ISSN 0911-5730
UVSOR-29
May 2002

UVSOR

ACTIVITY REPORT

2001

Ultraviolet Synchrotron Orbital Radiation Facility
Institute for Molecular Science

CONTENTS

2. Instrumental Developments

3. Gas Phase Spectroscopy

4. Solid State Spectroscopy 1 (IR, VUV, etc)

5. Solid State Spectroscopy 2 (XAFS, PES, etc)

6. Surface and Photochemistry

ULTRAVIOLET SYNCHROTRON ORBITAL RADIATION

UVSOR

UVSOR FACILITY

INSTITUTE FOR MOLECULAR SCIENCE

岡崎国立共同研究機構　分子科学研究所

極端紫外光実験施設

Outline of the Ultraviolet Synchrotron Orbital Radiation Facility

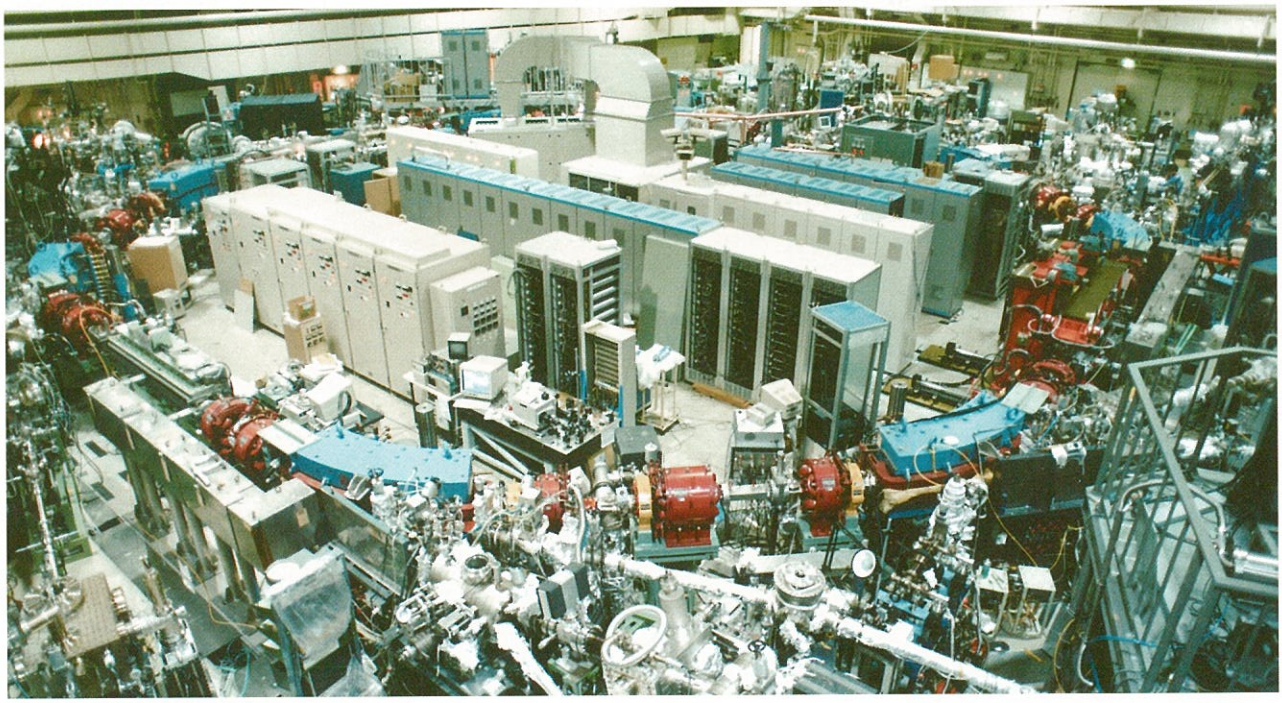

What is UVSOR?

The Institute for Molecular Science (IMS) is a national institute used by scientists who investigate new functional synthesis, reaction path ways, the utilization of photon energy and/or chemical energy etc., and basic researches on the structures and functions of molecules and molecular aggregates (clusters). The ultraviolet synchrotron orbital radiation facility (UVSOR) at the IMS is a synchrotron radiation light source research facility. Various investigations for molecular science are promoted at UVSOR with the use of synchrotron radiation.

What is synchrotron radiation?

It is well-known that an electron emits electromagnetic radiation when the electron is accelerated. The radiation is also emitted when the electron traverses a magnetic field. If the velocity of the electron is almost the speed of light, the radiation emission pattern is concentrated markedly onto the forward direction, being tangential to the orbit of the electron. This is called "synchrotron radiation". Synchrotron radiation has a continuous spectrum ranging from infrared/visible light to ultraviolet/X-ray wavelengths. And synchrotron radiation also has many excellent properties such as being tightly collimated, highly polarized, sharply pulsed, and partly coherent. Various spectra of the radiation from the sources available at UVSOR are shown in the right figure.

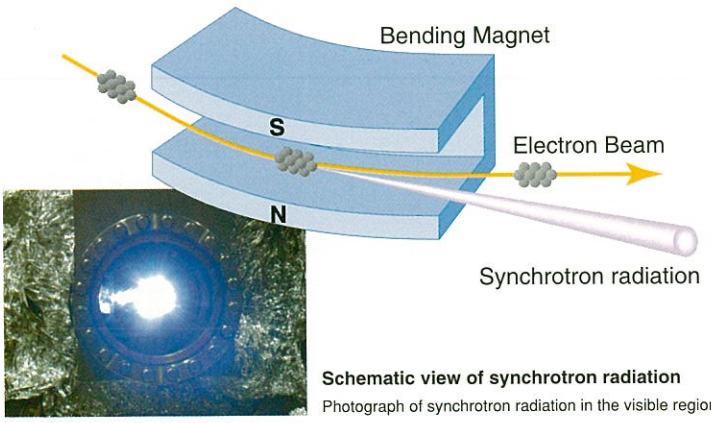

Schematic view of synchrotron radiation

Photograph of synchrotron radiation in the visible region

The Synchrotron Radiation Spectrum of UVSOR

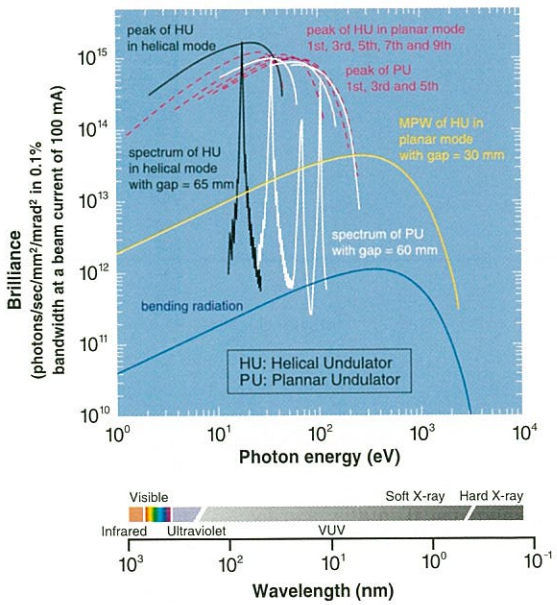

750 MeV Storage Ring

The UVSOR facility is composed of three accelerators, that is, a 15 MeV linear accelerator for electron injection, a booster electron synchrotron (about 8.5 m diameter) for accelerating the electron beam up to 600 MeV, and a 750 MeV storage ring for producing synchrotron radiation.

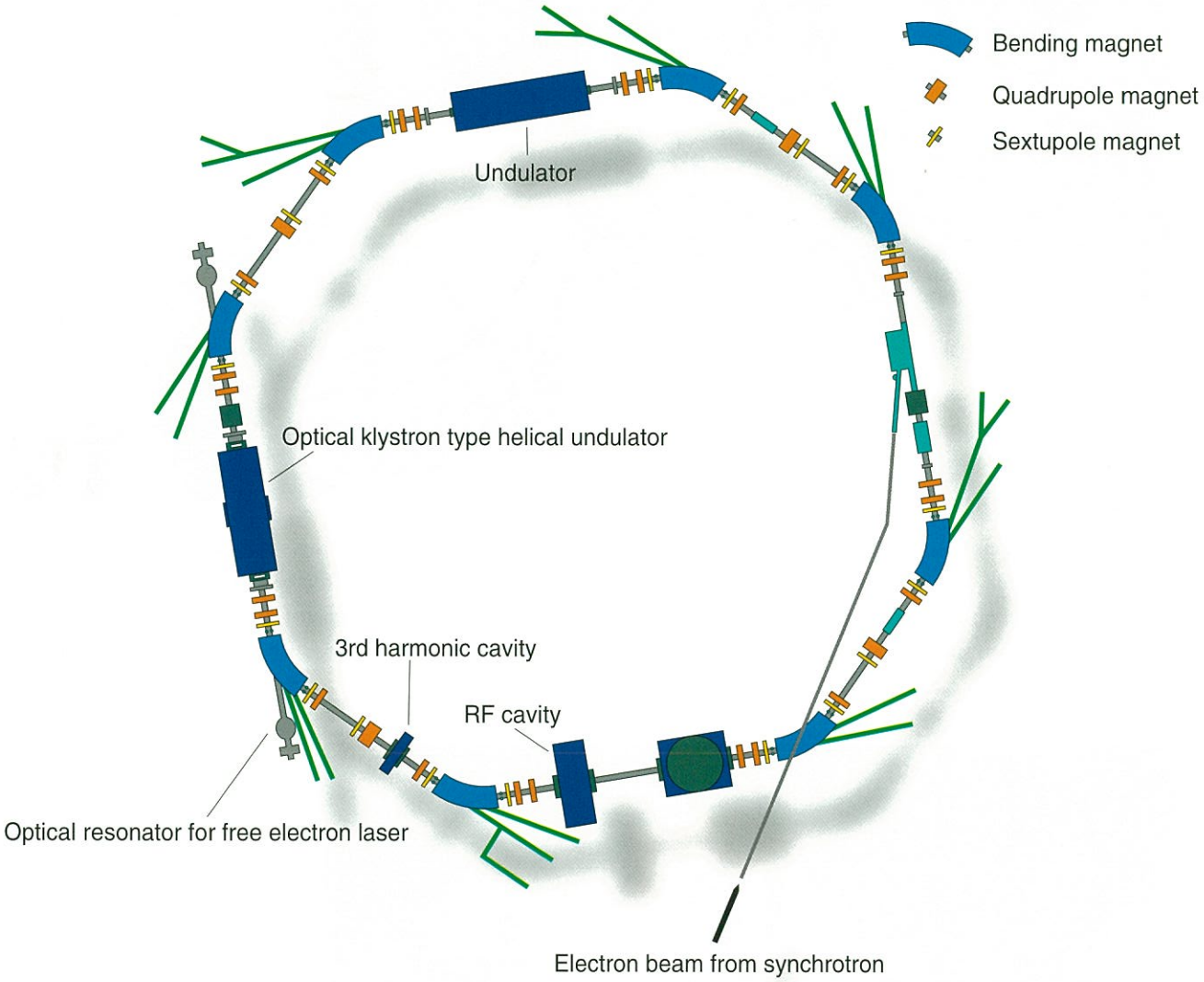

UVSOR Storage Ring

The storage ring has a quasi-octagonal shape with the combination of 8 bending magnets and 8 straight sections. In straight sections, undulators which are used for producing higher brightness synchrotron radiation and a RF cavity which is used for compensating energy loss through emitting synchrotron radiation are installed. There are 2 branch beamlines at each bending magnet section at UVSOR.

General parameters of the storage ring

Circumference	53.2 m
Energy	750 MeV (600 MeV at injection)
Number of bunches	Multi-bunch mode: 16
	Single bunch mode: 1
Initial stored current	Multi-bunch mode: 200 mA (max. 500 mA)
	Single bunch mode: 60~70 mA
Beam lifetime	Multi-bunch mode: 8 h (at 200 mA)
	Single bunch mode: 1 h (at 50 mA)
Beam sizes	0.39 mm (horizontal)/0.27 mm (vertical)
Pulsed light period	Multi-bunch mode: 11 ns
	Single bunch mode: 176 ns
Pulsed light width	~1ns with a harmonic cavity system (min. 20 ps)
Vacuum pressure	~1×10^{-10} Torr

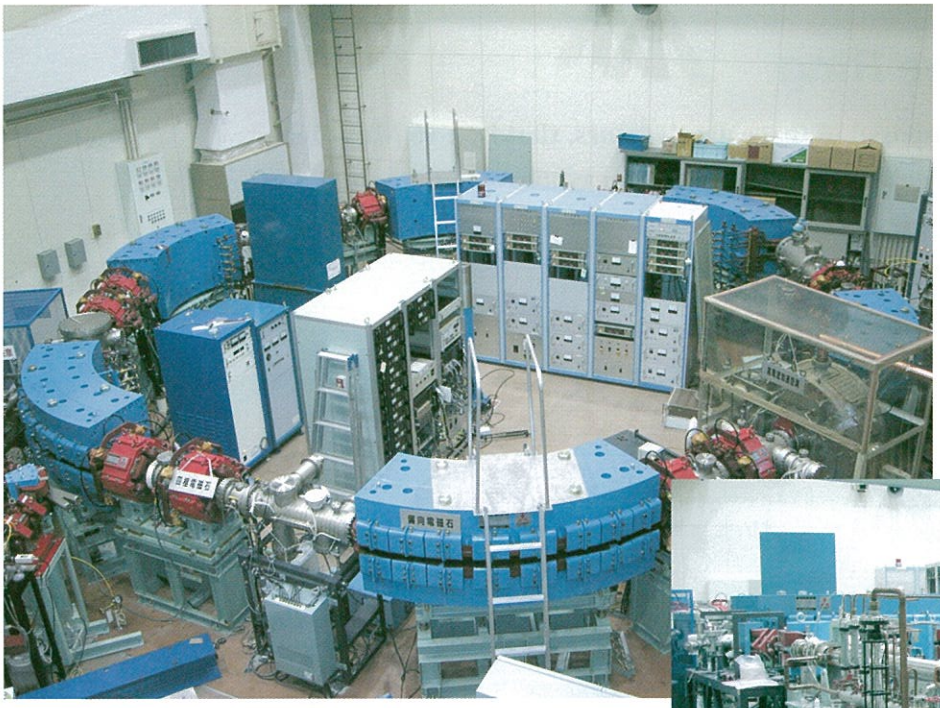

600MeV Electron Synchrotron

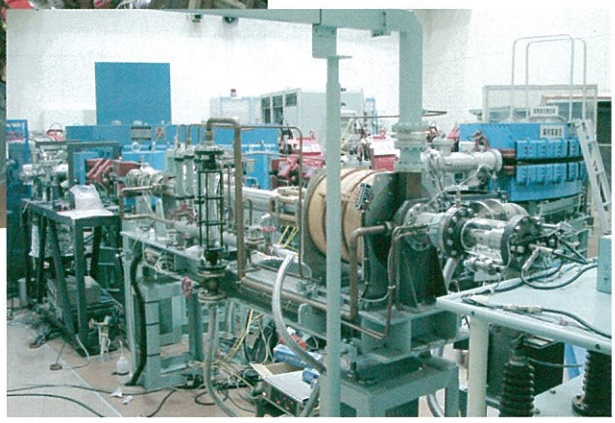

Electron Gun & Linac

Injectors

The injection system for the UVSOR storage ring comprises a linac and a booster synchrotron. The linac generates electrons with an electron gun and accelerates them to an energy of 15 MeV. The accelerated electron beam is injected to the booster synchrotron which raises the energy to 600 MeV. At this energy the electron beam is extracted from the booster synchrotron and transferred to the storage ring. The energy of stored electron beam in the storage ring is then raised to an operation energy of 750 MeV.

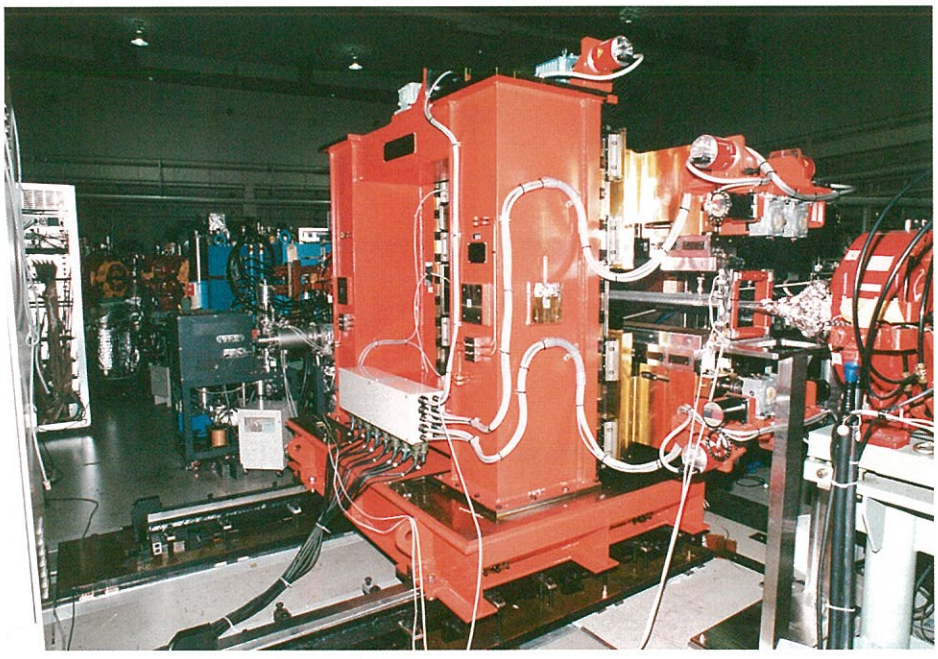

Helical Undulator

Undulator

An undulator is a device having periodic magnetic structures, which generate beams of radiation with higher brightness than the bending magnets. One of the two undulators installed in the storage ring of UVSOR has helical fields which produce circularly polarized radiation. This device is called "helical undulator" due to the movement of electrons within. It generates completely circularly polarized radiation ranging from 5 to 43 eV.

Free Electron Laser

The free electron laser (FEL) system is composed of an undulator and an optical resonator which consists of two mirrors facing each other at both ends of the undulator. Owing to the interaction of the high energy electron beam in the undulator field and the radiation in the optical resonator, laser action with positive gain takes place. At UVSOR, the shortest wavelength of FELs all over the world was successfully achieved by utilizing a helical optical klystron in 1997. Since 2000 the FEL has been used for users' researches.

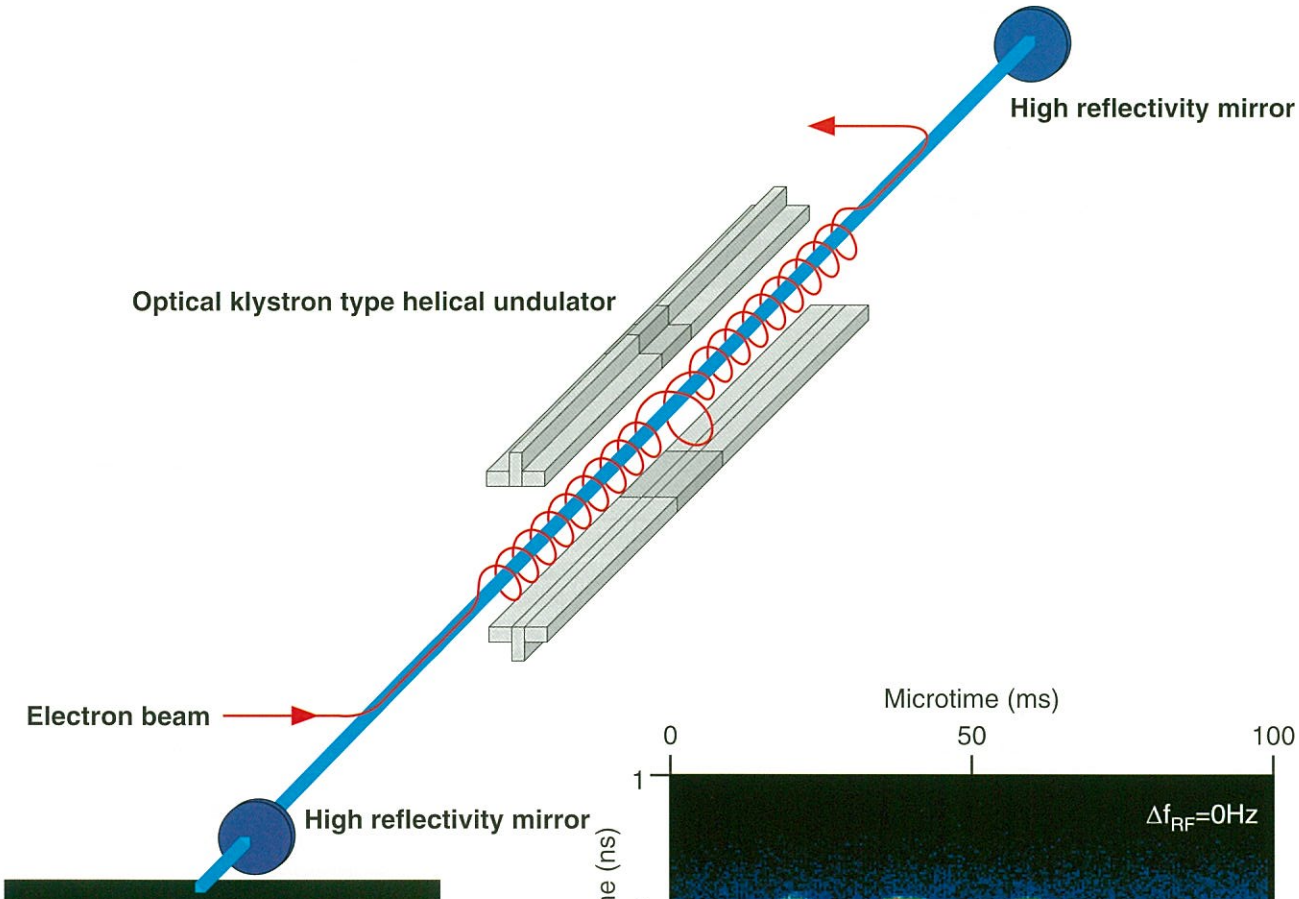

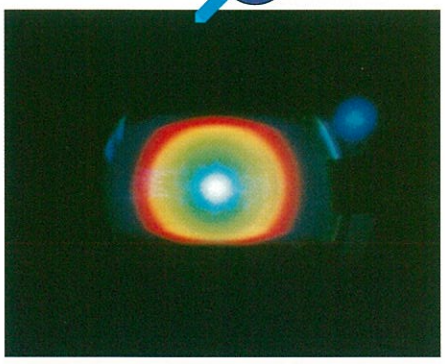

FEL lasing in the visible region

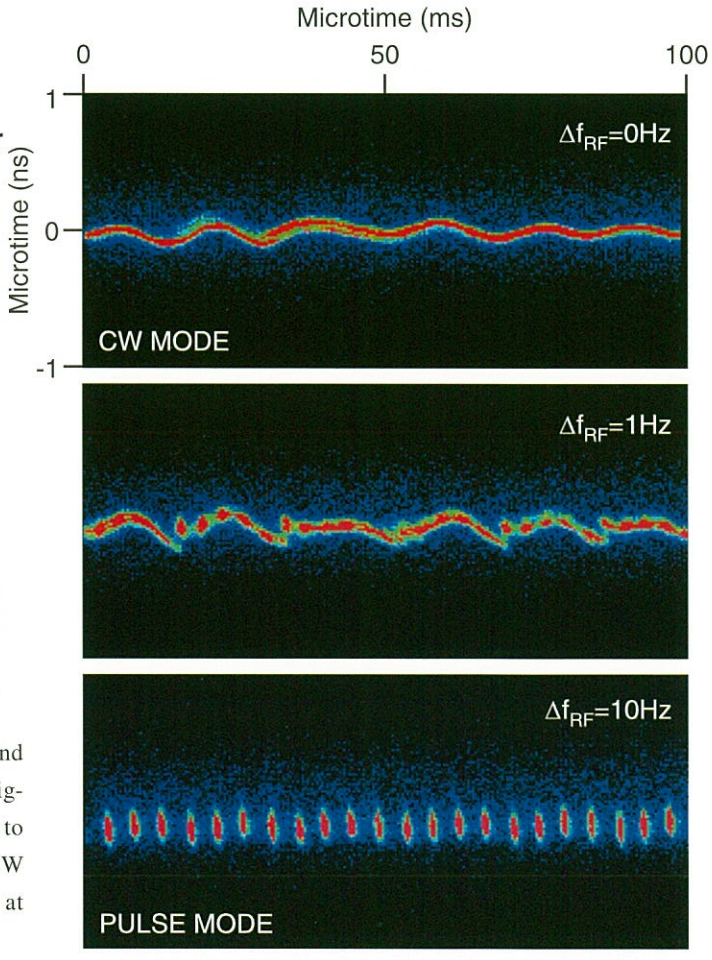

An accurate synchronization between an optical pulse and an electron beam is required for the stable FEL lasing. Figures show variation of temporal structure of FEL owing to only a small detuning. In users' experiments, the stable CW mode is kept using a feedback system developed at UVSOR.

Experiments using Synchrotron Radiation at UVSOR

In order to perform experiments using synchrotron radiation, a pre-focusing mirror system for introducing the radiation to an experimental setup, a monochromator for selecting a certain photon energy, and an instrument for data taking are required. A total combination of these elements is called "beamline" and every beamline is numbered. At UVSOR, priority has been given to the research fields related to the following subjects; 1) spectroscopic investigations (absorption, reflectivity and luminescence), 2) photoelectron spectroscopy, 3) photochemistry, 4) basic processes of chemical reaction, 5) photochemistry of solid state and surfaces, and 6) syntheses of new materials by photoexcitation. The preparation of beamline systems for such research fields results in growing scientific activities at UVSOR. The list of all available beamlines at UVSOR and their related experimental apparatuses are summarized below.

Beamlines of UVSOR

Beamline	Monochromator	Wavelength Region	Experiment
BL1A	Double Crystal	2.1 - 0.3 nm	Solid state (photoemission)
BL1B	1m Seya-Namioka	650 - 30 nm	Solid state (absorption)
BL2A	1m Seya-Namioka	400 - 30 nm	Bioscience (irradiation)
BL2B1	2m Grasshopper	60 -1.5 nm	Solid & Surface (photoemission, absorption)
BL2B2	18m Spherical Grating	60 - 6 nm	Gas(photoemission, photodissociation)
BL3A1	None (Filter, Mirror)	50 -15 nm	Solid & Irradiation (photodissociation)
BL3A2	2.2 m Constant Deviation Grazing Incidence	100- 10 nm	Gas & Solid (photoionization & photodissociation)
BL3B	3m Normal Incidence	400- 30 nm	Gas (photoemission)
BL4A1	Multi-Layered-Mirror Monochromator	23- 13 nm Mo/Si MLMs	Irradiation
BL4A2	——		Lithography
BL4B	Varied-line Spacing Plane GratingMonochromator	1.5- 14 nm	Gas(photoemission,photodissociation)& Solid (photoemission)
BL5A	SGM-TRAIN	250 - 5 nm	Solid (absorption) Free Electron Laser
BL5B	Plane Grating	200 - 2 nm	Calibration, Gas & Solid (photodissociation & absorption)
BL6A1	Martin-Puplett FT-IR Michelson FT-IR	3000 - 30 mm	Solid (absorption)
BL6A2	Plane Grating	650 - 8 nm	Solid (photoemission)
BL6B	None		Irradiation
BL7A	Double-crystal	1.5 - 0.8 nm	Solid (absorption)
BL7B	3m Normal Incidence	1000 - 50 nm	Solid (absorption)
BL8A	None (Filter)		Irradiation & Users' Instruments
BL8B1	15 m Constant Deviation Grazing Incidence	40 - 2 nm	Gas & Solid (absorption)
BL8B2	Plane Grating	650 - 8 nm	Solid (photoemission)

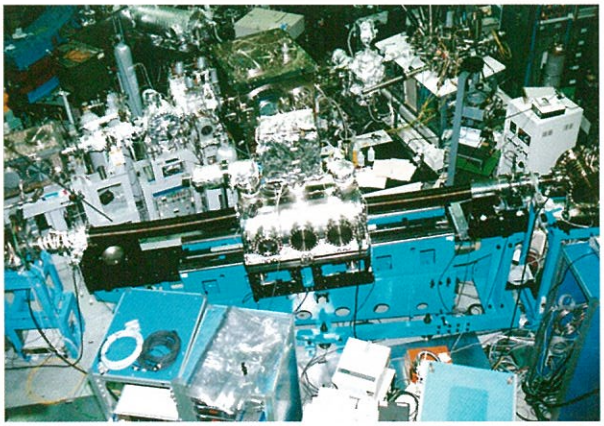

Spectrometer "SGM-TRAIN"

1 Absorption spectroscopy

Observation of absorption spectra of photons on materials (molecules).

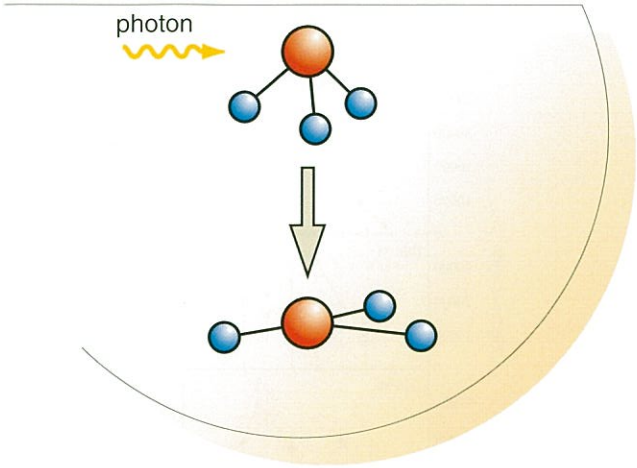

2 Photoelectron spectroscopy

Observation of electrons' emission from materials (molecules) irradiated with synchrotron radiation photons.

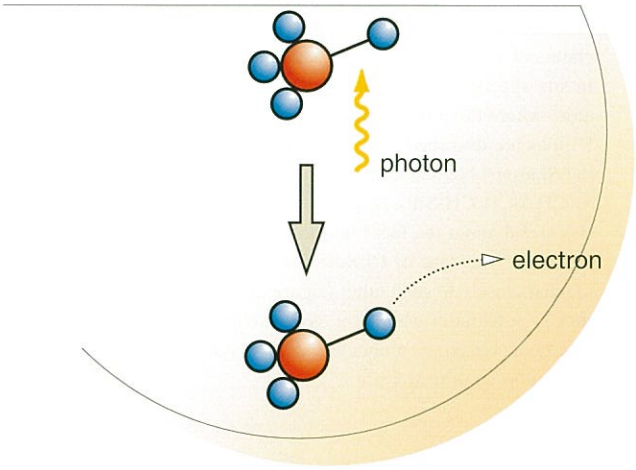

3 Photochemistry

Studies of chemical reactions using synchrotron radiation photons.

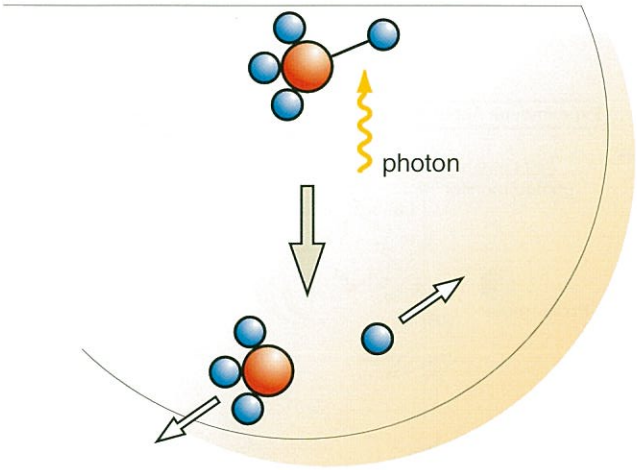

4 Basic processes of chemical reaction

Studies on behavior of ions and radicals using synchrotron radiation photons.

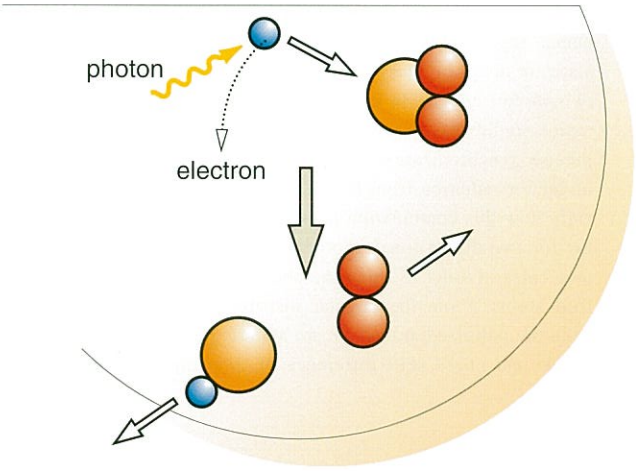

5 Photochemistry of solidstate (surface)

Studies of the dynamical behavior of solidstate(surfaces) irradiated with synchrotron radiation photons.

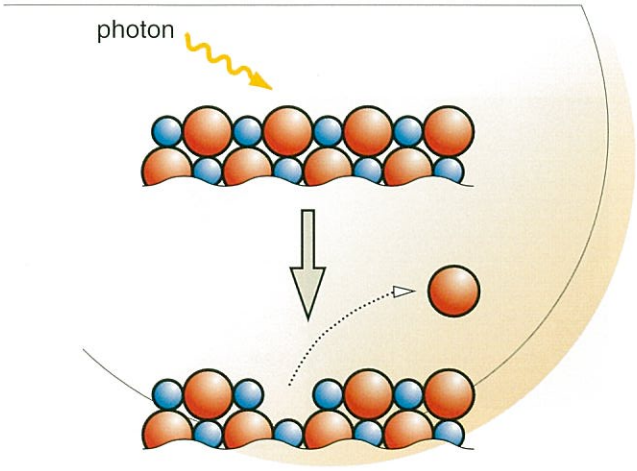

6 New functional synthesis by photoexcitation

Synthesis of a new molecule using synchrotron radiation photons.

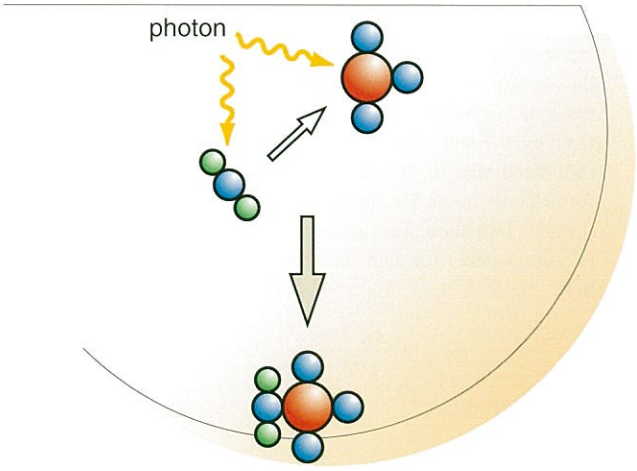

Recent Research Activities at UVSOR

Examples of recent research activites are presented here.

Investigation of Ion Desorption Caused by Core-Level Excitation – Application to Optical Knife –

Monochromatized synchrotron radiation can excite the core electrons of an atom in a specific chemical environment selectively, discriminating the core electrons from those of atoms in different chemical environments. This site-specific excitation often results in site-specific fragmentation, which occurs selectively around the atom where the photoexcitation has taken place. In fact, the H^+ and F^+ ions are desorbed by the photoionizations of the 2p electrons of the Si atoms bonded to the methyl groups and the fluorine atoms in $Si(CH_3)_3CH_2CH_2SiF_3$, respectively (figure c). However, one should be careful about the fact that the site-specific fragmentation is negligible for the case of $Cl_3SiSi(CH_3)_3$ in which the two Si sites are located closely to each other (figure a). The site-specific fragmentation is potentially useful for synthesizing materials through selective bond breaking: monochromatized synchrotron radiation could be used as an optical knife.

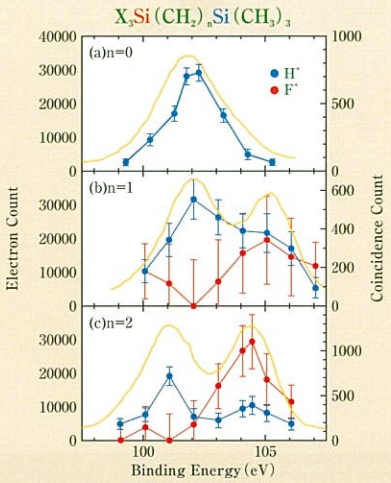

Experiments combining laser with synchrotron radiation

Combining laser with synchrotron radiation has attracted widespread attention of molecular scientists, in connection with possibilities for conducting various types of pump-probe or double resonance experiments on spectroscopy and dynamics of rovibronic states in detail by making the most use of different features of the two photon sources. In UVSOR, laser-synchrotron radiation combination studies have been realized for many molecular systems by a precise synchronization of a mode-locked Ti:sapphire laser with undulator radiation from BL3A2. The illustration shows schematically how this combination technique is combined with an apparatus for two-dimensional photoelectron spectroscopy of atoms and molecules in order to study the photoionization dynamics of polarized atoms. From the angular distribution of the photoelectrons from the polarized atoms, we are able to gain insight into the magnitude and phase shift difference of transition dipole matrix elements.

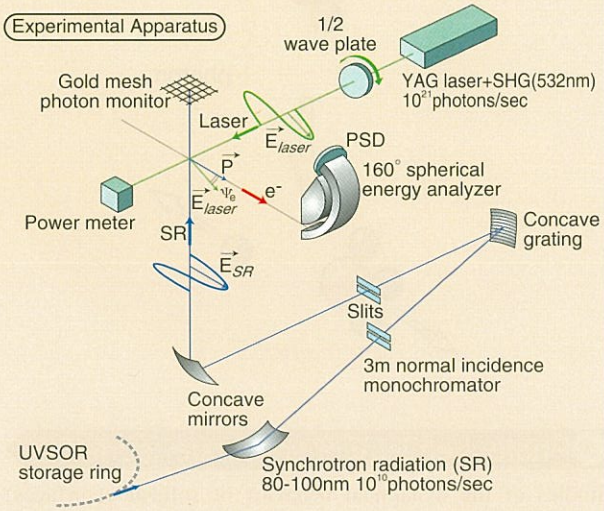

Silicon Nanostructure Self-Formation by illumination of Synchrotron Radiation

Si wafers covered with oxide were irradiated by Synchrotron Radiation (SR) at ~700 ℃. The surface was observed by scanning tunneling microscope (STM) after several hours illumination of SR. On the surface, we found unique self-formed Si nanostructures, for example, a single monolayer thick stripe of which width was quantized by 7x7 unit cells of surface reconstruction, as shown in upper right-hand side in the figure. Because these nanostructures were formed only in the SR illuminated area, any position can be chosen for their formation. This area selective formation of nanostructures may be suitable for application of biochip and biosensor fabrication.

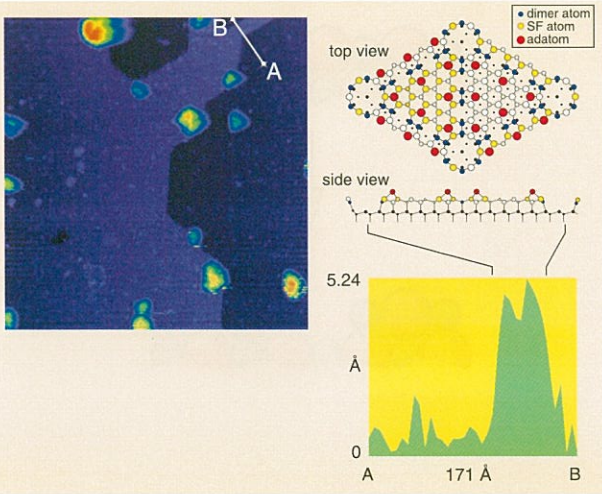

Reflection spectra of nitride ternary alloys

The blue LED has become a popular LED today, along with the red, yellow and green ones. This is due to the drastic development of the III-V nitrides thin films growth technique, because the III-V nitrides (mainly GaN) are the key material of blue LED. Furthermore, III-V nitride ternary (or more) alloys are the probables of the violet and ultraviolet LEDs. Since the UVSOR is a wide wavelength range lightsource, we can investigate the basic optical properties of these III-V nitride alloys using reflectance (see figure), emission and excitiation spectra at visible (red to violet), ultraviolet and vacuum ultraviolet regions.

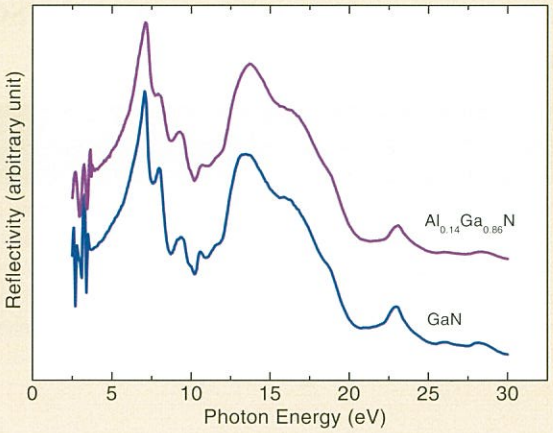

Resonant Photoelectron spectra of Nickel Complexes

When materials absorb a soft x-ray photon, electrons are emitted with various kinetic energies.Emitted electron with kinetic energy linearly increased to the incident x-ray is called photoelectron. Electron, which has the constant kinetic energy regardless of the x-ray energy is known as Auger electron. We have discovered a new kind of emitted electrons in nickel complex with cyano ligands (dotted line in the figure); they slow down as x-ray energy increases. Detail behavior of these electrons, as well as photoelectrons and Auger electrons, shed light onto the bonding and electronic structure of the nickel complexes.

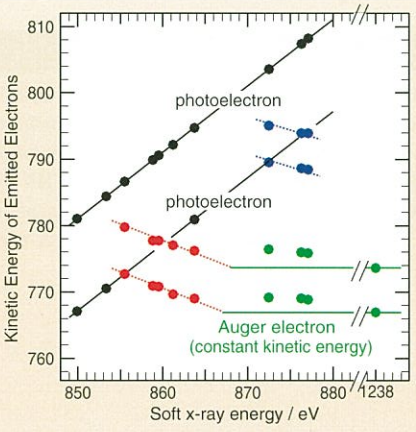

Study of electronic excited states of ozone

Ozone is one of the most important molecules in chemistry since ozone in the stratosphere absorbs UV light emitted from the sun and protects humanity from the exposure by the UV light. In view of this ozone effect, many experimental and theoretical exertions have been devoted to the spectroscopic studies of ozone. In order to explore the electronic states of ozone, we have constructed an ozone supply apparatus on the beamline BL8B1 at UVSOR facility. The photoabsorption spectra (left figure) and time-of-flight spectra of ion photofragments (right figure) have been successfully measured for the first time in the soft X-ray region 520-555 eV. These data are particularly useful for the determination of electronic states of ozone.

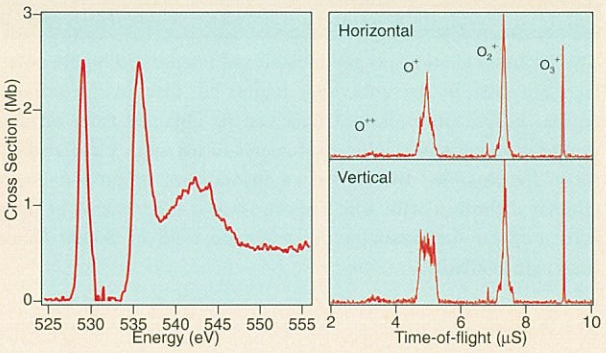

Absorption spectra of amino acids

Due to the fact that oxygen did not exist in the atmosphere of the earth before the onset of photosynthesis, vacuum ultraviolet radiation may have been a driving energy source of the molecular evolution prior to the orgin of life.

Vacuum ultraviolet absorption spectra of amino acids are being measured at UVSOR in an attempt to study the molecular evolution driven by the vacuum ultraviolet radiation.

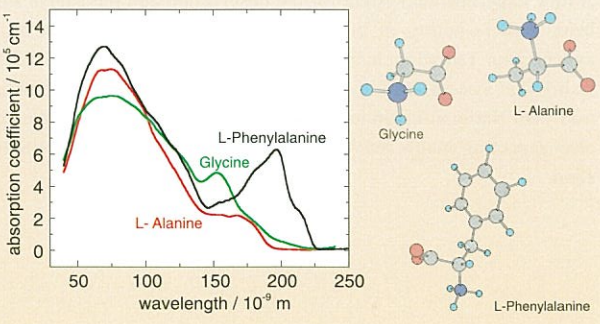

Equipments at UVSOR

There are a lot of unique equipments at UVSOR.
Some are shown in the following:

Photoelectron spectro-microscope with the combination of SR and Laser

A newly developed photoelectron spectro-microscope that can measure the specific small area of the sample has been installed at BL6A2. The femto-second laser system was also installed to conduct the combination experiment with SR and laser. Using this system, photoelectron micro-spectroscopic studies of various photo-induced phenomena can be conducted.

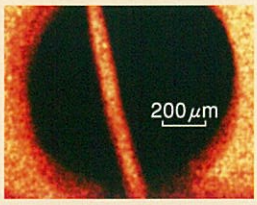

Calibration apparatus of optical elements

Synchrotron radiation contains soft X-ray which is absorbed by the air and is accessible in wide energy range. Thus synchrotron radiation can be used as "standard light" for the calibration of optical elements. Beamline BL5B has a purposed-build UHV calibration apparatus for optical elements. Calibration experiments of various soft X-ray optical elements, such as mirrors of soft X-ray telescope for satellites, are performed.

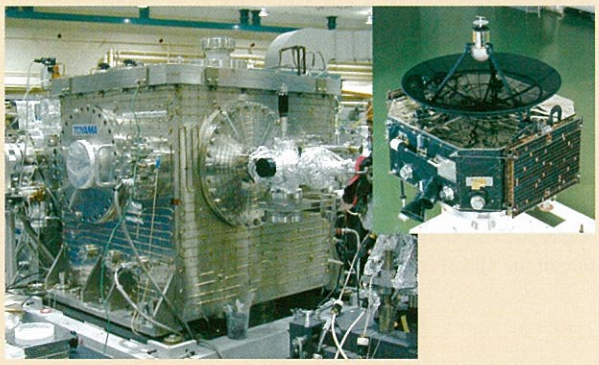

Infrared magnetic circular dichroism measurement apparatus

Synchrotron radiation has good features of intense and highly polarized not only in the ultraviolet region but also in the infrared region. Elliptically polarized light can be obtained from off-axis synchrotron radiation and measurements of magnetic circular dichroism are possible. BL6A1 has an apparatus of infrared magnetic circular dichroism with which spectroscopic experiments of magnetic circular dichroism in the magnetic field of 80000 Gauss (max) are available.

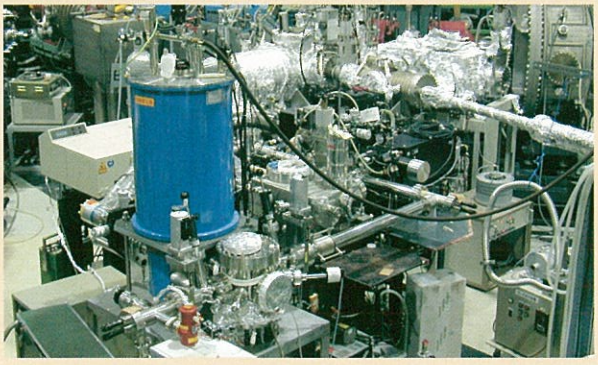

Irradiation Apparatus for Biology

A new experimental system for the observation and the analysis of behavioral responses of micro-organisms to ultraviolet light from synchrotron radiation has been constructed at beamline BL2A. Using this system, biology experiments have started in collaboration with National Institute for Basic Biology and the IMS. We are also expecting many active bioscientists to come to use UVSOR soon.

Collaborations

The synchrotron radiation of UVSOR is available for researchers within the Institute for Molecular Science (IMS) and from other universities and institutes. Various investigations related to molecular science are performed using UVSOR by IMS researchers mainly belonging to the Department of Vacuum UV Photoscience. Biology experiments using synchrotron radiation of UVSOR are performed in the collaboration between National Institute for Basic Biology and IMS.

Many researchers outside IMS visit UVSOR to use synchrotron radiation. The number of visiting researchers is about 800 from 60 institutes per year. International collaboration is also active and the number of visiting foreign researchers is over 80 from 10 countries.

UVSOR calls for proposals twice a year and also accepts proposals from industries (charged).
All the work using UVSOR are reported in the UVSOR ACTIVITY REPORT and the number of refereed publication is more than 60 since 1996.

Number of accepted proposals

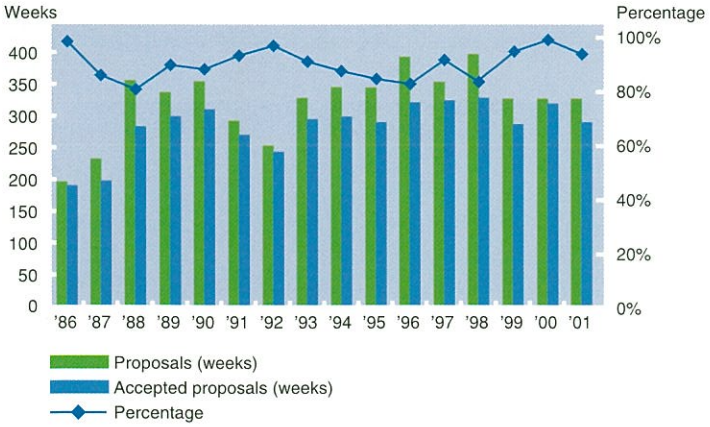

Number of published papers

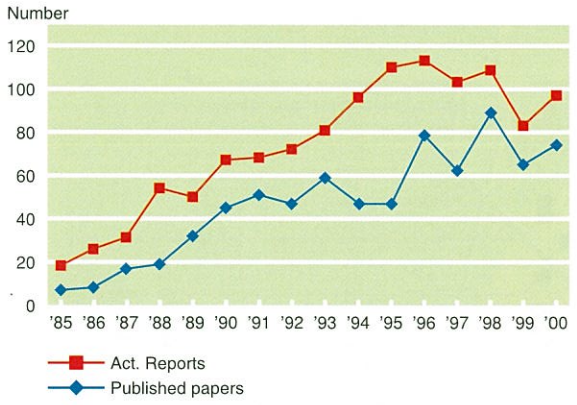

UVSOR joint studies

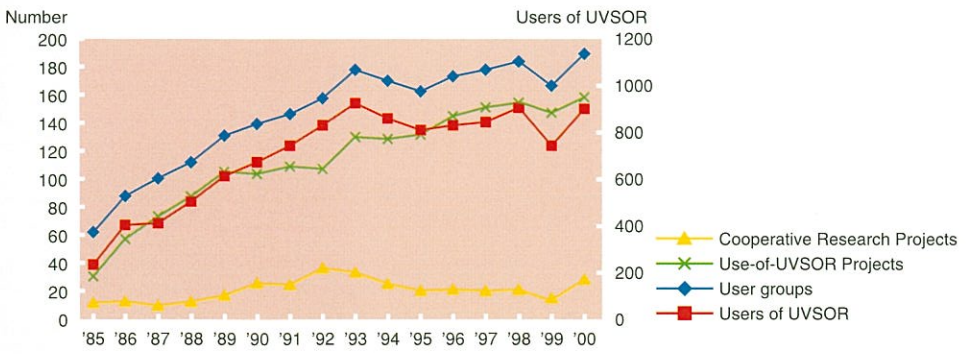

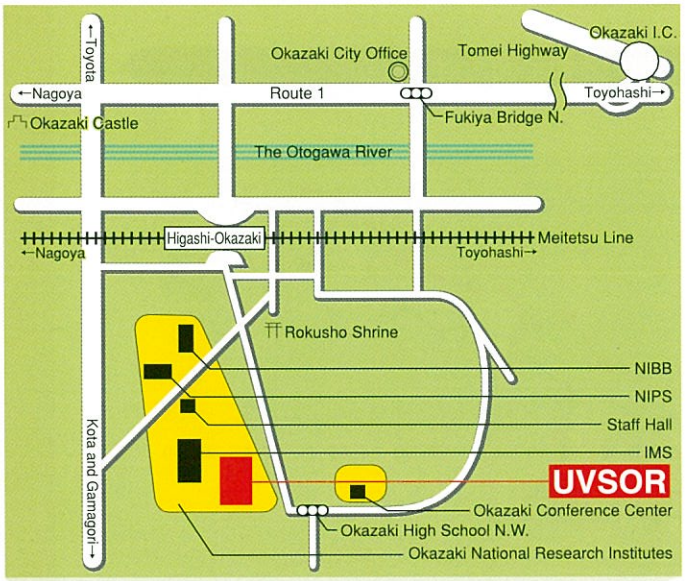

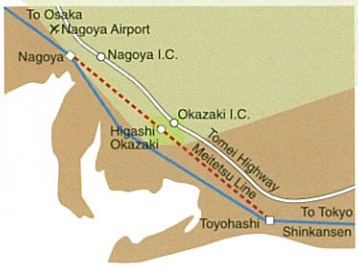

UVSOR

Ultraviolet Synchrotron Orbital Radiation Facility

Institute for Molecular Science,Okazaki National Research Institutes

Myodaiji, Okazaki 444-8585, Japan
TEL: 81-564-55-7402 FAX:81-564-54-7079 http://www.uvsor.ims.ac.jp

INSTITUTE FOR MOLECULAR SCIENCE, OKAZAKI NATIONAL RESEARCH INSTITUTES

UVSOR
ACTIVITY REPORT
2001

edited by
H. Hagiwara, M. Hosaka, E. Shigemasa, K. Takahashi

PREFACE

This Activity Report covers the research activities done at the UVSOR facility in the Institute for Molecular Science (IMS) in FY2001. This is the eighth volume in the red-covered activity report series for the second 10 years in UVSOR. For these years the total beamtime, beamlines, and users are in a steady state; that is, ~40 weeks/year (~2,500 hours/year), ~20 beamlines, and ~800 users/year (with ~180 projects/year). However, some of the equipment is gradually being behind the times in comparison with undulator-based highly brilliant synchrotron facilities in the world. In recent three years, we discussed with our Ministry (MEXT) an additional budget for the upgrade of the light source of UVSOR to enhance our activities even for the third 10 years. Finally we have succeeded in getting it for FY2002. We hope that the UVSOR will begin supplying low-emittance ~27 nmrad photons and 2 or 3 additional undulator beamlines from the autumn in 2003.

In FY2001 one associate professor of three, one research associate of four and one technical associate of six left the UVSOR facility. Dr. Masao Kamada and Dr. Shigeru Kouda moved to the Synchrotron Light Application Center, Saga University, as professor and research associate, respectively, in October and July in 2001. Mr. Toshio Kinoshita retires upon completion of 19 years of service and support this March. These changes are our great loss, but fortunately we succeeded in having two new members. In August 2001 Dr. Akira Mochihashi came as a new research associate from the Photon Factory, the Institute of Material Structures Science. He belongs to the light source division. In April 2002, Dr. Shin-ichi Kimura comes back as associate professor from Kobe University. He will reinforce infrared spectroscopy and high-resolution photoemission of correlated materials in UVSOR.

I attach herewith a report by Dr. A. M. Bradshaw. He is one of the two distinguished foreign councilors of the IMS during FY2001-02. We are very grateful to him for a valuable report to evaluate the present status and future of the UVSOR facility. After receiving his report, we received great news about the approval of the upgrade plan from MEXT. We will further elaborate our future programs by taking into account his comments.

March, 2002

Nobuhiro Kosugi
Director of UVSOR

THE UVSOR FACILITY: A SHORT APPRAISAL

INTRODUCTORY REMARKS

UVSOR is known mainly in the international community for its fine work in molecular photoionisation, photochemistry and macromolecular physics. The author of this brief survey, a former scientific director of BESSY with research interests in molecular photoionisation and surface science, has been familiar with the research carried out at UVSOR for many years, but visited the facility itself for the first time during his stay at IMS from 21st – 24th October 2001.

STATUS OF THE BEAM LINES

The machine has four straight sections two of which are used for insertion devices - a linear undulator (BL3A) and an undulator for circularly polarised light (BL5A), which is also used as an optical klystron for a free electron laser experiment. BL3A is equipped with an irradiation facility as well as with a constant deviation SGM used for the study of dissociative multiple photoionisation, unique among synchrotron radiation facilities. On BL5A there is a highly flexible SGM with an energy range of 5 - 250 eV which is used for high resolution spin- and angle-resolved photoemission studies of solids and surfaces. More insertion device beam lines are planned following an upgrade of the machine which is discussed below. There is also an impressive mono-chromator park on the bending magnet beam lines, including a further eight grazing-incidence monochromators and two crystal monochromators. A variable line spacing PGM has just finished trials on a bending magnet beamline (BL4B). Altogether there is a total of twenty measuring stations, including normal-incidence monochromators and beam lines for white light and IR. Eleven of these stations are used by outside users, i.e. by scientists from institutions other than IMS.

A BRIEF OVERVIEW OF THE RESEARCH PROGRAMME

It is not possible in such a brief account to do justice to the extensive research programme. The examples of world-class research work chosen by the author in the following are necessarily subjective and certainly influenced by his own research interests, as well as by some of the very fine talks he heard at a symposium held during his visit.

Both fluorescent decay and laser-induced fluorescence have been used to study the photofragmentation of molecules such as H_2O, OCS and CH_3CN following excitation with UV synchrotron radiation as well as to characterise the frag-ments. Similarly, the coincidence techniques PIPICO and AEPIPICO have been employed to study fragmentation in core-ionised CF_4, CD_3OH and CH_3CO, CD_3CN, respectively. The latter study was particularly interesting in that two-body dissociation with rearrangement was found to accompany N 1s resonant Auger decay to give CD_2^+ and DCN^+ alongside the "normal" products ($C_2D_3^+$ and N^+) and (CD_3^++ and CN^+). Similarly exciting is the increased level of understanding of core level photoabsorption of diatomic molecules achieved by both new experiments and theory. In particular, a very simple experiment has recently been conceived for the new variable line-spacing PGM in which two identical detectors register the photoion current at 0° and 90° to the **E** vector of the incident synchrotron radiation. Since the absorption cross section will be largest when the transition dipole is aligned parallel to the **E** vector the aniso-tropy in the ion distribution will reflect the symmetry of the excited states. Thus for a linear molecule it is possible to distinguish between final states of π and σ symmetry. In the case of core level excitation of N_2 a previously unidentified state of π symmetry was found at 419 eV in the region of the σ shape resonance. Recent calculations by the same group show that this could be a bound state involving a triple excitation. Combined synchrotron radiation and laser experiments are likely to play a more important role at UVSOR in the future: The technique has already been used to study the time dependence of photo-induced phase transitions in inorganic systems as well as of the surface photovoltage (SPV) effect in semi-conductors. It was found, for example, that both for the GaAs(100) surface and for a GaAs-GaAsP superlattice that the laser-induced photoelectron core level shift is due to the SPV and that its decay can be observed on a microsecond timescale. Beamline BL6A2 has been upgraded for experiments of this kind and combined with a facility for photoemission investigations on surfaces with a spatial resolution in the micron range. A deeper understanding of the preparation and properties of Si surfaces has also been obtained, in particular of the hydrogen adlayers resulting from etching techniques. Infrared reflection-absorption spectroscopy played an important role in these measurements. Single crystal surface science studies at UVSOR have also shed new light on the chemisorption of simple molecules on metal surfaces. For example, it was shown that N_2O adopts a lying-down geometry on the Pd(110) surface and already dissociates at about 120 K, giving rise to several N_2 desorption states and leaving oxygen on the surface. Studies of the electronic structure and molecular orientation of polymer films continue at UVSOR, if not with the same intensity as in the past. Recently, angle-resolved photoemission and NEXAFS have been used to show that the heterocyclic pendant group in poly(9-vinylcarbazole) exhibits a larger average tilt angle at the surface than that expected on the basis of random orientation.

PLANNED UPGRADE AND FUTURE EMPHASIS

As is now widely known, an undulator is a periodic magnetic structure, or insertion device, which is inserted into the straight section of a storage ring, causing the electron (or positron) beam to oscillate transversally about its prescribed orbit. The intense beam of radiation produced in the forward direction is strongly peaked at one wavelength on account of the quasi-coherent addition of the radiation emitted from the points of maximum excursion. UVSOR is a so-called second-generation synchrotron radiation source which was planned and constructed at a time when the principle of the undulator was already known, but essentially untested. Third generation sources built in the last ten years are those which contain a large number of straight sections for undulators and wigglers. These, rather than the bending magnets, then provide the most important sources of synchrotron radiation on the storage ring. (The periodic excursions from the orbit are larger in the wiggler due to a stronger magnetic field and there is no quasi-coherent addition of the emitted radiation.) UVSOR has currently two undulators and a short wiggler with superconducting magnets which is intended as a "wavelength shifter".

A modification to the lattice of the storage ring ("upgrade") is currently in the planning stage. This will create – without changing the circumference – four new short straight sections which can also be used for insertion devices. The new lattice can be created by replacing all the separate quadrupole and sextupole magnets of the old lattice with "combined function" magnets which have both quadrupole and sextupole fields. The bending magnets would remain un-changed. A further attractive feature of the upgrade would be the lower emittance (27 nm-rad as opposed to 165 nm-rad) which is an important factor in obtaining high spectral resolution and high photon flux on the various mono-chromators installed on the beam lines. The use of specially constructed *in vacuo* undulators with gaps as narrow as 10 mm will give access to the photon energy range up to 500 eV with the first and third harmonics. The short length available (1.5 m) for the undulators in the new straight sections means that the flux and pseudo-monochromaticity will be somewhat lower at these photon energies than on storage rings with electron energies in the 1–2 GeV range. However, UVSOR will still become competitive in this important soft x-ray region where very exciting work is currently being performed at facilities such as MAX II (Lund), ALS (Berkeley), ELETTRA (Trieste) and BESSY II (Berlin).

At the same time, the author of this report is of the opinion that it is very important to maintain, and to expand, the undulator capacity for photon energies from 10 to 100 eV. Storage rings with electron energies of the order of 750 MeV optimally provide first-harmonic

undulator radiation in this photon energy range. The last few years has seen a reduction in the number of such facilities available worldwide. BESSY I has been closed; Super-ACO in Orsay will suffer the same fate when the construction of SOLEIL begins; MAX I is used as part of the injection system for MAX II; the ISSP ring in Tokyo has been dismantled; further, it is not clear how long the UV ring in Brookhaven will remain in operation. UVSOR has the unique opportunity – particularly with the upgrade – of becoming the prime facility world-wide offering undulator radiation of very high spectral brilliance in the far UV up to 100 eV primarily for experiments in surface and solid state physics, for fundamental photoionisation studies (e.g. in the inner valence region) and for photochemistry.

The scientific programme already has many highlights, a few of which have been described briefly above. In line with the mission of IMS the main thrust of these activities lies in photochemistry (including surface photochemistry), molecular photoionisation and polymer science. However, there are several areas, particularly in surface and solid state physics, which are not as strongly represented as they could be, even though UVSOR has a very good monochromator park. (After the upgrade it will no doubt improve further!) This imbalance is all the more surprising since the ISSP ring is no longer in operation and one might have expected that outside users particularly in the area of solid state physics would have shown greater interest in coming to Okazaki. It therefore seems necessary – parallel to the implementation of the upgrade – to recruit new users or to initiate new activities at IMS itself in areas such as high energy and high angular resolution photoemission, spin-polarised photoemission, high spatial resolution photoelectron microscopy and photoelectron diffraction. This would establish UVSOR as an important multi-disciplinary, and internationally unique, facility with its most important areas of research focussed on the far UV.

A. M. Bradshaw
Garching, November 2001

Current Status of Light Source and Beamlines

UVSOR Light Source in 2001

Masahiro KATOH

UVSOR Facility, Institute for Molecular Science,
Okazaki 444-8585 Japan

1. Machine Operation

In 2001, the UVSOR accelerator complex was operated for 40 weeks (including machine tunings) as scheduled. Monthly statistics of the operation time is shown in Figure 1. Three weeks in this year were assigned for single bunch users operation and other two weeks were dedicated for machine studies. We had four shut down period, around the new years day (two weeks), in spring (three weeks), in summer (three weeks) and in autumn (one week).

In autumn, there were a few troubles on the injector. One was the breakdown of the electron gun. Another was on the function generator of the magnet power supply of the synchrotron. Fortunately they were quickly recovered. The users time was canceled only on two days in total.

Typical operation pattern in a week is as follows. Monday and Saturday morning (from 9 to 13 o'clock), are assigned for machine tunings and machine studies. From Tuesday to Friday, the machine is operated for users. The beam is injected twice a day, at 9 and 13 o'clock. The beam is stopped at 18 o'clock. It can be extended until 21 o'clock as requested by users. On Thursday, the beam is injected additionally at 17 o'clock and is stopped at 21 o'clock. The filling beam current is 250 mA in multi-bunch mode and 70 mA in single bunch mode. Typical beam current histories in both modes are shown in Figure 2.

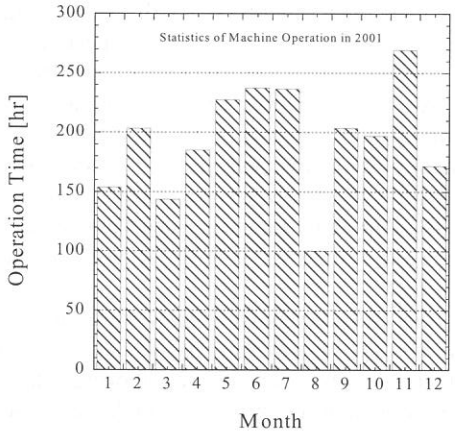

Fig. 1. Monthly statistics of the operation time in 2001.

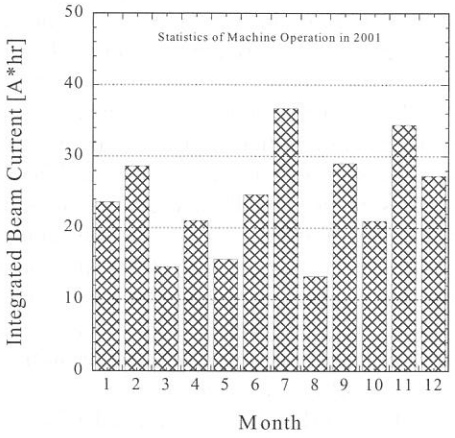

Fig. 2. Monthly statistics of the integrated beam current in 2001.

2. Improvements

2-1. Beam position monitor system

New beam position monitor (BPM) system (Figure 3) was successfully commissioned [1]. This system is capable of measuring the beam position at 16 BPM heads located around the ring, every second with resolution of a few microns.

This system has revealed orbit movements in various time scales. There can be seen slow drift of order of few hundreds of microns in horizontal and vertical can be seen in time scale of hours. There is an orbit movement correlating with the change of the cooling water temperature in a time scale of 10 minutes, which will be described in the following sub-section.

The origins and the mechanisms of these orbit movements are under investigation. We are going to construct an orbit stabilizing system based on this new BPM system.

2-2. Cooling water system

The new BPM system described in the preceding sub-section has revealed an orbit movement in a time scale of 10 minutes. Soon it is found to strongly correlate with the temperature of the cooling water, which is oscillating with amplitude of a few degrees. This large modulation was soon found to be due to a malfunction of the temperature stabilizing system. During the summer shutdown, we replaced the

temperature control unit. The temperature stability was greatly improved as well as the orbit stability.

2-3. High Coupling Operation

In the single bunch mode, the beam lifetime is strongly limited by Touschek effect. To improve the lifetime, we tried a high coupling operation, in which the skew quadrupole magnets were excited to increase the XY coupling. The larger emittance in vertical effectively suppressed the Touschek effect. We could improve the lifetime by a factor of 2. We have tested the high coupling mode during a single bunch users run. Longer lifetime resulted in larger integrated photon flux during a run for many users. However, some users claimed that the larger emittance resulted in lower photon flux in their experiment. We will choose high or low coupling modes depending on the users experiments.

2-4. Survey on the storage ring magnets

As a preparation for the upgrade project [2], we have surveyed the storage ring magnets. This is the first time to survey over the whole ring since its construction. Some modern devices, such as a laser tracker, were used instead of old equipments that were used during the construction. Same method will be used during the reconstruction in the upgrade project.

The results showed that there are global distortions in horizontal plane and in vertical direction. However, the deviations between the neighboring magnets are in the order of a few hundred microns, which was better than expected.

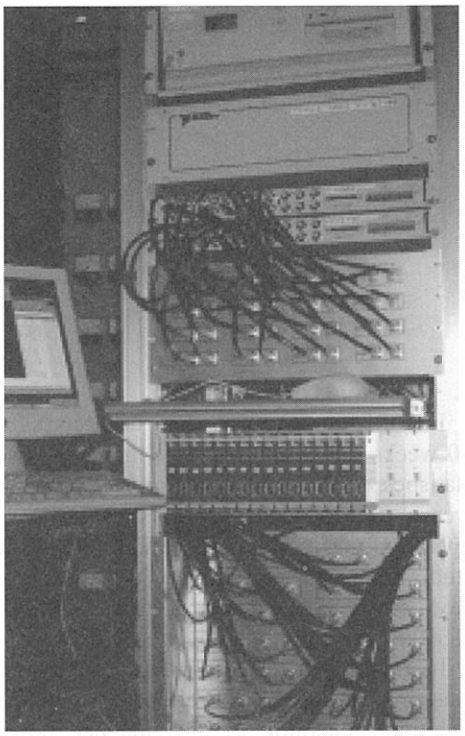

Fig. 3 New Beam Position Monitor System

3. Researches and Developments

3-1. Field measurement on the prototype of the multi-pole magnet for the upgrade project

In the new lattice for UVSOR storage ring [2], which has four new short straight sections and much smaller emittance (27nm-rad), all the quadrupoles and sextupoles will be replaced with combined function magnets, which have capabilities of producing both quadrupole and sextupole fields by utilizing auxiliary windings. A prototype was constructed and the field measurement was done. It was confirmed that the magnet can produce the required field strengths [3].

3-2. Development of In-vacuum undulator

In the new lattice described in the previous section, each straight section has small vertical betatron function, which enables us to install in-vacuum and small gap devices. A prototype of such a device is now under construction. This undulator will be installed at the straight section between B06 and B07, after removing the super-conducting wiggler, in March 2002. A precise field measurement and adjustment were finished. Final Vacuum conditioning is in progress.

3-3. Free Electron Laser

In July 2001, we have achieved 1.2W average output power on UVSOR-FEL in visible region [4]. This is the world highest record of the output power from a storage ring FEL. By using this high power FEL and brilliant undulator radiation in combination, we have succeeded in observing two-photon excitation of Xe atom [5].

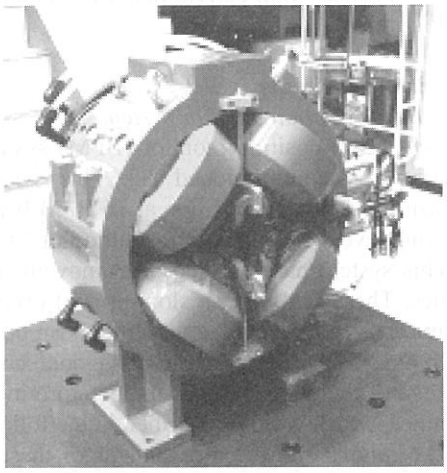

Fig. 4 Prototype of the combined-function multi-pole magnet

References

[1] K. Hayashi et al., Proceedings of the 13th Symposium on Accelerator Science and Technology, 372-374 (2001)

[2] M. Katoh et al., Nuclear Instruments and Methods in Physics Research A, **467-468** (2001), 68-71
[3] J. Yamazaki et al., in this report
[4] M. Hosaka et al., in this report
[5] T, Gejo et al., in this report

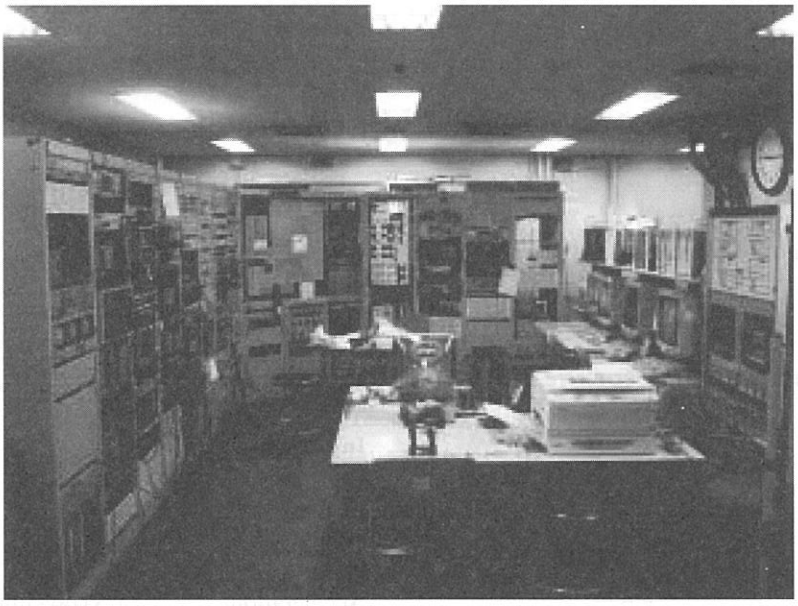

Control Room of UVSOR

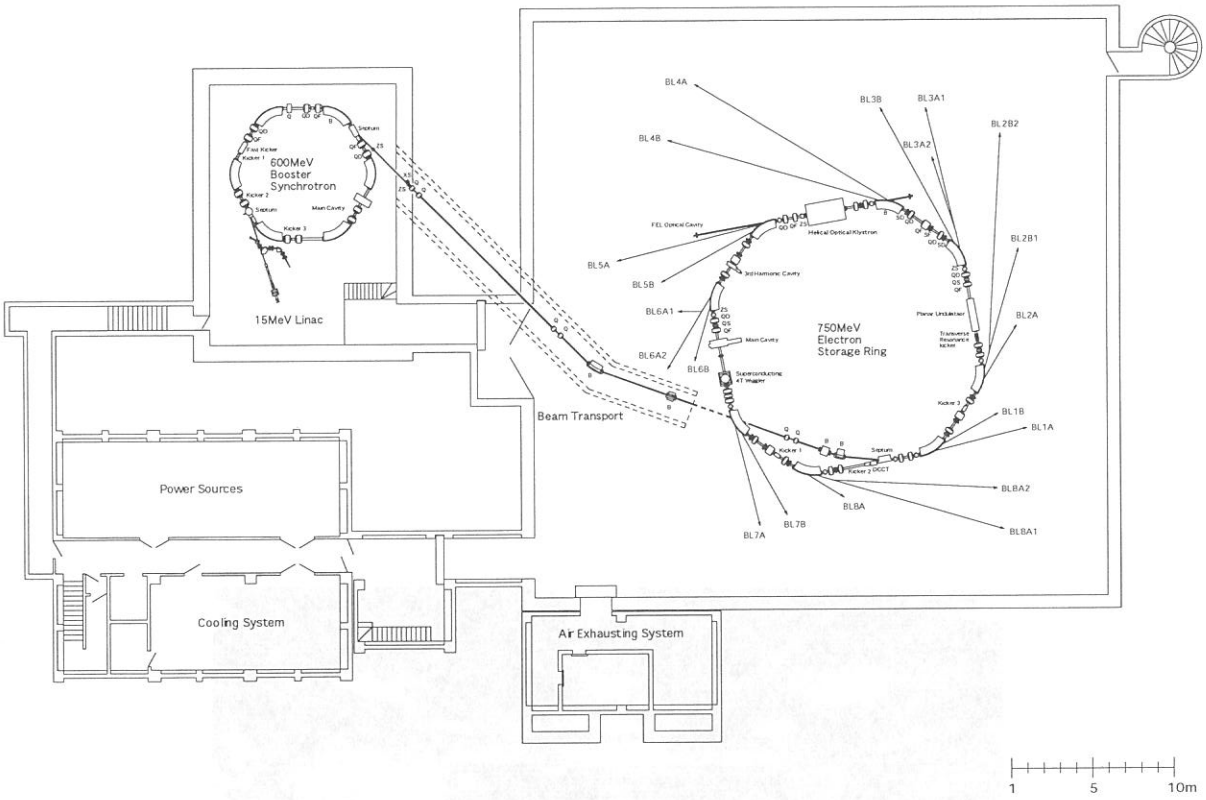

UVSOR Accelerator Complex

Parameters of UVSOR Storage Ring

Circumference	53.2 m
Lattice	DBA ×4
Straight Sections	3 m ×4
Beam Energy	750 MeV
Bending Radius	2.2 m
RF Frequency	90.115 MHz
Harmonic Number	16
RF Voltage	46 kV
Mom. Comp. Factor	0.026
Betatron Tunes	(3.16, 1.44)
Natural Energy Spread	4.2×10^{-4}
Natural Emittance	165 nm-rad
Natural Bunch Length	160 psec[#1]
Max. Beam Current	300mA (multi-bunch)[#2] 70 mA (single bunch)

#1) About three times longer with harmonic cavity on

Parameters of UVSOR Injector

Injection Linac

Energy	15 MeV
Length	2.5 m
Frequency	2856 MHz
Acceleration	2π/3Traveling Wave
Klystron Power	1.8 MW
Energy Spread	～1.6MeV
Repetition Rate	2.6 Hz

Booster Synchrotron

Energy	600 MeV
Lattice	FODO ×8
Circumference	26.6 m
Beam Current	32 mA (8-bunch filled)
Bending Radius	1.8 m
Betatron Tune	(2.25, 1.25)
Mom. Comp. Fac.	0.138
Harmonic Number	8
RF Frequency	90.115 MHz
Repetition Rate	2.6 Hz

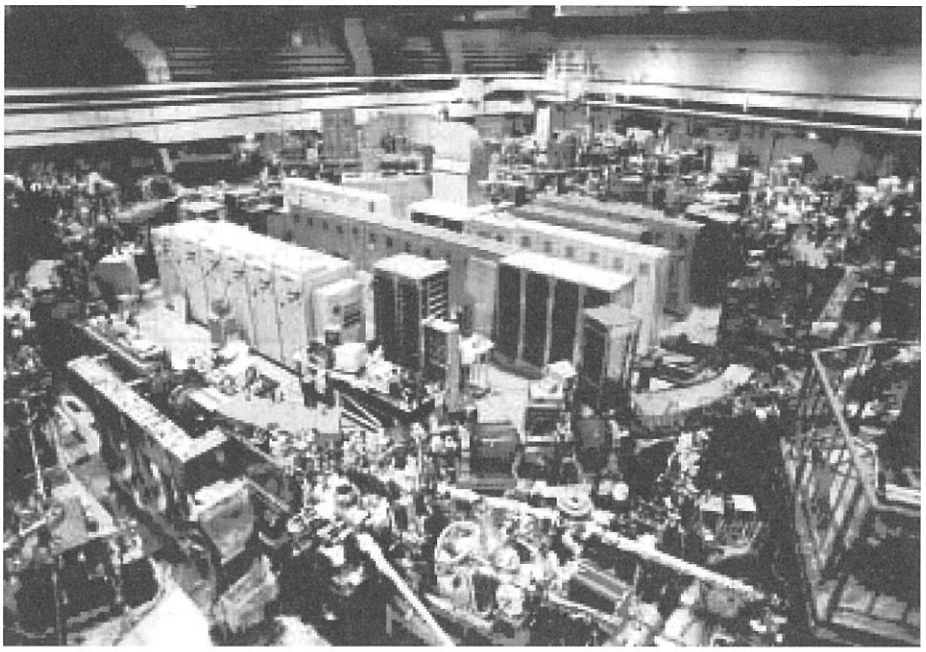

UVSOR Storage Ring

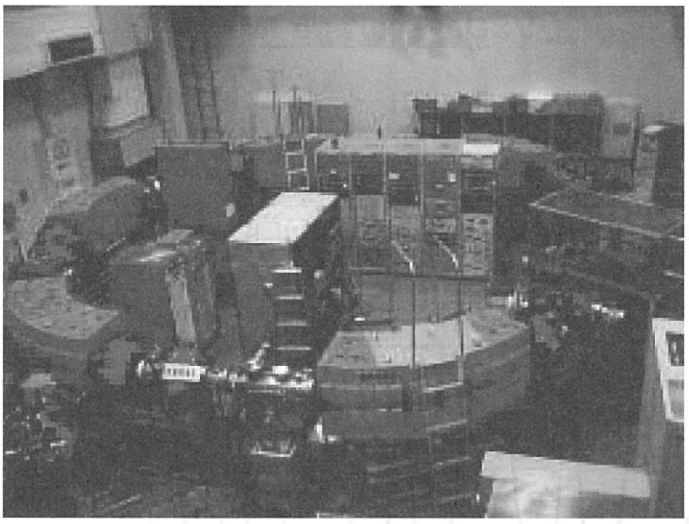

Booster Synchrotron

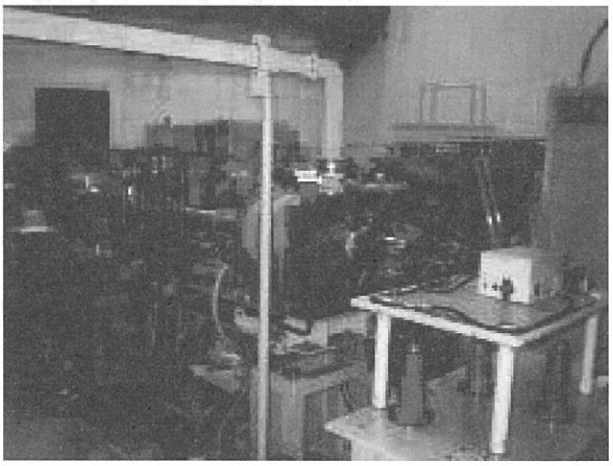

Injection Linac

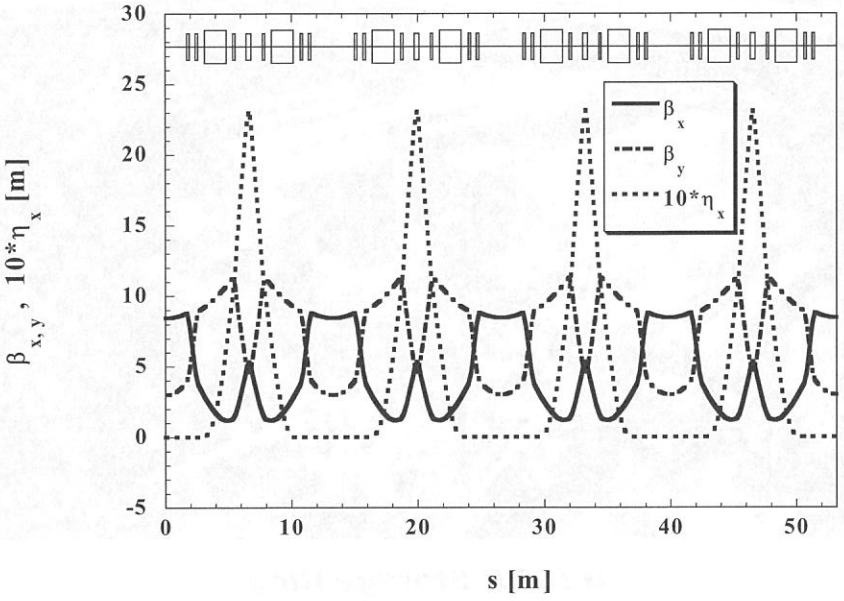

Optical Functions of UVSOR Storage Ring

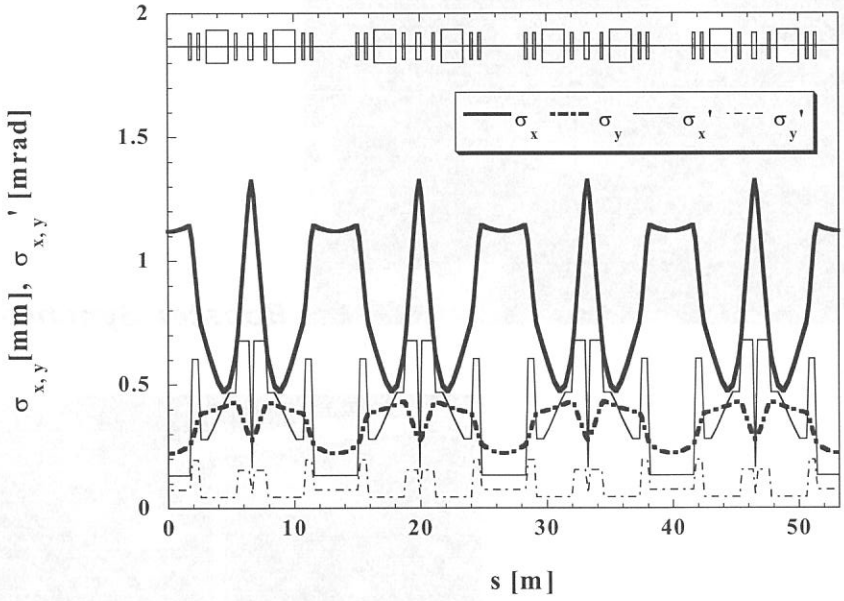

Beam Size and Divergence of UVSOR Storage Ring

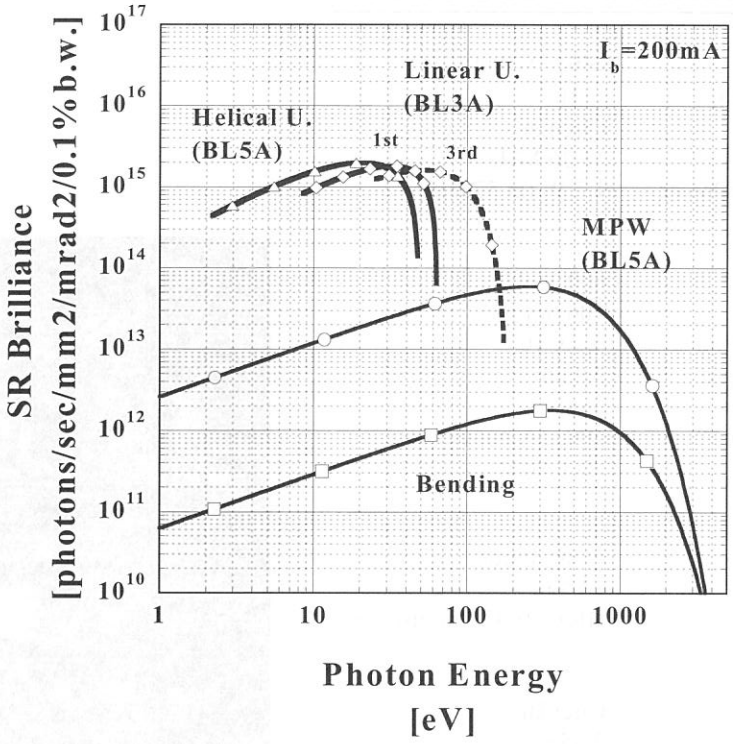

Synchrotron Radiation Spectra at UVSOR

Light Source Parameters

Bending Magnets	
Bending Radius	2.2 m
Critical Photon Energy	425 eV

Linear Undulator (BL3A)	
Number of periods	24
Period Length	84 mm
Total Length	2016 mm
Remanent Field	0.9 T
Magnetic gap	30 – 90 mm
Deflection parameter (K)	0.6 – 3.6

Helical Undulator/Optical Klystron (BL5A)	
Number of periods	18
Period length	110 mm
Length of dispersive part	302.5 mm
Total Length	2351.2 mm
Remanent field	1.3 T
Magnetic gap	30 – 150 mm
Deflection parameter (K)	0.07 – 4.6 (helical mode) 0.15 – 8.5 (linear mode)

Basic Parameters of UVSOR-FEL

Free Electron Laser	
Wave Length	240～570 nm
Spectral Band Width	$\sim 10^{-4}$
Polarization	Circular
Pulse Rate	11.26 MHz
Maximum Average Power	1.2 W (at 570nm)
Storage Ring	
Beam Energy	600 MeV
Natural Emittance	106 nm-rad
Natural Energy Spread	3.4×10^{-4}
Natural Bunch Length	3.4 cm
Number of Bunches	2 or 4
Max. Beam Current	100 mA/bunch
RF Frequency	90.1 MHz
Optical Cavity	
Type	Fabry Perot
Cavity Length	13.3 m
Mirror	HfO_2, Ta_2O_5 multi-layer
Optical Klystron	
Polarization	Circular
Length	2.35 m
Period Length	11 cm
Number of Periods	9 + 9

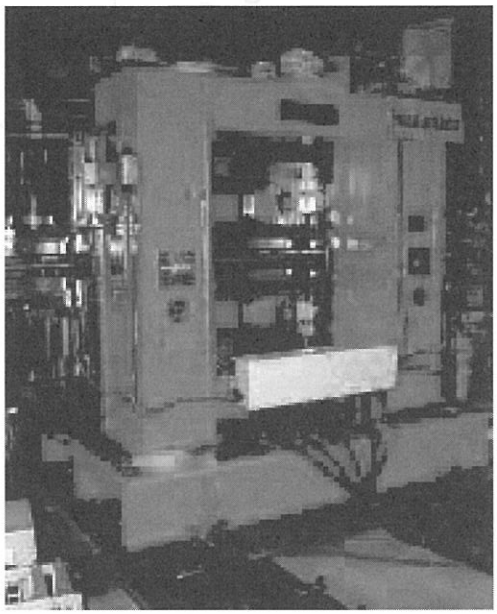

BL5A Helical Undulator (Optical Klystron for FEL)

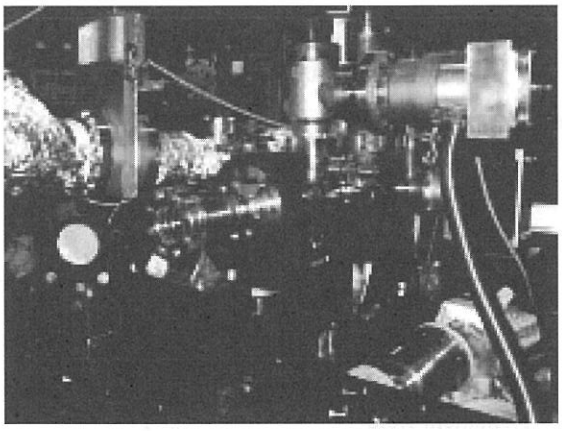

Optical Cavity for FEL at BL5A

Beamlines in 2001

Eiji SHIGEMASA

UVSOR Facility, Institute for Molecular Science

Eight bending magnets and two insertion devices are available for utilizing Synchrotron Radiation (SR) at UVSOR. There is a total of 20 operational beamlines, which are classified into two categories. 11 of them are so-called "Open beamlines", which are open to scientists of universities and research institutes belonging to the government, public organizations, private enterprises and those of foreign countries. The rest of the 9 beamlines are so-called "In-house beamlines", which are dedicated to the use of the research groups within IMS. We have two soft X-rays (SX) stations each equipped with a double-crystal monochromator (DXM), eight extreme ultraviolet (EUV) and SX stations with a grazing incidence monochromator, four vacuum ultraviolet (VUV) stations with a normal incidence monochromator (NIM), one infrared (IR) station equipped with FT interferometers, one station with a multi-layer monochromator, and four non-monochromatized stations for irradiation of white-light. Discussion with users, concerning the improvements and upgrades of the beamlines at UVSOR, has been continuously held as series of UVSOR workshops. As a result, about one third of the beamlines have been upgraded in recent years. More recently, discussion for the rebuilt and rearrangement of several old beamlines has been initiated, on the basis of the review and evaluation report on the present status of UVSOR in 2000. The following is a summary list concerning the status of the beamlines in 2001.

<Open beamlines>

BL1B covers the wavelength region ranging from 650 to 30 nm with the use of a Seya-Namioka type NIM. Standard measurements such as photoabsorption, reflection, and luminescence can be conducted at low temperatures down to 10 K. A variety of sample materials such as liquid, high pressure gases, and bio-specimens etc. can be measured easily by introducing appropriate windows. A second-monochromator system has been upgraded recently. The computer control system of the monochromator as well as the motor drivers has been renewed. The instruments including the multi-channel analyzer and detectors have been improved for time-resolved experiments. Several interesting experiments such as two-photon excitation, photo-reflectance, photoionization of liquid, and others are in progress.

BL2B1 consists of a Grasshopper monochromator, which covers the photon energy region from 20 to 800 eV, a double-pass cylindrical mirror analyzer (CMA), and an electron–ion coincidence apparatus. This beamline has been used mainly for surface science because the experimental chamber is equipped with useful instruments for surface science such as LEED, Auger, Ar-ion gun, and gas-inlet system. Photoelectron spectroscopy and electron–ion coincidence spectroscopy can be carried out on adsorbed surface and bulk material. There was no serious problem with the monochromator and photoelectron spectrometer. However, the performance of the

monochromator is far from satisfactory in comparison with more recently constructed monochromators. Discussion with users, concerning the future plan of this beamline, has been initiated in 2001.

BL3A1/BL3A2 can share intense synchrotron radiation from a planar-type undulator. At BL3A1, the intense undulator radiation has been used without the monochromator for SR stimulated processes such as etching and chemical vapor deposition (CVD), light-amplification, desorption, and luminescence experiments. In 2001 two color experiments for Xe atoms utilizing SR from BL3 undulator and Free Electron Laser (FEL) from BL5 optical klystron have been successfully performed on BL3A1. BL3A2 is composed of a constant-length Spherical Grating Monochromator (SGM) and a rotatable time-of-flight (TOF) mass spectrometer for gas samples. Either undulator radiation or dipole radiation can be used as a light source at this beamline. Recently BL3A2 has been mainly used with the undulator radiation for SR-Laser combined experiments in a gas phase. It has been decided that the undulator and beamlines will be renewed in 2003.

BL5A is utilized for photoemission spectroscopy on solids and surfaces in the photon energy ranging from 5 to 250 eV using an SGM-TRAIN monochromator. The beamline is fitted for experiments of both valence bands and shallow core levels. The experimental station is composed of a high-resolution photoelectron spectrometer, and a spin- and angle-resolved photoelectron spectrometer. Apart from SR from a bending magnet, circularly polarized radiation from a helical undulator is available at this beamline. The combined experiments with SR and the powerful laser system consisting of a TiS laser, RegA and OPA have been carried on in recent years. The preparation to use the undulator radiation in the low energy region is under way.

BL5B is mainly used for calibration of various optical elements and detectors in the photon energy region from VUV to SX. There are no similar beamlines at other facilities in Japan. BL5B has been contributing to many fields of research such as astro-science, nano-science, synchrotron science and technology for a long time. The beamline consists of a plane grating monochromator (PGM) and three experimental chambers in tandem, which are utilized for calibration of optical elements using a goniometer, optical measurements of solids, and photo-stimulated desorption experiments. The project for improving the goniometer will begin around the end of the fiscal year of 2001.

BL6A1 is used as a unique IR and FIR beamline. This beamline is composed of FT-IR and FT-FIR interferometers, which covers wide wavelength range from sub-milli to near IR region. Numerous research work on molecular sciences, using different experimental techniques such as high-pressure with a diamond anvil cell, magnetic circular dichroism, and time-dependence, have been carried out. In 2001, a gate valve with a window has been installed in between the experimental and mirror chambers, in order to make alignment of samples with the photon beam without breaking the vacuum condition.

BL7A was constructed at the first construction stage of the UVSOR facility in the mid 1980s for SX spectroscopy. This beamline has been providing SX in the photon energy range from 0.6 to 3 keV without a 4T-wiggler and up to 6 keV with it, using a DXM. However, the 4T-wiggler was shutdown completely due to

a mechanical problem on the cryogenic system in 1999. It has been confirmed that the photon intensity from the KTP crystals without the wiggler is almost the same as that from YB_{66} crystals combined with the wiggler. A new in-vacuum undulator will be installed at the straight section, where the wiggler lies, in March 2002. Accordingly, all the activity on this beamline will be transferred to BL1A.

BL7B consists of a 3-m NIM working in the photon energy range from near IR to VUV with a high resolving power. This beamline is mainly used for absorption, reflection, and fluorescence spectroscopy on solids. Although the installation of the monochromator was time-consuming, it has been shown that the performance of BL7B is sufficiently high to carry out spectroscopic investigations on solid samples with high resolution. New software to control the monochromator has been developed and tested in 2001, thanks to Prof. K. Fukui of Fukui University.

BL8A has no monochromator and is simply equipped with a differential pumping stage that makes it useful for measurements on gases as well as on solids. A focusing mirror having toroidal shape can be used to obtain a smaller irradiation area, if necessary. There is no permanent end-station installed at this beamline that enables users to install their own instruments brought from their institute or university. The UVSOR facility will support the installation of the users' experimental setup. Experiments on SR-CVD and SR-etching have extensively been carried out on this beamline in recent years.

BL8B1 is used for coincidence spectroscopy on gas samples in the photon energy range from 30 to 800 eV, where the K-shell ionization thresholds of chemically important elements like C, N, and O lie, using a high-resolution constant-deviation constant-length SGM. The experimental chamber at the end-station is composed of a TOF and a CMA, which makes it possible to perform the coincidence measurements between energy-analyzed electrons and photoions. Total electron yield measurements on solid samples are also possible. In 2001, the front-end valve with a possibility of making the vacuum condition worse, has been replaced. Modification to the scanning mechanism of the monochromator is scheduled in April 2002.

<In-house beamlines>

BL1A has been used for photoelectron spectroscopy on solids in the photon energy region from 600 to 3000 eV, with the use of a DXM. An analyzer chamber is equipped with a high-resolution hemispherical electron energy analyzer (SCIENTA SES200). In 2001, the experimental system has been removed from BL1A. This beamline will be used for XAFS experiments as an open beamline from the fiscal year of 2002.

BL2A was constructed for spectroscopic investigations on gas samples and have produced many scientific results. The monochromator installed at BL2A is a Seya-Namioka type NIM. Recently this beamline has been rearranged for bioscience and has been utilized by bio-scientists in the Okazaki organization. However, it is unfortunate that there has been no activity on this beamline through 2001.

BL2B2 is an EUV and SX beamline used for gas phase experiments. The monochromator is a Dragon-type SGM, which has commissioned in 1999. Angle-resolved ion yield measurements have been performed for SF_6 and rare gases on this beamline. New experiments for fullerene samples have been initiated in 2001.

BL3B consists of a 3-m NIM and an angle-resolved electron energy analyzer with a two-dimensional detector. This beamline has been used for spectroscopic investigations in gas phase, and has been providing interesting results for a long time. However, the performance of the 3-m NIM has become unsatisfactory in recent years. In 2001, the gratings installed were replaced for achieving higher performance.

BL4A1/4A2 are used for investigations on the reaction mechanism of SR stimulated processes. A multilayered-mirror monochromator for investigating the SR etching processes is installed at BL4A1. There is no monochromator but two branch lines (scanning tunneling microscopy (STM) and infrared reflection absorption spectroscopy) on BL4A2. SR assisted desorption processes of SiO_2 on Si substrates have been studied aggressively by STM observations lately.

BL4B is a new high-resolution beamline in the SX region (100 1000 eV). The monochromator is a Varied-line-spacing PGM. This beamline is utilized for various spectroscopic studies with high resolution in the SX range. There is no permanent experimental instrument installed at this beamline. The performance tests have been terminated at the end of January 2001. Several novel results for simple molecules have emerged from this beamline, using photoabsorption, angle-resolved photoion yield spectroscopy, and photoelectron spectroscopy under high-resolution condition in 2001. Very recently, new spectroscopic investigations on surfaces and solids have also begun.

BL6A2 is composed of a PGM and a photoelectron spectromicroscopy equipment (micro-ESCA, VG ESCALAB 220i-XL). The post-focusing mirror system has been completely changed in order to get a smaller spot for the micro-ESCA system. The achievement of the performance has been successfully tested. The femto-second laser system has also been installed to conduct the combination experiments of SR and lasers.

BL6B has been renewed for nano-scale photochemical reaction experiments. There is no monochromator on this beamline. An STM apparatus that can be operated under ultra high vacuum condition (UHV-STM) has been installed at BL6B, in order to make in situ observation for the reaction processes on Si surfaces stimulated by SR irradiation. It is in the planning stage to transfer the UHV-STM instrument to BL7A where the installation of a new in-vacuum undulator is programmed in March 2002.

BL8B2 is utilized for angle-resolved photoelectron spectroscopy on various organic solids such as molecular crystals, organic semiconductors, and conducting polymers. This beamline consists of a PGM, which covers the photon energy region form 2 to 150 eV, a sample preparation, a measurement, and a cleaning chamber. A high-performance multi-channel photoelectron spectrometer has been installed and its coordination has been terminated in 2001.

All users are required to refer to the beamline manuals and the UVSOR guidebook (latest revision in 1999), on the occasion of conducting the actual experimental procedures. Those wishing to use the open and in-house beamlines are recommended to contact the stationmaster/supervisor and the representative, respectively. For updated information of UVSOR, http://www.uvsor.ims.ac.jp/.

Table I. Station masters and supervisors of open beamlines in 2001*

Beamline	Station Master	Sub Master	Supervisor
1B	M. Hasumoto	M. Kamada	M. Kamada
2B1	K. Takahashi	E. Nakamura	M. Kamada
3A1	M. Kamada	E. Nakamura	M. Kamada
3A2	N. Kondo	T. Gejo	E. Shigemasa
5A	K. Takahashi	M. Hasumoto	M. Kamada
5B	M. Hasumoto	N. Nakamura	E. Shigemasa
6A1	E. Nakamura	O. Matsudo	M. Kamada
7A	E. Shigemasa	N. Kondo, O. Matsudo	E. Shigemasa
7B	M. Hasumoto	M. Kamada	M. Kamada
8A	T. Gejo	E. Nakamura	E. Shigemasa
8B1	T. Gejo	N. Kondo	E. Shigemasa

*Before October 2001. Prof. M. Kamada was promoted to Saga University on October 1, and since then the name of "M. Kamada" in Table I is tentatively replaced to "E. Shigemasa".

Table II. Representatives of in-house beamlines in 2001.

Beamline	Representative	Affiliation
1A	N. Kosugi	Dep. VUV Photoscience
2A	N. Kosugi	Dep. VUV Photoscience
2B2	K. Mitsuke	Dep. VUV Photoscience
3B	K. Mitsuke	Dep. VUV Photoscience
4A	T. Urisu	Dep. VUV Photoscience
4B	E. Shigemasa/N. Kosugi	UVSOR/Dep. VUV Photoscience
6A2*	M. Kamada*	UVSOR*
6B	T. Urisu	Dep. VUV Photoscience
8B2	K. Okudaira	Dep. VUV Photoscience

*Before October 2001. The current representative of BL6A2 is Prof. T. Urisu.

Beamlines at UVSOR

Beam Line	Monochromator, Spectrometer	Wavelength Region	Acceptance Angle (mrad) Horiz.	Vert.	Experiment
BL1A	Double Crystal	2.1 - 0.3 nm	4	1	Solid (photoemission)
BL1B	1-m Seya-Namioka	650 - 30 nm	60	6	Solid (absorption)
BL2A	1-m Seya-Namioka	400 - 30 nm	40	6	photoabsorption
BL2B1	2-m Grasshopper	60 - 1.5 nm	10	1.7	Solid & surface (photoemisson)
BL2B2	18-m Spherical Grating	60 - 6 nm	15	6	Gas (photoionization, photodissociation)
BL3A1	None (Filter, Mirror)	(U)	0.3	0.3	Solid & irradiation (photodissociation)
BL3A2	2.2-mConstant Deviation Grazing Incidence	100 - 10 nm (U)	10 0.3	4 0.3	Gas & solid (photoionization & photodissociation)
BL3B	3-m Normal Incidence	400 - 30 nm	20	6	Gas (photoemission)
BL4A1	Multi-Layered-Mirror Monochromator	13 - 23 nm Mo/Si MLMs	16.6	12.8	Irradiation
BL4A2	None				SR-CVD
BL4B	Varied-line-spacing Plane Grating Monochromator	15 - 1.5 nm	7.5	2	Gas (photoionization, photodissociation) & solid (photoemission)
BL5A	None SGM-TRAIN	(OK) 250 - 5 nm	10	3	FEL Solid (photoemission)
BL5B	Plane Grating	200 - 2 nm	10	2.2	Calibration, gas (photodissociation) & solid (absorption)
BL6A1	Martin-Puplett FT-IR Michelson FT-IR	3000 - 30 mm 100 - 1 mm	80 80	60 60	Solid (absorption)
BL6A2	Plane Grating	650 - 8 nm	10	6	Solid & surface (photoemission)
BL6B	None		8.3	6	Irradiation
BL7A	Double Crystal	1.5 - 0.8 nm	2	0.3	Solid (absorption)
BL7B	3-m Normal Incidence	1000 - 50 nm	65	10	Solid (absorption)
BL8A	None (Filter)		25	8	Irradiation & user's Instrum.
BL8B1	15-m Constant Deviation Grazing Incidence	40 - 2 nm	10	1.5	Gas (photoionization, photodissociation) & solid (absorption)
BL8B2	Plane Grating	650 - 8 nm	10	6	Solid (photoemission)

SGM-TRAIN: spherical grating monochromator with translating and rotating assembly including normal incidence mount

U: with an undulator

OK: with an optical klystron

BL1A

Soft X-Ray Beamline for Photoelectron-Photoabsorption Spectroscopy

BL1A is a soft X-ray beamline for photoabsorption spectroscopy. The beamline is equipped with a focusing premirror and a double crystal monochromator [1]. The monochromator serves soft x-rays in the energy range from 585 to 4000 eV by using several kinds of crystals such as β-Al_2O_3, beryl, KTP ($KTiOPO_4$), quartz, InSb, and Si crystals. The throughput spectra are shown in Fig. 1. Typical energy resolution ($E/\Delta E$) of the monochromator is about 1500 for beryl and InSb. The apparatus for photoelectron and photoabsorption spectroscopies was removed from the beamline last summer. The experimental setup for photoabsorption spectroscopy of BL7A will be moved to this beamline, which will be opened for the researchers outside IMS from May, 2002.

Reference

[1] A. Hiraya et al., *Rev. Sci. Instrum.*, **63** (1992) 1264.

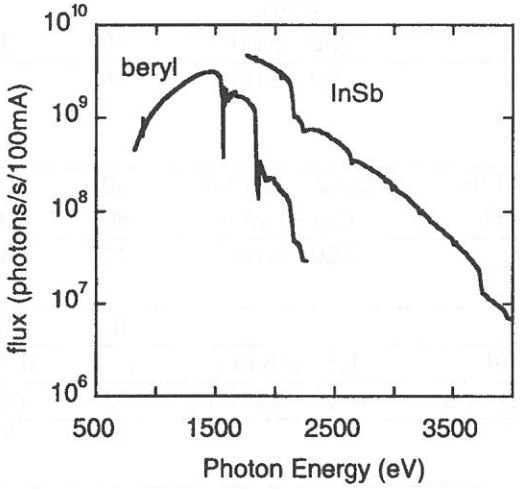

Figure 1. Throughput spectra of the double crystal monochromator at BL1A.

Specification

Monochromator:	double crystal monochromator
Monochromator crystals: (2*d* value, energy range)	β-Al_2O_3 (22.53Å, 585-1609eV), beryl (15.965Å, 826-2271eV), KTP (10.95Å, 1205-3310eV), quartz (8.512Å, 1550-4000eV), InSb (7.481Å, 1764-4000eV), Si (6.271Å, 2104-4000eV)
Resolution:	$E/\Delta E$= 1500 for beryl and InSb
Experiment:	photoabsorption spectroscopy for solid

BL1B

Seya-Namioka Monochromator for General Purposes

BL1B has been constructed to perform various spectroscopic investigations such as absorption, reflectivity, and luminescence in a condensed phase. This beamline consists of a pre-focusing mirror, a 1-m Seya-Namioka type monochromator, and post-focusing mirrors with different focal lengths. Three gratings of 600, 1200, and 2400 l/mm can cover the wavelength region ranging from 40 to 650 nm. The post mirror with a longer focal length is usually used with an LiF window to separate the vacuum condition of the monochromator from a main experimental station, which make experiments for liquids and bio-specimens possible, while the other is mainly utilized for solid-state spectroscopy.

The output flux from this monochromator is about 10^{10} photons/sec. around 200 nm with 0.1 mm slit openings. The spectral distributions for two gratings measured by a conventional photomultiplyer are shown in Fig. 1 A second monochromator (Spex 270M) and a LN-cooled CCD detector (Princeton Inc.) are available for luminescence measurements, together with a liquid helium-flow type cryostat. To perform time-resolved experiments, a TAC system is also available.

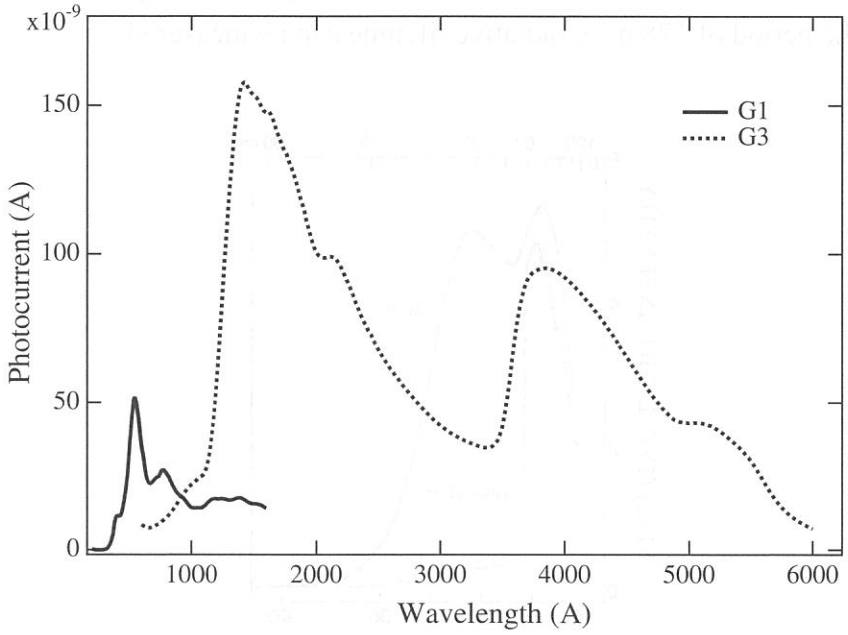

Figure 1. Photocurrent from the Seya-Namioka monochromator on BL1B.

Specification

Monochromator: 1-m Seya-Namioka type
Energy range: 40 to 600 nm (2-30 eV)
Resolution: E/ΔE~ 1000 at 100 nm
Experiments: Absorption, reflection, luminescence spectroscopy for solids

BL2A

Gas Phase Photoabsorption and Fluorescence Spectroscopy

Photoabsorption cross section and fluorescence excitation spectra of gaseous sample are simultaneously measured in a vacuum cell or effusive jet condition. The primary photons in the 30-400 nm region are dispersed by a 1-m Seya monochromator. Higher order light in the 80-120nm range is suppressed by using a long channel with a cross section 2.5 × 5.0 × 170 mm long filled with argon gas at a pressure ~ 0.3 Torras shown in Figure 1. No filter is used between 30 and 80 nm since the photon flux at $\lambda < 40$ nm is very weak (see Figure 1). The gas filter and cell are placed in a main chamber, which is evacuated by a 600 *l*/s turbo molecular pump (SII, STP600C). A LiF window is used for the measurement at the $105 < \lambda < 210$ nm range as usual. Thus the total photoabsorption cross section and fluorescence excitation spectra are available in the wide wavelength region 30-210 nm without or with little contamination by the higher order light. Dispersed fluorescence and polarity of emission from the excited fragment are also measurable in addition to the total photoabsorption and emission cross sections. In the single bunch operation of synchrotron radiation with the period of 178 ns, a radiative lifetime can be measured.

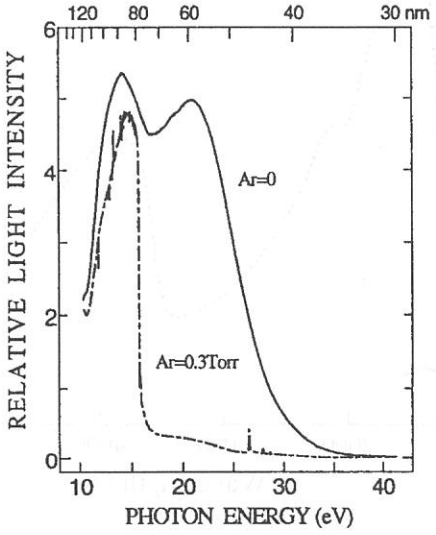

Figure 1. Transmitted I_0 intensity with and without an Ar gas filter.

Specification

Monochromator: 1-m Seya — Wavelength range: 30-400nm

Resolution: $E/\Delta E$= 1000 at 100 nm — Grating: 1200 line/mm blazed at 96nm

Experiments: Vacuum cell or effusive jet, Total photoabsorption cross section, Fluorescence cross section, Dispersed fluorescence, Radiative lifetime, Emission polarity

BL2B1

Soft X-ray Beamline for Solids and Surfaces

BL2B1 has been used for soft X-ray absorption and photoelectron spectroscopies of solids and surfaces. A 2-meter grazing incidence monochromator ('Grasshopper' type, Mark XV; Baker Manufacturing Co.) is installed, which serves soft X-rays in the energy range from 95 to 1000 eV using a 1800 l/mm grating. The resolving power is better than 600 at C K-edge (about 290 eV). A double-pass cylindrical mirror analyzer (CMA), a LEED of reverse type, a quadrupole mass spectrometer, and an ion-gun for sputtering are installed in the analyzing chamber. A pulsed leak-valve and a variable leak-valve are also installed. The samples can be cooled with a liquid helium cryostat. The base pressure of the analyzing chamber is better than 1×10^{-10} Torr. The photoelectron spectroscopy including constant initial-state spectroscopy (CIS) and constant final-state spectroscopy (CFS) can be conducted using the double-pass CMA. Besides these standard photoemission measurements, electron-ion-coincidence (EICO) spectroscopy can be carried out on adsorbed surfaces and bulk materials. In 1999, a new version of an EICO instrument has been installed, resulting in better efficiency on collecting data. The users who plan to perform the EICO measurement should make contact with the EICO users group. The sample preparation chamber equipped with a load-lock chamber is connected to the analyzing chamber. Sample treatments such as cleaving, filing, and deposition can be made under the ultra-high vacuum condition.

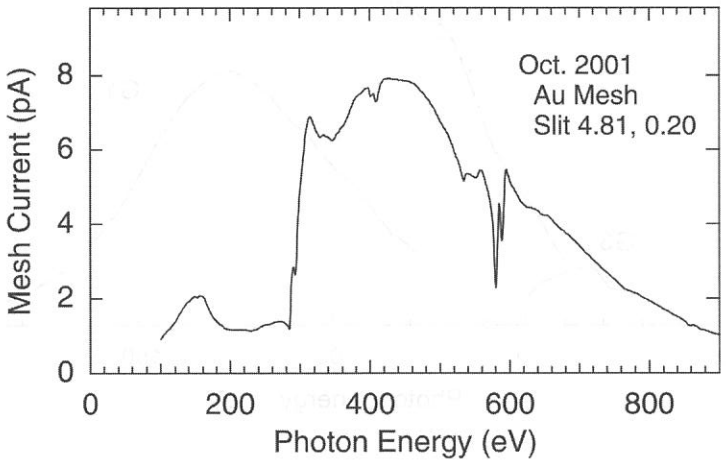

Figure 1. The photoelectron yield from a Au mesh of 90 % transmission located between the refocusing chamber and the sample.

Specification

Monochromator	: 2 m grasshopper type
Energy range	: 95-1000 eV (1800 l/mm)
Resolution of photon	: < 0.4 eV at 300 eV
Resolution of photoelectron	: < 0.3 eV for hν = 150 eV
Experiment	: Photoelectron spectroscopy, X-ray absorption spectroscopy, Electron-ion-coincidence spectroscopy

BL2B2

Beamline for Gas Phase Photoionization and Photodissociation Dynamics

This beamline has been developed for the purpose of studying ionization, excitation and decay dynamics involving inner-valence electrons or 2*p* electrons of the third row atoms. The monochromator is a spherical grating Dragon-type with 18 m focal length. High throughput (1×10^{10} photons s^{-1}) and high resolution ($E/\Delta E$ = 2000 - 8000) are achieved simultaneously under the condition of the ring current of 100 mA [see Fig. 1 and M. Ono *et al.*, *Nucl. Instrum. Meth. Phys. Res. A* **467-468**, 577 (2001)]. A second-order light of 7 % is contained at a photon energy of 45.6 eV (G3).

The optical system consists of two prefocusing mirrors, an entrance slit, spherical gratings (G1, G2 and G3), two folding mirrors, a movable exit slit and a refocusing mirror. The monochromator is designed to cover the energy range of 23 - 205 eV with the three gratings: G1 (2400 lines mm^{-1}, R = 18 m) at 80 - 205 eV; G2 (1200 lines mm^{-1}, R = 18 m) at 40 - 100 eV, G3 (2400 lines mm^{-1}, R = 9.25 m) at 23 - 50 eV. The including angles are 160° for G1 and G2, and 140° for G3. The detailed parameters of the optical elements are described elsewhere [H. Yoshida and K. Mitsuke, *J. Synchrotron Radiat.* **5,** 774 (1998)].

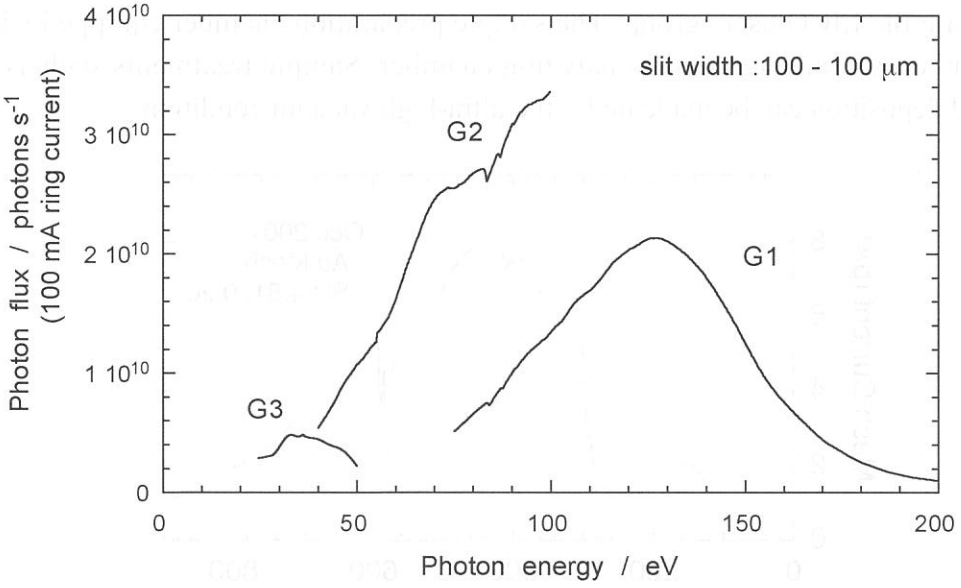

Figure 1. Photon flux at the end station at a 0.1 A ring current when the entrance- and exit-slit widths are set to 100 μm. The SR is provided from a bending magnet.

Specification

Monochromator: 18-m spherical grating grazing-incidence of Dragon-type
Energy Range: 6 – 54 nm (23 – 205 eV)
Resolution: $E/\Delta E$ = 2000 – 8000 (ΔE = 5 – 45 meV)
Experiments: TOF mass spectrometry, Symmetry-resolved photoabsorption spectroscopy, and Two-dimensional photoelectron spectroscopy

BL3A1

Irradiation Port for Undulator Radiation

BL3A1 has been mainly used for irradiation experiments such as photo-chemical reaction, SR-CVD, photo-etching, irradiation damage effects in condensed phase, light amplification induced by core-revel excitation. The experiments that need a very high intensity photon beam, namely, luminescence yield measurements and time-response measurements of SR-induced desorption, are also performed on this beamline.

A planar-type undulator installed in a long straight section of the UVSOR storage ring provides an intense quasi-monochromatic radiation to BL3A1. The undulator has 24 periods with a period length of 80 mm. The photon energy ranging from 8 to 52 eV can be covered by the fundamentals with K-values from 0.62 to 3.6, although higher harmonics are also generated at the same time.

This beamline has no monochromator between the undulator and the sample chamber. The radiation is introduced into the sample chamber only by a toroidal focusing mirror through a pinhole with 1 mm in diameter followed by a metallic filter (Al, Sn, or In). A gold mesh is installed in the sample chamber to monitor the photon beam intensity. The photocurrent measured using the monochromator at BL3A2 is shown in the figure below, when the undulator gap was set at 60 mm. The photon flux at the sample position is estimated to be about 10^{14} photons/sec.

A differential pumping system can be utilized for experiments in a gas phase. MgF_2 windows can also be installed to isolate the sample chamber from the beamline, which make experiments for high-pressure gases, liquids, and bio-specimens possible. A monochromator (Jobin-YvonHR-302), a VUV monochromator (home-made, normal-incident type), a helium storage-type cryostat and a TAC system are available.

Specification

Type	: planar-type undulator
Source emittance	: 164 nmrad
Period	: 80 mm
Number of periods	: 24
Magnetic field	: Kmax 3.6
Photon Fulux	: 10^{14} photons/s at 34eV
Energy range	: 8-52eV

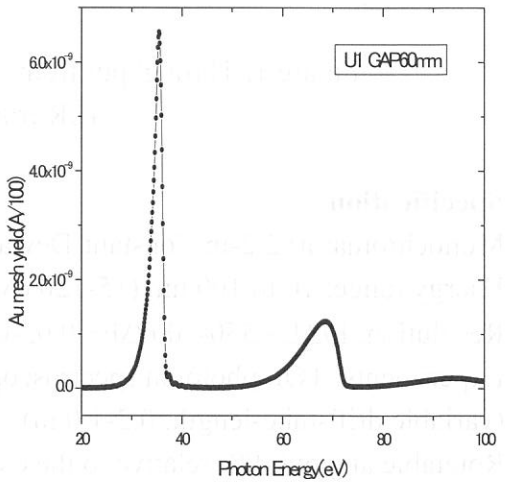

BL3A2

Gas-Phase Dissociative Photoionization Apparatus

BL3A2 has been constructed to study the formation of multiply charged molecular ions and their dissociation processes. The monochromator is a constant-deviation grazing incidence type with 2.2-m focal length (2.2-m CDM) and covers wide wavelength region (10-100 nm) where many kinds of molecules and multiply charged ions are effectively measured. Fig. 1 shows the absolute photon flux for each grating installed to CDM, with the use of the dipole radiation. Higher intensity photon beam is available by introducing the undulator radiation to CDM. The apparatus at the end station contains an angle-resolved time-of-flight mass spectrometer equipped with automatic data acquisition system for photoion-photoion coincidence measurements. It has been decided that the undulator and beamline will be renewed in 2003.

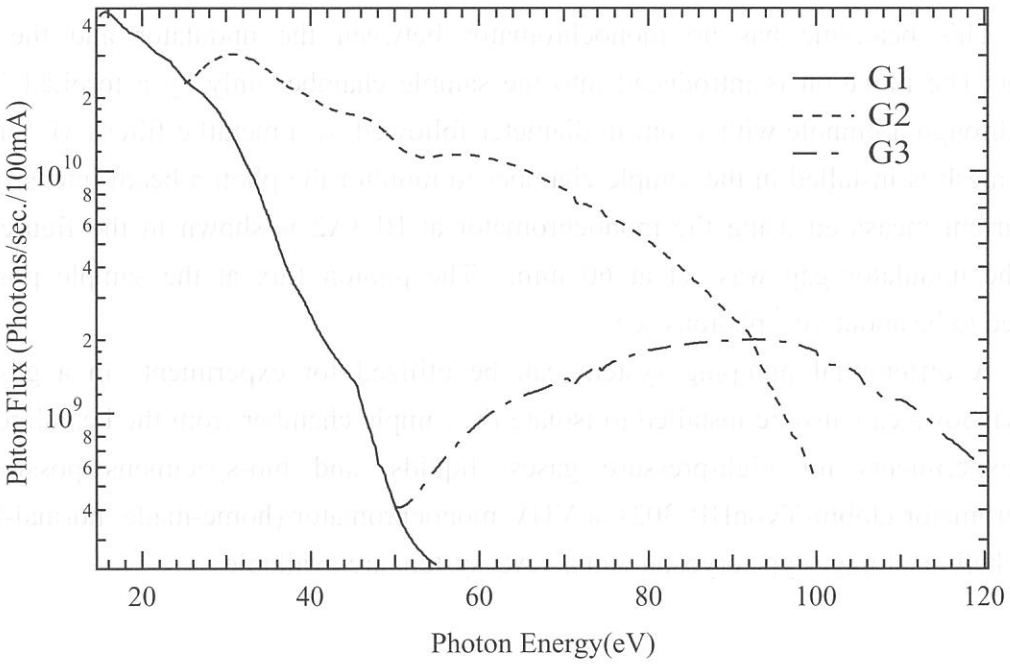

Figure 1. Throughput from the 2.2-m CDM monochromator on BL3A2.
(SR from the bending magnet)

Specification

Monochromator: 2.2-m Constant-Deviation Grazing-incidence
Energy range: 10 to 100 nm (15-120 eV)
Resolution: E/ΔE~ 550-800 (ΔE~ 0.03-0.18 eV)
Experiments: TOF photoion spectroscopy for gaseous targets
(variable drift-tube-length: 0.2-1.0 m)
Rotatable angle: 0-90° relative to the electric vector of SR

BL3B

Beam line for Gas Phase Two-Dimensional Photoelectron Spectroscopy

This beam line is devoted to studies of elementary atomic and molecular processes induced by excitation of valence electrons. A monochromator is a vertically dispersed normal incidence type with 3m focal length and 10° angle between the incident and diffracted photon beams. The maximum wavelength resolution of 0.007nm is narrow enough to separate vibrational levels of excited states for various molecules. A main component in an experimental chamber is a spherical sector electrostatic energy analyzer which has been designed and setup for photoelectron spectroscopy. One can perform two-dimensional photoelectron spectroscopy with good resolution (≤ 30meV) in which the photoelectron yield is measured as a function of both photon energy and electron kinetic energy (binding energy). A two-dimensional spectrum, usually represented as a contour plot, contains rich information on photoionization dynamics and properties of superexcited states. For more details, please see the following papers: K. Mitsuke *et al.*, *J. Electron Spectrosc. Rel. Phenom.* **79**, 395 (1996); H. Hattori and K. Mitsuke, *ibid.* **80**, 1 (1996); H. Hattoriet *al.*, *J. Chem. Phys.* **106**, 4902 (1997); Y. Hikosakæt *al.*, *ibid.* **105**, 6367 (1996); Y. Hikosakæt *al.*, *ibid.* **107**, 2950 (1997); **110**, 335 (1999); K. Mitsukæt *al.*, *J. Electron Spectrosc. Rel. Phenom.* **112**, 137 (2000).

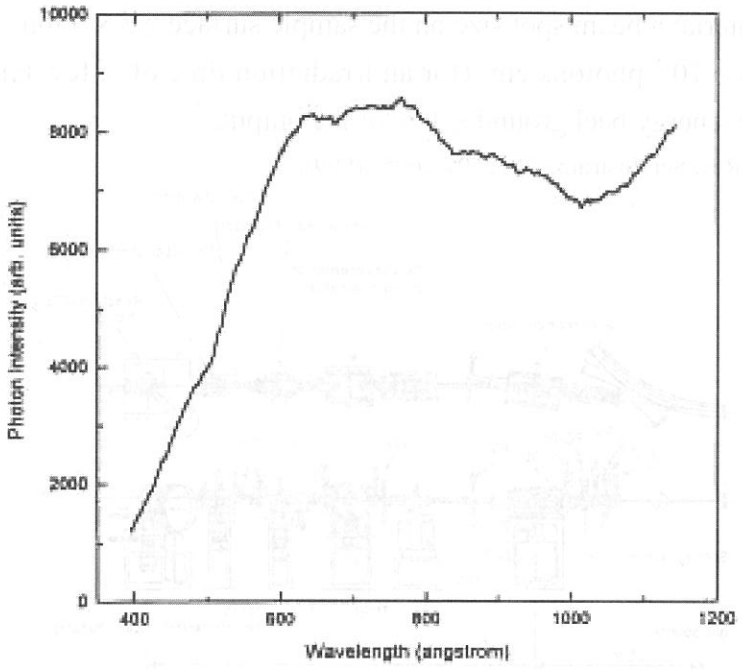

Figure 1. Relative photon intensity at the sample point.

Specification

Monochromator: Vertically dispersed normal incidence type with 3 m focal length
Grating: aberration-corrected concave type with 1200 lines/mm grooves
Energy Range: 30 – 200 nm (6 – 40 eV)
Resolution: $E/\Delta E$ = 14000 at 100 nm (ΔE = 0.9 meV) with the slit widths of 10μm
Experiments: TOF mass spectrometry and Two-dimensional photoelectron spectroscopy

BL4A1

Multilayered-mirror monochromator beam line for the study of synchrotron radiation stimulated process

A multilayered-mirror (MLM) monochromator beam line designed specially for synchrotron radiation (SR) stimulated process experiments has been constructed for the first time. The most important point in constructing an MLM monochromator beam line for the study of SR-stimulated processes is the optimization of the beam line optics to obtain a large photon flux. The second most important point is to remove the background existing in the low energy region caused by the total reflection. Optimization concerning the reduction of the low-energy background due to the total reflection has been made for the combination of the Mo/Si MLMs and the C filter. Mo/Si MLMs have a (normal incident) reflectivity of over 60% can be made for the energy region around 100eV, which contains the core electron binding energies of Al and Si (important material in semiconductor processes). The beam line was designed by the criteria; a beam spot size on the sample surface $\geq 3 \times 3$ mm^2, a density of total irradiated photons $\geq 10^{18}$ photons/cm^2 (for an irradiation time of a few tens of minutes to a few hours) and low-energy background ≤ 1 % of the output. [1]

[1] H. Mekaru, et. al., Rev. Sci. Instrum., 70, 2601-2605 (1999).

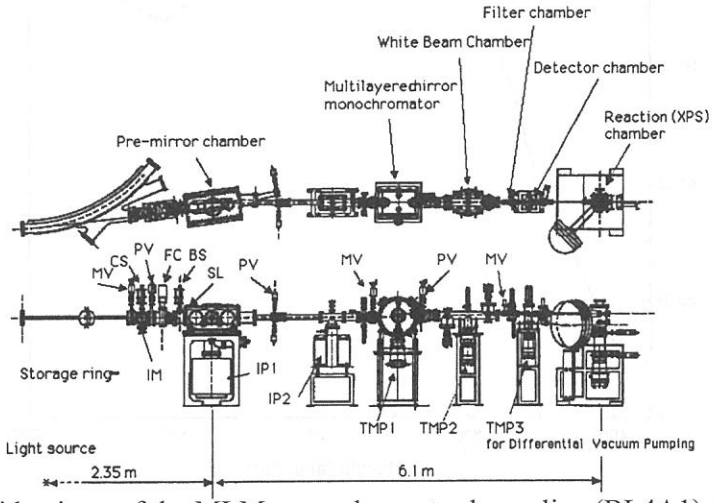

Figure 1. Top and side views of the MLM monochromator beam line (BL4A1) constructed at the UV-SOR facility of the IMS.

Specifications

Monochromator:	Multilayered-mirror monochromator
Wavelength range:	13.3 - 22.5 nm
Resolution:	5 - 9 eV (FWHM)
Experiments:	Excitation energy dependence of the SR processing

BL4A2

SR-CVD beam line

This beam line is used for SR-CVD and photo-etching experiments. The beam line has no monochromator for high photon flux to irradiate and consists of only two mirrors. One is for focussing and the other is for branching. At the beam line, the gas supply and extinction system is equipped for using legally controlled high pressure gasses such as SiH_4, Si_2H_6 and GeH_4. They are commonly used to CVD of semiconductor crystals.

The SR-CVD and photo-etching chambers are connected to the beam line as shown in Fig. 1. In those chambers, IRRAS system is installed to study surface photochemistry on Si surfaces adsorbed by various kinds of molecules.

BL4A2 has one branch for ultra high vacuum STM chamber. Now, the branch is under construction.

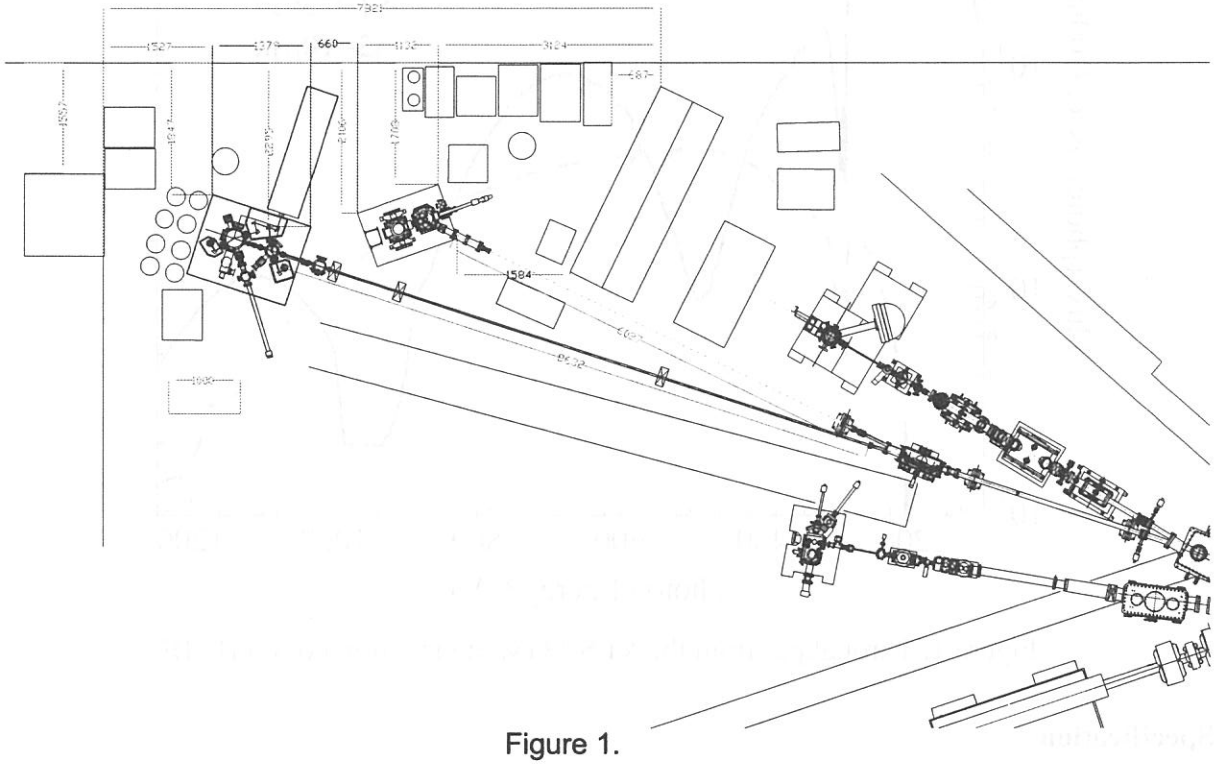

Figure 1.

Specifications

Spectral range: whole range of synchrotron radiation from UVSOR

BL4B

Varied-line-spacing Plane Grating Monochromator for Molecular Soft X-ray Spectroscopy

The beamline BL4B equipped with a varied-line-spacing plane grating monochromator (VLS-PGM) was constructed for various spectroscopic investigations in a gas phase and/or on solids in the soft X-ray range. Two holographically ruled laminar profile plane gratings with SiO_2 substrates are designed to cover the photon energy range from 80 eV to 1000 eV. The gratings with the groove densities of 267 and 800 l/mm cover the spectral ranges of 75-300 and 220-1000 eV, respectively, and are interchangeable without breaking the vacuum. Fig. 1 shows the absolute photon flux for each grating, with the entrance- and exit-slit openings set at 25 and 10 μm, respectively. Under this condition, the corresponding resolving power is expected to be more than 3000.

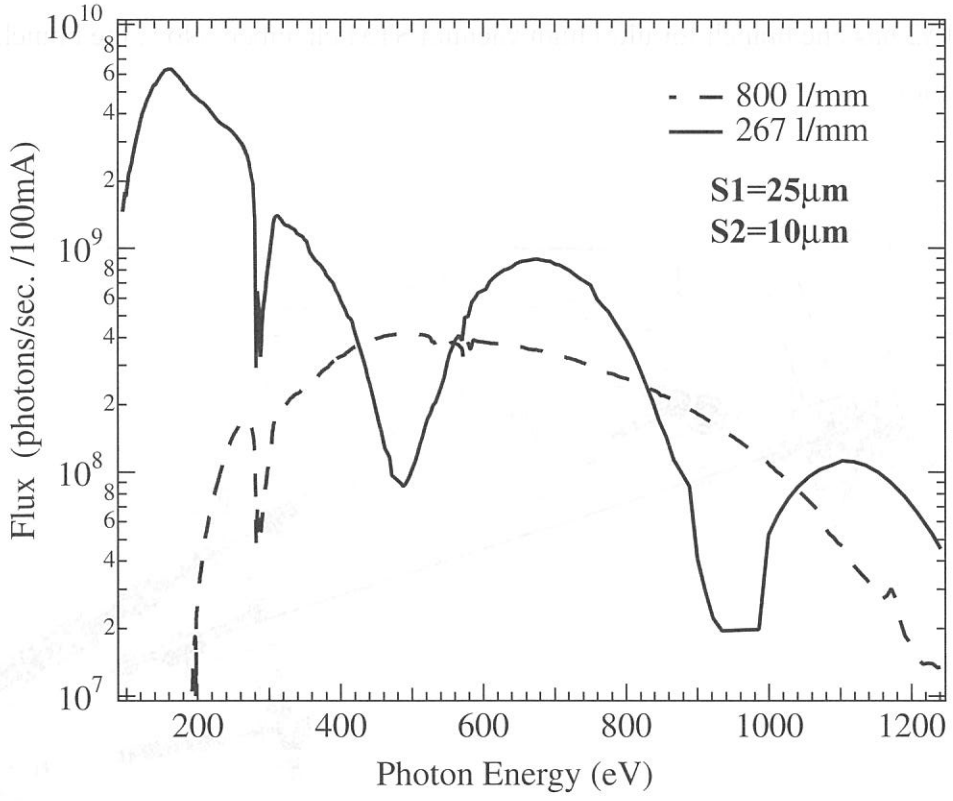

Figure 1. Throughput from the VLS-PGM monochromator on BL4B.

Specification

Monochromator: Varied-line-spacing plane grating monochromator

Energy range: 75 to 1000 eV

Resolution: $E/\Delta E > 5000$ (at maximum)

Experiments: Soft X-ray spectroscopy (mainly, angle resolved photoion spectroscopy for gaseous targets and photoelectron spectroscopy for gaseous and solid targets)

BL5A

Photoelectron Spectrometer for Solids and Surfaces

This beamline is designed for spin- and angle-resolved photoemission study for solids and surfaces with the circularly polarized synchrotron radiation from a helical undulator and for high-resolution photoemission spectroscopy with bending magnet radiation. The beamline consists of a Spherical Grating Monochromator with Translational and Rotational Assembly Including a Normal incidence mount (SGM-TRAIN), a spin- and angle-resolved photoelectron spectrometer, and a high-resolution photoelectron spectrometer.

The SGM-TRAIN is an improved version of a constant-length SGM to aim the following points; (1) wide energy range of 5-250 eV, (2) high resolving power, (3) use of linearly and circularly polarized light, (4) reduction of second-order light, and (5) two driving modes by a computer control. The second-order light is well suppressed by using laminar-profile gratings and combinations of mirrors and gratings.

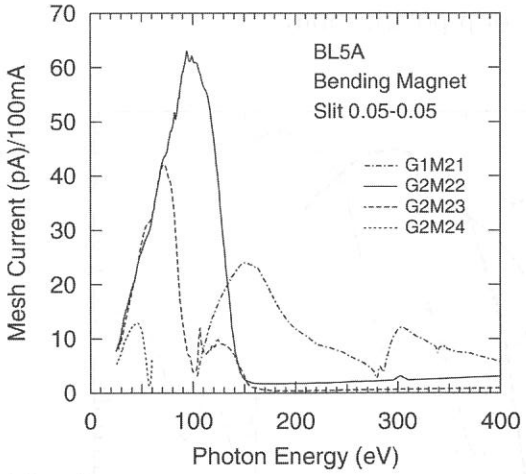

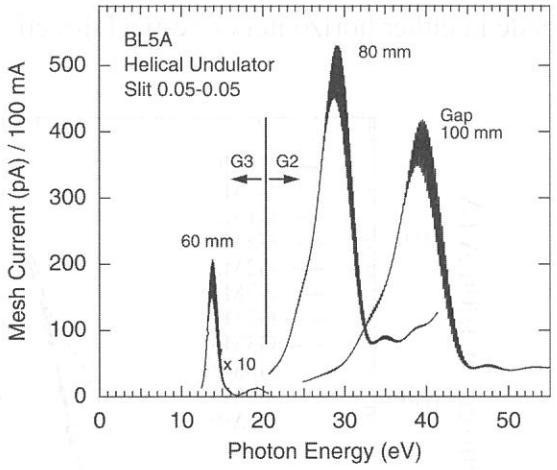

Specifications

1. Monochromator
   - Type : SGM-TRAIN
   - Energy range : 5-250 eV
   - Resolution : 0.5-80 meV (with slits width of 0.01 mm)
   - Flux : 3×10^{10} photons/s for bending magnet radiation (at 120 eV with slits width of 0.1 mm)
     1×10^{12} photons /s for undulator radiation in MPW mode
2. Main Instruments
   - Two-levels UHV chamber (1×10^{-10} Torr)
   - Hemispherical electron energy analyzer (OMICRON, EA125-HR)
   - Spin- and Angle-resolved spectrometer (low-energy diffused scattering type)
   - LEED of reverse type (OMICRON)
   - Ion-gun (ULVAC-Phi)
   - Low-temperature cryostat (above 30 K)
3. Helical Undulator (Optical Klystron)

Number of periods	18
Period length	110 mm
Fundamentals	2-45 eV (Circularly polarized)

BL5B

Calibration Apparatus for Optical Elements

BL5B has been constructed to perform calibration measurements for optical elements and detectors. This beamline is composed of a plane grating monochromator (PGM) and three end stations in tandem. The most upstream station is used for calibration measurements of optical elements, the middle one for optical measurements for solids and the last for photo-stimulated desorption experiments. The experimental chamber at the most downstream station is sometimes changed to a chamber for photoemission spectroscopy.

The calibration chamber is equipped with a goniometer for the characterization of optical elements, which has six degrees for freedom; X-Y translation of a sample, and interchange of samples and filters. These are driven by pulse motors in vacuum. Since the polaziation of synchrotron radiation is essential for such measurements, the rotation axis can be made in either horizontal or vertical direction (s- or p-polarization).

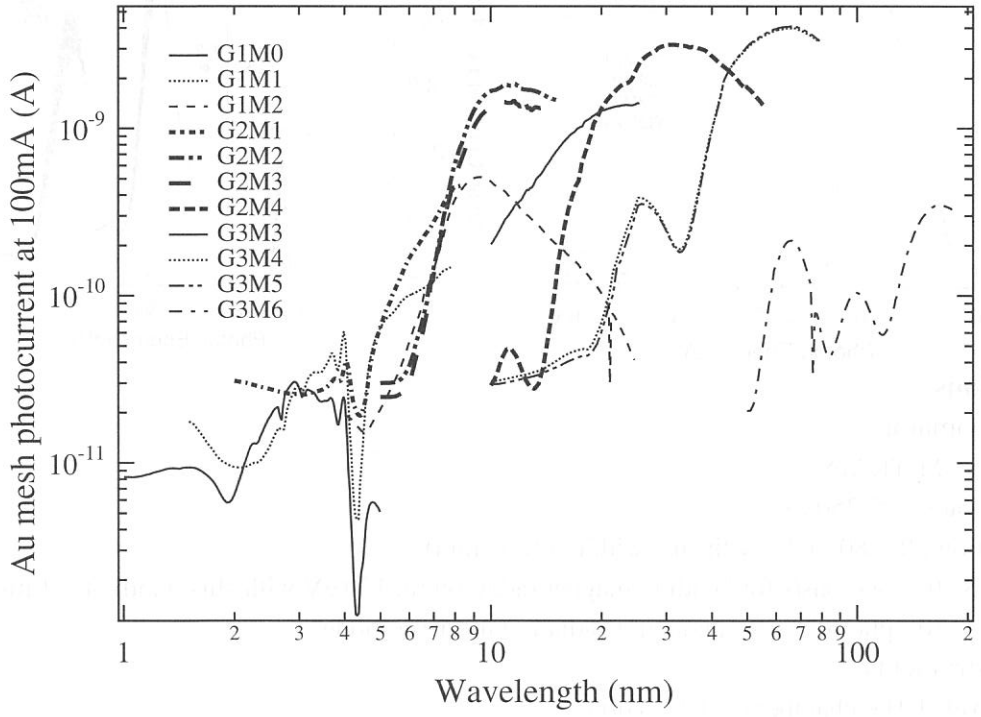

Figure 1. Throughput spectra of BL5B measured by a gold mesh.

Specification

Monochromator: Plane grating

Energy range: 2 to 200 nm (6-600 eV)

Resolution: E/ΔE~ 500

Experiments: Calibration of optical elements, absorption of solids, photo-stimulated desorption from rare gas solids

BL6A1

Fourier-Transform Middle and far Infrared spectrometers for solids

UVSOR covers a very wide energy region from a soft-X ray to a millimeter wave. BL6A1 was constructed in order to cover a long wavelength part in the spectral distribution of UVSOR from a near infrared to a milli-meter wave. Beamline are composed of two kinds of interferometers, a Martin Puplett type and a Bruker-IFS66v. The spectrum from 1 μ m to 3 μ m regions is measureable by changing of three kinds of detectors, MCT, Si-bolometer and InSb hot electron detector, according to each available region. Owing to the high brightness of the SR in the long wavelength region, the present spectroscopic system is specially favorable to the transmission and reflection measurements on so tiny specimens..

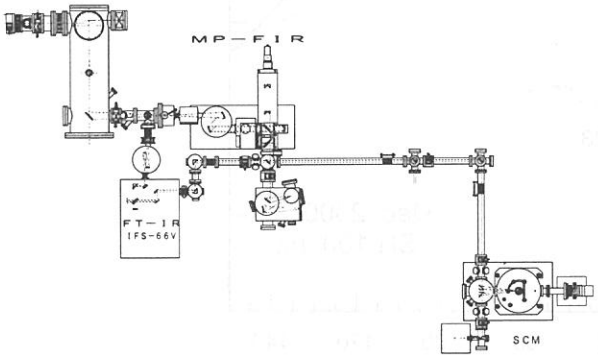

Top view of BL6A1

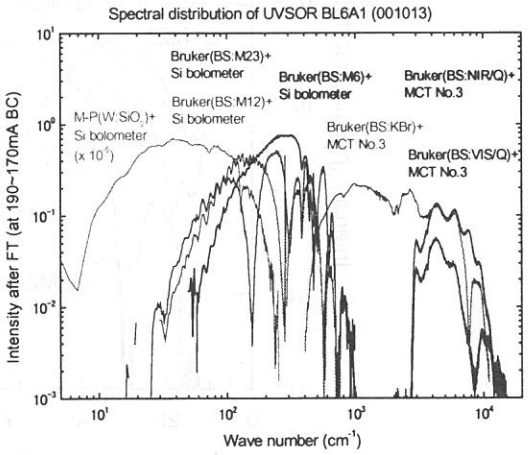

Throughput spectra of BL6A1

Spccification

Energy resolution :	500-20000
Energy range :	0.0005-1.5eV
Interferometers :	5-300cm^{-1} by Martin-puplett interferometer
	50-30000cm^{-1} by Michelson type interferometer
Detectors :	Si bolometer(20-1000cm^{-1})
	Ge bolometer(with polyethylene window,30-300cm^{-1})
	Ge bolometer(with quartz window,10-200cm^{-1})
	InSb bolometer(5-50cm^{-1})
	MCT(400-10000cm^{-1}) Photovoltaic type MCT(400-10000cm^{-1},time response10nsec)

BL6A2

Photoelectron Spectro-microscope for Solids and Surfaces

The beamline BL6A2 has been used for photoelectron spectroscopy on solids and surfaces with bending magnet radiation. The beamline consists of a Plane Grating Monochromator (PGM) and a photoelectron spectro-micrometer.

The PGM has several combinations of mirrors and gratings to cover the wide energy range of 2-150 eV with less higher-order light. Since the monochromator has no entrance slit, the resolving power depends on the beam size and the divergence. The beamline has been re-arranged in order to have a small spot for the photoelectron spectro-micrometer. Also the femto-second laser system was installed to conduct the combination experiments with synchrotron radiation and laser.

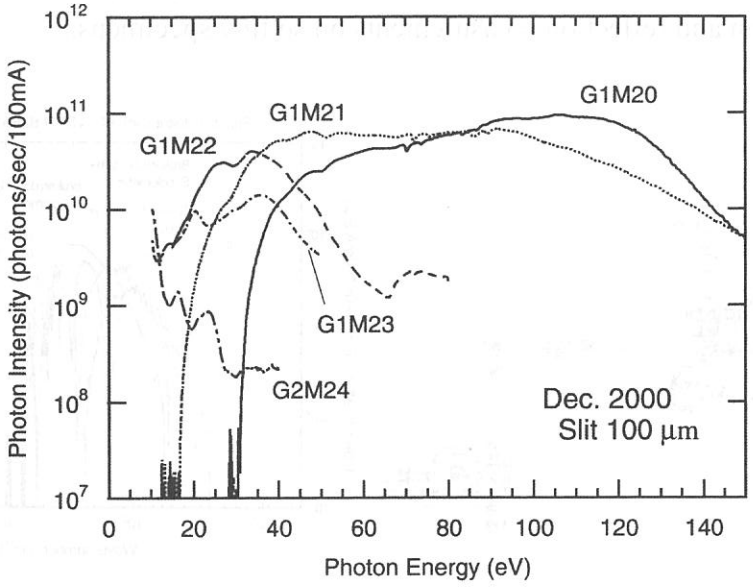

Figure 1. Through-put from the PGM monochromator on BL6A2.

Specifications

Monochromator

Type : Plane Grating Monochromator

Energy Range : 2-150 eV

Resolution : 0.1 eV at 70 eV

Photoelectron spectro-micrometer

Type : ESCALAB 220i-XL (FISONS Instruments)

Spatial Resolution : 20 μm for spectroscopy

: 2 μm for imaging

Others : XPS, LEED, Ion-gun

Laser

Type : Hurricane (Spectra Physics)

Fundamentals : 750-800 nm

BL6B

UHV-STM beam line

This beam line is constructed for the atom level characterization of the SR illuminated surfaces by the in situ observation of STM. The beam line is very simple and has only one bent cylindrical mirror as optical components for high flux of photons to irradiate.

The STM experimental system designed so that the SR beam can illuminated the sample surface just under the STM chip, the STM observation can be made just after the SR illumination without the sample transfer. The short undulator which is going to be inserted to the strait part of the storage ring and emit the beam for BL7A, is under construction. The beam line and the UHV-STM station are going to be moved to the end of the new BL7A after the completion of the undulator.

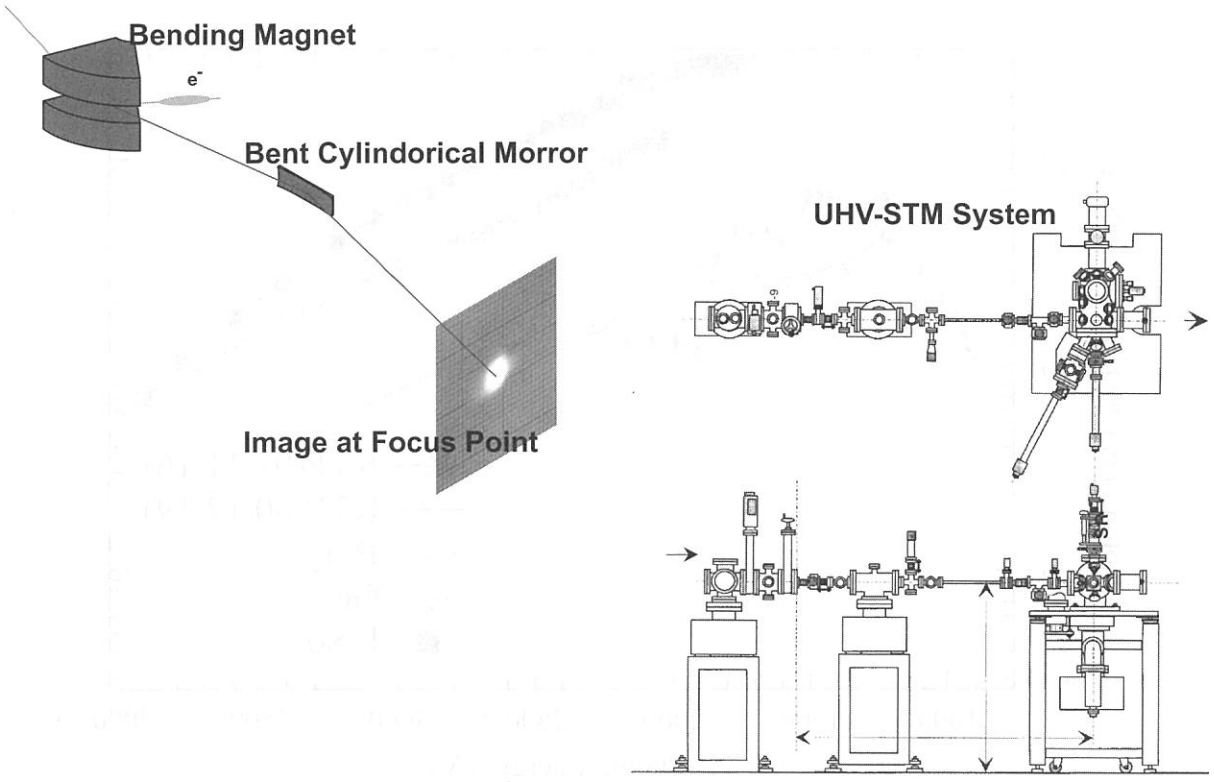

Specification

Specification: whole range of synchrotron radiation from UVSOR

Beam spot size at focus point: 4.5 mm x 4.5 mm

BL7A

Soft X-ray Spectrometer for Solids

The beamline BL7A equipped with a double crystal monochromator was constructed for spectroscopic investigation on solids in the soft X-ray range (0.6 to 5 keV). In order to make the NEXAFS experiments at the Mg (~1300 eV) and Al (~1550 eV) *K*-edges possible, a pair of $KTiOPO_4$ [KTP] (011) crystals was. In the past, it has been necessary to use beryl and quartz crystals to approach these two edges. It is found that the photon intensity from the KTP crystals without the wiggler is almost the same as that from the YB_{66} crystals combined with the wiggler.

Fig. 1 shows the absolute photon flux curves for several monochromator crystals over the photon energy range 800~4000 eV. The photon energy ranges suitable for Beryl, KTP, InSb, and Ge crystals are 0.83-1.5 keV, 1.2-2.5 keV, 1.8-4.0 keV, and 2.0-4.0 keV, respectively. It has been decided that all the activity on this beamline will be transferred to BL1A during the periodic shut down in the spring of 2002.

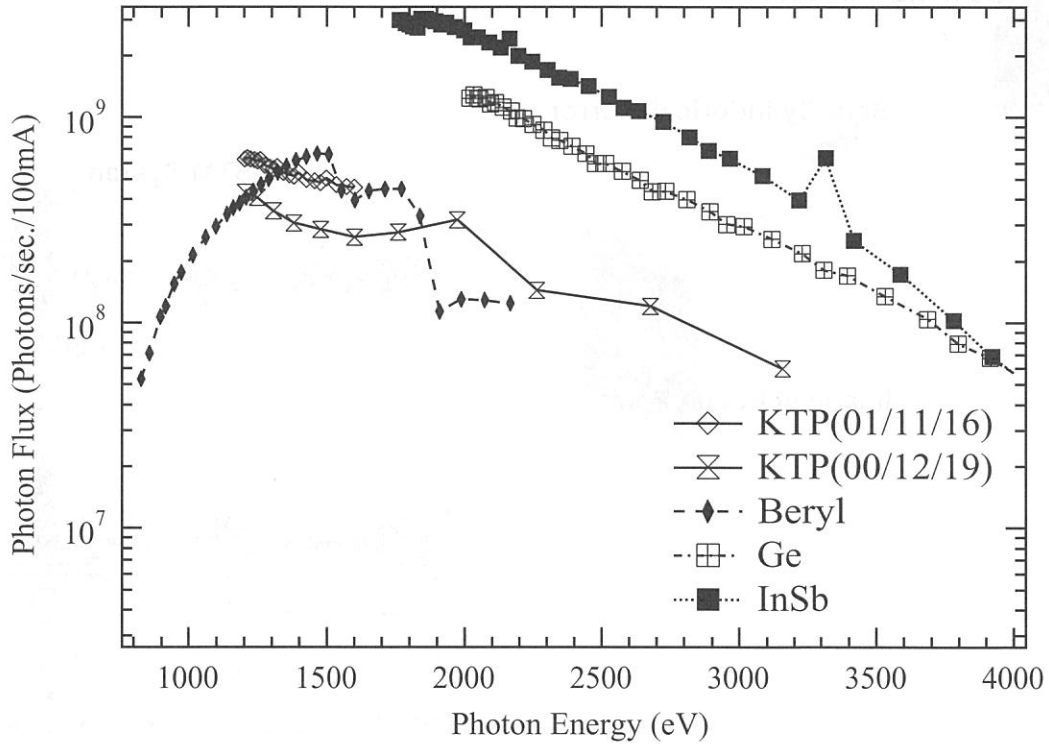

Figure 1. Absolute photon fluxes of main monochromator crystals on BL7A.

Specification

Monochromator: Double-Crystal

Energy range: 0.6~4.0 keV

Experiments: X-ray absorption (by total electron- or fluorescence-yield methods)

BL7B

3-m Normal Incidence Monochromator for Solid-State Spectroscopy

BL7B has been constructed to provide sufficiently high resolution for conventional solid-state spectroscopy, enough intensity for luminescence measurements, a wide wavelength coverage for Kramers-Kronig analyses, and the minimum deformation to the polarization characteristic of the incident synchrotron radiation. This beamline consists of a 3-m normal incidence monochromator which covers the vacuum ultraviolet, ultraviolet, visible and infrared, i.e. the wavelength region of 40–1000 nm, with three gratings (1200, 600, and 300 l/mm). Two interchangeable refocusing mirrors provide two different focusing positions. For the mirror with the longer focal length, an LiF or a MgF_2 window valve can be installed in between the end valve of the beamline and the focusing position.

Fig. 1 shows absolute photon intensity for each grating with the entrance and exit slit openings of 0.5 mm. A silicon photodiode (AXUV-100, IRD Inc.) was utilized for measuring the photon intensitiy and the absolute photon flux was estimated, taking the quantum efficiency of the photodiode into account.

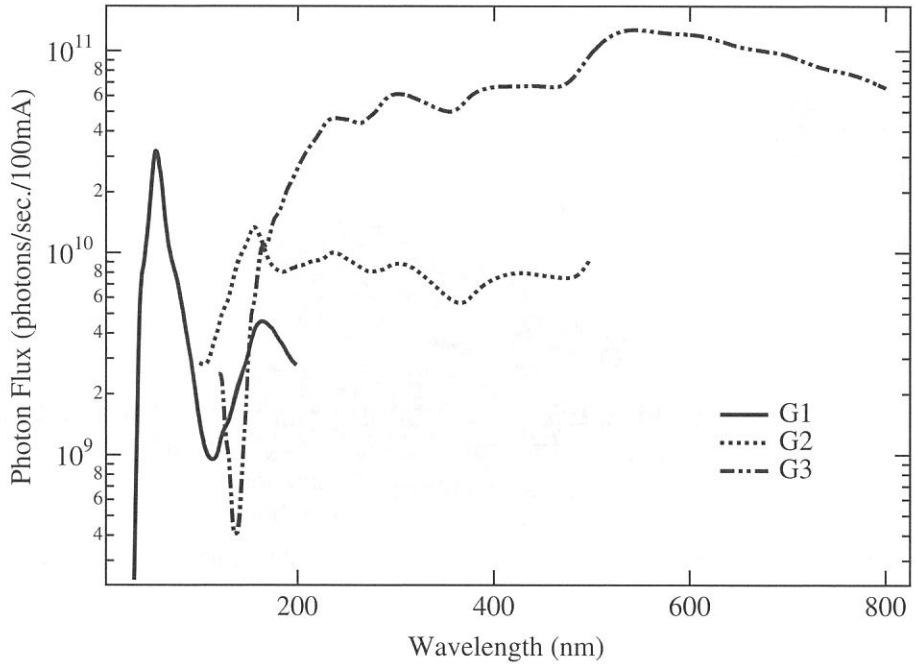

Figure 1. Throughput spectra of BL7B measured by a silicon photodiode.

Specification

Monochromator: 3-m Normal Incidence Monochromator
Energy range: 50 to 1000 nm (1.2-25 eV)
Resolution: $E/\Delta E$= 4000-8000 for 0.01 mm slits
Experiments: absorption, reflection, fluorescence spectroscopy, mainly for solids

BL8A

Free Port

BL8A was constructed as a free port. Synchrotron radiation is introduced into a sample chamber either directly or through a focusing mirror. Main experiments performed at BL8A are photochemical reaction, SR-CVD, photo-etching, irradiation damage effects in a condensed phase.

Since this beamline has no monochromator between the bending magnet and the sample chamber, the samples brought by users can be irradiated by white light. A gold mesh is installed in the sample chamber to monitor the intensity of the incident radiation.

The beamline consists of a front-end chamber, a focusing pre-mirror chamber and a differential pumping system with three stages. By the use of this system, one can perform various experiments at the reaction chamber under vacuum condition up to 0.5 Torr, while keeping ultra high vacuum at the pre-mirror chamber. This means that any kind of experiment in a gas phase is also possible at the reaction chamber without any windows.

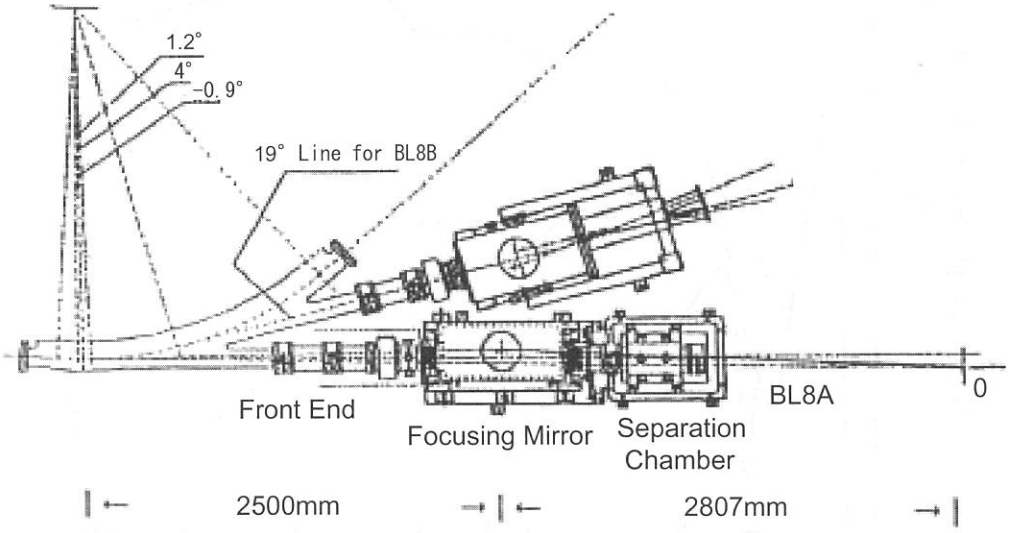

Specification

Acceptal angles (with mirror) : 25 mrad (horizontal) × 8mrad (vertical)
(without mirror) : 7.7 mrad (horizontal) × 8mrad (vertical)
Beam spot size :3mm (horizontal) × 2mm (vertical)
Energy range: Whole energy range of the dipole radiation at UVSOR

BL8B1

Photoabsorption and Photoionization Spectrometer

BL8B1 was constructed for various spectroscopic investigations in a gas phase under high resolution condition in the photon energy range from 30 to 800 eV, where the 1s ionization thresholds of chemically important elements like C, N, and O lie. The monochromator is a constant-deviation constant-length spherical grating type (CDCL-SGM). With three gratings (G1: R = 15 m; 1080 l/mm, G2: R = 15 m 540 l/mm, G3: R = 7.5 m; 360 l/mm), this monochromator is designed to cover the photon energy region of interest mentioned above. The typical resolving powers achieved are about 4000 at 400 eV and 3000 at 245 eV. The absolute photon flux for each grating measured by a silicon photodiode is shown in Fig. 1, with the slit openings of 10 μm.

The experimental chamber with a time-of-flight mass spectrometer and a photoelectron energy analyzer is installed at the downstream of the monochromator. This allows us to carry out photoelectron - photoion coincidence (PEPICO) and photoion - photoion coincidence (PIPICO) measurements. Measurements of absorption, electron yield and emission spectra of solid samples are also feasible.

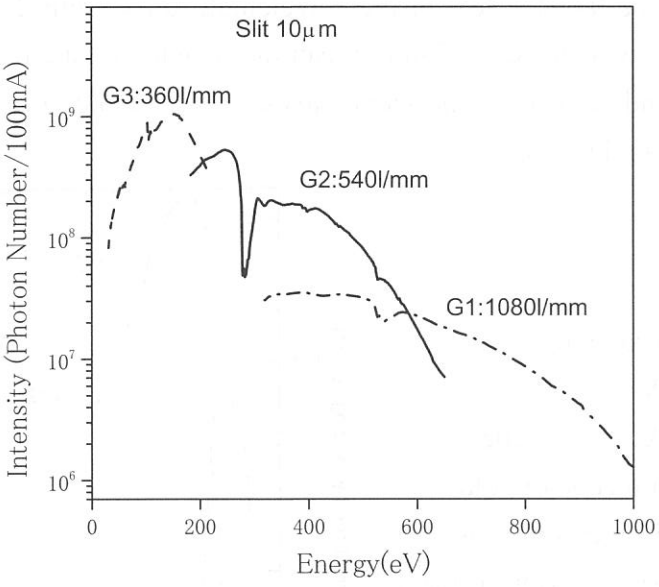

Figure 1. Absolute photon fluxes measured by a Si photodiode

Specification

Monochromator: Constant-deviation constant-length spherical grating type

Wavelength range: 30 to 800 eV

Resolution: $E/\Delta E$ = 4000 at 400 eV and 3000 at 245 eV

Available Experiments: Photoabsorption spectroscopy for gas and solid samples, coincidence experiments for gas samples

BL8B2

Angle-Resolved Ultraviolet Photoelectron Spectrometer for Solids

BL8B2 is a beamline for angle-resolved ultraviolet photoemission spectroscopy (ARUPS) system which is designed for measuring various organic solids such as molecular crystals, organic semiconductors, and conducting polymers. The beamline consists of a plane-grating monochromator (PGM), a sample preparation chamber with a fast entry Load-Lock chamber, a measurement chamber with an accurate for temperature dependence (base pressure 1×10^{-10}Torr), a cleaning chamber (base pressure 1×10^{-10}Torr), and a sample evaporation chamber (base pressure 3×10^{-10}Torr). The cleaning chamber is equipped with a back-view LEED/AUGER, an ion gun for Ar^+ sputtering, and an infrared heating unit. The PGM consists of premirrors, a plane grating, focusing mirror, and a post-mirror, with an exit slit. It covers the wide range from 2 to 150eV with exchanging two gratings (G1: 1200l/mm, G2: 450l/mm) and five cylindrical mirrors. The toroidal mirror focuses the divergent radiation onto the sample in the measurement chamber. The spot size of the zeroth-order visible light at the sample surface is about $1\times1mm^2$. The energy resolution at a slit width of 100μm was found to be 0.004-0.3eV in the wavelength range from 2 to 130eV. A hemi-spherical electron energy analyzer of 75mm mean radius with an angular resolution less than 2° can be rotated around vertical and horizontal axes. The sample mounted on a manipulator can be also rotated around two axes.

Specification

Monochromator:

Plane Grating Monochromator

Energy range: 2-150eV

Resolution: 100meV at 40eV as determined by the Fermi edge of gold

Experiment: Angle-resolved photoelectron spectroscopy (ARUPS) for various organic solids

Polarization: 85~91% at 500nm

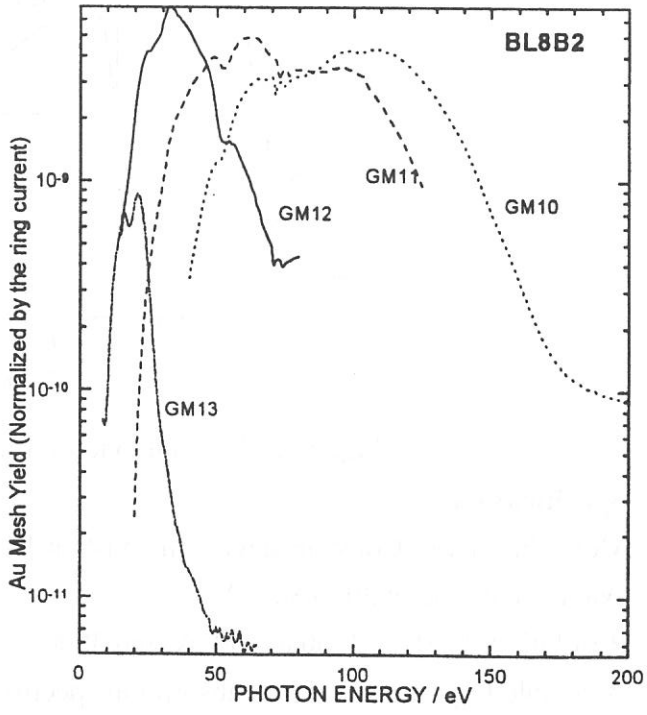

Figure Throughput spectra of plane-grating monochromator at BL8B2 with 100 μm exit slit.

Accelerators and Beam Physics

New BPM System

K. Hayashi, M. Katoh, M. Hosaka, A. Mochihashi, T. Kinoshita, J. Yamazaki, Y. Takashima, T. Honda[A], S. Koda[B]

Institute for Molecular Science, Myodaiji, Okazaki, Japan
[A)]KEK-PF, Oho, Tsukuba, Japan
[B)]Saga University, Honjo-machi, Saga, Japan

A new beam position monitor system was successfully comissioned at UVSOR storage ring. The new system comprises 16 signal-processing modules, which are commercial products of Bergoz Co. [1]. In these modules, the bunch signals are filtered at the RF frequency (90MHz). The 90MHz signals are down-converted to an intermediate frequency. They are amplified and detected. In the new system, all the electrodes are connected directly to the modules. There are no switches. Typical length of the cables is about 15 m. The lengths of four cables for one BPM head are adjusted with an accuracy of a few cm. The modules output two DC-voltage signals, which are proportional to the beam position in horizontal and vertical. They are AD-converted with 16-bit resolution and a cycle of 1 kHz. The data are averaged over one second to improve the resolution. The data are stored in a PC and sent to the main control system [2]. A schematic drawing of the system is shown in Figure 1.

The standard deviations of the beam position data were measured for various values of beam current, as shown in Figure 2. For the beam current higher than 10 mA, the standard deviations are smaller than a few microns.

New system has revealed orbit drifts in various time scales. In Figure 3, typical orbit drifts in a users run are shown. UVSOR is typically operated for users as follows. After the beam injection, the beam energy was ramped from 600MeV to 750MeV and the orbit was corrected. Then the users experiments start. The data in Figure 3 started also at this moment. There can be seen a rapid drift, especially in horizontal, during the first ten minutes. In vertical, there can be seen a slow drift in time scale of hours. The amplitudes of the drift motions are a few hundreds of microns.

In Figure 4, another example of the orbit movement is shown. These data were taken when the temperature control system of the cooling water was malfunctioned. The temperatures of the cooling water of the magnets and the vacuum chambers were fluctuated with amplitudes of about 2 degree and periods of about 10 minutes. This was caused by periodic on and off of the cooling tower. There can be seen orbit movements in horizontal and vertical synchronized with the temperature changes. The amplitudes are about a few tens of microns.

The beam position monitor system at UVSOR was replaced this year. New system was successfully commissioned. It is providing a set of beam position data every second with a resolution of a few microns. It saves the time for orbit correction significantly. It has revealed the orbit drift at UVSOR in users operations. Their origins will be investigated further with the beam position data. The orbit stabilizing system will be constructed based on the new system in future.

References

[1] http://www.bergoz.com
[2] N. Kanaya et al., Nucl. Instr. Meth. A 352 (1994) 166

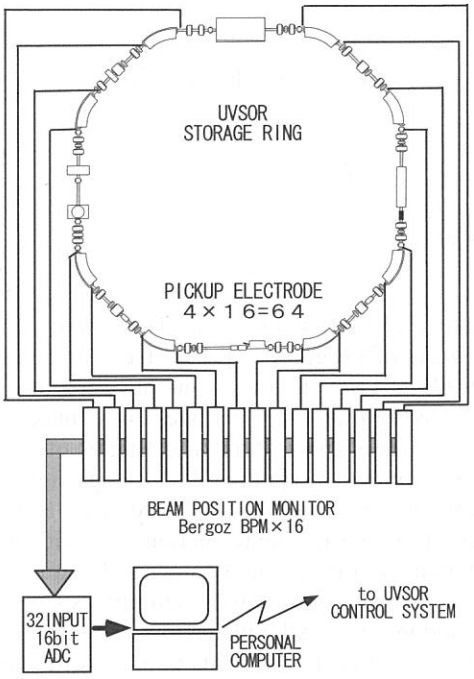

Fig.1 Schematic drawing of new BPM system

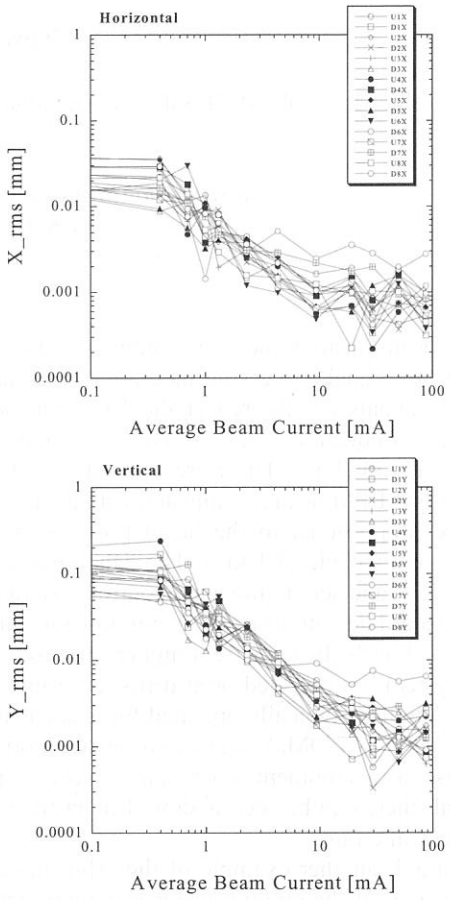

Fig. 2 Standard deviations of beam position data. Those for five samplings are shown against various beam currents. The data from all 16 BPMs are shown. The upper is horizontal and the lower vertical.

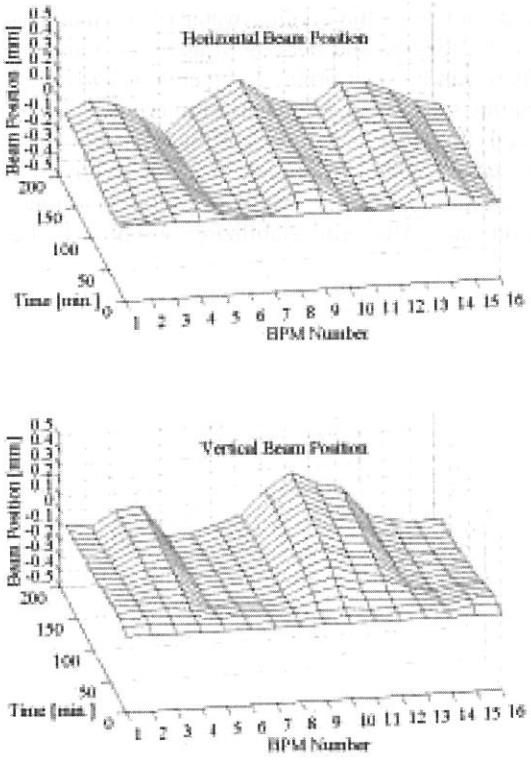

Fig. 3 Typical orbit drift observed during a users operation
The upper is the horizontal data and the lower the vertical data. The data interval is about 10 minutes.

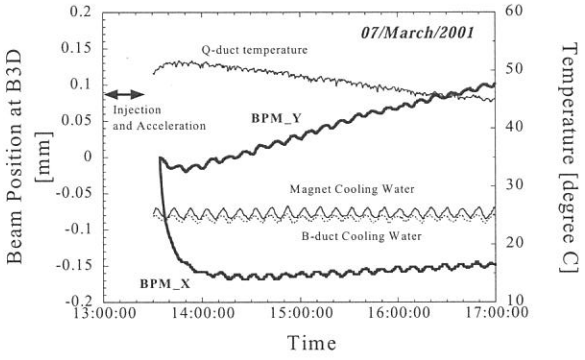

Fig. 4 Orbit movement caused by temperature fluctuations of the cooling waters for magnets and vacuum chambers Beam position at one BPM (B3D) is shown.

DEVELOPMENT OF COMBINED-FUNCTION FOCUSSING MAGNET

J. Yamazaki, M. Katoh, Y. Hori, M. Hosaka, A. Mochihashi, T. Kinoshita, K. Hayashi,
Y. Takashima, S. Koda[A],
Institute for Molecular Science, Myodaiji, Okazaki, Japan
[A)]Saga University, Honjo-machi, Saga, Japan

In the upgrade plan of UVSOR that will be started in FY2002, the original magnetic lattice will be modified to reduce the emittance and to increase the number of straight sections for insertion devices. We have completed the lattice design [1].

In the new lattice, the space limitation is very severe. In some of the modern light sources, sextupoles are integrated in the quadrupole magnets, to save the space and reduce the cost [2, 3]. They are successfully operational. We decided to introduce this type of magnet. There are several types of configuration. We have adopted the configuration as shown in Figure 1. The shape of the iron core is same as ordinary quadrupoles. The auxiliary coils on the pole face (sextupole coils) produce both dipole and sextupole fields. Other auxiliary coils on the poles (dipole correction coils) eliminate the dipole field. The main parameters of the magnet are summarized in Table 1.

A prototype was constructed as shown in Figure 2. Field measurements were completed. Some results from the field measurements are shown in Figure 3, 4 and 5. It was proved that the quadrupole and sextupole field required from the lattice could be achieved well below the maximum excitation current. It was also proved that the dipole field could be eliminated by exciting the dipole correction coils, for the typical operational currents of quadrupole and sextupole. However, at around the maximum excitation of quadrupole and sextupole where the iron core is saturated, it was found that the dipole field could not eliminated even with the maximum excitation of the dipole correction coils. In the final design, this point will be improved either by increasing the maximum current of the correction coils or by increasing the thickness of the iron cores.

References

[1] M. Katoh et al., Nucl. Inst. Meth. A467-8 (2001), 68
[2] M. Barthes et al., Proc. 9th International Conference on Magnet Technology (Zurich, 1985), p.114
[3] M. Eriksson, Proc. Of 5th European Particle Acc. Conf. (Sitges, 1996), 72

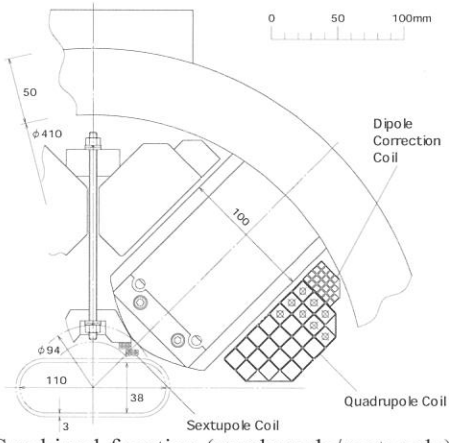

Fig.1 Combined-function (quadrupole/sextupole) magnet (cross-sectional view)

Table 1. Parameters of combined-function magnet

Core Length	0.2 m
Bore Diameter	94 mm
Quadrupole Coil	625A x 24 turns
Sextupole Coil	400A x 4 turns
Dipole Correction Coil	40A x 21 turns
Maximum Quadrupole Field	15 T/m
Maximum Sextupole Field	35 T/m^2

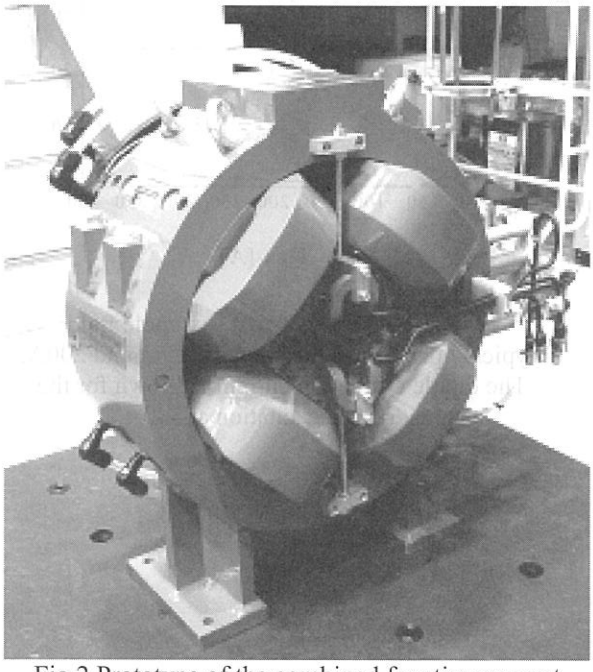

Fig.2 Prototype of the combined function magnet

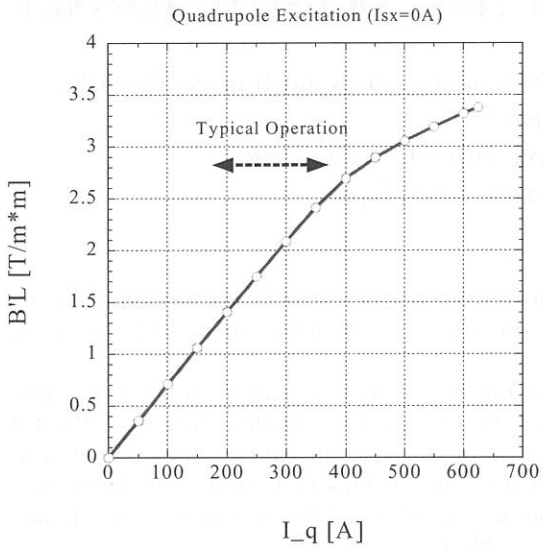

Fig.3 Excitation curve of quadrupole field
Typical operational current will be around 400A.

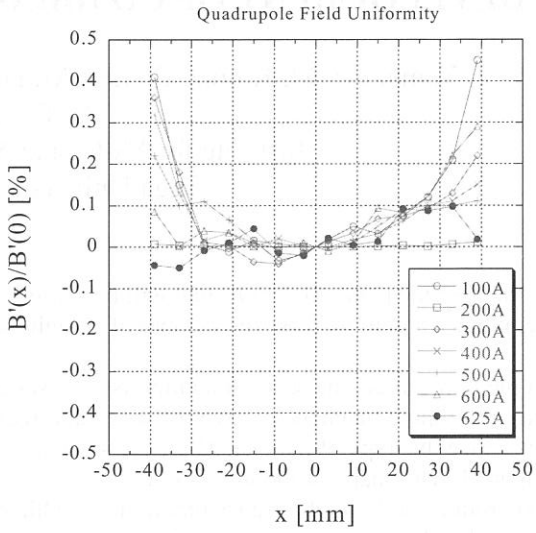

Fig.4 Excitation curve of quadrupole field
Typical operational current will be around 400A. The end shimming is optimised at the maximum excitation current (625 A).

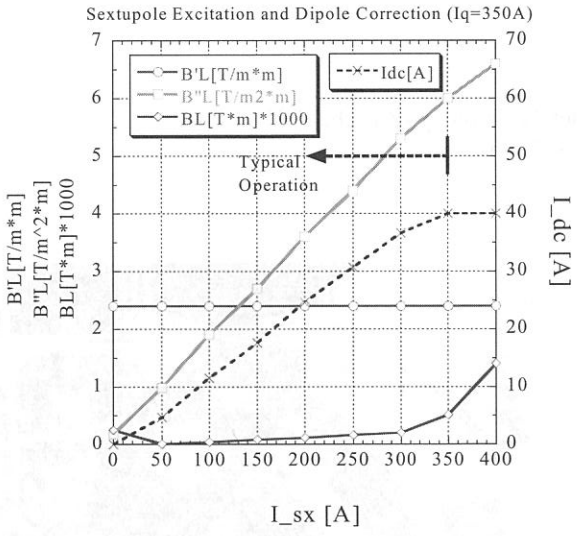

Fig.5 Excitation curve of sextupole field
Typical operational current will be around 200A.
The dipole correction current is shown for the quadrupole excitation at 300A.

Vertical Instability in Multi Bunch Operation in UVSOR

A. Mochihashi, K. Hayashi, M. Hosaka, M. Katoh, T. Kinoshita, J. Yamazaki, Y. Takashima*

UVSOR Facility, Institute for Molecular Science, Myodaiji, Okazaki 444-8585, Japan
**Institute for Molecular Science, Myodaiji, Okazaki 444-8585, Japan*

In the UVSOR electron storage ring a vertical beam instability has been observed in a multi bunch operation, even though it is very weak enough to neglect influence on SR users. To verify the cause of the instability, we have observed betatron oscillation for single/multi bunch condition in the UVSOR storage ring. Firstly, we have observed dependence of a vertical tune on the beam current at the single bunch condition. In the experiment, we analyzed beam signals from a pick-up electrode with a spectrum analyzer and observed the betatron oscillation of the beam. Figure 1 shows the dependence of the vertical tune on the beam current in the single bunch condition. The ordinate of the figure corresponds to the measured tune shifts from the tune of the highest beam current in the experiment. As seen in Fig. 1, the tune tends to decrease linearly as the beam current increases. From the experiment, the current dependence of the vertical tune $\left(\frac{\Delta\nu_y}{\Delta I_b}\right)_{exp.}$ is estimated at (-53.8 $\pm$ 4.03) $\times 10^{-6}$ /mA. Such dependence in the single bunch condition seems to be caused by a wake field that causes head-tail instability[1]. The current dependence of the tune $\left(\frac{\Delta\nu_y}{\Delta I_b}\right)$ due to the wake field is approximately given by[1]:

$$\frac{Z_0^{\parallel}}{n} \approx \frac{2q\gamma b^3\omega_y}{\epsilon_0 c r_e R C}\left(\frac{\Delta\nu_y}{\Delta I_b}\right), \tag{1}$$

where $\frac{Z_0^{\parallel}}{n}$ is longitudinal impedance of the storage ring, q an electron charge, γ the Lorentz factor of the beam, b radius of vacuum chamber, ω_y the vertical betatron oscillation frequency, ϵ_0 the dielectric constant of the free space, c the speed of light, r_e the classical electron radius, R the average radius of the storage ring and C the circumference of the ring, respectively. With the experimental value of $\left(\frac{\Delta\nu_y}{\Delta I_b}\right)$ and Eq. (1) we estimated that the longitudinal impedance is 2.46$\pm$0.20 Ω. An analysis of the longitudinal impedance from bunch lengthening in UVSOR[2] has concluded that $\frac{Z_0^{\parallel}}{n} = 1.6\ \Omega$, that is almost the same value as the analysis from the theory of the head-tail instability.

Secondly, we have observed the dependence of the vertical tune on the beam current in the multi bunch condition in which a series of 12 bunches (a bunch train) followed by a series of 4 empty buckets (a bunch gap) are stored in the ring. Because vertical spontaneous oscillation has been observed in the multi bunch condition we have measured the vertical tune by observing the spontaneous oscillation, not using RF-KO method. In the experiment, the vertical tune was observed above 169.4 mA because the spontaneous oscillation was not able to be observed below the beam current. Figure 2 shows the change in the vertical tunes in the multi bunch condition. The ordinate of the figure corresponds to the measured tune shifts from the tune of the highest beam current in the experiment. To emphasize phenomena in the multi bunch condition, we subtracted the current dependence of the vertical tune in the single bunch condition $\left(\frac{\Delta\nu_y}{\Delta I_b}\right)_{exp.}$ from the multi-bunch experiment. As seen in the figure, the change in the tune due to the change in the beam current still remains after the subtraction, and especially, the tune has step-like changes around the bunch current of 15 and 30 mA. Such a change in the tune in the multi bunch condition could be caused by trapped ion effect[3][4]. According to the classical theory of the ion trapping, an electric field induced by the ions trapped by the electron beam could increase the tune, and the change in the tune is proportional to the ion density. Because a trapping condition of the ions depends not only on configuration of the bunch train but also on a beam size, the condition differs at different positions in the ring under the same configuration of the ring. We calculated a ratio of the total area of regions where the ions are trapped to the area of the whole UVSOR-ring in various configurations of the bunch train. The results are shown in Fig. 3 and 4. These figures show with contour lines the ratio for various configurations of the train. In the calculation[5], ion species of CO^+ and CO^{2+}, which are the main components of the residual gas molecules in the UVSOR-ring, are assumed. As seen in these figures, the ratio has sudden changes at the bunch train length of 12 bunches around the bunch current of 15 mA in CO^+ and 30 mA in CO^{2+}. The bunch current at the sudden changes in the calculation corresponds to the bunch current in which the vertical tune has step-like changes, namely, the tune increases at the bunch current where the ratio also increases and has little change at the bunch current where the ratio also has little change. Therefore, it is

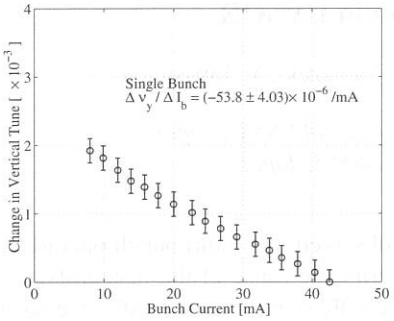

Figure 1: Dependence of the vertical tune on the beam current in the single bunch condition.

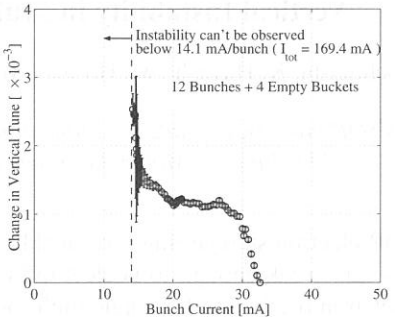

Figure 2: Dependence of the vertical tune on the beam current in the multi bunch condition.

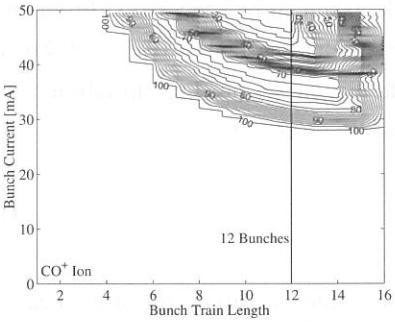

Figure 3: The ratio of the area of the regions where the CO^+ ions are trapped to the area of the whole ring for various bunch train lengths.

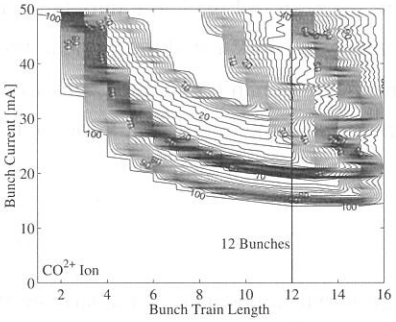

Figure 4: The ratio of the area of the regions where the CO^{2+} ions are trapped to the area of the whole ring for various bunch train lengths.

supposed that the change in the tune observed in the multi bunch condition is caused by the change in the trapping condition of the residual gas ions. To verify the cause of the vertical instability, more detailed experiments for the phenomenon are necessary. Development of a bunch-by-bunch beam diagnostic system and bunch-by-bunch beam diagostics with the system are future plans.

References

[1] A. W. Chao,
Physics of Collective Beam Instabilities in High Energy Accelerators,
(Wiley-Interscience Publication, New York, 1993)

[2] M. Hosaka, J. Yamazaki, T. Kinoshita and H. Hama,
UVSOR Activity Report 1997, p. 29.

[3] R. D. Kohaupt,
DESY, Interner Berichit No. H1-71/2, 1971.

[4] Y. Baconnier, G. Brianti,
CERN Internal Report No. CERN/SPS/80-2(DI), 1980.

[5] A. Mochihashi, T. Kasuga, T. Obina, Y. Tanimoto,
in *Proceedings of the International Workshop on Two-Stream Instabilities in Particle Accelerators and Storage Rings, Tsukuba, 2001.*(to be published)

Feasibility Study of Generation of Ultrashort Pulses of Synchrotron Radiation at UVSOR

Y.Takashima, M.Katoh[A], M.Hosaka[A], A.Mochihashi[A], T.Honda[B], T.Kinoshita[A], J.Yamazaki[A], K.Hayashi[A], Y.Hori[A,B]

Department of VUV Photo-science,Institute for Molecular Science, Okazaki 444-8585 Japan
[A)]UVSOR Facility, Institute for Molecular Science, Okazaki 444-8585 Japan
[B)]Photon Factory, Institute of Materials Structure Science, High Energy Accelerator Research Organization (KEK), Tsukuba, 305-0801 Japan

1. Introduction

We have been considering a method for the generation of ultrashort pulses of synchrotron radiation from UVSOR storage ring.

A pulse width of synchrotron radiation is the same as a bunch length of electron beam circulating in a storage ring and is usually several tens to several hundreds picoseconds. In order to obtain ultrashort photon pulses, we have been studying the feasibility of the bunch slicing technique [1,2]. The bunch slice can be achieved by using a femtosecond laser pulse passing together with an electron bunch through in an undulator. We tune the undulator to the wavelength of the laser, so that the energy of electrons overlapped with the laser are modulated by the interaction with the laser field. If the energy modulation is several times lager than the r.m.s. energy spread of the electron beam, the modulated electrons are separated spatially when the electrons pass through a dispersive section as shown in Fig. 1. The sliced electrons emit displaced synchrotron radiations in bending magnets or insertion devices. We can obtain ultrashort photon pulses by using a collimator and optical systems in order to transmit and focus on the radiations emitted from sliced electrons.

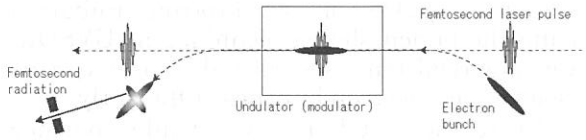

Fig.1. Sketch of bunch slicing technique.

2. Experimental Equipment

Fig. 2 shows an example of experimental setup to generate ultrashort photon pulses. We will use the existing BL5A undulator as an energy modulator in which circulating electrons interact with the laser pulses.

A mode-locked Ti-sapphire laser and an ultrafasst regenerative amplifier is used to make femtosecond laser pulses which should have enough power to make sufficient energy

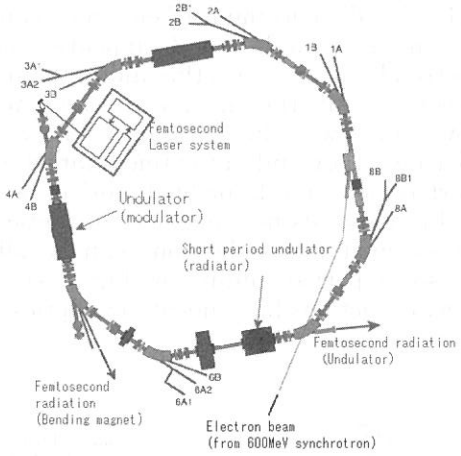

Fig. 2. Layout of experimental equipment.

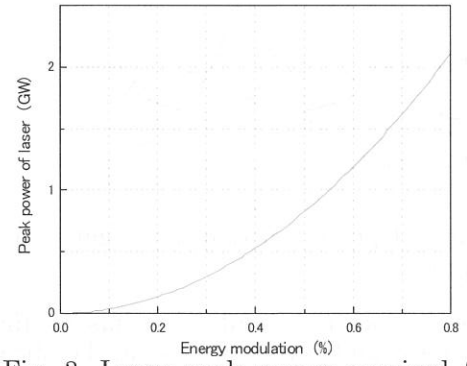

Fig. 3. Laser peak power required for energy modulation.

modulation in order to slice the electron bunches. Fig. 3 shows the required peak power of the laser to make the energy modulations. In this calculation, we supposed that the energy of electron beam was 750 MeV, the wave length and the pulse width of the incident laser were 800 nm and 100 fs, respectively. We also supposed the horizontal beam spread of UVSOR storage ring was about 0.5 mm (r.m.s.), and the value of the horizontal dispersion function in the bending magnet was about 0.6 m. If we intend to spread the electron bunch up to 2.5 mm (r.m.s.), 0.4 % of energy modulation is needed and we have to employ 500 MW peak power laser.

The intensity of the ultrashort radiation is proportional to the number of sliced electrons. The width of the laser pulse is about 10^{-4} of the bunch length, and in addition, the repetition rate of the laser pulse (1 kHz) is about 10^{-5} of the RF frequency of UVSOR storage ring, so that the averaged intensity of the radiation is 10^{-9} of the intensity of synchrotron radiation from UVSOR storage ring under the normal operation.

In order to improve the intensity of the radiation, we have been considering using the short period undulator as a radiator which will be installed for BL7 of UVSOR storage ring [3,4]. The displacement of electrons caused by the energy modulation disappears when the electron bunch reaches the undulator since the dispersion function is free at the undulator. However, if we adjust the optics between the existing BL5A undulator (modulator) and the short period undulator (radiator) to be locally isochronous using negative-α optics, the energy modulated electrons can be sliced in the short period undulator. Fig. 4 shows the optical functions for a negative-α optics.

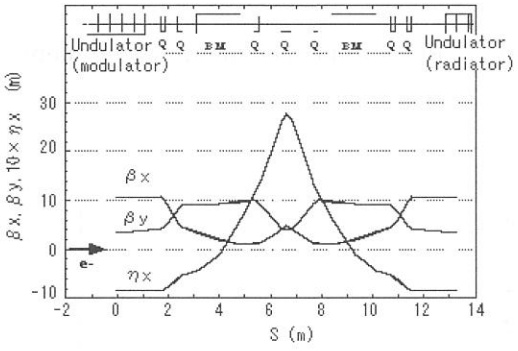

Fig. 4. Optical functions for negative-α optics.

Beam tracking simulations has confirmed that the modulated electrons can be sliced at the short period undulator. The SAD code developed in KEK for accelerator design [5] was used for the simulations. Fig. 5 shows the spatial distribution of electrons at the short period undulator. The electrons of the width of 100 fs in a bunch were modulated their energy up to 0.8 % randomly in the existing BL5A undulator and then traveled to the short period undulator.

3. Intensity of Ultrashort pulse radiation.

We calculated the spectra of ultrashort synchrotron radiation on the following assumptions: the r.m.s. spread of the sliced electrons was five times larger than the natural spread and the radiations emitted from the electrons displaced over three times

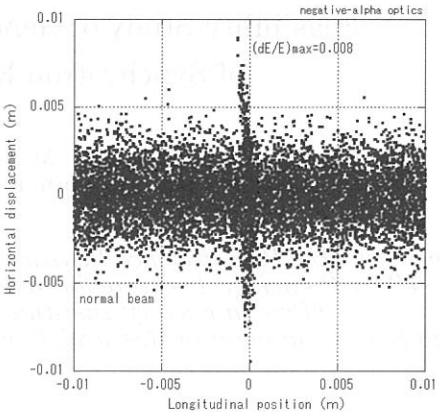

Fig. 5. Spatial distribution of electrons in BL7 short period undulator calculated by using SAD code.

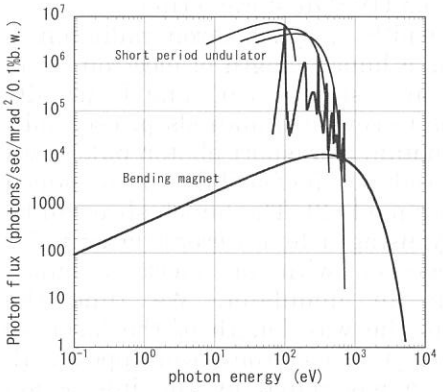

Fig. 6. Photon flux of ultrashort synchrotron radiation from short period undulator and BL5 bending magnet.

of the natural r.m.s. spread were observed. The wavelength and repetition rate of the incident laser were 800 nm and 1 kHz, respectively. Fig. 6 shows the photon fluxes generated in the short period undulator and BL5 bending magnet.

4. Summary

We have been planning to generate ultrashort pulse of synchrotron radiation using the bunch slicing technique at UVSOR. A commercial femtosecond pulse laser can be used to slice electron bunches sufficiently.

For further studying, we should consider methods to improve the peak intensity of the radiation.

References

[1] A.A.Zholents and M.S.Zolotorev, Phys. Rev.Lett., 76, 912 (1996)
[2] R.W.Schoenlein et al., SCIENCE, 287, 2237 (2000)
[3] M.Katoh et al., UVSOR Activity Report, UVSOR-28, 37 (2000)
[4] M.Katoh et al., Nucl. Instr. and Meth. A 467-468, 68 (2001)
[5] KEK Accelerator Theory Group, http://acc-physics.kek.jp/SAD/sad.html

Improvement of out-coupled power of the UVSOR-FEL

Masahito HOSAKA, Shigeru KODA, Akira MOCHIHASHI, Masahiro KATOH, Jun-ichiro YAMAZAKI, Kenji HAYASHI, Yoshifumi TAKASHIMA Tatsuo GEJO, Eiji SHIGEMASA, Eiken NAKAMURA, and Hiroyuki HAMA[a]

Institute for Molecular Science, Myodaiji, Okazaki 444-8585, Japan

[a]*Laboratory of Nuclear Science, Tohoku University, Sendai 980 Japan*

Storage ring free electron lasers (SRFELs) likely have a potentiality for scientific application as a unique light source because of, in addition to variable wavelength, good coherence and temporal feature. Recently an experiment using SRFEL combined with synchrotron radiation (SR) was begun at UVSOR. As the first experiment we have tried to demonstrate the relevance of SRFEL for a pump/probe experiment in the gas phase molecular science that is the double-resonant excitation of Xe [1]. Since the application experiment was planned, efforts to improve the performance of the FEL have been made from the application point of view. We have already developed a feedback system leading to a stable laser [2], with reduced jittering and intensity fluctuations that spoil a quality of the experimental data. Another significant requirement is out-coupled laser power of the FEL. In this report, we present efforts to increase the out-coupled laser power of the UVSOR-FEL and show the latest result.

The out-coupled power of SRFEL at the saturation is approximately given by,

$$P \approx \eta_c J_\varepsilon \sigma_\varepsilon e^{-1/2} P_{SR} \qquad [1]$$

where η_c (= transmittance/cavity loss) is the efficiency of a optical cavity, $J_\varepsilon (\approx 2)$ is the damping partition number of the synchrotron damping, σ_ε is the induced energy spread due to the FEL interaction and P_{SR} is the synchrotron radiation power. Since P_{SR} is proportional to the number of electrons stored in the storage ring, it is crucial to increase the stored electron beam in the storage ring. Therefore we tuned the booster synchrotron and the injection condition and succeeded to store the electron beam of more than 100 mA/bunch. However, Touschek life time of the electron beam is considerably short when the beam current is high. Then we increased the x-y coupling of the electron beam from 2% to 6 % using skew-quadrupole magnets and increased the life time.

In order to maximize the optical cavity efficiency in the region of the wavelength used for the application experiment, we have chosen a multilayer coating of Ta_2O_5/SiO_2 on the fused silica substrates for the cavity mirrors. Since the FEL gain large at a high beam current, numbers of layers were decided to reduce to be 19 and 21 layers for the rear mirror from which the laser is extracted and the front mirror, respectively, to obtain high transmission rate. Measured initial transmission rates at the wavelength of 570 nm were 0.2 % and 0.1 % for the 19-layer and the 21-layer mirrors, respectively. The round-trip loss in the optical cavity was initially measured to be 0.35 %, meanwhile the expected FEL gain is ~ 5 % at a beam current of 100 mA/bunch.

Beside optimizing the basic conditions for the lasing given in Eq [1], we have also developed a new operation of the storage ring: 4-bunch operation. In the ordinary FEL operation, two electron bunches are

stored with an equal spacing in the ring, whereas, in the 4-bunch operation, two more bunches are added next to the initial bunches. Then the stored beam current is simply doubled and the extracted power as well. Prior to this operation, we have investigated an effect of the coupled-bunch instability, which would be commonly predicted to be occurred. However, because there is an additional cavity operated at a third-harmonic frequency of the main cavity has been installed on the UVSOR to suppress the coupled-bunch instability in a multi-bunch operation for the user SR machine time, we could find a proper tuning angle for a passive operation of the harmonic cavity to stabilize the 4-bunch operation.

Fig.1 shows the demonstration of the FEL lasing in the visible region around 570 nm. The extracted power exceeds 1 W and is the highest in the SRFELs so far. Using the FEL, the application experiment has been carried out successfully and the relevance of SRFEL for it has been shown [1]. We are planning to extend the high power operation to the UV region.

References

[1] T. GEJO, E. SHIGEMASA, E. NAKAMURA, M. HOSAKA, S. KODA, A. MOCHIHASHI, M. KATOH, J. YAMAZAKI, K. HAYASHI,Y. TAKASHIMA and Hiroyuki HAMA, UVSOR ACTIVITY REPORT 2001 (2001)

[2] S. Koda, M. Hosaka, J. Yamazaki, M. Katoh, H. Hama, Nucl. Instr. and Meth., A 474 (2001) 211.

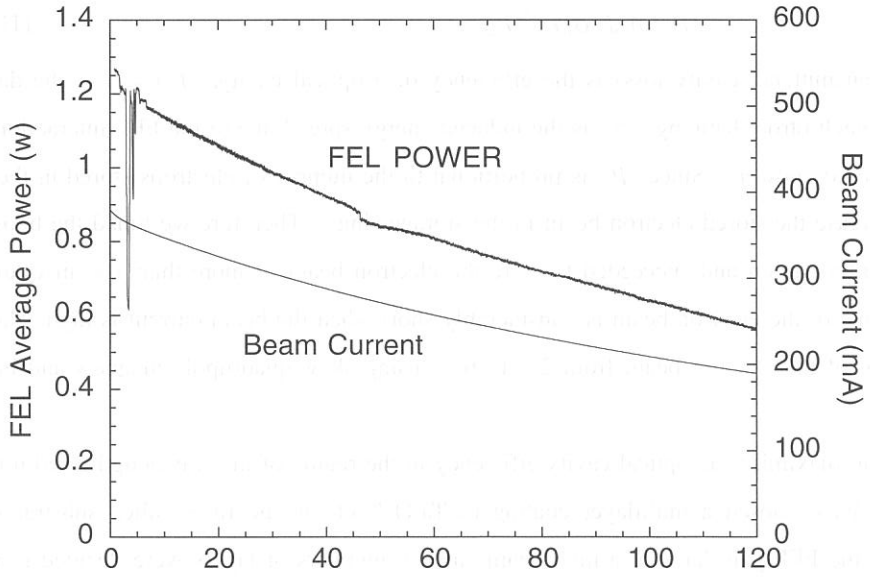

Fig. 1 Demonstration of the FEL lasing in the 4-bunch operation of the UVSOR storage ring. The extracted power exceeds 1 W.

In-Vacuum Undulator for UVSOR BL-7A

A. Mochihashi, K. Hayashi, M. Hosaka, M. Katoh, T. Kinoshita, J. Yamazaki, Y. Takashima[A], H. Kitamura[B], T. Hara[B], T. Tanaka[B]

UVSOR Facility, Institute for Molecular Science, Myodaiji, Okazaki 444-8585, Japan
[A]Institute for Molecular Science, Myodaiji, Okazaki 444-8585, Japan
[B]SPring-8, Institute of Physical and Chemical Research (RIKEN), Mikatsuki-cho 679-5148 Japan

An upgrade plan for the UVSOR[1] mainly aims to realize (1) smaller emittance and (2) more straight sections for insertion devices. The high brilliance beam optics is very suitable for insertion devices with narrow gap such as an in-vacuum undulator because vertical betatron functions for all the straight sections in the ring are very small ($\sim$1m). The in-vacuum undulator has been utilized as one of standard types of the insertion devices in SPring-8, and much technical knowledge for the undulators has been stored so far. However, there is no precedent in which this kind of the undulator has been installed in lower energy electron storage ring such as the UVSOR. Going ahead of the upgrade project, we plan to install the undulator and have a performance test in UVSOR BL-7A. Table 1 shows main parameters of the undulator. The minimum gaps of the magnetic poles are 20/10 mm for present/upgraded lattice, respectively. The period length is 36 mm, that results in very wide tunability in VUV and soft X-ray region, as shown in Fig. 1.

For the narrow gap undulators, a wall-current effect, that can cause not only heating of the magnetic poles but also beam instabilities, can't be neglected. We have estimated resistive wall heating on the magnetic poles by the wall-current for the single/multi bunch operation. The results are shown in Fig. 2. In this figure the gap height of 10 mm, that corresponds to the minimum value of the gap, is assumed. According to the calculation, the heating power in the maximum beam current in routine single/multi bunch operation (70/300mA in single/multi bunch operation) is about 0.2 W in the single bunch and 0.3 W in the multi bunch operation, therefore, it is expected that the heating effect is not so serious in our case. We have also estimated growth rates of resistive wall instability induced by the magnetic gap in the undulator. Figure 3 shows the growth rates for both the present and the upgraded lattice of the UVSOR when the beam current is 300 mA. According to the calculation, the growth rates are smaller than the radiation damping time even though in the minimum gap height, therefore, it is also expected that the effect of the resistive wall instability is not so serious in our case, too.

Installation of the in-vacuum undulator has been completed in March 2002. Figure 4 shows a photograph of the undulator just after the installation. After several basic performance test, we plan to investigate performance of the undulator as a light source in detail with the electron beam.

Magnet Type	Pure Permanent (Nb-Fe-B)
Remanent Field	1.17 Tesla
Period Length	36 mm
Number of Period	26
Magnetic Length	936 mm
Overall Length	1.4 m
Minimum Gap	10 mm (Low-β Optics)
	20 mm (Present Optics)
Max. K-parameter	2.27 (Low-β Optics)
	1.15 (Present Optics)
Polarization	Linear (Horizontal)

Table 1: Main parameters of in-vacuum undulator

References

[1] M. Katoh, *et al.*,
UVSOR Activity Report 2000, p. 38.

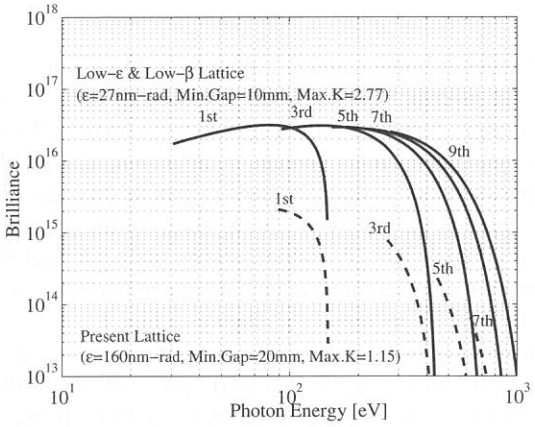

Figure 1: Calculated brilliance for the in-vacuum undulator.

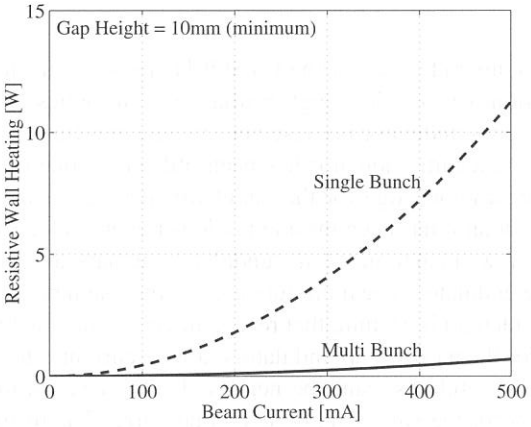

Figure 2: Calculation of the resistive wall heating on the magnetic poles in the in-vacuum undulator.

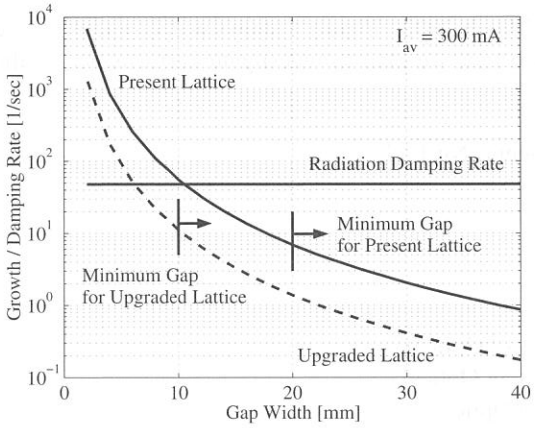

Figure 3: Calculation of the growth rates due to the resistive wall instability by the magnetic poles in the in-vacuum undulator.

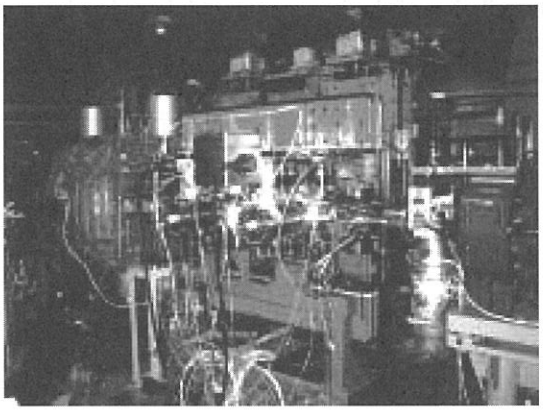

Figure 4: A photograph of the in-vacuum undulator just after the installation.

Instrumental Development

(BL8A)

Carbon contamination of SR mirror

Eiken Nakamura[1], Mikito Tadano[2], Hiroshi Sakai[2], Nobuhiro Terumuma[2], Masami Hasumoto[1], Junji Urakawa[2], Takashi Naito[2], Yasunori Tanimoto[2], Eiji Shigemasea[1]

[1] *Institute for Molecular Science, Okazaki 444-8585, Japan*

[2] *High Energy Accelerator Research Organization , 1-1 Oho Tsukuba 305-0801,Japan*

When SR irradiates an optical device, it is known well that carbon contamination will arise in an irradiation part. Carbon pollution of the optical device is a serious problem for the measurement of a SR beam line. Some kinds of optical measurement in carbon region have been made under the very difficult situation according to the experience of UVSOR. At KEK-ATF, the beam size measurement experiment in a visible region has been affected. It is coped with by exchanging the optical element polluted until now. It is important to remove or mitigate carbon contamination for the measurement of SR beam lines. We aim at finding the environment in which carbon contamination does not generate.

In order to investigate the growth rate of carbon contamination, the experiment has been performed by BL8A. The growth rate was compared by the measurement of the reflective intensity of laser light of 670nm with different conditions. The reflective intensity from SR irradiation part and a non-irradiation part was simultaneously measured, and the surface temperature and surface current of a mirror were also measured. We used three kinds of mirrors (Au coat mirror, Al coat mirror and Pt coat mirror). The experiment of this time was to measure the difference of reflection materials, gas purge effect and magnetic field effect.

Fig.1 shows the reflectivity as function of dose in three kinds of reflection materials of Au, Al and Pt. The material's dependence of the carbon contamination was clearly measured. However, an inspection of mirrors after SR irradiation indicates the contamination on both Al coat mirror and Au coat mirror, and not it on Pt coat mirror.

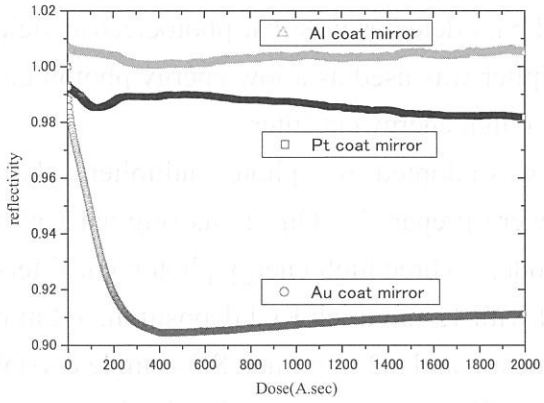

Fig.1: Reflectivity as a function of dose for reflection materials.

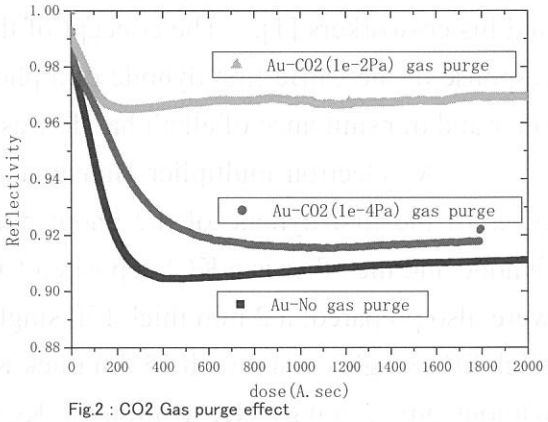

Fig.2 : CO2 Gas purge effect

The effect of a CO2 gas purge was investigated about an Au coat mirror (Fig.2). The reflection rate changes according to CO2 gas pressure. It is not clear whether the change comes from ozone generation by CO2-photon reaction or photon decrease by the absorption. The magnetic field effect was measured on Au coat mirror. There was no remarkable change in reflectance. However, the surface current was changing according to magnetic field intensity (Fig.3).

We have also measured about other effects. Interesting results were provided and can be expected in future experiment.

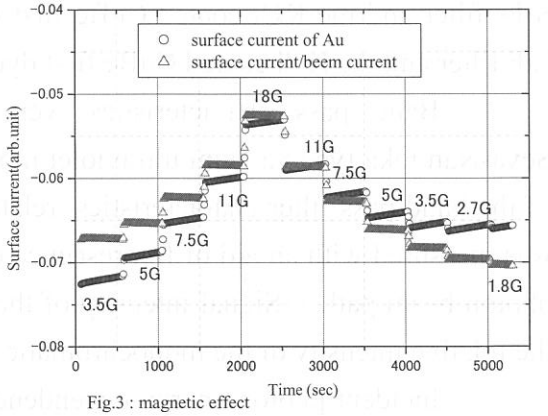

Fig.3 : magnetic effect

Referrence

[1] T.Naito et.al., *UVSOR Activity Report*, 2000, P63

(BL1B)

Characteristics of Vacuum Ultraviolet Region Band Pass Photon Detector for Inverse Photoelectron Spectrometer

Shojun Hino, Hiroyuki Kagitani and Kentaro Iwasaki

Faculty of Engineering and Graduate School of Science and Technology,
Chiba University, Inage-ku, Chiba Japan 263-8522

Inverse photoelectron spectroscopy is a powerful tool to investigate unoccupied electronic states. Inverse photoelectron spectrometer can be classified mainly into two categories according to the way of the measurement of emitted photon; one is using a monochromator of vacuum ultraviolet region and the other is using a photon band pass filter. We are now constructing an inverse photoelectron spectrometer equipped with the band pass filter constituted with an photo multiplier and an alkali halide window material, since band pass filters are less expensive and easily assembled to the vacuum chamber. In this report we describe the characteristics of our band pass photon detector of vacuum ultraviolet region.

Band pass detectors were fabricated according to the design proposed by Yokoyama and his co-workers [1]. The concept of their band pass detector was that photoelectric yield response of the CuBe first dynode of a photo multiplier was used as a low energy photon cut filter and transmittance of alkali halide was used as a high energy cut filter.

An electron multiplier Hamamatsu R595 was adopted as a photo multiplier. Two types of the first dynode of the photo multiplier were prepared. One is its original CuBe dynode and the other is a KCl deposited CuBe dynode. Three high energy photon cut filters were also prepared; a 2 mm thick LiF single crystal with 15 nm thick KCl deposition, a 2 mm thick SrF_2 single crystal with 15 nm thick KCl deposition and a 2 mm thick SrF_2 single crystal without any coating. Deposition of KCl onto the filters served to make the band pass narrower. We examined three types band pass detectors; detector A consists of the KCl coated SrF_2 filter and the normal CuBe first dynode, detector B consists of the KCl coated SrF_2 filter and the KCl coated CuBe first dynode and detector C consists of the KCl coated LiF filter and the KCl coated CuBe first dynode.

Band pass characteristics were measured at BL1B of UVSOR (a 1 meter Seya-Namioka type vacuum ultraviolet monochromator). Before and after the measurement of the band pass filter characteristics, relative photon intensity of the monochromatized light was measured with an aid of fluorescence emitted from a sodium salicylate film placed at the photon beam path. Signal intensity of the band pass detectors was normalized according to the relative intensity of the monochromatic light.

Incident photon energy dependence of three band pass detectors is shown in Fig. 1. Detector A has maximum sensitivity at 9.47 eV with 0.7 eV full width at half maximum

(FWHM) and its sensitivity is pretty low. Detector B shows maximum sensitivity at 9.5 eV with 0.5 eV FWHM. Deposition of KCl onto the first dynode (detector B) improves the sensitivity of the photon detector about three time compared with no KCl coated one (detector A) and pass energy width by 0.2 eV. It seems that detector B can be used as a narrow and sensitive band pass photon detector. The behavior of detector C is quite different from that of detectors A and B. Detector C has maximum sensitivity at 11.48 eV and with much wider FWHM of 1.85 eV. Its sensitivity is about ten times better than that of detector B, which is advantageous for the inverse photoelectron measurement of organic materials that is easily damaged by irradiation of electron beam. However, its wide FWHM together with a shoulder structure at 10.5 eV could be a serious problem for the materials that have unoccupied states situated very closely each other. Thus the best choice for the photon detector in the inverse photoelectron measurement may be detector B for less electron beam sensitive materials with crowded unoccupied states and detector C for electron beam sensitive materials with widely spaced unoccupied states.

References

[1] K. Yokoyama, K. Nishihara, K. Mimura, Y. Hari, M. Taniguchi, Y. Ueda, and M. Fujisawa, Rev. Sci. Instrum. 64, 87 (1993).

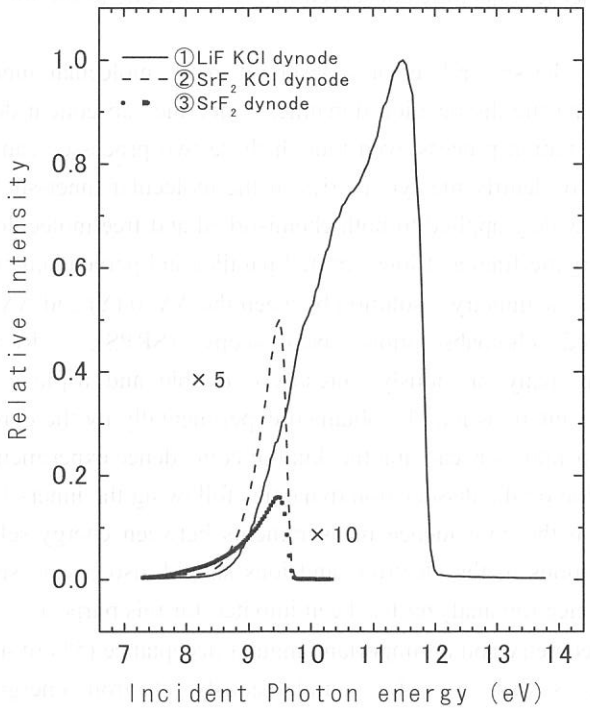

Fig. 1 Spectral response of three band pass photon detectors.

(BL4B)

New Apparatuses for Coincidence Measurements towards Understanding Dissociation Dynamics of Inner-Shell Excited Molecules

E. Shigemasa, N. Kondo, E. Nakamura, and T. Gejo

Institute for Molecular Science, Okazaki 444-8585, JAPAN

Thanks to the rapid progress of experimental techniques related to synchrotron radiation, vibrational spectroscopy in the inner-shell excitation region of low-Z molecules becomes feasible. The findings in the recent observations of the resonant Auger processes and their theoretical analyses impel us to give up the traditional idea that the molecular dissociation starts at the Auger final state where the Auger transition is terminated. This means that the Auger decay can not be treated separately from the primary photoexcitation process, that is, "break down of the two step model". In the case of photoionizaiton processes, the so-called post collision interaction (PCI) effect, which occurs in the Auger decay followed by near-threshold inner-shell photoionization due to the interaction between the Auger electron and the corresponding photoelectron, is known to illustrate such a situation. In addition, the contribution of multiple excitations owing to the electron correlation makes molecular inner-shell excitation processes near the thresholds complicated. Threshold electron spectroscopy (TES) is one of the most powerful techniques for probing the multiple excitations. A novel threshold electron spectrometer has been constructed for this purpose. The spectrometer is composed of a lens system based on the penetrating field technique [1] and an electrostatic analyzer (Comstock inc. AC-901 model), and its performance test is just beginning to be carried out. It is seen from the trajectories for photoelectrons with 5 meV kinetic energy shown in Fig. 1 that the potential well collects the threshold electrons over all angles. The asymmetric trajectories observed in Fig. 1 are due to the influence of the potential on the gas nozzle.

The interpretation of the spectral features observed in the molecular inner-shell excitation spectra is essential towards understanding the dissociation dynamics, since the subsequent decay processes never happen without the primary photoexcitation process even though these two processes can not be treated separately as mentioned above. In order to identify the symmetries of the molecular inner-shell excited states, polarization dependent studies have been widely applied to both chemisorbed and free molecules. For diatomic molecules, the measurements of the energetic fragment ions emitted parallel and perpendicular to the electric vector of the incident light achieve complete symmetry resolution between the $\Delta\Lambda=0$ (Σ) and $\Delta\Lambda=1$ (Π) transitions [2], which is called symmetry-resolved photoabsorption spectroscopy (SRPS). Recent high-resolution SRPS measurements for N_2 reveal many previously unresolved double and triple excitations. Further detailed information on the multiple excitations may be obtained experimentally by the combination of SRPS and TES. The construction of a new apparatus for realizing this kind of coincidence experiments has begun.

For detailed investigation on the dissociation dynamics following the inner-shell excitation and ionization, it is indispensable to perform the coincidence measurements between energy-selected electrons and ions, in which the angular distributions of the electrons and ions should also be measured. The construction of a high luminosity electrostatic electron analyzer has been initiated for this purpose. The design of the analyzer is based on a double toroidal geometry and an important angular acceptance (5% of 4π) [3]. Its two-dimensional position sensitive detection system provides simultaneously electron energy and angular distribution measurements. Fig. 2 shows a three dimensional view of the mechanical setup of the double toroidal analyzer. The test operation will be started in the near future.

References

[1] R.I. Hall et al., *Meas. Sci. Tech.* **3**, 316 (1992).

[2] E. Shigemasa et al., *Phys. Rev. A* **45**, 2915 (1992).
[3] C. Miron et al., Rev. Sci. Instrum. **68**, 3728 (1997).

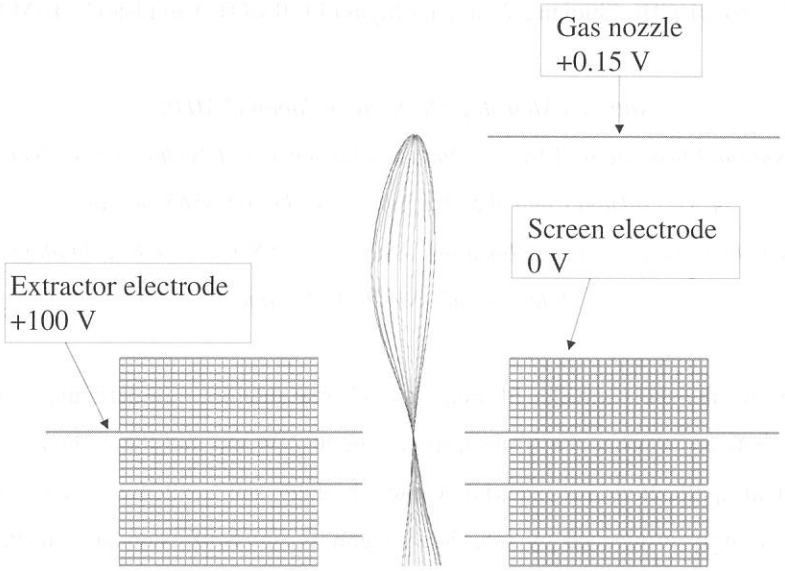

Fig. 1. Electron trajectories in the penetrating field geometry.

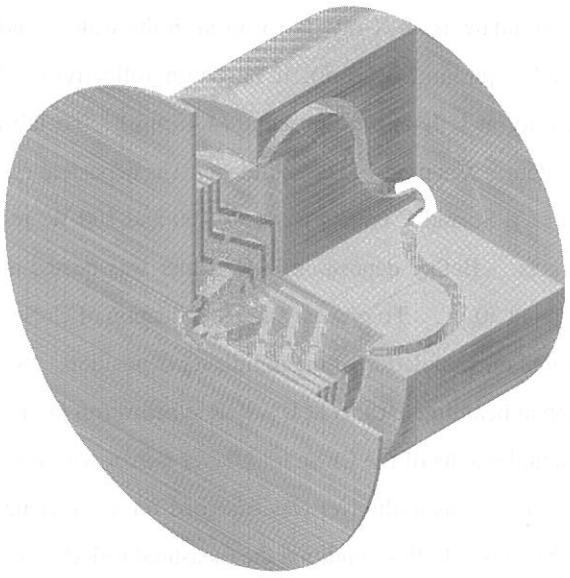

Fig. 2. Three dimensional view of the double toroidal analyzer.

(BL5B)

Reflectivity Measurements of Cr/Sc and Cr/C Multilayers for Soft X-rays

Tadayuki OHCHI, Shiqiang WEI*, Toshiyuki FUJIMOTO and Isao KOJIMA

National Metrology Institute of Japan (NMIJ),
National Institute of Advanced Industrial Science and Technology (AIST)
AIST Tsukuba Central 5, Tsukuba, Ibaraki 305-8565, Japan
**National Synchrotron Radiation Laboratory, University of Science and Technology of China*
Hefei, Anhui 230029, P.R.China

X-ray multilayers for the short wavelength range are of great interest. In particularly, multilayers for the water window region between the oxygen K-absorption edge at 2.34 nm and the carbon K-absorption edge at 4.38 nm have important applications for material science, biology and medicine. The reflectivity of such a multilayer mirror is strongly influenced by interface roughness, inter-diffusion and fluctuation of the layer thickness, because the layer thickness is extremely small. Thus fabricating multilayer with high performance is very difficult in this region. In order to fabricate the high performance X-ray multilayer mirror, it is necessary to prepare the multilayer films with high precisely and to analyze their structural properties for the improvement of its performance.

Cr/Sc multilayer mirror is a candidate as an X-ray mirror used in the water window region. Especially at just above the Sc L-absorption edge (around 3.11nm), it has high reflectivity. On the other hand, Cr/C multilayer mirror has high reflectivity at C K-absorption edge (4.48 nm). To fabricate these mirrors the r.f. magnetron sputtering deposition system [1] was used. The multilayer was deposited on SiO_2 wafer under an argon gas atmosphere. The rf powers of Cr, Sc and C targets were 50, 100 and 100 W, respectively. The argon gas flow rate was 2.5 sccm for all targets. Before deposition, SiO_2 wafer was heated at 200 °C in 30 minutes for cleaning and then cooled down to about 30 °C. To prevent surface oxidation of Cr/Sc multilayer, a carbon film of about 2 nm in thickness was deposited on completion of the multilayer deposition. Soft X-ray reflectivities were measured with s-polarized radiation at beamline BL-5B at UVSOR synchrotron facility.

Figure 1 and 2 show experimental results of the Cr/Sc multilayer mirror with periodic thickness of about 3.4 nm and 50 layer pairs (Multilayer #1). This multilayer was designed for a wavelength of 3.37 nm (C VI 1s-2p emission) and an incident angle of 60 deg. In this condition the measured reflectivity was about 8.74 % shown in Fig. 1. This was about 40 % of the reflectivity with an ideal interface. The main reason of reduction of reflectivity is roughness. In this case, roughnesses on the top interface of Cr and Sc layers were about 0.5 and 0.6 nm, respectively. The maximum reflectivity around Sc L-absorption edge shown in Fig. 2 was about 20.4 % at the wavelength of 3.16 nm and the incident angle of 62.5 °.

Figure 3 shows the result of the Cr/Sc multilayer mirror with periodic thickness of about 1.95 nm and 80 layer pairs (Multilayer #2). This multilayer was designed for an incident angle of 30 deg. In this condition the measured reflectivity was about 1.3 %. The reflectivity around Sc L-absorption edge 2 was about 4.3 % at the wavelength of 3.12 nm and the incident angle of 36.6 °.

The reflectivity of the Cr/C multilayer mirror with periodic thickness of about 5.18 nm and 8 layer pairs (Multilayer #3) was measured. This multilayer was designed for a wavelength of 4.47 nm (C Kα line) and an incident angle of 60 deg. The reflectivity was about 0.5 % at an incident angle of 55 deg. It was very low and an incident angle was different from designed one. This was because thickness of carbon layer was fluctuated caused by unstable carbon plasma.

References

1) T. Fujimoto, B. Li, I. Kojima, S. Yokoyama, and S. Murakami, *Rev. Sci. Instr.*, 70, 4362 (1999).

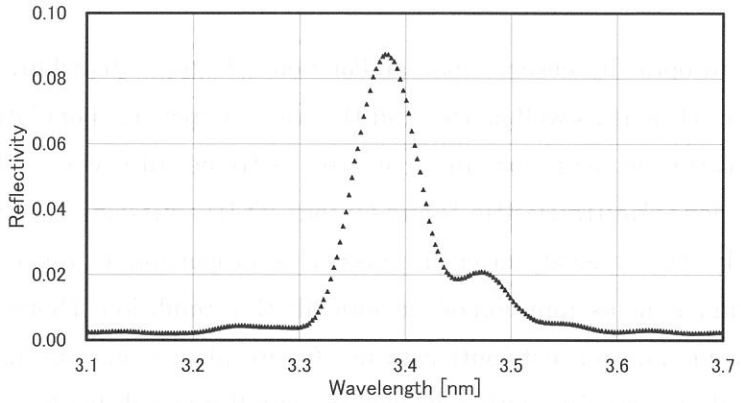

Fig. 1 Reflectivities of Multilayer #1 at an incident angles of 60.0 deg.

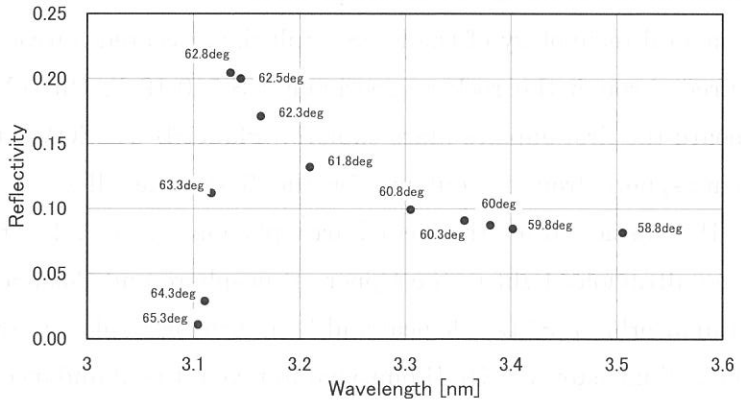

Fig. 2 Peak reflectivities of Multilayer #1 at each incident angle.

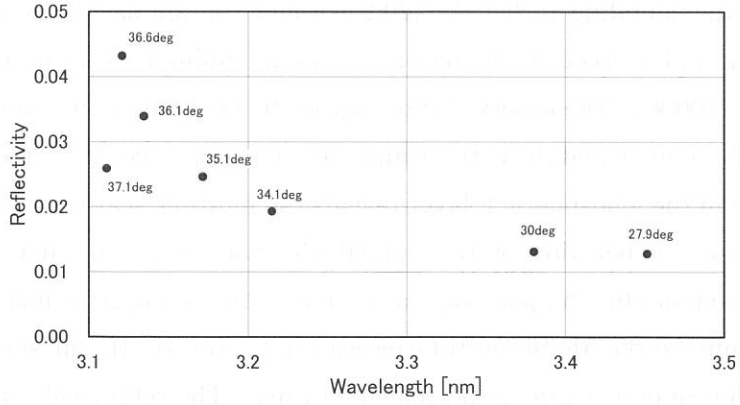

Fig. 3 Peak reflectivities of Multilayer #2 at each incident angle.

(BL5B)

Optical Characteristics of Mo/Si Multi-layer Evaporated using the Magnetron DC/RF Sputtering System

[A]M. Nakamura, [A]T. Murachi, [B]I. Yoshikawa, [A]Y. Takei, and [C]A. Yamazaki

[A] *Department of Earth and Planetary Science, University of Tokyo, Bunkyo-ku 113-0033*

[B] *Institute of Space and Astronautical Science, Sagamihara, Kanagawa 229-8510*

[C] *Communications Research Laboratory, Koganei, Tokyo 184-8795*

We study to optically observe ions and/or neutral atoms distribution in space plasma environments, where O^+ ions as well as He^+ and He are an important population. These particles have resonance scattering emission lines in the extreme ultraviolet (EUV) region. The wavelengths of He^+ ions (He II), He (He I) and O^+ ions (O II) emissions are 30.4nm, 58.4nm and 83.4nm, respectively. The intensity of each emission is proportional to column density of each scattered particle under the assumption of the optically thin condition. Therefore a 2-D snap shot brings the macroscopic plasma distribution to us. *In-situ* plasma measurements limited to the very close vicinity of one satellite with a low-energy cutoff has a difficulty in identifying global distribution and transport mechanisms of the cold plasmas.

The fundamental technology of the Mo/Si multi-layer coated mirror for detecting He II emission was acquired through the rocket experiments S-510-19 [1]. Our eXtreme Ultra-Violet (XUV) Scanner onboard the first Japan's Mars explorer, Planet-B (NOZOMI) took the imaging of the terrestrial plasmasphere from its outside for the first time all over the world [2), 3)] and discovered the He II emission from the near-Earth plasma sheet [4]. In the near future the Telescope of EXtreme ultraviolet light in the Upper- atmosphere and Plasma Imager component (UPI-TEX) for the Lunar orbiter, SELenological and ENgineering Explorer (SELENE), which will be launched in 2005, will measure the He II emission to reveal the abundance and distribution of He^+ ions in the terrestrial plasmasphere. Furthermore we developed the extreme ultraviolet (XUV) sensor for the sounding rocket SS-520-2 without contamination from the very strong H Lyman-α emission, and succeed in the observing the altitudinal variation of the O II emission from 150 through 1100 km. The observed intensity of the O II emission beyond an expectation at the topside ionosphere indicated the extraordinary O^+ ions lying over the ionosphere. And also the high emission rate in the ionospheric F layer reveals the multiple scattering effects.

For the next generation of the optical observation we are developing the imaging spectroscopy instruments for the planetary atmosphere and ionosphere imaging in a broadband EUV range. We improve the Mo/Si multi-layer coating for the He II emission described above to apply the mirror for an observation in a broadband range. The reflectively of a Mo/Si coated test piece mirror, which was evaporated using the magnetron DC/RF sputtering system at the Communications Research Laboratory (CRL), was measured to estimate the optical constant.

Figure shows the measured reflectively of the test piece at 30.4-nm wavelength (point) and calculated values for the Mo 5nm/Si 33nm multi-layer coating (curve). Since two wave structures resemble each other, we consider that the test piece has the thickness coating for this calculation.

We will re-design the thickness of each coated layers with the optical constant estimated by the measurements. We evaporate a multi-layer coated mirror for the broadband EUV range, and evaluate its reflectivity to put it to practical use.

Reference

1) I. Yoshikawa et al., *J. Geophys. Res.*, *102*, 19,897, 1997.

2) M. Nakamura et al., *Geophys. Res. Lett.*, *27*, 141, 2000.

3) I. Yoshikawa et al., *J. Geophys. Res.*, *106*, 26,057, 2001.

4) I. Yoshikawa et al., *Geophys. Res. Lett.*, *27*, 3,567, 2000a.

5) M. Nakamura et al., *UVSOR Activity Report*, 152, 1998.

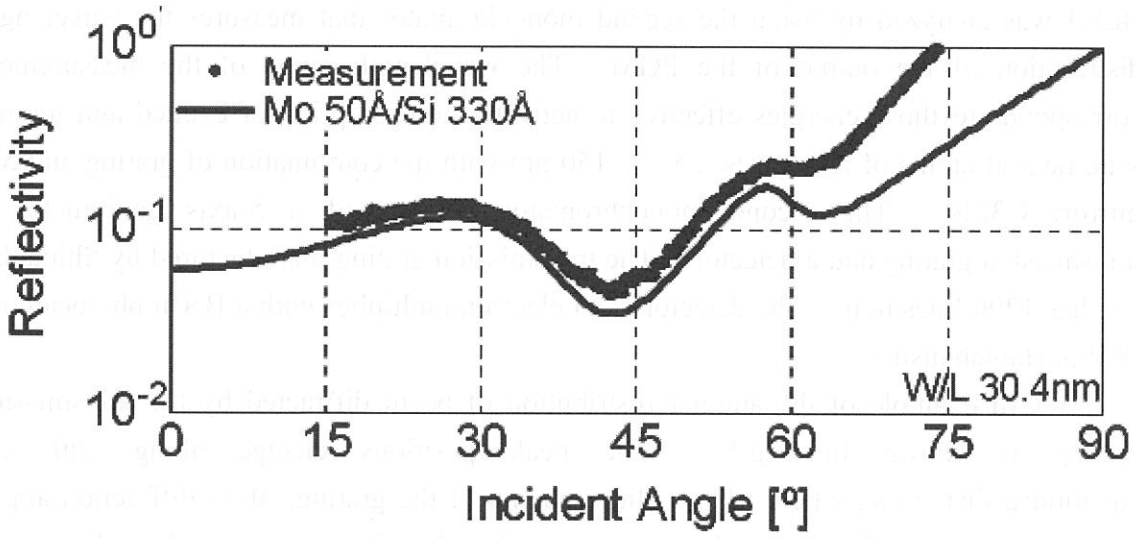

Figure. Reflectivity of the test Mo/Si multi-layer coated mirror. The points represent the measured value, and the black curve shows the calculation of the Mo 5nm/Si 33nm multi-layer reflectivity.

(BL5B)

Evaluation of higher order light of the PGM at BL5B

Makoto Sakurai, Takashi Adachi[1], Takato Hirayama[2], and Ichiro Arakawa[1]

Department of Physics, Kobe University, Kobe 657-8501

[1]Department of Physics, Gakushuin University, Toshima, Tokyo 171-8588

[2]Department of Physics, Rikkyo University, Toshima, Tokyo 171-8501

We have reported the results of measurements of absolute photo-desorption yields from the surface of solid Ne[1], Ar [2, 3] and Kr [4] by the irradiation of synchrotron radiation at excitonic excitation regime. Since the desorption yield depends on the energy of incident photon, the efficiency changes with the contribution of higher order light. Then, the higher order distribution of the output light of the monochromator (PGM) of BL5B was analyzed by using the second monochromator that measures the wavelength distribution of the output of the PGM. The wavelength range of the measurement corresponds to those energies effective to activate the desorption of excited and ground state neutral atoms of rare gases; 25 ～ 150 nm with the combination of grating and M2 mirror: G3M4. The second monochromator consists of a 5-axis goniometer, a transmission grating and a detector. The transmission grating manufactured by Shimadzu Co. has 1200 lines/mm. The detector is an electron multiplier with a BeCu photocathode (R595, Hamamatsu).

An example of the angular distribution of beam diffracted by the transmission grating is shown in Fig.1. The peak positions change along with the equation: $d \sin\theta = n\lambda$, where d is a line spacing of the grating, θ is diffraction angle, n is an order of diffraction, and λ is the wavelength. Broken curves show the change of the position of the first order diffraction peaks of the original wavelength, and dashed curves show those of the first order diffraction peaks of the second order light (i.e. with half of the original wavelength). Higher order contribution obviously increases with the wavelength.

Since the diffraction angles of the first order diffraction ($n=1$) of original wavelength (λ) and the second order diffraction ($n=2$) of the second order light ($\lambda/2$) coincide, theoretical diffraction efficiency of a transmission grating is used to determine the second order contribution. The relative photon number for each order light is calculated from the measured intensity taking into account the quantum efficiency of the detector, and is converted to the absolute photon number using the current of a beam

intensity monitor (a gold plate) as shown in Fig.2. Since the efficiency becomes higher when incident photon energy increases, the intensities of higher order in Fig.1 are too emphasized. The higher order lights are negligible for shorter wavelength region, however, they become comparable with the first order at wavelengths longer than 70 nm. These data are utilized to obtain the absolute desorption yield of rare gases.

References

[1] I. Arakawa, T. Adachi, T. Hirayama and M. Sakurai, Surf. Sci. **45**1, 136 (2000).

[2] T. Adachi, T. Hirayama, I. Arakawa and M. Sakurai, UVSOR Act. Rep. 1999, UVSOR-**2**7, 178 (2000).

[3] T. Adachi, T. Hirayama, I. Arakawa and M. Sakurai, UVSOR Act. Rep. 2000, UVSOR-**2**8, 208 (2001).

[4] T. Adachi, T. Hirayama, I. Arakawa and M. Sakurai, in preparation.

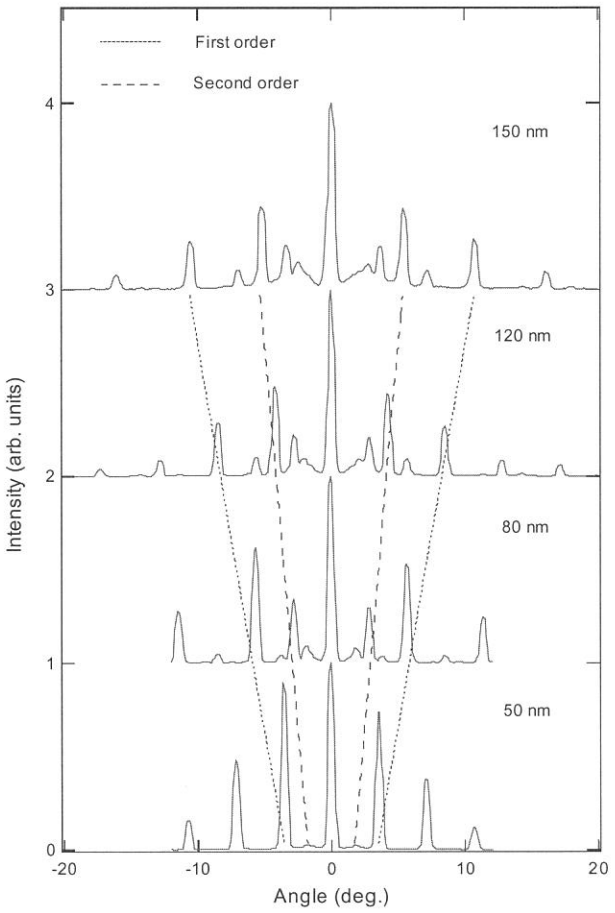

Fig.1 Angular distributions of the diffracted beams for various incident photon wavelengths.

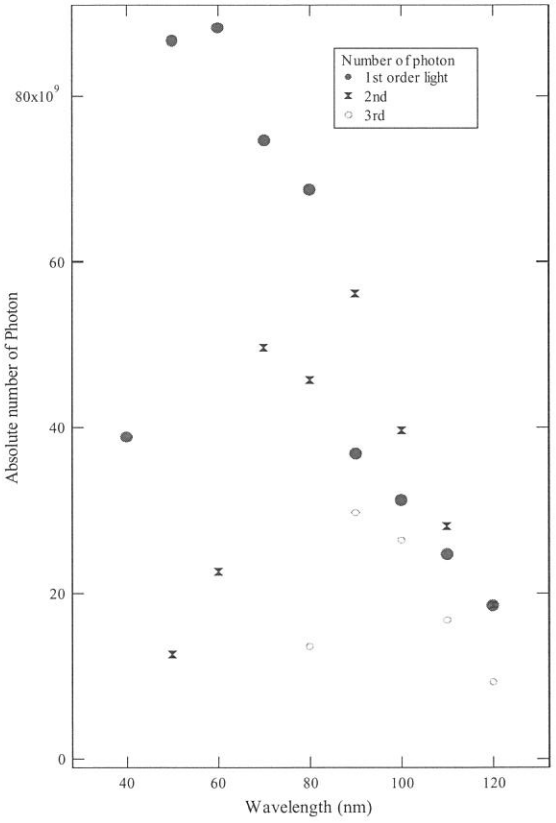

Fig.2 Photon number for each order light at various wavelengths.

Gas Phase Spectroscopy

(BL2B2, 3A2, 3B, 4B, 8A1)

(BL8B1)

Study on Dissociation Processes of Core-excited Methanol Using Auger Electron-Photoion Coincidence Measurements

Y. Senba [a], Y. Mishima [a], M. Morita [a], Y. Suto [a], T. Goya [a], H. Yoshida [a], T. Gejo [b], K. Mase [c] and A. Hiraya [a]

[a] *Department of Physical science, Hiroshima University, Higashi-Hiroshima 739-8526, Japan.*

[b] *UVSOR, Institute for Molecular science, Okazaki 444-8585, Japan*

[c] *Photon Factory, Institute of Materials Structure Science, Tsukuba 305-0801, Japan*

Photofragmentation processes of core-excited methanol (CH_3OH) have been investigated.[1, 2] Initial-excited-state dependence in partial ion yield was observed for several fragment ion. For instance, suppressions of OH^+ and COH^+ yields were observed only at O1s→3sa' excitation. Since core-excited molecules mainly dissociate via various Auger decay processes, Auger electron-photoion coincidence (AEPICO) measurements for C1s and O1s excited CD_3OH were performed.

Experiments were carried out at a soft X-ray beamline BL8B1. Experimental procedure was described elsewhere.[3] Briefly, a cylindrical-mirror type electron energy analyzer (CMA)[4] and a reflectron-type time-of-flight mass spectrometer (R-TOF)[5] were used for the coincidence measurements. Electrons and ions were extracted by an electrostatic field of 40 V/cm. In such an experimental condition, energy resolution (E/ΔE) of CMA was estimated to be ~40 and mass resolution (M/ΔM) of R-TOF ~45.

Figures 1 and 2 show the total ion yield spectra for C1s and O1s excitation regions, respectively. Observed peaks around 288 and 534 eV are assigned to C1s→3sa' and O1s→3sa', respectively.[1] AEPICO spectra were obtained for these excitations and some of them are shown in Figs. 3 and 4. The intensities of OH^+ (mass: 17) and COH^+ (mass: 29) for O1s→3sa' in Fig. 4 are very weak in comparison with those for C1s→3sa' in Fig.3. Moreover, even when we change the Auger electron energy, that is, final state energy (FSE), the intensities of OH^+ and COH^+ are still quite low in comparison with those of other fragments, for instance CD_3^+ and DCO^+. These results would suggest the ultra-fast dissociation of O-H bond for CD_3OH at O1s→3sa' excitation. The time scale of such dissociation is considered to be several femtoseconds and is comparable with that of Auger decay.

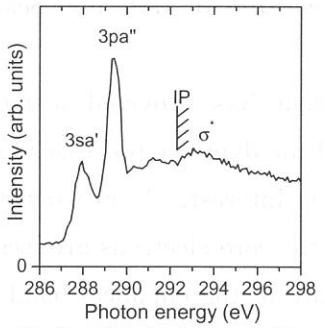

Fig.1. Total ion yield spectrum obtained for C1s excitation region.

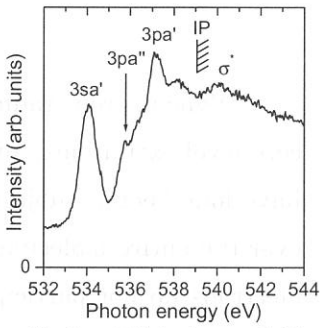

Fig.2. Total ion yield spectrum obtained for O1s excitation region.

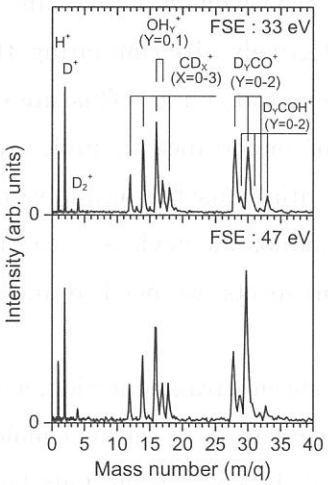

Fig.3. AEPICO spectra obtained for C1s→3sa'.

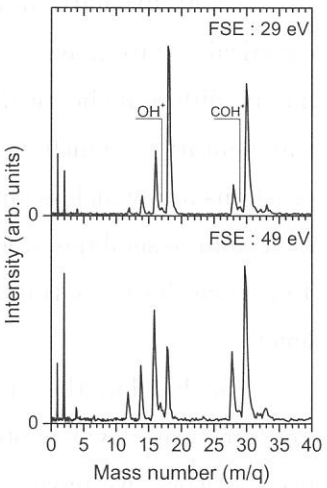

Fig.4. AEPICO spectra obtained for O1s→3sa'.

[1] A. Hempelmann et al., J. Phys. B: At. Mol. Opt. Phys., 32 (1999) 2677.

[2] T. Tokushima et al., SPing-8 User Experiment Report 7 (2001) 126.

[3] Y. Senba et al., to be published.

[4] T. Gejo et al., UVSOR Activity Report 1999, 27 (2000) 68.

[5] A. Hiraya et al., J. Electron Spectrosc. Relat. Phenom. 101-103 (1999) 1025.

(BL2B1)

Site-Specific Fragmentation Caused by N:1*s* Core-Level Photoionization of N_2O Condensed on a Si(100) Surface

Shin-ichi NAGAOKA, Akiko FUJII, Shin-ichiro TANAKA,[A] Kazuhiko MASE[B] and Kazutoshi TAKAHASHI[C]

Department of Chemistry, Faculty of Science, Ehime University, Matsuyama 790-8577

[A]Department of Physics, Graduate School of Science, Nagoya University, Chikusa-ku, Nagoya 464-8602

[B]Photon Factory, Institute of Materials Structure Science, High Energy Accelerator Research Organization, 1-1 Oho, Tsukuba 305-0801

[C]Institute for Molecular Science, Okazaki 444-8585

Synchrotron radiation has provided a powerful means to obtain information about core-level excitations, and the dynamic processes following the core-level excitations in molecules have long been a subject of interest. In contrast to valence electrons that are often delocalized over the entire molecule, the core electrons are localized near the atom of origin. Although core electrons do not participate in the chemical bonding, the energy of an atomic core-level in the molecule depends on the chemical environment around the atom. A shift in the energy levels of core electrons that is due to a specific chemical environment is called a chemical shift.

Monochromatized synchrotron radiation can excite core electrons of an atom in a specific chemical environment selectively, discriminating the core electrons from those of like atoms having different chemical environments. This site-specific excitation often results in site-specific fragmentation, which is of importance in understanding localization phenomena in chemical reactions and which is potentially useful for analyzing the structures and properties of molecules, molecular assemblies, and nanoscale devices by controlling matter at the level of individual atoms. To realize these exciting prospects, we need to understand what controls behavior at the atomic level.

To elucidate the site-specific fragmentation, we have studied the spectroscopy and dynamics following core-level photoionization of various molecules condensed on surfaces [1-5]. In the present work, we have used the energy-selected-photoelectron photoion coincidence (ESPEPICO) method to study the site-specific fragmentation caused by N:1*s* photoionization of N_2O condensed on a Si(100) surface. Since the chemical environment of the terminal N atom (N_t) is different from that of the central N atom (N_c), N_2O shows occurrence of different chemical shifts [6]. Thus N_2O may show site-specific fragmentation. The Si surface was cooled to about 50 K by flowing cold helium gas, and the sample was prepared by exposing the surface to N_2O gas at 10 L (1L = 1×10^{-6} Torr•s).

Figure 1 shows the photoelectron spectrum, which has two peaks in the region of N:1*s*

electron emission. The lower energy and higher energy peaks were respectively assigned to N_t:1*s* and N_c:1*s* electron emissions by comparison with the X-ray photoelectron spectrum obtained in the vapor phase [6]. The photoelectron spectrum thus clearly shows that the chemical shifts (binding energies) at the two nitrogen atoms are different.

Figure 2 shows the ESPEPICO spectra obtained with emission of the N_t:1*s* and N_c:1*s* electrons. N^+ (and/or O^+) and N_2O^+ ions are desorbed coincidentally with N:1*s* electrons. The site-specificity for these ions in N_2O condensed on a Si(100) surface is less remarkable than expected. The reason for this is thought to be that the two nitrogen sites are close to each other. In fact, we previously showed that site-specificity in $X_3Si(CH_2)_nSi(CH_3)_3$ (X=F or Cl, *n*=0-2) decreases with decreasing distance between the two silicon sites [3]. As in $X_3Si(CH_2)_nSi(CH_3)_3$, effective electron migration among the two nitrogen sites is probably responsible for the absence of site-specificity. Since the site specificity to a site adsorbed to a substrate is enhanced by electron transfer from the substrate to that site, we now attempt to perform the ESPEPICO experiments of N_2O adsorbed on a Si(100) surface.

References

[1] S. Nagaoka, K. Mase, M. Nagasono, S. Tanaka, T. Urisu and J. Ohshita, J. Chem. Phys. **107**, 10751 (1997).

[2] S. Nagaoka, K. Mase and I. Koyano, Trends Chem. Phys. **6**, 1 (1997).

[3] S. Nagaoka, K. Mase, M. Nagasono, S. Tanaka, T. Urisu, J. Ohshita and U. Nagashima, Chem. Phys. **249**, 15 (1999).

[4] K. Mase, S. Tanaka, S. Nagaoka and T. Urisu, Surf. Sci. **451**, 143 (2000).

[5] S. Nagaoka, S. Tanaka and K. Mase, J. Phys. Chem. B **105**, 1554 (2001).

[6] K. Siegbahn, C. Nordling, G. Johansson, J. Hedman, P. F. Hedén, K. Hamrin, U. Gelius, T. Bergmark, L. O. Werme, R. Manne, and Y. Baer, *ESCA Applied to Free Molecules* (North-Holland, Amsterdam, 1969).

Figure 1 (bottom). Photoelectron spectrum of N_2O taken at a photon energy of 442.5 eV.

Figure 2 (right-hand side). ESPEPICO spectra of N_2O taken at a photon energy of 467.2 eV. (a) N_t:1*s* electron emission. (b) N_c:1*s* electron emission.

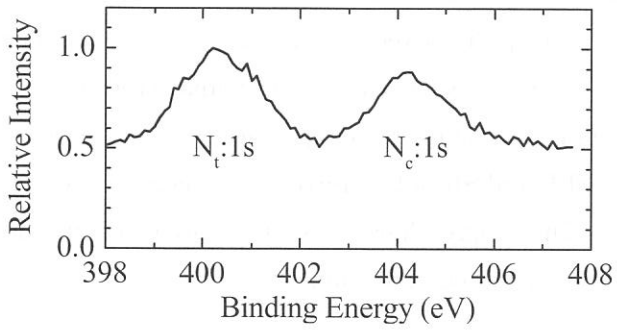

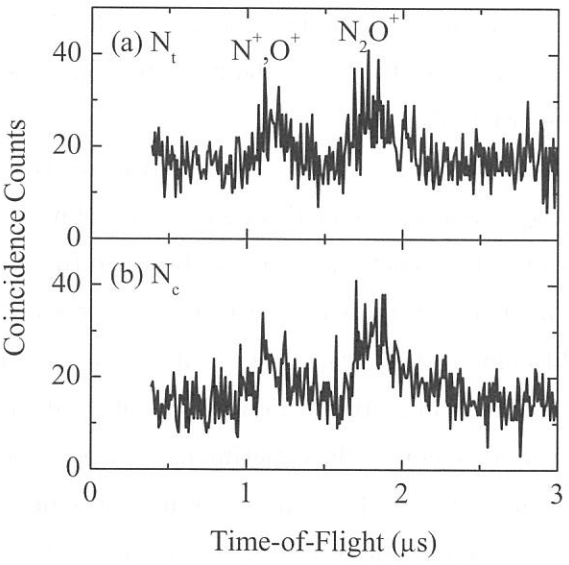

(BL3A1, BL7B)

Pump /Probe Experiments with FEL and SR Pulses at UVSOR

Tatsuo GEJO, Eiji SHIGEMASA, Eiken NAKAMURA, Masahito HOSAKA, Shigeru KODA, Akira MOCHIHASHI, Masahiro KATOH, Jun-ichiro YAMAZAKI, Kenji HAYASHI, Yoshifumi TAKASHIMA and Hiroyuki HAMA[a]

Institute for Molecular Science, Myodaiji, Okazaki 444-8585, Japan

[a]Laboratory of Nuclear Science, Tohoku University, Sendai 980 Japan

Introduction

Storage Ring Free Electron Laser (SRFEL or FEL) has been developed as a powerful light source owing to its high power, high coherence and unique temporal feature. Pump and probe experiments using FEL and synchrotron radiation (SR) pulses have been tried to perform for the last decade, because the FEL pulse naturally synchronizes with the SR one.

Very recently, as the first gas-phase experiment combined FEL with SR, we have carried out the two-photon double-resonant excitation on Xe atoms, utilizing a SR pulse as a pump and an FEL pulse as a probe light. Here we report the present status and future plan for the combined experiments with FEL and SR at UVSOR. The first experimental results on the two-photon double-resonant excitation of the Xe* $5p^5nf$ autoionization states using the combination of a mode-locked laser and SR have already been demonstrated by Meyer's group at LURE. In the present work, the combination of FEL and the undulator radiation was chosen in place of the former.

Experiments

The experiments were done on the undulator beamline BL3A1 and bending-maget-based beamline BL7B at UVSOR. At BL3A1, no monochromator is installed. Therefore, an LiF filter was employed to suppress higher order harmonics of the undulator radiation. The estimated photon flux of BL3A1 is about 1×10^{13} photons/sec/0.1%B.W at I = 100 mA and that of BL7B is in the order of 10^9.

The FEL pulses were extracted through the backward mirror and transported to experimental stations through a series of multi-layer mirrors. The flight path of FEL, which was adjusted to synchronize timing between the FEL and the SR pulses, was about 30 m. A focusing mirror (f = 10 m) was placed in the center of the flight path to keep the beam size of FEL small throughout the transport. About 69 % of the extracted power were transferred to the experimental station. Fine-tuning of the delay timing was made by using a movable optical delay system (50 cm) at the experimental station. The FEL and SR pulses introduced coaxially crossed an effusive jet of Xe atoms from a gas nozzle. The singly charged Xe ions produced in the interaction region were detected by means of a conventional channeltron.

Results and discussion

The fundamental harmonic of the undulator was adjusted to be 10.4 eV, in order to prepare the Xe* $5p^5 5d$ intermediate states as a first step. The Xe* $5p^5 4f$ autoionization resonance can be excited within the wavelength region of FEL as a second step. Because the lifetime of the intermediate states is quite short (600 ps), the synchronization between the SR and laser pulses is essential in this experiment.

During the experiment, there were serious background signals due to scattered stray light of SR pulses (typically about 10^5 counts/sec), which made it difficult to detect the real ion signals. Therefore, for searching the real signals, we temporarily employed the Q-switching technique. In this technique, much larger peak power of FEL is provided, although the duration of lasing becomes relatively short (~ 0.2 msec). However, if events are selected only during this duration, the improvement of signal to noise ratio (S/N) by a factor of 100 can be achieved.

After the precise alignment of the beams and the gas nozzle position by the Q-switching technique, we have measured the ion yield spectrum for the autoionization Xe* $5p^5 4f$ resonance using a CW FEL (Fig. 1). During the measurement, a newly developed feedback system was operated to stabilize the lasing. The asymmetric line shape described by the Fano formula has been clearly observed in Fig. 1.

In order to realize the angular distribution measurements of photoelectrons, considerable reduction of the background signals is necessary. Therefore we used the same experimental setup and performed the same measurement at BL7B, where a high-resolution monochromator is installed. The count rate for this measurement is about 200 counts/sec, which is about 1/1000 in comparison with the case when the undulator radiation was used. Figure 2 shows the two-photon ionization signals of Xe as a function of the wavelength of SR. Although the photon intensity of SR at BL7B is high enough to obtain total ion yield spectrum, it is not high enough to measure the angular distribution of photoelectrons.

We are planning to carry out similar experiments in the shorter wavelength region (around 400 nm) of FEL, where higher Rydberg series of the Xe* $5p^5 nf$ states via the Xe* $5p^5 5d$ intermediate state are accessible.

Reference [1] M. Gisselbrecht, A. Marquette and M. Meyer, J. Phys. B31 L977 (1998)

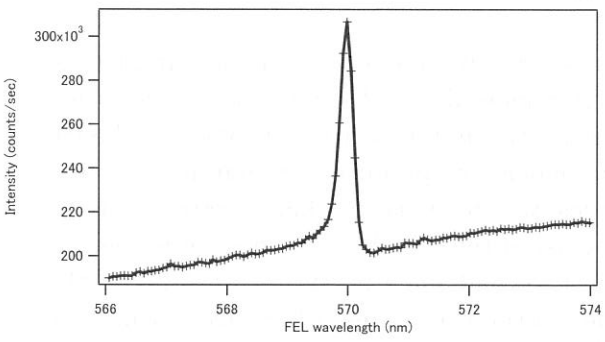

Fig. 1 Two-photon ionization signal of Xe as a function of the wavelength of FEL

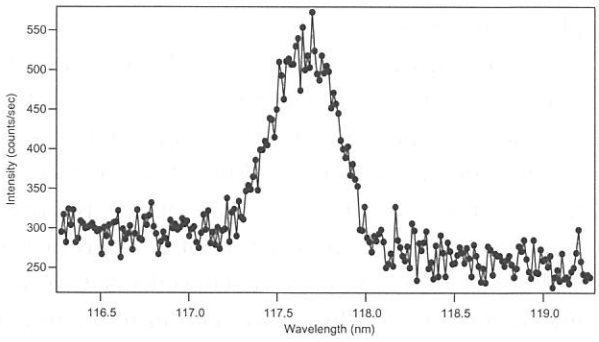

Fig. 2 Two-photon ionization signal of Xe as a function of the wavelength of SR

(BL3A2)

Molecular and Dissociative Single and Double Photoionization of CS_2 and Ionic Fragmentation of CS_2^+ and CS_2^{2+} in the Range from 20 to 120 eV

Toshio MASUOKA, Masahiro KATO, and Ataru KOBAYASHI

Department of Applied Physics, Graduate School of Engineering,, Osaka City University, Sugimoto 3, Sumiyoshi-ku, Osaka 558-8585

In order to study molecular and dissociative single and double photoionization and subsequent dissociation processes of CS_2, we have studied these processes with time-of-flight mass spectrometry and the photoion-photoion-coincidence (PIPICO) method by use of synchrotron radiation in the photon energy range of 20-120 eV. The TOF mass spectra and the PIPICO spectra were measured at an angle of ~55° with respect to the polarization vector where the second-order Legendre polynomial is close to zero. Under these conditions, the effects of anisotropic angular distributions of fragment ions are minimized. Appropriate optical filters (Sn and Al) were used to eliminate higher order radiation. To obtain accurate ion branching ratios, the radio frequency (rf) signal of the storage ring was used as the start signal of a time-to-amplitude converter (TAC) under the single bunch mode operation of the storage ring.

The present study focuses on the determination of the ratio of double to single photoionization (σ^{2+}/σ^{+}) as a function of photon energy. Second, the ion branching ratios for the individual ions produced from the parent CS_2^+ and CS_2^{2+} ions are separately determined. Third, the dissociation ratio of the parent CS_2^{2+} ions into two ionic fragments is determined. Some of the results are presented in this report.

Shown in Fig. 1 is a typical PIPICO spectrum measured at a photon energy of 72.5 eV. Only two dissociation channels of CS_2^{2+}, namely $S^+ + CS^+$ and $S^+ + C^+ + S$, are observed, whereas Lablanquie *et al.* [1] observed three dissociation channels $S^+ + C + S^+$ in addition to the above two channels. From the spectral profile of the coincident peaks, the discrimination against energetic ions is little, if any. The threshold of double ionization forming molecular CS_2^{2+} is at 27.0 ± 0.5 eV in good agreement with 27.05 ± 0.02 eV (the best previously reported value) measured by TPEsCO spectroscopy [2]. Metastable CS_2^{2+} ions are observed in the mass spectra. The ratio of double to single photoionization is shown in Fig. 2, increasing monotonically with photon energy. Since the $S^+ + C + S^+$ channel is not measured in the present experiments, the ratios in Fig. 2 should be regarded as representing a lower limit. Since the reliable total photoabsorption cross section of CS_2 in this wide photon energy range has not been reported, the σ^{2+}/σ^{+} ratios can not be converted to the absolute cross sections for single and double photoionization.

Ion branching ratios for the individual ions respectively produced from the parent CS_2^+ and CS_2^{2+} ions are determined separately, thus enabling more detailed study of the dissociation processes of the CS_2^+ and CS_2^{2+} ions. These results are shown in Figs. 3 and 4. Looking at the ion branching ratios of CS_2^+ (Fig. 3), we notice that the major ions produced are parent CS_2^+ and their ratios still increase at higher photon energies which suggests that electronic states contributing to the production of the parent CS_2^+ ion exist at these higher energies. Other details of Figs. 3 and 4 will be discussed elsewhere. Because we had some technical problems in the measurements of the ion-detection efficiency and the ion counting rates, which are essential to evaluate the σ^{2+}/σ^{+} ratios, the present results should be regarded as preliminary ones.

REFERENCES

[1] P. Lablanquie *et al.* JCP 82, 2951 (1985). [2] M. Hochlaf *et al.* CP 234, 249 (1998).

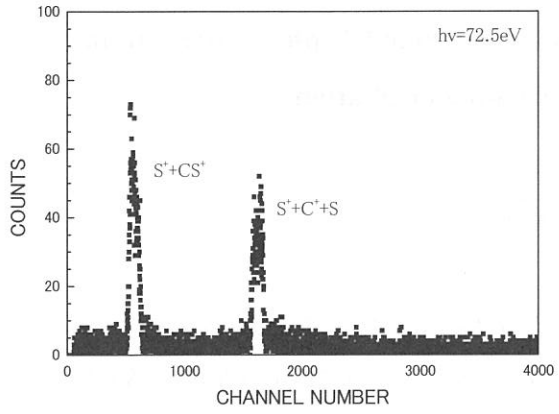

FIG. 1. A typical PIPICO spectrum measured at a photon energy of 72.5 eV.

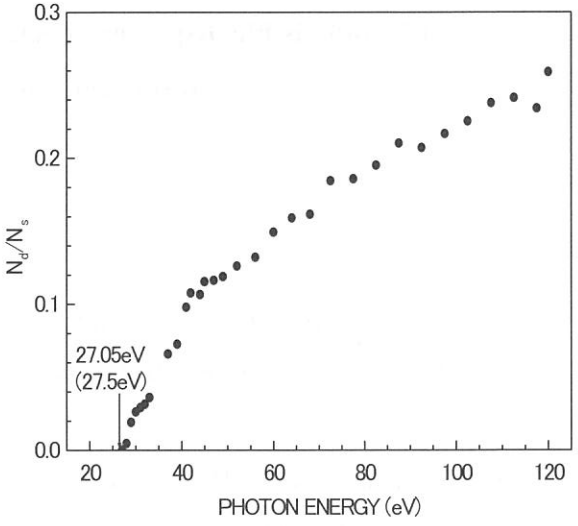

FIG. 2. Ratios of double to single photo-ionization cross section of CS_2.

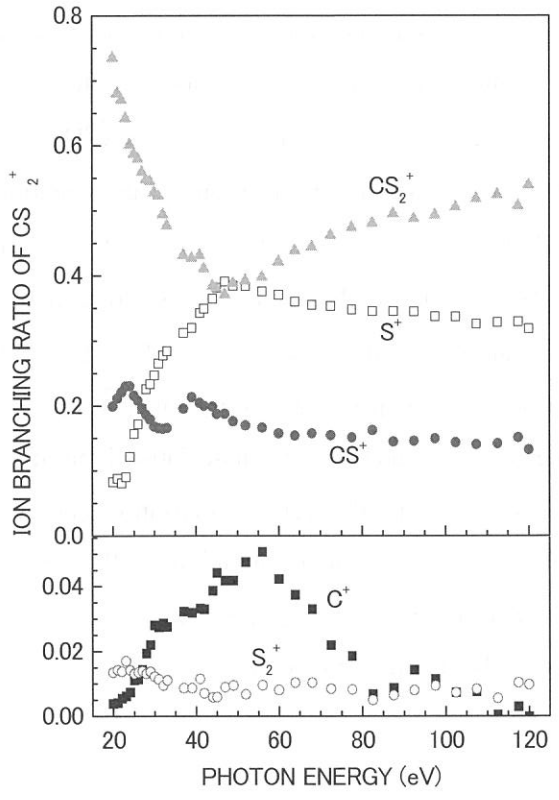

FIG. 3. Ion branching ratios of single photo-ionization of CS_2.

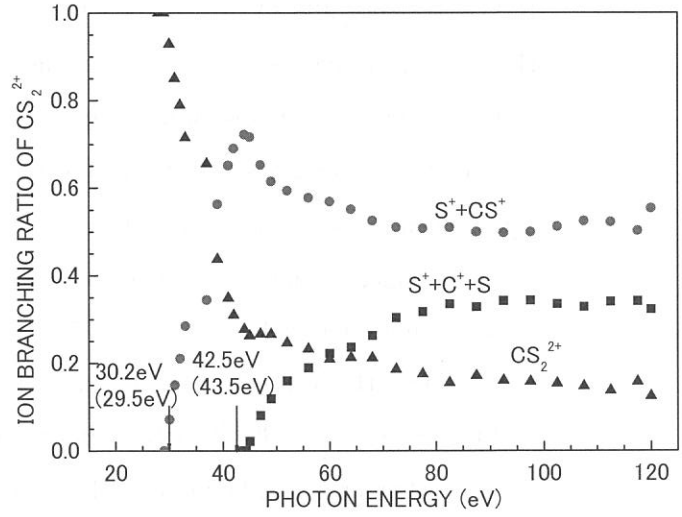

FIG. 4. Ion branching ratios of double photo-ionization of CS_2.

(BL3A2)

UV and visible dispersed spectra from the extreme UV photodissociation of the water using synchrotron radiation

Koichiro Mitsuke

Institute for Molecular Science, Myodaiji, Okazaki 444-8585, Japan

Department of Structural Molecular Science, The Graduate University for Advanced Studies

The photofragmentation of H_2O has been studied by fluorescence spectroscopy at photon energies between E_{hv} = 19.8 – 54.5 eV [1]. The primary photon beam was monochromatized undulator radiation supplied from the UVSOR synchrotron radiation facility. The fluorescence in the wavelength range of 280 – 720 nm was dispersed with an imaging spectrograph. The dispersed spectra in Figure 1 exhibit the hydrogen Balmer lines of $H^*[n\,^2L'_{J'} \rightarrow 2^2L''_{J''}(n=3-9)]$ and the emission band systems of $H_2O^+[\tilde{A}^2A_1(0,v'_2,0) \rightarrow \tilde{X}^2B_1(0,0,0)]$, $OH^+(\tilde{A}^3\Pi_\Omega, v' \rightarrow \tilde{X}^3\Sigma^-, v'')$, and $OH(\tilde{A}^2\Sigma^+, v' \rightarrow \tilde{X}^2\Pi_\Omega, v'')$. The fluorescence cross sections for these transitions have characteristic dependences on E_{hv} and vibrational quantum numbers. The cross section summed over the Balmer lines takes a minimum value at E_{hv} = 21.7 eV and steadily increases with increasing E_{hv} beyond 24.9 eV. This behavior is understood as that the superexcited states correlating with $H^*(n\geq3)$ + $OH(\tilde{A}^2\Sigma^+)$ are too repulsive to be accessible at E_{hv} = 21.7 eV by the Franck-Condon transitions from $H_2O(\tilde{X}^1A_1)$. The appearance energy of the $OH^+(\tilde{A}^3\Pi_\Omega, v' \rightarrow \tilde{X}^3\Sigma^-, v'')$ transitions is found to be ca. 27 eV. This value is much higher than the dissociation limit of 21.5 eV for the $OH^+(\tilde{A}^3\Pi_\Omega)$ + H(n=1) channel, but agrees well with the vertical ionization energy to $H_2O^+[(1b_1)^{-2}(4a_1)^1\,^2A_1]$ that has been assumed to correlate with the above dissociation limit in the literature [2]. The vibrational distribution of $OH^+(\tilde{A}^3\Pi_\Omega)$ evaluated from the $OH^+(\tilde{A}^3\Pi_\Omega, v' \rightarrow \tilde{X}^3\Sigma^-, v'')$ band intensities is similar to the prior distribution in the rigid-rotor harmonic-oscillator approximation.

Reference

[1] K. Mitsuke, *J. Phys. B,* submitted.

[2] J. Appell and J. Durup, *Int. J. Mass Spectrom. Ion Phys.* **10**, 247 (1972/73).

Figure 1. Dispersed fluorescence spectra of H_2O encompassing the wavelength region 300 – 700 nm at six photon energies between E_{hv} = 19.8 and 43.5 eV. The $2_0^{v'}$ symbols in the panel of E_{hv} = 19.8 eV designate the vibrational progression in the bending mode ν_2 of the $H_2O^+[\tilde{A}^2A_1(0,v'_2,0) \rightarrow \tilde{X}^2B_1(0,0,0)]$ transition. The hydrogen Balmer lines $H^*[n\,^2L'_{J'} \rightarrow 2^2L''_{J''}(n=3-9)]$ are indicated by the ($n \rightarrow 2$) marks.

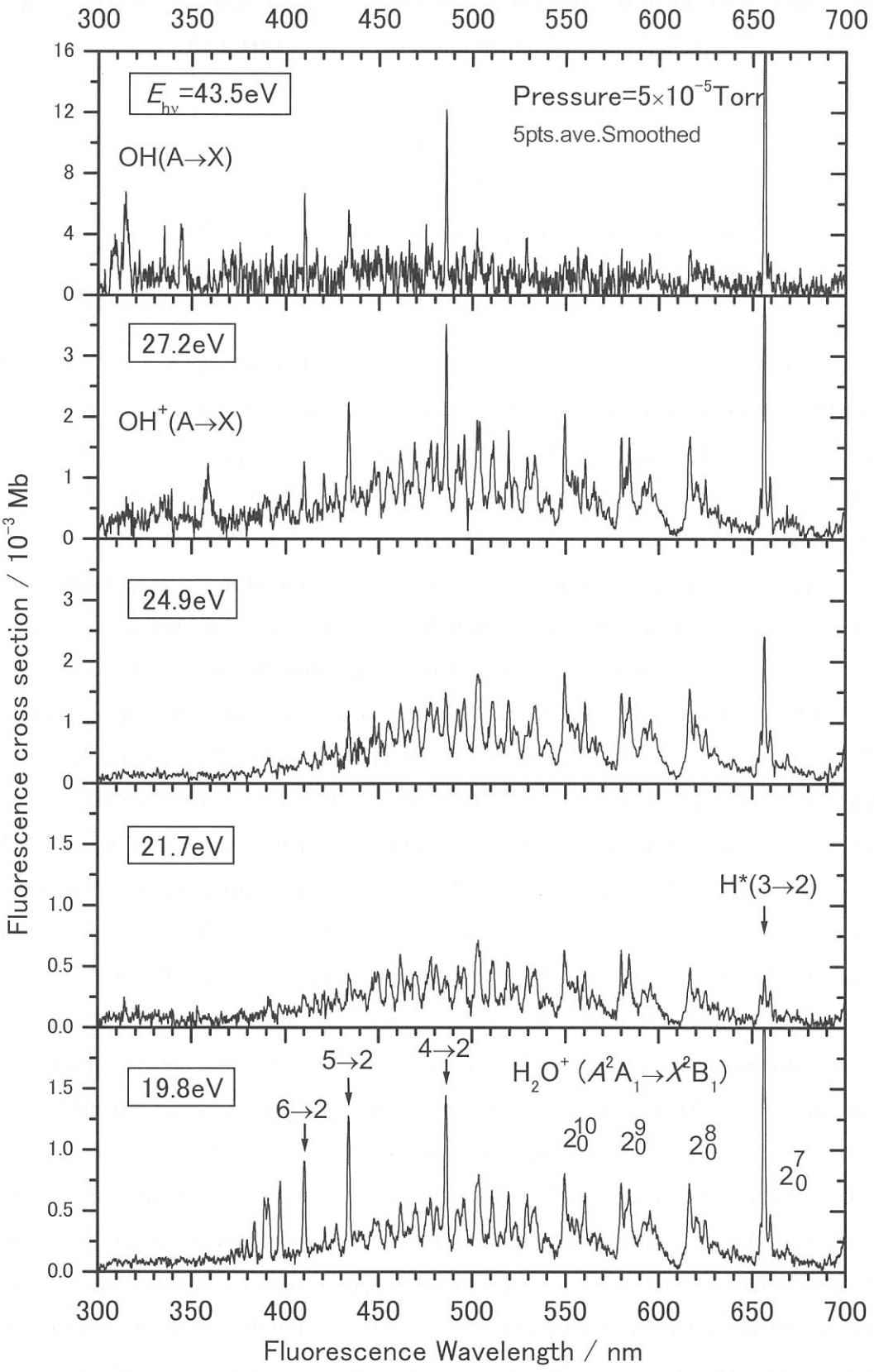
$E_{h\nu}$=43.5eV
Pressure=5×10^{-5}Torr
5pts.ave.Smoothed
OH(A→X)
27.2eV
OH$^+$(A→X)
24.9eV
21.7eV
H*(3→2)
19.8eV
6→2
5→2
4→2
H$_2$O$^+$ (A^2A$_1$→X^2B$_1$)
2_0^{10}
2_0^9
2_0^8
2_0^7
Fluorescence cross section / 10^{-3} Mb
Fluorescence Wavelength / nm

(BL3A2)

Development of the apparatus for high-resolution dispersed spectroscopy and fluorescence excitation spectroscopy at BL3A2

Koichiro Mitsuke

Institute for Molecular Science, Myodaiji, Okazaki 444-8585, Japan
Department of Structural Molecular Science, The Graduate University for Advanced Studies

The sample gas was expanded under an effusive jet condition through a multichannel capillary plate, and subjected to the irradiation of monochromatized undulator radiation (E_{hv}= 15 – 55 eV). The fundamental light or its third harmonic of the undulator radiation was dispersed by a monochromator of constant deviation grazing-incidence type with a 2.2 m focal length. A typical photon intensity and spectral resolution of the synchrotron radiation were $(2 – 8) \times 10^{14}$ photons s^{-1} cm^{-2} and 2.4 Å (FWHM, 83 meV at 20.85 eV), respectively, with entrance- and exit-slit widths of 300 μm. There exists contamination of the light by passage of a second order through the monochromator from the second undulator harmonic. The concentration of the second-order light was estimated to be no less than 10% at E_{hv} = 15 eV.

The fluorescence was collected by an optical detection device in Fig. 1 made up of spheroidal and spherical mirrors facing each other across the photoexcitation region (*PR*), i.e. the source of the fluorescence [1]. One focal point of the spheroidal mirror fell at *PR*, while the other focal point was at the surface of an optical-fiber bundle of 45 cm long. The fluorescence light was reflected back to *PR* by the spherical mirror with its focal point at *PR*, and was then focused onto the surface of the fiber bundle by the spheroidal mirror. This detection system can collect light from about 62% of the full-sphere solid angle. The fluorescence passed through the optical-fiber bundle (transmission ~ 55% at 400 nm).

Two types of monochromators were used to disperse the fluorescence (*e.g.* Fig.2). In dispersed fluorescence spectroscopy we utilized a 300 mm focal-length imaging spectrograph equipped with a liquid-nitrogen cooled CCD array detector of 26.8 mm wide (the dispersion direction) and 8 mm high. Normally 600 and 1200 grooves/mm gratings having nominal blaze wavelengths of 300 and 500 nm were chosen. The overall detection efficiency, including the spheroidal and spherical mirrors, fiber bundle, and imaging spectrograph, was estimated to be $(1 - 5)\times10^{-3}$ with the entrance slit width of the spectrograph being 250 μm. When we fulfilled fluorescence excitation spectroscopy by scanning the wavelength of synchrotron radiation, we replaced the imaging spectrograph by a 100 mm focal-length monochromator and a photomultiplier tube. In this case, the overall detection efficiency was estimated to be $(1.4 \pm 0.3)\times10^{-3}$ at the entrance- and exit-slit widths of the monochromator of 2 mm. All spectra were corrected by the wavelength dependence of the relative detection efficiency.

Reference

[1] K. Mitsuke and M. Mizutani, *Bull. Chem. Soc. Jpn.* **74**, 1193 (2001).

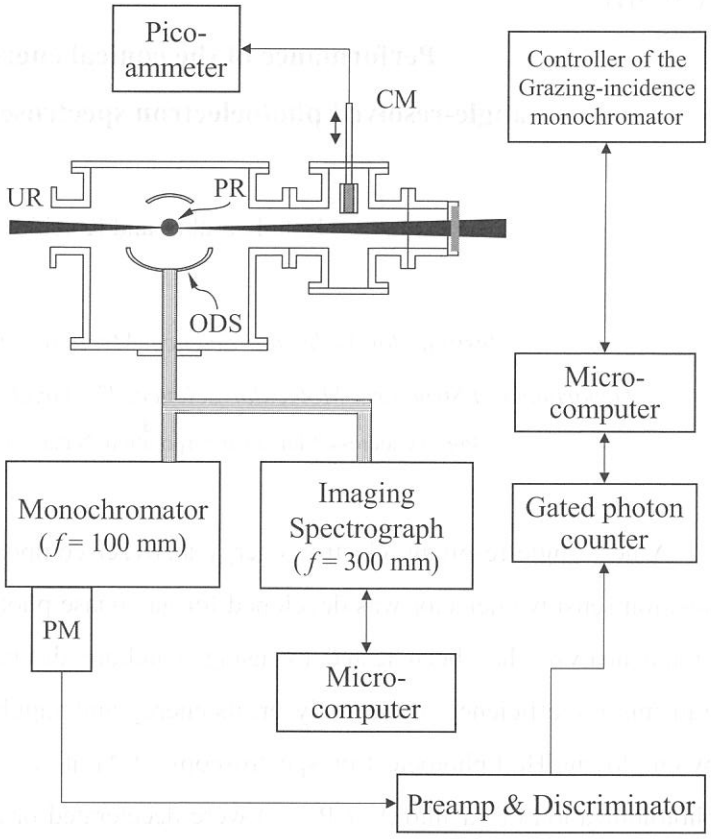

Fig. 1. Schematic diagram of the apparatus for dispersed fluorescence spectroscopy and fluorescence excitation spectroscopy. UR, monochromatized undulator radiation; PR photoexcitation region (not to scale); ODS, optical detection system composed of spheroidal and spherical mirrors and an optical-fiber bundle; CM, gold-mesh current monitor; PM, photomultiplier.

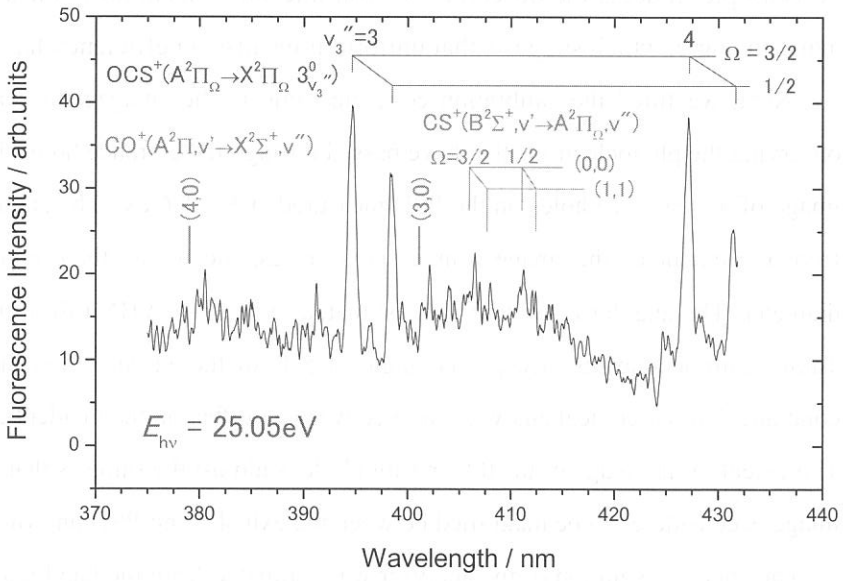

Fig. 2. Dispersed fluorescence spectra of OCS encompassing the wavelength region 375 – 431 nm at E_{hv} = 25.05 eV. The spectrum was measured by using the imaging spectrograph equipped with a 1200 grooves/mm grating which has a nominal blaze wavelength of 300 nm. The entrance-slit width was set to 250 μm. The thin short vertical lines indicate two spin-orbit components (Ω = 3/2 and 1/2) of the vibrational bands of the $OCS^+[A^2\Pi_\Omega(0,0,0) \rightarrow X^2\Pi_\Omega(0,0,\nu_3'')]$ transition with $\nu_3'' = 3$ and 4. The thin long vertical lines indicate the two spin-orbit components of the vibrational bands of the $CS^+(B^2\Sigma^+,\nu' \rightarrow A^2\Pi_\Omega,\nu'')$ transition. The (ν',ν'') mark denotes the band due to the transition from the upper ν' to lower ν'' vibrational states. The thick vertical lines indicate the band origins of the $CO^+(A^2\Pi_\Omega,\ \nu' \rightarrow X^2\Sigma^+,\ \nu''=0)$ emission-band system.

(BL3B)

Performance of the conical energy analyzer for angle-resolved photoelectron spectroscopy developed at BL3B

Kota Iwasaki [a] and Koichiro Mitsuke

Institute for Molecular Science, Myodaiji, Okazaki 444-8585, Japan

Department of Structural Molecular Science, The Graduate University for Advanced Studies

[a] Present address: Shimadzu corporation, Nakagyo-ku, Kyoto 604-8511, Japan

A new angle-resolving electron energy analyzer composed of a conical electrostatic prism and a position sensitive detector was developed for gas-phase photoelectron spectroscopy. The performance of the analyzer has been tested by using a helium discharge lamp. Namely, we have tested the transmission efficiency of the analyzer, its energy and angular resolutions, and background count rate by employing He I photoelectron spectroscopy of Ar atoms. The 5.3 and 5.5eV electrons produced by photoionization of Ar into $Ar^+(^2P_{3/2,1/2})$ were decelerated or accelerated and made to pass through the analyzer. Since the light is unpolarized, the nascent photoelectron angular distribution is expected to be isotropic. Indeed, the observed electron intensity was almost constant over the whole range of the azimuth angle, which suggests that uniform transmission efficiency has been realized.

Next, we fitted the calibration cone electrode in the analyzer to evaluate the angular resolution by observing the photoelectrons that have passed through the entrance holes. Figure 1 shows a typical electron image of the entrance holes on the PSD measured at E = 5.6 eV. The angular resolution can be determined from the extent of the image. Three spots correspond to the three entrance holes of 1.5 and 2mm in diameter. The angular resolution was estimated to be 3° (FWHM) from the spot size for the 1.5mm hole. Taking into account the acceptance angle of 5.4° of the entrance hole from the sample volume, we can conclude that our conical analyzer has a converging effect on the incident electrons in the azimuth direction. The extent of the image of the 0.5 or 1 mm hole is almost the same as that of the 1.5 mm hole. The electron image is considered to be magnified between the exit slot and PSD unit owing to the fringing-field effect.

The energy resolution of the analyzer was estimated from the band-width of the $Ar^+(^2P_{3/2,1/2})$ peaks in a photoelectron spectrum. The spectrum was obtained by plotting the total electron counts within the image of the entrance hole of ϕ2 mm on the PSD, as a function of the potential difference between the gas cell and inner cone electrode. Figure 2 shows the photoelectron spectrum thus measured. The $Ar^+(^2P_{3/2,1/2})$ bands have symmetric Gaussian profile. It is thus likely that there exists no distortion in the electric field acting upon the photoelectrons from the gas cell. The signal to background ratio was found to be 10 - 20.

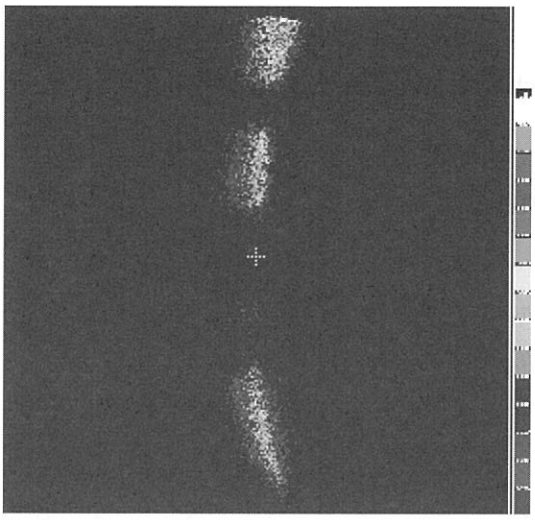

Fig. 1. Photoelectron image on the PSD. Three spots represent the image of three entrance holes bored through the inner cone electrode. The top spot is truncated along the edge of the PSD.

The minimum band-width of 60±1 meV (FWHM) has been achieved at E = 1.4 eV, i.e. the best energy resolution of $\Delta E/E$ = 0.043. This value amounts to 130 % of the resolution expected from our simulation of the electron trajectories. This deterioration can be explained by the assumption that we cannot optimize the deceleration voltages applied to the annular lens system yet. Conceivably, the lens system extracts superfluous electrons with large incident angles with respect to the mean trajectory in the dispersion plane under the present experimental conditions.

Reference

[1] K. Iwasaki and K. Mitsuke, *Surf. Rev. Letters,* in press.

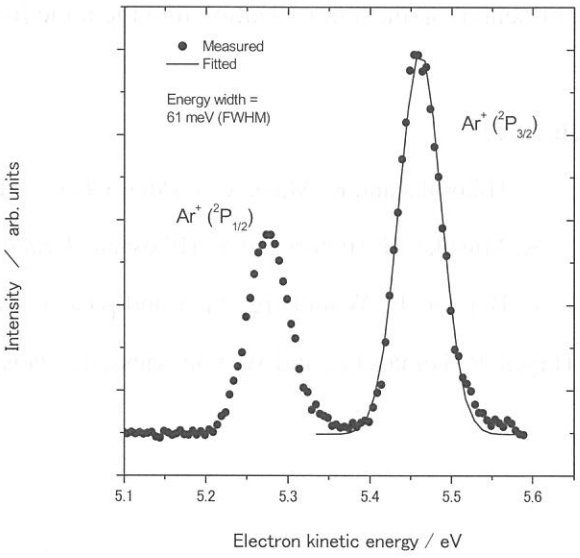

Fig. 2. He photoelectron spectrum of Ar. Two peaks are attributed to the $Ar^+(^2P_{2/3,1/2})$ bands. The ratio of the peak intensities is two and agrees with that of their statistical weights.

(BL3B)

Formation and autoionization of a dipole-forbidden superexcited state of CS_2

Yasumasa Hikosaka [a] and Koichiro Mitsuke [b]

[a] *Photon Factory, Institute of Materials Structure Science, 1-1 Oho, Tsukuba, 305-0801, Japan*

[b] *Institute for Molecular Science, Myodaiji, Okazkai 444-8585, Japan*

Department of Structural Molecular Science, The Graduate University for Advanced Studies

We have measured 2D-PESs of CS_2 in the $E_{h\nu}$ region of 14.60 - 15.35 eV, in order to investigate excitation and decay mechanisms of superexcited states [1,2]. The 2D-PESs show pronounced formation of the (0,0,1) levels of $CS_2^+(\tilde{X}\,^2\Pi_g$ and $\tilde{B}\,^2\Sigma_u^+)$ from a superexcited state at $E_{h\nu}$ = 14.88 eV. This unusual vibrational excitation of ions in the ν_3 mode results from autoionization of the (0,0,1) level of the dipole-forbidden state which has been assigned to the $3d\sigma_g$ $CS_2^*(R_C)$ state conversing to $CS_2^+(\tilde{C}\,^2\Sigma_g^+)$. The primary photoexcitation to the (0,0,1) level of the $3d\sigma_g$ state is considered to become allowed by vibronic interaction with the $5p\sigma_u$ $CS_2^*(R_C)$ state. We have additionally uncovered that the preference in autoionization of the $3d\sigma_g$ state into the final ionic states depends on their vibrational levels. The preference concerning the ionic (0,0,0) levels is explained in terms of the vibronic interaction that remains until autoionization, while the vibronic interaction is relatively uninfluential on the autoionization into the ionic (0,0,1) levels.

Reference

[1] Y. Hikosaka and K. Mitsuke, *J. Phys. Chem. A* **105,** 8130 (2001).

[2] K. Mitsuke, H. Hattori and Y. Hikosaka, *J. Electron Spectrosc. Relat. Phenom.* **112**, 137 (2000).

[3] P. Baltzer, B. Wannberg, M. Lundqvist, L. Karlsson, D.M.P. Holland, M.A. MacDonald, M.A. Hayes, P. Tomasello, and W. von Niessen, *Chem Phys.* **202,** 185 (1996).

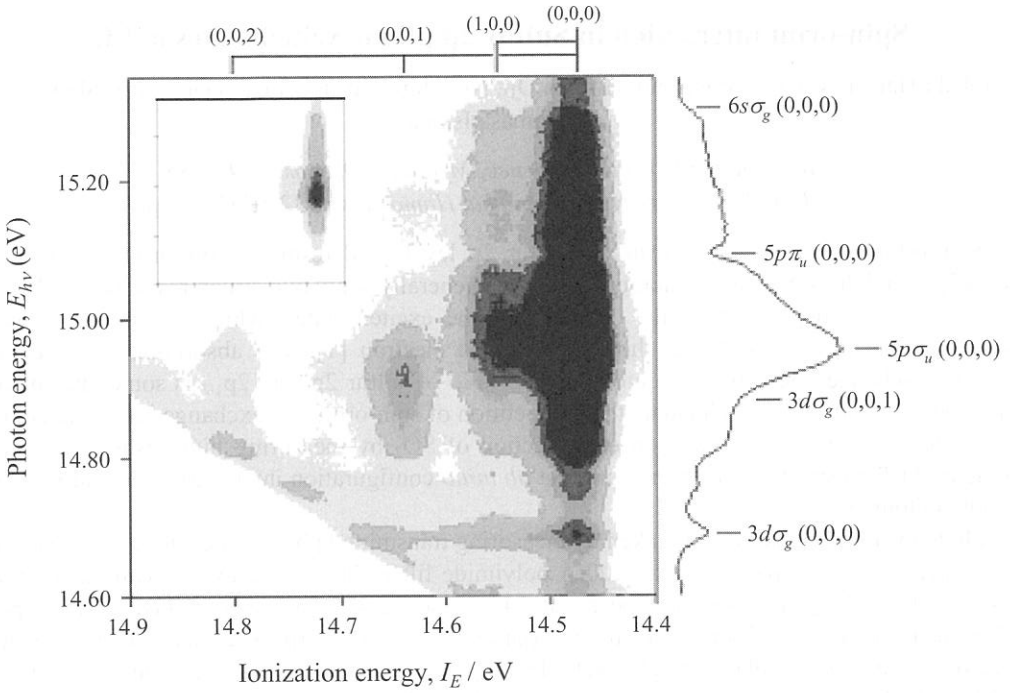

Fig. 1. Two-dimensional photoelectron spectrum for the $CS_2^+(\tilde{B}\ ^2\Sigma_u^+)$ band and its vicinities measured in the photon energy range of 14.60 - 15.35 eV. The electron yield is presented as a function of both photon energy E_{hv} and ionization energy I_E by the plots with eight tones from light to dark on a linear scale. The curve in the right panel shows a constant ionic state spectrum, which is obtained by summing electron counts along the I_E axis at each E_{hv}. Five resonances of Rydberg states converging to $CS_2^+(\tilde{C}\ ^2\Sigma_g^+)$ are observed at E_{hv} = 14.69, 14.88, 14.95, 15.09, and 15.31 eV. The former two states are first assigned in this work.

Fig. 2. One-dimensional photoelectron spectrum for the $CS_2^+(\tilde{B}\ ^2\Sigma_u^+)$ band, which is obtained by summing electron counts in Fig. 1 at every I_E over the E_{hv} = 14.80 - 14.95 eV range along the E_{hv} direction. Vibrational levels are indicated at the I_E positions reported in Ref. [3].

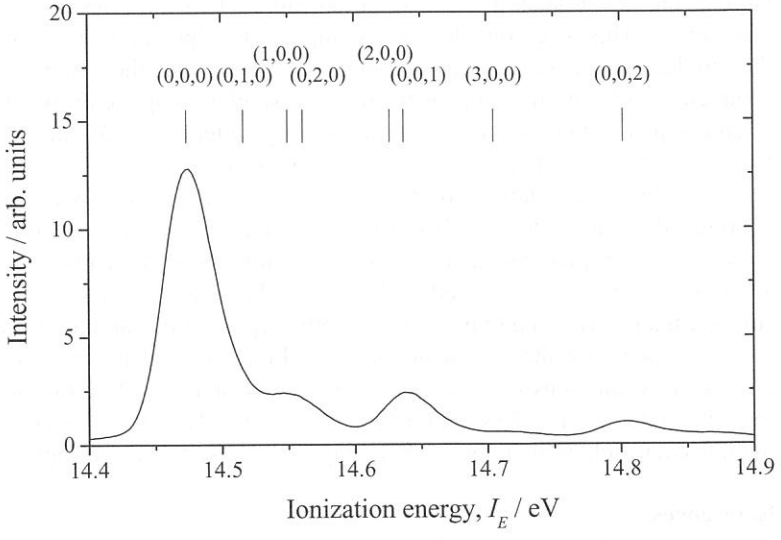

(BL4B)

Spin-orbit interaction in Sulfur 2p photoexcited states of SO_2

Takaki Hatsui, Mitsuru Nagasono, Hiroshi Oji, Nobuhiro Kosugi, Tatsuo Gejo, Eiji Shigemasa
Toshimasa Ishida*

Institute for Molecular Science, Myodaiji, Okazaki 444-8585
** Shizuoka University, Hamamatsu, Hamamatsu 432-8561, Japan*

Spin-orbit interaction is large in the sulfur 2p levels and resulting spin-orbit-split levels are well described as $2p_{3/2}$ and $2p_{1/2}$. Sulfur 2p photoexcited states generally show two structures separated by ~1 eV. The separation is, however, dependent on the character of the excited states, which can be explained by large exchange interaction between sulfur 2p hole and excited electron [1]. The absorption cross-section is also affected by the exchange interaction; the cross-section ratio of sulfur $2p_{3/2}$ to $2p_{1/2}$ is sometimes deviated from statistical value of 2:1. In order to elucidate the competition of spin-orbit and exchange interactions in detail, we have investigated anisotropy of absorption cross-section of SO_2 by measuring high-resolution angle-resolved photoion yield (ARPIS) spectra, and by carrying out *ab initio* configuration interaction calculations based on the Breit-Pauli hamiltonian.

Photoabsorption spectra were taken by measuring transmitted photon intensity using a Si diode. A few Torr SO_2 gas pressure was separated by a 1200 Å polyimide filter. Photon energy was calibrated by measuring Ar $2p_{3/2}$-4s* and Kr $3d_{3/2}$-5p absorption peaks at 244.4 and 92.425 eV, respectively. ARPIS spectra were measured by using two channeltron set in the 0° (parallel) and 90° (perpendicular) directions relative to the electric vector of the linearly polarized light. Retardation grids were used to detect energetic photoions (>3 eV). Ab initio MO calculations were performed using the GSCF3 code.

Figure 1 shows high-resolution photoabsorption and ARPIS spectra. In this report, we focus on excitations to π^* (b_1), σ^* (a_1), σ^* (b_2), and 4s (a_1). Figure 2 shows a part of ARPIS spectra of SO_2, where I_0 (I_{90}) corresponds to ion yields in the direction parallel (perpendicular) to the electric vector of the linear polarized incident light. This region includes only the S 2p excitation to the lowest unoccupied orbital of $\pi^*(b_1)$ symmetry. The S 2p orbitals have a_1, b_2 and b_1 symmetries, resulting in three S 2p-$\pi^*(b_1)$ excited states of B_1, A_2, and A_1 symmetries. The ground state symmetry is A_1 and the $A_2 \leftarrow A_1$ excitation is dipole-forbidden; that is, the $a_1 \rightarrow b_1^*(B_1)$ and $b_1 \rightarrow b_1^*(A_1)$ excitations should be observed in Figure 2. Theoretical calculations predicts that $a_1 \rightarrow b_1^*(B_1)$ and $b_1 \rightarrow b_1^*(A_1)$ excitations have nearly the same oscillator strengths (Table 1a). Considering the spin-orbit interaction, each singlet excitation is mixed with two triplet excitations, resulting in three excited states in each symmetry. The transition dipoles to the B_1 states are orthogonal to the molecular plane and these transitions give only I_{90} yields; on the other hand, the transitions to the A_1 states give both I_0 and I_{90} yields. In Figure 2, three electronic states of B_1 symmetry show vibrational fine structures, where the lowest electronic state is very weak, and the second ($^2P_{3/2}$) is stronger than the third ($^2P_{1/2}$). On the other hand, only two electronic states of A_1 symmetry appears in Figure 2, where one is located in the $^2P_{3/2}$ manifold, and the other is in the $^2P_{1/2}$ manifold. The $^2P_{1/2}$ feature seems to be slightly stronger that the $^2P_{3/2}$ feature, though the $^2P_{3/2}$ branch is as twice large as the $^2P_{1/2}$ branch in the case of ionization. This indicates that exchange interaction is essential in the A_1 symmetry. This is reasonable, considering that the $2p(b_1)$ and $\pi^*(b_1)$ orbitals are oriented parallel. Furthermore, the singlet excited state is quite higher in energy than the triplet excited state, and the lowest state of A_1 symmetry hardly borrows intensity from the singlet component; therefore, the lowest state is almost invisible. Theoretical calculations shows that the exchange interaction (Δ_{ST} in Figure 3a) in A_1 symmetry (1.5 eV) is much larger than Δ_{ST} in the B_1, and B_2 symmetries (<0.2 eV).

In the excitation to σ^* (a_1), broad bands were observed. Since the S $2p_{1/2}$-$\sigma^*(a_1)$ excitation is overlapped by the S $2p_{3/2}$-$\sigma^*(b_2)$, it is not straightforward to extract anisotropy information of each excitation. However, theory predicts that oscillator strength for S 2p-$\sigma^*(a_1)$ is dominated by $b_1 \rightarrow a_1^*(B_1 \leftarrow A_1)$ as in Table 1b. Thus, S $2p_{1/2}$-$\sigma^*(b_2)$ is expected to show the polarization dependence similar to S $2p_{3/2}$-$\sigma^*(b_2)$, where I_{90} yield is stronger than I_0. Based on this analysis, both S $2p_{3/2}$-$\sigma^*(b_2)$, and S $2p_{1/2}$-$\sigma^*(b_2)$ excitations show $I_0 > I_{90}$, which is in accordance with theoretical predictions (Table 1c, and Figure 3c). In Figure 1, both S $2p_{3/2}$-$4s(a_1)$, and S $2p_{1/2}$-$4s(a_1)$ excitations were revealed to be anisotropic ($I_0 > I_{90}$). Because of the Rydberg character of 4s orbital, exchange interaction is less than 0.1 eV (Figure 3d). Oscillator strengths, however, are rather strongly perturbed by molecular field as in Table 1d, resulting in the observed anisotropy.

References

[1] N. Kosugi, R.G. Cavell, A.P. Hitchcock, Chem. Phys. Lett., 265 (1997) 490.

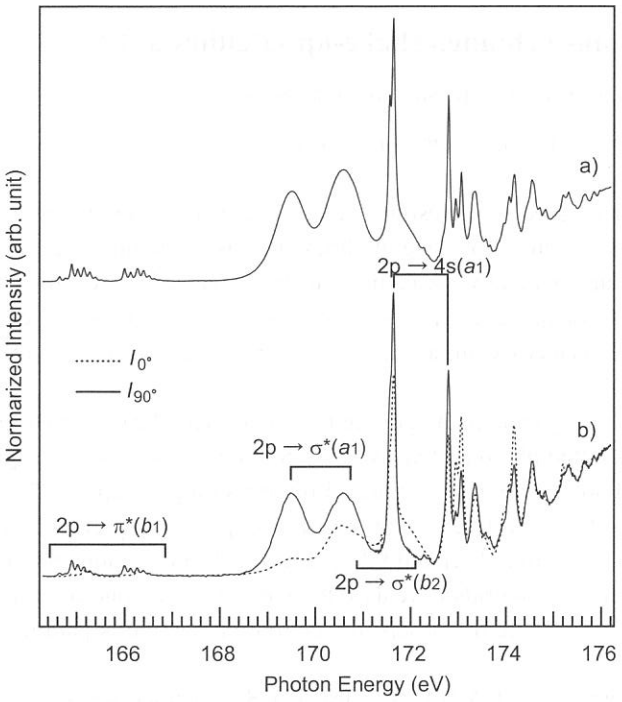

Figure 1. Sulfur 2p photoabsorption spectrum (a) and angle-resolved photoion-yield spectra for SO_2.

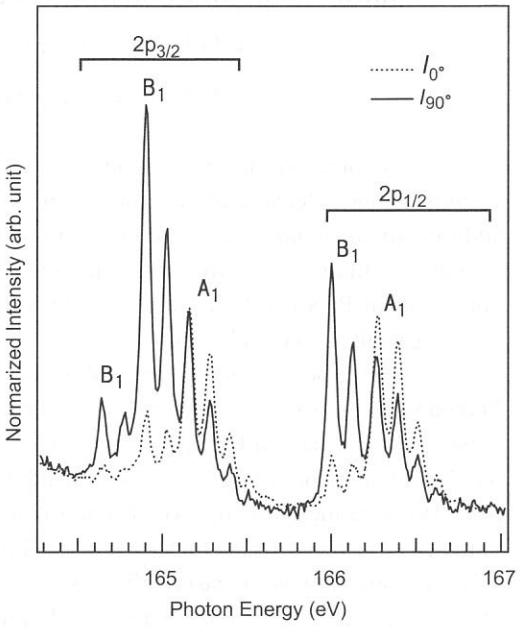

Figure 2. Angle-resolved ion-yield spectra for sulfur 2p→π* (b_1) transition.

Table 1. Theoretical osillator strengths for non-relativistic excited states.

(a) 2p → π*(b1)	Osillator strength for singlet
B1 [2pz (a1) → b1]	f=0.0016
A1 [2px (b1) → b1]	f=0.0016
A2 [2py (b2) → b1]	forbidden

(b) 2p → σ*(a1)	Osillator strength for singlet
A1 [2pz (a1) → a1]	f=0.0003
B1 [2px (b1) → a1]	f=0.0319
B2 [2py (b2) → a1]	f=0.0016

(c) 2p → σ*(b2)	Osillator strength for singlet
B2 [2pz (a1) → b2]	f=0.0124
A2 [2px (b1) → b2]	forbidden
A1 [2py (b2) → b2]	f=0.0127

(d) 2p → 4s*(a1)	Osillator strength for singlet
A1 [2pz (a1) → a1]	f=0.0016
B1 [2px (b1) → a1]	f=0.0050
B2 [2py (b2) → a1]	f=0.0016

Figure 3. Theoretically obtained correlation diagram of relativistic and non-relativistic states. Singlet states and it's perturbed states are indicated by thick lines. Percentages of each non-relativistic singlet component in relativistic states are indicated. Dipole forbidden states are omitted for clarity.

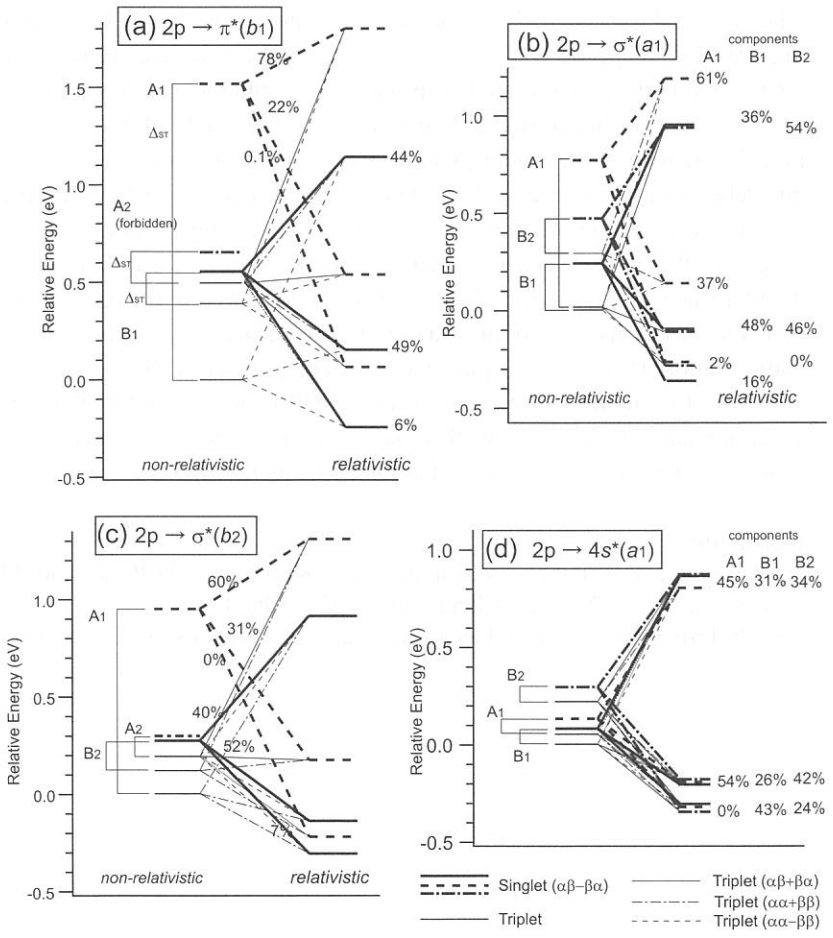

(BL4B)

Sulfur 2p photoexcited states and spin-forbidden shake-up satellites of CS_2

Takaki Hatsui , Mitsuru Nagasono, Eiji Shigemasa, Nobuhiro Kosugi

Institute for Molecular Science, Myodaiji, Okazaki 444-8585

Photoelectron spectroscopy (PES) is widely used to investigate the one-electron energy level in various matters. Because of electron correlation effect, spectra show satellite lines such as shake-up satellites in addition to main lines. These correlation satellites are generally weak but can be enhanced by exciting at resonances. In this report we for the first time demonstrate that even spin-forbidden and invisible (dark) states in non-resonant PES can be observed by PES at the resonances with strong singlet-triplet mixing via spin-orbit coupling of the 2p core electrons.

All experiments were carried out at varied-line-spacing plane grating monochromater beamline BL4B. Photoabsorption spectra are taken by measuring transmitted photon intensity using Si diode. A few Torr CS_2 gas pressure was separated by 1200 Å polyimide filter. Photon energy is calibrated by measuring Ar $2p_{3/2}$-4s* and Kr $3d_{3/2}$-5pabsorption peaks at 244.4 and 92.425 eV, respectively. Angle-resolved photoion yield spectra (ARPIS) were measured by two channeltrons set in the 0° (parallel) and 90° (perpendicular) directions relative to the electric vector of the linearly polarized light. Retardation grids were used to detect energetic photoions (>3 eV). PES spectra were measured by a SES-200 analyzer, where the observed electron momentum is parallel to the electric vector of the linearly polarized light.

Figure 1 shows high-resolution photoabsorption and ARPIS spectra of CS_2. Distinct anisotropy is observed above 165 eV, in sharp contrast to the lower S $2p\rightarrow3\pi_u$* resonances. These information on symmetry of excited states combined with *ab initio* theoretical investigation provides detail insight on the competition of spin-orbit and exchange interactions. Here, we focus on PES and do not discuss on ARPIS results further. Similar discussion is presented in this issue for SO_2.

Figure 2 shows PES recorded at S $2p_{3/2}\rightarrow3\pi_u$* resonance and non-resonant PES below the resonance. The ground state CS_2 has $\cdots(6\sigma_g)^2(5\sigma_u)^2(2\pi_u)^4(2\pi_g)^4$ electronic configuration in $D_{\infty h}$. Main bands, $^2\Pi_g$, $^2\Pi_u$, $^2\Sigma_u$, $^2\Sigma_g$ states are observed. Satellite bands 0, 1", 2, 2', 2", 3, and higher-energy structures are clearly enhanced, whereas satellites 1, and 1' are not. Here satellite numbering 1, 1', 2 and 3 follows the previous study[1]. In the high-resolution spectra (Figure 3), these satellites 1-3 are clearly resolved. Satellites 0, 1", 2', and 2" have not been found in the previous studies measured at excitation energies below 100 eV.

Within the (*LS*) coupling scheme, excited state of S $2p_{3/2}\rightarrow3\pi_u$* transition is described as strongly mixed state with singlet and triplet non-relativistic states, where the intensity comes from dipole-allowed singlet non-relativistic state. Intermediate states in the resonant PES have a large triplet contribution, which opens up transitions to ionized quartet states in addition to doublet states. Satellite 0 is not observed in non-resonant spectrum; therefore it can be assigned to the transition to a quartet state. Satellite 1 is assigned to the lowest doublet shake-up state with $^2\Pi_u$ symmetry [1,2] allowed in the non-resonant PES spectra. Satellite 0 is possibly explained as transition to the quartet ionized states $^4\Pi_u$ with a dominant $\cdots(6\sigma_g)^2(5\sigma_u)^2(2\pi_u)^4(2\pi_g)^2(3\pi_u)^1$ configuration. Difference in spin state makes the quartet satellite 0 lower than its counterpart doublet satellite 1.

In summary, we have measured ARPIS and resonant PES of CS_2. We have successfully found quartet shake-up state in the resonant PES via the S $2p_{3/2}\rightarrow3\pi_u$* resonance. The spin-orbit mixing in the intermediate state opens up transitions to dark states such as quartet shake-up.

References

[1] P. Baltzer, B. Wannberg, M. Lundqvist, L. Karlsson, D.M.P. Holland, M.A. MacDonald, M.A. Hayes, P. Tomasello, W. von Niessen, Chem. Phys. 202 (1996) 185.

[2] J. Schirmer, W. Domcke, L.S. Cederbaum, W. von Niessen, L. Åsbrink, Chem. Phys. Lett., 61 (1979) 30.

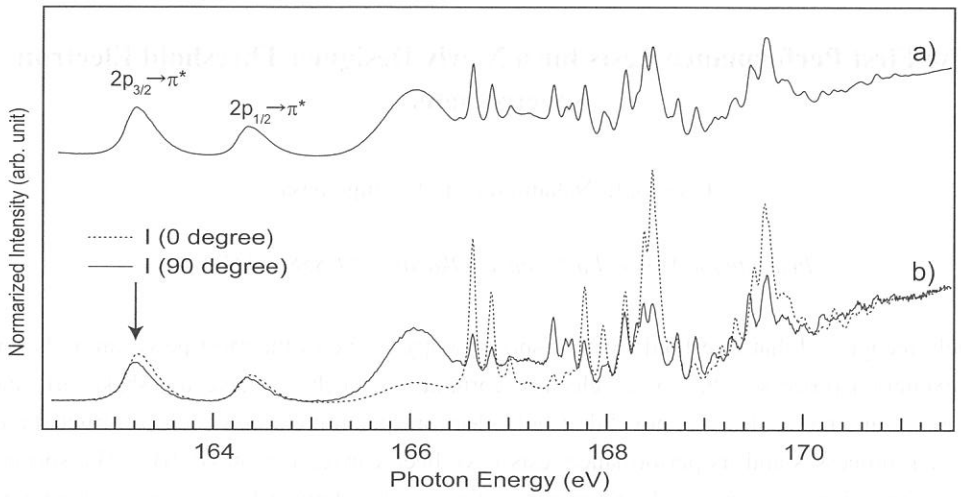

Figure 1. Photoabsorption Spectrum (a) and angle-resolved ion yield spectra (b) of CS_2. Resonant photoelectron spectra are measured at the excitation energy indicated as an arrow.

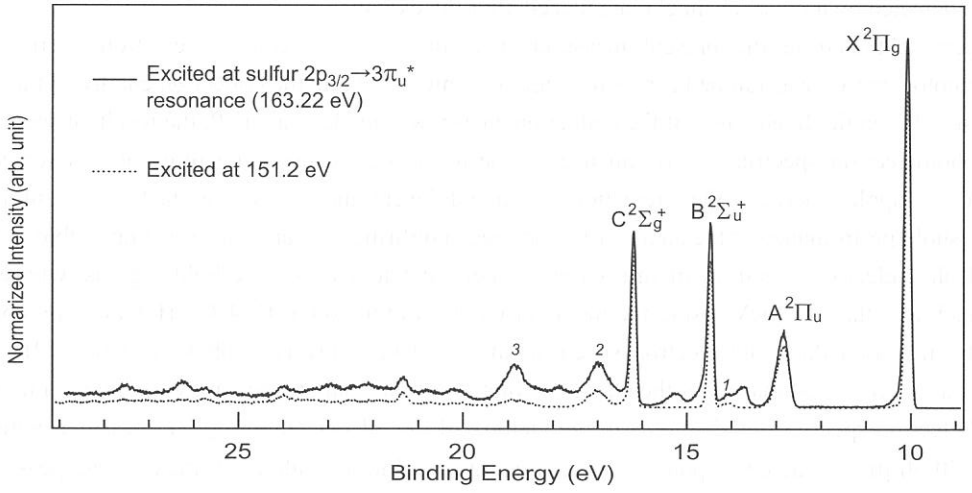

Figure 2. Low-resolution resonant photoelectron spectrum of CS_2 recorded at $2p_{3/2}\rightarrow3\pi_u*$ resonance (163.22 eV). Non-resonant photoelectron spectrum recorded below sulfur 2p excitation region (151.2 eV) is shown for comparison.

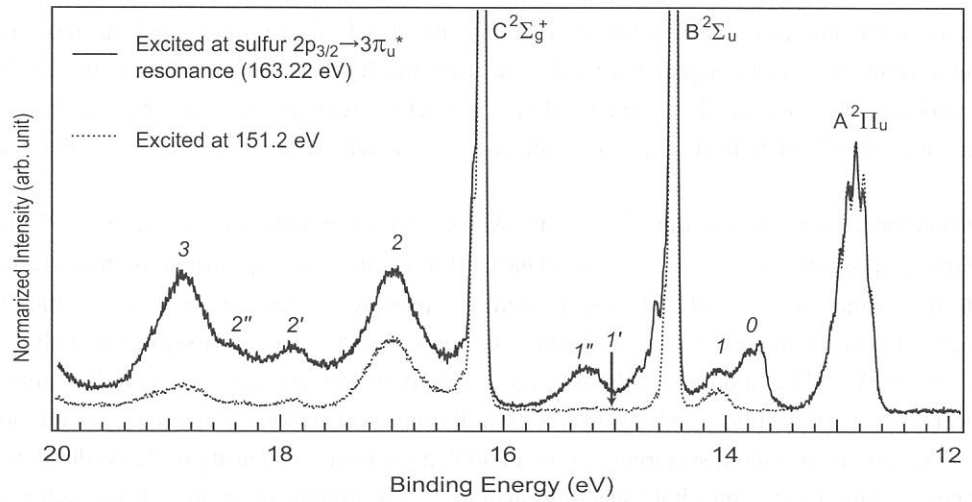

Figure 3. High-resolution resonant photoelectron spectrum of CS_2 recorded at $2p_{3/2}\rightarrow3\pi_u*$ resonance (163.22 eV). Non-resonant photoelectron spectrum recorded below sulfur 2p excitation region (151.2 eV) is shown for comparison.

(BL4B)

The First Performance Tests for a Newly Designed Threshold Electron Spectrometer

T. Gejo, E. Nakamura, and E. Shigemasa

Institute for Molecular Science, Okazaki 444-8585, JAPAN

It is widely recognized that threshold electron spectroscopy is one of the most powerful tools for probing the multiple excitation processes due to the electron correlations, such as shake up, shake off, and double ionization, in atoms and molecules. A novel threshold electron spectrometer has been constructed recently for investigating such processes and its performance tests have been carried out on BL4B. The spectrometer is composed of an input lens system based on the penetrating field technique [1] and an electrostatic analyzer (Comstock inc. AC-901 model). The lens system was designed for optimum collection and focusing of low energy electrons. By performing suitable adjustment of the potentials applied to the grids of the lens, it is possible to collect and focus electrons with energies from 0 to about 10 eV. Electrons passing through the analyzer were detected by a micro channel plate placed after the exit slit.

The spectra obtained in the present measurements correspond to constant electron energy spectra. Namely, the photon energy was ramped across the region of interest, while the collection energy of the analyzer was held fixed. When the fixed value of the collection energy was made equal to 0, the resultant spectrum was a threshold photoelectron spectrum. To enhance the performance for detecting threshold photoelectrons a draw-out field was applied between the interaction region and the entrance to the lens stack [1]. Unfortunately the actual threshold performance of the analyzer has not been confirmed so far, since it is impossible to measure the threshold photoelectron spectrum of rare gases in their first ionization threshold regions, whose natural widths are much less than 10 meV, using the monochromatized radiation at BL4B. However, by comparing the previously measured threshold electron spectrum in Kr 3d near-threshold photoionization [2] with that measured by our analyzer, estimation of the energy resolution of the analyzer becomes possible. Fig. 1 shows the threshold electron spectrum of Kr atoms in the vicinity of the 3d ionization region, measured with the slit openings of 120-50 μm. The corresponding photon energy resolution is about 50 meV. The peak width of the 5p Rydberg state in Fig. 1 is about 135 meV which is due to the natural width of the state (~100 meV) and the finite energy width of the incident radiation and the analyzer. Assuming that the total width observed can be expressed as the vector sum of the individual contributions with Gaussian profiles, it seems safe to say that the energy resolution of the analyzer is better than 80 meV. It is obvious from the spectrum of Fig. 1 that the threshold spectrum contains peaks due to the ionic states and also Rydberg states, and the ionic peaks are broadened and asymmetric when compared with the peaks for the Rydberg states. This is the result of post collision interaction (PCI), which is due to the Coulomb interaction between the slow photoelectron produced by the primary near-threshold ionization process and the fast Auger electrons generated by the subsequent decay process.

The threshold photoelectron spectrum of N_2 in the *K*-shell excitation region is shown in Fig. 2 along with the photoabsorption spectrum except for the π^* resonance. For the threshold spectrum, asymmetric slit widths of 125 and 50 μm for the entrance and exit slits, respectively, provide an energy resolution of ~200 meV over the photon energy region of interest, while the photoabsorption spectrum has been measured with the energy resolution of ~60 meV. The similar threshold spectrum with poorer energy resolution has already been reported in Ref. 3. The prominent π^* resonance and Rydberg transitions converging to the ionization threshold are present in the threshold spectrum. It is found that the relative intensity of the Rydberg transitions to higher n states are larger in the threshold spectrum than in the absorption spectrum. This result is common to the atomic case, where relative probability for an excited state for undergoing shake off increases with greater n. The peak corresponding to the N 1s threshold photoelectrons exhibits the energy shift to higher energy side

and asymmetry due to the PCI effect. There are at least two additional broad bands centered at ~415 and ~420 eV in the threshold spectrum, where the double excitations and σ* shape resonance are observed in the absorption spectrum. For further detailed discussions on these structures, improvement on the total performance of the experimental setup and additional information on the excited states are obviously necessary.

References

[1] R.I. Hall et al., *Meas. Sci. Tech.* **3**, 316 (1992).

[2] L. Avaldi et al., J. *Phys. B* **24**, 427 (1991).

[3] L.J. Medhurst et al., *J. Chem. Phys.* **89**, 6096 (1988).

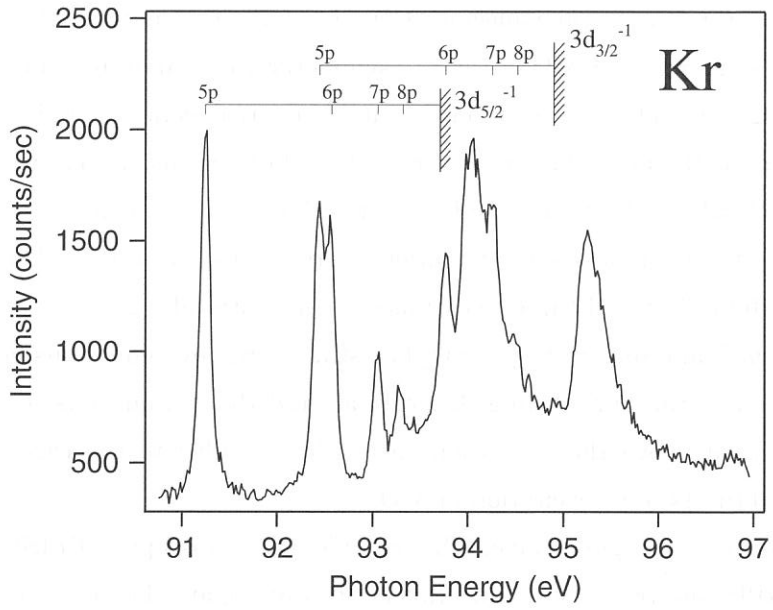

Fig. 1. Threshold photoelectron spectrum obtained in the region of the 3d subshell of Kr.

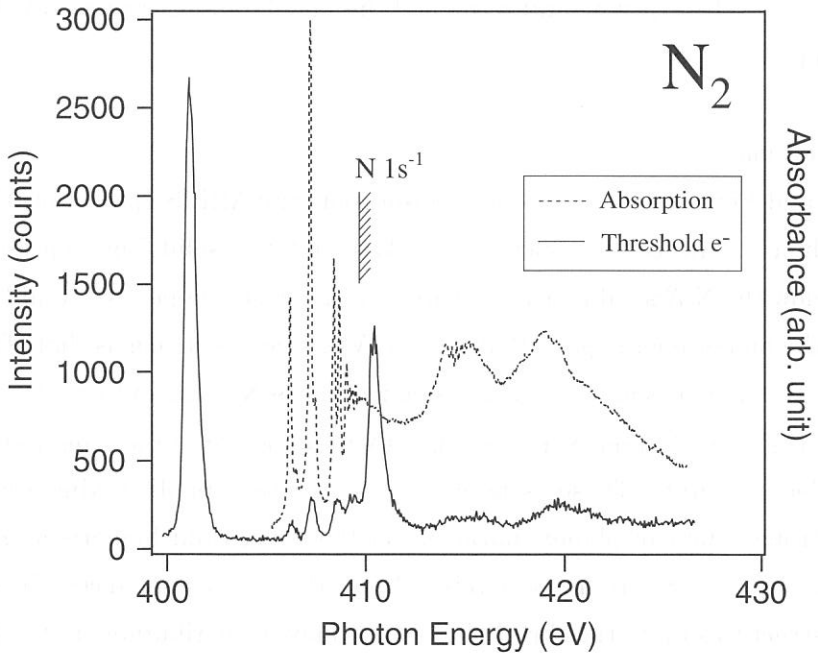

Fig. 2. Threshold photoelectron spectrum obtained in the *K*-shell excitation region of N_2.

(BL4B)

Angle-resolved photoion spectra of NO_2 in the N *K*-edge region

T. Gejo, E. Shigemasa, M. Nagasono, H. Oji, T. Hatsui and N. Kosugi

Institute for Molecular Science, Myodaiji, Okazaki 444-8585, Japan

Introduction

The NO_2 molecule has a bent structure with terminal oxygen atoms and belongs to the point group C_{2v}. Comparing to other liner tri-atomic molecules, NO_2 has one additional electron as an unpaired electron to the linear molecules CO_2 of the $D_{\infty h}$ symmetry with three unoccupied orbitals, $2\pi_u^*$, $5\sigma_g^*$, and $4\sigma_u^*$, and N_2O of the $C_{\infty v}$ symmetry with three unoccupied orbitals, $3\pi^*$, $8\sigma^*$, and $9\sigma^*$. The $(2\pi_u^*)^1$ and $(3\pi^*)^1$ states of CO_2 and N_2O are degenerate and are stabilized in a bent geometry due to the Renner-Teller effect, where $2\pi_u^*$ of CO_2 is split into in-plane π^* ($6a_1^*$) and out-of-plane π^* ($2b_1^*$), where the former and the latter have bent and linear stable geometries, respectively, and the former is lower in excitation energy than the latter. Thus, NO_2 has one half-filled valence orbital $6a_1^*$ and three unoccupied valence orbitals, $2b_1^*$, $7a_1^*$, and $5b_2^*$, which correspond to $3b_1^*$, $9a_1^*$, and $6b_2^*$ in SO_2. NO_2 has still strong covalent bonds between N and O even with an electron in the antibonding $6a_1^*$ orbital, and the N and O 1s$\rightarrow 5b_2^*$ excitation is expected to be observed above the ionization thresholds, similar to the case of the 1s$\rightarrow 4\sigma_u^*$ excitation in CO_2 and the 1s$\rightarrow 9\sigma^*$ excitation in N_2O.

Here we report the angle-resolved photoion yield spectroscopy (ARPIS) of NO_2 in the N *K*-edge region. ARPIS spectroscopy is a useful tool to investigate the symmetry of the K-shell excited states. In electric dipole transitions induced by the linearly polarized light, the transition probabilities relate to the molecular orientation with respect to the direction of the electric vector of the incident light . The experimental setup and the calculation procedure have been described in the previous report.

Results and Discussion

Fig. 1a and Fig. 1b display the photoabsorption and ARPIS spectra of NO_2 in the N *K*-edge region with a resolution of ~3000. The dots and the solid line represent I_{90} and I_0, respectively. Below the N *K*-shell ionization thresholds, two strong peaks, A and B, are observed. The intensity of the higher-energy peak B at 403.26 eV is twice as strong as that of the lower peak A at 401.03 eV. The higher peak B is easily assigned to the N 1s $2a_1\rightarrow 2b_1\pi^*$ (B_1) transition, and the lower peak A is assigned to the N 1s $2a_1\rightarrow 6a_1^*$ (A_1), as a result of the unpaired electron in the half-filled $6a_1$ valence orbital. These assignments are also reasonable, taking account of weak Σ (in plane) and strong Π (out of plane) characters of the lower- and higher-energy peaks in the ARPIS spectra as shown in Fig.1b, respectively. Above these two resonances, the spectra exhibit relatively weak structures up to the thresholds, which may be attributable to the Rydberg states and the Rydberg-valence mixed states. The excitation to $7a_1^*$ is expected to be less contributive to the spectral intensity, considering that $7a_1^*$ of NO_2 corresponds to $5\sigma_g^*$ in CO_2 and $8\sigma^*$ in N_2O

with s-type character on the central atom and the excitation from the K-shell to the s-type state should be weak. In the continuum, only one broad band around 416 eV is observed and is attributed to a σ^* continuum shape resonance originating from the strong σ* anti-bonding orbital of $5b_2$*.

Fig. 1c represents the blowup of the photoabsorption spectra of NO_2 in the N K-edge region with a resolution of ~5000. The calculations indicate that the valence and Rydberg transitions converging to the triplet ionization threshold are dominant. The triplet and singlet separation is observed for the 3s Rydberg states, C and D, where the total spin coupling is doublet and the exchange effect involving the Rydberg electron is estimated to be 0.18 eV at the most from the difference in their term values. Furthermore, the calculations show that the $7a_1$* valence is completely dissolved in the Rydberg sea and cannot be assigned to a specific peak. The $7a_1$* valence is mainly mixed into the s-type Rydberg, especially the 3s and 4s Rydberg (assigned to features C and G in Fig. 1), but the intensity contribution is expected to be small, as mentioned above. The features E/F, I/J, and M are mainly attributed to p-type Rydberg transitions converging to the triplet ionization threshold. Moreover, it is found from the calculations that the 1s→d$b_1(\pi)$ triplet channel is relatively strong among the 1s→d-type transitions and the features H, L and P have the same type of contributions.

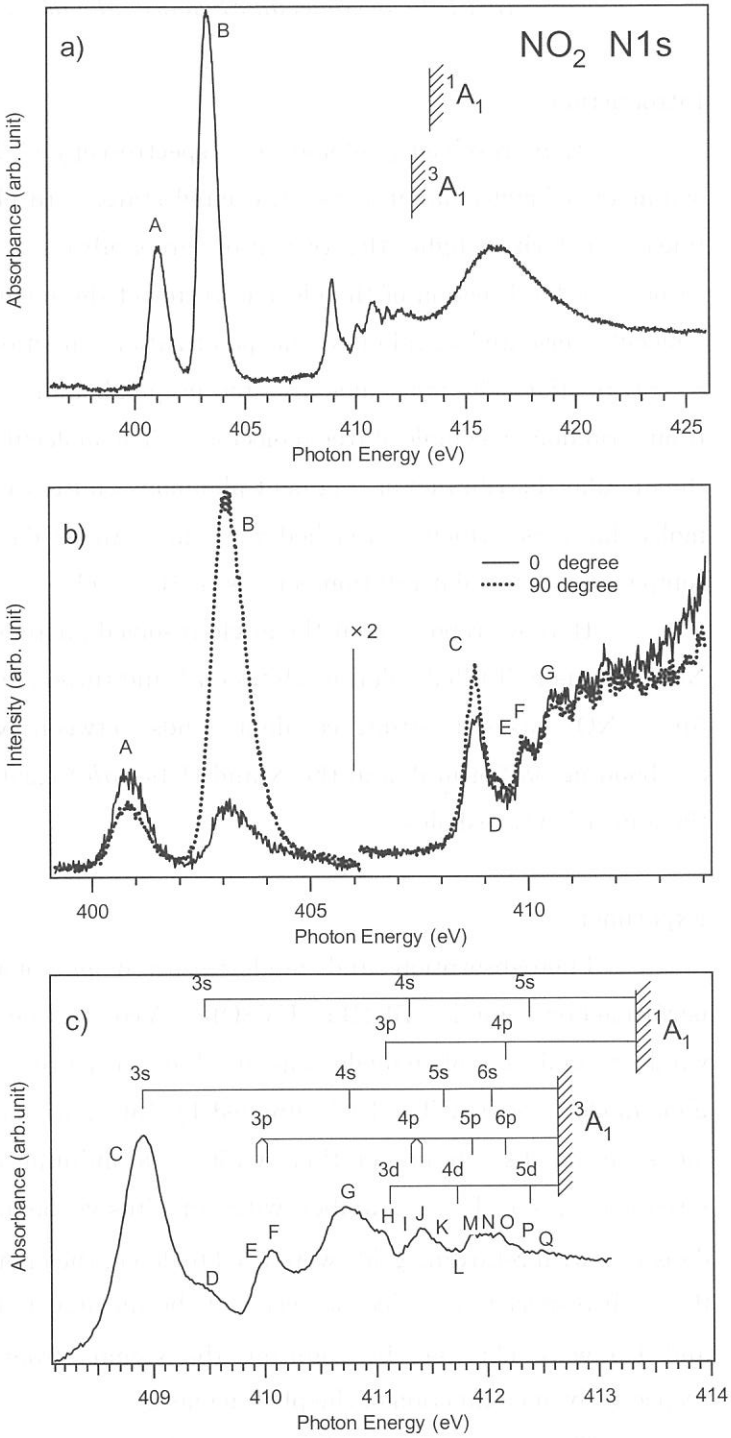

Figure 1. a) Absorption spectrum of NO_2 in the N K-edge region. b) Angle-resolved ion yield spectra of NO_2. Dotted and solid lines denote I_{90} and I_0 ion yields, respectively, in the N K-edge region. c) Absorption spectrum of NO_2 in the Rydberg excitation region.

(BL4B)

Angle-resolved photoion spectra of NO_2 in the O *K*-edge region

T. Gejo, E. Shigemasa, M. Nagasono, H. Oji, T. Hatsui and N. Kosugi

Institute for Molecular Science, Myodaiji, Okazaki 444-8585, Japan

Introduction

Angle-resolved photoion yield spectroscopy (ARPIS) is a useful tool to investigate the symmetry of molecular inner-shell excited states. In electric dipole transitions induced by the linearly polarized light, the transition probabilities relate to the molecular orientation with respect to the direction of the electric vector of the incident light. For the $\sigma \rightarrow \sigma$ transitions the molecules oriented parallel to the polarization direction are selectively excited, while for the $\sigma \rightarrow \pi$ transitions the molecules oriented perpendicular to the direction are preferentially excited from a random ensemble of free molecules. The molecular orientation will be directly reflected in the angular distribution of fragment photoions emitted immediately from a repulsive potential of molecular ions, which is reached by a fast Auger decay of the *K*-shell vacancy ($\tau \sim 10^{-14}$ sec) compared to molecular rotation periods ($\tau \sim 10^{-10}$ sec).

Here we report about the angle-resolved photoion spectra of NO_2 in the O *K*-edge region. NO_2 has one half-filled valence orbital $6a_1$* and three unoccupied valence orbitals, $2b_1$*, $7a_1$*, and $5b_2$*. NO_2 has still strong covalent bonds between N and O even with an electron in the antibonding $6a_1$* orbital, and the N and O 1s$\rightarrow 5b_2$* excitation are expected to be observed above the ionization thresholds.

Experiment

Photoabsorption and angler-resolved photoion yield (ARPIS) measurements were performed on beamline BL4B at UVSOR. A conventional gas cell system having leak tight thin windows and the photodiode was used to measure the photoabsorption spectra. A silicon photodiode (model AXUV-100) supplied by International Radiation Detectors Inc. was used to measure the absolute photon flux. A 1500 Å aluminum window from Luxel is installed to the up stream of gas cell. A chamber with an effusive beam nozzle was used. Two identical ion detectors with retarding grids were used to detect the energetic photoions (>2eV) emitted at 0° and 90° with respect to the electric vector of the incident light, respectively. The ARPIS spectra (I_0 and I_{90}) were obtained by counting the signals from the 0° and 90° positioned detectors, respectively, as a function of the photon energy.

The O 1s core-to-valence excited states of NO_2 were calculated by multi-reference configuration interaction including single and double excitations (MR-SDCI) [1]. The molecular geometries for the calculations were taken from those for the ground states. The CI calculations were carried out using SCF (self consistent field) orbitals for the 1s ionized states, which were obtained from the use of the GSCF3 code [2,3]. Symmetry-adapted molecular orbitals were used

even for the O 1s excited states with a localized character, which can be taken into account through MR-SDCI.

Results and discussion

Fig. 1a shows the photoabsorption spectrum of NO_2 in the O *K*-edge region with an energy resolution of ~5000. Fig. 1b demonstrates the ARPIS spectra with a resolution of ~3000. The dots and the solid line denote I_{90} and I_0, respectively. The splitting caused by the interaction between two O 1s orbitals ($1b_2$ and $1a_1$) is expected to be negligible. The lowest two features A and B are simply assigned to the O 1s $1a_1/1b_2 \rightarrow 6a_1^*(A_1,B_2)$ and O 1s $1a_1 \rightarrow 2b_1^*(B_1)$ transitions, respectively, where the O 1s $1b_2 \rightarrow 2b_1^*(A_2)$ transition is dipole forbidden. Fig. 1a shows rather strong features in the Rydberg excitation region, and a comparatively strong and broad enhancement above the ionization thresholds. The latter is assigned to the O 1s$\rightarrow 5b_2^*$ shape resonence, though Jürgensen and Cavell [4] assigned the shape resonance to the a_1 symmetry.

The excited states converging to the triplet ionized state are lower in energy than the states converging to the singlet. Similar to the case of the N 1s excitation, the calculations manifest that the $7a_1^*$ valence is completely dissolved in the Rydberg sea and cannot be assigned to a specific peak. The $7a_1^*$ valence is mainly mixed into the s-type Rydberg, especially the 4s and 5s Rydberg (assigned to the features D and E in Figure 1). In contrast to the central N 1s excitation, the terminal O 1s to $7a_1^*$ excitation is strongly contributive to the spectral intensity, as discussed in the O 1s and terminal N 1s excitations of CO_2 and N_2O.

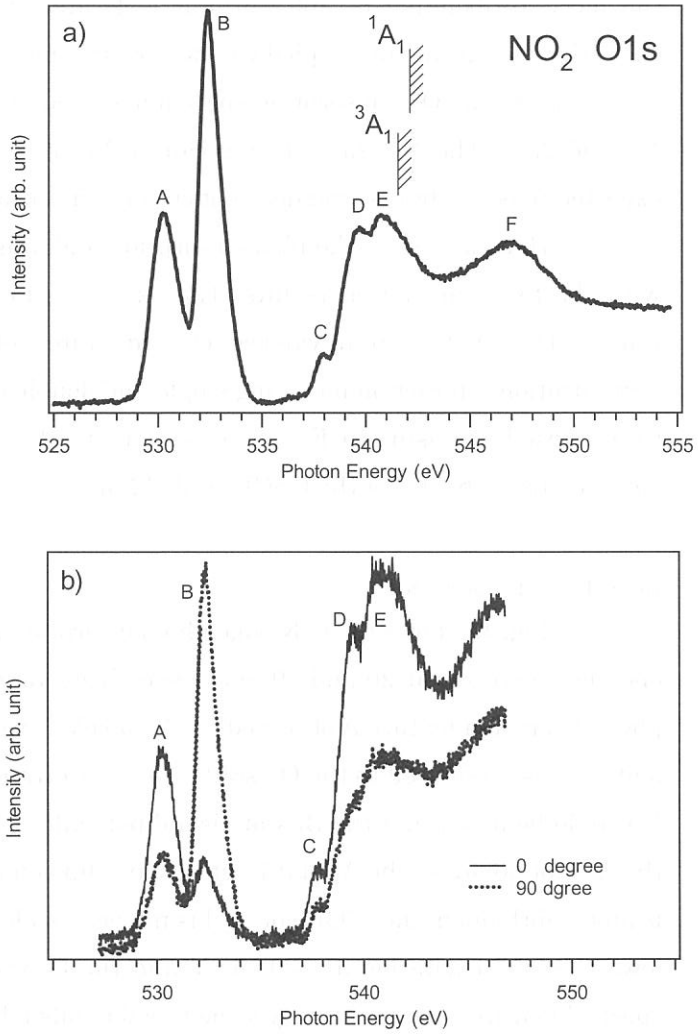

Figure 1. a) Absorption spectrum of NO_2 in O *K*-edge region. b) Angle-resolved ion yield spectra of NO_2 in the O *K*-edge region. Dotted and solid lines denote I_{90} and I_0 ion yields, respectively.

References

[1] E. Rühl et al., *J. Chem. Phys.* 116 (2002) 3316. [2] N. Kosugi and H. Kuroda, *Chem. Phys. Letters.*, 74 (1980) 490. [3] N. Kosugi, *Theoret. Chim. Acta*, 72, (1987) 149. [4] A. Jürgensen and R.G. Cavell, *Chem. Phys.* 257 (2000) 123.

(BL4B)

Angle-resolved photoion spectra of SO_2

T. Gejo, E. Shigemasa, M. Nagasono, H. Oji, T. Hatsui and N. Kosugi
Institute for Molecular Science, Myodaiji, Okazaki 444-8585, Japan

Introduction

The SO_2 molecule has three unoccupied valence orbitals, $3b_1$*, $9a_1$* and $6b_2$*, which can be associated with the three S 3p orbitals, where SO_2 has an electronic structure of $S^{4+}[(3s)^2(3p)^0]\cdot(O^{2-})_2$ in the limit of an ionic bonding picture and the $3b_1$, $9a_1$ and $6b_2$ orbitals correspond to out-of-plane S3p π (π_{out}), in-plane S3p π (π_{in}) and in-plane S3p σ, respectively [1]. All the S1s ($1a_1$) excitations to the $3b_1$*, $9a_1$* and $6b_2$* orbitals are dipole-allowed and are found to be lying below the S1s→Rydberg excitations with the term values of 10.4, 5.7, and 4.8 eV, respectively [1]. The chemical bond between S and O is not so strong, and even the excitation to the most antibonding σ* ($6b_2$) orbital is located below the ionization threshold. The single excitations to all the unoccupied valence orbitals are observed below the ionization threshold even in the case of the O1s absorption spectra assigned previously, though there are two O 1s orbitals, $1b_2$ and $2a_1$. The $1b_2$–$2a_1$ splitting caused by the interaction between the two O 1s orbitals is expected to be negligible and does not change the situation.

Here we report the photoabsorption and anlgle resolved photoion specta of SO_2, together with the SCF calculation results. The experimental setup has been described at the previous report. The O 1s core-to-valence excited states of SO_2 were calculated by multi-reference configuration interaction including single and double excitations (MR-SDCI). The CI calculations were carried out using SCF (self consistent field) orbitals for the 1s ionized states, which were obtained from the use of the GSCF3 code [2,3].

Results and discussion

Fig. 1a shows the O K-edge photoabsorption spectrum of SO_2. The entrance and exit slit openings were set at 20 and 10 μm, respectively, to get a resolving power of ~5000. The lowest photoabsorption feature A observed at 530.56 eV is well separated from the higher features. The feature A is attributed to the O 1s$\sigma(2a_1)$→$\pi^*(3b_1)$ transition, considering its term value of 9.27 eV. It should be noted that the B_1 state is a dipole-allowed out-of-molecular plane (π*) transition from the A_1 ground state, the A_1 and B_2 states are dipole-allowed in-plane transitions, and the A_2 state is dipole-forbidden; the $\pi^*(3b_1)$ orbital is not accessible from the O 1sσ ($1b_2$) electron. Between the lowest 1s→π* excitation at 530.56 eV and the O K-shell ionization threshold at 539.83 eV, the spectral feature is dominated by some broad bands labeled as B, C, and D at ~535 eV (term values of ~5eV) arising from the 1s→in-plane excitations, which consist of the O 1s→$9a_1$* (dipole-allowed B_2 from $1b_2$ and A_1 from $2a_1$) and O 1s→$6b_2$* (dipole-allowed A_1 from $1b_2$ and B_2 from $2a_1$) transitions. The structures E, F, and G are comparatively weak and have term values of 2.24, 1.63, and 0.75 eV, respectively; therefore, they are possibly assigned to the lowest s-type (4s or 5s)

and p-type (4p or 5p) Rydberg transitions. In the continuum, two broad bands are observed around 540.80 and 542.69 eV, which are attributable to double excitations or S 3d-type shape resonances, because there are no other singly excited valence states than the $1s \rightarrow 3b_1^*$, $9a_1^*$ and $6b_2^*$ transitions.

Fig. 1b indicates the present O K-edge ARPIS spectra of SO_2, where the dots and the solid line represent I_{90} and I_0, respectively. The peak A is definitely assigned to the O $1s(2a_1) \rightarrow \pi^*(3b_1)$ excitation, and F is assigned to the O $1s(2a_1) \rightarrow 4pb_1$ or $5sa_1$ Rydberg excitation ($B_1 \leftarrow A_1$). The peak G is probably assigned to the O $1s(1b_2/2a_1) \rightarrow 4pa_1$ and $4pb_2$ Rydberg excitations. However, the features B, C and D in Fig. 1 are difficult to assign even with the help of the ARPIS spectra.

In order to assign these peaks more accurately we have performed the SCF-CI calculations. The calculated results show that both the $1b_2 \rightarrow 9a_1^*$ (B_2) and $2a_1 \rightarrow 9a_1^*$ (A_1) transitions contribute to the feature B but $1b_2 \rightarrow 9a_1^*$ (B_2) is much stronger than $2a_1 \rightarrow 9a_1^*$, and that both the $1b_2 \rightarrow 6b_2^*(A_1)$ and $2a_1 \rightarrow 6b_2^*(B_2)$ transitions contribute to the feature C but $1b_2 \rightarrow 6b_2^*(A_1)$ is much stronger. That is, the $9a_1^*$ orbital is lower in energy than the $6b_2^*$ orbital, similarly to the case of the S 1s excitation [1]; however, the excitations from the b_2-symmetry core orbital are dominant in the case of the O 1s excitation, resulting in the inverse retarding potential dependence of the asymmetry prameters for $9a_1^*$ and $6b_2^*$ in comparison with the S 1s (a_1) excitation. The feature D is assigned to the O $1s(1b_2/2a_1) \rightarrow 4sa_1$ Rydberg excitation. The calculation also shows that E is assigned to the O $1s(2a_1) \rightarrow 4pb_1$ or O $1s(1b_2/2a_1) \rightarrow 4pa_1$ Rydberg excitation and F is assigned to the O $1s(1b_2/2a_1) \rightarrow 4pb_2$ or O $1s(2a_1) \rightarrow 3db_1$ Rydberg excitation.

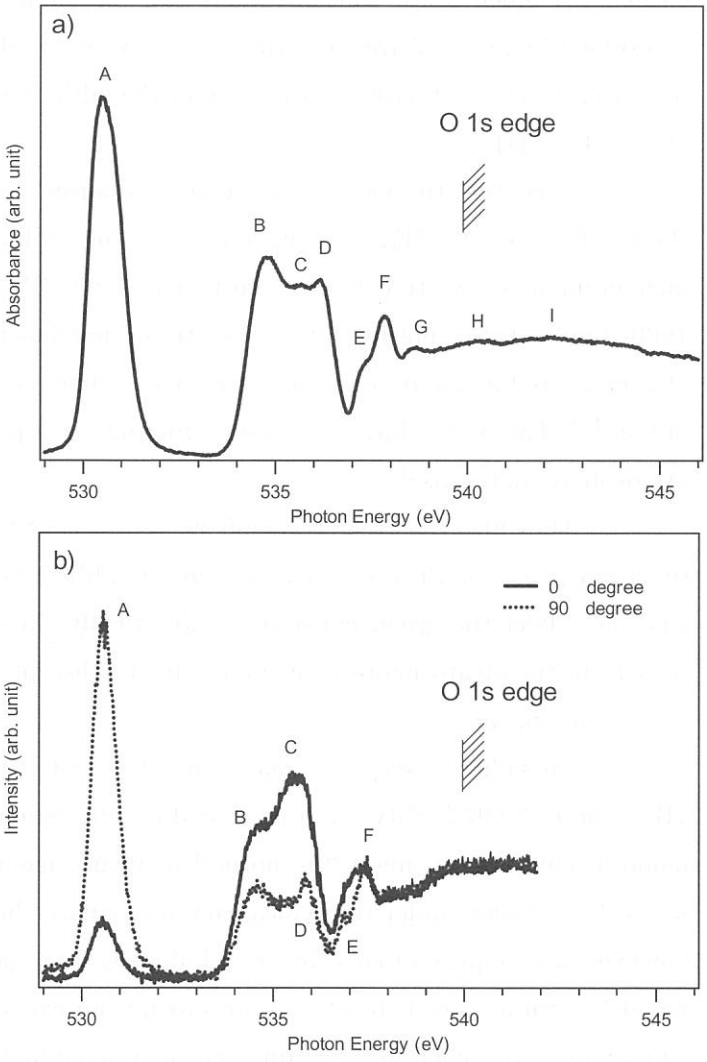

Figure 1. a) Absorption spectrum of SO_2 in the O K-edge region. b) Angle-resolved ion yield spectra of SO_2. Dotted and solid lines denote I_{90} and I_0 ion yields, respectively.

References

[1] J. Adachi et al. Chem. Phys. Letters, 294 (1998) 559. [2] N. Kosugi and H. Kuroda, Chem. Phys. Letters., 74 (1980) 490. [3] N. Kosugi, Theoret. Chim. Acta, 72, (1987) 149.

(BL7B)

The measurement of absorption spectra of Trifluoromethyl Sulfur Pentafluoride in VUV region

Tatsuo GEJO, Eiji SHIGEMASA , Kenshi TAKAHASHI [A)] and Yutaka MATSUMI [A)]
Institute for Molecular Science, Myodaiji, Okazaki 444-8585, Japan
[A)]STEL, Nagoya Univ. Honohara 3-13, Toyokawa, 442-8507, Japan

Global warming or green house effect is one of the major issues for environmental chemistry. Although CO_2, CH_4, and N_2O play a major role on the green house effect in air, some gases with much lower concentrations can contribute to the global warming because of their exceptionally large infrared absorption. For example, SF_6 has 22,200 times larger global warming potential (GWP) over a100-year time than CO_2 although it is currently present in the atmosphere at only 4 ppt [1].

Recently Sturges et al. detected Trifluoromethyl sulfur pentafluoride (SF_5CF_3), which is chemically close to SF_6, at Antarctic deep consolidated snow (firn) [1]. This Antarctic firn measurement shows that the concentration of SF_5CF_3 have increased from near zero in the late 1960s to about 0.12 ppt in 1999, whose trend matches to recent global warming tendency. They also measured a radiative forcing of SF_5CF_3, which is 0.57 watt per square meter per parts per billion [1]. This is the largest radiative forcing, on a per molecule basis, of any gas found in the atmosphere up to this date.

They also reported stratospheric profiles of SF_5CF_3 and suggested that it is long-lived in the atmosphere (on the order of 1000 years) [1]. If this is true, the irreversible accumulation of this gas may affect the green house effect drastically. In order to access this effect and lifetime of SF_5CF_3 in the stratosphere more precisely, its absorption spectra and cross sections in the VUV region are crucial.

This photoabsorption measurement of SF_5CF_3 in VUV region was performed at Beamline 7B in the UVSOR facility, Institute for Molecular Science. Synchrotron radiation at UVSOR was monochromated by using a 3-m normal incidence monochromator (NIM). The energy resolution was $\lambda/\Delta\lambda$ = 10000 under the typical conditions with the slit widths of 100 μm. High photon flux, however, was required to obtain the reliable signal to noise ratio and hence the slit widths of the monochromator were kept at 500 μm during the experiment. A photoabsorption cell was 33 cm long and was attached to the main experimental chamber. The typical sample pressure in the cell was 10 Pa, which was measured by a Baratron manometer. An LiF filter with a thickness of 1.5 mm was installed in front of the cell in order to keep the monochromator in good vacuum condition. The intensity of the photon beam transmitted through the cell was monitored by using a silicon photodiode (IRD Inc, AXUV-100). The photoabsorption cross sections were calculated by using the Beer-Lambert expression. The data were checked to ensure there is no line saturation effect.

Fig 1 shows the absorption spectra of SF_5CF_3 in VUV region. In this figure, two strong peaks were observed: One peak around 107 nm (A) and another one around 130 nm (B). The peak similar to A is also observed in SF_6, whereas the equivalent to the peak B was not observed. Therefore one can suggest that the peak B arises from the transition from the lone pair electron of CF_3.

Based on these data, we will estimate the lifetime of SF_5CF_3 in the stratosphere.

[1] W. T. Sturges et al., Science 289, 613(2000)

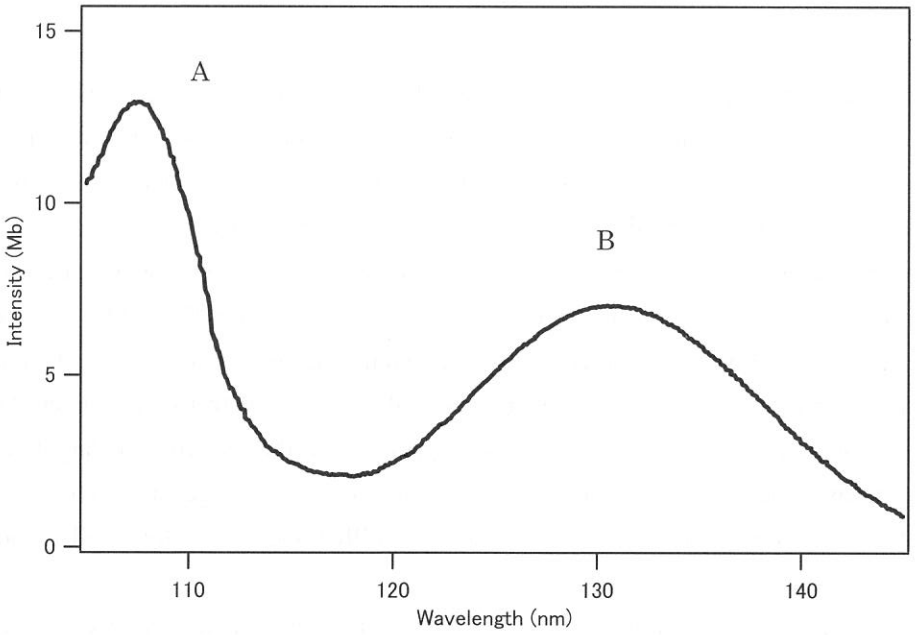

Fig. 1: The absorption spectra of SF_5CF_3 in the VUV region

(BL8B1)

Molecular size effect on the site-specific fragmentation of the N and O *K*-shell excited oxoalkanenitrile molecules

Tomoki MORITA, Kazumasa OKADA, Toshio IBUKI,[a] Yuichi HAGA,[a] Shuichiro TANIMOTO, Tatsuo GEJO,[b] Ko SAITO, and Keiichi OHNO

Department of Chemistry, Hiroshima University, Higashi-Hiroshima 739-8526

[a] *Kyoto University of Education, Kyoto 612-8522*

[b] *Institute for Molecular Science, Okazaki 444-8585*

An attractive concept of photochemistry is selective bond activation of a molecule by tuning the photon energy to specific electronic and/or vibrational transitions. Monochromatized soft x-ray synchrotron radiation can excite core electrons of a molecule. Because of the localized nature of core electrons, an intriguing possibility is that the bond rupture will be also localized around the atomic site of excitation. Evidence for such selective photochemistry has been found in studies on the fragmentation of a few molecules since the pioneering work by Eberhardt et al. [1], showing the C^+ and O^+ fragment ions were characteristically enhanced in the carbonyl C(1s) $\rightarrow \pi^*$ excited acetone. The question then arose as to the correlation of the created core hole and the removal of valence electrons via Auger decay with the molecular fragmentations. In later studies, it became apparent that the selectivity is largely determined by the electronic decay of the core-hole state [2]. Since then, relatively large number of studies has been performed with an Auger electron–photoion coincidence (AEPICO) technique for detailed understanding of the fragmentation mechanisms.

On the other hand, the idea of chemical activation and the non-statistical effects on reaction emerged up in the field of unimolecular reactions [3]. Dissociation pattern can be viewed as the outcome of the competition between the bond rupture in the activated site and energy randomization over the activated molecule. Thus in order to have more insights into the site-specific photochemistry of core-excited molecules, it is of great interest to determine whether the initial memory of core excitation preserves against the energy randomization. In our recent study on the fragmentation of the N and O *K*-shell excited CH_3OCOCN and CH_3OCOCH_2CN molecules, the fragmentation patterns were essentially identical for the smaller molecule, while marked site-specific fragmentation was observed for the other molecule [4]. This result infers that the site-specific fragmentation following core excitation depends on the molecular size. In this report, we present the results of a consecutive study concerning the molecular size effect on the site-specific fragmentation following the excitation of core electrons in a polyatomic molecule.

The experiments were performed on the beamline BL8B1 at the UVSOR facility. Photoabsorption spectra were observed in the N and O *K*-shell regions of gaseous pyruvonitrile (CH_3COCN), cyanoacetone (CH_3COCH_2CN), and 4-oxopentanenitrile ($CH_3CO(CH_2)_2CN$) molecules. A Samson-type ion chamber with 10-cm long electrodes was mounted on the main chamber and used for the measurement. The ion current was fed to a picoammeter and stored in a personal computer, together with the sample pressure. The energy scale was calibrated using the major soft x-ray peaks of N_2 and O_2.

The photoelectron–photoion coincidence (PEPICO) spectra were acquired at some typical photon energies by using a reflectron type time-of-flight (RTOF) mass spectrometer. An effusive flow of sample

gas was introduced into the main chamber through a gas nozzle orthogonal to both the photon beam axis and the spectrometer tube. A high electrostatic field was applied across the collision region so as to collect the energetic fragment ions with kinetic energies up to ≅10 eV. The flight time of ions was measured with a TAC. The output pulse height from the TAC was analyzed with an MCA and the obtained spectrum was then transmitted to a personal computer. The axis of the spectrometer was set at the magic angle with respect to the photon polarization direction for suppressing anisotropic effect in the photoabsorption process. An Al thin filter was inserted upstream in order to reduce the scattered stray light. Incident soft x-ray flux was monitored by an Au mesh and recorded simultaneously as the photocurrent. All spectra were normalized by the photocurrent in order to correct for fluctuations in dispersed photon flux. The CH_3COCN sample for the experiment was obtained commercially and the other two samples were prepared according to the published methods [5, 6].† All samples were used after being degassed by several freeze–pump–thaw cycles.

Figure 1 shows the RTOF mass spectra acquired at the $N(1s)^{-1}$ and $O(1s)^{-1}$ ionizations of gaseous $CH_3CO(CH_2)_2CN$ molecule. The photofragment ions heavier than m/e=60 were negligible. Clear dependence of the photofragmentations on the atomic site of excitation can be found in the present study as well. It is worthwhile to note that the abundant photofragment ions are H^+ and CN^+ at the N *K*-shell ionization, while heavier photofragments such as the CH_3C^+ and CH_3CO^+ ions are greatly produced at the O *K* edge: The yields of the latter two photofragments are 1.5 and 2.4 times larger in the $O(1s)^{-1}$ ionization than those in the $N(1s)^{-1}$ ionization, respectively. The abundant production of these photofragment ions is reasonably explained by the bond fission around the carbonyl group. That is, for the $CH_3CO(CH_2)_2CN$ molecule the photofragmentation basically occurs at the limited site of initial excitation. By contrast, core excitation of the smallest CH_3COCN molecule does not show any difference in fragmentation patterns regardless of the sites and states of the initial excitation. Core-excited CH_3COCH_2CN molecule gives the middle result among the molecules studied.

†The authors are grateful to Mr. M. Yamashita and Professor Y. Yamamoto at Hiroshima University for their help in the synthesis of the samples.

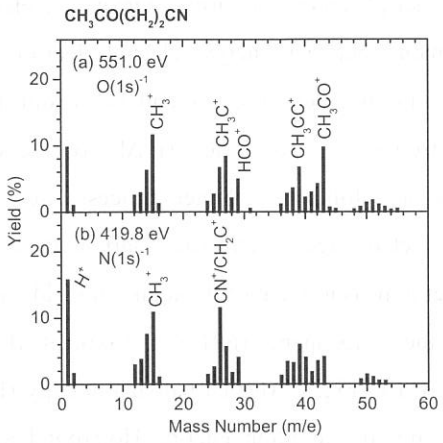

Fig. 1: The RTOF mass spectra of $CH_3CO(CH_2)_2CN$ excited at the $O(1s)^{-1}$ and $N(1s)^{-1}$ ionizations. The spectra are presented as percentage yields calculated from the peak areas.

References

[1] W. Eberhardt, T. K. Sham, R. Carr, S. Krummacher, M. Strongin, S. L. Weng, and D. Wesner, *Phys. Rev. Lett.* **50**, 1038 (1983).

[2] W. Eberhardt, E. W. Plummer, I.-W. Lyo, R. Reininger, R. Carr, W. K. Ford, and D. Sondericker, *Aust. J. Phys.* **39**, 633 (1986); W. Eberhardt, E. W. Plummer, I.-W. Lyo, R. Carr, and W. K. Ford, *Phys. Rev. Lett.* **58**, 207 (1987).

[3] W. Forst, "Theory of Unimolecular Reactions," Academic Press, New York (1973).

[4] T. Ibuki, K. Okada, K. Saito, and T. Gejo, *J. Electron Spectrosc. Relat. Phenom.* **107**, 39 (2000).

[5] L. Claisen, *Ber. Deutsch. Chem. Gesell. (Berlin)* **25**, 1776 (1892).

[6] Y. Kawasaki, A. Fujii, Y. Nakano, S. Sakaguchi, and Y. Ishii, *J. Org. Chem.* **64**, 4214 (1999).

(BL8B1)

Study on Dissociation Dynamics of Core-exited Trifluoromethane in the F K-shell Excitation Region using Auger Electron-Photoion-Photoion Coincidence Measurement

Y. Suto [a], H. Yoshida [a], M. Aratake [a], Y. Senba [a], T. Gejo [b], K. Mase [c], and A. Hiraya [a]

[a] *Department of Physical Science, Hiroshima University, Higashi-Hiroshima 739-8526, Japan.*
[b] *UVSOR, Institute for Molecular Science, Okazaki 444-8585, Japan.*
[c] *Photon Factory, Institute of Materials Structure Science, Tsukuba 305-0801, Japan.*

Core-excited molecules are unstable and Auger decay follows rapidly. Auger electrons are emitted with various kinetic energies and as a consequence, various Auger-final states of singly charged ions are produced. When the energy of Auger-final state is higher than the threshold of double ionization, it can be autoionized into doubly charged ion. This dication often dissociate into ion pair by Coulomb repulsion. To elucidate the detail of the dissociation dynamics of core-excited organic molecules, especially those from the dication produced by auto ionization, Auger electron–photoion–photoion coincidence (AEPIPICO) measurements have been applied to CH_3CN [1] and $(CH_3)_2CO$ [2]. In the present study, we have investigated the dissociation dynamics of trifluoromethane (CHF_3) in the F K-Shell excitation region.

Experimental procedure was described elsewhere [3]. Briefly, a double-focusing time-of-flight (TOF) mass spectrometer [4] and a cylindrical-mirror type electron energy analyzer (CMA) [5] were used for the coincidence measurements between energy-selected electrons and fragment ions. A weak electrostatic field (40 V/cm) was applied to the interaction region and as a result, mass resolution ($M/\Delta M$) of the TOF was estimated to be ~30 and electron energy resolution ($E/\Delta E$) of the CMA ~25. Correlations between two ions produced by an autoionization following Auger process are recorded in a fast multiscaler by using the signal of an energy-selected Auger electron as a start signal and the ion signals as multi-stop signals.

After a measurement of the total ion yield curve for CHF_3 at F1s excitation region, we set the photon energy to top of the σ^* resonance (691 eV). A typical AEPIPICO 2-D map obtained for the Auger electron energy of 657 eV is shown in Fig.1. Auger-final-state energy (FSE) of 34 eV is calculated by subtracting the electron energy from the initial excitation energy. Horizontal and vertical axes are the flight time of first and second ion, respectively. Various ion pairs such as F^+/CF^+, F^+/CHF^+, F^+/CHF_2^+ and F^+/CH^+ are observed. The slope of the coincidence peak for the ion pair F^+/CHF_2^+ produced by two-body dissociation is –1. The slope of –1 indicates that the initial momenta of two ions produced by dissociation of dication have same amplitude with opposite direction. Fig.2(a) shows a part of AEPIPICO 2-D map at F^+/CF^+ ion pair region in Fig.1. Slope of the coincidence peak is estimated to be not –1 but about –0.6. This implies a sequential dissociation of the parent dication CHF_3^{2+}. A plausible dissociation mechanism to form this ion pair is considered as follows.

$$CHF_3^{2+}\ (FSE=34eV) \rightarrow F^+ + CHF_2^+ \rightarrow F^+ + CF^+ + H + F\ (or\ HF)\ \ldots\ (1)$$

For this process, slope of the coincidence peak is calculated to be -0.63. The value is in good agreement with the experimental one. Fig.2(b) shows the same part of AEPIPICO 2-D map as Fig.2(a), but obtained for FSE of 59

eV. The slope of this peak is almost –1. The dissociation mechanism is considered as follows.

$$CHF_3^{2+}\ (FSE=59eV) \rightarrow CF_2^{2+} + H + F\ (or\ HF) \rightarrow F^+ + CF^+ + H + F\ (\ or\ HF)\ \ldots\ (2)$$

These observations reveal, for the first time, different dissociation mechanisms for different dicationic states having different Auger-final-state energy.

References

[1] Y. Senba *et al.*, UVSOR Activity Report 2000, 28 (2001) 84.
[2] H.Yoshida *et al.*, UVSOR Activity Report 2000, 28 (2001) 88.
[3] Y. Senba *et al.*, to be published.
[4] A. Hiraya *et al.*, Journal of Electron spectroscopy and related phenomena 101-103 (1999) 1025.
[5] T. Gejo *et al.*, UVSOR Activity Report 1999, 27 (2000) 68.

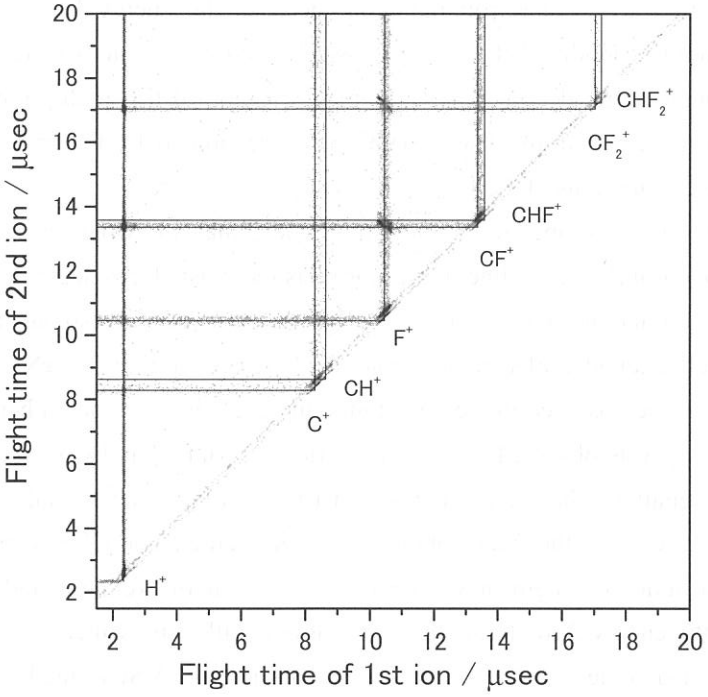

Fig.1. AEPIPICO spectrum obtained for the F1s to σ* (691eV) and for Auger electron energy of 657eV. (FSE=34eV)

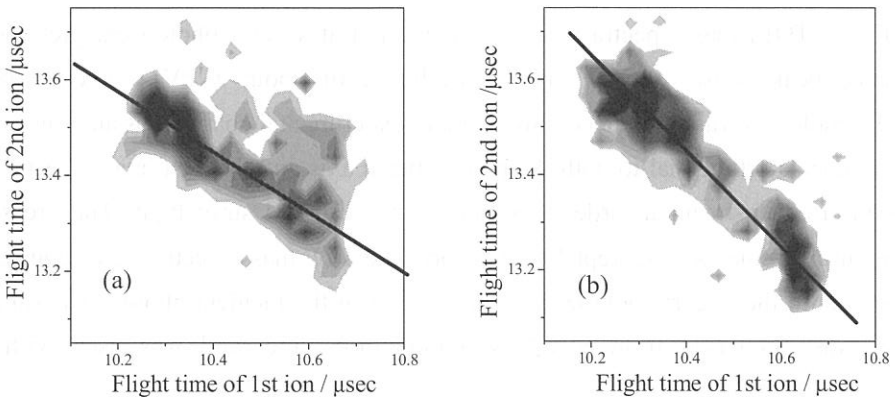

Fig.2. Part of AEPIPICO 2-D maps at F^+/CF^+ ion pair region measured with the final state energy of (a) 34 and (b) 59eV. Reference lines are also shown, which slopes are calculated to be (a) –0.63 and (b) –1.

(BL8B1)

Fragmentation of the C *K*-shell excited CF_3CN molecule studied by angle-resolved TOF mass spectroscopy: Vibrational modes acting as an internal energy reservoir

Shuichiro TANIMOTO, Kazumasa OKADA, Toshio IBUKI,[a] Ko SAITO, and Tatsuo GEJO[b]

Department of Chemistry, Hiroshima University, Higashi-Hiroshima 739-8526

[a] *Kyoto University of Education, Kyoto 612-8522*

[b] *Institute for Molecular Science, Okazaki 444-8585*

Inner-shell electrons of the atom in a specific chemical environment of a molecule can be selectivity excited with a tunable soft x-ray synchrotron radiation, because the energy levels of the inner-shell electrons differ from one atom to another. When the inner-shell electron is photoexcited, a multiply ionized molecule is produced through Auger decays. The Coulomb explosion of this multiply charged molecular ion follows the loss of bonding electrons. The dynamics can be probed by the measurement of mass, angular, and kinetic energy distributions of the fragment ions.

Trifluoroacetonitrile (CF_3CN) is one of the intriguing molecules in two respects. Firstly, we can selectively excite a specific atom (F, N, or either C). Fluorine is the most electronegative atom and induces the largest chemical shift around it in the molecule. Secondly, we can investigate the fragmentation dynamics of the inner-shell excited molecule noticing the linearity of the C–C≡N skeleton. Whether anisotropic fragmentation can be observed in the polyatomic molecule is our concern here. In our previous study [1], a strong anisotropy was observed for the energetic CF_3^+, CF_2^+, and CN^+ fragment ions at the $\pi_{CN}^* \leftarrow$ N(1s) resonance excitation. That is, the Π–Σ symmetry transition basically holds. This report gives an outline of our subsequent work on the fragmentation of the *K*-shell excited CF_3CN molecule. We show that the kinetic energy distribution of fragment ions depends on the site of excitation and the fragmentation competes with intramolecular energy flow. The detailed discussion will be presented elsewhere [2].

The experiments were performed on the beamline BL8B1 at the UVSOR facility. Photoabsorption spectrum was observed at room temperature in the C *K*-shell region with the energy resolution $E/\Delta E$ better than 2000. The experimental setup, procedure, and the obtained photoabsorption spectrum have been given in Ref. [3], and we do not repeat here.

The time-of-flight (TOF) mass spectra were also measured at several photon energies including the prominent resonance peaks observed. An energy resolution of about 1 eV was employed for the measurement. The sample gas was introduced into the main experimental chamber as an effusive molecular beam through a gas nozzle orthogonal to both the photon beam axis and the TOF mass spectrometer tube. An Al filter was inserted upstream in order to suppress the scattered stray light. The pressures in the chamber during the measurements were kept 1×10^{-5} Torr. The TOF mass spectra were acquired at 0° and 90° angles with respect to the linearly polarized electric vector of the incident photon. The sample gas for the present study was purchased from SynQuest Laboratories, Inc. and was used without further purification.

The mass spectral profiles of CN^+, CF_2^+, and CF_3^+ peaks were reproduced by the fitting method developed by Saito and Suzuki [4] to obtain the anisotropy β parameters and kinetic energy distributions. The kinetic energies and the β parameters for the components were determined so as to minimize the

difference between the experimental data and the calculated profile. Figure 1 shows the derived kinetic energy distributions of the CN^+, CF_2^+, and CF_3^+ fragment ions generated at the $C_N(1s)$ and $C_F(1s)$ excitations into the π^*_{CN} level. The kinetic energy distribution of CN^+ was expressed well by a Gaussian function with the maximum at KE ~ 2.7 eV, while those of CF_2^+ and CF_3^+ were split into two components: One is a sharp component with a maximum around 0.1 eV and another is a broad distribution with a maximum at 1.3 and 1.1 eV for the CF_2^+ and CF_3^+ ions, respectively. These high kinetic energies are interpreted by a simple relation of $M(CN^+)/M(CF_n^+) \times 2.7 = 1.4$ and 1.0 eV for CF_2^+ and CF_3^+, respectively, where $M(CN^+)/M(CF_n^+)$ is the mass ratio between the CN^+ and CF_n^+ fragment ions. That is, the axial-recoil approximation is valid for the production of the energetic CN^+ and CF_n^+ fragment ions.

The kinetic energy distributions at the $C_F(1s)$ excitation are as wide as those at the $C_N(1s)$ excitation. We cannot see, however, low kinetic energy components for the CF_2^+ and CF_3^+ fragment ions. A dependence of the kinetic energy distribution of the fragment ions on the site-specific excitation is observed for the first time. That is, fragmentation into the CF_n^+ ions following the $C_N(1s)$ excitation competes with the intramolecular energy flow from the initially excited C_N atom to the CF_3 group. We can claim that most of the CF_3^+ ions are formed with kinetic energies and a part of CF_3^+ (about 20 %) would be produced after energy redistribution through the C–C≡N skeleton into the vibrational modes within the CF_3 group. When a $C_F(1s)$ electron of the CF_3 group is initially excited, energy flow from the CF_3 group to the terminal N atom would occur. However, the CN group is not an effective energy reservoir because it has only one vibrational mode, and thus at any excitation mode the CN^+ fragment ion does not have a small kinetic energy component. The CF_3 group acts as an internal energy reservoir.

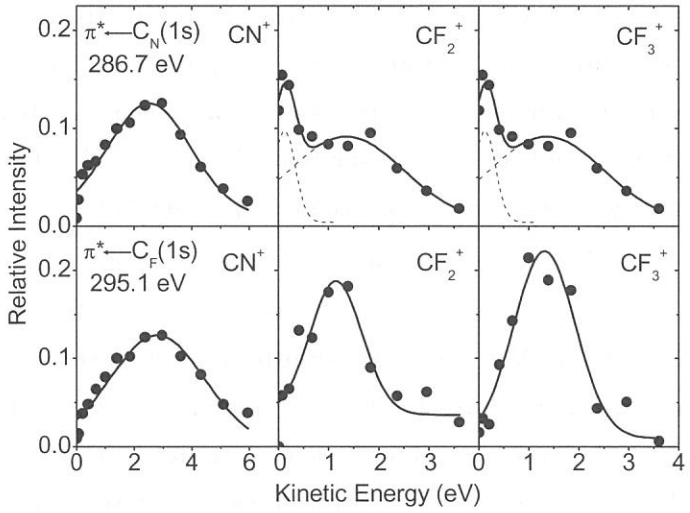

Fig. 1: Kinetic energy distributions of the CN^+, CF_2^+, and CF_3^+ fragment ions generated at the $C_N(1s)$ and $C_F(1s)$ excitations into the π^*_{CN} level.

References

[1] T. Ibuki, K. Okada, T. Gejo, and K. Saito, *Chem. Phys. Lett.* **328**, 147 (2000).

[2] T. Ibuki, K. Okada, S. Tanimoto, K. Saito, and T. Gejo, *J. Electron Spectrosc. Relat. Phenom.*, in press.

[3] K. Okada, S. Tanimoto, T. Ibuki, K. Saito, and T. Gejo, *Chem. Lett.*, 1046 (2001).

[4] N. Saito and I. H. Suzuki, *Int. J. Mass Spectrom. Ion Processes* **82**, 61 (1988).

(BL8B1)

Ultra-fast Dissociation of Core-exited Trifluoromethane in the C K-shell Excitation Region

H. Yoshida [a], Y. Suto [a], M. Morita [a], Y. Senba [a], T. Gejo [b], K. Mase [c], and A. Hiraya [a]

[a] *Department of Physical Science, Hiroshima University, Higashi-Hiroshima 739-8526, Japan.*

[b] *UVSOR, Institute for Molecular Science, Okazaki 444-8585, Japan.*

[c] *Photon Factory, Institute of Materials Structure Science, Tsukuba 305-0801, Japan.*

Core-excited species are unstable and decay processes follow rapidly. The most dominant decay process is resonant Auger electron emission. In some case, the nuclear motion is so fast that dissociation takes place on the same scale as Auger electron emission. Such dissociation in core-excited states is termed "ultra-fast dissociation" and its time scale is considered to be several femtoseconds. It was observed at first for HBr at the Br3d$\rightarrow\sigma^*$ excitation by detecting the atomic Auger emission from the core-excited fragment Br^* [1]. The electronic decay from the core-excited fragment was also observed for CH_2F_2, CHF_3, and CF_4 at the C1s$\rightarrow\sigma^*$ excitation [2]. Those were tentatively assigned to the electron emission from C^* or CF^*. To elucidate the detail of the ultra-fast dissociation processes for CHF_3, Auger electron–photoion coincidence (AEPICO) measurements have been carried out at the soft x-ray beamline BL8B1.

The experimental procedure was described elsewhere [3]. The resonant Auger spectrum following the C1s$\rightarrow\sigma^*$ excitation ($h\nu$=294.7eV) is shown in Fig.1. Horizontal axis is indicated as a scale of Auger-final-state energy (FSE). Spectator-type Auger transitions are observed around 40 and 60 eV, while participant-type around 20 eV. The weak shoulder structure observed at 26 eV is ascribed to the Auger transition from the fragment [2]. Coincidence spectra between energy-selected Auger electrons and fragment ions were measured for various Auger-final-state energies. When the FSE is set to 17 eV, CF_3^+, CF_2^+, and CF^+, which would be produced from the participant-type molecular Auger-final states, are observed in Fig.2(a). On the other hand, only CF^+ is appeared in Fig.2(b) when the FSE is set to 26 eV. This is a clear evidence for the Auger decay from not C^* but CF^* fragments. Such a considerable enhancement for CF^+ yield can not observed for the other core-excited states, for instance, C1s$\rightarrow$3p. We, thus, conclude that after C1s$\rightarrow\sigma^*$ excitation in CHF_3, the ultra-fast dissociation (1) and consequent Auger decay of the fragment (2), as described bellow, take place in competition with the resonant Auger decay within several femtoseconds.

$$CHF_3^*(C1s^{-1}\,\sigma^*) \rightarrow CF^*(C1s^{-1}\sigma^*) + H + F + F \quad (1)$$
$$\rightarrow CF^+ + e^- \quad (2)$$

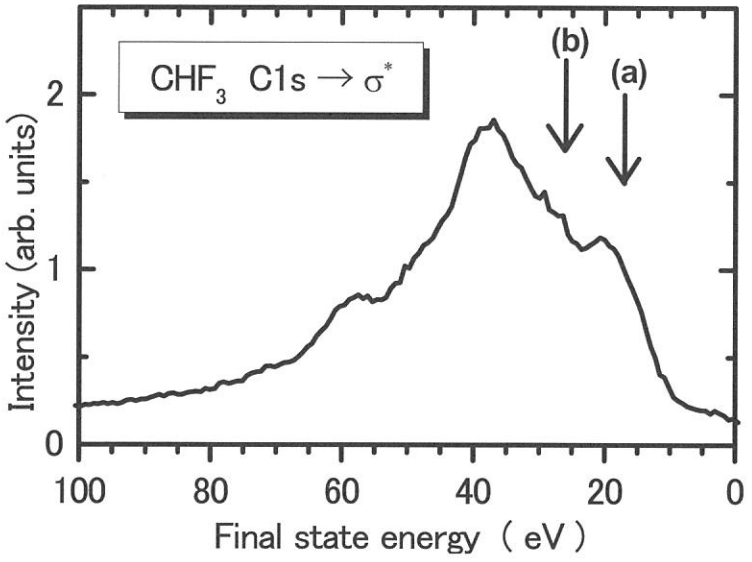

Fig.1 Auger electron spectrum for CHF_3 at C1s→σ^* excitation

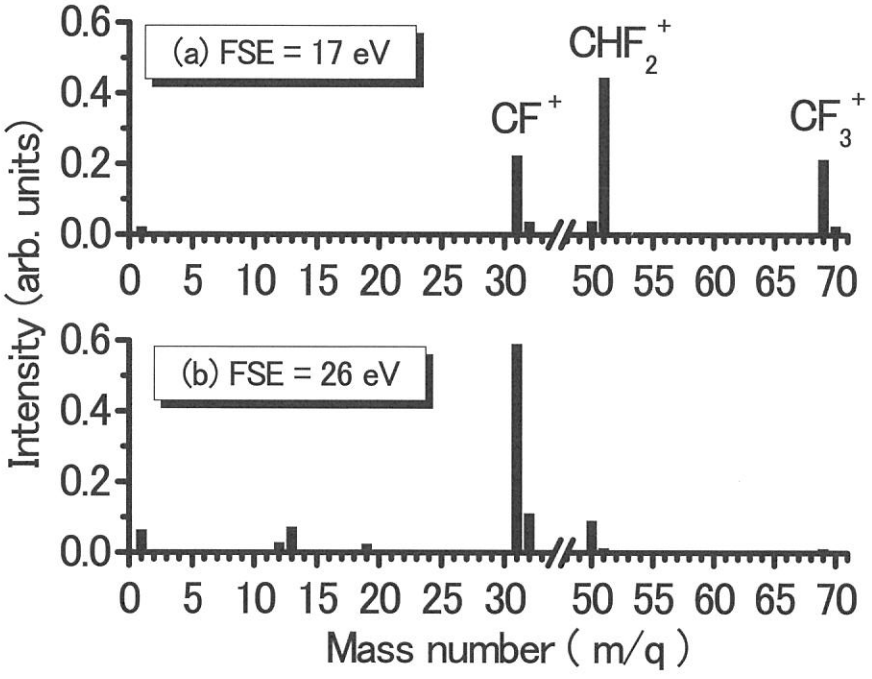

Fig.2 AEPICO spectrum for CHF_3 at C1s→σ^* excitation

References

[1] P. Morin and I. Nenner, Phys. Rev. Lett., 56 (1986) 1913.

[2] K. Ueda et al., J. Electron Spectrosc. Relat. Phenom., 79 (1996) 441.

[3] Y. Senba et al., to be published.

Solid State Spectroscopy I
— IR, VUV, etc. —

(BL1B, 3A1, 6A1, 7A, 7B)

(BL1B)

Vacuum-ultraviolet reflectance spectroscopy of transition-metal oxides

Yoshinori TOKURA [1,2,3], Shigeki MIYASAKA [2], Yasujiro TAGUCHI [1], Katsuhiro TOBE [1], Kyoko ISHIZAKA [1], Takahumi SAITO [4], and Taka-hisa ARIMA [4]

[1] *Department of Applied Physics, University of Tokyo, Tokyo 113-8656*

[2] *Joint Research Center for Atom Technology (JRCAT), Tsukuba 305-0046*

[3] *Correlated Electron Reseach Center (CERC), National Institute of Advanced Industrial Science and Technology(AIST), Tsukuba 305-0046*

[4] *Institute of Materials Science, University of Tukuba, Tsukuba 305-8573*

One of the most important characteristics of the correlated electron systems is the drastic re-construction of electronic structure over an energy scale of eV with changes of temperature, doping concentration, and/or external field. Therefore, optical reflectivity measurement over a wide energy range and the optical conductivity spectra derived from the reflectivity spectra provide us with very useful information about the strongly correlated electron systems.

We measured the reflectivity spectra of several transition-metal oxides, including Mn-, Ni-, Co-, Mo- and V-oxides, for an energy range of 4 eV < E < 35 eV at room temperature using the beam line BL1B. The measured reflectivity data, together with the lower-energy data below 6 eV, were used to derive the optical conductivity spectra or dielectric function via the Kramers-Kronig analysis. As an example, imaginary part of the dielectric function of perovskite-type V-oxide, YVO_3, are shown below.

This compound is well known as a typical Mott-Hubbard insulator that has orbital-ordered ground state as well as intermediate-temperature phase whose patterns determine the respective spin-ordering pattern (G-type and C-type). The compound is also of current great interest because of thermally induced magnetization reversal. As shown in the figure, the ε_2 spectra show small anisotropy even at room temperature, which is above the spin- and orbital-ordering temperatures. These spectral features are attributed to robust spin- and orbital-correlation .

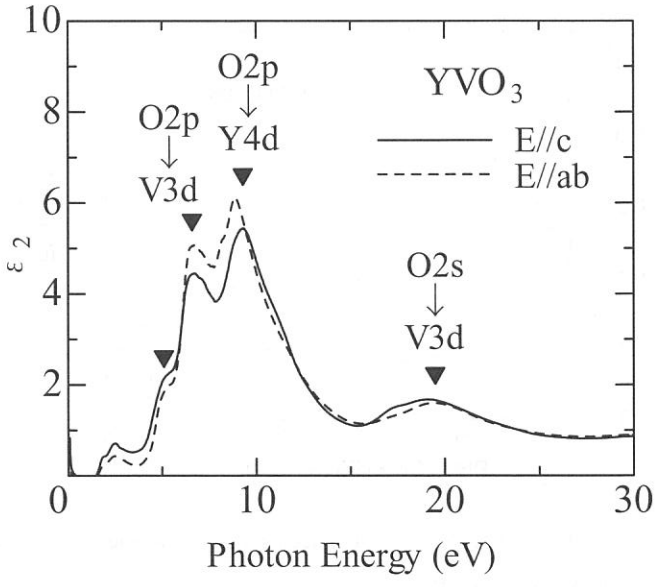

(BL1B)

Extreme-Ultraviolet Reflectivity Spectra and Electronic Structures of $PbWO_4$

Masami FUJITA

Japan Coast Guard Academy, Wakaba, Kure 737-8512

Hiroshi YOKOTA, Yoshiyuki INABE, Michihiro HORIMOTO and Minoru ITOH

Department of Electrical and Electronic Engineering, Shinshu University, Nagano 380-8553

Lead tungstate ($PbWO_4$) has been received intense attention as a promising candidate for scintillating substance [1]. On the other hand, its basic optical properties, such as reflectivity spectra or dielectric constants, have not been established experimentally until now. Very recently, remarkable dichroism has been observed on the reflectivity spectra by us [2] and other groups [3,4]. However, there are some discrepancies among these results. In the present study, polarized reflectivity spectra of $PbWO_4$ crystals with scheelite structure have been measured in the extreme ultraviolet up to 30 eV.

Single crystals of $PbWO_4$ were obtained from the Institute of Solid State Physics of Russian Academy of Sciences and the Materials Research Laboratory of Furukawa Company. Reflectivity spectra were measured at 8 K on the cleaved surfaces of (011) plane, with the electric vector parallel ($\boldsymbol{E} \parallel \boldsymbol{a}$) and perpendicular ($\boldsymbol{E} \perp \boldsymbol{a}$) to the a-axis [2].

Figure 1 shows typical reflectivity spectra of $PbWO_4$ in the 3–30 eV region. A strong exciton band 1 is observed for the polarization $\boldsymbol{E} \parallel \boldsymbol{a}$. The intensity of the exciton band 1 for $\boldsymbol{E} \perp \boldsymbol{a}$ is very small. Several polarization-dependent structures are also observed in the high-energy region. A strong peak 2 is observed at 5.3 eV for $\boldsymbol{E} \perp \boldsymbol{a}$, while such a peak is not observed for $\boldsymbol{E} \parallel \boldsymbol{a}$. One may see a structure 3 around 6.5 eV. The broad peak 4 observed for both polarizations probably corresponds to the prominent peak observed in the 8–9 eV region in Refs. 3 and 4. The reflectivity decreases gradually above 9 eV and shows a minimum at around 12–14 eV. The structures in the 4–10 eV region are mainly ascribed to the transitions from the valence band to

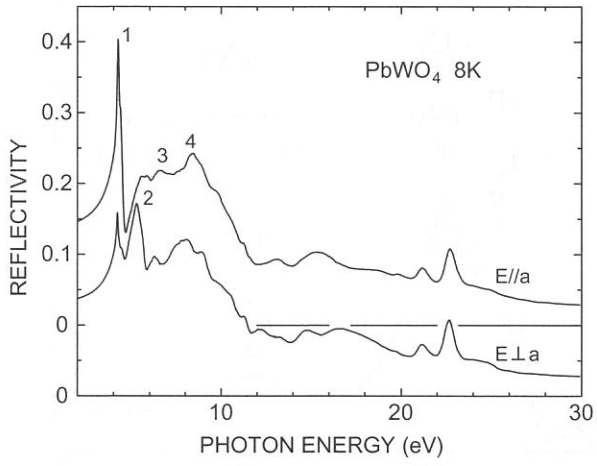

Fig. 1 Reflectivity spectra of scheelite $PbWO_4$ in the 3–30 eV region at 8 K.

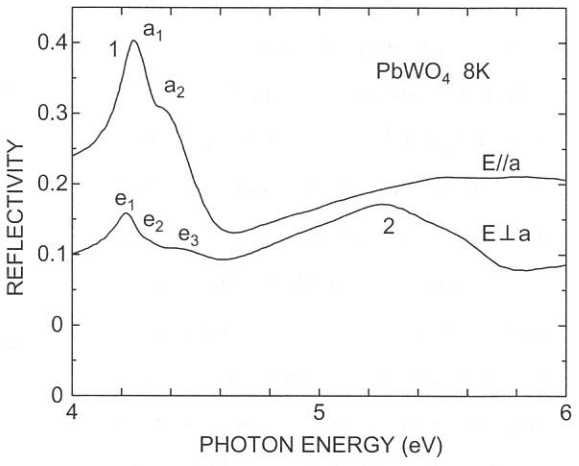

Fig. 2 Reflectivity spectra of scheelite $PbWO_4$ in the exciton-band region at 8 K.

the bottom of the conduction band, since the calculated width of the valence band is about 5.5 eV (see below). Sharp peaks due to the transition from the Pb^{2+} 5*d* core level to the 6*p* level are observed in the 19–25 eV region, indicating that the Pb^{2+} 6*p* state contributes appreciably to the bottom of the conduction band. It is supposed that the exciton transition in $PbWO_4$ would involve the cationic Pb^{2+} $6s \rightarrow 6p$ excitation as well as the charge transfer from oxygen to tungsten.

In Fig. 2 are shown reflectivity spectra in the exciton-band region on an expanded scale. We can see two structures a_1 and a_2 for the polarization $\boldsymbol{E} \,//\, \boldsymbol{a}$ and three structures e_1, e_2 and e_3 for $\boldsymbol{E} \perp \boldsymbol{a}$. The fine structures a_1 (e_1) and a_2 (e_2) would originate from the spin-orbit splitting of the Pb^{2+} 6*p* state. The structure e_3 is likely to be assigned to the longitudinal exciton-polariton mode peculiar to anisotropic crystals, since the light wave with the polarization $\boldsymbol{E} \perp \boldsymbol{a}$ propagates as an extraordinary ray in the crystal.

We are now calculating the electronic structure of scheelite $PbWO_4$ by using the DV-Xα method. A preliminary result of simple $[PbW_4O_{16}]^{6-}$ cluster is presented in Fig. 3. It appears that the valence band is built up of mixed Pb(6*s*)-O(2*p*) state, and the conduction band is composed of mixed Pb(6*p*)-W(5*d*) state. This result is fairly consistent with the above interpretation of the fine structures in the exciton-band region.

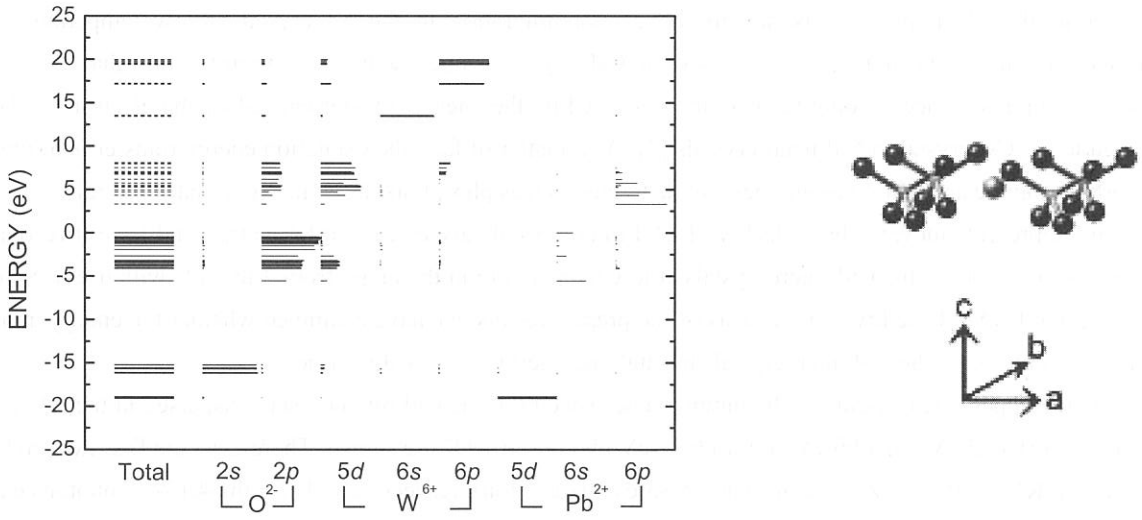

Fig. 3 Electronic structure of $PbWO_4$ calculated by DV-Xα method (right-hand side: simple $[PbW_4O_{16}]^{6-}$ cluster).

The authors would like to thank Dr. D. L. Alov and Dr. Y. Usuki for supplying the single crystals.

References

[1] M. Nikl: Phys. Status Solidi A **178** (2000) 595.

[2] M. Fujita, M. Itoh, M. Horimoto, Y. Usuki, M. Kobayashi and M. Nikl: J. Phys. Soc. Jpn. **70** (2001) 1439.

[3] I. A. Kamenskikh, V. N. Kolobanov, V. V. Mikhailin, I. N. Shpinkov, D. A. Spassky and G. Zimmerer: Nucl. Instrum. Methods Phys. Res. A **467-468** (2001) 1423.

[4] M. Kirm *et al.*: *Proc. 9th Int. Symposium on the Physics and Chemistry of Luminescent Materials*, ed. C. Ronda and A. M. Srivastava (Electrochemical Society, Pennington, NJ) in press.

(BL1B)

Luminescence of CuI Microcrystals Dispersed in KI Matrix under Matrix Excitation

[A]T. HIRAI, [B]Y. HARADA, [C]S. HASHIMOTO and [A]T. ITOH

[A]*Division of Materials Physics, Graduate School of Engineering Science, Osaka University, Toyonaka, 560-8531, Japan*

[B]*Applied Physics, Osaka Institute of Technology, Osaka, 535-8585, Japan*

[C]*Department of Environmental Science, Faculty of Science, Osaka Women's University, Sakai, 590-0035, Japan*

Lots of studies have been conducted on optical properties of semiconductor mesoscopic particles dispersed in insulator matrices so far. Almost all the studies have focused on the optical properties of the semiconductor particles in the visible or near ultraviolet spectral regions. Accordingly, we have focused our attention on the far and vacuum ultraviolet spectroscopy of the semiconductor particles dispersed in insulator matrices.

One of our great interests in this subject is the excitation energy transfer from the insulator matrix to the semiconductor particles through the interface. In other words, we expect that the excitation of the matrix by photons or electrons can efficiently give the luminescence of the semiconductor particles: the matrix-sensitized luminescence. In the past, KI crystals doped with Tl^+ impurity ions have been reported to occur the energy transfer to the Tl^+ impurity ions due to the exciton migration in the KI crystal at low temperature [1]. Furthermore, it has been recently proposed in CsI crystals doped with Na^+ impurity ions that the X-ray stimulated luminescence at room temperature is caused by the energy transfer carried by the electrons or holes created in the CsI crystal to NaI nano-crystals [2]. As a matter of fact, the excitation energy transfer is of utmost importance on the application to luminescent materials such as phosphors, laser and scintillator crystals.

In the present study, we have dealt with CuI microcrystals dispersed in a KI matrix, and have investigated the luminescence from the CuI microcrystals at low temperature in the range from 3 to 7 eV with use of SOR at BL1B in the UVSOR facility. On the basis of the present results, we have examined whether the energy transfer from the KI matrix to the CuI microcrystals through the interface is possible or not.

On the upper side of figure 1, the luminescence spectra of the CuI microcrystals dispersed in the KI crystal excited by (a) 4.13-eV, (b) 4.96-eV and (c) 6.42-eV photons at 10 K are shown. There exist the first exciton band of CuI and KI at 3.05 eV ($Z_{1,2}$ exciton) and 5.83 eV (1s exciton), respectively. Thus, the 4.13-eV photons excite only the CuI microcrystals, and most of the 6.42-eV photons are absorbed by the KI matrix. In addition, the absorption band around 4.7 eV and the luminescence band around 3.1 eV, which originate from isolated Cu^+ ions, can be observed in KI crystals doped with Cu^+ impurity ions [3]. Supposed that there are a lot of Cu^+ ions in the KI crystal, the 4.96-eV photons are expected to excite the Cu^+ ions. Firstly, we can see in Fig. 1(a) the luminescence line at 3.05 eV ascribed to bound excitons and the luminescence band around 2.95 eV due to donor-acceptor pair transitions, which come from CuI microcrystals regarded as bulk crystals. In addition, the luminescence at the higher-energy side of the luminescence line at 3.05 eV is probably assigned to confined excitons in CuI nano-crystals. Secondly in Fig. 1(b), the luminescence line and bands from the CuI microcrystals can be seen like Fig. 1(a). It should be pointed out that the luminescence band originating from the Cu^+ impurity ions is not observable. This fact suggests that very few Cu^+ ions are left in the KI crystal because they have almost precipitated as CuI microcrystals in our sample. Thirdly, there appear two luminescence bands ascribe to type I and type II self-trapped excitons (STEs) in KI at 4.15 eV and 3.31 eV in Fig. 1(c), compared to Fig.1 (a) and (b). From the results, we should notice that the luminescence of the CuI microcrystals around 3 eV could be observed in addition to the STE luminescence of KI even under the interband excitation of KI. Finally, Fig 1(d)

shows the excitation spectrum monitored at 3.05 eV at 10 K. Below ~ 5.5 eV, the spectrum corresponds to the optical transition of CuI. On the other hand, the spectrum above 6 eV is quite similar to the excitation spectrum for the luminescence band of Tl^+ ions reported in KI crystal heavily doped with Tl^+ ions [1], although the 3.05-eV luminescence contains not only the exciton luminescence of CuI but also the STE luminescence of KI. According to [1], the Tl^+ luminescence is caused by the energy transfer due to the exciton migration in the KI crystal. Consequently, the results suggest that the CuI luminescence under the excitation on the intrinsic absorption of KI is strongly correlated to the excitonic process in the KI matrix.

References

[1] H. Nishimura and M. Tomura, J. Phys. Soc. Japan, **39**, 390 (1975)
[2] H. Nishimura, Kotaibutsuri (in Japanese), **35**, 243 (2000)
[3] R. Oggioni and P. Scaramamelli, phys. stat. sol. , **9**, 411 (1965)

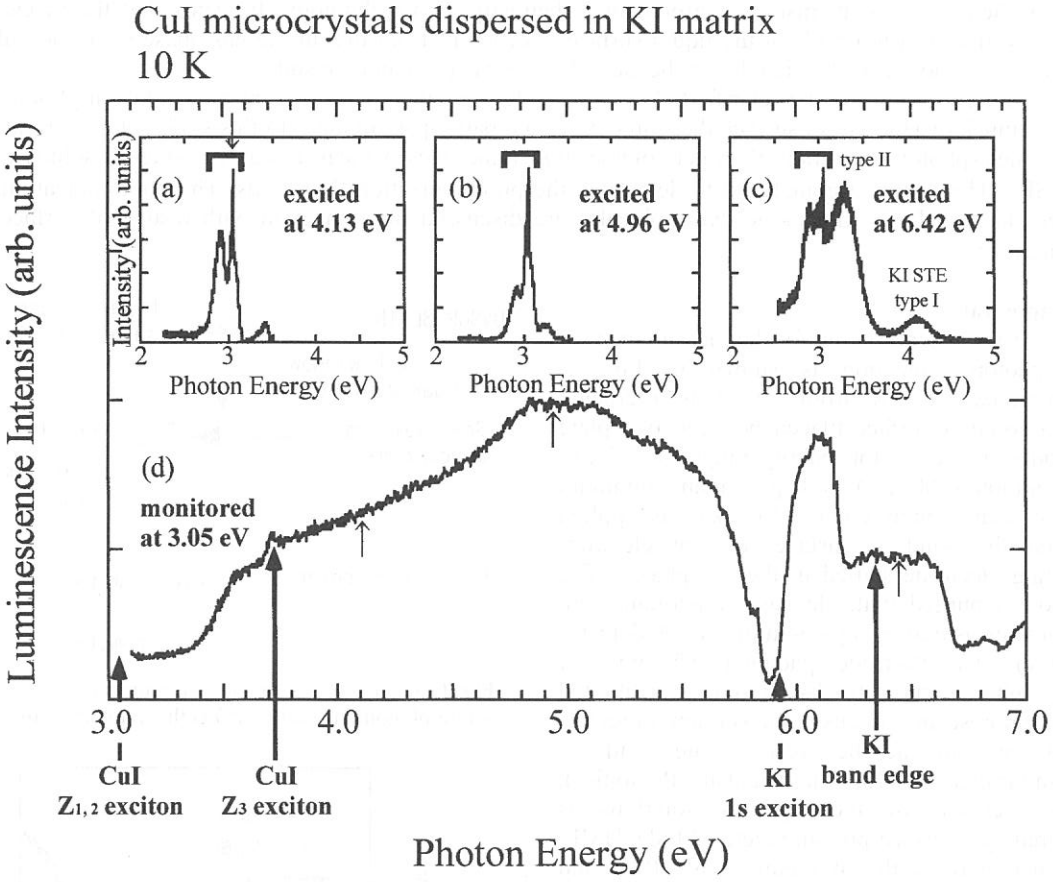

Figure 1. Luminescence spectra of CuI microcrystals dispersed in KI matrix excited at three different photon energies (upper) and the excitation spectrum monitored at 3.05 eV (lower) at 10 K.

(BL1B)

Photoionization of Adsorbed Rhodamine Dyes at the Aqueous Solution Surfaces

Toshio Ishioka, Koichiro Seno, Akira Harata, and Yoshihiko Hatano

Department of Molecular and Material Sciences, Interdisciplinary Graduate School of Engineering Sciences, Kyushu University, Kasugakoen 6-1, Kasuga-shi, Fukuoka 816-8680, Japan

Photoionization of molecules has been of great importance both in fundamental and applied sciences. Such studies have been in progress with powerful photon sources such as lasers and synchrotron radiation (SR).[1] SR covers higher and wider photon energy regions than laser radiation so that SR is used for the photoionizing of molecules not only in the gas phase but also in the condensed phase or at the surface to characterize molecular states or to analyze photoionization mechanisms.

A solute in a bulk solution is known to photoionize at a lower photon energy than the ionization potential in the gas phase due to neighboring solvent molecules around a solute molecule. However, photoionizing behavior of adsorbed molecules at an aqueous solution surface has hardly studied even though there are a wide variety of surface-active molecules and their adsorption behavior has a great importance in physical chemistry, biochemistry, environmental chemistry, and technology. It seems that the mechanism of photoionization of a molecule at the liquid surface is different from that in the gas phase or in the bulk liquid phase but it has not been clarified due to the lack of precise experimental results.

Furthermore, it is not clarified also how a solute interacts with solvent molecules on photoionization and how much distance from surface the solute molecule participate in that. In this study, photocurrent induced by the single-photon ionization of water-soluble rhodamine dyes is measured at the aqueous solution surfaces using SR. The results are analyzed to determine the photoionization thresholds. The photoionization process and the state of these rhodamine dye molecules are discussed in connection with results of surface tension measurements.

Experimental

Experimental setup for the measurement of single-photon ionization is shown in Fig. 1. Monochromatized SR from BL1B is irradiated upon a solution surface placed between two plate electrodes in the photon energy range of 4-7 eV. The solution (400 μL) is kept on an aluminum plate so that a high voltage (0.8 kV) is applied between the solution surface and an electron-collecting electrode settled in the gas phase. The cell box is purged with He gas. Photoionization current is measured by a pico-ammeter (Model 617, Keithley). The electrode spacing is 5.5 mm. A relative photon intensity distribution is calibrated by the fluorescence intensity of sodium salicylate coated on an acrylic resin plate with a photomultiplier (1P28, Hamamatsu Photonics). Surface tension of the aqueous solutions is measured by a surface-pressure meter (Model HMB, Kyowakaimen) of the Wilhelmy type. RhB and Rh101 (reagent grade, Nacalai) are used as received. Rh6G is purified by recrystallization. Water is purified by a Milli-Q system (Milli-Q Academic, Millipore). Aqueous solutions with a concentration ranging 0-100 μmol dm^{-3} are prepared. In all measurements, the temperature is controlled at 25±1°C under atmospheric pressure.

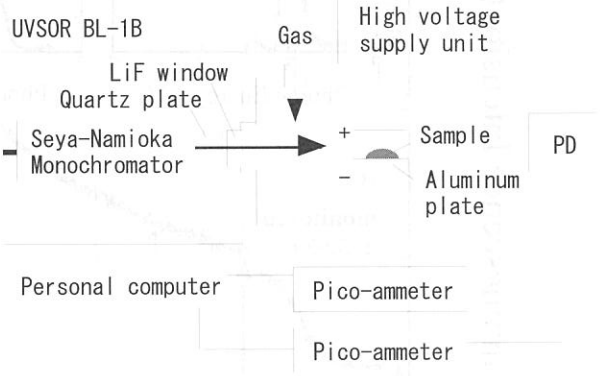

Fig. 1 Schematic diagram of experimental setup for single-photon ionization. PD is the photodetector.

Results and Discussion

Photocurrent spectra at the surface of both pure water and the aqueous solutions of RhB, Rh6G, and Rh101 are shown in Fig. 2, where the photocurrents are normalized with the SR photon intensities. The photocurrent for the surface of pure

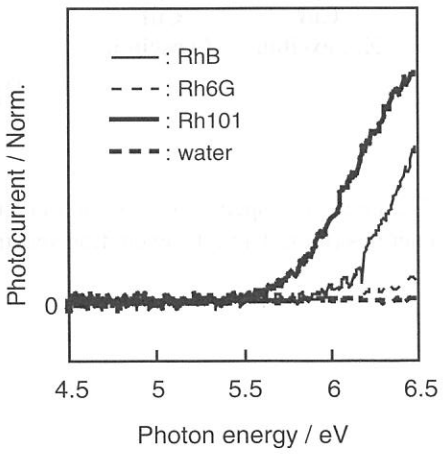

Fig. 2 Photocurrent spectra at the surfaces of pure water and rhodamine aqueous solutions with a concentration of 10 μmol dm^{-3}.

water is not detected in this experimental accuracy. The photocurrents increase with the photon energy above their threshold photon energies. It has been known that the photocurrent, I, near the photoionization threshold, E_{th}, is expressed with an empirical power law,[2]

$$I = C\,(E_{ex})^{\alpha} = C\,(h\nu - E_{th})^{\alpha}, \qquad (1)$$

where C is a constant, E_{ex} is the excess energy, and $h\nu$ is the incident photon energy. The values of E_{th} for rhodamine dyes at the aqueous solution surfaces are determined by fitting Eq. (1) with the exponent $\alpha = 2.5$ to the curves in Fig. 2. A plot of the 0.4 power of the photocurrent vs the photon energy is on a straight line. The values of E_{th} for RhB, Rh6G and Rh101 are determined to be 5.6, 5.6 and 5.3 eV, respectively. The photoionization threshold of a solute in a bulk solution can be related to the ionization potential in the gas phase, IP,

$$E_{th} = IP + P^{+} + V_0, \qquad (2)$$

where P^{+} is the polarization energy of the resultant positive ion and V_0 is the electron affinity in the solvent. Timoshenko et al. derived the value of IP for RhB to be 6.7 eV.[3] Assuming that V_0 in Eq. (2) at the surface is negligible, we can estimate the value of P^{+} at the aqueous solution surface from IP and the obtained photoionization threshold. The value of P^{+} for RhB at the aqueous solution surface is calculated to be –1.1 eV, which is larger than that value in bulk solution estimated from the Born's equation (–0.5 eV).[4] It suggests that probed molecules by single-photon ionization measurements are positioned at a depth from the surface where the resultant positive ion sufficiently interacts with solvent water molecules, and that the value of V_0 cannot be negligible even for molecules at the water surface.

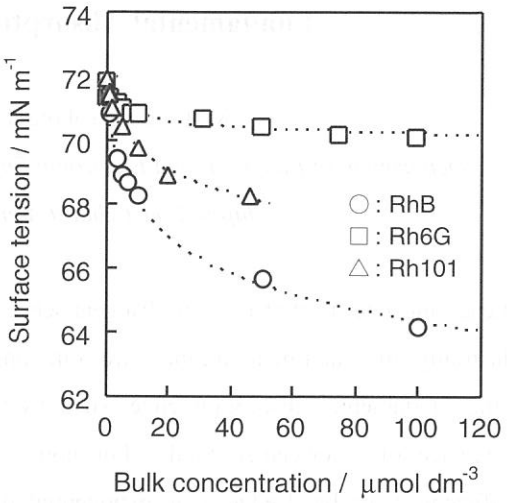

Fig. 3 Bulk concentration dependence of surface tension of the rhodamine aqueous solutions.

Table 1 Experimental results for threshold, signal intensity and surface excess. Concentration of the solutions is 10 μmol dm^{-3}.

Sample	Threshold / eV	Signal intensity / arb. units	Surface excess / μmol m^{-2}
RhB	5.6	1	0.20
Rh6G	5.6	0.16	0.05
Rh101	5.3	2.7	0.13

To discuss the relation between the signal intensity and the amount of solute molecules at the surface, it is necessary to know the number density of rhodamine molecules at the aqueous solution surface. Surface tension measurements are known to be useful for its purpose and the dependence of the surface tension of the rhodamine solutions on their bulk concentration were measured and the result is shown in Fig. 3. Surface tension of each rhodamine aqueous solution decreases with the bulk concentration, which indicates that each rhodamine molecule is adsorbed positively to the surface. The surface excess of each rhodamine molecule can be deduced by applying the thermodynamic equations for the data in Fig. 3 and the result at a 10 μM dye concentration is listed in Table 1 as well as the photoionization threshold and the signal intensity at 6.2 eV. The signal intensity difference between Rh6G and RhB can be regarded as the difference in the surface excess. While, the signal intensity of Rh101 which is much larger than that of RhB despite of smaller surface excess is caused by the difference in the photoionization threshold.

However, there is still a detailed discrepancy in the relation between the surface excess and the photoionization signal intensity. Possible causes of the discrepancy are differences between the rhodamine dyes in photoionization crosssection, direction of the transition moment, depth profile of the molecules and so on. It is important to quantify those values to clarify the cause of the discrepancy though we do not have enough data to discuss them at the present stage and further experiments are now in progress.

References

1. Y. Hatano, *Phys. Rep.-Rev. Sec. Phys. Lett.*, **1999**, *313*, 109.
2. R. A. Holroyd, J. M. Preses, and N. Zevos, *J. Chem. Phys.*, **1983**, *79*, 483.
3. M. M. Timoshenko, I. V. Korkoshko, V. I. Kleimenov, N. E. Petrachenko, Yu. V. Chizhov, V. V. Ryl'kov, and M. E. Akopyan, *Dokl. Phys. Chem.*, **1981**, *260*, 138.
4. M. Born, *Z. Phys.*, **1920**, *1*, 45.

(BL1B)

Fundamental Absorption Edge of $PbWO_4$ Crystals

M. Itoh, H. Yokota, H. Kunisaki, and M. Fujita[A]

Department of Electrical and Electronic Engineering, Shinshu University, Nagano 380-8553

[A]*Japan Coast Guard Academy, Wakaba, Kure 737-8512*

Lead tungstate ($PbWO_4$) is a birefringent scheelite-type crystal consisting of tetragonal unit cell. In this industrially-important material, there are some unresolved problems on optical transmission in the region of the fundamental absorption edge, such as the spectral behavior of the low-energy tail and the appearance of color-center band. For non-metallic solids, it has been found that the absorption coefficient at the band edge is an exponential function of the photon energy at a certain temperature. This dependence is called Urbach rule [1]. Spectral behavior of the fundamental absorption tail in $PbWO_4$ crystals was investigated by Loo [2], who claimed that the Urbach rule does not hold for this material. In the present study, we focus our attention on the low-energy tail of the fundamental absorption of $PbWO_4$.

Single crystals of $PbWO_4$ used in the present experiment were grown by Dr. Usuki. The specimen having a freshly cleaved (011) surface was mounted on the copper holder in a variable-temperature cryostat of He-flow type. Optical transmission measurements were carried out using the ordinary ray ($\boldsymbol{E} \,//\, \boldsymbol{a}$) as a light source.

Figure 1 shows a typical example of the absorption spectra of $PbWO_4$ at $T = 6$ K near the fundamental absorption edge. The results of four crystals cut out of the same or different ingots are presented in this figure. A single absorption band is clearly seen at 3.5 eV for all samples. Its intensity varies from sample to sample. This band is typical of $PbWO_4$ crystal, but the origin is still controversial [3]. The 3.5-eV band overlaps with the tail part of the fundamental absorption. This makes the true shape of the low-energy tail obscure. Fortunately, there is no or little influence of such overlap in the spectrum indicated by asterisk. This spectrum was taken for a crystal with 2.1-mm thickness, the quality of which seems to be the best among the samples investigated.

The absorption coefficients obtained for the best-quality sample at various temperatures are plotted on a logarithmic scale in Fig. 2. The open circles represent the experimental data. The straight lines converge to a point (E_0, α_0), indicating that the Urbach rule certainly holds for $PbWO_4$. From the converging point, we get $E_0 = 4.33$ eV and $\alpha_0 = 4.2 \times 10^7$ cm^{-1}. The steepness parameter σ at various temperatures is presented by open circles in Fig. 3. The temperature dependence of σ is expressed as $\sigma(T) = \sigma_0(2k_BT/h\nu)\tanh(h\nu/2k_BT)$. The solid line is the least-squares fit of this equation to the experimental data, with the high-temperature steepness parameter $\sigma_0 = 0.82$ and the average phonon energy $h\nu = 32$ meV.

According to the Sumi-Toyozawa theory [4], the parameter σ_0 is inversely proportional to the strength of the exciton-phonon interaction. The present value $\sigma_0 = 0.82$ is smaller than the critical value (1.50), above which an exciton becomes self-trapped. This fact strongly suggests that the exciton-phonon interaction is strong in $PbWO_4$. In fact, it is known that the intrinsic luminescence of this tungstate appears at 2.80 eV, and is attributed to radiative decay of self-trapped excitons [5].

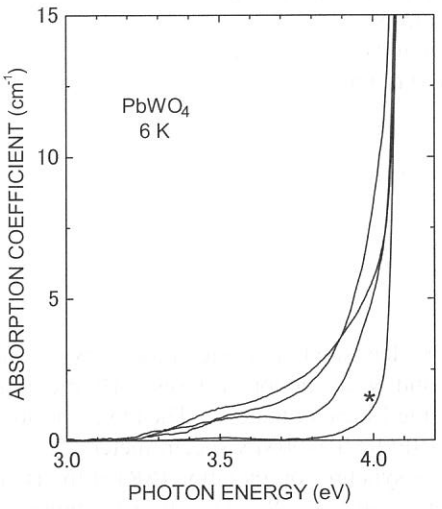

Fig. 1

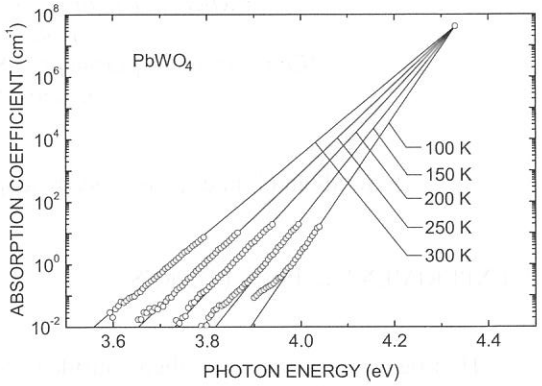

Fig. 2.

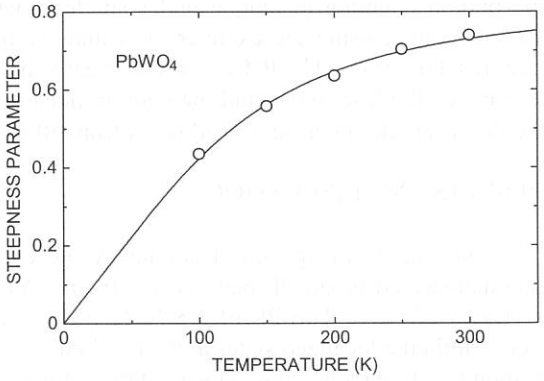

Fig. 3

References

[1] M. V. Kurik: Phys. Status Solidi A **8** (1971) 9.

[2] W. van Loo: Phys. Status Solidi A **27** (1975) 565.

[3] M. Nikl: Phys. Status Solidi A **178** (2000) 595.

[4] H. Sumi and Y. Toyozawa: J. Phys. Soc. Jpn. **31** (1971) 342.

[5] M. Itoh and M. Fujita: Phys. Rev. B **62** (2000) 12825.

(BL1B)

Photoluminescence Properties of Hydrogenated Amorphous Silicon Nitride

Norihide *KASHIO*, Hiromitsu *KATO*, Kwang Soo *SEOL**, Takashi *NOMA*** and Yoshimichi *OHKI*

Department of Electrical, Electronics and Computer Engineering,
Waseda University, 3-4-1, Shinjuku-ku, Tokyo 169-8555.
**RIKEN (The Institute of Physical and Chemical Research),*
Wako-shi, Saitama 351-0198.
***Engineering Department 1, System-LSI Division, Sanyo Electric Co. Ltd.,*
Oizumi-Machi, Gumma 370-0596.

Category 4. Solid- and liquid- phase spectroscopy 1 (IR, VUV, etc)

I. EXPERIMENTAL PROCEDURES

Hydrogenated amorphous silicon nitride (a-SiN_x:H) films were deposited on a silicon monocrystal substrate by plasma-enhanced chemical vapor deposition using SiH_4, NH_3 and N_2 as monomer gases. By increasing the SiH_4 flow rate from 150 to 350 sccm, samples A to C shown in Table I were obtained. The atomic ratio of N to Si, denoted by x, was calculated from XPS spectra obtained with a JEOL JPS-90MX spectrometer.

For PL measurements, two photon sources were used. One is synchrotron radiation (SR) at the BL1B line of UVSOR Facility and the other is a KrF excimer laser with a wavelength of 248 nm (=5.0 eV), a pulse width of 25 ns, and a pulse energy of ~100 mJ/cm^2. Using SR, PL and PL excitation (PLE) spectra were measured at 10 K under multi-bunch operation, while PL decay characteristics were measured at 10 K by a time-correlated single photon counting technique under single-bunch operation. Time-resolved PL spectra were obtained at room temperature using the excimer laser and a monochromator equipped with an intensified charge-coupled device (ICCD) array. The ICCD array was gated by a pulse generator connected to a delay circuit and the delay time between the laser pulse and the gate-on pulse was monitored with an oscilloscope. The gate-on duration or the PL observation period was adjusted from 50 ns to 4 μs so that clear PL spectra could be obtained.

II. RESULTS AND DISCUSSION

Figure 1 shows PL spectra of samples A to C excited by photons with an energy of 5.0 eV from SR at 10 K. A gaussian-shaped broad PL band is observed. As x increases, the PL peak energy shifts to a higher energy from 1.9 to 2.7 eV. The PL of a-SiN_x:H films is considered to be due to recombination of photogenerated carriers within the localized states at the band tails. As shown in Fig. 2, the threshold energy of the PLE spectra, corresponding to the optical band gap energy, shifts to a higher energy with an increase in x. Thus, an increase in the band gap energy is responsible for the blue-shift of the present PL peak. To investigate PL properties further, we have measured time-resolved PL spectra using samples B and C that have stronger PL intensities than sample A. The height of the time-resolved PL spectrum was divided by the gate-on duration, and is shown as a function of the delay time for samples B and C in Fig. 3(a). The PL decays nonexponentially, ranging from ~10^{-8} to 10^{-3} s, which indicates that the PL has a broad lifetime distribution. Therefore, it is convenient to analyze the PL decay by assuming a distribution function $G(\tau)$ of lifetime τ. The distribution function $G(\tau)$ is expressed by the equation,

$$G(\tau)=\text{const}\ I\ (d\log I/d\log \tau), \quad (1)$$

where I is the PL intensity and τ is the lifetime. Figure 3(b) shows the product $\tau G(\tau)$ or the lifetime distribution drawn by choosing $G(\tau)$ so as to yield the best fits to the decay. The lifetime distribution $\tau G(\tau)$ has a component that stretches over a wide range from 10^{-6} to 10^{-3} s. Radiative tunneling recombination is considered to be the main recombination mechanism of this component. In Fig. 3(b), a steep drop in $\tau G(\tau)$ is seen at $\approx 10^{-7}$ s. The PL decay at this early stage was investigated using SR. Figure 4 shows the nanosecond-order decay of PL excited by SR photons with an energy of 5.0 eV, observed in sample B by monitoring at 2.2 eV at 10 K. The decay is nonexponential and can be expressed by a stretched exponential function,

$$I'(t)\propto(\tau'/t)^{1-\beta}\exp[-(t/\tau')^{\beta}], \quad (2)$$

where I' is the PL intensity, t the time, τ' the effective lifetime, and β a parameter that has a value between 0 and 1. The curve in Fig. 4 is the least-squares fit to Eq. (2) of the decay profile. The nanosecond-order decays of the PLs in samples A and C excited by 5.0 eV photons from SR at 10 K were monitored at each excitation peak, namely, at 1.9 eV for sample A and 2.7 eV for sample C. Figure 5 shows the effective lifetime τ' and parameter β, each as a function of x. It is found that τ' increases from 10 to 16 ns with an increase in x, while β is constant at 0.4 independent of x. This fast decay component is considered to be due to an exciton-like recombination. The time-resolved PL and nanosecond-order PL decay measurements indicate that the photogenerated carriers in the band-tail states recombine first through an exciton-like mechanism and then through a radiative tunneling mechanism.

Table I. The ratio of the source gases and N/Si ratio of the a-SiN_x:H films synthesized.

Sample	gas ratio (=NH_3/SiH_4)	x (=N/Si)
A	5.5	0.91
B	7.5	0.97
C	12.5	1.26

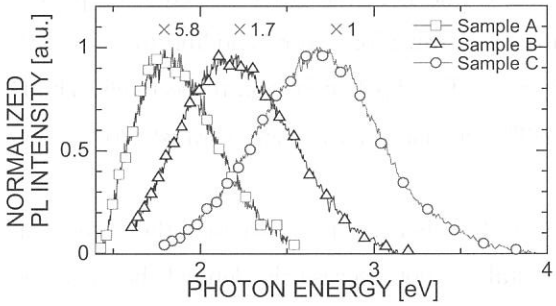

Fig. 1. PL spectra at 10 K observed in samples with different N/Si ratios (x). Numerals beside the spectra are their magnifications.

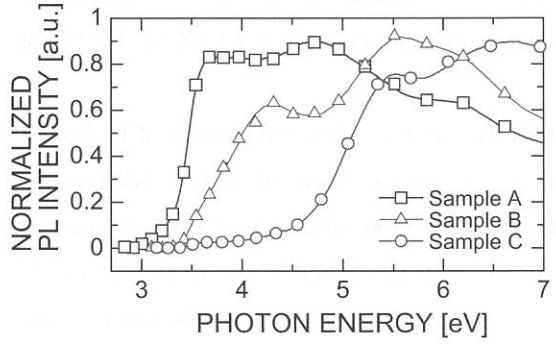

Fig. 2. PLE spectra at 10 K observed in samples with different N/Si ratios (x).

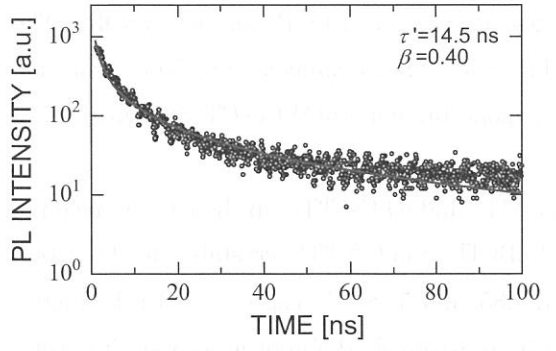

Fig. 4. PL decay at 10 K in sample B monitored at 2.2 eV. Excitaion was done by SR photons with an energy of 5.0 eV.

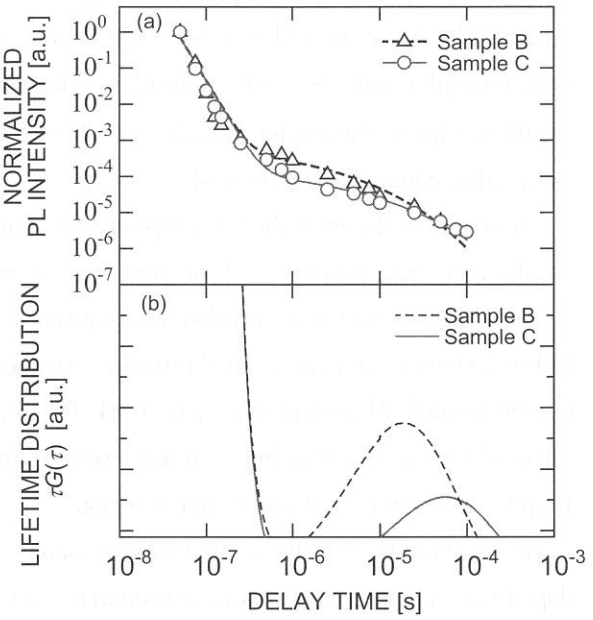

Fig. 3. (a) PL decays and (b) PL lifetime distribution measured in samples B and C, excited by the KrF excimer laser at room temperature. The lifetime distribution stretches over the time range from 10^{-8} to 10^{-3} s.

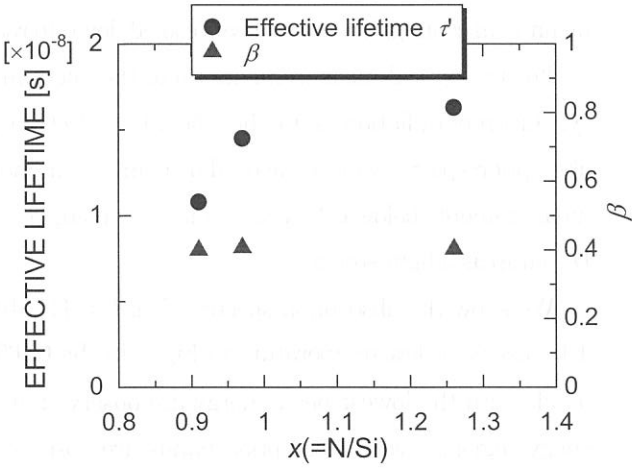

Fig. 5. Effective lifetime τ' and parameter β each as a function of x at 10 K.

(BL1B)

Optical Absorption Bands of Cesium Halides Doped with Tl^+ Ions

Taketoshi KAWAI, and Satoshi HASHIMOTO

Department of Environmental Sciences, Faculty of Science, Osaka Women's University, Daisen-cho, Sakai City, Osaka 590-0035, Japan

It has been well-known that the Tl^+-type centers in alkali halides exhibit several absorption bands in the energy region below the absorption band edge of host crystals. In alkali halides with the NaCl-type crystal structure, these absorption bands are labelled A, B, C and D in the order of increasing photon energy. The A, B and C bands are originated from intraionic transitions corresponding to $^1S_0 \rightarrow ^3P_1$ (spin-orbit allowed), $^1S_0 \rightarrow ^3P_2$ (vibration induced) and $^1S_0 \rightarrow ^1P_1$ (dipole allowed), respectively. The D bands are due to the exciton transition perturbed by the Tl^+-type ions or the charge transfer transition from halogen ions to Tl^+-type ions[1,2].

In alkali halides with the CsCl-type crystal structure, on the other hand, the origin of the absorption bands appearing below the absorption edge of host crystals is not necessarily defined, because the systematic study on the absorption bands of the Tl^+-type centers doped in the CsCl-type alkali halides is lacking. Though there are a small number of studies on CsI:Tl^+ having the absorption bands in the lower energy region[3-5], optical studies on CsBr:Tl^+ and CsCl:Tl^+ are limited[6,7], especially in the vacuum ultraviolet energy region. In this report, we present the optical absorption spectra of CsX:Tl^+ (X=Cl, Br, I) up to the vacuum ultraviolet energy region.

The preparation of the sample was as follows. At first, rapidly quenched bulk ingots of Cs-halides doped with Tl^+ impurity ions were prepared from the melt containing corresponding Tl-halide powders in Cs-halide powders. Next, a small fragment of the ingots was placed on a step of the cell made by putting one smaller quartz or sapphire plate on top of the larger plate. When it was heated above the melting point of the Cs-halides in a nitrogen atmosphere, the melt was percolated into the gap of the cell through capillary action. After infiltrating into a whole area of the cell, thin crystal was grown in the gap by natural cooling. The crystal was cooled down to room temperature within one hour.

For the optical measurements up to the vacuum ultraviolet energy region, the light source was the synchrotron radiation from the 750 MeV electron storage ring at the BL-1B line of UVSOR. The absorption spectra were measured by using a 1 m monochromator of Seya-Namioka type. The absorption measurements below 6.1 eV were made by using a grating monochromator (JASCO CT25CS) attached a D_2 lamp as a light source.

We show the absorption spectra of (a) CsI:Tl^+, (b) CsBr:Tl^+, and (c) CsCl:Tl^+ in the energy region of 4.1～7.8 eV at low temperature in Fig.1. In the CsI:Tl^+, CsBr:Tl^+, and CsCl:Tl^+ crystals, the absorption bands with the lowest peak energy are observed at 4.27, 4.85, and 5.18 eV, respectively. In the higher enegy region, several absorption bands are observed with no extremely different absorption intensity. These absorption bands become close to each other in a sequence of CsCl:Tl^+ → CsBr:Tl^+ → CsI:Tl^+ crystals.

The lowest absorption bands have been assigned to the A absorption bands of the Tl^+-type centers by several authors[3,4,6]. On the other hands, the origin of the higher energy bands has not necessarily been demonstrated. The temperature evolution of the higher energy bands is not characteristic of the Tl^+ centers in NaCl-type alkali halides. From the spectra changes in the $CsBr_{1-x}$ CsI_x : Tl^+ ($0.0 \leqq x \leqq 1.0$) mixed crystals and the temperature dependence of the absorption bands, we assign the higher energy bands to the charger transfer or perturbed exciton transition bands[8]. The B and C bands are not given in our assignment. The difference of the absorption bands between the CsCl-type and NaCl-type alkali halides may be explained in terms of the ion arrangements around the Tl^+ ion. To clear up this problem, further studies of optical transitions in the CsCl-type ionic crystals doped with the Tl^+-type ions are needed.

References

[1] A. Ranfagni, D. Mugnai, M. Bacci, G. Viliani, and M. P. Fontana: Advances in Physics 32 (1983) 823.

[2] P. W. M. Jacobs: J. Phys. Chem. Solids 52 (1991) 35.

[3] K. Asami, T. Naka, and M. Ishiguro : phys. stat. sol. (b) 104 (1981) 145.

[4] M. J. Stillman, P. W. M. Jacobs, K. Oyama Gannon, and D. J. Simkin : phys. stat. sol. (b) 124 (1984) 261.

[5] V. Nagirnyi, A. Stolovich, S. Zazubovich, V. Zeplin, E. Mihokova, M. Nikl, G. P. Pazzi, and L. Salvini: J. Phys. : Condensed Matter 7 (1995) 3637.

[6] V. Nagirnyi, S. Zazubovich, and N. Jaanson: phys. stat. sol. (b) 175 (1993) 155.

[7] E. Mihokova, V. Nagirnyi, M. Nikl, A. Stolovich, G. P. Pazzi, S. Zazubovich, and V. Zeplin: J. Phys. : Condensed Matter 8 (1996) 4301.

[8] T. Kawai, N. Ichimura, and S. Hashimoto: phys. stat. sol. (b) 277 (2001) 587.

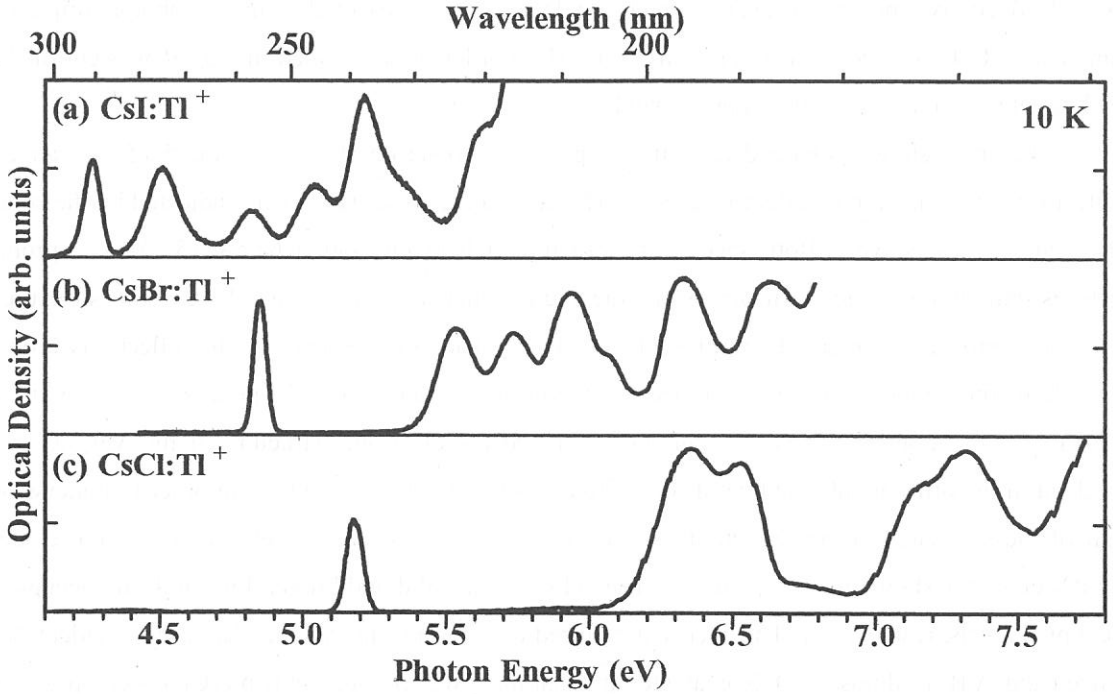

Figure 1 Absorption spectra in Cs-halides doped with Tl^+ centers

(BL-1B)

Reflection Spectra and Electronic Structure of Forsterite (Mg_2SiO_4) Single Crystals

Mamoru KITAURA[A], Hideyuki NAKAGAWA[B] and Akimasa OHNISHI[C]

[A]*Fukui National College of Technology, Sabae 918-8057*

[B]*Department of Electric and Electronics Engineering, Fukui University, Fukui 910-8057*

[C]*Department of Physics, Yamagata University, Yamagata 990-8560*

Magnesium silicate, Mg_2SiO_4, is one of the silicate minerals which make up the majority of the earth's crust and mantle. This material takes two kinds of crystal phases: forsterite with olivine structure, and ringwoodite with spinel structure. They have been studied from the interest in geophysics and crystal chemistry. The electronic structure of forsterite has been investigated by X-ray emission and photoelectron spectroscopy [1]. As far as we know, there is no report on the electronic structure of forsterite except this investigation. In the present study, polarized reflection spectra of forsterite have been measured using synchrotron radiation, in order to obtain the information on its electronic structure. The results obtained here will be applicable to predict the structure, physical and chemical properties of forsterite under ultra-high pressures in the earth's deep interior.

The crystals of forsterite were grown in air by a floating zone (FZ) technique. The orientation of crystal samples was determined by the X-ray analysis. The crystal samples were mounted on a Cu holder of a He-flow-type cryostat. The present experiments were carried out at BL-1B of UVSOR facility. The synchrotron radiation (SR) dispersed with a 1-m Seya-Namioka monochromator was used as a light source. The spectral bandwidth of the SR was fixed to 0.1 nm. The electric vector of the SR is perpendicular to the *b*-axis. Reflectivity spectra of near normal incidence were measured using a photomultiplier tube (Hamamatsu R105) coated with sodium salycilate. High order light included in the SR was cut off by the LiF plate set up in the front of the sample chamber.

Figure 1 shows polarized reflectivity spectra of forsterite at 10 K in the 5-25 eV range. The spectra for the polarization parallel to the *a*-axis (E || a) and the *c*-axis (E || c) are indicated by the solid and broken curves, respectively. Both spectra are structure rich in the region below 15 eV. The prominent structures exhibit remarkable anisotropy. In the higher energy region above 15 eV, the structures are considerably broad, as compared with those below 15 eV. The rapid decrease in the reflectivity around 20 eV would be due to plasmon excitation, because the plasmon energies for the polarization E || a and E || c are estimated to be about 23 eV. We further calculated the electronic structure of the Mg_9SiO_4 cluster embedded in the orthorhombic lattice of forsterite by using the DV-$X\alpha$ method, in order to understand the origin of the structures in the reflectivity spectra of Fig. 1. The energy level diagram of the embedded Mg_9SiO_4 cluster is shown in Fig. 2. In the left hand side, the solid and broken lines indicate occupied and unoccupied levels, respectively. The energy is referred to the top of the valence band. It is evident that the valence band (VB) is almost of O 2*p* character and that the lower conduction band (CB) is composed of the Mg 3*s* orbital with contribution from the Si 3*s* orbital. Therefore, it is most likely that the optical transitions

in the region near the fundamental gap are attributed to the O 2*p* → Mg 3*s* transitions, which are indeed of allowed type. Although the anisotropy of the structures in the region below 15 eV is not explained at present, they reflect the joint density of states between the VB and the lower CB. In addition, we expect that the transitions from the VB to the Mg 3*p* conduction states take place at around 15 eV. This type of the transitions is essentially forbidden, and thus the structures in the region above 15 eV are not so remarkable, as compared with those below 15 eV.

Reference

1. M. A. Al-Kadier, C. Tolon, D. S. Urch: J. Chem. Soc. Faraday Trans. 80 (1984) 669.

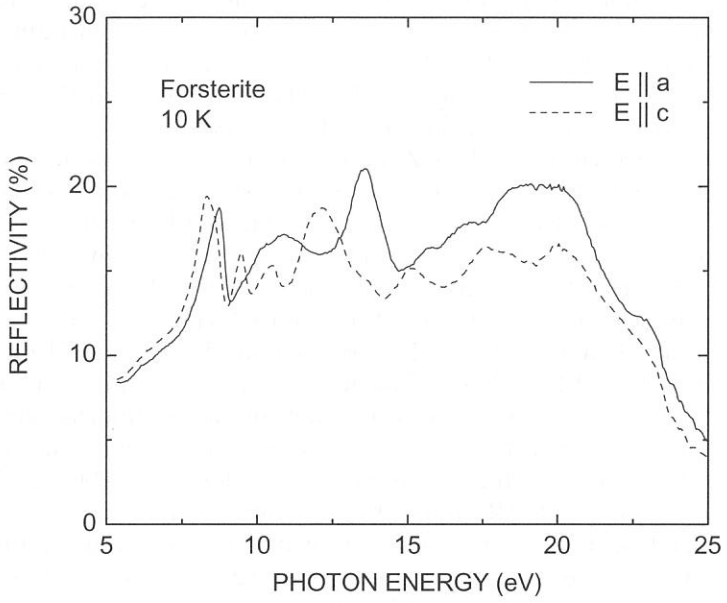

Fig. 1: Polarized reflectivity spectra of forsterite at 10 K in the 5-25 eV range. The spectra were measured for the polarization parallel to the *a*-axis (solid curve) and the *c*-axis (broken curve).

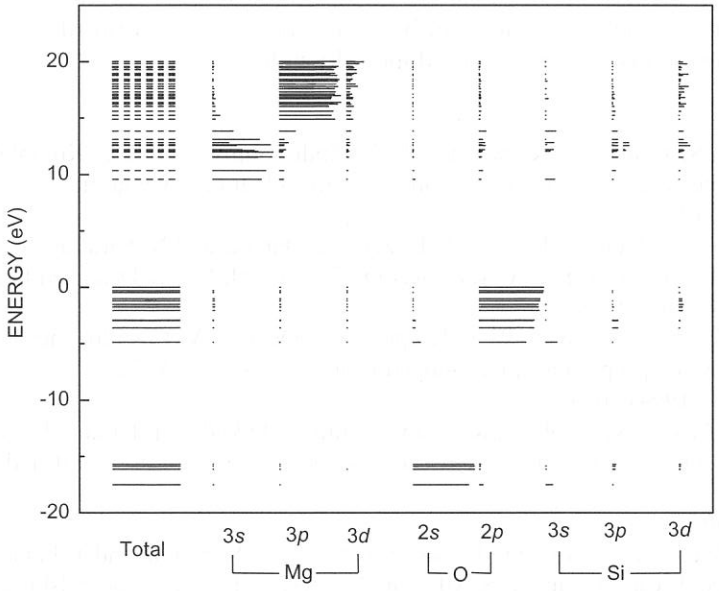

Fig. 2: Energy level diagram of the Mg_9SiO_4 cluster embedded in the orthorhombic lattice of forsterite.

(BL1B)

Observation of New Excitation Channels of Cerium Ion through Absorption by Various Fluoride Host Crystals

Toshimasa Kozeki, Yuji Suzuki, Masahiro Sakai, Hideyuki Ohtake and Nobuhiko Sarukura

Institute for Molecular Science (IMS), Myodaiji, Okazaki 444-8585, Japan

Kiyoshi Shimamura and Tsuguo Fukuda

Tohoku University, 2-1-1 Katahira, Aoba-ku, Sendai 980-8577, Japan

Cerium-ion-doped crystals [1,2] are already known as practical tunable ultraviolet laser media pumped with the fourth harmonic of an Nd:YAG laser. A 60-mJ output from Ce:LiCAF was already demonstrated with large Czochralski (CZ)-grown crystal [3-5], and if other pumping schemes were available, it would expand the applicability of this laser medium. In this paper, we report finding new excitation channels of Cerium ion through Ce:LiCAF, Ce:LiSAF, and Ce:LiSCAF crystals and they coincide completely with the transmission edge of each crystal.

Fluoride crystals were grown using the CZ method. Commercially available AlF_3, CaF_2, SrF_2 and LiF high-purity powders (>99.99 %) were used as the starting material. Growth orientation was controlled by using *a*-axis- oriented seed crystals. The pulling rate was 1 mm/h and the rotation rate was 10 rpm. The growth was carried out in an Ar gas atmosphere and the starting material was melted at 1120 K. Sodium ions were co-doped for the charge compensation.

The transmission, luminescence and excitation characteristics of various fluoride crystals including Ce:LiCAF, Ce:LiSAF, and Ce:LiSCAF were measured using an Ultraviolet Synchrotron Orbital Radiation Facility (UVSOR) with a 1-m focal length Seya-Namioka monochrometer with a photo-multiplier. The luminescence spectrum of Cerium-ion-doped fluoride crystals is known to peak around 290 nm [1]. Therefore, we measured the excitation characteristics of Cerium-ion-doped fluoride crystals with an observation wavelength of 290 nm through band-pass filters. As shown in Fig. 1, the peaks (B) and (C) in the excitation spectrum corresponded to the absorption of Cerium ions. Excitation channels (A) at around 115, 118 and 119 nm for each fluoride crystal coincided roughly with the transmission edges of 112, 118 and 123 nm, respectively. It is interesting that these excitation channels roughly coincide with the bandgaps of each crystal. This result confirmed that these excitation channels can be considered as electrons transfer from the host crystal to the active Cerium ions. A schematic of energy levels and a possible decay channel in the crystal is shown in Fig. 2.

In conclusion, the excitation channels of Cerium ions through fluoride host crystals were observed. These excitation channels indicate the bandgap of the host crystals, and can be used as a potential pumping channel including electron-beam pumping or vacuum ultraviolet pumping, for the future scaling of high-power Cerium-ions-doped fluoride lasers.

References:

[1] M. A. Dubinskii, V. V. Semashko, A. K. Naumov, R. Y. Abdulsabirov, and S. L. Korableva, "Ce^{3+}-doped colquiriite –a new concept of all-solid-state tunable ultraviolet laser," J. Mod. Opt. **40** (1993) 1.

[2] Z. Liu, K. Shimamura, K. Nakano, T. Fukuda, T. Kozeki, H. Ohtake, and N. Sarukura, "High-Pulse-Energy Ultraviolet Ce^{3+}:$LiCAF_6$ Laser Oscillator with Newly Designed Pumping Schemes," Jpn. J. Appl. Phys. **39** (2000) L466.

[3] C. D. Marshall, J. A. Speth, S. A. Payne, W. F. Krupke, G. J. Quarles, V. Castillo, and B. H. T. Chai, "Ultraviolet laser emission properties of Ce^{3+}-doped $LiSrAlF_6$ and $LiCaAlF_6$," J. Opt. Soc. Am. B **11** (1994) 2054.

[4] Z. Liu, T. Kozeki, Y. Suzuki, N. Sarukura, K. Shimamura, T. Fukuda, M. Hirano, H. Hosono "Chirped-pulse amplification of ultraviolet femtosecond pulses by use of Ce^{3+} $LiCaAlF_6$ as a broadband, solid-state gain medium" Opt. Let. **26** (2001) 301.

[5] K. Shimamura, S. L. Baldochi, N. Mujilatu, K. Nakano, Z. Liu, N. Sarukura, and T. Fukuda, "Growth of Ce-doped $LiCaAlF_6$ and $LiSrAlF_6$ single crystals by the Czochralski technique under CF_4 atmosphere,"

J. Crystal Growth **211** (2000) 302.

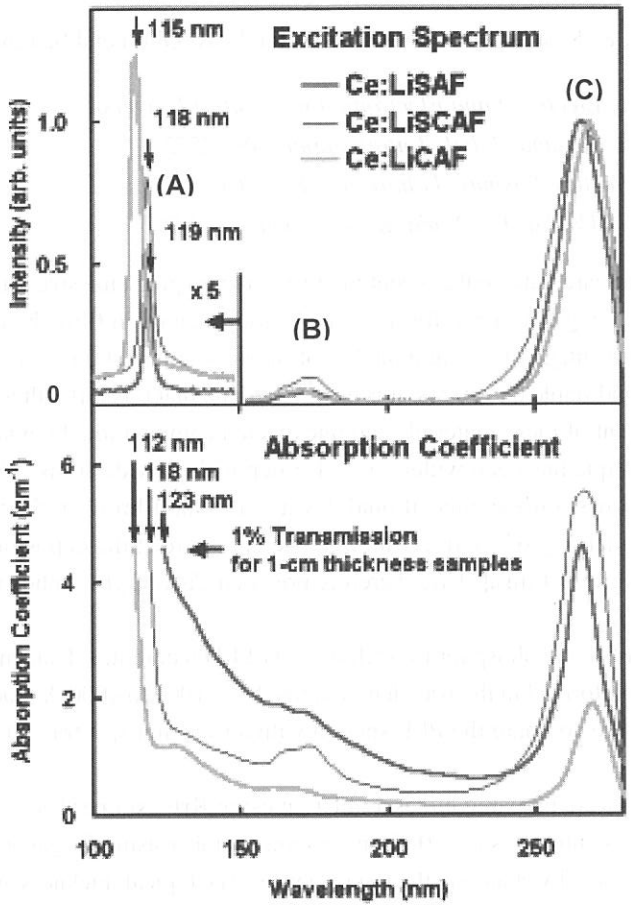

Fig. 1. The excitation spectrum and absorption coefficient curve for Ce:LiCAF, Ce:LiSCAF and Ce:LiSAF crystals.

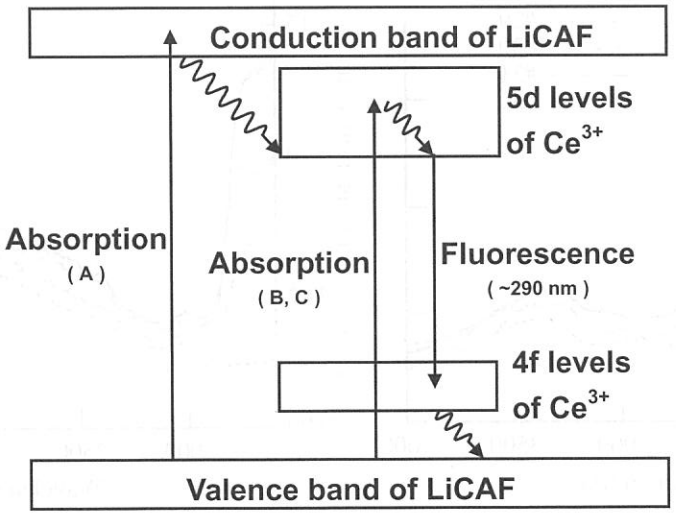

Fig. 2. Schematic of energy levels and possible decay channel in Cerium ions doped crystal.

(BL-1B)

Optical spectra of $CaAl_2O_4:Eu^{2+}$ phosphor thin film prepared by PLD technique

T. Kunimoto*, K. Kakehi, R. Yoshimatsu, S. Honda, K. Ohmi and S. Tanaka

Dept. of Electrical and Electronic Eng., Tottori University
Koyama, 4-101, Tottori, Japan, 680-8552
**Venture Business Laboratory, Kobe Univerisity*
Rokkodai, 1-1, Nada, Kobe, Japan, 657-8501

There is resurgence in phosphor research due to the recent interest in developing emissive flat panel displays. Efficient and stable three-color phosphors are being developed for these applications, and thin film phosphor materials have been attracted much attention due to the advantage of the high quality of pictures. It is well known that oxide phosphor is the promising materials for the efficient and stable phosphors. It is however found that it is difficult to make the complex oxide hosts because of the high melting point of these materials and unexpected compositional deviation.[1] On the contrary, Pulsed laser deposition (PLD) technique has been widely used for depositing oxide films.[2] The advantages for this method include some aspects as follows: little compositional deviation in the film from the target oxide, low growth temperature of substrate, and the availability of relatively high oxygen pressure at the deposition which could facilitate sufficient oxygen incorporation to as-grown films.[3] We therefore prepared $CaAl_2O_4:Eu^{2+}$ phosphor thin films using PLD technique.

We report on the optical spectra of oxide phosphor thin films using PLD technique. Transmission, reflection and PL excitation (PLE) measurement were performed in the wavelength range from 1000 to 4000 Å. Each spectra were corrected by sodium salicylate as a reference. We compare the PLE spectra with absorption spectra and obtain the quantum efficiency for the Eu^{2+} blue emission.

$CaAl_2O_4:Eu^{2+}$ phosphor thin films were prepared by laser ablation using KrF excimer laser (248 nm). The films were deposited on 25×12.5 mm^2 quartz glass substrates at 200 °C in vacuum chamber using O_2 gas injection with 5 sccm flow rate. Obtained films have various thickness by changing the laser fluence. The typical thickness are 500 Å for #29 film and

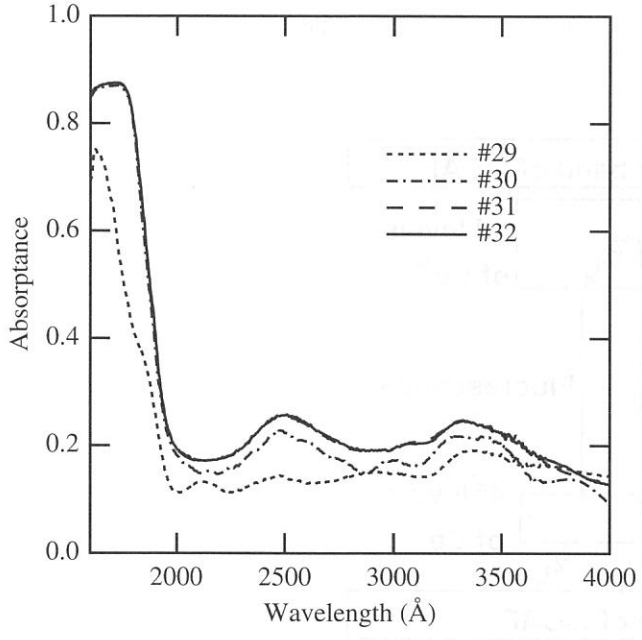

Fig. 1 Absorption spectra of $CaAl_2O_4:Eu^{2+}$ thin films. The films were deposited using various laser fluence (#29 ; 0.5 J/cm^2, #30 ; 1.0J/cm^2, #31 ; 1.5 J/cm^2, #32 ; 2.0 J/cm^2)

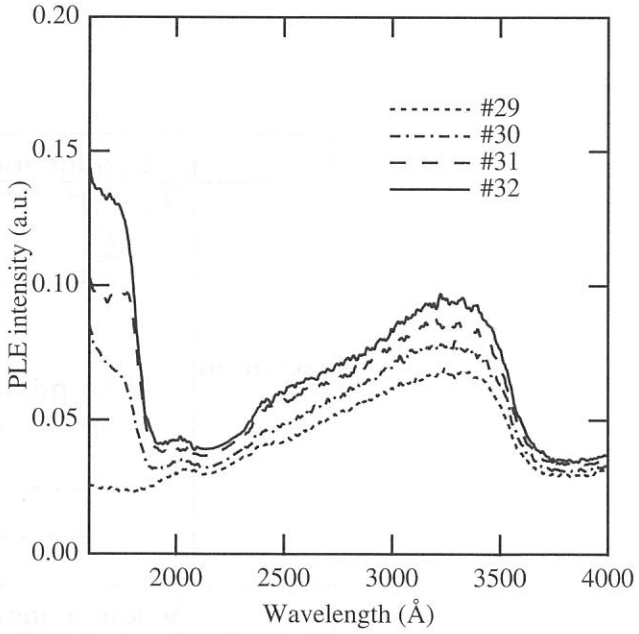

Fig. 2 PL excitation spectra of $CaAl_2O_4:Eu^{2+}$ thin films. The monitor wavelength is 4410 Å.

3000 Å for #32 film. The deposited films crystallized by post-annealing at 950 °C, however the number of diffraction peaks varies with film thickness. The annealed films exhibit the emission band peaking at 4410 Å mainly.

Figure 1 shows the absorption spectra of annealed films. We obtained the absorptance A using following relation,

$$A = 1 - R - T, \quad (1)$$

where T and R are transmittance and reflectance, respectively. The Absorptance increases with increasing the film thickness. The absorption edge structure is observed at 1930 Å and is attributed to the interband transition of host $CaAl_2O_4$. The absorption band observed in the range from 2200 to 3700 Å is associated with the $4f^7$ to $4f^6 5d$ transition of Eu^{2+} ion situated in 9-coordinated Ca(III) site of $CaAl_2O_4$ crystal.

As illustrated in the PLE spectra of Fig. 2, excitation band corresponding to the interband transition of host crystal is observed below 1950 Å, and the direct excitation bands of Eu^{2+} ions are also observed in the range from 2200 to 3600 Å. The position of these excitation bands is consistent with absorption spectrum. The thick thin films (#30, #31, #32) show the relatively strong PLE intensity of the host excitation band. On the contrary the PLE intensity of host excitation band of #29 film is quite weak. The PLE intensity of host excitation band and Eu^{2+} direct excitation bands also increases with increasing the film thickness.

Figure 3 shows the spectral quantum efficiency (QE) of $CaAl_2O_4$:Eu^{2+} phosphor thin films. We obtain QE as following procedure. QE is usually determined by the ratio of the light output and absorptance. The light output is proportional to the measured emission intensity, that is also called PL excitation spectrum $I_{exc}(\lambda)$. In this report, we neglect the wavelength independent factor relating the excitation spectrum to the light output, then QE is finally obtained as

$$QE = I_{exc}(\lambda)/A. \quad (2)$$

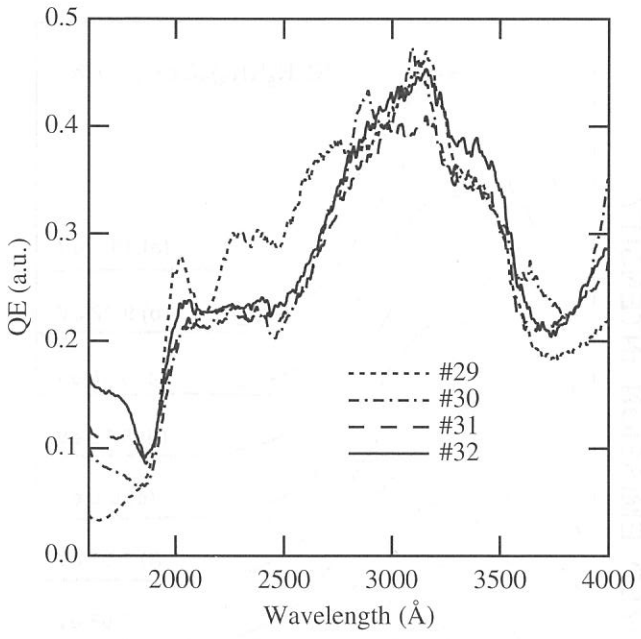

Fig. 3 Quantum efficiency (QE) of $CaAl_2O_4$:Eu^{2+} thin films. QE is determined by the ratio of PLE intensity and absorptance.

As shown in Fig. 3, the QE of Eu^{2+} direct excitation band is relatively high and is almost constant. On the contrary, the QE of host excitation band is quite low and significantly varies with the film thickness. This fact suggests that the migration rate of absorbed energy by host crystal varies with the size of the crystal on the film. Thus, in order to obtain the efficient $CaAl_2O_4$:Eu^{2+} phosphor thin film, it is necessary to increase the size of the crystal.

In summary, Transmission, reflection and PL excitation (PLE) measurement were performed in the wavelength range from 1000 to 4000 Å. We compare the PLE spectra with absorption spectra and obtain the quantum efficiency for the Eu^{2+} blue emission. Quite low QE of host excitation band and its film-thickness dependence are observed.

This work is supported by "Research for the Future Program" through grant JSPS-RFTF 96 R 12501 from "Japan Society for the Promotion of Science" (JSPS).

REFERENCE

[1] C. Sella, J.C. Martin and Y. Charreire: Thin Solid Films **90** (1985) 181.

[2] P. Yu, Z. K. Tang, George K. L. Wong, M. Kawasaki, A. Ohtomo, H. Koinuma and Y. Segawa: Pro. Int. Conf. on the Phys. of Semicond. **2** (1996) 1453.

[3] M. Kawasaki, J. Gong, M. Nantoh, T. Hasegawa, K. Kitazawa, M. Kumagai, K. Hirai, K. Horiguchi, M. Yoshimoto and H. Koinuma: Jpn. J. Appl. Phys. **32**(1993) 1612.

(BL-1B)

Intrinsic Luminescence in $(C_2H_5NH_3)_2CdCl_4$ Single Crystals

[A] Akimasa OHNISHI and [B] Mamoru KITAURA

[A] *Department of Physics, Yamagata University, Yamagata 990-8560*

[B] *Fukui National College of Technology, Sabae 916-8507*

Alkylammonium Cadmium Chloride, $(C_2H_5NH_3)_2CdCl_4$, is a layered ionic crystal of perovskite-type. In the crystal, it has been reported that a largely stokes-shifted luminescence band appears at 2.50 eV under excitation at 5.90 eV into the excitonic absorption region, and at 2.25 eV under excitation at 10.3 eV above the band gap energy. [1] These bands have been supposed to be of intrinsic nature. However, we recently clarified that the lowest exciton absorption band is peaked at 6.19 eV, different from the previous report. [2,3] This finding suggests that the excitation for the intrinsic luminescence occur above 6.19 eV. It is evidence, therefore, that the 2.50 eV band, which is strongly excited in the low energy tail of the lowest exciton absorption, is not intrinsic luminescence. In the present study, recombination luminescence of $(C_2H_5NH_3)_2CdCl_4$ has been investigated in detail under excitation at various photon energies, in order to reconsider the intrinsic luminescence.

$(C_2H_5NH_3)_2CdCl_4$ single crystals were grown at RT by evaporating the aqueous solution containing stoichiometric amounts of $C_2H_5NH_3Cl$ and $CdCl_2$. Samples were cleaved in a plane perpendicular to the *c*-axis, mounted on a Cu holder of a He flow-type cryostat and then were cooled to 7 K. Experiments were performed using synchrotron radiation (SR) from a beam line 1B of UVSOR. Luminescence was analyzed by a Spex 270M monochromator equipped with a CCD detector or a R955 photomultiplier.

Figure 1 shows luminescence spectra of $(C_2H_5NH_3)_2CdCl_4$ measured under excitation at various energies. As shown in Fig. 1(a), a luminescence band is observed at 2.14 eV, when the crystal is excited at 10.8 eV above the

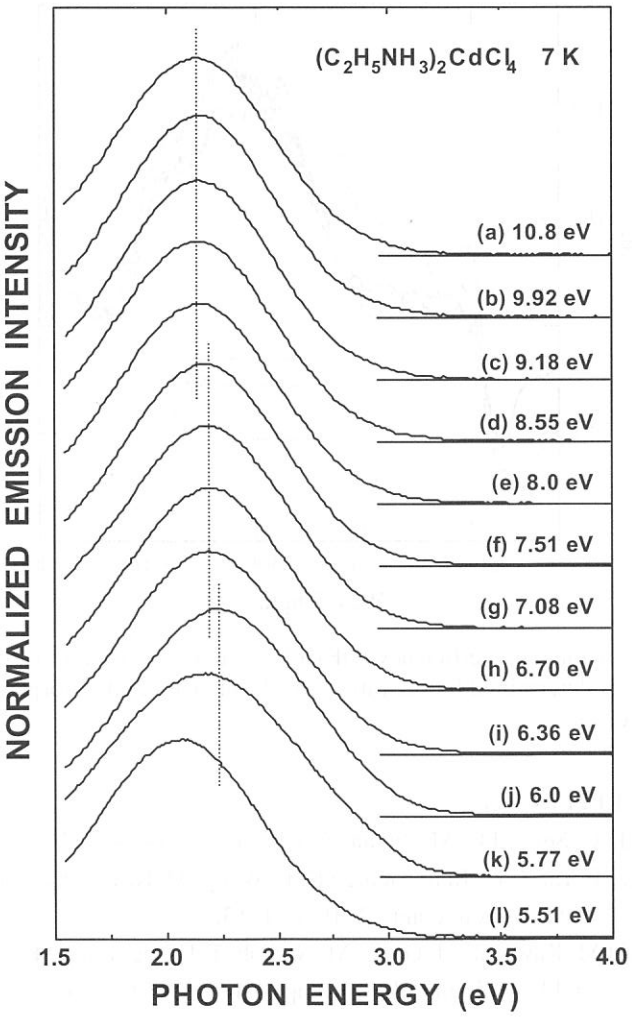

Fig. 1

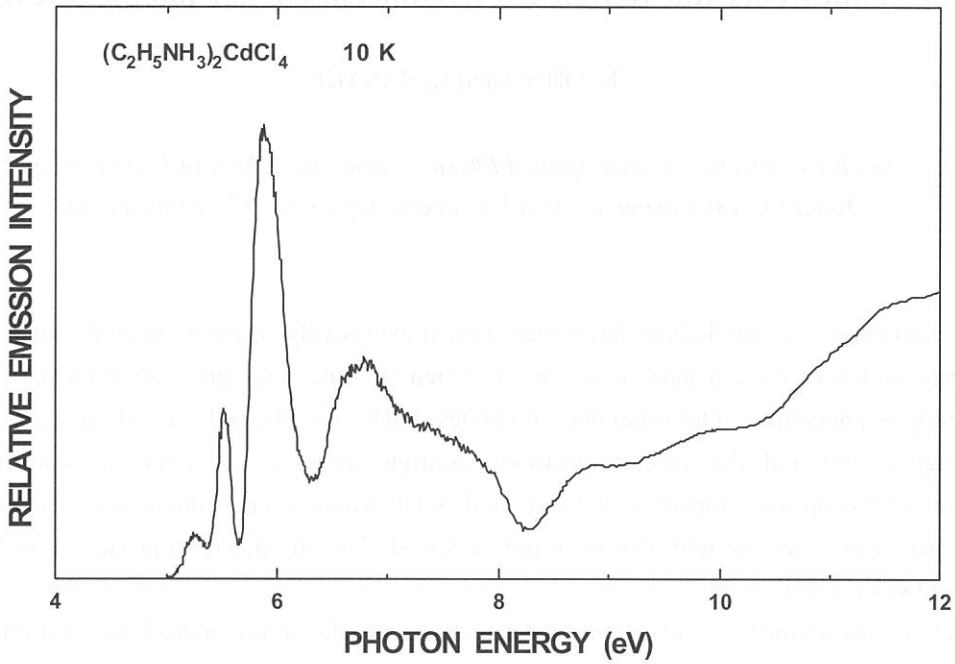

Fig. 2

band gap energy of 6.81 eV. This band appears under excitation above around 8.0 eV (Fig. 1(a) – (e)). In Fig. 2, the excitation spectrum detected at 2.14 eV is shown. The dips at 6.2 eV and 8.2 eV correspond with the peak positions of two kinds of exciton absorption bands, which are due to the transitions from the same Cl *3p* valence band to the conduction bands composed of Cd *5s* and NH_3 *s*-like states, respectively. [2,3] The excitation spectrum indicates high emission yield even below 8.0 eV. When the crystal is excited in the 6.2 – 8.0 eV range, another luminescence band appears at 2.19 eV, as seen in Fig. 1(f) – (i). Thus, the efficiency in the 6.2 – 8.0 eV range is due to the excitation of the 2.19 eV band. On the other hand, it was found that the 2.14 eV and 2.19 eV bands rapidly degrade during prolonged irradiation of excitation lights.

From the results mentioned above, the 2.14 eV and 2.19 eV luminescence bands are undoubtedly assigned to intrinsic luminescence of $(C_2H_5NH_3)_2CdCl_4$. The existence of such two intrinsic luminescence bands suggests that there are two recombination processes of electrons and holes in this crystal. From rapid degradation of their intensities, we speculate that they come from recombination of two kinds of spatially correlated electron-hole pairs.

References

(1) A. Ohnishi, T. Yamada, T. Yoshinari, I. Akimoto, K. Kan'no and T. Kamikawa; J. Electron Spectrosc. Relat. Phenom. **79** (1996) 163.

(2) A. Ohnishi, K. Tanaka, T. Yoshinari: J. Phys. Soc. Jpn. **68** (1999) 288.

(3) A. Ohnishi, K. Tanaka, M. Kitaura, T. Otomo and T. Yoshinari: J. Phys. Soc. Jpn. 70 (2001) 3424.

(BL1B)

Luminescence due to Relaxed Excitons in Orthorhombic $SnCl_2$

N. OHNO and K. SASAKI

Division of Electronics and Applied Physics, Graduate School of Engineering, Osaka Electro-Communication University, Neyagawa 572-8530, Japan

Optical properties of lead halides have been studied extensively so far by several groups. Especially, luminescence studies of these materials have been carried out since they give complimentary information on the photolysis phenomena. Orthorhombic tin halides, $SnBr_2$ and $SnCl_2$, have the same crystal structure (space group *Pmnb*) and the similar electronic configurations as orthorhombic lead halides. The investigation of the optical properties of $SnBr_2$ and $SnCl_2$ would deepen our understanding the energy relaxation processes in this system. However, only a few studies on optical properties of Sn halides have been reported so far [1-3].

Reflection measurements of our group for $SnBr_2$ have revealed a pronounced polarization dependence of the first exciton band at 3.4 eV [4]. The polarization dependence has been well interpreted as a cationic interband transition in Sn^{2+} ($5s \rightarrow 5p$) under the crystal field with C_S symmetry. The logarithmic plot of the fundamental absorption spectra has been found to give a straight line [4], that is, the absorption tail of $SnBr_2$ is well described by the Urbach rule. The obtained small value of the steepness parameter $\sigma_0 = 0.7$ suggests that the electron-phonon interaction is in a strong case in $SnBr_2$, and the free carriers are easily self-trapped. In fact, a luminescence bands with a large Stokes shift was observed under the band-to-band excitation at low temperatures [5,6].

In the present study, reflection and photoluminescence spectra of $SnCl_2$ have been examined at BL1B in the UVSOR facility to obtain the new information on exciton relaxation process in this system. The $SnCl_2$ granule crystals were first purified by distillation in vacuum, and the single crystals were grown by the sublimation method. Figure 1 shows the reflection spectrum up to 12 eV measured at 10 K. One can see a prominent peak at 4.51 eV due to the first exciton transition. The peak energy is almost the same as that reported by Voloshinovskii (4.52 eV at 4.2 K) [3]. There are also seen several sharp peaks at 4.9 and 5.9 eV, and broad peaks in the higher energy region. The structures from 4.5 eV to ~ 9 eV are obviously due to the optical transition from the valence bands. The first exciton transition in $SnCl_2$ is probably ascribed to a cationic interband transition in Sn^{2+} ($5s \rightarrow 5p$) as in the case of $SnBr_2$. However, the optical measurement for polarization dependence is needed to make assignments to the electronic structures in $SnCl_2$.

Figure 2 shows the luminescence and excitation spectra of $SnCl_2$ measured at 10 K. The luminescence spectra are taken under the excitation with 4.13 and 4.48 eV photons. Two luminescence bands peaking at 2.05 and 2.67 eV are observed under the excitation with 4.48 eV photons, while the 2.67 eV band appears under the excitation with 4.13 eV photons. These luminescence bands have a Gaussian lineshape and a large Stokes shift from the lowest exciton energy. The obtained results are almost the same as those reported by Pidzyrailo *et al* [1].

Luminescence excitation spectra were examined for photons emitted at 2.05 and 2.67 eV, respectively. As can be seen in Fig. 2, the 2.05 eV band is stimulated with photons in the low energy region of the first exciton band. On the other hand, the 2.67 eV band is strongly excited with photons in the region of the

lowest exciton band. These excitation spectra exhibit a sharp decrease in intensity as the excitation energy is in the region of the band-to-band transition. The present results suggest that the 2.67 eV band is of intrinsic in origin and is related to the annihilation of self-trapped excitons, and the 2.05 eV band is due to the annihilation of self-tapped excitons perturbed by some impurity.

It is found that the integrated intensity of the 2.67 eV band begins to decrease rapidly at around 30 K, while that of the 2.05 eV band begins to increases at the same temperature. The anti-correlated relation in intensities of these luminescence bands strongly suggests that the self-trapped excitons begin to migrate above 30 K and the exciton energy transfers to the 2.05 eV impurity center.

The authors acknowledge M. Tanaka for her assistance in crystal preparation, optical measurements and data analysis.

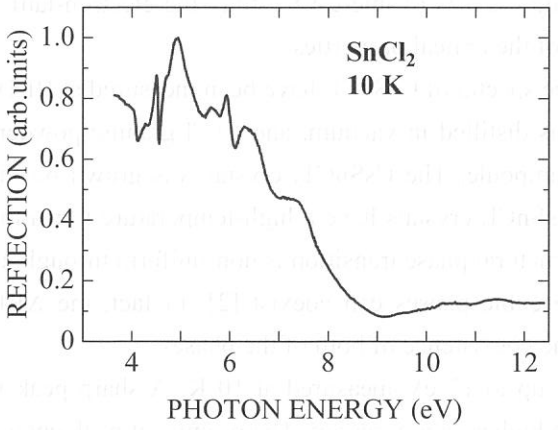

Fig. 1. Reflection spectrum of $SnCl_2$ crystal measured at 10 K.

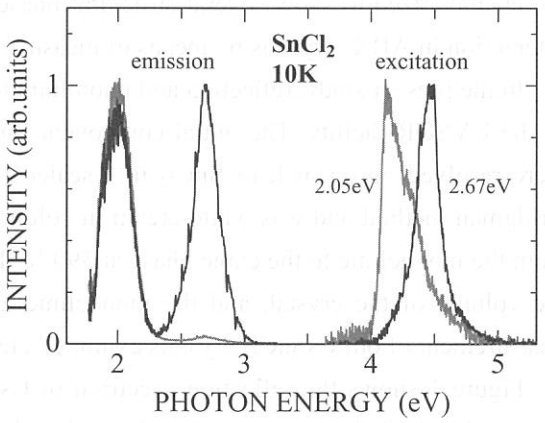

Fig. 2. Luminescence and excitation spectra of $SnCl_2$ measured at 10 K.

References

[1] N.S. Pidzyrailo, A.S. Voloshinovskii, N.G. Stan'ko and Z.A. Khapko: Sov. Phys. Solid State **24** (1982) 708.
[2] A.S. Voloshinovskii, S.V. Myagkota, N.S. Pidsyrailo and Z.A. Khapko: Opt. Spectrosc. **52** (1982) 457.
[3] A.S. Voloshinovskii: Phys. Solid State **35** (1993) 1588.
[4] N. Ohno, Y. Yamasaki, H. Yoshida and M. Fujita: Phys. Status Solidi (b) **223** (2001) 352.
[5] Y. Yamasaki and N. Ohno: UVSOR Activity Report **2000** (2001) 114.
[6] Y. Yamasaki and N. Ohno: Int. J. Mod. Phys. B **15** (2001) 4009

(BL1B)

Photoluminescence of $CsSnCl_3$ Crystal

N. OHNO and K. SASAKI

Division of Electronics and Applied Physics, Graduate School of Engineering, Osaka Electro-Communication University, Neyagawa 572-8530, Japan

The compounds of ABX_3 type (A=Cs, Rb; B=Pb, Sn; X=C1, Br, I) have some interesting optical and electrical properties. For example, free exciton luminescence was found in $CsPbCl_3$ crystal, and $CsSnBr_3$ crystal is of quasi-metal type [1], while $CsSnCl_3$ crystal has dielectric properties. Moreover, these crystals are characterized to show several structural phase transitions. It is of interest to study the electron-lattice interaction in ABX_3 crystals by means of measurements of the optical properties.

In the present study, reflection and photoluminescence spectra of $CsSnCl_3$ have been measured at BL1B in the UVSOR facility. The initial component $SnCl_2$ was distilled in vacuum, and CsCl granule powders were resolved into a melt of $SnCl_2$ in a sealed Pyrex ampoule. The $CsSnC1_3$ crystal was grown by the Bridgman method and was white-cream in color. The $CsSnCl_3$ crystals have a high-temperature transition from the monoclinic to the cubic phase at 390 K. This structural phase transition is non-uniform throughout the volume of the crystal, and the monoclinic and the cubic phases can coexist [2]. In fact, the XRD measurement of our $CsSnCl_3$ crystals exhibited clearly the coexistence of both of the phases.

Figure 1 shows the reflection spectrum of $CsSnC1_3$ up to 12 eV measured at 10 K. A sharp peak is observed at 4.38 eV. There are several broad peaks in the higher energy region. The prominent peak energy is close to the absorption peak of the monoclinic phase reported by Voloshinovskii *et al* (4.0 eV at 77 K) [2], thus it can be assigned as the lowest exciton transition of the monoclinic phase. A small structure is observable at 3.6 eV, which is probably due to the lowest exciton transition of the cubic phase since the absorption peak of the cubic phase is located at 3.5 eV at 77 K [2]. It is to be noted that these lowest exciton energies are almost the same as the first exciton energy of orthorhombic $SnCl_2$ [3,4]. The lowest exciton transitions in $CsSnC1_3$ are ascribed to the cationic interband transition in Sn^{2+} ($5s \rightarrow 5p$) as in $SnCl_2$ [4] and $SnBr_2$ [5].

Luminescence spectra of $CsSnC1_3$ measured at 10 K are shown in Fig. 2. The 2.11 eV band with a full-width at half maximum of 0.26 eV is observed under the excitation with 3.32 eV photons. When the excitation is made with 4.23 eV photons, a luminescence band with an asymmetric lineshape is observed peaking at 2.65 eV. The luminescence excitation spectra for these bands are shown in Fig. 3. The 2.11 eV band is stimulated with photons in the region of the lowest exciton band of the cubic phase, while the 2.67 eV band is strongly excited with photons in the region of the lowest exciton energy of the monoclinic phase. The present results suggest strongly that they are of intrinsic in origin and is related to the annihilation of self-trapped excitons in the respective phases.

It is found that the integrated intensity of the 2.11 eV band begins to decrease at around 40 K, while that of the 2.65 eV band decreases gradually at 20 K and then diminishes at around 50 K. The estimated activation energies using Arrhenius's formula are 37 meV for 2.11 eV band, and 9 and 48 meV for the 2.65 eV band. The two-step thermal quenching of the 2.65 eV band indicates that this luminescence band consists of composite bands.

The authors acknowledge Y. Kitaguchi for her assistance in crystal preparation, optical measurements and data analysis.

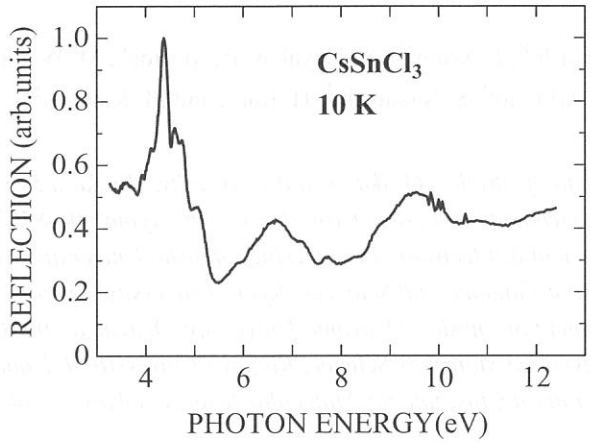

Fig. 1. Reflection spectrum of $CsSnCl_3$ crystal measured at 10 K.

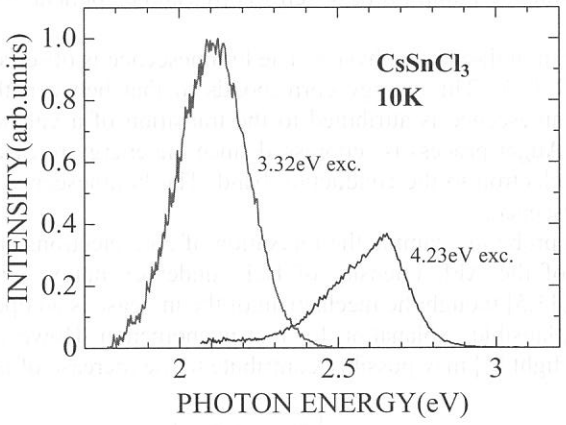

Fig. 2. Luminescence spectra of $CsSnCl_3$ crystal measured at 10 K.

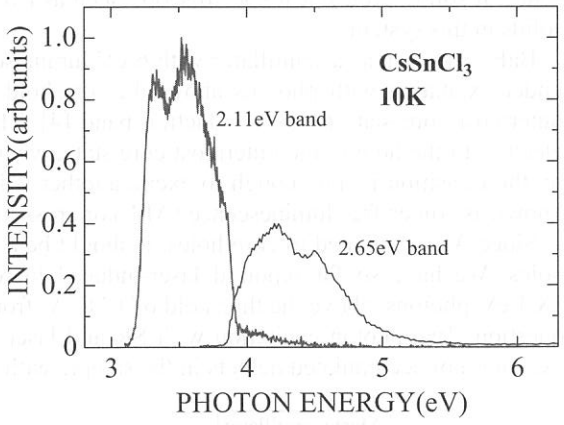

Fig. 3. Excitation spectra of $CsSnCl_3$ crystal measured at 10 K.

References

[1] S. Clark, C. Flint and J. Donaldson, Phys. Chem. Sol. **42** (l981) 133.
[2] A.S. Voloshinovskii, S.V. Myagkota, N.S. Pidzyrailo and M.V. Tokarivskii: J. Appl. Spectrosc. **60** (1994) 226.
[3] A.S. Voloshinovskii: Phys. Solid State **35** (1993) 1588.
[4] N. Ohno and K. Sasaki: UVSOR Activity Report **2001** (2001) in press.
[5] N. Ohno, Y. Yamasaki, H. Yoshida and M. Fujita: Phys. Status Solidi (b) **223** (2001) 352.

(BL1B)

Two-Photon Spectroscopy of Core Electrons in BaF_2 with Synchrotron Radiation and Laser

T. Tsujibayashi[a], J. Azuma[b], K. Hayakawa[c], M. Itoh[c], M. Watanabe[d], O. Arimoto[e], S. Nakanishi[f], H. Itoh[f], and M. Kamada[g]*

[a]*Department of Physics, Osaka Dental University, Hirakata 573-1121*
[b]*Department of Physics, Kyoto University, Kyoto 606-8502*
[c]*Department of Electrical & Electronic Engineering, Shinshu University, Nagano 380-8553*
[d]*Department of Fundamental Sciences, Kyoto University, Kyoto 606-8501*
[e]*Department of Physics, Okayama University, Okayama 700-8530*
[f]*Department of Advanced Materials Science, Kagawa University, Takamatsu 760-8526*
[g]*UVSOR Facility, Institute for Molecular Science, Okazaki 444-8585*

We have been constructing a spectroscopic system in which both synchrotron radiation (SR) and laser are used as light sources [1-3]. A combination of the wide spectral range of SR, from X-ray to infrared, and the high power of lasers is a powerful tool for investigating dynamical behaviors of excitations in inner-shell electronic states of solids. Non-linear spectroscopy such as two-photon and pump-probe spectroscopy can be applicable to solids in this system.

BaF_2 is known as a scintillator with 6-eV luminescence in high-energy physics. The luminescence is observed under excitation with photons above the threshold of 17.8 eV. This energy corresponds to that between the outermost core state to the conduction band [4]. The luminescence is attributed to the transition of a valence electron to the hole in the outermost core state, where an Auger process is suppressed since the energy released by the transition is not enough to excite another valence electron to the conduction band. The luminescence is known as Auger-free luminescence (AFL) or cross luminescence.

Since AFL is related to core holes, it should be a good probe to examine the relaxation of core electrons and holes. We have so far reported laser-induced increase of the AFL intensity of BaF_2 under excitation with 18.4-eV-photons, above the threshold of 17.8 eV, from SR [3,5] though the mechanism of the increase is an open question. Two-photon excitation with SR and laser is a plausible explanation for that phenomenon. However, excitation of accumulated defects in the sample with laser light [6] may possibly contribute to the increase of the

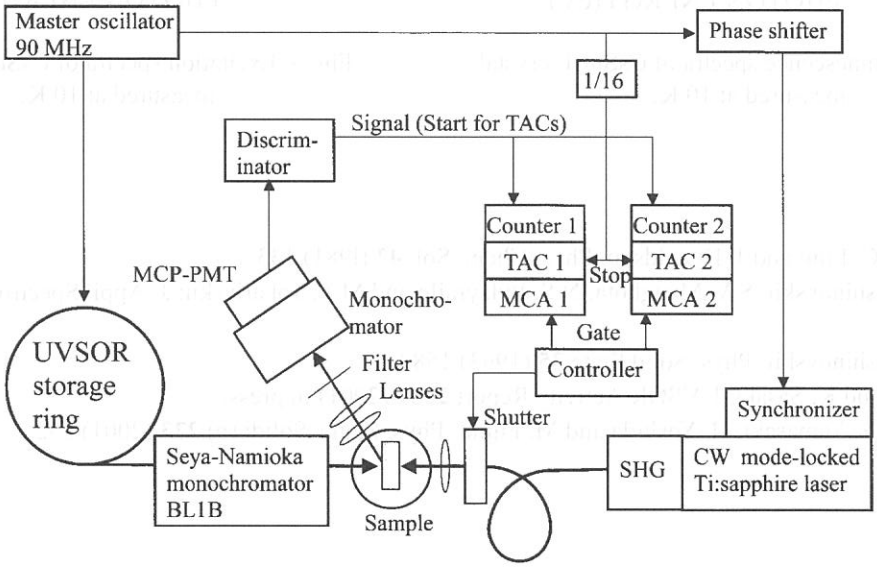

Fig. 1 The block diagram of the experimental setup.

* Present address: *Synchrotron Light Application Research Center, Saga University, 1 Honjyou, Saga 840-9502.*

AFL intensity through changing the branching ratio between decay channels of the core holes. In order to avoid this complexity we lowered the photon-energy of SR below the threshold to 16.7 eV so that AFL is not observed under excitation only with SR. Temporal behavior of the luminescence was measured to clarify whether the luminescence is a consequence of two-photon absorption or not.

The block diagram of the measuring system is depicted in Fig. 1. The laser light was guided to the sample by a 50-m-long optical fiber. The duration of the pulse was stretched from 160 fs to about 0.3 ns during the travel through the fiber. The duration of the laser pulse is comparable to that of the SR pulse under the single bunch operation. The pulse shapes of the laser and SR are shown by solid and broken lines, respectively, in the upper panel of Fig. 2. The temporal behavior of AFL was obtained through the time-correlated single photon counting method. As shown in Fig. 1, MCA1 and MCA2 accumulated the signal when the shutter was open and closed, respectively. The temperature of the sample was kept at 295 K.

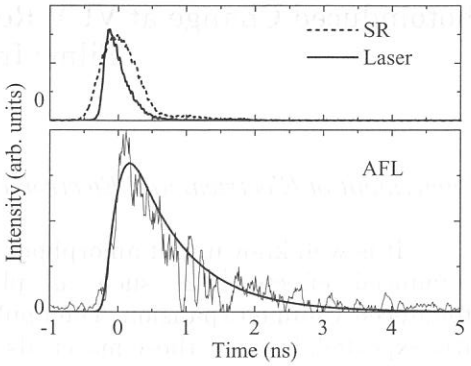

Fig. 2 Upper panel: pulse shapes of SR (broken line) and laser light (solid line). Lower panel: temporal behavior of AFL under excitation with SR (16.7 eV) and laser (3.1 eV). The smooth curve is obtained through convolution analysis (see the text).

The rough curve in the lower panel of Fig. 2 shows temporal behavior of AFL under simultaneous excitation with 16.7-eV-photons of SR and 3.1-eV-photons of the laser. The component of the luminescence caused by scatter and higher harmonics of the Seya-Namioka-type monochromator was eliminated by subtraction of the data on MCA2 (excitation with SR alone) from those on MCA1 (excitation with SR and laser light). We performed convolution analysis of the experimental data. Convoluting the laser pulse shape with an exponentially decaying function was not satisfactory. The smooth curve in the figure was obtained by convoluting the product of SR and laser pulse shapes with an exponentially decaying function with the time constant of 0.8 ns, which is the usual lifetime of AFL. The curve explains the experimental data successfully. This result suggests that the luminescence originates from two-photon absorption of SR and laser light.

References

[1] S. Asaka *et al.*: Rev. Sci. Instrum. **69** (1998) 1931.
[2] S. Asaka *et al.*: UVSOR Activity Report **26** (1999) 34.
[3] T. Tsujibayashi *et al.*: UVSOR Activity Report **28** (2001) 112.
[4] M. Itoh *et al.*: Solid State Commun. **65** (1988) 523.
[5] J. Azuma *et al.*: Nucl. Instrum. & Methods A **467-8** (2001) 1452.
[6] M. Watanabe *et al.*: UVSOR Activity Report **26** (1999) 66.

(BL5B)

Photoinduced Change at VUV Reflection Spectra of Amorphous Chalcogenide Films Induced by BG Light

Koji HAYASHI

Department of Electrical and Electronic Engineering, Gifu University, Gifu 501-1193, JAPAN

It is well known that amorphous chalcogenide semiconductor materials show a variety of photoinduced effects [1,2] such as photodarkening, photoinduced structural change and photoinduced volume expansion. The application of the amorphous materials to optical devices is greatly expected, because these materials are very sensitive to the light. Among those phenomena, the most prominent phenomenon is the so-called photodarkening, which is a parallel shift of the optical absorption edge to lower energy side after irradiation with light whose energy corresponds to the optical bandgap (bandgap (BG) light). This darkened state is removed by annealing near the glass-transition temperature. The X-ray diffraction [3] and the volume change [4,5] of the films before and after irradiation with BG light suggest that the photodarkening is due to a change of the local structure of the amorphous network. Although a large number of studies have been done on the photoinduced phenomena, there is rarely a photoinduced phenomenon in which the details of the mechanism is clarified. These phenomena were studied by exciting outer core electrons with the irradiation of the visible light with the energy corresponding to the optical bandgap or sub-bandgap. Little attention has been give to photoinduced effects by exciting inner core electrons with the irradiation of higher energy photon. To obtain a wide knowledge of the photoinduced effects, it is necessary to investigate photoinduced phenomena on wide energy region. In the previous reports[6], we reported the photodarkening in amorphous chalcogenide films by the irradiation of the vacuum ultra-violet (VUV) light. In our recent study, we observed interesting photoinduced change in the photoconductivity and the total photoyield of amorphous chalcogenide films by the irradiation of the VUV light and the BG light[7-9]. In this report, we investigate the photoinduced change at the VUV reflection spectra of amorphous chalcogenide films induced by BG light.

Samples used for the measurement were amorphous chalcogenide (a-As_2Se_3 and a-As_2S_3) films. Thin films of amorphous chalcogenide were prepared onto quartz substrates by conventional evaporation technique. A typical thickness of an amorphous film was around 0.7 μ m. After evaporation, samples were annealed near the glass transition temperature for two hours in a vacuum with a pressure of 10^{-4} Pa. A xenon arc lamp or a high pressure mercury lamp with IR-cut-off filter were used as a light source. Before the measurement of the VUV reflection spectra, half area of the sample was irradiated with the BG light to the degree in which the sample sufficiently produced the photodarkening. The measurement of the VUV reflection spectra was performed at room temperature at the BL5B beam line of the UVSOR facility of the Institute for Molecular Science. For the measurement of the reflection spectra, the incident angle was near normal to the sample surface and the reflectivity was measured by a silicon photodiode. We also monitored the spectrum of light source by measuring the photoyield of the gold mesh. The reflection spectra were obtained by normalizing the spectra by the spectrometer system response.

Figure 1 shows the VUV reflection spectra of a-As_2S_3 film at room temperature in the photon energy region between 42eV and 50eV. One main peak was observed in this energy region. This peak around 44eV corresponds to the 3d core level of As atom. It can be seen in the figure that the peak of the spectrum observed from the area which irradiated with BG light slightly shifts toward the low energy side and the FWHM becomes narrower as compared to the spectrum observed from the area which dose not irradiate with BG light. It seems to relate these spectral change to the structural change induced by irradiation with BG light. As for the origins of the spectral change, it is not clear. Further analysis of these spectra is now in progress. We also investigate the photoinduced change at the spectra of a-As_2Se_3 films. Method for accurately measuring the peak position and for removing the effect of the higher order light are examined at present. The detailed experiments and analysis will be done in the next step.

This work was partly supported by grants-in-aid for Scientific Research from the Ministry of Education, Science and Culture of Japan.

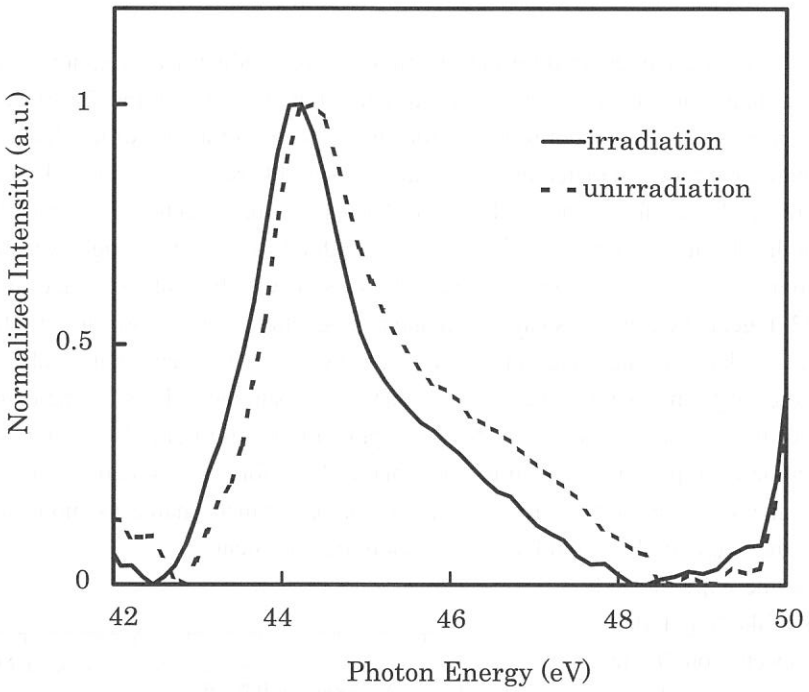

Fig. 1. VUV reflection spectra of a-As_2S_3 film at room temperature in irradiation area (solid line) and unirradiation area (broken line) of BG light.

REFERENCES

[1] Ke. Tanaka, Rev. Solid State Sci., 4(1990)641.
[2] K. Shimakawa, A. Kolobov, and S. R. Elliott, Adv. Phys., 44(1995)475.
[3] Ka. Tanaka: Fundamental Physics of Amorphous Semiconductors, ed. F. Yonezawa, (Springer, Berlin, 1981), p.104.
[4] Ka. Tanaka: Proc. A.I.P. Conf. Structure and Excitations of Amorphous Solid, ed. G. Lucovsky and G.L. Galeemer, Vol.31, (A.I.P., New York, 1977), p.148.
[5] S. R. Elliott, J. Non-Cryst. Solids, 81(1986)71.
[6] K. Hayashi, D. Kato, and K. Shimakawa, J. Non-Cryst. Solids., 198-200(1996)696.
[7] K. Hayashi, A. Hirai, and K. Shimakawa, UVSOR Activity Report 1996(1997)116.
[8] K. Hayashi, UVSOR Activity Report 1997(1998)118.
[9] K. Hayashi, UVSOR Activity Report 1998(1999)105.

(BL5B), (BL8B1)

Magnetic Kerr Rotation Measurement on Ni around Its $M_{2,3}$ Edges

K. Saito, M. Igeta, T. Ejima, T. Hatano and M. Watanabe

Institute of Multidisciplinary Research for Advanced Materials, Tohoku University
Katahira 2-1-1, Aoba-ku, Sendai 980-8577

In the previous study, we have reported for the first time the longitudinal Kerr rotation measurement on Co around its $M_{2,3}$ edges utilizing the developed magnetic Kerr rotation apparatus in the 50-70 eV at BL5B of the UVSOR facility.[1] The measured longitudinal Kerr rotation angle spectra for angles of incidence of $\theta = 65°$ and $\theta = 80°$ have been compared with the calculated ones from the measured Faraday rotation angle spectrum using the Maxwell-Fresnel approach. It was found that both spectra had the similar spectral shape and θ-dependence of the rotation angle, but the absolute value of the measured longitudinal Kerr rotation angle was larger than that of the calculated one from the Faraday rotation spectrum. The reason was thought to be due to the fact that the magnetic field of 0.82 T generated by the shared permanent magnetic circuit could saturate the magnetization parallel to the Co film plane in the longitudinal Kerr rotation measurement, but could not saturate the magnetization perpendicular to the plane in the Faraday rotation measurement, because the demagnetizing field is strong. In the case of the Ni film, it is expected that the applied magnetic field of 0.82 T is strong enough to saturate the magnetization even perpendicular to the film plane. Therefore in this study, by the use of the same apparatus, the similar measurements on a Ni film were performed, which enable us more direct comparison between the results of the magnetic Kerr and Faraday rotation measurements.

Figure 1 shows, the experimental and calculated results of the longitudinal Kerr rotation angle spectra on 98 nm thick Ni film, for the *s*-polarized incident light at the angle of incidence of $\theta = 65°$. The experimental result is plotted by open circles, and the calculated one, by dashed curve which is obtained through Maxwell-Fresnel approach from the result of the Faraday rotation measurement on a 31.5 nm thick Ni film at BL8B1 of the UVSOR.[2] Each measurement was performed at room temperature. Both spectra are almost the same, as seen in Fig. 1. Therefore, we conclude that the consistency between the magnetic Kerr and Faraday rotation measurements was confirmed directly. Now we are proceeding with the study on magnetic multilayer systems.

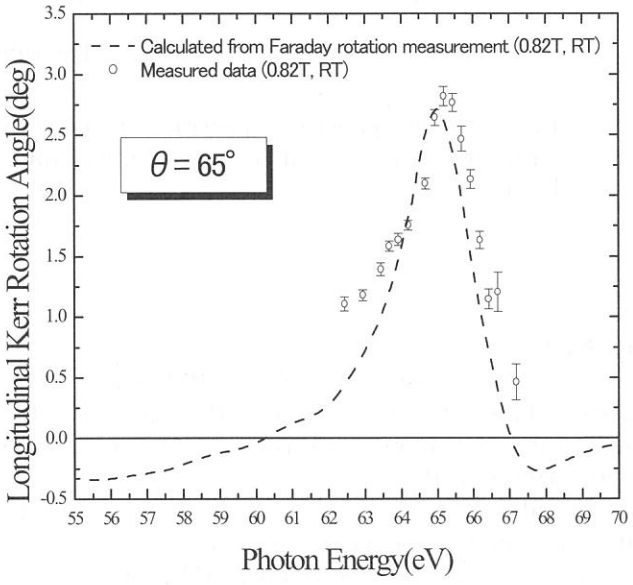

Fig. 1. Longitudinal Kerr rotation angle spectra of 98 nm thick Ni film on Si wafer for *s*-polarized incident light around Ni $M_{2,3}$ absorption edges, at angle of incidence of $\theta = 65°$.

References

1) K. Saito, M. Igeta, T. Ejima, T. Hatano and M. Watanabe, UVSOR Activity Report 2000 (2001) 124.
2) T. Hatano, W. Hu, K. Saito and M. Watanabe, J. Electr. Spectr. Rel. Phenom. **101** (1999) 287.

(BL6A1)

Magneto-Optical Study on Electronic Structure of $Ce_{1-x}La_xSb$ (x = 0, 0.1) in the Infrared Region

S. Kimura[1,2], T. Nishi[1], H. Iwata[1], M. Okuno[1], H. Kitazawa[3] and G. Kido[3]

[1]*Graduate School of Science and Technology, Kobe University, Nada-ku, Kobe 657-8501*
[2]*Japan Science and Technology Corporation*
[3]*National Research Institute for Metals, Tsukuba, 305-0047*

Cerium monoantimonide (CeSb) is a typical strongly correlated semimetal with 4*f* electrons. It has a complex magnetic phase diagram with 16 magnetic phases. [1] The main mechanism is known to be the mixing effect between the Ce 4*f* and the Sb 5*d* states, so-called the *pf* mixing effect. [2] Due to the *pf* mixing effect, the band structure near the Fermi level drastically changes with magnetic phases. The change of the electronic structure has been detected by magneto-optical experiments in the infrared region by us [3] and the other groups [4,5]. The change of the electronic structure produces a large magneto-optical effect because of the strong polarization of the electronic structure. Until now, we revealed the detail mechanism of the strong magneto-optical effect. The main origin is the mixing effect between Sb 5*p* and Ce 5*d* induced by the *pf* mixing (*pf* + *pd* mixing). [6]

In our magnetic circular dichroism measurement of CeSb, a peak was found at 0.4 eV in the $\sigma_+(\omega)$ spectrum in the ferromagnetic phase in contrast to the $\sigma_-(\omega)$ spectrum. According to a theoretical prediction, the peak shifts to the lower energy side in $Ce_{1-x}La_xSb$ ($x > 0$) because the *pf* mixing and also the *pd* mixing are suppressed by the La substitution.

To confirm the theoretical prediction, we measured the magnetic circular dichroism of $Ce_{0.9}La_{0.1}Sb$ in the ferromagnetic phase. Because of the weak *pf* mixing intensity, the ferromagnetic phase appears at lower temperatures than 5 K. Then we made a new cryostat that is a continuous liquid helium flow type and reaches down to 4.0 K for the infrared magneto-optical apparatus at BL6A1.

Figure 1 indicates the magnetic circular dichroism of optical conductivity of $Ce_{0.9}La_{0.1}Sb$ and CeSb in these ferromagnetic phases. The spectral tendency is similar to each other, i.e., the $\sigma_+(\omega)$ is higher (lower) intensity than the $\sigma_-(\omega)$ around 0.4 eV (above 0.6 eV and below 0.25 eV). Since it originates from the polarization of the electronic structure in the ferromagnetic phase, the outline of the electronic structure is similar to each other. The different point of the spectral shape is the peak at 0.35 eV in CeSb shifts to 0.25 eV in $Ce_{0.9}La_{0.1}Sb$. This is considered to originate from the weak *pf* mixing effect as theoretically predicted.

[1] J. Rossat-Mignod *et al.*, J. Magn. Magn. Mater. **52**, 111 (1985).
[2] H. Takahashi and T. Kasuya, J. Phys. C: Solid State Phys. **18**, 2697, 2709, 2721, 2731, 2745, 2755 (1985).
[3] S. Kimura *et al.*, J. Phys. Soc. Jpn. **69**, 647 (2000).
[4] R. Pittini *et al.*, Phys. Rev. Lett. **77**, 944 (1996).
[5] F. Salghetti-Drioli *et al.*, Solid State Commun. **109**, 687 (1999).
[6] F. Ishiyama and O. Sakai, J. Phys.Soc. Jpn. **71** (2002) in press.

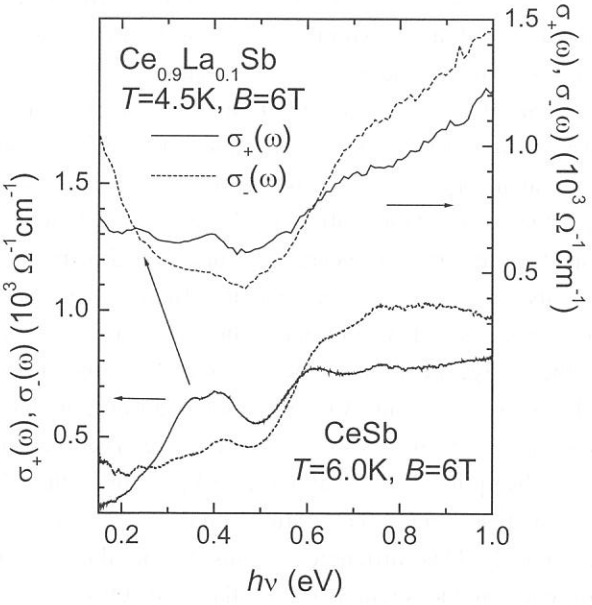

Fig. 1. Magnetic circular dichroism of $Ce_{0.9}La_{0.1}Sb$ and CeSb in the ferromagnetic phase.

(BL6A1)

Far-infrared and Millimeter Wave Spectra of Iodide Doped Silver Phosphate Glass

Teruyoshi AWANO

Department of Applied Physics, Tohoku Gakuin University, Tagajo 985-8537

Enhancement of ionic conductivity by doping of PbI_2 in $AgPO_3$ glass was reported previously[1]. Swenson et al. investigated mechanism of the enhancement on the PbI_2-$AgPO_3$ glass by diffraction measurements and reverse Monte Carlo simulation[2]. They explained the increase of ionic conductivity by that the doped Pb^{2+} substitute Ag^+ which is connected with non-bonding oxygen and the released Ag^+ contribute to ionic conduction. The doped I^- extend space between PO_4 chains and conduction channel for Ag^+ is expanded.

The enhancement of ionic conductivity by metal iodide doping has also been reported on BiI_3 and CdI_2 and NaI[3]. The increase of ionic conductivity is proportional to dopant concentration and valence of the metal ion. This paper reports results of far-infrared and millimeter wave spectra of BiI_3-$AgPO_3$ and CdI_2-$AgPO_3$ glasses to investigate the effect of valence numbers of cations on the enhancement of ionic conductivity.

BiI_3 or CdI_2 doped $AgPO_3$ glasses were obtained by quenching melt of product after reaction of $NH_4H_2PO_4$, $AgNO_3$ and BiI_3 or CdI_2 at 400℃ for two hours after pre-heating at 200℃ for 12 hours. Far-infrared and millimeter wave reflectivity spectra were measured by SPECAC Murtin-Puplett interferometer. Optical constants were obtained by Kramers-Kronig analysis.

Fig. 1 shows reflectivity spectra of $AgPO_3$, $(BiI_3)_{0.05}(AgPO_3)_{0.95}$ and $(CdI_2)_{0.05}(AgPO_3)_{0.95}$ glasses. Dotted line shows the reflectivity of pure silver phosphate glass. Solid and dashed line shows that of BiI_3 or CdI_2 doped glass respectively. Intensity change was observed at 100 cm^{-1} peak in the doped glasses. Fig. 2 shows absorption spectra obtained by Kramers-Kronig analysis from the reflectivity spectra. The reflectivity was extrapolated as constant at lower and higher energy region than the measured one. Absorption peaks were observed at 550, 460, 350 and 125 cm^{-1} in $(BiI_3)_{0.1}(AgPO_3)_{0.9}$ glass. Former three peaks, which are assigned as bending and torsional modes of PO_4 unit[4, 5], were observed at the same positions and at the same intensities as those in $AgPO_3$ glass, although the last peak was located at lower position and at more strength than in $AgPO_3$, in which the Ag-O vibration absorption is at 133 cm^{-1} as shown in fig. 3, which is the magnified one of fig. 2. In $(CdI_2)_{0.1}(AgPO_3)_{0.9}$, the peak was at 129 cm^{-1} and the position shift were little than that of $(BiI_3)_{0.05}(AgPO_3)_{0.95}$, although the strength is more than that in $AgPO_3$ as shown in fig. 3. Other peaks in $(CdI_2)_{0.1}(AgPO_3)_{0.9}$ were at the same positions as those in $AgPO_3$ as shown in fig.2. The shift of the 125 cm^{-1} peak in $(BiI_3)_{0.1}(AgPO_3)_{0.9}$ glass from that in $AgPO_3$ seems to be due to the following mechanism.

A part of silver ions in $AgPO_3$ are replaced by bismuth ions in $(BiI_3)_{0.1}(AgPO_3)_{0.9}$ because the doped Bi^{3+} couples by covalent bond with a nonbonding oxygen. Therefore the intensity of Ag-O vibration decreases as shown by dashed line in fig. 3. The Gaussian curve was drown as the intensity decreased 15 percent in $(BiI_3)_{0.05}(AgPO_3)_{0.95}$ because one doped Bi^{3+} ion must alternates three Ag^+ ions for the charge neutrality. The released Ag^+ ions couple with iodine ions and Ag-I vibrational absorption band grows as at 115 cm^{-1} as shown in the figure. The intensity of the absorption band is drown as 30 percent of the 133 cm^{-1} band in $AgPO_3$. This ratio should be 15 percent in this model. This difference seems to be due to the difference of the strength of oscillator. Bi-O absorption band of the intensity of 5 percent of original Ag-O band is

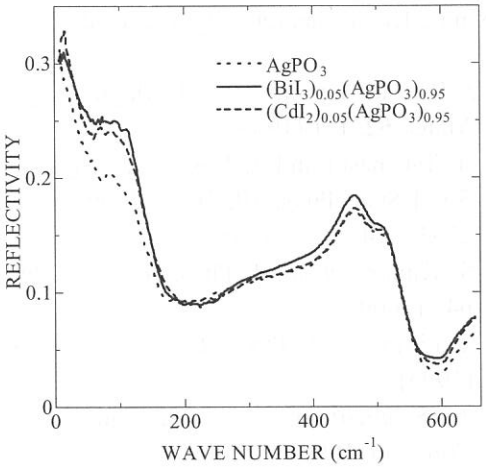

Fig. 1. Reflectivity spectra of pure and doped silver phosphate glasses.

also drawn at 150 cm^{-1} [4] in the figure. Net absorption spectrum by these spectral change is shown by thick solid line. This simulation spectrum agrees with the observed one around 100 cm^{-1}. In $(CdI_2)_{0.1}(AgPO_3)_{0.9}$, the peek shift was smaller than that of $(BiI_3)_{0.05}(AgPO_3)_{0.95}$. This seems to be due to that Cd-O vibrational frequency is almost the same as that of Ag-O [4], because the mass of cadmium ion is almost the same as that of silver ion. The changeless of three absorption bands shows that the glass network structure itself is not affected by the metal doping.

The far-infrared spectral change showed the mechanism of the enhancement of ionic conductivity in BiI_3-$AgPO_3$ and CdI_2-$AgPO_3$ glasses. A doped metal ion substitutes a silver ion which is connected with a nonbonding oxygen. The released silver ion is coordinated weakly with an iodine ion and conducts easily. This mechanism are the same as that in PbI_2-$AgPO_3$ glass.

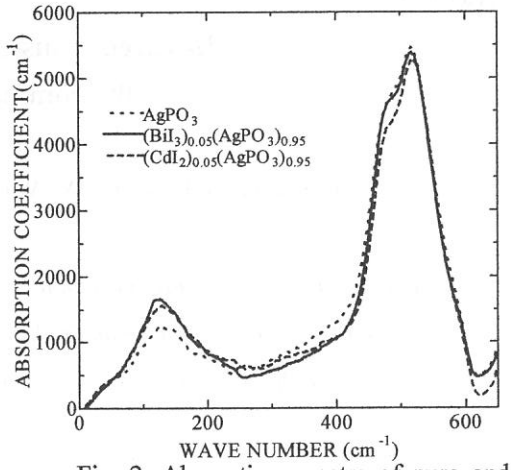

Fig. 2. Absorption spectra of pure and doped silver phosphate glasses obtained from the reflectivity spectra by Kramers- Kronig analysis.

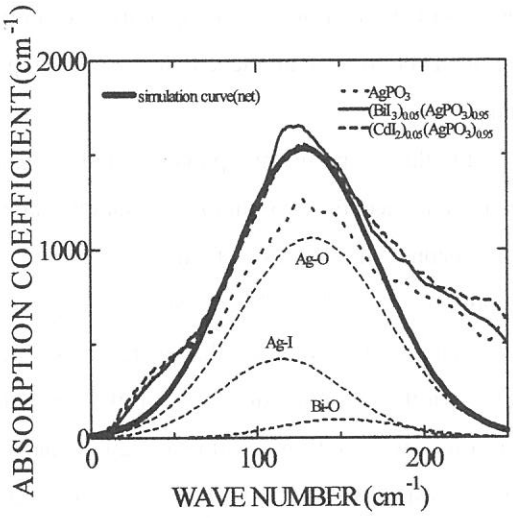

Fig. 3. Magnified spectra of fig. 2 and simulation curves of Ag-O, Ag-I, Bi-O vibration absorption and the net curve of them.

REFERENCES

[1] J. P. Malugani, R. Mercier and M. Tachez, Solid State Ionics, 21 (1986) 131.

[2] J. Swenson, A. Matic, C. Gejke, L. Boerjesson, W. S. Howells and M. J. Capitan, Phys. Rev. B60 (1999) 12023.

[3] H. Nakajin, H. Takahashi and T. Sakuma, Annual meeting of the Physical Society of Japan 1999, 31a-ZE-10.

[4] B. N. Nelson and G. J. Exarhos, J. Chem. Phys. ,71 (1979) 2739.

[5] K. Wakamura, J. Katagi and H. Takahashi, Physica B263-264 (1999) 799.

(BL6A1)

Infrared transient absorption obtained from the combined laser-SR experiment

J. Azuma, M. Iwanaga[A], M. Watanabe[B], M. Kitaura[C], M. Itoh[D] and M. Kamada[E]

Dept. of Phys., Kyoto Univ., Graduate school of Human and Environmental Studies, Kyoto Univ.[A], *Faculty of Integrated Human Studies, Kyoto Univ.*[B], *Fukui National College of Technology*[C], *Faculty of Engineering, Shinshu Univ.*[D], *UVSOR, Institute for Molecular Science*[E]

Transient absorption measurement is a powerful technique to investigate the photo-excited states in condensed matters. Some important results have been obtained by this technique in the visible region[1,2]. It is necessary to expand the spectral range to the infrared (IR) region in order to apply to other interesting topics which cannot be studied in the usual technique in the visible region[3]. It is well known that synchrotron radiation (SR) is a brilliant light source not only in the X-ray or vacuum ultra violet region but also in the IR region. Therefore we are developing the technique of the infrared transient absorption measurement by using SR and laser.

In this experiment, photo-excited states were generated by two-photon excitation using the second harmonics of the regenerative amplified Ti:sapphire laser (Spectra Physics, Hurricane). The wavelength, average power, pulse width and repetition rate of the second harmonics were 400 nm, 250 mW, 120 fs, and 1 KHz, respectively. The measurement was performed in the energy range of 80～13000 cm^{-1} with the rapid-scan Michelson interferometer (Bruker, IFS-66V) by using quartz, KBr and mylar beam splitters. A HgCdTe detector and a Si borometer were used for the energy range of 400～13000 cm^{-1} and 80～500 cm^{-1}, respectively. The transient absorption was obtained from the difference between the transmitted IR intensities with and without the laser excitation. The single crystal of lead bromide was used as a sample in this experiment.

In lead halides, it has been strongly

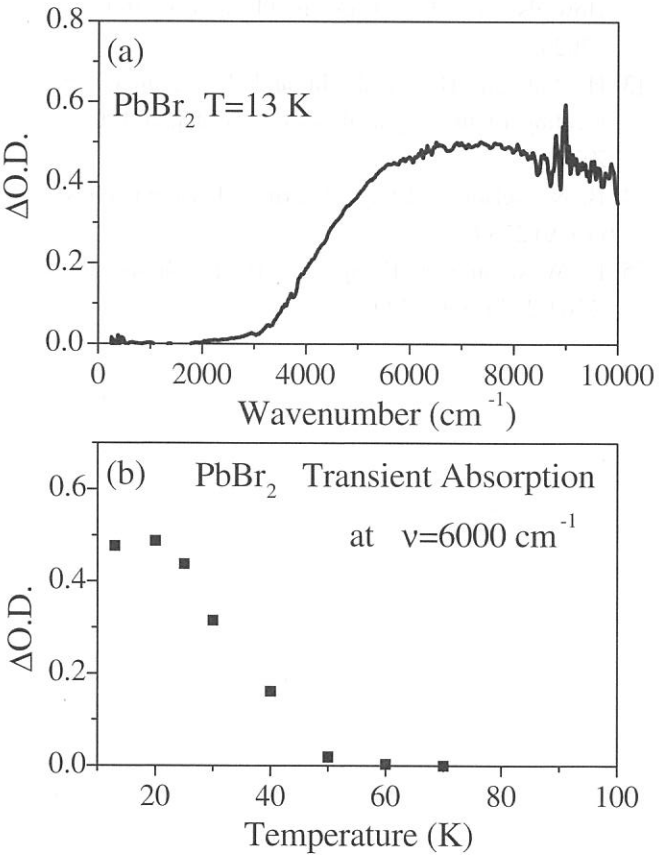

Fig.1 (a): Transient absorption spectrum in lead bromide at 13 K. (b): Temperature dependence of the transient absorption at 6000 cm^{-1}.

suggested that the free electron-hole pair is relaxed into the spatially separated pair of a self-trapped electron and a self-trapped hole by the strong electron-lattice interaction[4,5]. This is an interesting suggestion which pushes us to study the relaxation process of the photo-excited states.

Figure 1(a) shows the transient absorption spectra of lead bromide at 13 K. One can see that a broad transient absorption band appears above 3000 cm^{-1}. This absorption band disappeared instantly after the laser excitation was stopped. This indicates that the absorption is not due to the sample damage caused by the laser irradiation.

Figure 1(b) shows the temperature dependence of the transient absorption at 6000 cm^{-1}. It is clear that the transient absorption decreases around 40 K. The electron-spin-resonance measurement performed by Iwanaga *et al.* has clarified that the V_k-type hole center (Br_2^- dimer center) is induced as a self-trapped hole by the photo-excitation and disappears above 40 K[6]. This result indicates that the observed transient absorption is due to the self-trapped hole. The present experiment is the first optical observation about the self-trapped hole in lead halides.

It is important to investigate the time evolution of the transient absorption originating from the self-trapped hole in order to clarify the relaxation dynamics of the photo-excited state in lead halides. Therefore we are planning to apply the time-resolved technique to this transient absorption measurement.

References

[1] T. Kobayashi, T. Saito and H. Ohtani, Nature **414**, 531 (2001).

[2] S. Iwai, S. Tanaka, K. Fujinuma, H. Kishida, H. Okamoto and Y. Tokura, Phys. Rev. Lett. **88**, 057402 (2002).

[3] M. Nagai, R Shimano and M. Kuwata-Gonokami, Phys. Rev. Lett. **86**, 5759 (2001).

[4] M. Iwanaga, M. Watanabe and T. Hayashi, Phys. Rev. B **62**, 10766 (2000).

[5] M. Kitaura and H. Nakagawa, J. Phys. Soc. Jpn. **70,** 2462 (2001).

[6] M. Iwanaga, J. Azuma, M. Shirai, K. Tanaka and T. Hayashi, cond-mat/0201264.

(BL6A1&7B)

Optical response of $Cu_{1-x}Zn_xIr_2S_4$ due to metal-insulator transition

L. Chen[1], M.Matsunami[1], T.Nanba[1], G.Cao[2] and T.Matsumoto[2]

1.*Graduate School of Science and technology, Kobe University, Nada-ku, 657-8501, Kobe, Japan*

2.*National Research Institute for Metals, 1-2-1Sengen, Tsukuba, 305-0047, Japan*

The mother material $CuIr_2S_4$ of the thiospinel system $Cu_{1-x}Zn_xIr_2S_4$ undergoes a temperature-induced metal-insulator (M-I) transition around 226 K and its precise change in the optical conductivity spectrum due to MI transition has been reported. [1] The Zn substitution for Cu suppresses the MI transition temperature (T_{MI}), resulting in the complete suppression of the MI transition for $x > 0.4$ and also appearance of superconductivity for $x>0.25$ [2]. From the measurements of magnetic susceptibility, X-ray diffraction, and photoelectron spectroscopy, the appearance of the insulating state is to be explained in terms of charge ordering of the Ir3+ and Ir^{4+} ions due to the Ir^{4+} dimerization coupled with the slight deformation of the S-octahedron surrounding the Ir ion. From the band calculation [2], it has been pointed out that the hybridization band across the Fermi level (E_F) formed by the Ir-5d (t_{2g}) and S-3p states play an important role in its material properties. However, the precise study of the change in the electronic structure has not been done on the M-I transition. We have measured the temperature dependence of the optical reflection spectra of $Cu1_{-x}Zn_xIr_2S_4$ (x=0, 0.1, 0.3, 0.4 and 0.5) samples in the energy regions of 0.005-30 eV in order to study the change in the electronic structure very close to the E_F due to the Zn substitution for Cu. Measured reflection spectrum of $Cu_{1-x}Zn_xIr_2S_4$ **in** the temperatures of 8-300 K and its optical conductivity spectrum, $\sigma(\omega)$, obtained by a Kramers-Kronig transformation of the reflection spectrum are shown in Fig.1 for x=0.1. In metallic state above $T_{MI} \sim 130$ K, the Drude part was found to be composed of two components which correspond to the two branches around Γ at B.Z across the E_F in the energy band calculation. Each branch gives rise to a different Drude component because of the difference in the effective mass and lifetime. The continuous Drude components in metallic state lose its intensities below T_{MI} and the interband peak appeared in insulating state in the lower energy part of the spectrum although the higher energy part ($h\nu \geq 3eV$) does not almost change. Only slight change in the whole spectrum except the the lower energy part means that the change in material properties like a MI transition is induced by the change in the electronic state very close to E_F.

The lowest energy interband peak (L) at 0.5 eV for x=0 split into two peaks L_1 and L_2 for x=0.1 and 0.3. The intensities of these peaks do not increase with increasing of Zn substitution as shown in Fig.2. This means that the electronic states very close to the E_F does not come from Zn but the degree of the hybridization between the Ir-5d(t_{2g}) and S-3p states is affected by the Zn substitution.

References

[1] M.Hayashi et al.:Physica **B** 281&282(2000)631.

[2] T.Furubayashi *et al.*: J.Phys.Soc.Lapan **63**(1994)3333.

[3] T.Oda. *et al.* : J.Phys.:Condens.Matter **7**(1995)4433.

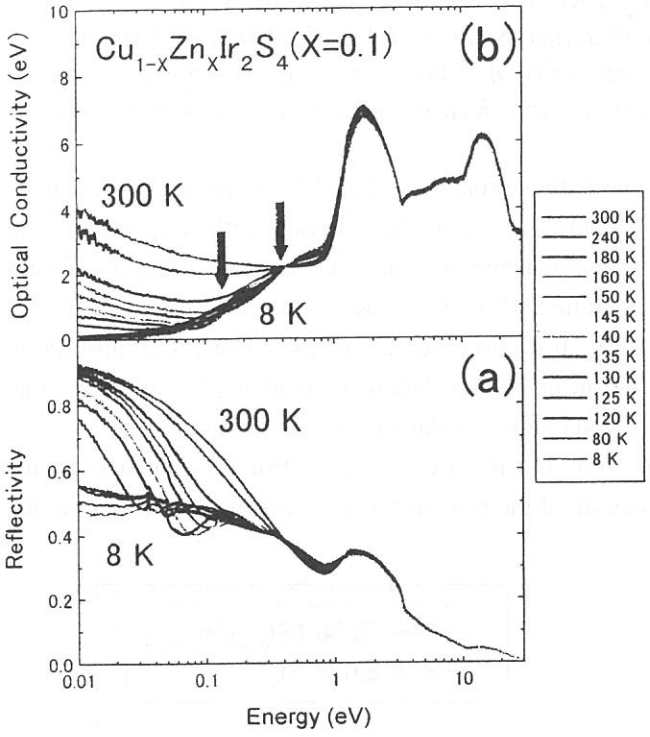

Fig.1

Measured reflection (b) $Cu_{0.9}Zn_{0.1}Ir_2S_4$ and its optical conductivity spectra, σ(a).

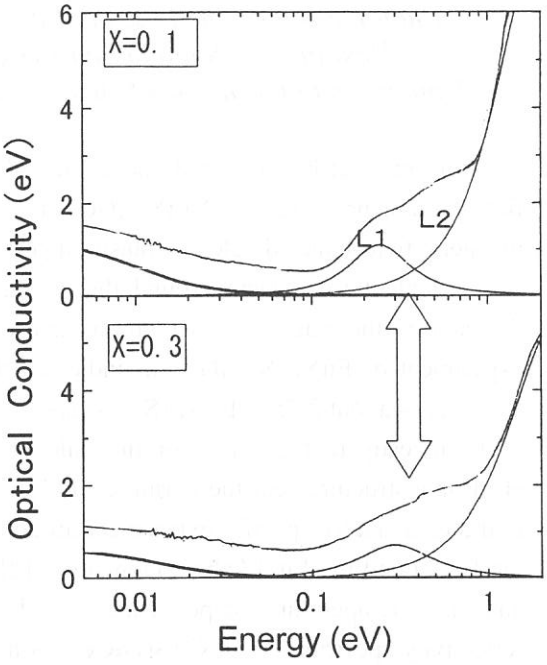

Fig.2 Splitting of the lowest energy interband peak (L) around 0.4 eV for x=0 to the peaks L_1 and L_2 for x=0.1 and 0.3, and its dependence on Zn substitution.

(BL6A1)

Temperature-Induced Valence Transition of $EuNi_2(Si_{0.25}Ge_{0.75})_2$ Studied by Eu 4*d*-4*f* Resonant Photoemission and Optical Conductivity

S. Kimura[1], M. Okuno[1], H. Iwata[1], T. Saitoh[2], T. Okuda[3], A. Harasawa[3], T. Kinoshita[3], A. Mitsuda[3], H. Wada[4] and M. Shiga[4]

[1]*Graduate School of Science and Technology, Kobe University, Nada-ku, Kobe 657-8501*
[2]*Photon Factory, Institute of Materials Structure Science, KEK, Tsukuba, 305-0801*
[3]*Institute for Solid State Physics, University of Tokyo, Kashiwa, 277-8581*
[4]*Dapartment of Materials Science and Engineering, Kyoto University, Kyoto 606-8501*

Some rare-earth compounds have the valence transition property induced by temperature, magnetic fields and/or pressure. $EuNi_2(Si_{1-x}Ge_x)_2$ (x = 0.70 - 0.82) is one of the materials with temperature- and magnetic field-induced valence transition.[1] The mean valence of Eu ion in $EuNi_2(Si_{0.25}Ge_{0.75})_2$ changes from trivalent to divalent around the critical temperature (T_V) of 115 K as the temperature increases detected by the magnetic susceptibility and the Eu 2*p* absorption measurements. The Eu 2*p* absorption experiment of $EuNi_2(Si_{0.21}Ge_{0.79})_2$ indicated that the mean valence below T_V is about 2.8, whereas, that above T_V is about 2.25. $EuNi_2(Si_{0.25}Ge_{0.75})_2$ is expected to take similar valences.

To investigate the origin of the valence transition of $EuNi_2(Si_{0.25}Ge_{0.75})_2$ from the change of the electronic structure near the Fermi level (E_F), we measured the resonant photoemission (RPE) spectra that is the elementally specific experiment around the Eu 4*d* and the Eu 3*d* absorption edges [2] and the temperature dependence of the reflectivity spectrum of $EuNi_2(Si_{0.25}Ge_{0.75})_2$ in the infrared - vacuum-ultraviolet range [3]. The material with trivalent Eu ion, $EuNi_2Si_2$, was also examined for the reference. The optical conductivity ($\sigma(\omega)$) spectra are compared to the RPE spectra and the change of the electronic structure due to the valence transition is discussed.

The Eu 4*d*-4*f* RPE experiment was performed at the beam line 11D of Photon Factory, where a high energy-resolution electron spectrometer, SCIENTA SES-200, is equipped. The total resolution of the monochromator and the electron analyzer was estimated to be about 50 meV at $h\nu \sim$ 140 eV. The sample was set several temperatures of 15 – 300 K controlled by continuous flow of liquid helium and a heater. Samples was scraped *in situ* by a diamond file under ultra-high vacuum. The infrared reflectivity spectra were recorded at the beam line 6A1of UVSOR.

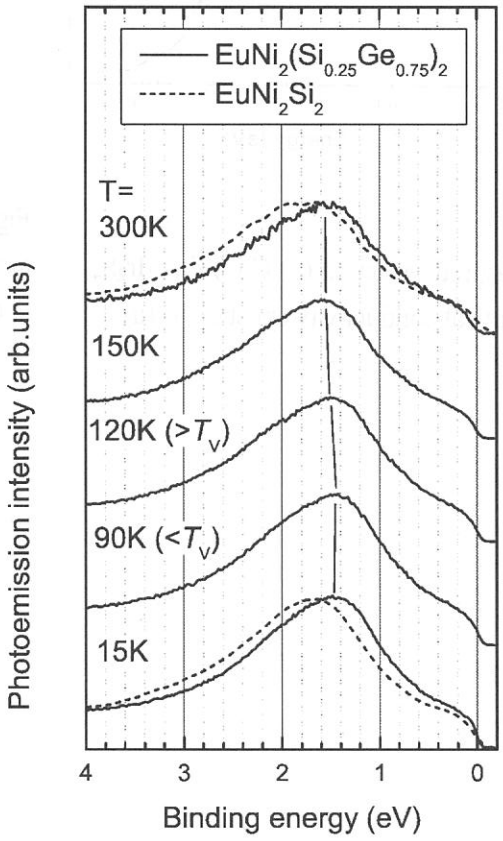

Fig. 1. Temperature dependence of off-resonant photoemission spectrum of $EuNi_2(Si_{0.25}Ge_{0.75})_2$ (solid lines) at $h\nu$ = 135.9 eV. The spectra of $EuNi_2Si_2$ at 15 and 300 K are also plotted for the reference (dotted lines).

The change of the other electronic structure due to the valence transition is examined by using the off-RPE spectra. Figure 1 is the temperature dependence of the off-RPE spectrum of $EuNi_2(Si_{0.25}Ge_{0.75})_2$ at $h\nu$ = 135.9 eV. The spectra of $EuNi_2Si_2$ at 15 and 300 K are also plotted. The spectra mainly correspond to the Ni 3*d* partial density of states. In $EuNi_2Si_2$, the peak is located at higher binding energy (E_B) side than that of $EuNi_2(Si_{0.25}Ge_{0.75})_2$. The peak of $EuNi_2Si_2$ expands with increasing temperature but the peak energy does not shift. On the other hand, the peak of $EuNi_2(Si_{0.25}Ge_{0.75})_2$ that is located at 1.5 eV below T_V slightly shifts to the high E_B by 0.1 eV above T_V. This indicates that the valence of Ni slightly decreases above T_V. At the Eu site, Eu^{2+} is dominant above T_V. Therefore both mean valences of Eu and Ni decrease above T_V. The reason is that the mixing between Eu^{3+} 4*f*-hole and Ni 3*d* becomes weak above T_V because the Eu^{3+} state decreases.

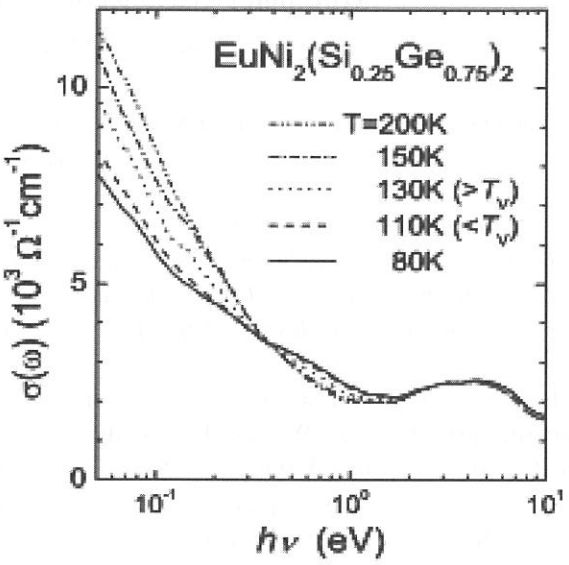

Fig. 2. Temperature dependence of optical conductivity spectrum ($\sigma(\omega)$) of $EuNi_2(Si_{0.25}Ge_{0.75})_2$.

The character of carriers is considered. Since the 4f state has no density at the E_F of E_B = 0 and the Ni 3*d* state has the density at the E_F, the conduction band originate from the Ni 3*d* state. The density of the Ni 3*d* state on the E_F decreases as the temperature increases despite that of $EuNi_2Si_2$ does not change with the temperature. The change appears in the $\sigma(\omega)$ spectrum in Figure 2. The $\sigma(\omega)$ spectrum below 2 eV that has a gentle slope to the low energy side below T_V gradually changes to the steep slope above T_V. The change is different from that of a normal metal, *i.e.*, the slope becomes gentle as the temperature increases because the relaxation time becomes long in a normal metal. The short (long) relaxation time means that the mixing intensity between the Ni 3*d* conduction band and the Eu^{3+} 4*f*-hole states is strong (weak). Therefore the mixing intensity below T_V is larger than that above T_V. This is consistent with the valence transition from trivalent to divalent with increasing temperature.

The photon energy at which the $\sigma(\omega)$ spectrum becomes minimum corresponds to the plasma frequency of carriers. The square of the photon energy is proportional to the carrier density. Since the photon energy of the minimum $\sigma(\omega)$ shifts to the low energy side with increasing temperature, the carrier density below T_V is higher than that above T_V. This result is consistent with the temperature dependence of the Ni 3*d* states on the E_F observed in Fig. 1. Therefore the carrier mainly originates from the Ni 3*d* states.

Reference

[1] H. Wada *et al.*, J. Phys., Condens. Matter **9** (1997) 7913.

[2] T. Kinoshita *et al.*, J. Phys. Soc. Jpn. **71** (2002) 148.

[3] S. Kimura *et al.*, J. Phys. Soc. Jpn.**71** (2002) in press.

(BL6A1)

Millimeter Wave Reflection Measurements of $LiNiO_2$ Using UVSOR and Coherent SR

Hitoshi Ohta, Kanji Kawakami[A], Yuta Nagasaka[A], Takao Nanba[A], Atushi Hirano[B], Ryoji Kanno[B], T. Takahashi[C] and T. Matsuyama[C]

Molecular Photoscience Research Center, Kobe University, 1-1 Rokkodai, Nada, Kobe 657-8501
[A]The Graduate School of Science and Technology, Kobe University, 1-1 Rokkodai, Nada, Kobe 657-8501
[B]Department of Chemistry, Faculty of Science, Kobe University, 1-1 Rokkodai, Nada, Kobe 657-8501
[C]Research Reactor Institute Kyoto University, 1010 Noda, Kumatori, Sennan, Osaka 590-0494

$LiNiO_2$ is known as a super ionic conductor and also a promising material for the positive electrode of the Li ion secondary batteries. We have been studying the millimeter wave reflection measurements of $LiNiO_2$ and related substances using UVSOR [1-6]. We found the drastic increase of the reflection of $LiNiO_2$ above 300 K in the millimeter wave region [1, 6], and we suggested that this increase of reflection is related to the motion of Li ion in the system. However, it is difficult to extend our measurement below 5 cm^{-1} in UVSOR. As the coherent SR of Kyoto University in Kumatori has a potensial to extend our study, we started a measurement using coherent SR and compared it with the result using UVSOR.

The reflection measurements of $LiNiO_2$ sintered sample with a diameter of 10 mm have been performed in the spectra region from 5 to 60 cm^{-1} and 5 to 18 cm^{-1} using the beam line BL6A1 of UVSOR and the coherent SR produced by the LINAC of Kyoto University in Kumatori, respectively. The measurement using coherent SR was limited down to 5 cm^{-1} due to the sample diameter. The temperature was changed from 300 to 380 K. The gold plate was used as a reference and InSb detector was used as a detector. Figure 1 shows our results for $LiNiO_2$ sample. The results of UVSOR and coherent SR observed at 300, 340 and 380 K are consistent within the limit of the S/N ratio. From these results we can extend our study below 5 cm^{-1} using the larger diameter sample and discuss about the origin of the reflection in high temperature.

[1] H. Ohta *et al.*: UVSOR Activity Report 1996 (1997) 182.
[2] H. Ohta *et al.*: UVSOR Activity Report 1997 (1998) 128.
[3] H. Ohta *et al.*: UVSOR Activity Report 1998 (1999) 158.
[4] H. Ohta *et al.*: UVSOR Activity Report 1999 (2000) 93.
[5]H. Ohta *et al.*: UVSOR Activity Report 2000, (2001) 121.
[6] H. Ohta *et al.*: Jpn. J. Applied Phys. **39** (2000) Suppl. 39-1, 409-410.

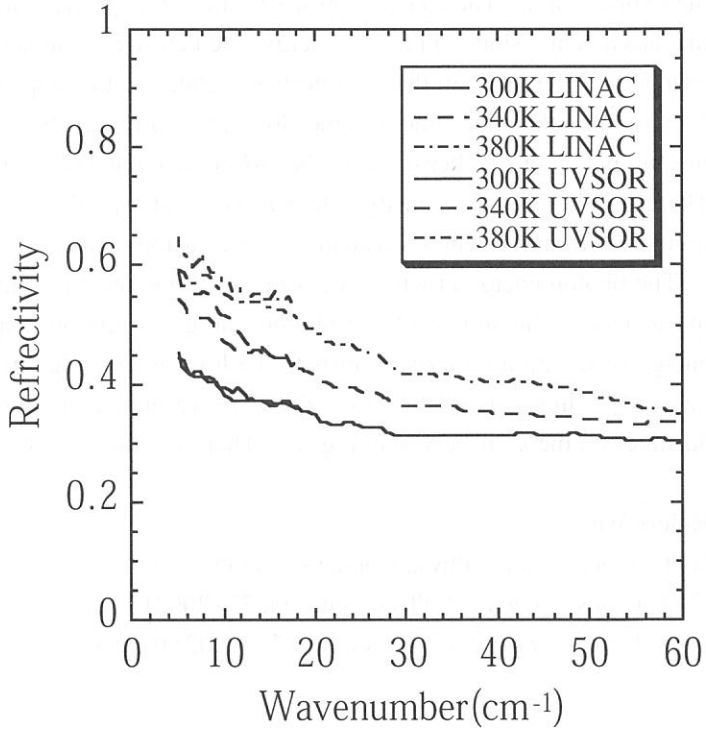

Fig. 1 Reflection spectra of $LiNiO_2$.

(BL7B)

Excitonic properties of lead-halogen-based self-organized low-dimensional crystals

Kenichiro Tanaka[a, b], Takayuki Takahashi[a, b], Takashi Kondo[a, b]

[a]*Department of Materials Science, The University of Tokyo, 7-3-1 Hongo, Bunkyo-ku, Tokyo 113-8656, Japan*

[b]*Core Research for Evolutional Science and Technology, Japan Science and Technology Corporation (CREST)*

The large family of the lead-halogen-based perovskite-type crystals have been attracted much attention because of their unique crystal structures and the optical properties. They are self-organized low-dimensional crystals, where $[PbI_6]$ octahedra form zero-, one-, two- or three-dimensional networks. In these crystals, excitonic absorption peaks are clearly observable, mainly because they are tightly confined in the $[PbI_6]$ networks. In the past study, it has shown that the excitonic effects are strengthened according as the dimensionality of the $[PbI_6]$ octahedra networks are lowered. Further investigation of the excitonic properties of these materials needs the clarification of the electronic structure of these materials. Thus we measured the reflectivity spectra in this study on $(C_6H_{13}NH_3)_2PbI_4$ (two-dimensional crystal), $(CH_3NH_3)PbBr_3$ (three-dimensional crystal), and $[NH_2SC(=NH_2)NH_2]_3PbI_5$ (one-dimensional crystal) at 18 K. The light was focused onto the sample with nearly normal incidents and the reflected light was detected by Si photodiode. Figure shows the absorption spectra of $(C_6H_{13}NH_3)_2PbI_4$, $(CH_3NH_3)PbBr_3$ and $[NH_2SC(=NH_2)NH_2]_3PbI_5$ evaluated from the Kramers-Kronig transformation of the reflectivity spectra obtained in this study. In each crystal, the clear exciton absorption lines were clearly observed. The oscillator strength of the lowest-energy exciton $(C_6H_{13}NH_3)_2PbI_4$, $[NH_2SC(=NH_2)NH_2]_3PbI_5$ and $(CH_3NH_3)PbBr_3$ are evaluated to be 0.8, 0.5 and 0.03 per $[PbI_6]$ octahedron unit, respectively. The excitons confined in lower structures such as $(C_6H_{13}NH_3)_2PbI_4$ and $[NH_2SC(=NH_2)NH_2]_3PbI_5$ have much higher oscillator strength than the three dimensional crystal $(CH_3NH_3)PbBr_3$. The origins of the absorption band appeared above the lowest-energy excitons are under investigation by several measurements such as two-photon absorption and electroabsorption spectroscopy.

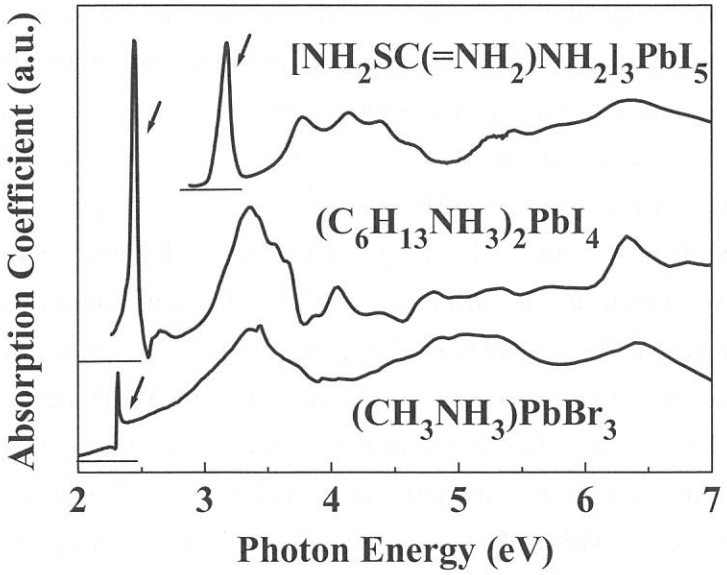

Fig. The absorption spectra of $[NH_2SC(NH_2)NH_2]_3PbI_5$, $(C_6H_{13}NH_3)_2PbI_4$ and $(CH_3NH_3)PbBr_3$ at 18 K. The arrows show the lowest-energy exciton.

(BL6A1)

Infrared magnetic circular dichroism in the colossal magneto- resistance pyrochlore $Tl_2Mn_2O_7$

H. Okamura, T. Koretsune, M. Matsunami, S. Kimura, T. Nanba,
H. Imai[A], Y. Shimakawa[A], Y. Kubo[A]

Department of Physics and Graduate School of Science and Technology, Kobe University, Kobe 657-8501.
[A]Fundamental Research Laboratories, NEC Corporation, Tsukuba 305-8501, JAPAN

Physics of the colossal magneto-resistance (CMR) phenomena has been one of the central issues of condensed matter physics in the last several years. In particular, the ferromagnetic perovskite manganites, e.g., $La_{1-x}Sr_xMnO_3$, have attracted much attention [1]. More recently, the $Tl_2Mn_2O_7$ pyrochlore has been attaining increasing interest, since it exhibits a CMR that is comparable to those observed for the perovskites [2]. $Tl_2Mn_2O_7$ is also a ferromagnet, and its resistivity (ρ) drops rapidly upon cooling through $T_c \sim 120$ K. Near and above T_c, an external magnetic field of 7 T reduces ρ by a factor of ~ 10. Although these features appear very similar to those for the perovskites, various studies have suggested that the underlying mechanism should be very different from that in the perovskites [2]. In order to study the electronic structures of $Tl_2Mn_2O_7$, we have measured its optical reflectivity spectra under magnetic fields at BL6A1 [3], and observed an infrared (IR) magnetic circular dichroism (MCD). Figure shows the reflectivity spectra (top graphs) and the MCD spectra (bottom graphs) of $Tl_2Mn_2O_7$ at 40 K under magnetic fields of 4 T and 6 T measured under the Faraday configuration. Here, the MCD spectra are shown as the difference of the reflectivity spectra when the field direction is changed from parallel to antiparallel to the light propagation direction, normalized by the average spectra of the two configurations. A clear MCD signal is observed exactly at the plasma edge of the reflectivity, and it grows with increasing magnetic field. Using this MCD signal, the Kerr rotation can be calculated. The rotation angle is of the order of a few degrees. This MCD signal decreases with increasing temperature, and it becomes very weak above ~140 K. In addition, the MCD grows with magnetic field even at 40 K, where the magnetization is almost saturated below 0.5 T. Our analyses have shown that a simple magneto-plasma model is able to account for the basic features of this MCD signal. In this model, an MCD arises from the coupled Drude-cyclotron motion of a plasma, and a ferromagnetic spin order is not required to produce an MCD. For an MCD in a

ferromagnetic material, the magnitude of the observed MCD signal is known to be proportional to the spontaneous magnetization, and also the MCD is a result of a spin-orbit coupling that connects the spin state of the electrons with the circular polarization of light. The observations that the observed MCD is not proportional to the magnetization and that the MCD is basically reproduced by a classical magneto-plasma suggest that the spin-orbit coupling is rather weak in this compound. Further analyses are in progress for a better understanding of this compound.

References

[1] See, for example, Y. Tokura et al. J. Phys. Soc. Jpn. **63**, 3931 (1994).

[2] Y. Shimakawa et al., Nature **379**, 53 (1996); Phys. Rev. B **55**, 6399 (1997).

[3] H. Okamura et al., Phys. Rev. B 64, 180409(R) (2001).

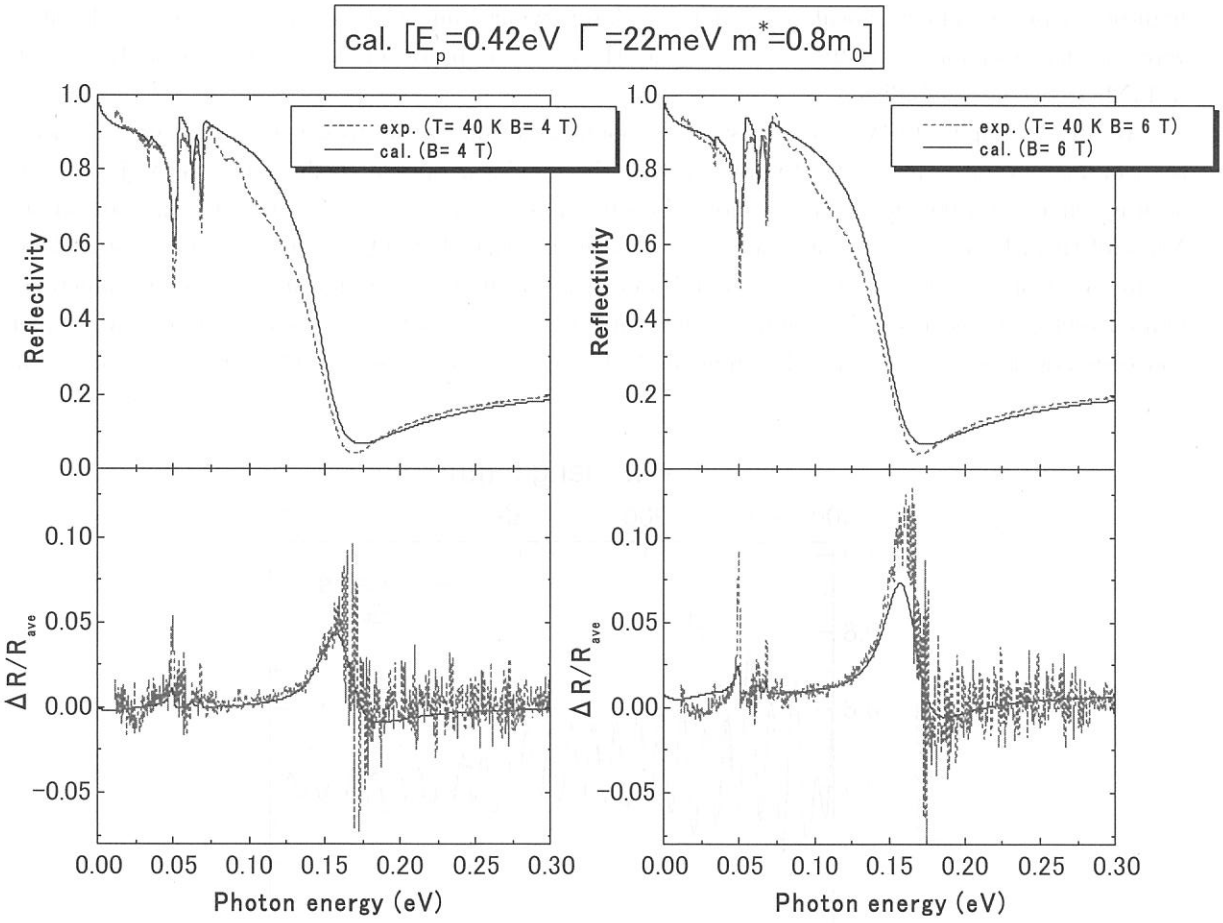

FIGURE: Top graphs: optical reflectivity spectra of $Tl_2Mn_2O_7$ at 40 K, under magnetic fields of 4 T and 6 T. Bottom graphs: the MCD spectra, given as the difference of reflectivity spectra when the magnetic field direction is flipped.

(BL6A1)

Transmittance spectra of GaAs and GaP in far-infrared region

Ichiro Shoji and Takunori Taira

Laser Research Center for Molecular Science, Institute for Molecular Science,
38 Nishigonaka, Myodaiji, Okazaki 444-8585, Japan

Demands for wide-tunable infrared (IR) coherent light sources are growing because they can be used for a variety of applications, including spectroscopy, chemical monitoring, biomedical applications, and atmospheric and environmental sensing. Frequency down conversion of 1 μm pump sources such as Nd:YAG lasers which uses optical parametric oscillation or difference-frequency generation is a promising approach to obtain coherent light in the IR region. It is necessary to satisfy the phase-matching condition between the pump, signal, and idler light in order to realize high conversion efficiency. The conventional phase-matching method using birefringence in nonlinear-optical crystals limits the wavelength range and materials applicable, while quasi-phase matching (QPM) technique which periodically modulates the magnitude of the nonlinear-optical coefficient has many advantages and has been intensively studied. Especially, recent developments in fabrication of periodically poled $LiNbO_3$ (PPLN) [1] have realized high-power pulse and cw optical parametric oscillators which emit up to 4 μm. However, highly efficient wavelength conversion using PPLN is difficult for the wavelengths longer than 6 μm because IR absorption in $LiNbO_3$ becomes significant.

We are developing QPM devices using compound semiconductors to generate IR light. Compound semiconductors have large optical nonlinearities; the nonlinear optical coefficient of GaAs is 170 pm/V at wavelength of 1.06 μm, which is more than 6 times larger than that of $LiNbO_3$ [2]. In addition, Many of them have longer absorption cutoff wavelengths than $LiNbO_3$; GaAs is transparent as long as 16 μm [3]. Moreover, the crystal-growth and processing technologies are matured for semiconductors [4]. Our current target is developing highly efficient mid-IR sources, but it would be attractive if the frequency conversion devices generating far-IR can be made by use of compound semiconductors. We have measured

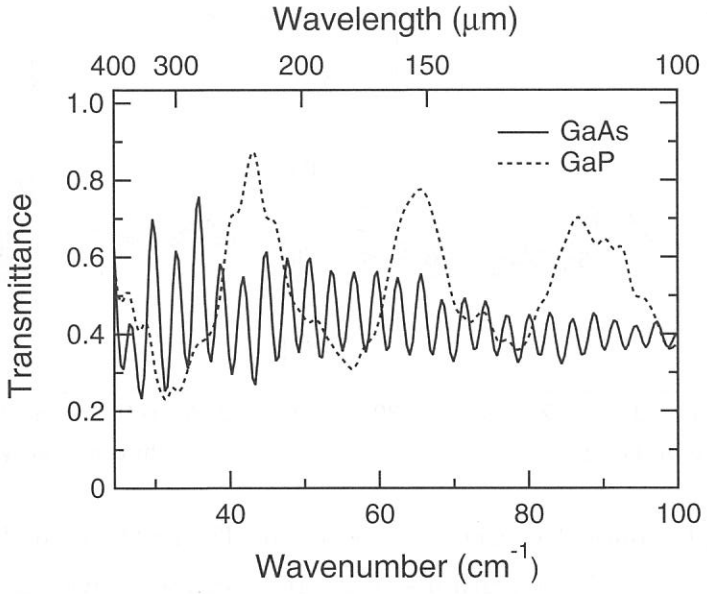

Fig 1. Transmittance spectra of the undoped GaAs and GaP in far-IR region.

transmittance spectra of GaAs and GaP, which are popular compound semiconductors, in far-IR region to investigate the possibility for far-IR generating materials.

Absorption spectra of semiconductors strongly depend on the dopant concentration. Semi-insulating or high-resistivity samples are suitable for frequency-conversion devices because the optical absorption is much lower. We have prepared an undoped GaAs and GaP samples grown by Hitachi Cable and Sumitomo electric, respectively. The resistivities were both $\geq 10^7\ \Omega\,\mathrm{cm}$, the thicknesses were 470 and 75 μm, respectively, and their both facets were optically polished. The absorption spectra were measured with the Martin-Puplett Fourier interferometer (Specac) at the beam line BL6A1. Using the Si bolometer, we made measurements in the wavelength range of 100–400 μm (25–100 cm^{-1}). The step and the total displacement of the moving mirror were 25 μm and 6.4 mm, respectively.

Figure 1 shows the obtained transmittance spectra. We found that both GaAs and GaP are transparent in the measured region, although transmittances are lower than in the near-IR region because the refractive indices in far-IR are much higher. The modulations in the obtained spectra are due to the interference effects caused by the multiple reflections of the beam since the samples were plane-parallel plates.

We have found that GaAs and GaP are attractive materials for the frequency conversion devices generating far-IR light.

References

[1] L. E. Myers, R. C. Eckardt, M. M. Fejer, R. L. Byer, W. R. Bosenberg, and J. W. Pierce, J. Opt. Soc. Am. B **12,** 2102 (1995).

[2] I. Shoji, T. Kondo, A. Kitamoto, M. Shirane, and R. Ito, J. Opt. Soc. Am. B **14,** 2268 – 2294 (1997).

[3] I. Shoji, S. Kurimura, and T. Taira, "Infrared absorption spectrum of GaAs," UVSOR ACTIVITY REPORT 2000.

[4] S. Koh, T. Kondo, M. Ebihara, T. Ishiwada, H. Sawada, H. Ichinose, I. Shoji, and R. Ito, "GaAs/Ge/GaAs sublattice reversal epitaxy on GaAs (100) and (111) substrate for nonlinear optical devices," Jpn. J. Appl. Phys. **38,** L508 – L511 (1999).

(BL7A)

In situ measurement of luminescence from silica glass under soft X-ray irradiation

Tomoko Yoshida[A], Tetsuo Tanabe[A], Hisao Yoshida[B]

[A]*Center for Integrated Research in Science and Engineering, Nagoya University, Nagoya 464-8603, Japan*

[B]*Department of Nuclear Engineering, Graduate School of Engineering, Nagoya University, Nagoya 464-8603, Japan*

Introduction

Radiation effects on silica glasses are one of the main concerns for their application as optical windows, insulators and optical fibers under fusion and fission environments.[1] Although the radiation damage of silica in nuclear environments has been widely studied, the detailed damaging process and damage structure are still unknown. That is mainly because the effect of ionizing radiation, which is very important in optical materials like silica, is mixed up with the displacement effect. Recently, we have made in-situ luminescence measurements of silica glasses induced by in-reactor irradiation. This in-situ measurement was very useful for the observation of dynamic effects of ionizing radiation on the electrical property of a silica [2,3] and we have applied this technique to study effects of other ionizing radiations (such as gamma-ray, X-ray VUV and UV lights) on silica.

The present work is our first trial to observe soft X-ray radiation effects on silica. We have measured the luminescence from a silica glass under the irradiation of soft X-ray near Si K-edge, and investigated the origin of the luminescence.

Experimental

The samples used in this work was a fused silica glass (T-1030) of 13 mm diameter and 2 mm thickness produced by Toshiba Ceramics, Japan. The measurement of luminescence of a fused silica glass induced by soft X-ray irradiation (1.8-1.9 keV) was carried out on the beam line 7A at UVSOR, Institute for Molecular Science with a stored current of 100-200 mA. The luminescence was focused by a lens in the UHV chamber to the monochromator (CP-200, JOBIN YVON) and detected by a multi-channel analyser (OMA III, EG&G PRINCETON APPLIED RESEARCH). The wavelength range (λ) from 300 to 800 nm was measured because the photon detecting efficiency in the regions of $\lambda <$ 300 nm and $\lambda >$ 800 nm were reduced drastically. The luminescence yield spectrum was also measured by a photomultiplier (Hamamatsu Photonics R955).

Results and Discussion

Fig. 1 shows the observed luminescence spectra of the fused silica glass under the irradiation of soft X-rays near Si K-edge (1848 eV). An intense emission band at around 400 nm was observed. Similar luminescence spectra have been measured for silica glasses under in-reactor or UV irradiation [2,3], and we have concluded that the present XEOL, 400 nm band emission, originates from an intrinsic $B_{2\beta}$ center [4] due to the electron excitation by soft X-ray.

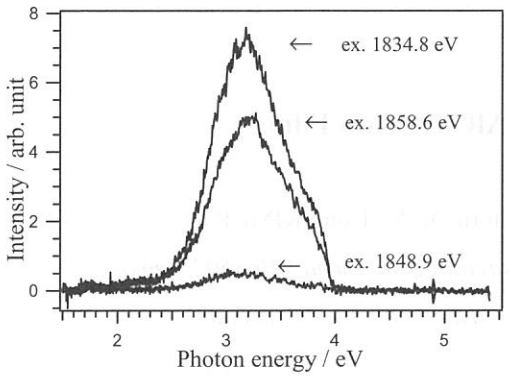

Fig.1 Optical luminescence spectra of a fused silica glass excited by soft X-ray with the energy of 1834.8 eV, 1848.9 eV and 1858.6 eV.

It is noteworthy that the intensity of the 400 nm emission band changed with the excitation energy of soft X-ray (Fig.1). Therefore, we also measured a photoluminescence yield (PLY) spectrum of the 400 nm band and showed in Fig. 2(a) together with X-ray absorption (Si K-edge XANES) spectrum (Fig. 2(b)) recorded in the photocurrent mode for the same fused silica glass. It is rather surprising to see nice correspondence between the PLY and XANES spectra. Three processes are controlling the photoluminescence yield. One is penetration depth or energy deposition per unit volume of the incident soft X-ray. But one should note that only very small fraction of the deposited energy is used for activation or electron excitation of the $B_{2\beta}$ center. Nevertheless, two following processes can be distinguished. One is electron excitation density and the other is relaxation probability of the excited electrons through the $B_{2\beta}$ emission. However, in the present stage, none of above three processes are evaluated quantitatively and further studies are necessary.

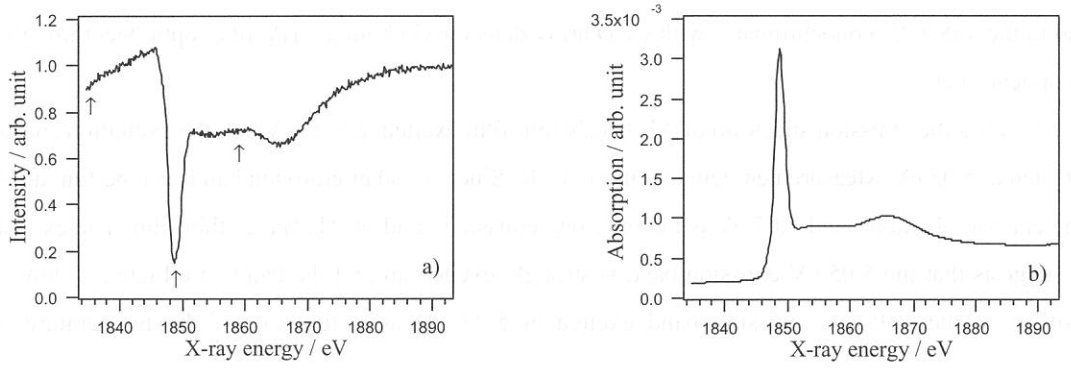

Fig. 2 The comparison between a) the luminescence yield spectrum of the 400 nm band and b) Si K-edge XANES spectrum of a fused silica glass.

Acknowledgements

The authors are grateful to Prof. Eiji Sigemasa, Prof. Masao Kamata and Mr. Eiken Nakamura of UVSOR for their great help and cooperation in the luminescence measurements.

References

[1] F.W. Clinard Jr., L.W. Hobbs, in: Physics of Radiation Effects in Crystal, Elsevier, Amsterdam, 1986, p. 442.

[2] T. Yoshida, T. Tanabe, T. Ii, T. Hara, M. Sakai and Y. Inaki, *Nucl. Instr. and Meth. B*, 166-167 (2000) 476.

[3] T. Ii, T. Yoshida, T. Tanabe, T. Hara, M. Okada and K. Yamaguchi, *J. Nucl. Mater.* 283-287 (2000) 898.

[4] R. Tohmon, H. Mizuno, Y. Ohki, K. Sasagane, K. Nagasawa, Y. Hama, *Phys. Rev. B* 55 (1989) 1337.

(BL7B)

Luminescence Spectra of AlGaN Thin Films

Kazutoshi FUKUI, Kazuya EBISU[1], Satoru ODA[1], Kouji KIMURA[1]

Research Center for Development of Far-Infrared Region, Fukui 910-8507, Japan

[1] Faculty of Engineering, Fukui University, Fukui 910-8507, Japan

The group III-nitride semiconductors (AlN, GaN and InN) are promising materials for applicateions in opt-electronic devices. The ternary alloy $Al_{1-x}Ga_xN$ is complete solid solution and varies its band gap from 3.4 eV (blue) to 6.2 eV (ultraviolet). We have been performed the reflectance measurements at the visible – vacuum ultraviolet region [1]. In this report, we represent the emission and excitation spectra, and decay profiles.

AlGaN samples were made by MOCVD method at RIKEN on SiC substrates. The luminescence experiments were carried out as follows; a) excitation : BL7B (3.4 – 25 eV) b) luminescence : VIS – UV monoochromator (1.5 – 6.2 eV) with a CCD array c) vacuum : in the range of 10^{-9} Torr d) temperature : 17 K – 60 K e) time resolved measurement : TAC method with MCP-PMT under the single bunch operation. A single UV optical fiber cable, which was dedicated for ultra high vacuum (UHV) and had 0.6 mm core diameter, were used for detecting VIS and UV luminescence in the UHV chamber. VIS and UV luminescence lights were introduced to the VIS-UV monochromator with CCD array detector via both a UHV fiber optic feedthrough and a flexible optical fiber.

Figure 1 shows the emission spectrum of $Al_{70}Ga_{30}N$ thin film excited at 5.25 eV and the excitation spectrum that is detected at 5.05 eV. Measurement temperature is 17 K. Since no other emission bands can be found below 4.7 eV, the emission band around 5.05 eV is the only one emission band of $Al_{70}Ga_{30}N$ thin film. The excitation spectrum suggests that the 5.05 eV emission band is strongly excited around the band gap. Figure 2 shows the decay profiles of the 5.05 eV emission band excited at 5.25 eV as a function of the temperature. The

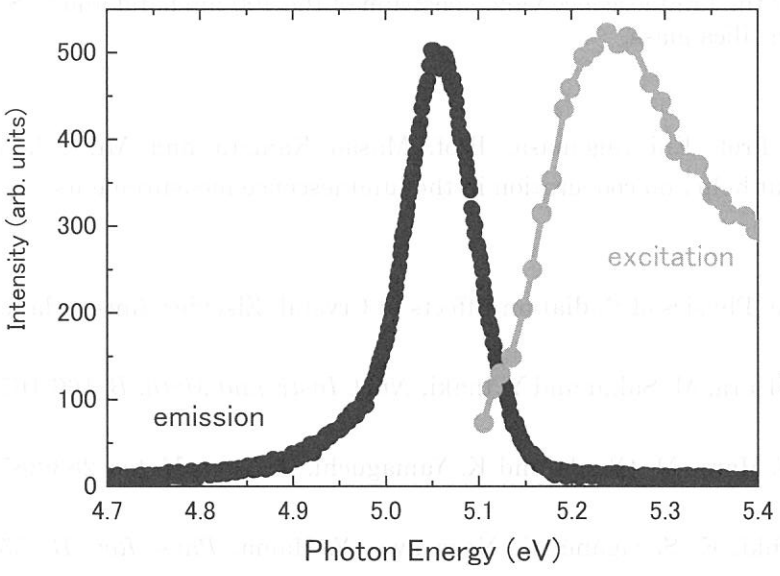

Fig.1
Excitation spectrum and emission spectrum of $Al_{0.7}Ga_{0.3}N$ at 17 K. The detected energy of the excitation spectrum and the excitation energy of the emission spectrum are 5.05 eV and 5.25 eV, respectively.

experimental results are plotted by the closed circles. Each decay profile consists of (i) sharp peak at around 0 time which is similar to the time structure of the excitation SR light (ii) non-linear decay curve in semi logarithmic graph (iii) no intensity without the noise level can observed just before 0 time. It is also clear that the overall decay time is decreasing with increasing temperature. These results suggest that there are more than three thermal activation type decay processes, one of them has the very fast decay time ($< 10^{-1}$ nsec), and the decay times of all processes are less than SR bunch period (177 nsec). The solid curves in fig. 2 are the fitting results of the combination of the two single exponential curves. Then it is concluded that there are at least three decay processes. The decay times at 17 K of $Al_{70}Ga_{30}N$ sample are $< 10^{-1}$, 0.95 and 12 nsec, for example.

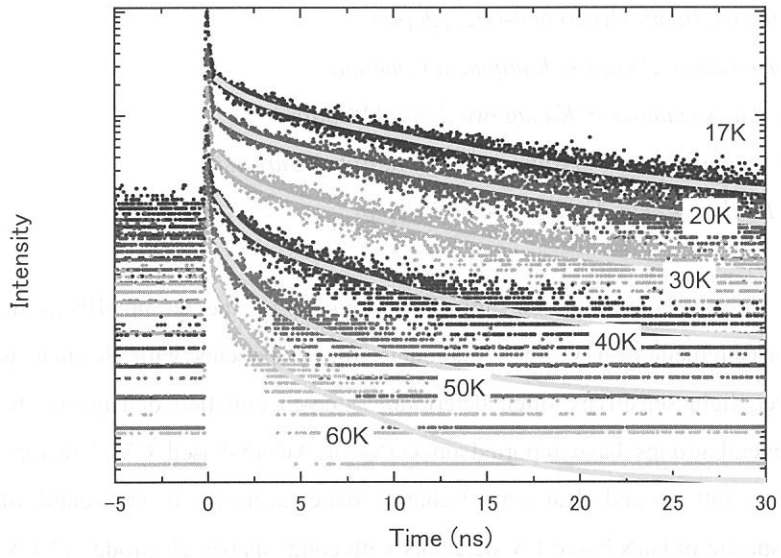

Fig.2
Decay profile of the 5.05 eV emission band excited at 5.25 eV. The measurement temperature range is from 17 K to 60 K

References

[1] K. Fukui, H. Miura, A. Okada, Q. Guo, S. Tanaka, H. Hirayama and Y. Aoyagi, Proceedings of International Workshop on Nitride Semiconductors, IPAP Conference Series 1, (2000.11) 647-650.

(BL7B)

Responsivity spectra of GaN based UV detectors in VUV region using transparent electrode

Atsushi Motogaito[1], Keiichi Ohta[1], Kazumasa Hiramatsu[1], Youichiro Ohuchi[2], Kazuyuki Tadatomo[2], Yutaka Hamamura[3] and Kazutoshi Fukui[4]

[1]*Deptartment of Electrical and Electronic Engineering, Mie University, 1515 Kamihama, Tsu, Mie 514-8507, Japan*

[2]*Telecommunication & Photonics Research Laboratory, Mitsubishi Cable Industries, Ltd., 4-3 Ikejiri, Itami, Hyogo 664-0027, Japan*

[3]*Nikon Corporation, Precision Equipment Company, 1-10-1 Asamizodai, Sagamihara, Kanagawa 228-0828, Japan*

[4]*Research Center for Development of Far-Infrared Region, Fukui University, 3-9-1 Bunkyo, Fukui, Fukui 910-8507, Japan*

Ultraviolet (UV) detectors are one of the most attractive devices in the group III-nitride semiconductors. Currently, for the measurement of UV light, photodetector components with Si such as photodiodes are mainly used. However, light sensitivity often deteriorates due to radiation damage in the vacuum ultraviolet (VUV) region. Several groups have reported on GaN- or AlGaN-based UV detectors. They have good responsivity from 250 to 360 nm and clear cut-off characteristics at a cut-off wavelength of λ_c=360 nm. We reported responsivity spectra of GaN based UV detectors with comb-shaped electrode in VUV region for the first time [1, 2]. The small responsivity in VUV region is caused by the photoemission of Au and GaN.

In this report, the responsivity spectra of UV detectors with transparent Au electrode structure to suppress the photoemission of GaN and Au are described.

The UV detectors used in this study adopt the Schottky contacts with a transparent electrode. They consist of a 3-μm-thick n-GaN layer ($n=2.0\times10^{18}$ cm^{-3}) and a 1.5-μm-thick i-GaN layer ($n=1.0\times10^{16}$ cm^{-3}) on a (0001) sapphire substrate. These layers are grown by metalorganic vapor phase epitaxy (MOVPE). The Au/Ni Schottky contact is deposited on i-GaN. The thickness of Au and Ni are 10 nm and 1 nm, respectively. The diameter of detectors is 6.5 mm.

Prior to the characterization of responsivity, the transmittance of Au in VUV region is estimated by counting the number of transmitted photons into Au membrane. Figure 1 shows transmission spectra of 10-nm-thick Au electrode. The transmittance of 10-nm-thick Au is about 0.4-0.5 in UV and VUV region and almost agreed with calculation. Thus the 10-nm-thick Au is enough thickness to transmit VUV light into Au electrode.

The responsivity spectra of detectors for photon energy are measured. Figure 2 shows the

responsivity spectra. In this measurement, the ampere meter does not measure the photoemission current of Au. Dark current is about 1-2 pA. It is corresponding to about the order of 10^{-5} A/W in Fig.2. No responsivity at the energy lower than 3.4 eV (the absorption edge of GaN) can be observed clearly. This indicates that these detectors can be used only in the UV or VUV region. The ratio of responsivity between UV and visible regions is about 5×10^{3}. The maximum responsivity of this detector is 0.15 A/W at $h\nu$=3.5 eV (λ=354 nm). The responsivity for VUV light is about 0.01 A/W. Furthermore, the photoemission current of GaN (I_{GaN}) is not detected by other measurement. It is considered that the total current measured by ampere meter is equal to diode current. Therefore, the both photoemission current of GaN and Au are not observed in this measurement and the higher responsivity is realized in this structure.

References

[1] A. Motogaito, M. Yamaguchi, K. Hiramatsu, M. Kotoh, Y. Ohuchi, K. Tadatomo, Y. Hamamura and K. Fukui: Jpn. J. Appl. Phys. **40**, L368 (2001).

[2] A. Motogaito, M. Yamaguchi, K. Hiramatsu, M. Kotoh, Y. Ohuchi, K. Tadatomo, Y. Hamamura and K. Fukui: UVSOR Activity Report 2000, 136 (2001).

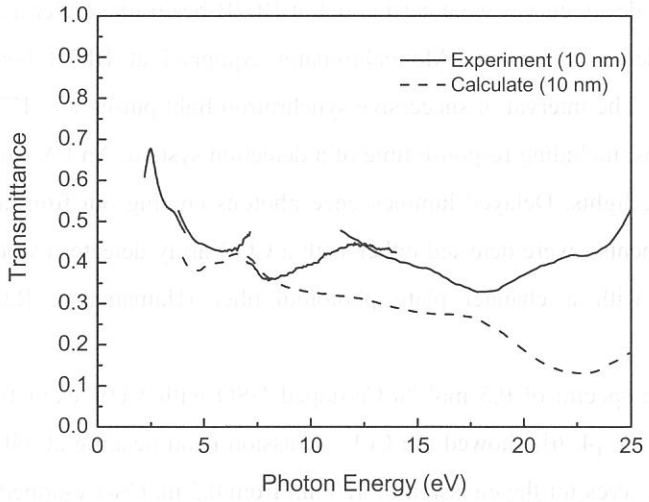

Fig.1 Transmittance spectra of 10-nm-thick Au

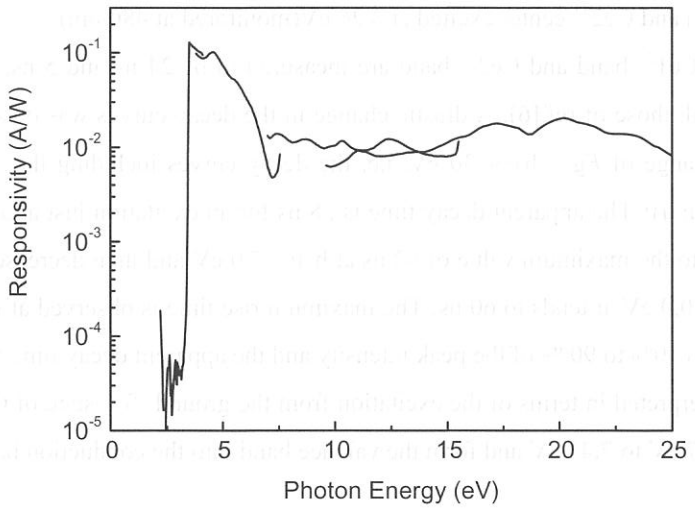

Fig.2 Responsivity spectra of UV detector with transparent Au

(BL7B)

Luminescence Decay of Ce-doped GSO under Excitation of VUV with Energy less than 30 eV at Room Temperature

S.Shimizu [a], A.Ejiri [b] and S. Kubota [a]

[a] *Rikkyo University, Nishi-Ikebukuro 3, Tokyo, 171 Japan*

[b] *Meiji University, Higashi-Sanda, Tama, Kawasaki, 214 Japan*

It is well known that the efficient scintillation photons are produced mainly through recombination of electron-hole pairs created by ionization processes with charged particles [1,2]. However, the details of the electron-hole recombination process in Ce-doped GSO (Gd_2SiO_5) have not been investigated yet, except refs.[3,4]. The purpose of this experiment is to study the energy transfer of electrons and holes to Ce^{3+} activator centers and to study the scintillation mechanism of Ce-doped GSO.

The measurements of decay curves were carried out at BL7B beam line under a single bunch operation of UVSOR. A normal incidence Mcpharson Monochromator equipped at BL7B beam line was used VUV excitation of the specimen. The interval of successive synchrotron light pulses was 177.6 ns and the duration of the pulses was about 550 ps, including response time of a detection system. An UV optical fiber cable was used for detecting luminescence lights. Delayed luminescence photons coming out from a monochromator (Model SP-300i, Princeton Instruments), were detected either with a CCD array detector (Model 1340PB) for emission spectra measurement or with a channel plate photomultiplier (Hamamatsu, R3809U) for decay curve measurement.

The observed emission spectra of 0.5 mol % Ce-doped GSO with VUV excitation at $h\nu$ higher than the band-gap energy Eg (~6.2 eV [4, 6]) showed the $Ce1^{3+}$ emission band peaking at 440 nm as reported in [5,6]. Figure 1 shows the decay curves for the emission of 420 nm from 0.5 mol % Ce-doped GSO under excitation of VUV photons between $Eg < h\nu < 30$ eV, together with the decay curves of the $Ce1^{3+}$ center excited at 3.64 eV(monitored at 420 nm) and $Ce2^{3+}$ center excited at 3.26 eV(monitored at 480 nm).

The decay times of $Ce1^{3+}$ band and $Ce2^{3+}$ band are measured to be 24 ns and 5 ns, respectively, and these results are consistent with those of ref.[6]. A drastic change in the decay curves was observed for the excitation photon energies in the range of $Eg < h\nu < 30$ eV; i.e. the decay curves including the initial build-up and the decay strongly depend on $h\nu$. The apparent decay time is 58 ns for an excitation just above the band gap energy of 6.2 eV and increases to the maximum value of 92 ns at $h\nu = 7.0$ eV and then decreases to 60 ns at $h\nu = 10.0$ eV. For 10.0 eV$< h\nu <$ 30.0 eV, it tends to 60 ns. The maximum rise time is observed at $h\nu = 7.0$ eV. The initial build-up time t_b that from 10% to 90 % of the peak intensity and the apparent decay time t_a are shown in Fig.2.

Those results are interpreted in terms of the excitation from the ground $^8S_{7/2}$ state of Gd^{3+} ion into the higher excited multiplets of 6.27 eV to 7.41 eV and form the valence band into the conduction band [7].

Acknowledgements

The authors would like to express their gratitude to Dr. K.Fukui of UVSOR facility for his assistance to perform the experiment at UVSOR.

References

[1] A. Lempicki, A.J. Wojtowicz and E. Berman, Nucl. Instr. and Meth. A 333 (1993) 304.

[2] T. Doke, E. Shibamura and S. Kubota, J. Phys. Soc. Jap. 68 (1999) 2433.

[3] H. Ishibashi, Nucl. Intstr. and Meth. A294 (1990)271.

[4] Z.A. Racholo, I.A. Tale, V.D. Ryzhikov, J.L. Jansons and S.F. Burochas, Nucl. Trans Radiat. Meas. 21 (1993) 121.

[5] H. Suzuki, T.A. Tombrello, C.L. Melcher and J.S. Schweitzer, Nucl. Instr. and Meth. A 320 (1992)263.

[6] H. Suzuki, T.A. Tombrello, C.L. Melcher, C.A. Peterson and J.S. Schweitzer, Nucl. Instr. and Meth. A 346(1994)510.

[7] S.Shimizu, H.Ishibashi, A. Ejiri and S. Kubota, Nucl. Instr. and Meth. (2002), in press.

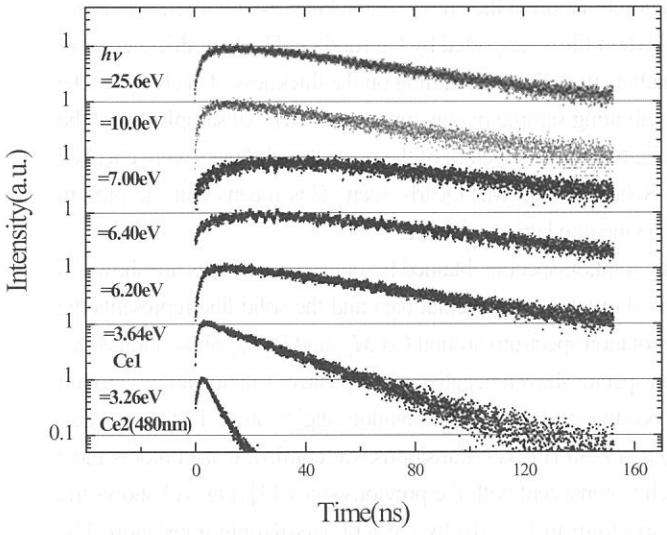

Fig.1. Decay curves of 0.5 mol % Ce-doped GSO under excitations by photons of various energies.

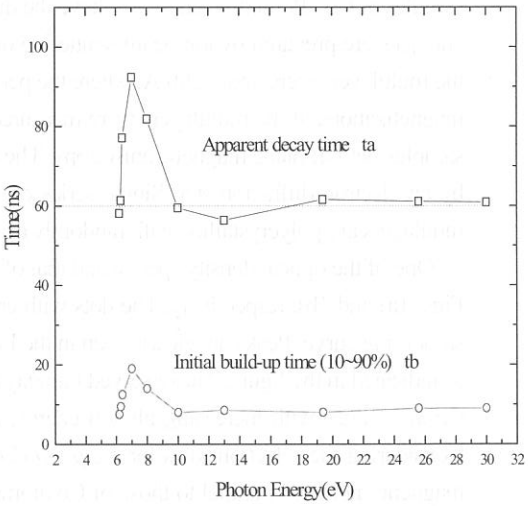

Fig.2. Apparent decay time and initial build-up times (10~90%) from 0.5 mol % Ce-doped GSO as a function of excitation photon energy. The curves are drawn only to guide the eyes. The dotted straight line is the expected decay time ~60 ns for sufficiently large photon energy.

(BL8B1)

Extreme Ultraviolet Faraday Rotation Spectra of Co / Pt Multilayers on Collodion Films

M. Igeta, K. Saito, T. Ejima, T. Hatano and M. Watanabe

Institute of Multidisciplinary Research for Advanced Materials, Tohoku University
Katahira 2-1-1, Aoba-ku, Sendai 980-8577, Japan

Many magnetic multilayers have been studied by the magnetic circular dichroism (MCD) measurements in the extreme ultraviolet, soft X-ray and hard X-ray regions. Among them, Co / Pt multilayers carefully grown to <111> direction have been investigated intensively to clarify the origin of their novel character of the perpendicular magnetic anisotropy (PMA) [1-3]. In the previous work by Nakajima *et al.* [3], it was proposed that the PMA is caused by the Co 3*d* - Pt 5*d* hybridization, which is highly localized at the Co / Pt interface. So it is interesting to investigate the magnetic properties and hybridization effect of Co / Pt multilayers grown to other directions without special treatment.

The Faraday rotation measurements on Co / Pt multilayers on collodion films were performed in the 55-80 eV region. The degree of linear polarization of the incident beam was more than 96 % in the energy region of the present experiment. The full bandwidth of the monochromatized incident beam was about 0.1 eV. The Faraday rotation apparatus consists of a magnetic circuit, a sample holder and a rotating analyzer unit [4]. A field of 8.2 kOe was generated by the magnetic circuit composed of four Sm / Co permanent magnets. The samples are situated, as the multilayer plane was perpendicular to the magnetic field. The polarization states of incident and transmitted beams were monitored by a rotating analyzer unit mounting Al / YB_6 and Mo / Si reflection multilayer polarizers. Twelve samples of Co / Pt multilayers which have the different combination of the one-layer thicknesses of both materials (t_{Co} and t_{Pt}) were prepared by ion-beam-sputtering onto collodion films supported by Cu meshes. The total thicknesses of the multilayers were about 200 Å, where the period numbers were 5-24 depending on the thickness of each layer. The magnetizations of the multilayers were measured by a vibrating sample magnetometer (VSM). All samples were the samples with in-plane magnetic anisotropy. The crystallinity and the structure of the present multilayers were checked by an electron diffractometer. Single series of Debye-Scherrer rings was clearly seen. This means that the present mutilayers are polycrystalline with randomly oriented having one lattice constant.

One of the optical density spectra and that of Faraday rotation spectra obtained by our measurements are shown in Figs. 1a) and 1b), respectively. The dots with error bars show the experimental data and the solid line represents the smoothing curve. Peaks are clearly seen in the Faraday rotation spectrum around Co-$M_{2,3}$ and Pt-$N_{6,7}$ absorption edges as indicated in the figure. The observed Faraday rotation spectra show a negative and a positive rotation angles around Co-$M_{2,3}$ edges with increasing photon energy, and a positive and a negative rotation angles around Pt-$N_{6,7}$ edges. Considering the selection rules for the $p \rightarrow d$ (Co-$M_{2,3}$) and $f \rightarrow d$ (Pt-$N_{6,7}$) transitions, we confirm that Pt atoms have magnetic moments parallel to those of Co atoms, which is consistent with the previous study [3]. Fig. 1c) shows the MCD spectrum calculated from the Faraday rotation spectrum in Fig. 1b) by the Kramers-Krönig translation. The spectral shape at the Pt-$N_{6,7}$ edges is somewhat different from that of the previous result [3], but similar to that of $CoPt_3$ alloy which shows the unusual profile due to the Fano effect [5]. Therefore, in the present experiment, the magnetization state in Pt seems to be similar to that in $CoPt_3$ alloy. However, the ratio of the MCD magnitudes for Co-$M_{2,3}$ and Pt-$N_{6,7}$ edges is about 1/3 in $CoPt_3$ alloy, but about 1 in the present multilayer, of which t_{Co} / t_{Pt} is about 1/3, so that the present samples are not $CoPt_3$ alloy.

Here, we assume that the peak-to-peak values of Faraday rotation angles around Co-$M_{2,3}$ and Pt-$N_{6,7}$ edges are proportional to the total magnetic moments of Co and Pt layers, respectively. In Figs. 2a) and 2b), the peak-to-peak values of the rotation angles around Co-$M_{2,3}$ edges per unit thickness of Co layer (normalized by the total thickness of the Co layers) and those around Pt-$N_{6,7}$ edges per unit thickness of Pt layer (normalized by the total thickness of the Pt layers) are plotted against the Co and Pt one-layer thicknesses (t_{Co} and t_{Pt}), respectively. Except for the samples with 3 Å thick Co one-layer, the peak-to-peak values for Co-$M_{2,3}$ edges per unit thickness of Co layer are almost the same,

but decrease gradually with the increase in Co one-layer thickness. The similar behavior was found in the case for Pt-$N_{6,7}$ edges. This means that each magnetic moment of Co and Pt atoms is almost constant, so that the magnetization of Co and Pt is not localized at the interface, but volumetric in our case. The reason why the values decrease with the increase in Co one-layer thickness may be due to the fact that the out-of-plane magnetization of these samples are not saturated, which was checked by the VSM. For the samples with 3 Å thick Co one-layer, rapid decrease with the increase in Pt one-layer thickness may be due to the disordered-alloying effect at the interface, where Co atoms become minor and are dispersed among Pt atoms.

In summary, the magnetization of Pt is not localized at the Co / Pt interface, but volumetric in the present samples. The state of hybridization is similar to that of $CoPt_3$. This conclusion is different from the previous experiment [3], which may be due to the difference in the growth direction and suggests that the PMA manifests itself in the multilayers grown to <111> direction.

References

[1] D. Weller, Y. Hu, J. Shöhr, M. G. Samant, B. D. Hermsmeier, C. Chappert, Phys. Rev. B **49** (1994) 12888.

[2] J. Thiele, C. Boeglin, K. Hricovini, F. Cheyrier, Phys. Rev. B **53** (1996) 11934.

[3] N. Nakajima, T. Koide, T. Shidara, H. Miyauchi, H. Fukutani, A. Fujimori, K. Ito, T. Katayama, M. Nývlt, Y. Suzuki, Phys. Rev. Lett. **81** (1998) 5229.

[4] T. Hatano, W. Hu, K. Saito, M. Watanabe, J. Electr. Spectr. Rel. Phenom. **101-103** (1999) 287.

[5] T. Shishidou, S. Imada, T. Muto, F. Oda, A. Kimura, S. Suga, T. Miyahara, T. Kanomata, T. Kaneko, Phys. Rev. B **55** (1997) 3749.

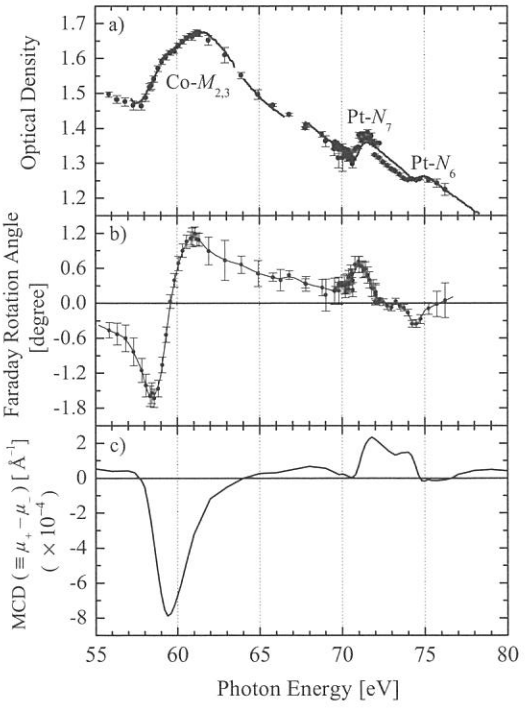

Fig. 1. a) Absorption and b) Faraday rotation spectra of Co (22.0 Å) / Pt (13.8 Å) multilayer in the 55-80 eV region, and c) MCD spectrum calculated from the Faraday rotation spectrum by the Kramers-Krönig translation.

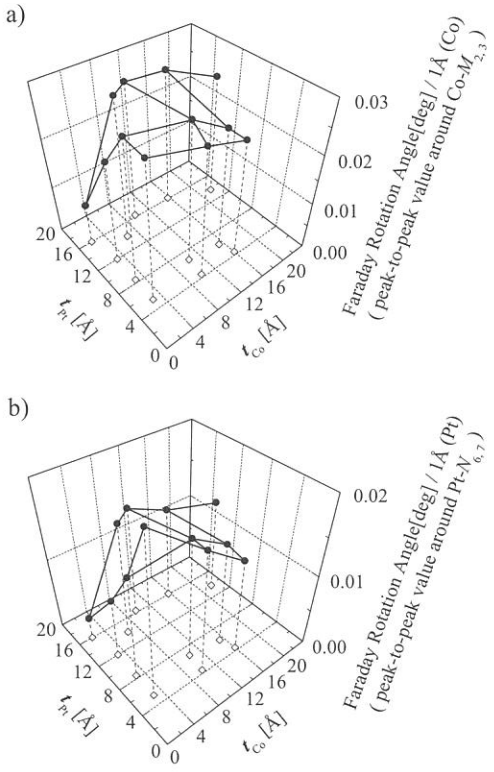

Fig. 2. a) Faraday rotation angles around Co-$M_{2,3}$ absorption edges per 1 Å thick Co layer and b) those around Pt-$N_{6,7}$ absorption edges per 1 Å thick Pt layer, as functions of Co and Pt one-layer thicknesses (t_{Co} and t_{Pt}).

Solid State Spectroscopy II
— XAFS, PES —

(BL1A, 5A, 5B, 6A2, 7A, 8B1, 8B2)

(BL-7A)

Structural Analysis of Amorphous Al_2O_3-Y_2O_3 Films

Naoshi OZAWA[1], Takeshi YAO[1] and Teiichi HANADA[2]

[1] *Graduate School of Energy Science, Kyoto University, Kyoto, 606-8501 Japan*

[2] *Graduate School of Human and Environmental Studies, Kyoto University, Kyoto, 606-8501 Japan*

Among rare earth oxides, Y_2O_3 has higher melting point than that of Al_2O_3 and is applied for a laser crystal and a heat-resisting material. Y_2O_3 is also used as a mother material for producing tri-valence rare earth ion phosphor and the applications for an optical waveguide and a thin film luminescent material have been reported. In this study, the structure of Al_2O_3-Y_2O_3 amorphous films were analyzed from Al-K XANES and Y-K_{III} XANES spectra. Samples were synthesized by means of rf-spattering, a method by which amorphous material can be easily obtained from material with high melting point.

Al_2O_3-Y_2O_3 amorphous film samples with Y_2O_3 content from 9 to 82 % were prepared. X-ray absorption was measured by BL-7A at UVSOR, Institute for Molecular Science, Okazaki, Japan. The storage ring was operating at electron energy of 750 MeV. The spectra were collected in a total electron yield mode at room temperature by an electron multiplier, using $KTiPO_4$ (KTP) (011) double crystal monochromator.

Figure 1 shows Al-K XANES spectra of the samples. $AlPO_4$ and Al_2O_3 were used as references of Al with coordination number (CN) 4 and 6, respectively. The peak intensity at about 1566 eV decreased with the increase of Y_2O_3 content. It is considered that the decrease of Al with CN 4 is indicated. Figure 2 shows Y-L_{III} XANES spectra of the samples. Spectra of Y_2O_3 and $LaYO_3$ are shown as a reference of Y with CN 6 and spectrum of YVO_4 is shown as a reference of Y with CN 8. The Y-L_{III} XANES spectra of the samples were almost unchanged with the Y_2O_3 content and were similar to that of YVO_4. This indicates that CN of Y in Al_2O_3-Y_2O_3 amorphous films is 8, regardless of the Y_2O_3 content.

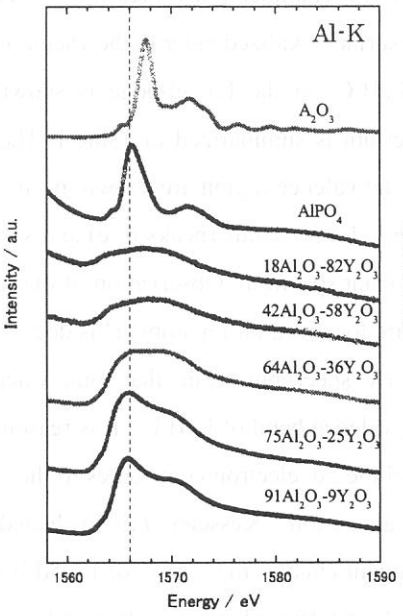

Fig.1 Al-K XANES spectra of Al_2O_3-Y_2O_3 amorphous films

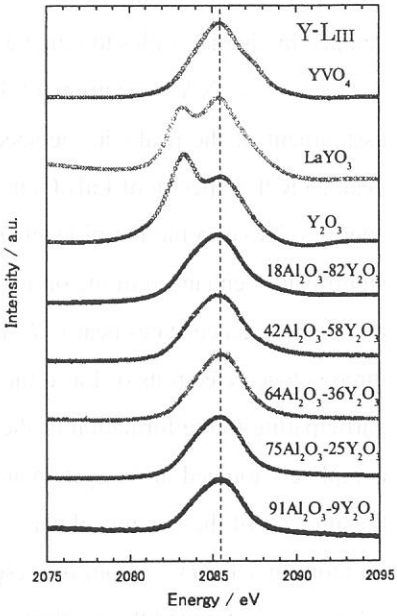

Fig.2 Y-L_{III} XANES spectra of Al_2O_3-Y_2O_3 amorphous films

(BL1A)

La 3d-edge Photoabsorption and Resonant Photoelectron Spectroscopy of Rare-earth Borocarbide LaB_2C_2

Hiroshi Oji,[a] Shinji Hasegawa,[a] Kazuya Suzuki,[b] and Nobuhiro Kosugi[a]

[a]*Institute for molecular Science, Myodaiji, Okazaki 444-8585, JAPAN*

[b]*Graduate School of Engineering, Yokohama National University, Hodogawa-ku, Yokohama 240-8501, JAPAN*

In rare-earth borocarbides RB_2C_2 (R: rare-earth (RE) metals) rare-earth metal cations are intercalated in the planar BC sheets. These intercalation compounds show interesting electronic and magnetic properties, such as superconducting behavior (T_c=2.4K for LuB_2C_2[1]). Therefore, it is important to know their electronic structure in order to clarify the mechanism of these properties. In the present study, the La 3d X-ray absorption spectroscopy (XAS) and valence-band resonant photoelectron spectroscopy (RPES) were used to reveal the partial density of states at the core-excited atom for lanthanum borocarbide (LaB_2C_2). Use of the relatively high energy photons of BL1A at the UVSOR facility (hν~830eV) allows us to perform the bulk-sensitive measurement.

The measurement of X-ray absorption and photoelectron spectra was performed at the BL1A soft X-ray beamline equipped with the double crystal monochromator. A pair of beryl ($10\bar{1}0$) crystal was used as a monochromator crystal, where the bandpass of monochromatized light was 0.6eV around 850eV. The XAS spectra were measured by the total electron yield mode. A SCIENTA SES-200 hemispherical electron energy analyzer was used for the measurement of RPES spectra. The energy resolution of the analyzer was set to be ~0.4eV and the total energy resolution for the measurements of the photoelectron spectra was ~0.7eV. The intensity of the spectra was normalized by the mesh yield (I_0). A polycrystalline flake of LaB_2C_2 cleaved in the atmosphere was introduced in the UHV chamber (base pressure: $<3X10^{-10}$Torr), and the sample surface was scraped by diamond files to remove surface oxidized layer in the vacuum just before the experiment.

The XAS spectrum of LaB_2C_2 in the La 3d-edge is shown in Fig. 1. According to Ref. 2, the assignment of the peaks in the spectrum is summarized in Table I. The off- (hν=826.4eV) and on- (834.3eV, peak 2) RPES spectra of LaB_2C_2 in the valence region are shown in Fig. 2. Abscissa corresponds to the binding energy relative to the Fermi level (E_F). La 5p bands (peaks d, e) and some bands near to the E_F (peaks a-c) are significantly enhanced in the on-resonant spectrum. Observation of the resonance effect on the valence suggests that some valence states near to E_F are localized on La atom. This does not support the complete donation of the three valence electrons of La to the BC sheet, but means that some valence (5d or 6s) electrons of La atom are participating to the formation of the valence band of LaB_2C_2. It is reasonable to expect that the $6s^2$ electrons are completely ionized in the system and the $5d^1$ electron contributes to the valence band. This is in agreement with the analysis of the theoretical band calculation.[3] Kesseler *et al.* evaluated the number of electrons localized on a La atom in a $La@C_{82}$, from the resonant enhancement ratio of La 5d band to that of La 5p. According to their scheme, we estimated the number of La 5d derived-valence electron localized on a La atom in LaB_2C_2 roughly to be 0.3.

References

1) J. van Duijn et al, *Phys. Rev.* **B62** (2000) 6410.

2) B. T. Thole et al. *Phys. Rev.* **B32** (1985) 5107.

3) H. Harima and M. Shirai, *J. Phys. Soc.* submitted.

4) B. Kessler et al, *Phys, Rev. Lett*, **76** (1999) 2289.

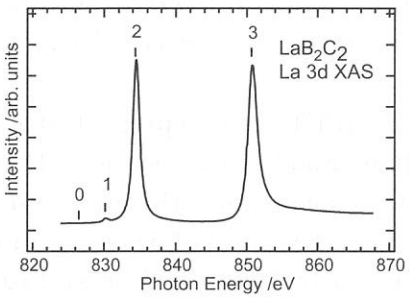

Fig. 1. La 3d-edge XAS spectrum of LaB_2C_2.

TABLE I. The assignment of the peaks in the XAS spectrum of LaB_2C_2.

Peak#	Peak Pos. /eV	Assignments
1	830.2	La $3d_{5/2}$ -> 4f ($^3D_1$)
2	834.3	La $3d_{5/2}$ -> 4f ($^3P_1$)
3	850.6	La $3d_{3/2}$ -> 4f ($^1P_1$)

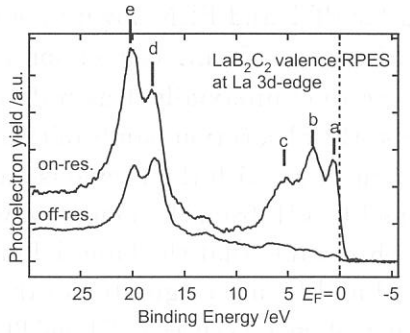

Fig. 2. Off- and on-resonant valence-band PES spectra of LaB_2C_2.

(BL-1B)

Anisotropic Absorption Spectra of Polyester Films due to Valence Electrons in Shallow and Deep Levels

Isuke OUCHI, Ikuo NAKAI[A] and Masao KAMADA[B]*

Faculty of Engineering, Tokushima Bunri University, Shido, Kagawa 769-2193
[A]*Faculty of Engineering, Tottori University, Koyama, Tottori 680-8552*
[B]*UVSOR, Institute for Molecular Science, Myodaiji, Okazaki 444-8585*

Polyethylene terephthalate (PET) is a representative aromatic polyester having a benzene ring in the main chain, and has been subject of study by many researchers with different interests, since long ago. Polyethylene 2,6-naphthalate (PEN) is similar polyester with a naphthalene ring instead of benzene. Both polymers can be extruded in sheet form, and, after biaxially drawn and crystallized, are utilized for variety of applications. Their optical and photo-physical properties have also been pursued. Absorption spectra of PET films in visible and ultraviolet regions manifest three bands between 300 and 190 nm; their nature was examined in detail, particularly for the first band at 300 nm.[1] The third band at 197 nm was found to consist of two peaks of different polarization by a molecular orbital calculation using π electron approximation, whereas it was not certain from experiments which of the two peaks had parallel polarization, because of the limit of the measurement in air or nitrogen.[1]

We have been trying to investigate the deep levels of valence electrons in oriented polyester films for the past years. At the present, optical constants and absorption spectra have been obtained for PET and PEN down to 50nm, or up to 24.7eV, from the reflection spectra by use of Kramers-Kronig conversion and Fresnel Formula. Fig. 1 illustrates the absorption spectra of uniaxially drawn PET and PEN films as a function of photon energy. Table I list the absorption bands of these films in relation to the peak position and polarization, comparing with the previous data obtained in air; absorption bands therein are denoted as I to VII, from the longer wavelength to the shorter.

If magnified, it is clearly observable that the band III of PET consists of two peaks as listed in Table I. Bands I, II and III are originated in the allowed $^1A_g \rightarrow {}^1B_u$ transitions due to $\pi \rightarrow \pi^*$ excitation; major difference between PET and PEN appears in this region.

The rest of the region, consisting of Bands IV to VII, resembles each other in spectral shape and peak positions, although there are minor differences in the polarization and shape. These bands must be caused by the transitions associated with σ electrons. The number of valence σ electrons in a repeat unit of PET and PEN are 54 and 68, respectively; the ratio of these numbers must be equal to the ratio of the integrated area of the peaks of each polymer, if taken for isotropic samples. The peak area is larger for PEN than PET, but not in proportion to 68 vs. 54, because of the anisotropy of the sample and mostly of the inevitable error caused by the method of approximation in the calculation of Kramers-Kronig conversion.

The feature in the region near Bands VI and VII resembles that for other polymers

---

● Present address: Saga University

such as polystyrene and PMMA as recorded by electron energy loss spectroscopy many years ago[2,3]. This may be understandable from the fact that a majority part of most polymers consists of carbon and hydrogen atoms.

	PET				PEN			
Band No.	absorption peak	polarity	previous data*		absorption peak	polarity	previous data**	
	A (eV)		exp.	calc.	A (eV)		exp.	cal.
VII	800 (15.5) vvs	∥			800 (15.5) vvs	∥		
VI	930 (13.3) vs	∥			920 (13.5) vs	∥		
V	1100 (11.3) sh	⊥			1100 (11.3) sh	⊥		
	1200 (10.3) sh	∥			1230 (10.3) sh	∥		
IV	1480 (8.4) sh	⊥			1550 (8.0) sh	∥		
					1700 (7.3) sh	⊥		
								n.a.
III	1860 (6.7) vs	∥	(6.29)	(6.44)	2200 (5.6) vs	∥		
	1970 (6.3) vs	⊥		(6.33)	2400 (5.2) vvs	∥	(5.5)	
					2500 (5.0) sh	∥	(4.8)	
II	2420 (5.1) vs	∥	(5.09)	(5.27)	2780 (4.5) sh	∥		
	2500 (5.0) vs	∥			2880 (4.3) s	∥	(4.2)	
					2990 (4.1) sh	∥	(4.0)	
I	2800 (4.4) sh	⊥			3260 (3.8) sh	∥		
	2900 (4.3) w	⊥	(4.26)	(4.66)	3410 (3.6) w	∥	(3.7)	
	3000 (4.1) w	⊥	(4.13)		3580 (3.5) w	∥	(3.5)	

Table 1. **Absorption peaks of PET and PEN films**
Peak intensity is denoted by the abbreviation; vvs=extremely strong, vs=very strong, s=strong, w:=weak, sh= shoulder. Also, * designates the reference [1]; ** [3].

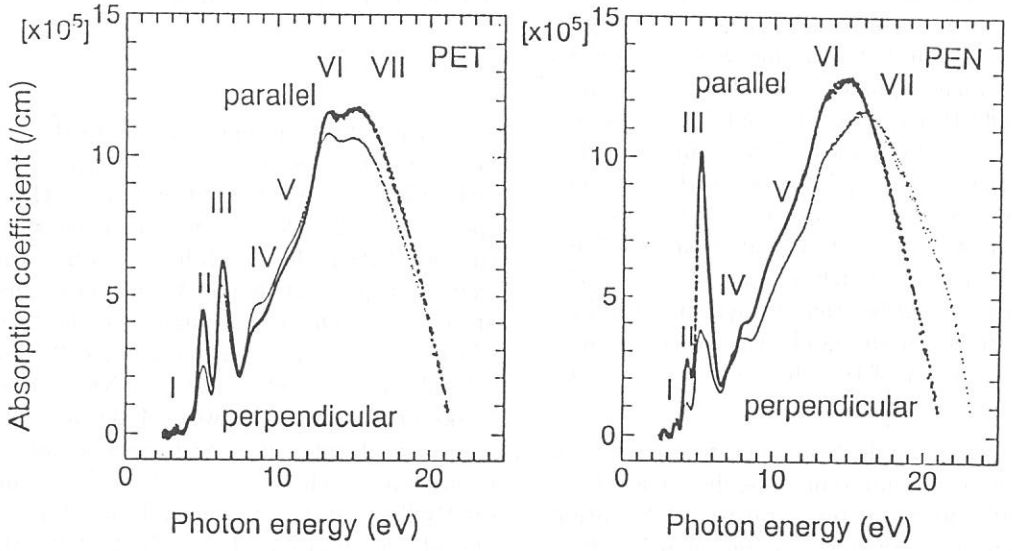

1) I. Ouchi, Polym. J., 15 (1983) 225.
2) T. Inagaki, E.T. Arakawa, R.N. Ham,M.W. Williams, Phys Rev., B15 (1977)3243.
3) J.Jritsko and R.W. Bigelow, J. Chem. Phys. 69 (1978) 4162.

(BL 2B1)

Orientation of Ammonia on ZnO(10$\bar{1}$0)

K.Ozawa, T. Hasegawa, K. Edamoto, K. Takahashi* and M. Kamada*

Department of Chemistry, Tokyo Institute of Technology, Ookayama, Meguro-ku, Tokyo 152, Japan
**Institute for Molecular Science, Myodaiji, Okazaki 444-8585*

The orientation of ammonia (NH_3) adsorbed on the ZnO(10$\bar{1}$0) surface at room temperature has been investigated by near-edge X-ray absorption fine structure (NEXAFS) spectroscopy. The NEXAFS technique is a well established method to determine the orientation of a wide variety of adsorbed species on the surfaces [1]. However, no such attempt has been made so far for adsorbed ammonia, partly because the NEXAFS spectra of adsorbed NH_3 show only broad resonance features with a poor dependence on the electric vector of the light [2]. Regarding adsorbed ammonia, therefore, electron stimulated desorption ion angular distribution (ESDIAD), photoelectron diffraction (PhD), and X-ray emission spectroscopy (XES), etc., have been used to investigate the orientation of adsorbed NH_3. The present study demonstrates that the polarization dependent NEXAFS measurements combined with curve fitting analysis are also capable to determine the orientation of adsorbed NH_3

The N K-edge NEXAFS spectra were measured at beam line 2B1 with the N KLL Auger electron yield mode with a constant final state energy of 375 eV. The ZnO(10$\bar{1}$0) sample was oriented so that the incidence plane of the light was parallel to the [000$\bar{1}$] azimuth. The NEXAFS spectra were normalized by photon flux estimated from the photocurrent of a gold mesh at the entrance of the UHV chamber. The photon energy was calibrated using the absorption feature at 284.5 eV in the photocurrent, which is associated with the π^* resonance of highly oriented pyrolitic graphite (HOPG) formed on the gold mesh as a contaminant. The accuracy of the photon energy is $\pm$ 0.5 eV.

Our recent photoelectron spectroscopy study has revealed that ammonia adsorbs molecularly on ZnO(10$\bar{1}$0) at room temperature. Adsorption reaches saturation at the coverage of 0.5 (3.0×10^{14} cm^{-2}). Fig. 1 shows a series of the N K-edge NEXAFS spectra from the NH_3-saturated ZnO(10$\bar{1}$0) surface as a function of the incidence angle of the light θ_i relative to the surface normal. All the NEXAFS spectra do not exhibit a sharp resonance as is often observed for the adsorbates with the π conjugated system [1]. However, at least three resonances are resolved at $\sim$ 401, 404 and 407 eV (indicated by bars in the bottom spectrum). The N-K edge excitation spectra for the free NH_3 molecule [3] have shown a threshold excitation peak at 400.6 eV and an intense peak at 402.3 eV, which are assigned to the transitions of the N 1s electrons to the $4a_1$ and 2e molecular orbitals, respectively. For free NH_3, three more peaks are observed between 402.8 and 404.2 eV with a weak intensities and are associated to the transitions to the N $3p_z$ (a_1), 4s (a_1), and $4p_{x,y}$ (e) Rydberg states, respectively [3]. Since ammonia adsorbs molecularly on ZnO(10$\bar{1}$0), the excitation features found in free NH_3 should be also observed in the adsorption system, although the position and the width of the peaks as well as the intensity ratio of the peaks are considered to be modified because of the bonding interaction of the molecular orbitals of NH_3 with the substrate or-

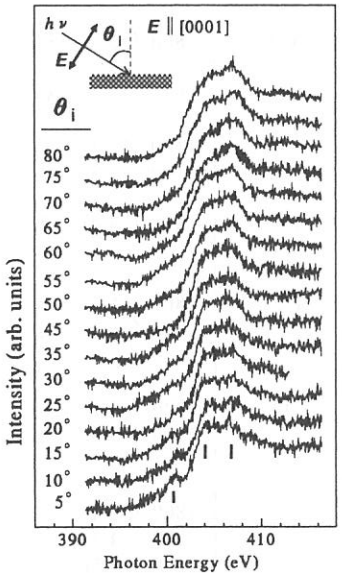

Fig. 1. The N K-edge NEXAFS spectra at various incidence angle θ_i of the light. The angle is measured from the surface normal direction. The incidence plane of the linearly polarized light is parallel to the [000$\bar{1}$] azimuth.

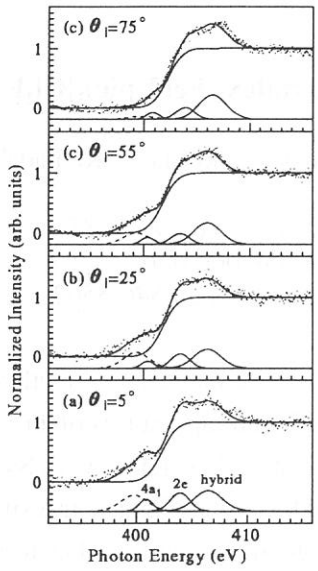

Fig. 2. The results of curve fitting analysis for the NEXAFS spectra. Four Gaussian functions for the resonance features and an error function for the continuum step are assumed. The line through the dots are the best fitted results.

bitals [2]. We, therefore, interpret the peaks at 401 and 404 eV as the excitations of the N 1s electron to the $4a_1$ and 2e orbitals of adsorbed NH_3, respectively. The third peak at 407 eV can be related to the excitation to the hybrid Rydberg states formed between the N $3p_z$ and N 4sp orbitals of NH_3 and the substrate Zn 4sp orbitals.

Fig. 1 shows that the observed peaks at 401, 404 and 407 eV exhibit a rather weak, but an obvious polarization dependence. In order to quantify the polarization dependence of these peaks, the NEXAFS spectra were decomposed by the curve fitting procedure using Gaussian functions for the peaks and an error function for the continuum step [1]. A selected set of the result is shown in Fig. 2. Apart from the peaks at 401, 404 and 407 eV, which are related to the $4a_1$, 2e and hybrid Rydberg states, respectively, another peak (shown by dashed line) is requisite to reproduce the low energy tail. The origin of this peak for the present system is unclear, but the NH_3 $3a_1$–Zn 4sp antibonding state could be responsible for the low energy tail.

Because of the large overlap between the $4a_1$ peak and the low excitation energy peak (dashed line), the intensity of these peaks seems to be correlated each other, especially at large θ_i where the $4a_1$ peak becomes a shoulder. Thus, the polarization dependence of the 4 a_1 peak intensity is ambiguous. On the other hand, the 2e and the hybrid peaks, which are well separated from the $4a_1$ and low excitation energy peaks, shows a clear polarization dependence.

Fig. 3 shows the θ_i dependent change in the

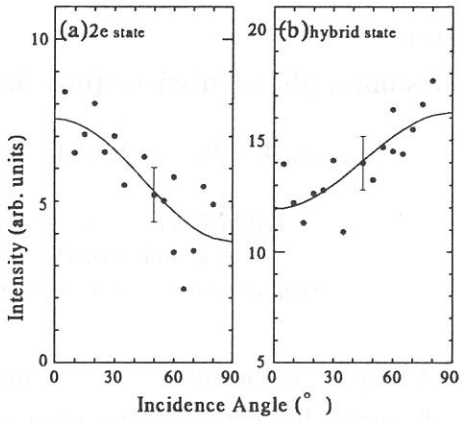

Fig. 3. The θ_i dependence of the intensities of the peaks, which are associated with (a) the 2e state and (b) the hybrid Rydberg state. Filled circles are the observed data. The solid lines are the best fit to the data using Eqs. 9a and 10a in Ref. [4].

peak intensities of these peaks. The 2e peak exhibits a decreasing trend with increasing θ_i. The 2e molecular orbitals are mainly composed of the N $3p_{xy}$ orbitals (the z axis is taken along the C_{3v} molecular axis). If NH_3 adsorbs with the C_{3v} axis tilted in the $[000\bar{1}]$ azimuth, the dependence of the 2e peak intensity on the incidence angle of light θ_i is expressed by Eq. 9a in Ref. [4]. The best fit to the data points is obtained at the molecular tilt of 33 ± 5° from the surface normal. On the other hand, the the peak associated with the hybrid states at 407 eV shows an increasing trend with increasing θ_i (Fig. 3b). This result implies that the molecular orbitals with the different symmetry from the 2e symmetry should be contribute significantly to the 407-eV peak. Namely, the Rydberg orbitals with the a_1 symmetry is responsible for the observed θ_i dependence. In such a case, the the θ_i dependent peak intensity can be fitted using Eq. 10a in Ref. [4] with the tilt angle of 41 ± 5°. Analysis of the intensity variation of these two resonances concordantly indicates that molecularly adsorbed ammonia on $ZnO(10\bar{1}0)$ is inclined in the $[000\bar{1}]$ azimuth.

References

[1] D.A. Outka and J. Stöhr, J. Chem. Phys. *88* (1988) 3539.

[2] J. Hasselström et al., J. Chem. Phys. *110* (1999) 4880.

[3] J. Schirmer et al., Phys. Rev. A *47* (1993) 1136.

[4] J. Stöhr and D.A. Outka, Phys. Rev. B *36* (1987) 7891.

(BL2B1)

Resonant photoemission study for spin-crossover complex $[Fe(2\text{-}pic)_3]Cl_2EtOH$

Kazutoshi Takahashi[A], Takeshi Tayagaki[B], Koichiro Tanaka[B], and Masao Kamada[C]

[A] *UVSOR Facility, Institute for Molecular Science, Okazaki 444-8585*
[B] *Department of Physics, Kyoto University, Kyoto 606-8502*
[C] *Synchrotron Light Application Center, Saga University, Saga 840-8502*

An organometal spin-crossover complex $[Fe(2\text{-}pic)_3]Cl_2EtOH$ (2-pic=2-aminomethyl-pyridine) shows the thermally-induced phase transition of two stages at critical temperatures of 114 and 121 K [1]. The high- and low-temperature phases correspond to the high-spin (HS) phase with S=2 and low-spin (LS) phase with S=0, respectively. In addition to the thermally-induced phase transition, $[Fe(2\text{-}pic)_3]Cl_2EtOH$ shows the dramatic change in chromic and magnetic properties due to the photo-induced phase transition, when it is excited by photons at low temperatures. Up to now, these thermally- and photo-induced phase transitions in $[Fe(2\text{-}pic)_3]Cl_2EtOH$ have been investigated mainly by optical and magnetic methods, but to our knowledge, there are a few works that highlight the electronic structure in the wider energy range [2]. In order to clarify the photo-induced phase transitions, it is also indispensable to understand the electronic structure in the wider energy range. In this study, we have carried out a resonant photoemission study at N 1s-2p and Fe 2p-3d excitation regions for $[Fe(2\text{-}pic)_3]Cl_2EtOH$.

Experiments have been carried out at the beam line BL2B1 in the UVSOR facility. Powder samples of $[Fe(2\text{-}pic)_3]Cl_2EtOH$ were synthesized at Kyoto university. The sample was attached on the sample holder using a carbon adhesive tape and introduced to measurement chamber without being exposed to air using a glove-bag filled with nitrogen gas and a load-lock chamber. The sample temperature was changed between 300 and 100 K using liquid nitrogen. The sample was irradiated by visible light from the Ar^+-ion laser of about 9 mW in multi-line mode at 100 K in order to cause the photo-induced phase transition. Photoemission spectra were measured using a double-pass CMA analyzer. Total energy resolution is about 1.5 eV for N 1s-2p excitation region.

Figure 1 shows the photoabsorption spectrum at the Fe $2p_{1/2}$ and $2p_{3/2}$ edges of $[Fe(2\text{-}pic)_3]Cl_2EtOH$ at HS phase. Figure 2 shows the difference spectra in valence band and Fe 3p regions at the Fe $2p_{1/2}$ and $2p_{3/2}$ edges of $[Fe(2\text{-}pic)_3]Cl_2EtOH$ at HS phase. Off-resonance spectrum (A) is also shown in Fig. 2. The features at 688 and 635 eV in kinetic energy correspond to the L_3VV and $L_3M_{23}V$ Auger lines, respectively. As shown in Fig. 2, spectral intensities of these features increase at Fe $2p_{2/3}$ edge. It is also found that the photoemission intensity of valence-band (feature 1) and satellite of Fe 3p (feature 3) increase at Fe $2p_{1/2}$ edge. Figure 3 shows the photoabsorption spectrum at the N 1s edge. The feature at 399 eV corresponds to the π^* resonance. On the other hand, the features at 406, 407.5, and 416 eV correspond to σ^* resonances. Figure 4 shows the difference spectra in valence-band and Fe 3p regions at the N 1s edge of $[Fe(2\text{-}pic)_3]Cl_2EtOH$ at HS phase. Off-resonance spectrum (A) is also shown in Fig. 4. The main features in the difference spectra correspond N KVV Auger lines. As shown in Fig. 4, it is found that the kinetic energy of the KVV Auger lines shift to lower kinetic energies with increasing the excitation energy from π^* resonance to σ^* resonance regions. In contrast with the Fe $L_{2,3}$ excitation region, it is found that the spectral intensity at valence-band and Fe 3p regions show almost no change at N K excitation region.

We have also measured photoabsorption and photoemission spectra for LS and photo-induced (PI) phases. It is found that the feature at 416 eV in the absorption spectrum at N K edge region broaden at LS phase and the energy separation of features around 407 eV increase at PI phase. It is considered that these spectral changes are indicative of the change in Fe-N bonding at thermally- and photo-induced phase transitions. However, we could not find electronic structure changes in resonant photoemission spectra at LS and PI phase with finite energy resolution in this study. Further investigations with higher energy resolution are in progress.

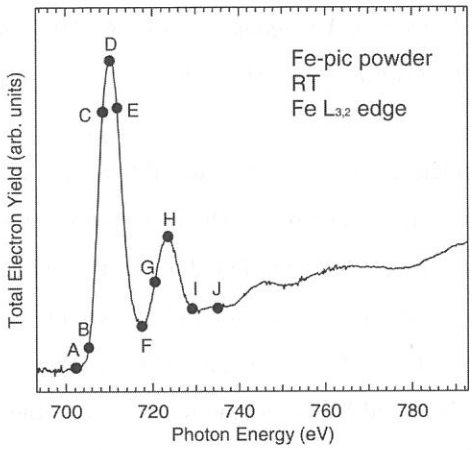

Figure 1. Photoabsorption spectrum at Fe $2p_{1/2}$ and $2p_{3/2}$ edges for high-spin phase.

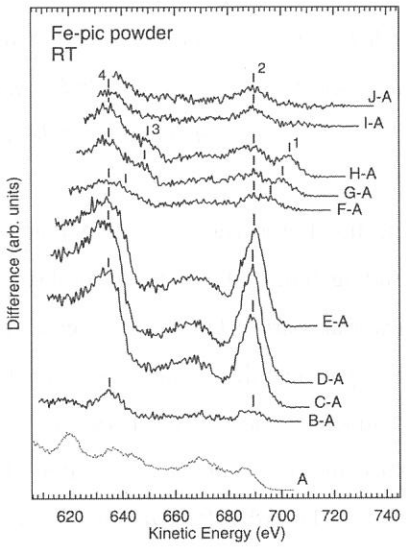

Figure 2. Difference photoemission spectra at Fe $2p_{1/2}$ and $2p_{3/2}$ edges for high-spin phase.

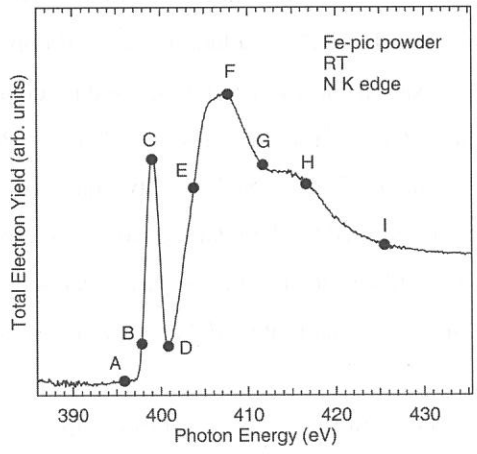

Figure 3. Photoabsorption spectrum at N 1s edge for high-spin phase.

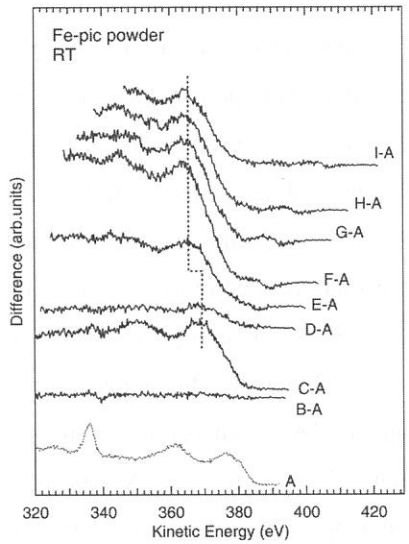

Figure 4. Difference photoemission spectra at N 1s edge for high-spin phase.

References

[1] P. Gutlich, *et al.*, Angew. Chem. **33**, 2024 (1994).

[2] M. Kamada *et al.*, UVSOR Activity Report **28**, 158 (2001).

(BL4B)

PES and NEXAFS study of DNA polynucleotides on silicon dioxide surfaces with and without iodine doping

Masashi Furukawa[1,2], Hiroyuki S. Kato[1], Masateru Taniguchi[2], Takaki Hatsui[3], Hiroshi Oji[3], Tadahiro Komeda[1], Tomoji Kawai[2], Nobuhiro Kosugi[3] and Maki Kawai[1]

[1] *RIKEN (The Institute of Physical and Chemical Research), Hirosawa, Wako, Saitama 351-0198, Japan*

[2] *The Institute of Scientific and Industrial Research, Osaka University, Mihogaoka, Osaka 567-0047, Japan*

[3] *Institute for Molecular Science, Myodaiji, Okazaki 444-8585, Japan*

Electrical properties of DNA double strands are being attractive as they are considered to be a candidate for the building block of functional molecular systems in nano-scale technology. Direct measurements of the electrical transport of DNA have been extensively reported, and thus it has been found out that double-stranded DNA polynucleotides with well-defined sequences, Poly(dG)·Poly(dC) and Poly(dA)·Poly(dT), show the hole-conductive and the electron-conductive behaviour, respectively ($\rho \sim 1$ Ω·cm) [1]. It has also been confirmed that the conductivity of Poly(dG)·Poly(dC) were increased by the iodine doping, i.e., hole-doping, while that of Poly(dA)·Poly(dT) were not changed [2]. In this study, both occupied and unoccupied electronic structure of such polynucleotides have been characterized by use of photoelectron spectroscopy (PES) and near-edge X-ray absorption fine structure spectroscopy (NEXAFS), aiming at the investigation of the origin of the iodine-doping effect as well as that of carrier conduction mechanism of DNA, which is currently a hot debate.

The specimens used in our experiments were synthesized DNA polynucleotides, Poly(dG)·Poly(dC) and Poly(dA)·Poly(dT), purchased from Amersham Pharmacia Biotech. DNA solutions were dropped onto SiO_2/*p*-Si(111) surfaces (ρ = 20–40 Ω·cm), blown off after the fixation for a few minutes. Iodine doping was achieved by sealing samples with elemental iodine in evacuated Pyrex glass ampoules for 6 hours. PES and NEXAFS measurements were performed at BL4B soft-X-ray beamline of the UVSOR facility, equipped with the double crystal monochrometor. NEXAFS measurements were performed by the total electron yield mode. A SCIENTA SES-200 hemispherical electron energy analyzer was utilized for the PES measurements. The PE spectra of Si 2p region (Binding energies (B. E.) of bulk of *p*-Si: 99.1 eV and SiO_2: 103.2 eV) were measured to calibrate the electron energy and intensity of the spectra.

Figure 1 shows the N 1s XP spectra of DNA polynucleotides on SiO_2/*p*-Si(111) surfaces with and without iodine doping. Two dominant components (lower B.E.: =N- and higher B.E.: -N- [3]) observed for non-doped samples were drastically changed in intensity ratio by doping iodine. For both polynucleotides with iodine doping, the intensity of higher B.E. component was stronger than that of lower one, while P 2p core levels did not show drastic differences in intensity and binding energy in their spectra (see Fig. 2). Nitrogen *K*-edge X-ray absorption spectra has also shown the significant difference between iodine-doped and non-doped polynucleotides samples, as shown in Fig. 3. As iodine were doped into DNA, second prepeak (π^*_{-N-} resonance [4]) were shifted toward the lower excitation energy, while first prepeak ($\pi^*_{=N-}$ resonance) were not shifted and

the intensity of second prepeak is stronger than the first one. It is concluded so far, from these PES and NEXAFS results, that iodine intercalates directly into the DNA base molecules (π stacking). We are currently analyzing these doping effects using molecular orbital calculations.

References

[1] K. –H. Yoo et al., Phys. Rev. Lett. **87,** 198102 (2001).

[2] M. Taniguchi et al., in preparation.

[3] L. S. Shlyakhtenko et al., Biophys. J. **77,** 568 (1999), and references therein.

[4] S. Mitra-Kirtley et al., J. Am. Chem. Soc. **115,** 252 (1993).

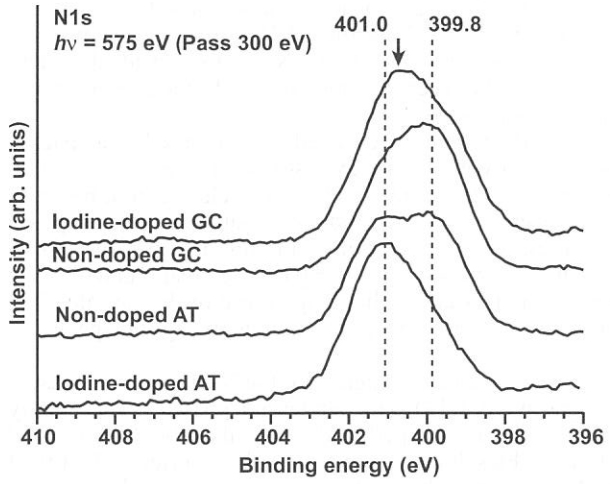

Fig. 1 N 1s XP spectra for DNA polynucleotides on SiO_2/*p*-Si(111) surfaces with and without iodine-doping ($h\nu$ = 575 eV).

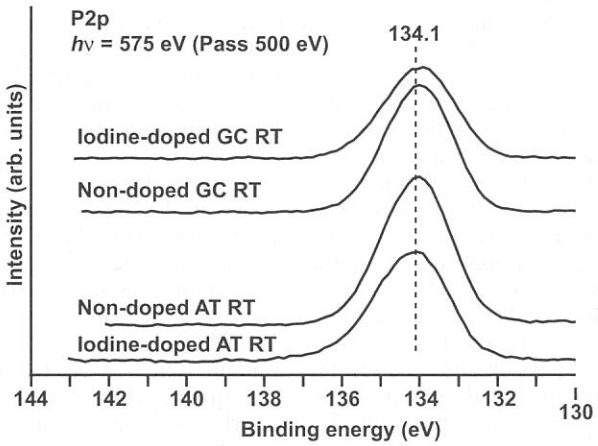

Fig. 2 P 2p XP spectra for DNA polynucleotides on SiO_2/*p*-Si(111) surfaces with and without iodine-doping ($h\nu$ = 575 eV).

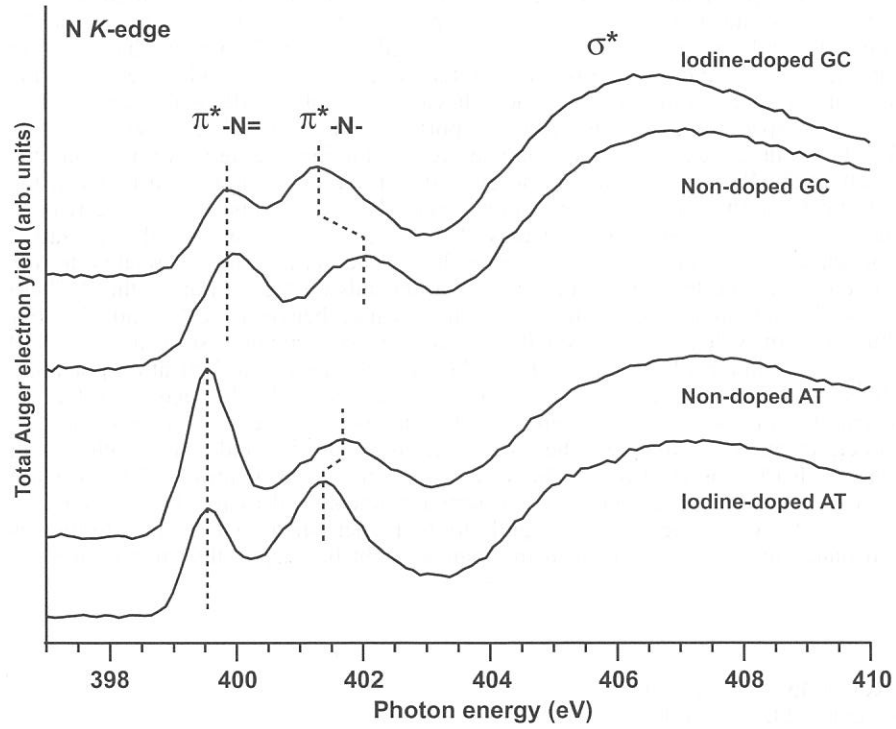

Fig. 3 Nitrogen K-edge absorption spectra spectra for DNA polynucleotides on SiO_2/*p*-Si(111) surfaces with and without iodine-doping.

(BL4B)

N 1s Photoabsorption of N_2 Trapped in Rare Gas Matrices

Mitsuru Nagasono , Hiroshi Oji, Takaki Hatsui, Eiji Shigemasa, and Nobuhiro Kosugi

Institute for Molecular Science, Myodaiji, Okazaki 444-8585, Japan

The N_2 molecule has been widely used as an ideal system to study the inner-shell excitation process. Many N 1s photoabsorption spectra have been reported for the gas phase (monomer [1-3] and clusters [4]), condensed phase [5,6], and surface-adsorbed phase of N_2 [7,8]. The gaseous N_2 spectra show a strong bound state resonance and a strong continuum resonance, even in low-resolution spectra. These features arise from the 1s-π^* excitation and the σ^* shape resonance, which are orthogonal to each other in the polarization dependence to the linearly polarized soft X-rays. The anisotropy is clearly observed in the angle-resolved photoion yield spectroscopy (ARPIS) of gaseous N_2 [1], and is used to determine the adsorption geometry of N_2 [8]. Furthermore, high-resolution inner-shell spectra of N_2 show many Rydberg excited states below the ionization threshold and several double and triple excitations near and above the threshold [2,3]. Some of them have diffuse character and should have environmental effects around the molecule. Thus, N_2 is also an ideal system from the viewpoints of the surrounding effect and of the difference between gas and solid. In the present work, we have measured N 1s excitation spectra of N_2 trapped in rare gas matrices.

The experiments were carried out at a new beamline BL4B, which is equipped with a varied-line-spacing plane grating monochromator. The monochromator was operated with an energy resolving power E/dE = 8000 at 400 eV photon energy. N 1s photoabsorption spectra were measured with an electron yield method, but with a transmission method for gaseous N_2. The rare gases used were Ne, Ar, Kr and Xe. Samples were prepared by mixing gaseous N_2 with rare gas in the high-vacuum stainless-steel vessel; before the mixing, the amounts of N_2 and rare gas were controlled by measuring the pressure in each vessel with a capacitance manometer. The gas mixtures were evaporated on an Au coated sample plate of a cryostat. The temperature of the sample plate was below 6.5 K. The ratios N_2 to rare gas were 1/10 and 1/1. Furthermore, N 1s photoabsorption spectra of the condensed and gaseous N_2 were also measured.

Figure 1 shows the N 1s photoabsorption spectra in the 1s-π^* resonance region for the N_2 in gaseous phase, rare gas matrix phases (the amount ratios of N_2 to rare gas were 1/10) and condensed phase. The energy position and the vibrational structure in all spectra are essentially unchanged, indicating that the 1s-π^* excited states do not have significant overlap with surrounding atoms. Flesch et. al. have recently reported red shift of 6 ± 1 meV of the 1s-π^* excitation in N_2 clusters relative to N_2 monomer due to dynamic stabilization that follows photoexcitaion [4]. Though there are also very small energy differences among the present data, argument about the energy shift would need more high-resolution measurement and more careful energy calibration on our spectrometer.

Figure 2 shows the N 1s photoabsorption spectra near the N 1s ionization threshold region, which contains Rydberg excitations, multiple excitations and a σ^* shape resonance. The excitations from N 1s to 3*s* and 3*p* Rydberg states are clearly identified in all spectra. The 3*s* and 3*p* excited states both exhibit blue shifts in photon energy in the matrix phase. Furthermore, compression of the Rydberg series is observed with the increasing the concentration of N_2 in the rare gas matrices. The behavior of the blue shifts is the same as that in UV photoabsorption spectra of NO trapped in the rare gas matrices reported by M. Chergui, et. al. [9].

The absolute energy for the Rydberg excitation is obtained by subtracting the term value from the ionization potential; then, the shift of the Rydberg excitation energy is determined by competition between the shifts of the ionization potential and the term value. The ionization potential becomes smaller with decreasing the distance between the N_2 and the neighbor atoms or molecules [10]. Thus the red shift of the ionization potential becomes larger as the cage size smaller. On the other hand, the term value is related to the antibonding character in the Rydberg state, and the antibonding character depends on the overlap of the Rydberg orbitals with the valence orbital of the neighbor species; that is, on the distance between the N_2 and neighbor species or the cage size. Thus the term value becomes smaller as the cage size smaller. Since the observed matrix effect exhibits a blue shift, the variation of the term value is larger than that of the ionization potential. The situation for the energy shift by the N_2 concentration effect is nearly the same as that by the cage size effect.

The double excitations near the threshold show a complicated behavior in some systems, though it is difficult to distinguish from Rydberg excitations and from other new electronic states in solid. The well-known double excitations at 415 eV can be clearly observed for all the spectra, though fine structures in the gas phase are disappeared in the matrices. However, the energy position is essentially unchanged as for the π^* resonance excitation. The σ^* shape resonance for the dense media shifts slightly to the higher energy with respect to the gas phase. The interatomic bond distance in the N_2 molecule in the matrix might be shorter than that of the gas phase.

References

[1] E. Shigemasa, et. al., Phys. Rev. A **45**, 2915 (1992).
[2] M. Neeb, et. al., Chem. Phys. Lett. **320**, 217 (2000).
[3] E. Shigemasa, et. al., to be published.
[4] R. Flesch, et. al., Phys. Rev. Lett. **86**, 3767 (2001)
[5] O. Björneholm et. al., Physica Scripta **T41**, 217 (1992)
[6] W. Wurth et. al., Physica Scripta **T41**, 213 (1992)

[7] L. Wenzel, et. al., Phys. Rev. B **40**, 6409 (1989).
[8] J. Stöhr, et. al., Phys. Rev. B **26**, 4111 (1982).
[9] M. Chergui, et. al., J. Chem. Phys. **85**, 2472 (1986)
[10] P. S. Bagus et. al., J. Electron Spectrosc. Relat. Phenom. **100**, 215 (1999)

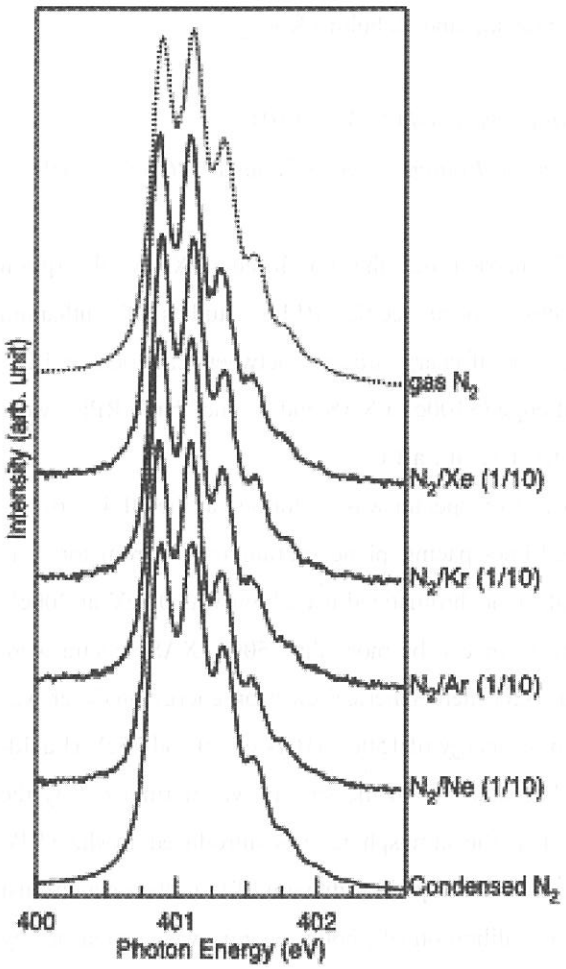

Figure 1. the N 1s photoabsorption spectra in the 1s-π^* resonance region for the N_2 in gaseous phase, rare gas matrix phases and condensed phase.

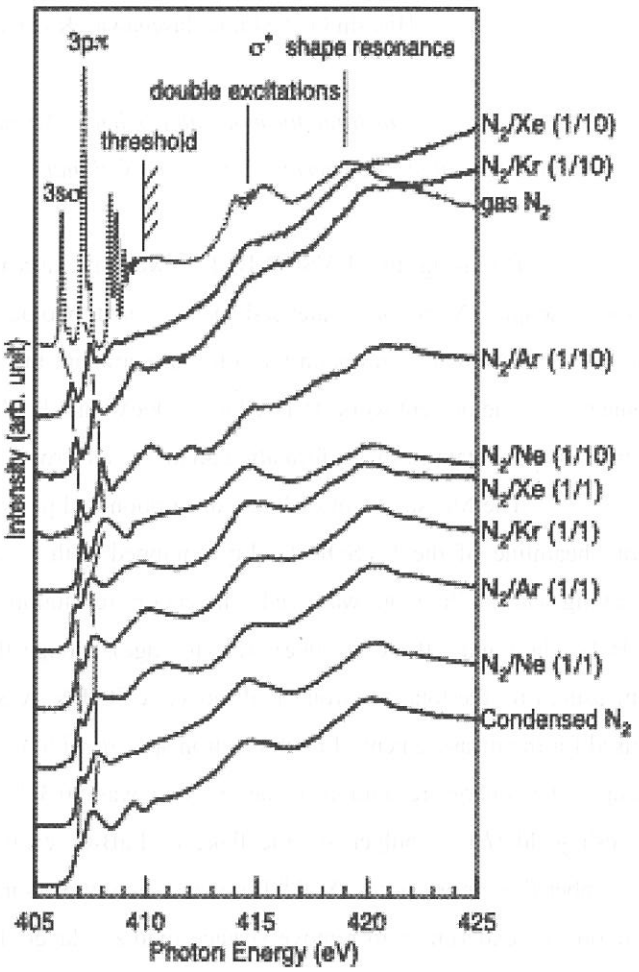

Figure 2. the N 1s photoabsorption spectra near the N 1s ionization threshold region for the N_2 in gaseous phase, rare gas matrix phases and condensed phase.

(BL4B)

B 1s- and La 4d-edge photoabsorption and Resonant Photoelectron Spectroscopy of Rare-earth Borocarbide LaB_2C_2

Hiroshi Oji,[a] Shinji Hasegawa,[a] Kazuya Suzuki,[b] and Nobuhiro Kosugi[a]

[a]*Institute for molecular Science, Myodaiji, Okazaki 444-8585, JAPAN*

[b]*Graduate School of Engineering, Yokohama National University, Hodogawa-ku, Yokohama 240-8501, JAPAN*

By using the UVSOR-BL1A, we have already carried out the La 3d-edge X-ray absorption spectroscopic (XAS) and valence-band resonant photoelectron spectroscopic (RPES) studies of lanthanum borocarbide (LaB_2C_2) to obtain the information about the dergee of charge transfer between La atoms and BC sheets.[1)] In the present work, B 1s-edge (~200eV) and La 4d-edge (~100eV) XAS and valence-band RPES were measured to obtain further information about the electronic structure of LaB_2C_2.

The Measurement of X-ray absorption and photoelectron spectra was performed at the BL4B soft X-ray beamline of the UVSOR facility equipped with varied-line-spacing plane grating monochromator. The grating with 267line/mm was used. The energy resolution of monochromatized used light was 0.1eV at 200eV (B 1s-edge) and 0.03eV at 100eV (La 4d-edge), though the $E/\Delta E$ can be more than 5000. XAS spectra were measured by the total electron yield mode. A SCIENTA SES-200 hemispherical electron energy analyzer was used for the measurement of photoelectron spectra with the pass energy of 150eV (B 1s-edge) and 75eV (La 4d-edge). The energy resolution of the analyzer was ~0.3eV. The intensity of the spectra was normalized by the mesh yield (I_0). A polycrystalline flake of LaB_2C_2 cleaved in the atmosphere was introduced in the UHV chamber (base pressure: $<3X10^{-10}$Torr), and the sample surface was scraped by diamond file in the vacuum just before the experiment to remove surface oxidized layer. The calibration of photon energy was carried out by assuming the π^* peak of h-BN as 191.8eV.[2)]

La 4d-edge XAS spectrum of of LaB_2C_2 is shown in Fig. 1. The assignments of the peaks are indicated in the figure.[3)] The valence- and inner-valence RPES spectra of LaB_2C_2 at various photon energies (indicated by numbers) are shown in Fig. 2. Abscissa corresponds to the binding energy relative to the Fermi level (E_F). La 5p bands (~20eV) are significantly enhanced in the on-resonant (La 4d) spectrum. Especially, an anomalous change of the photoemission branching ratio between $5p_{3/2}$ and $5p_{1/2}$ intensity can be seen. Actually, this anomaly is also observed in other La compounds. Ogasawara *et al.* attributed this to the multiplet dependence of the Auger transition probabilities.[3)] The intensity of the all valence- and inner-valence band begin to decrease from the photon energy of "5", and almost no structure can be observed at "10". Such a phenomenon was not observed in the RPES spectra at B K-edge as seen in Figs. 3 and 4.

References

1) See the page for BL1A.

2) R. Franke et al., *Chem. Phys.* **216** (1997) 243.

3) H. Ogasawara *et al., Solid State Commun.* **81** (1992) 645.

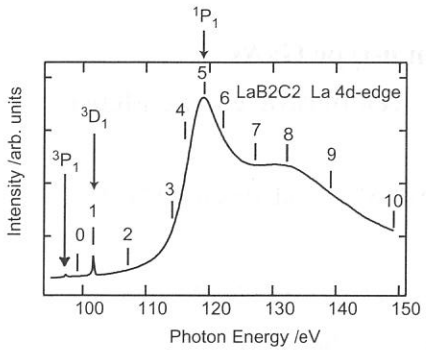

Fig. 1. La 3d-edge XAS spectrum of LaB_2C_2.

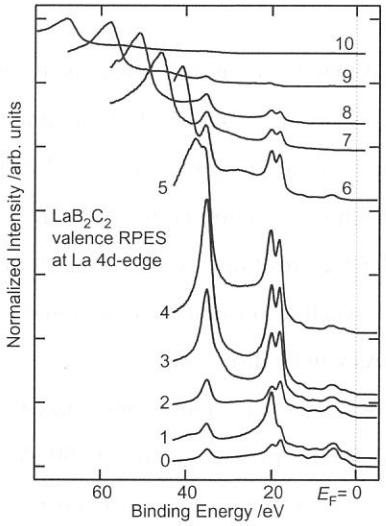

Fig. 2. The valence- and inner-valence RPES spectra of LaB_2C_2 at various photon energies.

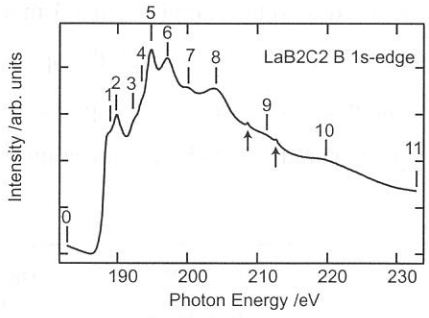

Fig. 3. B 1s-edge XAS spectrum of LaB_2C_2. (The small peaks indicated by the arrows are due to the La 3d absorption by 4th order light.)

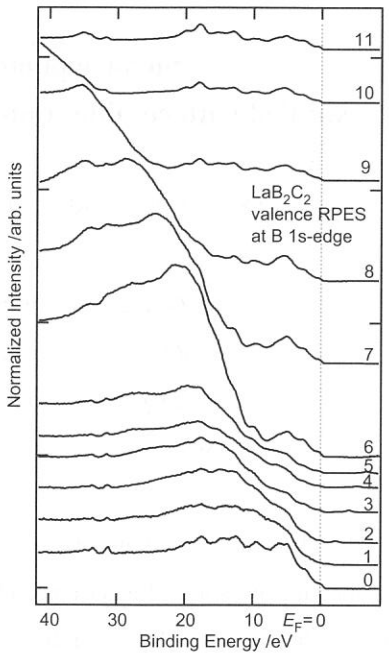

Fig. 4. The valence- and inner-valence RPES spectra of LaB_2C_2 at various photon energies.

(BL5A)

Surface photovoltage effects on n-type GaAs studied with combination of SR and laser : Temperature dependence

Senku TANAKA, Kazutoshi TAKAHASHI [A], Junpei AZUMA [B] and Masao KAMADA [C]

The Graduate University for Advanced Studies, Okazaki 444-8585

[A] *UVSOR Facility, Institute for Molecular Science, Okazaki 444-8585*

[B] *Department of Physics, Kyoto University, Kyoto 606-8502*

[C] *Synchrotron Light Application Center, Saga University, 840-8502*

The absorption of photon with energy larger than the bulk band-gap energy generates electron-hole pairs. The spatial separation of electrons and holes in the space-charge layers causes electromotive force called surface photovoltage (SPV) [1]. Recently, we proposed an approximate formula to give a simple relation of SPV with photocarrier density, temperature and initial band-bending. This approximation is in good agreement with the experimental results of the SPV effect on p-type GaAs [2]. In the present study we have measured the SPV effect on n-type GaAs using photoelectron spectroscopy combined synchrotron radiation (SR) and laser. The applicability of the approximation to the measurements of n-type GaAs will be discussed.

The experiments were performed at BL5A, UVSOR. SR was monochromatized with an SGM-TRAIN-type monochromator. The photon density was typically 3 x 10^9 photons/s·mm^2 at 100 eV. The base pressure of the experimental chamber was about 2 x 10^{-8} Pa. A hemispherical electron-energy analyzer (OMICRON EA125HR) was used for the photoelectron spectroscopy. The overall energy resolution was about 0.2 eV. We used a Ti: Sapphire laser system (COHERENT Mira 900-F) to cause the SPV effect. The wavelength of the laser was 800 nm and the repetition frequency was about 90 MHz (synchronized with SR). Laser light was transported to the experimental chamber using an optical fiber and focused onto the sample with a 3-mm radius spot. The temporal width of the laser pulses was expanded to about 100 ps by passing through the optical fiber. The spatial overlap between the laser and SR was adjusted by our eyes. We performed experiments on a Si-doped (1 x 10^{18} cm^{-3}) GaAs. The clean surface of the sample was prepared *in situ* by an annealing and ion sputtering.

Fig. 1 shows photoelectron spectra of an n-type GaAs. Solid and dotted lines represent the photoelectron spectrum with and without laser illumination, respectively. As can be seen from Fig. 1, the illumination of the laser results in a shift of the photoelectron spectrum toward lower kinetic energies. This shift originates from the SPV effect caused by the laser-excited carriers [2]. Fig. 2 shows the temperature dependence of the peak energy of the Ga-3d

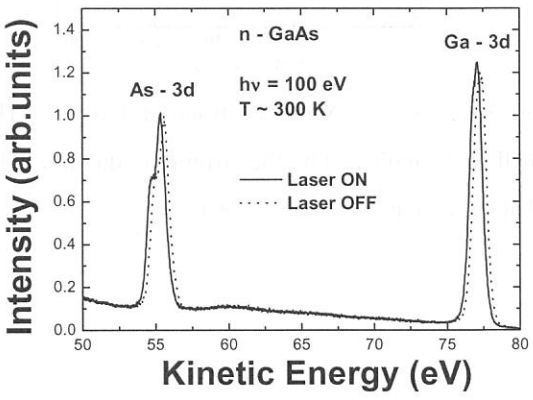

Figure 1. Effects of the laser illumination on an n-type GaAs surface.

photoelectron spectrum. Circle and triangle represent the peak energy of the Ga-3d with and without laser illumination, respectively. In the range over 350 K, the peak energy without laser illumination remains almost constant. In the range under room temperature, the peak energy shifted toward lower kinetic energies with decreasing temperature. The absolute values of the SPV shift of Ga-3d in the range of 80- 400 K are shown in Fig. 3 as dots. The SPV shift increased with decreasing temperature from 400 K to room temperature, while, the SPV shifts decreased on further cooling below ~275 K.

The present results are different from the behavior of p-type GaAs [2]. In the case of p-type GaAs, the SPV shifts increase with decreasing temperature. It is found that the peak energy without laser illumination remains nearly unaffected by the change of temperature in the p-type, while that is strongly affected in the n-type. Therefore, the temperature dependence of the initial band-bending values may explain the discrepancy of SPV shift. The simple formula of the SPV effect can be expressed as

$$\beta\Delta\Psi \exp(\beta\Delta\Psi) = \frac{\delta n}{n_0}\exp(\beta\Psi_0) \quad , \qquad (1)$$

where $\beta = e / kT$, e is the absolute value of electron charge and k and T have their usual meanings, $\Delta\Psi$ is SPV, δn is photoexcited carriers, and n_0 is the doping density. From Fig.2, we can obtain the temperature dependence of the initial band-bending values. The solid line of Fig. 3 represents the simulation of SPV that includes temperature dependence of the initial band-bending values. This simulation agrees qualitatively with the experimental result. The simulation is not complete in temperature range lower than 200 K. This disagreement may be attributed to the fact that the present experimental conditions are beyond the approximation. Further consideration is in progress.

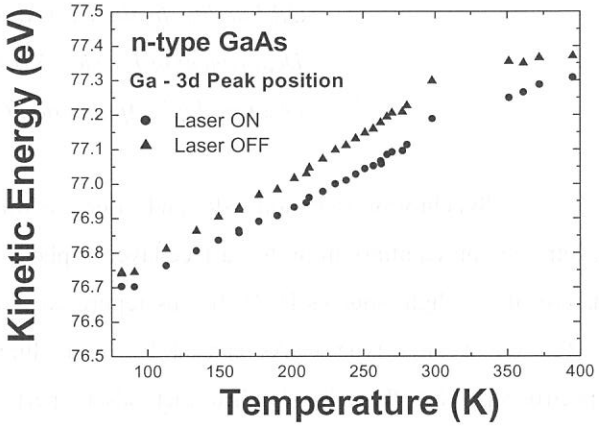

Figure 2. Temperature dependence of the peak energy of the Ga-3d photoelectron spectrum.

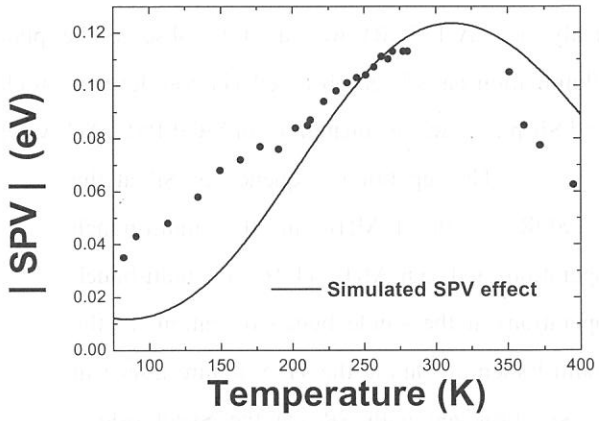

Figure 3. Temperature dependence of the SPV shifts.

In summary, we have studied the SPV effect on n-type GaAs. The simple approximate formula fairly explains the temperature dependences of the SPV in both of p-type and n-type GaAs.

References

[1] W. Mönch, *Semiconductor Surfaces and Interfaces* (Springer, 2001) 3rd ed.

[2] S. Tanaka et al., Phys. Rev. B **64** (2001) 155308.

(BL5A)

Surface photovoltage effects on n-type GaAs studied with a time-resolved photoelectron spectroscopy

Senku TANAKA, Kazutoshi TAKAHASHI [A], Junpei AZUMA [B] and Masao KAMADA [C]

The Graduate University for Advanced Studies, Okazaki 444-8585

[A] *UVSOR Facility, Institute for Molecular Science, Okazaki 444-8585*

[B] *Department of Physics, Kyoto University, Kyoto 606-8502*

[C] *Synchrotron Light Application Center, Saga University, 840-8502*

Synchrotron radiation (SR) and laser are widely used as useful light sources. We have studied the electronic non-equilibrium in the surface layer of photo-excited p-type GaAs using the combination of the pulse nature of two light sources [1-3]. In this report, we present the temporal change of the surface photovoltage (SPV) effect on n-type GaAs caused by laser illumination by means of a time-resolved photoelectron spectroscopy (TR-PES). Two kinds of methods are performed for measuring the TR-PES. One is the pump-probe method through the synchronization of SR and laser. The other uses the pick-out method through the gate circuit.

Experiments were performed at BL5A. A Si doped (1 x 10^{18} cm^{-3}) n-type GaAs was used for the measurements. We used the Ti: Sapphire laser (COHERENT Mira 900-F) and the regenerative amplifier (COHERENT RegA) as the excited light sources to cause the SPV effects. The OMICRON electron-energy analyzer (EA-125HR) was used to observe the photoelectron spectra. The SPV effects caused by laser illumination have been observed via core-level photoelectron spectra [3, 4]. The temporal overlap of the laser and SR pulses was evaluated by an MCP-PM/TAC system.

The repetition frequency of SR at the UVSOR is 90.115MHz in the multi-bunch operation and 5.63MHz (1/16 of multi-bunch operation) at the single bunch operation. In the multi-bunch operation, the Ti: Sapphire laser can be synchronized with SR via the Synchro-lock circuit. We obtain the TR-PES in the range of 11ns using this system. In the single bunch operation, if the laser pulses could be picked out via the AO modulator to synchronize with SR, the range of about 176 ns would be allowed to observe the TR-PES. Time resolution of the pump-probe method is restricted by the SR pulse width and it is typically about 1.5 ns.

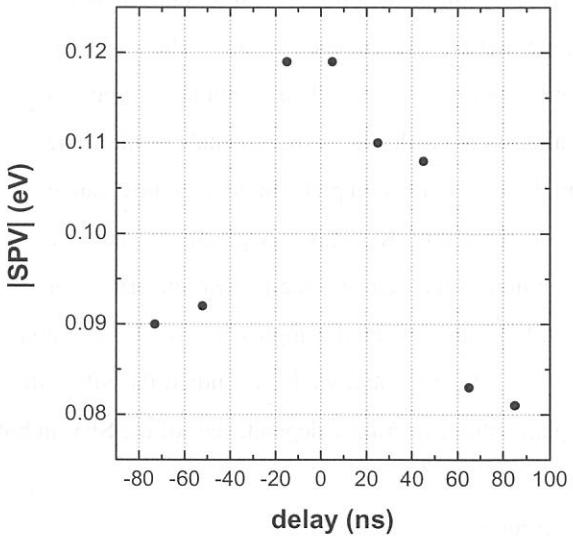

Figure 1. Time dependence of the SPV on an n-type GaAs.

Fig. 1 shows the measurement of the time dependence of SPV on n-type GaAs in the single bunch operation with different delays between the laser

and SR pulses. One can see the increase of the SPV around zero delay and it decreases gradually with time. We can also distinguish that the SPV lifetime is longer than 176 ns. Here we would like to emphasize that the laser pulses was not completely picked out to one by one ratio for a single SR-pulse because the rise time of the AO modulator were lager than 11ns. Although, a single pulse was not completely picked out, the pulse train of laser light was synchronized with an SR pulse.

The regenerative amplifier gave the laser light with the frequency of 10 to 300 kHz. The combination of this laser light and the gate system can provide TR-PES in the microsecond range. The gate circuit receives the photoelectron signal from the electron energy analyzer and the trigger signal from the laser system. The gate system can pick out the time-window for the time width in the range from 40 ns to 160 μs. The time resolution of this system is restricted by the time width of the photoelectron signals, which is about 0.1 μs. In Fig. 2 we present the TR-PES Ga-3d photoelectrons. The Ga-3d photoelectron spectrum without laser illumination is also shown for comparison. The frequency of the laser was 100 kHz. It can be seen that the Ga-3d photoelectron spectrum is shifted toward lower kinetic energies due to the SPV effects caused by laser illumination. It is also obvious that the shift value decreases with the delay time. The analyses in detail, such as the curve fitting of the core-level spectra and time constant of the SPV decay time, are now in progress.

To summarize, we have performed the time dependent experiments of the SPV effects on an n-type GaAs using the TR-PES. It was observed that the temporal change of the SPV effects in the range from nano-second to microsecond. These experimental results provide the better understanding for the dynamics of the SPV effects.

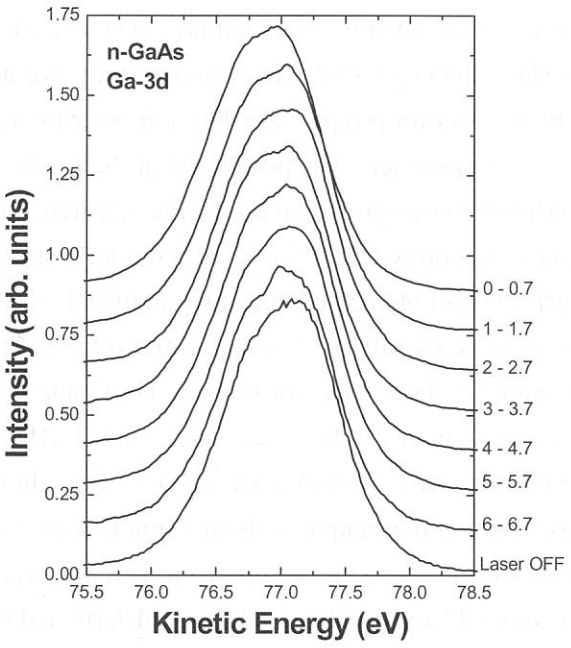

Figure 2. The time-resolved photoelectron spectra of the Ga-3d core-levels. Each figures of right side represents the pick out time in microsecond unit. The spectrum without laser illumination is shown for comparison.

References

[1] M. Kamada et al., UVSOR Activity Report, 1999, 180.

[2] S. Tanaka et al., UVSOR Activity Report, 2000, 154.

[3] S. Tanaka et al., Phys. Rev. B **64** (2001) 155308.

[4] S. Tanaka et al., UVSOR Activity Report, 2000, 152.

(BL6A2)

Surface photo-voltage effect on GaN(0001) studied by photoemission spectroscopy with the combination of SR and Laser

Kazutoshi Takahashi[A], Kousuke Hayakawa[B], Senku Tanaka[C], Junpei Azuma[D], Minoru Itoh[B], and Masao Kamada[E]

[A] *UVSOR Facility, Institute for Molecular Science, Okazaki 444-8585*
[B] *Department of Electrical & Electronic Engineering, Shinshu University, Nagano 380-8553*
[C] *The Graduate University for Advanced Studies, Okazaki 444-8585*
[D] *Department of Physics, Kyoto University, Kyoto 606-8502*
[E] *Synchrotron Light Application Center, Saga University, Saga 840-8502*

Surface photo-voltage (SPV) effects on semiconductor surface have been attracting considerable interest from the viewpoints of surface physics and practical applications for photo-electronic devices. Recently, several researchers have reported the SPV effects on Si(111) [1] or GaAs(100) [2] surfaces using the core-level photoemission spectroscopy with the combinational use of synchrotron radiation (SR) and laser. GaN has the large band-gap energy of 3.4 eV, thus it is expected to show the large SPV effect. In this study, we have performed the photoemission spectroscopy with SR and laser for p-type GaN(0001) in order to investigate SPV effects on GaN.

Experiment was performed at the beamline BL6A2, UVSOR Facility. The p-type Mg doped GaN(0001) was grown on a sapphire substrate with AlN buffer layer using MOVPE method. The hole concentration is 1.3×10^{17} cm^{-3} at room temperature determined by the Hall measurements. The clean surface was obtained by annealing in ultra-high vacuum at about 1000°C. X-ray photoelectron spectra showed Ga/N ratio of 1, indicating no loss of the nitrogen atom after the annealing. We used the Ti:Sapphire laser (Spectra-Physics, Hurricane) to cause the SPV effect. The output of the Ti:Sapphire laser was about 130 fs pulse duration and 1 kHz repetition rate. The third harmonic of the output from Hurricane ($h\nu$ = 4.66 eV) was used as the light source to cause the SPV effect. The diameter of the laser light at the sample is about 5 mm that covers the beam spot of SR. The Fermi level of the sample was determined by the comparison with a Au reference. It is found that the present sample shows the downward band-bending of 1.26 eV determined from the valence-band spectrum.

Figure 1. shows Ga 3d photoemission spectra of GaN(0001). Solid and dotted lines represent the spectra with and without laser irradiation, respectively. The intensity of the laser light is about 0.5 mW/cm^3. As shown in Fig. 1, the Ga 3d core-level shifts to the higher kinetic energy side under the irradiation of laser. It is also found that the spectral shape does not change with laser irradiation. In conjunction with our previous results for GaAs, it is considered that the observed peak shift originates from the SPV effect due to the spatial separation of electrons and holes excited by absorption of laser light in the space-charge region.

Figure 2 shows the dependence of the peak shift on the laser intensity. In Fig. 2, positive direction of peak shift corresponds to the shift to higher kinetic energies and the laser intensity of 100% corresponds to 50 mW/cm^2. As shown in Fig. 2, the peak shift due to the SPV effect increases with increasing laser intensity from 0.015% to about 1%. On the other hand, it is found that peak shift decreases with increasing laser intensity at the laser intensity above 5%, and finally Ga 3d peak shows

negative peak shift at the laser intensity of 50 and100 %. We found that the observed dependence on the laser intensity in the low laser intensity region less than 1% fits well with the theoretical relation between laser intensity and SPV effect which is described in detail elsewhere [3]. In this theoretical model, we assumed that the amount of the photo-excited carriers is in proportion with laser intensity and distribution of the surface state is uniform. It has been reported that this approximation is in good agreement with the experimental result of the SPV effects on p-GaAs(100). However, the dependence in the higher laser intensity region cannot be explained by the present simple formula. In order to fully explain the laser intensity dependence, the change of the surface electronic charge caused by many amounts of photo-excited carriers should be considered. Further investigations including the time-resolved measurement are needed to elucidate the SPV effects on GaN surface in detail.

In conclusion, we have performed the photoemission study for the SPV effects on p-GaN(0001) using synchrotron radiation and laser. It is found that Ga 3d core-level spectra show the peak shift due to the SPV effect. The dependence of the peak shift on the laser intensity at the laser intensity less than 0.5 mW/cm^2 can be explained by simple formula.

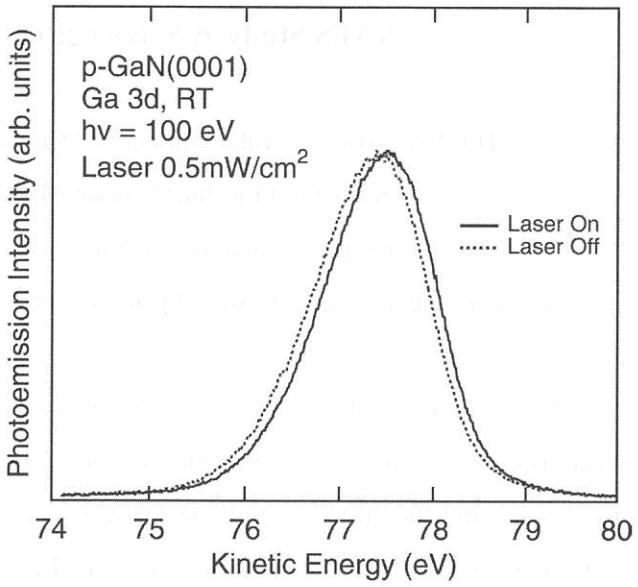

Figure 1. Ga 3d photoemission spectra with and without laser irradiation for p-GaN(0001).

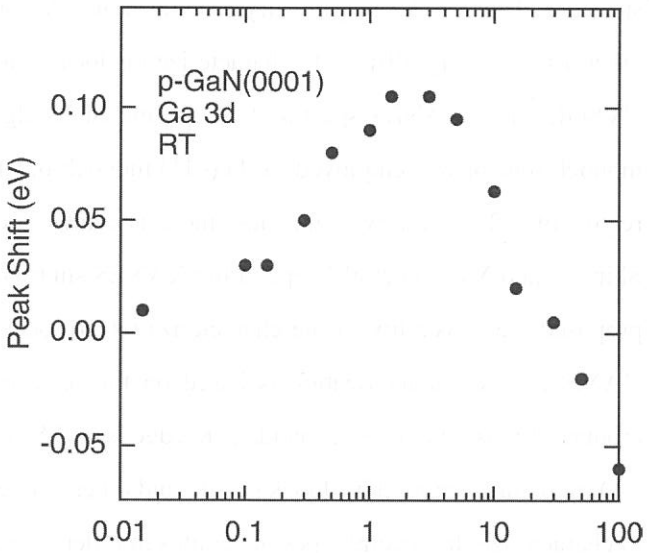

Figure 2. Laser intensity dependence of the peak shift due to the SPV effect on p-GaN(0001).

References

[1] J. P. Long *et al.* Phys. Rev. Lett. **64**, 1158 (1990).

[2] M. Kamada *et al.* Sur. Sci. **454-456**, 525 (2000).

[3] S. Tanaka *et al.* Phys. Rev. B **64**, 155308 (2001).

(BL7A)

XAFS Study at Si K-edge on Several Types of Zeolites

Hirofumi Aritani,* Yuko Fujimura,** Chikako Karatani,** Takayuki Murakami,**
Ken-ichiro Eguchi,** Masato Tamai,** and Atsushi Nakahira**

**Faculty of Engineering, Saitama Institute of Technology, Okabe, Saitama 369-0293, Japan.*;

***Faculty of Engineering & Design, Kyoto Institute of Technology, Sakyo-ku, Kyoto 606-8585, Japan.*

Silica-alumina (SiO_2-Al_2O_3) binary oxide is one of the typical compounds for use of fundamental materials or basic supports. Several types of silica-alumina materials such as aluminosicicates and mullites are present, and the structure of these materials is almost depend on the Si/Al ratio and heat-treated temperature. Zeolite materials with very low Si/Al ratios are well known as microporous ones, and have been applied widely to several engineering processes because of peculiar surface activity. Zeolites are open framework aluminosilicates consisting of SiO_4 and AlO_4 tetrahedra, interconnected *via* oxygen atoms. There are several types of zeolites (MFI, MOR, BEA, *etc.*) with original types of ordered framework structure. Thus the local symmetry around Si and Al ions in these zeolites is slightly different from each other. But it is very difficult to characterize the local structure around Si and Al ions. In BL7A beamline of UVSOR, clear XANES spectra at Al K- and Si K-edges have been obtained since YB_{66} double-crystal monochromator was employed.[1] KTP(011) monochromator gave more emission of soft X-ray source in the region of 1.2 - 2.1 keV,[2] and thus, more accurate XANES spectra can be obtained. In recent studies, Shimizu and Yoshida et al.[3] applied the XANES study to evaluate the local structure around Al ions. They proposed the possibility of the characterization of local structure by means of edge energy in Al K-edge XANES. This characterization is based on the relationship between the energy and the local structure around Al ions. On the other hand, Si K-edge XANES can give an information about the local symmetry of SiO_4 structure, reported by Tanaka et al.[3] and other workers. In our study, XANES at Si K-edge was applied to characterize the several types of zeolites in order to evaluate the possibility of characterization around Si atom. Another study of Al K-edge XAFS on these materials will be reported elsewhere.[5]

For zeolite samples, H-MOR (synthesized, [I]Si/Al_2=10 and [II]Si/Al_2=18), H-MFI ([I]Tosoh JRC-Z-1000H (Si/Al_2=1000) and [II]Tosoh HSZ-890H0A (Si/Al_2=1880)), H-BEA (JRC-HBEA-25, Si/Al_2=25) were employed. Quartz, Silica-gel, and silicic acid (SiO_2•xH_2O) were used for silica reference samples. The XANES at at Al K- and Si K-edges were measured in BL7A of UVSOR in a total electron yield mode at ambient temperature by using KTP(011) monochromator.

Figure 1 (Top) shows the Si K-edge XANES spectra of reference Si compounds. SiO_4 tetrahedra with T_d symmetry are dominant in quartz. The SiO4 tetrahedra in silica-gel and silicic acid contain several types of vacancy sites and/or hydrated species partly, and thus, mean symmetry of SiO_4 local structure is

lower than that of T_d structure in quartz. The prominent peak in XANES centered at 1853 eV is due to $1s$ - $3p$ electron in Si atom. In symmetric SiO_4 (T_d) tetrahedron, monolithic state of $3p$ band energy is present. In case of lower symmetry, the band should be broader, and intensity of the prominent peak should be lower. The results of XANES spectra indicate the structural feature about the lower symmetry in silica-gel and silicic acid than that in quartz. This structural result can hardly be obtained by means of other spectroscopy.

Middle of the figure shows the XANES of MOR zeolites. These results show the independence between the Si/Al atomic ratio and local symmetry in SiO_4 tetrahedra. These tetrahedra have low symmetry than silicic acid. Thus it is clear that local structure around Si in MOR framework has low symmetry by formation of mordenite structure with three-dimensional micropore. This feature is also seen in the XANES results of H-MFI. In contrast, intensity of the peak in H-BEA (with thenty-menbered ring in local framework) is larger than that in silicic acid, indicating the higher symmetry than in MOR or MFI. From these results, local symmetry around Si atom in zeolites depends on the framework structure of zeolites. It is likely that small pore size(s) and low-membered rings in the framework tend to give low symmetry in SiO_4 tetrahedra. Detailed characterization on zeolites and silica-alumina materials are now in progress. This work is partly supported by Asahi Glass Fundation.

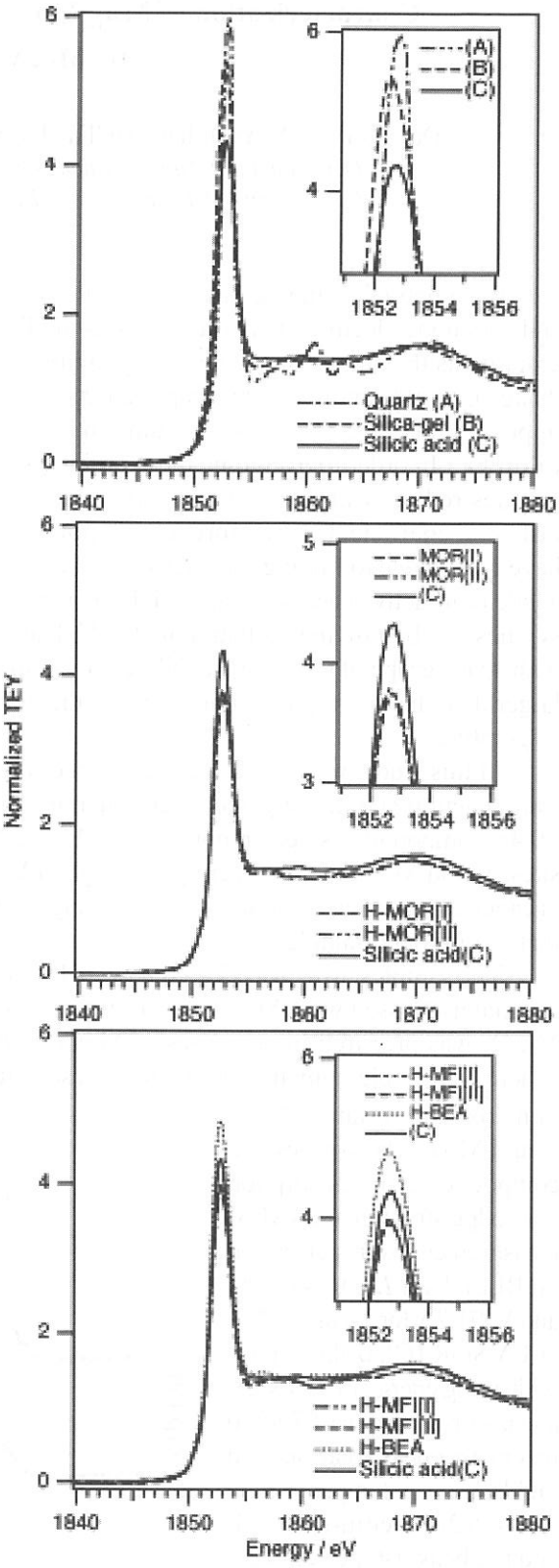

Fig. 1 Si K-edge XANES spectra of reference silica-type materials (top), H-MOR (middle), H-MFI, and H-BEA zeolites (bottom).

References

1. T. Kinoshita et al., *J. Synchrotron Rad.*, 5 (1998) 726.
2. Y. Takata et al., *J. Synchrotron Rad.*, 8 (2001) 351.
3. K. Shimizu et al., *Chem. Commun.*, **1996**, 1681.; H. Yoshida et al., *UVSOR Activity Report*, **1999**, 148.
4. T. Tanaka et al., *J. Phys. IV (Colloq. C2)*, **1997**, 913.
5. H. Aritani et al., *Chem. Mater.*, in press.

(BL7A, BL8B1)

Characterization of $Mn_{1-x}Mo_{2x}V_{2(1-x)}O_6$ as anode for Li Secondary Battery by Mo, V and Mn L-XANES

Daishu HARA, Yoshiharu UCHIMOTO, Hiromasa IKUTA, and Masataka WAKIHARA
Department of Applied Chemistry, Graduate School of Science and Engineering, Tokyo Institute of Technology, 2-12-1 Ookayama, Meguro-ku, Tokyo 152-8552, Japan

Commercial available lithium ion batteries consist of two Li-intercalation materials in both for cathode and for anode electrode materials. One is the lithiated transition metal oxide as the cathode, and the other is graphite as the anode. However, the graphite anode suffers from small capacity per unit weight (about 350 $Ahkg^{-1}$). Furthermore to attain rapid charge-discharging, the rate capability of graphite material needs to be improved, because of its poor lithium ion diffusion coefficient which is much lower than that of $LiCoO_2$ or $LiMn_2O_4$. In order to overcome these problems about the capacity and rate performance of graphite material, it is desired to synthesize novel anode materials having large capacity and high rate with high lithium ion diffusion coefficient. Therefore, considerable amount of attempts such as oxide, nitrides and intermetallics have been made to finding out alternative anode materials in place of graphite anode. Among them, the oxide anode is attractive because of their high capacity. In previous paper, we proposed novel oxide anode of MnV_2O_6 synthesized by polymer gellation method. The MnV_2O_6 compound had monoclinic brannerite type structure with space grope of *C2/m*, and exhibited reversible capacity of about 800 $Ahkg^{-1}$ which is more than two times larger than that of graphite. Furthermore, the brannerite MnV_2O_6 compound had better rate property than that of graphite.

In this study, we synthesized Mo doped MnV_2O_6 ($Mn_{1-x}Mo_{2x}V_{2(1-x)}O_6$ (x=0, 0.4)) by conventional solid-state reaction and investigated electrochemical properties. The crystal structure of $Mn_{1-x}Mo_{2x}V_{2(1-x)}O_6$ ($0 < x < 0.45$)compound has been reported that Mn and Mn vacancies are randomly distributed over the original Mn sites, V and Mo randomly occupy the original V sites in the parent MnV_2O_6. Therefore, we expect that these vacancies on Mn sites might work effectively for Li ion diffusion, which leads to higher rate performance than that of un-doped sample.

The samples, $Mn_{1-x}Mo_{2x}V_{2(1-x)}O_6$ (x=0, 0.4) were prepared by conventional solid-state reaction. The starting materials used were Mn_2O_3, V_2O_5 (99.9 % Soekawa chemicals) and MoO_3 (99.9 % Soekawa chemicals). Mn_2O_3 was prepared by pyrolysis of $MnCO_3$ (99.9 % Soekawa chemicals) at 600°C for 1day in air atmosphere. The stoichiometric amounts of these materials were mixed and ground in an agate mortar. To determine oxidation states of Mn, V and Mo on the synthesized compounds, X-ray absorption near edge structure (XANES) measurements were performed on BL8B1 for *L*-edges of Mn and V, BL7A for *L*-edge of Mo at UVSOR (Okazaki, Japan) with a ring energy of 750 MeV and a stored current of 70-220 mA in a mode of total electron yields at room temperature.

CR2032 coin-type cell and the beaker-type cell were selected for charge-discharge measurement. The working electrode was fabricated by doctor-blade technique on a copper-foil, spreading paste

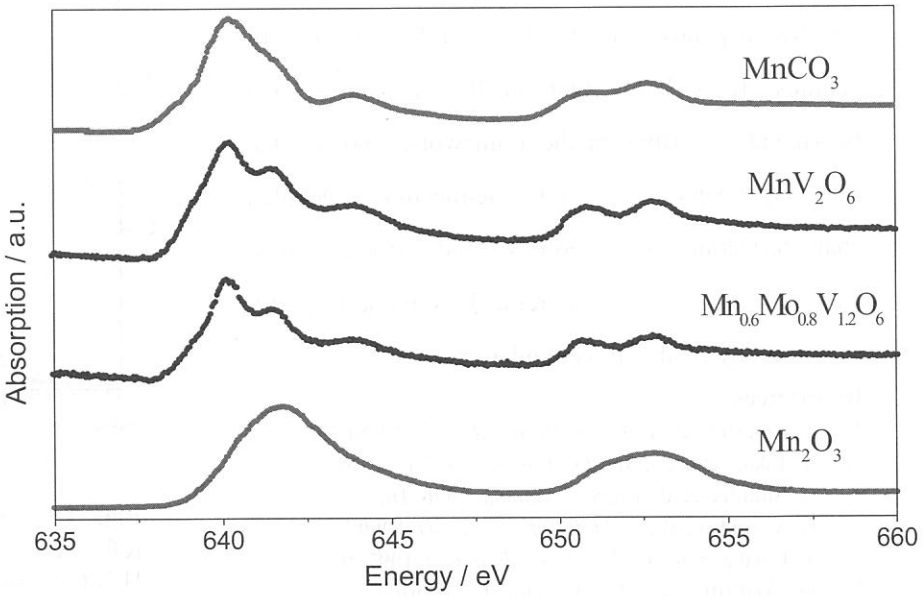

Fig.1. Mn *L*-edge XANES spectra for $Mn_{1-x}Mo_{2x}V_{2(1-x)}O_6$ (x=0, 0.4), $MnCO_3$ and Mn_2O_3.

consisted of 10 wt% polyvinylidenefluoride (PVDF) binder, 20 wt% acetylene black (conductive agent), 70 wt% active material of $Mn_{1-x}Mo_{2x}V_{2(1-x)}O_6$ (x=0, 0.4) and appropriate amount of n-metyl-2-pyrrolidinone (NMP) as solvent. After evaporating of NMP solvent in a furnace at 110°C in air atmosphere for 1day, the electrodes were roll-pressed and cut into disks. Lithium metal was used as the counter electrode. The electrolyte was 1M $LiClO_4$ dissolved in ethylene carbonate (EC) / diethyl carbonate (DEC) (volume ratio of 1:1) (received from Tomiyama pure chemical industries LTD.). All the cell assembling (Li | 1 M $LiClO_4$ in EC / DEC | $Mn_{1-x}Mo_{2x}V_{2(1-x)}O_6$ (x=0, 0.4)) was operated in a glove box filled with argon gas. The electrochemical measurements were carried out galvanostatically at various current densities at room temperature. Relaxation time between charge and discharge was set at 20 minutes.

L-edge XANES measurements of Mn, V and Mo for synthesized powdered $Mn_{1-x}Mo_{2x}V_{2(1-x)}O_6$ (x=0, 0.4) were carried out in order to investigate the oxidation states of Mn, V and Mo in the compounds. Fig. 1 shows the Mn L_{III}-edge XANES spectra of $Mn_{1-x}Mo_{2x}V_{2(1-x)}O_6$ (x=0, 0.4) together with those of $MnCO_3$ (Mn^{2+}) and Mn_2O_3 (Mn^{3+}) as references. The spectra in the figure show strong absorption features due to the spin-obit splitting of the Mn 2*p* core hole around 640 eV, and they correspond to the transition from $Mn2p^63d^n$ to $Mn2p^53d^{n+1}$. Mn L_{III} absorption peaks of $MnCO_3$ and Mn_2O_3 are apparent about 640 eV and 642 eV, respectively. This result indicates that the Mn L_{III} absorption edge shifts to higher energy with increasing the oxidation state of manganese. Both synthesized MnV_2O_6 and $Mn_{0.6}Mo_{0.8}V_{1.2}O_6$ exhibit the same feature of the spectra. Since the spectra of the edge jumps for $MnCO_3$ and $Mn_{1-x}Mo_{2x}V_{2(1-x)}O_6$ (x=0, 0.4) are very close to each other, Mn ions exist as close to Mn^{2+} in $Mn_{1-x}Mo_{2x}V_{2(1-x)}O_6$ (x=0, 0.4) compound. However, small peaks which correspond to Mn^{3+} are observed around 642 eV. Accordingly, small amount of Mn^{3+} beside main Mn^{2+} may include in the solid solution $Mn_{1-x}Mo_{2x}V_{2(1-x)}O_6$ (x=0, 0.4).

V L_{III}-edge XANES spectra of V_2O_5(V^{5+}), $VOSO_4$(V^{4+}) and $Mn_{1-x}Mo_{2x}V_{2(1-x)}O_6$ (x=0, 0.4) presented in Fig. 2 illustrate that the valence of V in $Mn_{1-x}Mo_{2x}V_{2(1-x)}O_6$ (x=0, 0.4) should be +5, because of very similar behavior of $Mn_{1-x}Mo_{2x}V_{2(1-x)}O_6$ (x=0, 0.4) and V_2O_5.

In the same way, Mo L_{III}-edge spectra of MoO_3 (Mo^{6+}) and $Mn_{0.6}Mo_{0.8}V_{1.2}O_6$ in Fig. 3 designate that the Mo oxidation state is +6 in $Mn_{0.6}Mo_{0.8}V_{1.2}O_6$ compound. In the absorption of Mo L_{III}-edge of MoO_3 and $Mn_{0.6}Mo_{0.8}V_{1.2}O_6$, the spectra split into two peaks due to splitting of d-orbital. In a pseudo-octahedral coordination, the first peak (t_{2g}) dominates, while in a pseudo-tetrahedral coordinates, the second peak (t_2) dominates. Consequently, Mo is coordinated pseudo-octahedrally with oxide ions in brannerite structure of $Mn_{0.6}Mo_{0.8}V_{1.2}O_6$.

In order to investigate the electrochemical performance of $Mn_{1-x}Mo_{2x}V_{2(1-x)}O_6$, (x=0, 0.4), the cells was subjected to charge-discharge cycles in constant current mode of 0.2 C. Cutoff voltage was set at 0.01 V and 2.50 V. The insertion process of Li into the active materials is defined as charge process, while the reverse holds for extraction process. The first Li insertion in MnV_2O_6 shows a large capacity of about 1000 $Ahkg^{-1}$ and that of $Mn_{0.6}Mo_{0.8}V_{1.2}O_6$ is about 1400 $Ahkg^{-1}$, these capacities are much larger than that of graphite (about 350 $Ahkg^{-1}$). Furthermore, $Mn_{0.6}Mo_{0.8}V_{1.2}O_6$ has larger charge-discharge capacity than that of MnV_2O_6.

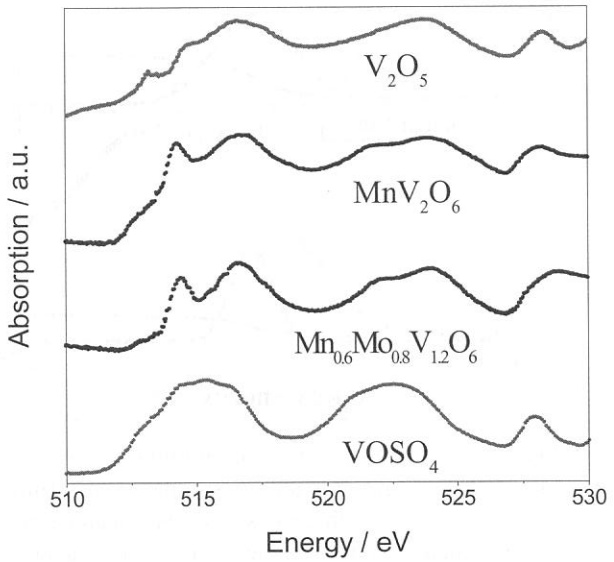

Fig.2. V *L*-edge XANES spectra for $Mn_{1-x}Mo_{2x}V_{2(1-x)}O_6$ (x=0, 0.4), V_2O_5 and $VOSO_4$.

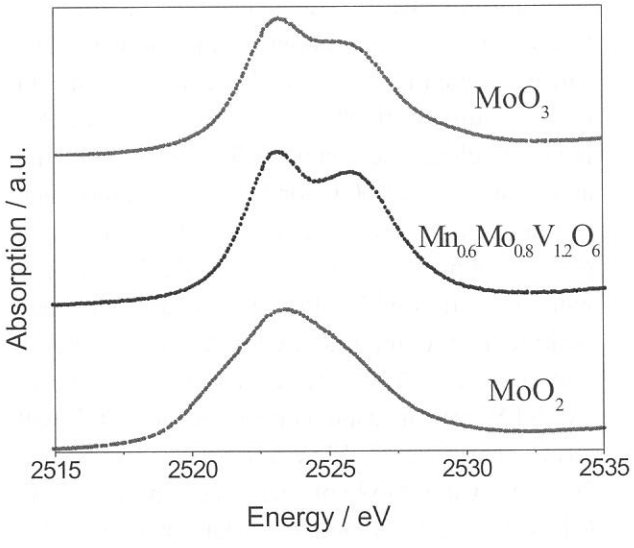

Fig.3. Mo *L*-edge XANES spectra for $Mn_{0.6}Mo_{0.8}V_{1.2}O_6$, MoO_2 and MoO_3.

(BL7A)

Al K-edge XANES of Surface Treated Natural Graphite by Aluminum

Sung-Soo KIM, Yoshihiro KADOMA, Hiromasa IKUTA, Yoshiharu UCHIMOTO and Masataka WAKIHARA

Department of Applied Chemistry, Graduate School of Science and Engineering, Tokyo Institute of Technology, 2-12-1 Ookayama, Meguro-ku, Tokyo 152-8552, Japan

Natural graphite can be thought as promising candidates for anode in lithium ion battery in terms of cost. However, it has been difficult to control the key parameters of carbon that affect their characteristics for use as anode because carbon materials have large variations in their electrical properties. Furthermore, it has been known that natural graphite flakes cannot deliver reasonable electrochemical performances such as reversible specific capacity, cycle life, rate capability, etc. Since an electrochemical reaction takes place on the surface of electrode, the control of surface properties can be thought as one of the critical factors. Therefore it needs to consider improvement by control surface properties that affect the electrochemical property of natural graphite. In this report, we investigated the influence of surface and/or structure modification by aluminum compound on electrochemical performances of natural graphite as anode in lithium ion battery. Furthermore the correlation between the local structure of amorphous-like aluminum oxide and electrochemical performance will be discussed with the results of Al *K*-edge XANES measurement.

The Aluminum-treated samples were prepared by aluminum tri-etoxide($Al(OC_2H_5)_3$, Soekawa Chemicals) treatment on NG2(Kansai chemicals). The NG2 graphite was soaked in ethyl alcohol solution containing 10wt% aluminum tri-etoxide, followed by ultrasonic treatment for 3 hours, filtration and drying above 200°C for 1 day in air atmosphere to remove residual of alcohol. On the other hand, pristine sample also prepared by alcohol soaking without Al tri-etoxide, ultrasonic treatment and heat treatment for comparison with Al-treated one. Al *K*-edge X-ray Absorption Near Edge Structure (XANES) were measured on BL7A at UVSOR with a ring energy of 750MeV and a stored current of 70-220mA in a mode of total electron yields. The KTP double crystal monochromator was used. The monochromator scanning angle step width was 0.003°, which corresponds to *ca.* 0.1eV at 1560eV.

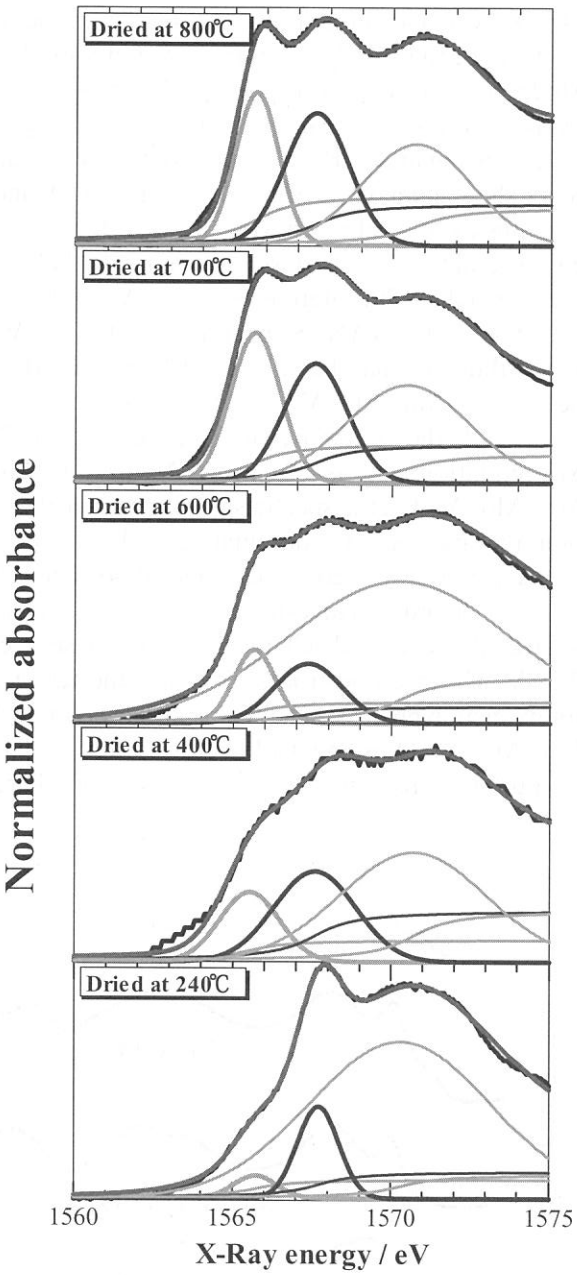

Fig.1. Al *K*-edge spectrum of alumina on the surface of natural graphite and its simulated spectrum which composed of three sets of Gaussian and arctangent function. Each samples were calcined at 800 ℃, 700℃, 600℃, 400℃ and 240℃.

The absolute energy scale was calibrated by using literature value of Al *K*-edge in α-Al_2O_3. The curve fitting for obtained XANES spectra was carried out with the REX2000 software by Rigaku.

The electrochemical measurement was carried out with the use of CR2032 coin-type cell. The working electrodes were prepared by doctor-blade technique on copper foil, spreading paste consisted of 10wt% polyvinylidenefluoride(PVdF) as binder, 10wt% acethylene black as conductive agent, 80wt% treated or pristine NG2 graphite and appropriate amount of 1-methyl-2-pyrrolidinone(NMP) as solvent. After drying of NMP solvent, the electrode was cut into disk (the weight of all sample was controlled around 4mg). Lithium metal was used as counter electrode. The electrolyte used was 1M $LiClO_4$ dissolved in ethylene carbonate(EC)/diethylene carbonate(DEC)(volume ratio 1:1). The cell assembly was operated in a glove box filled with argon gas. The specific capacity was measured by galvanostatically with current density 70mA/g, 175mA/g and 350mA/g in the ranges 0 to 2.5V on Hokuto Denko charge-discharge tester.

To investigate the correlation of Electrochemical performances with the local structure of alumina, we measured the Al *K*-edge XANES and electrochemical performance, especially in high rate Li intercalation/deintercalation to clear comparison, of samples which surface treated in different heat treatment temperature, because the structure of amorphous aluminum oxide is sensitive the preparation temperature. Since the accurate structures of alumina are not known except q-Al_2O_3, the structural analysis of amorphous-like alumina is not so simple. Recently, Al *K*-edge XANES measurement combining quantitative analysis was proposed to estimate the local structure of alumina[1]. It is well known that the XANES spectra of AlO_4 tetrahedra and AlO_6 octahedra were clearly identified in aluminum oxide. A white line 1566eV is characteristics of AlO_4 compound and the peaks at 1568eV and 1572eV can be assigned to AlO_6 octahedral compound. Normalized XANES spectra with the calcination temperature of the Al-treated graphite samples together with reference sample of α-Al_2O_3 (corundum) are shown in Fig. 1. The peak ratio of tetrahedral AlO_4 to octahedral AlO_6 in the XANES spectrum of $f¿$-Al_2O_3 (corundum) in our measurement is 7:93, which is in good agreement with that of Reference 1. We can observe a peak at 1565eV due to AlO_4 and two peaks at 1567eV and 1570eV due to AlO_6 and the difference of peak position between AlO_4 and AlO_6 was about 2eV. In addition, the relative intensity of AlO_4 and AlO_6 was varied with the calcination temperature. In the range of this study up to the 500°C of calcination temperature, the portion of AlO_4 increased, like that of previous report , this alumina phase can be thought as boehmite + g type alumina. From the above results of XANES of each sample, we can determine that the variation of local structure of aluminum oxide with calcinations temperature, and the influence of local structure of aluminum oxide on the electrochemical performances of graphite can be observed in Fig. 2. In Fig. 2 shows the charge-discharge profiles of pristine and Al-treated graphite samples, which calcined 300 and 500°C, during the first cycle and 30th cycle at current density is 350mA/g and cut-off voltage is 0.0-2.5V. Comparing the profiles of the potential curves of Al-treated sample with those of pristine sample, we could not observe the remarkable changes in electrochemical reactions from initial profiles. However, Fig. 2 clearly indicates that the cycle performance was improved by the Al-treatment and calcination temperature.

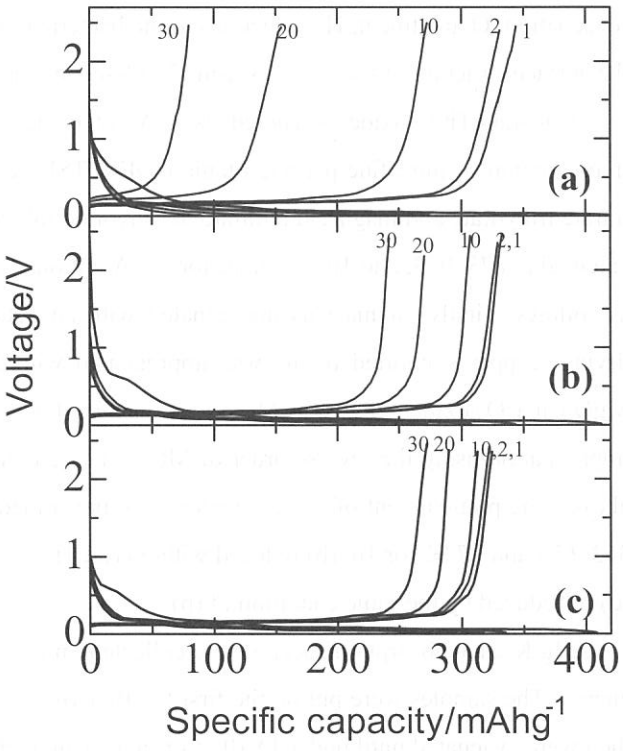

Fig.2. Voltage profile of 1,2,10,20,30th cycle of (a)pristine, (b)Al-treated (calcined at 300℃) and (c)Al-treated(calcined at 500℃) natural graphite electrode.

Refedences

[1] K.Shimizu, Y.Kato, T.Yoshida, H.Yoshida, A.Satsuma and T.Hattori, *Chem. Commun.*,**1999**, 1681 (1999).

(BL7A)

Mg K-edge XANES study of Cu-MgO/TiO_2 oxide for bactericidal materials

Tomomi Kosaka, Ayano Yamada, Yoko Hayashi and Sadao Hasegawa

Department of Chemistry, Tokyo Gakugei University, Koganei, Tokyo, 184-8501

Recently, many inorganic oxides (Ag-zeolite, Zn-hydroxyapatite, TiO_2...and so on) for bactericidal material were developed and investigated by the researchers of university and industry [1~3]. The mechanism of bactericidal effects was suggested as follows. ①The inhibition effect of noble metal ion(Ag^+, Cu^{2+}, Zn^{2+}...that is "Soft acid") which was dissolved from the materials to SH group of enzyme. ②The strong oxidation property of active oxygen species (hydroxyl radical, super oxide, hydrogen peroxide), was produced on the surface of materials under photo irradiation in the case of semiconductor oxide. However, its detailed explanation was still unclear and both suggestions were reliable. In our previous study[4], we prepared TiO_2-SiO_2-MgO tertiary oxide and investigated the OH radicals formation on that of surface contacted with water using the spin-trapping method. In the following experiment, we also investigated the effect of evacuation temperature to OH radical formation. The thermally reduced surface was formed on the TiO_2-SiO_2-MgO oxide by the evacuation at high temperature (over 773K) and the formation of OH radicals was increased. However, the stable electron state was formed by the thermally reduction (Cu^{2+}→Cu^+ or Cu^0) in the case of TiO_2-SiO_2-CuO. The quantity of active oxygen species was decreased by the results of the inhibition of hydrogen abstraction reaction. From these findings and background, we prepared Cu-MgO/TiO_2 oxides and investigated the effects of pretreatment (evacuation, O_2 treatment, H_2 reduction) to the bactericidal function in progress. In this report, we investigated the surface structure of these oxides using Mg K-edge X-ray Absorption Near Edge Structure analysis.

Cu-MgO/TiO_2 oxides (denoted as C-M/T) containing 25wt% Cu and 25wt% Mg were prepared by impregnation of ultra fine particle titania (IDEMITSU KOSAN, IT-S) with an aqueous solution of copper(Ⅱ) nitrate trihydrate and magnesium nitrate hexahydrate followed by drying in air at 383K for 24h. Then, they were calcined at 873, 973, and 1073K in air for 1h. Additionally, we also prepared two different kinds of these oxides as follows. Firstly, titania was impregnated with an aqueous solution of copper(Ⅱ) nitrate trihydrate. After drying, copper supported titania was impregnated with a magnesium nitrate hexahydrate solution, and then MgO/Cu/TiO_2 oxide(denoted as MC/T) was obtained. Cu/MgO/TiO_2 oxide (denoted as CM/T) was prepared by impregnation using the reverse order of MC/T. These oxides were calcined at the same temperature mentioned above. The pretreatment of these samples were performed in a vacuum cell: the samples were (a) evacuated at 383, 673 and 773K for 1h, (b) reduced with 50Torr H_2 for 1h at 473K, (c) oxidized in 50Torr O_2 for 1h at 473K, (d) re-reduced by the same condition of (b).

Mg K-edge absorption spectra were collected on the BL-7A facility at UVSOR, IMS with 750MeV of ring energy. The samples were put on the first Cu-Be dynode of electron multiplier using adhesive carbon tape, and then were evacuated until under $1X10^{-7}$ torr in a vacuum chamber. The spectrum was recorded in a total electron yield mode at room temperature using $KTiPO_4$ [KTP](011) double crystal monochromator (2d=10.954nm).

Mg K-edge XANES spectra of reference samples and MgO/TiO_2 calcined at 873 and 1073K(previous data)

[5] were shown in Fig.1. Fig.2 was also indicated that those of prepared samples (C-M/T, CM/T and MC/T) at various temperatures. It was found that the formation of $MgTiO_3$ was inhibited by Cu addition and 6-fold coordinated Mg (rock salt type structure) predominantly existed in all prepared samples. These results were corresponded to our previous data[5]. However, the characteristic difference of the spectra was detected in the samples calcined at under than 973K. Relative intensity of the peak around 1306eV in CM/T was more weaken than those of the other samples. It was indicated that the environmental structure of Mg was affected by the preparation and the effect of Cu addition was varied by the supporting method. Unfortunately, the effects of pretreatment to the XANES spectra were not shown in this experiment. The mechanism of bactericidal materials was so complex, theoretical and experimental efforts were more need. We believed that XAFS analysis was effective method to clarify this problem.

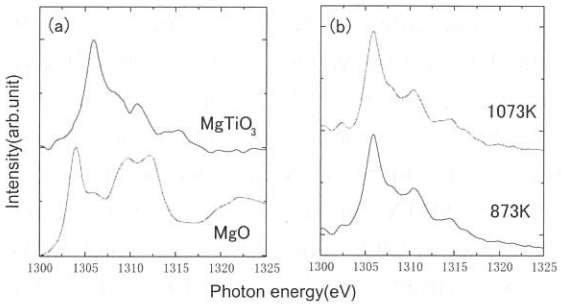

Fig.1 Mg K-edge XANES spectra of (a) reference samples and (b) 25wt% MgO supported titania

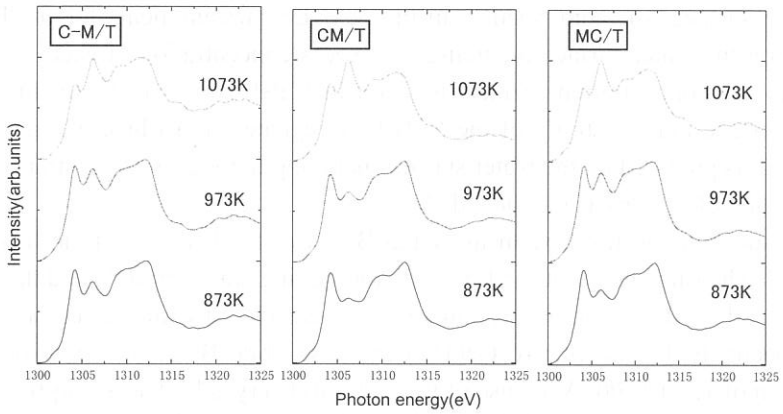

Fig.2 Mg K-edge XANES spectra of Cu and MgO supported titania

Acknowledgements

This work was supported by Grant-in-Aid for Scientific Research (S.H. and T.K.) from Ministry of Education, Culture, Sports, Science and Technology of Japan. T.K. also appreciated to INAMORI foundation.

References

[1] H.Kourai, Y.Manabe, Y.Yamada, J. Antibact. Antifung. Agents, **22**(10),(1994)595.

[2] Q.L.Feng, T.N.Kim, J.Wu, E.S.Park, J.O.Kim, D.Y.Lim and F.Z.Cui, Thin Solid Films, **335**(1998)214.

[3] Y.Kikuchi, K.Sunada, T.Iyoda, K.Hashimoto and A.Fujishima, J.Photochem.Photobiol.A:Chem., **106**(1997)51.

[4] A.Ikuo, M.Takagi, N.Kabasawa, Y.Yoshinaga, S.Teratani and S.Hasegawa, Appl.Surf.Sci., **121/122**(1997)513.

[5] T.Kosaka, A.Yamada, A.Miyaji, M.Shiraishi, and S.Hasegawa, UVSOR activity report 2000, 162.

(BL7A)

Characterization on the Surface of Polymer Ultra Thin Films Impregnated with Ruthenium-Polybipyridine Complex by XAS

Shuji MATSUO[1*], Tsutomu KURISAKI[2], Hisao YAMASHIGE[2], and Hisanobu WAKITA[1,2]

[1]*Advanced Materials Institute, Fukuoka University, Nanakuma, Jonan-ku, Fukuoka 814-0180, Japan*
[2]*Department of Chemistry, Faculty of Science, Fukuoka University, Nanakuma, Jonan-ku, Fukuoka 814-0180, Japan*

*Corresponding author: mashu23@hotmail.com

Poly(methyl methacrylate) (hereafter, PMMA) ultra thin films impregnated with (N,N′-di(hexadecyl)-2,2′-bipyridine-4,4′-dicarboxyamide)-bis(2,2′-bipyridine)ruthenium(II) diperchlorate complex (denoted as RuBP) have been prepared, and the characterization has been investigated by the X-ray absorption spectroscopy (XAS) [1]. So far, it was found from Ru L_3-edge, Cl K-edge, and Br L_3-edge X-ray absorption near-edge structure (XANES) spectra that (1) the RuBP complexes are impregnated only a single-side of the PMMA thin film, resulting that it gives hydrophilicity due to the RuBP complexes; (2) the Cl K-edge peak of ClO_4^- ions which are counter anions in RuBP complex is also observed in the Ru L_3-edge XANES spectrum; and (3) the intensity ratio between the peaks of Cl K-edge and Ru L_3-edge changes in the film-prepared conditions on the water surface, suggested that the surface of the RuBP-impregnated thin film chooses the anion on a water surface, for example ClO_4^- and OH^- ions. The ion-selectivity of the surface was confirmed from the XANES measurements for the RuBP-impregnated thin films prepared on the water surface including the excess concentration of each of ClO_4^-, Cl^-, and Br^- ions, compared with the concentration of the ClO_4^- ion in RuBP solution [2]. In this study, in order to investigate further surface ion-selectivity of the RuBP-impregnated thin films, we measured the XANES spectra for the thin films prepared on the water surface including the excess concentration of each of BrO_3^-, SO_4^{2-}, SO_3^{2-}, $S_2O_3^{2-}$, and SCN^- ions as mentioned above.

The X-ray absorption spectra were measured at BL7A of the UVSOR in the Institute of Molecular Science, Okazaki [3]. The ring energy of the UVSOR storage ring was 750 MeV and the stored current was 110–230 mA. S K- and Ru $L_{2,3}$-edge absorption spectra were recorded in the regions of 2420-2540 and 2800-3000 eV, respectively, by use of two Ge(111) crystals, while Br $L_{2,3}$-edge absorption spectra were recorded in the region of 1550-1700 eV by use of two KTP(011) crystals. The absorption was monitored by the total electron yield using a photomultiplier. The RuBP solution and RuBP-impregnated polymer thin film were prepared by the procedure as described elsewhere [1,4], here, each anion was in advance added to water. These anions were added as sodium salt, and the molar quantity of these anions was 50000 times that in the RuBP solution normally dropped on the water surface. The thin films were directly attached to carbon adhesive sheets, and the reference materials, for example powder of each sodium salt, were spread on the sheets. Each sheet was adhered to the first dynode of the photomultiplier.

The Ru L_3-edge XANES spectra for the RuBP-impregnated thin films prepared on the water surface including the excess concentration of each of BrO_3^-, SO_4^{2-}, SO_3^{2-}, $S_2O_3^{2-}$, and SCN^- ions are shown in Fig. 1 along with that of the RuBP powder and normal RuBP-impregnated thin film. The photon energy is calibrated by setting the Ru L_3-edge peak of the Ru metal to 2838.0 eV. The spectra are normalized to the Ru L_2-edge peak. In all the thin films, no peak A assigned to the Cl K-edge of ClO_4^- ion appears in the XANES spectra, though it appears in those of the RuBP powder and normal RuBP-impregnated thin film. This result suggests that few ClO_4^- ions exist at the RuBP-impregnated surface of the thin film, and another anion interacts with that instead. The S K-edge and Br L_3-edge XANES spectra for those thin films are

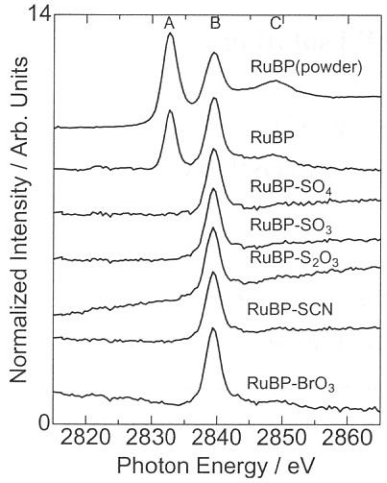

Fig. 1. Ru L_3-edge XANES spectra.

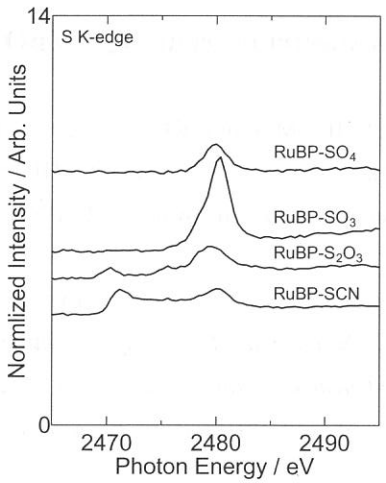

Fig. 2. S K-edge XANES spectra.

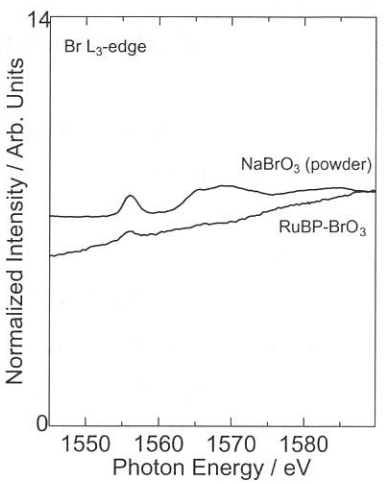

Fig. 3. Br L_3-edge XANES spectra.

shown in Figs. 2 and 3. The XANES spectra for the sodium salts of the S compounds as reference samples are presented in Fig. 4, and that of $NaBrO_3$ is also depicted in Fig. 3. The photon energy for the S K-edge and Br L_3-edge is calibrated by the references of Refs. 5 and 6, respectively. The spectra in Figs. 2 and 3 (only RuBP-BrO_3) are multiplied by the coefficient when the Ru $L_{2,3}$-edge XANES spectra are normalized to the Ru L_2-edge peak, that is, their spectra is comparable in the intensity with that of the Ru L_3-edge. In Figs. 2 and 3, all the anions exist as counter ions at the RuBP-impregnated surfaces of the thin films, though the peak intensity for the ClO_4^- ion in the normal RuBP-impregnated thin film is larger than that of all the anions except for RuBP-SO_3. The RuBP-impregnated surfaces of the thin films may be thus suggested to predominantly interact with another anion rather than BrO_3^-, SO_4^{2-}, $S_2O_3^{2-}$, and SCN^- ions. However, it is not understood why the SO_3^{2-} ions are predominantly adsorbed to the RuBP-impregnated surfaces of the thin film, compared with the other anions, and the peak positions (2480 eV) of RuBP-SO_3, -S_2O_3, and -SCN are similar to that of RuBP-SO_4, though the feature characteristic of each spectrum for RuBP-SO_3, -S_2O_3, and -SCN still remain. This will be clarified by progressing this study furthermore. In conclusion, it is found that the chemical state of the RuBP-impregnated surfaces of the thin film changes by anion added in advance to water.

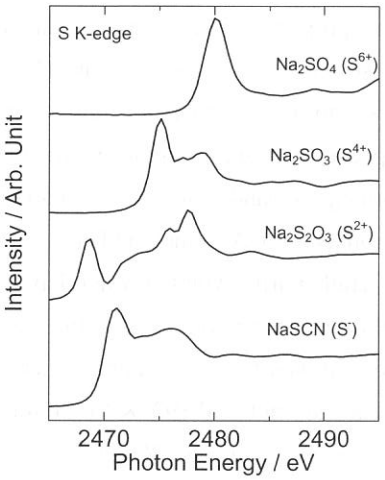

Fig. 4. The S K-edge XANES spectra for the sodium salts of the S compounds as reference samples

This study is supported by the Advanced Materials Institute of Fukuoka University.

References

[1] S. Matsuo, T. Nakano, S. Yamada, T. Matsuo, and H. Wakita, *J. Electron Spectrosc. Relat. Phenom.*, **113**, 193 (2001).

[2] S. Matsuo, S. Yamada, T. Matsuo, and H. Wakita, *Anal. Sci.*, (2002) *in press*.

[3] T. Murata, T. Matsukawa, S. Naoè, T. Horigome, O. Matsuodo, and M. Watanabe, *Rev. Sci. Instrum.*, **63** 1309 (1992).

[4] S. Yamada, Y. Tanaka, M. Kawazu, and T. Matsuo, *Supramol. Sci.*, **5** 379 (1998).

[5] H. Sekiyama, N. Kosugi, H. Kuroda, and T. Ohta, *Bull. Chem. Soc. Jpn.*, **59**, 575 (1986).

[6] T. Matsukawa, H. Okutani, and T. Kinoshita, *UVSOR Activity Reports*, 140 (1999).

(BL7A)

Zn-L_3 absorption spectrum from MgO-ZnO solid solutions

Teruyasu MIZOGUCHI [A], Masahiro KUNISU [A], Masafumi MATSUI [A],
Isao TANAKA [A], Hirohiko ADACHI [A], Tomoko YOSHIDA [B], Hisao YOSHIDA [C],
Shang-Di MO [D] and Wai-Yim CHING [D]

[A] *Department of Materials Science and Engineering, Kyoto University, Sakyo, Kyoto 606-8501, Japan*
[B] *Center for Integrated Research in Science and Eng., Nagoya University, Nagoya, 464-8603, Japan*
[C] *Department of Applied Chemistry, Nagoya University, Nagoya, 464-8603, Japan*
[D] *Department of Physics, University of Missouri-Kansas City, Kansas City, Missouri 64110-2499, USA*

Ceramic solid solutions are widely used not only for functional materials but also for engineering materials. Properties of the ceramic materials are dramatically changed by the kind of the doped solute. In order to control the properties intelligently, detailed knowledge of local structures around solutes is indispensable. X-ray absorption near edge structure (XANES) and electron energy loss near edge structure (ELNES) are versatile tools to analyze them. In this work, MgO-ZnO solid solutions are investigated by XANES and ELNES with special interests on the local structure around Zn in MgO. In order to interpret the experimental spectra, a first principles band-structure calculations were performed using the orthogonalized linear combination of atomic orbitals (OLCAO) method [1].

High purity MgO powder having rock-salt structure (2000A, Ube Materials Industries, Japan) and ZnO powder having wurzite structure (Seido Chemical Corp., Japan) were used as starting materials. Two powders were mixed by a magnetic-starrier in ethanol until they dry up. Sintering was done in air at 1623K for 3h for undoped ZnO, and 1933K for 2h for the doped/undoped MgO. The solubility limit of Zn in MgO was reported to be 38.7 at % at 1873K [2]. All specimens used in this work exhibit a single crystalline phase of a rock-salt structure by a standard powder x-ray diffraction method. XANES was obtained at BL-7A of the soft X-ray beam line of UVSOR, in the Institute for Molecular Science, Okazaki, Japan. Zn-L_3 edge spectra were collected in a total electron yield mode at room temperature using a beryl two-crystal monochrometer. The photon energy was calibrated at the Al K-edge (1568eV) from the beryl monochrometer. Samples were put on the first photocathode of electron multiplier by adhesive carbon tape. ELNES was measured using transmission electron microscopy (CM200 FEG Philips) operated at 200 kV with standard transmission geometry. A post-column imaging filter system (GIF, Gatan) with a slow-scan CCD camera was used in a spectroscopic mode.

Figure1 shows Zn-L_3 ELNES and XANES from wurzite-ZnO (w-ZnO). Two experimental spectra are in good agreement except for the fact that the present XANES shows higher energy resolution than that of the ELNES. As a result, fine structures of peaks A and B can be clearly seen only in the XANES. The theoretical spectrum obtained by the OLCAO method using a large supercell composed of 108 atoms is also shown in Fig. 1. Theoretical spectrum is found to reproduce the experimental spectra quantitatively well up to the peak C if we correct the absolute energy by 15 eV (1.4 %).

Figure 2 shows the Zn-L_3 XANES from the MgO-30mol% ZnO solid solution. The spectral features are clearly different from that of w-ZnO. The spectrum from w-ZnO is basically composed of 4-sets of peaks, A, B, C, and D. On the other hand, the 3-sets of peaks, A, B, and C, make the spectrum from the solid solution. The spectral difference can be ascribed to the difference of coordination number of Zn [3]. The calculated spectrum from an isolated Zn model is also shown in Fig. 2. The isolated Zn model was made up with the assumption that

an isolated Zn ion is present in the MgO matrix. The reproduction of the theoretical spectrum is satisfactory except for small discrepancy in the shape of the peak B. Although the peak B in the experimental spectrum is rather sharp, it shows a double peak in the isolated Zn model. The isolated Zn model should therefore be modified.

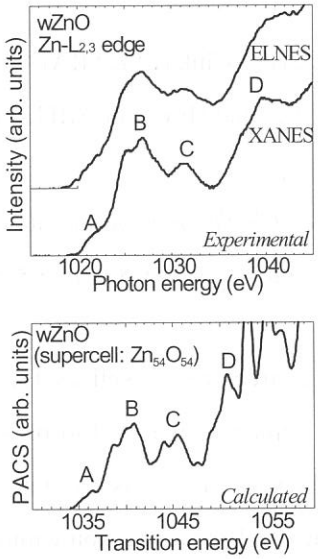

Fig. 1
(top) Zn-L_3 ELNES/XANES from w-ZnO and (bottom) the calculated spectrum by the OLCAO method using a large supercell composed of 108 atoms.

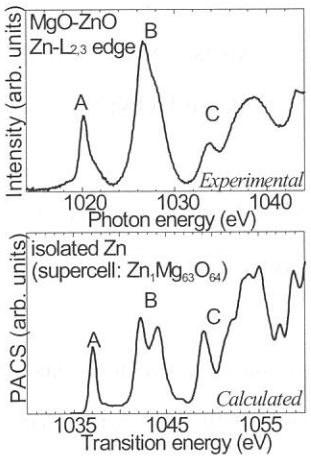

Fig. 2
(top) Zn-L_3 XANES from a MgO-30 mol % ZnO solid solution and (bottom) the calculated spectrum with the isolated Zn model using a $Zn_1Mg_{63}O_{64}$ supercell.

Figure 3 shows the dependency on Zn concentration for the Zn-L_3 XANES. Although the spectral features gradually change depending on the Zn-concentration, the change is not so significant. The doubled peak B found in the theoretical spectrum by the isolated-Zn model did not appear even in the 2.5%Zn specimen. This implies that the isolated-Zn model cannot be applied to the 2.5%Zn specimen, either. This is suggestive of the solute distribution far from random. Strong interaction among Zn atoms in the solid solution should occur even in the low-doped sample.

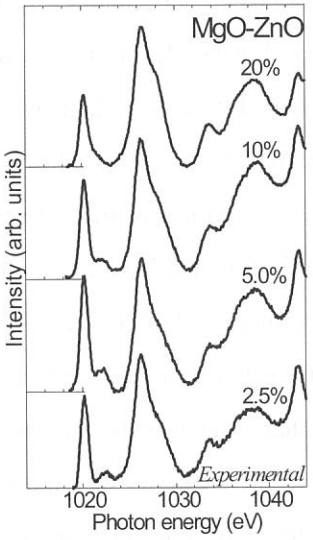

Fig. 3
Dependency on Zn concentration for the Zn-L_3 XANES.

REFERENCES

[1] S. D. Mo and W. Y. Ching, Phys. Rev. B. **62** (2000) 7901.

[2] E. R. Segnit, S. E. Hlland, J. Am. Ceram. Soc., **8** (1965) 409.

[3] T. Mizoguchi, M. Yoshiya, J. Li, F. Oba, I. Tanaka, and H. Adachi, Ultramicroscopy **86** (2001) 363.

(BL7A)

Microstructural control of calcium titanates with some oxides as a dopant and analysis of their local structure by Ca K- and P K-edge XAFS

Atsushi NAKAHIRA,* Ken-ichiro EGUCHI,* Chikako KARATANI,*
Yukako HONDA,* Takayuki MURAKAMI,* and Hirofumi ARITANI**

*Faculty of Engineering & Design, Kyoto Institute of Technology, Kyoto 606-8585, Japan
**Faculty of Engineering, Saitama Institute of Technology, Okabe, Saitama 369-0293, Japan

Calcium titanate, $CaTiO_3$, has the perovskite type structure as well as $BaTiO_3$ for ferroelectric materials. $CaTiO_3$ with the addition of some oxides as a doping is expected to possess the possibility of novel ferroelectric properties. Recently, according to Hayakawa et al, it was also reported that the usage of $CaTiO_3$ based materials with small amount of nickel led the exothermic reaction without H_2O in the case of the oxidation of methane. In this study, the evaluation of microstructure for $CaTiO_3$ with the addition of some oxides and its structural analysis around Ca and P atoms was carried out by means of Ca K- and P K-edge XAFS. In this report, obtained results and discussions about P K-edge XAFS were omitted.

As an initial material, $CaTiO_3$ powder, zirconium oxide powder, strontium oxide powder, and barium nitrate were selected. 5 wt% of their oxide powders and salt was added into $CaTiO_3$ powder and mixed in ethanol solvent for 24 hours by a ball-milling method. The slurry was dried with an evaporator and then in an oven at 50℃. The mixture of $CaTiO_3$ and other oxides or salt was molded with a stainless die. The compacts were heat-treated in an air atmosphere for 2 hours at 1100 - 1300°C. XAFS spectra at Ca K- and P K-edges were measured at BL7A of UVSOR by means of Ge(111) double-crystal monochromator. All samples were measured in a total electron yield mode.

Heat-treated $CaTiO_3$ with some additives was identified by X-ray diffraction (XRD) and composed of only $CaTiO_3$ phase without reaction phases. The XRD results indicated that these $CaTiO_3$ with some additives had the perovskite-type structure. It is suggested that the solid solution of Ba, Zr, and Sr into $CaTiO_3$ structure was performed. Fig. 1 shows XANES spectra of $CaTiO_3$ with some additives. $CaTiO_3$ has perovskite-type orthorhombic structure, and Ca ions are surrounded by 12 oxygen atoms in three types of slightly distorted square-planner CaO_4 tetrahedra. Thus the feature of XANES are quite different from those of CaO (CaO_6, O_h) and HAp (Ca-O_{10}). In case of $CaTiO_3$ with several additives (Sr, Ba, Zr, or La), the features of XANES spectra are almost similar to that of non-doped $CaTiO_3$. However, the transition intensities of each peak (especially, prominent peak at 4044 eV) on these samples have a little difference from each other. This result indicates that a little change was brought about in Ca local structure by addition of those dopants. Fig. 2 shows EXAFS oscillation waves of these samples in the range of Δk = 3.0 - 10.0

$Å^{-1}$. Slight difference of oscillations can be between $CaTiO_3$ and Ba-, La, or Zr-added one, supporting the structural change around Ca ions in minor. To clarify the difference, Fourier-transformed EXAFS analysis was introduced. The results of FT are shown in Fig. 3. In $CaTiO_3$, two types of Ca-O bonds are present in the range of 2.39 - 2.50 (8O) and 2.58 - 2.69 Å (4O). For FT-EXAFS, it seems that Ca-O scattering of these bonds are seen in the range of R = 2.2 - 3.2 Å (as shoulder and primary peaks). The FT peak at ca. 4.0 Å may be due to Ca-Ti scattering (3.84 Å as a real bond length). The feature of Ca-O peaks in 5wt% Sr-added $CaTiO_3$ is almost as same as those of $CaTiO_3$, however, the difference can be seen in 10wt% Sr-added $CaTiO_3$ from non-doped one. In addition, intensity of the peaks in higher shells ($R \geq 4.0$ Å) becomes large by Sr addition. These results show that Sr-insertion in $CaTiO_3$ perovskite give a successive change of local structure around Ca ions in minor. In cases of La- or Zr-added $CaTiO_3$, separate peaks due to Ca-O scattering can be seen at 2.4 and 3.3 Å. The peaks at 4.2 Å, which may be due to overlapped Ca-La or Ca-Zr scattering with Ca-Ti one, becomes large by metal-addition. These change of local structure around Ca ions in $CaTiO_3$ perovskite phase. The slight change of Ca local structure.

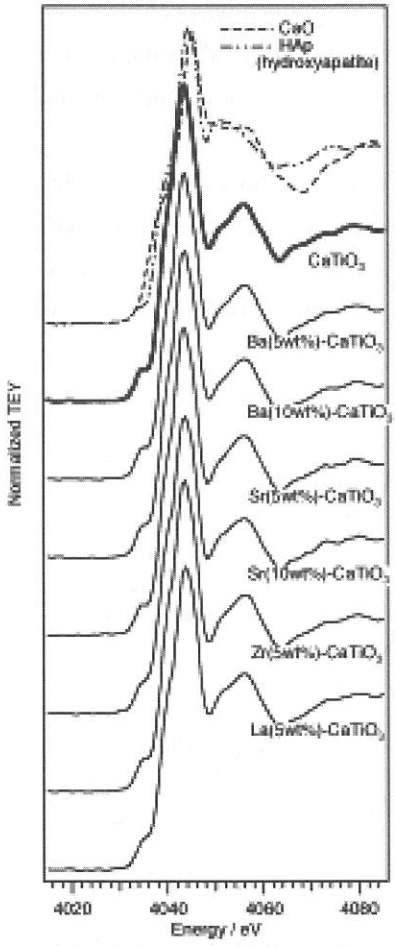

Fig. 1 Ca K-edge XANES.

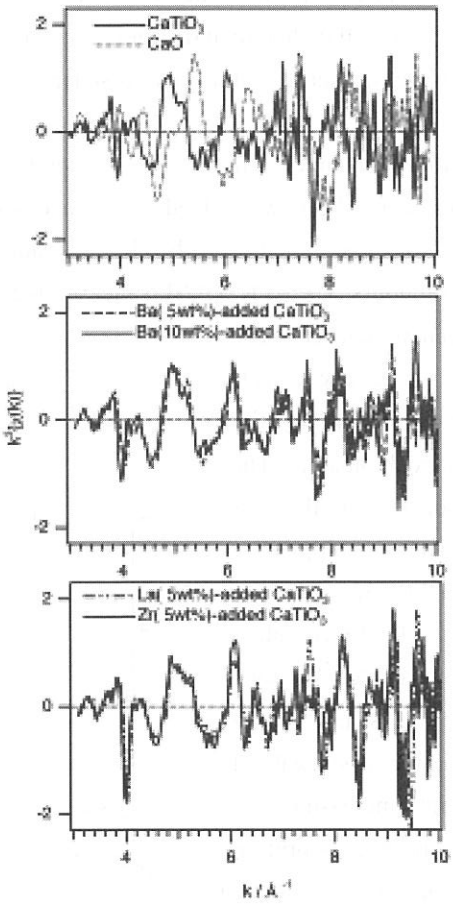

Fig. 2 EXAFS oscillations.

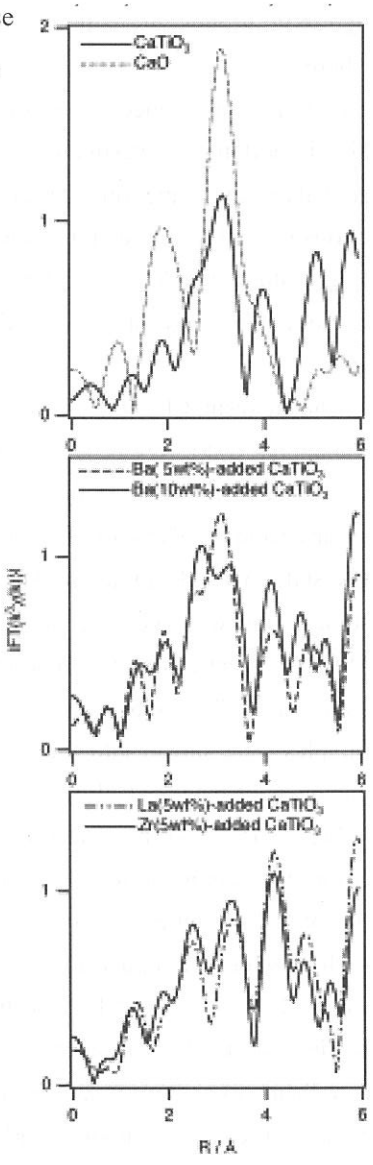

Fig. 3 FT-EXAFS (Δk=3-10).

(BL-7A)

An Electronic Study on the Analysis of Al K X-ray Absorption Near Edge Structure for on Aluminum Adsorbed Ion-exchange Resin

K. Shirozu[1], S. Matsuo[2], T. Kurisaki[1], T. Yokoyama[3], and H. Wakita[1,2]

[1]*Department of Chemistry, Faculty of Science Fukuoka University*
Nanakuma, Jonan-ku, Fukuoka 814-0180, Japan
[2] *Advanced Materials Institute, Fukuoka University*
Nanakuma, Jonan-ku, Fukuoka 814-0180, Japan
[3]*Department of Chemistry, Faculty of Science Kyushu University*
Hakozaki, Higashi-ku, Fukuoka 812-8581, Japan

Fulvic acid is a typical organic compound with aliphatic and/or aromatic carboxylic and phenolic hydroxyl groups in natural water. It is also a polymer which has molecular weight of 1000-10000. Therefore, it is important to understanding the behavior of aluminum ion with this acid on the environmental science. Thus for understanding the binding properties of aluminum ion to fulvic acid, it is also important to investigate the interaction between aluminum ion and some model compounds of fulvic acid that have functional groups such as carboxylic groups and amino groups in aqueous solution. We choose a chelate and cation exchange resin. But the structure of these model compounds was not clear yet. In this study, the Al K XANES spectra of the chelate and cation exchange resin adsorbing aluminum ion as model compounds for fulvic acid were measured and discussed steric structure of these compounds in solid state.

Chelate resin, Chelex 100, and cation exchange resin, Bio-Rex 70, were obtained from Bio-Rad Laboratories, Richmond, Calif., respectively. Each resin (2-5g) was added into aqueous solutions (100-200 cm^3, pH3) with various concentrations of aluminum ions and stirred for 24h. The resin adsorbing aluminum ions was filtered, air-dried and dried at 60°C for several hours. The Al K XANES measurements were carried out at the BL-7A of UV-SOR in the Institute for Molecular Science. The storage ring was operating at electron energy of 750 MeV. All spectra were recorded in total electron yield, using a KTP double-crystal monochromator. The samples were spread into the carbon film on the first photodynode made of CuBe of the electron multiplier.

Fig.1 shows Al K XANES spectra of the resin adsorbing aluminum ions and Al(CyDTA) complex. Al(CyDTA) complex contains six coordinated Al^{3+} ions, each of which is bonded to two N atoms and four O atoms. For Al K XANES spectra, the first peak of K-edge shifts higher energy with increasing the coordination number of aluminum ions. The absorption edges of the three compounds are located on the same energy level. The result shows that these compounds have similar surroundings of aluminum ions.

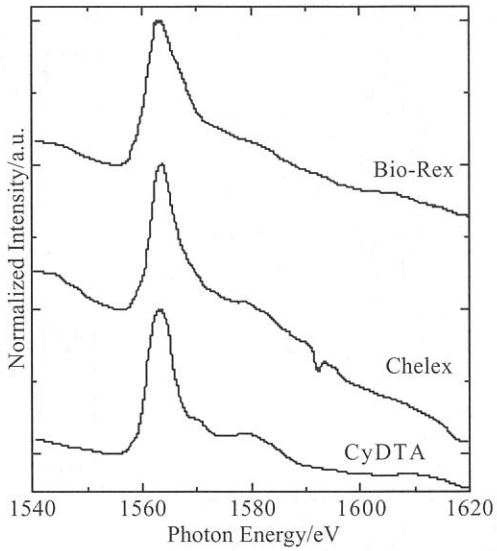

Fig. 1 Al K XANES spectra of the resin adsorbing aluminum ions and Al(CyDTA) complex

(BL8B2)

Ultraviolet Photoelectron Spectra of Surface Lattice Oxygen of $LiNiO_2$

T. Miyazaki[1], D. Yoshimura[2], K. Kamiya[2] and Yamaguchi[1]

[1] *Department of Applied Chemistry, Faculty of Engineering, Ehime University, Matsuyama, 790-8577*

[2] *Institutes for Molecular Science, Okazaki, 444-8585*

Several metal oxides have been utilized as catalysts of the oxidative coupling of methane (OCM). $LiNiO_2$ has an activity for the OCM reaction and a layered structure in which lithium and transition metal ions are alternately and regularly arranged to oxygen layers. We suggested that the anisotropic structure should be a key to the formation of the active sites for the OCM reaction. In this study, ultraviolet photoelectron spectra (UPS) were measured in order to examine electronic structures of the valence band of $LiNiO_2$. It should be carefully investigated, because the top of the valence band usually determines chemical activities and properties.

The measurements of ultraviolet photoelectron spectra were carried out at the BL8B2 of the UVSOR/IMS. $LiNiO_2$ was synthesized by solid phase reaction at 800℃ in the atmosphere. The surface treatments were carried out by a surface cutting under high vacuum and/or argon sputter. The $h\nu$-dependence of ultraviolet photoelectron spectra of $LiNiO_2$ was also measured at room temperature.

Ultraviolet photoelectron spectra of $LiNiO_2$ after the surface treatment are shown in Figs. 1 and 2. These spectra were measured with reference to E_F as zero of the energy scale. Fig. 1 is different demonstrating the effect of the surface contamination and/or modification by air. Fig. 2 shows the incident photon energy dependence of UPS of $LiNiO_2$. The intensity of these bands at E_b=6.9 eV and E_b=1.6, 2.7, 3.5 eV from the Fermi level shows maximum at around $h\nu$=40 eV and 55 eV, respectively. It seems likely to be a considerable possibility of orbital mixing between Li, Ni and O atoms.

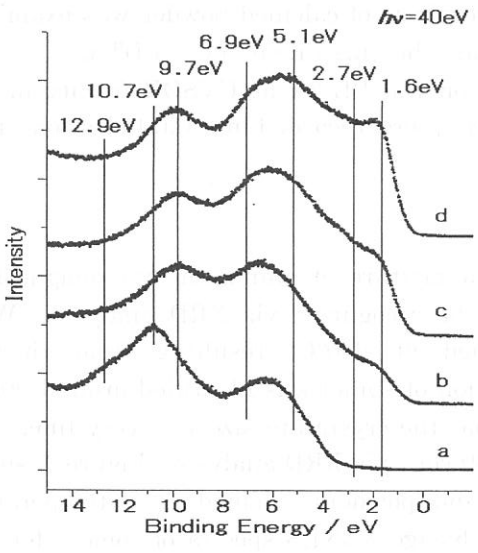

Fig.1. UPS of $LiNiO_2$, a) $LiNiO_2$ sample of no surface treatment; b)-d) $LiNiO_2$ sample after the surface cutting and argon sputter treatments.

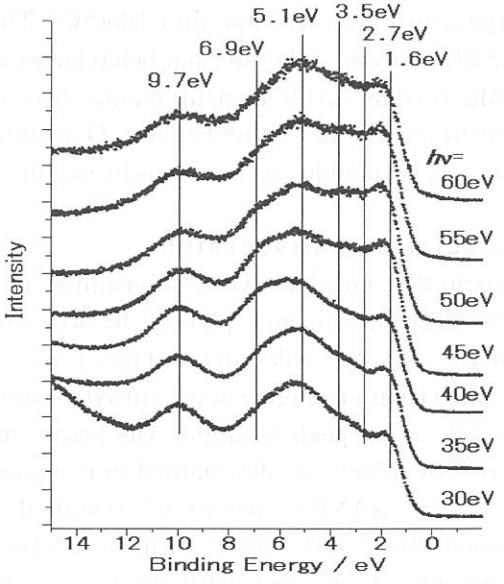

Fig.2. The $h\nu$-dependence of UPS of $LiNiO_2$ in the $h\nu$-region of 30 - 60 eV.

(BL7A)

Mg K-Edge XANES Study of Crystallization of $MgAl_2O_4$ Spinel Prepared from A Mixture of $Al(OH)_3$ and $Mg(OH)_2$ Activated Mechanically by Wet Milling

Takeshi SHIONO, Takushi MINAGI, Hirofumi ARITANI
Shinya OKUMURA and Toshihiko NISHIDA

Department of Chemistry and Materials Technology
Kyoto Institute of Technology
Matsugasaki, Sakyo-ku, Kyoto, 606-8585, Japan

1 Introduction

$MgAl_2O_4$ spinel is recognized as one of structural oxide materials because of high melting point (2015°C), superior resistance to chemical attacks strength and so on. However, it is very difficult to prepare dense polycrystalline spinel with high-purity and stoichiometric composition by a conventional method. Advanced synthesizing techniques have been applied to preparation of the powder with good sinterability[1-3]. Mechanochemical process is a well-known process that improves the reactivity of powders and gives new properties to them, using mechanical stress by agitating and milling processes. Despite mechanochemical phenomena are applied to various industrial fields in practice, few studies of quantitative mechanochemistry were carried out.

In the present study, the formation of spinel phase from a mixture of aluminum and magnesium hydroxide activated mechanically with wet-milling was investigated through X-ray diffraction (XRD) analysis and Mg K-edge X-ray near-edge structure (XANES).

2 Experimental

Aluminum hydroxide (Sumitomo Chemical Industries Co. Ltd. : C-31) and magnesium hydroxide (Ube Chemicals Co. Ltd. : UD-653) was used as raw materials for mechanical milling, without further heat treatment and purification. The average particles size were 50μm and 2.8μm respectively. For preparation of activated powder, the hydroxides were milled in hydrochloric solution with a Mg : HCl molar ratio of 1 : 0.01 by using a planetary ball-milling equipment (Fritsch Co. Ltd. : P-5). The milled hydroxide powders were calcined at a temperature between 300° and 1200°C. The crystalline phase of calcined powder was examined via XRD analysis. The thermal behavior was estimated at a heating rate of 5°C via DTA.

Mg K-edge XAFS measurements were carried out on the BL-7A at UVSOR facility in the Institute of the Molecular Science, Okazaki. The spectra were recorded in a total electron yield, using a beryl double crystal monochromater.

3 Results and Discussion

As-milled powders were determined to consist of a mixture of aluminum and magnesium hydroxides and no new phases by wet milling could be recognized via XRD analysis. With increase in the calcining temperature, MgO formed at 600°C, resulting from thermal decomposition of magnesium hydroxide and the formation of spinel was identified around 900°C. The diffraction peak of spinel was broad, indicating that the crystallite size was very fine. The fraction of spinel was determined to be approximately 49 vol% via XRD analysis. Figure 1 shows Mg K-edge XANES spectra of as-milled hydroxide and powders calcined at a temperature between 300°C and 1200°C. Figure 2 also shows Mg K-edge XANES spectra of some reference compounds. Compared with the figures, magnesium element is found to exist as a hydroxide until a calcining temperature of 600°C and formation of MgO could be recognized at 600°C. These results are in good agreement with those by XRD analysis. XANES spectrum at 900°C looks a combination of spectra for spinel and MgO. In order to examine the degree of reaction to

spinel, therefore, we tried to combine the XANES spectra of MgO and spinel in Fig.2, with changing the intensity ratio of each spectrum. Dashed line in Fig.3 shows the result of the combination for 57% MgO and 43% spinel. The combined curve was similar to the spectrum obtained at 900°C, as shown in Fig.1. The fraction of spinel, 43% would be good agreement with the result, 49% from XRD analysis, although the fraction was a little bit smaller.

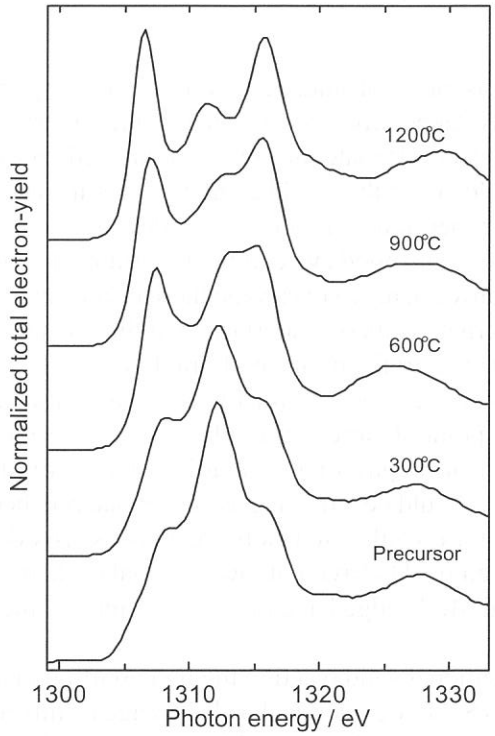

Fig.1. Mg K-edge XANES spectra of spinel precursor and powders.

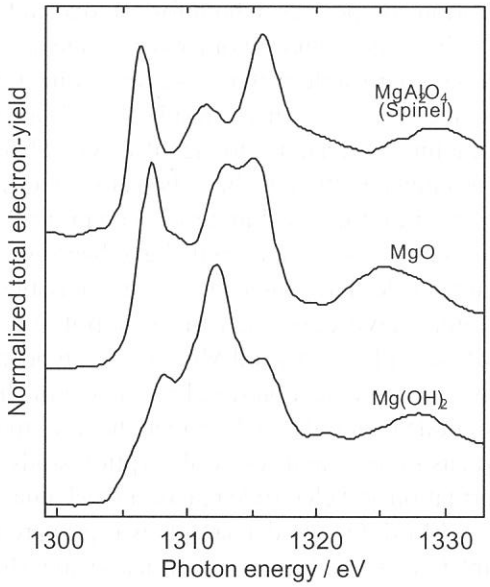

Fig.2 Mg K-edge XANES spectra of reference Mg compounds.

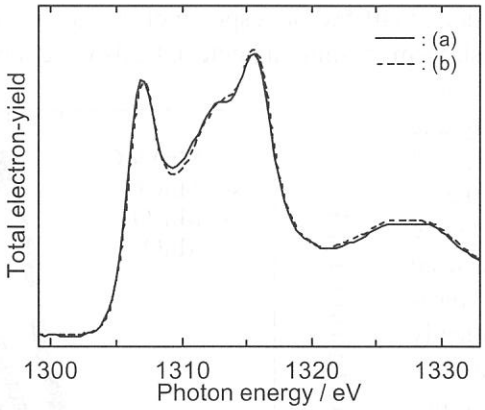

Fig.3. Combination of XANES spectra for spinel and MgO.
(a) spinel powder calcined at 900°C
(b) [spectrum of 57% MgO] + [spectrum of 43% spinel]

References

[1] R.J.Rratton, *J. Am. Ceram. Soc. Bull.*, **48**, 759 (1969).

[2] S.Hokazono, K.Manako and A.Kato, *Br.Ceram.Trans.J.*, **91**, 77 (1992).

[3] T.Shiono, K.Shiono, K.Miyamoto and G.Pezzotti, *J. Am. Ceram. Soc.*, **83**, 235 (2000). the result

(BL7A, BL8B1)

Mo and Mn *L*-XANES of $MnMoO_4$ for high capacity anode material of Li secondary battery

Yoshiharu UCHIMOTO, Seiichiro OGURA, Hiromasa IKUTA, and Masataka WAKIHARA
Department of Applied Chemistry, Graduate School of Science and Engineering, Tokyo Institute of Technology, 2-12-1 Ookayama, Meguro-ku, Tokyo 152-8552, Japan

The Li-ion rechargeable batteries are considered as the most suitable power sources for portable electronic devices due to their high capacity and energy density. Generally, Li-ion rechargeable batteries consist of intercalation compounds in both for cathode and for anode electrode materials. One is a lithiated transition metal oxide as the cathode and the other is graphite as the anode. However, the graphite anode material commonly used in Li-ion rechargeable batteries suffers from small capacity per unit weight (about 350mAh/g) and/or per unit volume due to its low density in spite of its low redox potential and good cycle life. Furthermore the rate capability of graphite material due to the diffusivity also needs improvement. To overcome these disadvantages, considerable amounts of attempts have been made to find out alternative anode materials, including metal oxide(MO, M=Co, Ni, Fe), tin-based material, vanadium-based oxide materials, in place of graphite anodes. Especially, vanadium based oxide materials have been researched as active materials for Li secondary battery, since the vanadium oxides have interesting characteristics in a standpoint of variety of oxidation state. Recently, several researchers have described the low potential Li-insertion behavior in vanadium based oxide such as RVO_4(R=In,Cr,Fe,Al,Y) and MnV_2O_6. Molybdenum oxides should be attractive as anode material, because they also have various oxidation state like vanadium. In this report, we synthesized molybdenum-based oxide $MnMoO_4$ as new anode material and described the lithium insertion/removal behavior at low potential cycle property. The XRD measurement and X-ray absorption study of Mn and Mo L-edge have provided insight on the structural transformation and electrode reaction mechaniam.

$MnMoO_4$ powder sample was prepared by conventional solid reaction method. Starting material used was $MnCO_3$(99.9% Soekawa chemicals) and MoO_3(99.9% Soekawa chemicals). This reagents mixed with stoichiometric ratio in agate mortar and the mixture was heat-treated at 600°C for 24h in air atmosphere. Then we could get crystalline $MnMoO_4$ powdered sample. The phase identification was carried out by powder X-ray diffractometry using Rigaku RINT2500V with CuK¥á radiation. The samples for the electrochemical measurement were prepared by mixing crystalline $MnMoO_4$, acethylene black as conductive agent and polytetraflouroethylene (PTFE) binder(55-40-5wt%, respectively) in an agate mortar and made in the form of film. The film was then cut into a disk form (5.4mm diameter). Cells were fabricated by coupling this disc with lithium foil of same area as counter electrode using microporous polyprophylene film(Celgard2400) as separator. 1M $LiClO_4$ dissolved in Ethylene Carbonate(EC)/DiEthlylene Carbonate(DEC) (vol ratio=1:1) was used as the electrolyte. The electrochemical measurement was carried out galvanostatically at various current densities at room temperature in a glove box under argon atmosphere. The cut-off voltage was set at 0.0 and 2.0V versus Li/Li^+. Mo *L*-edge X-ray Absorption Near Edge Structure (XANES) of synthesized powder were measured on BL7A at UVSOR (Okazaki, Japan) with a ring energy of 750MeV and a stored current of 70-220mA in a mode of total electron yields. The KTP double crystal monochromator was used. The absolute energy scale was calibrated by using literature

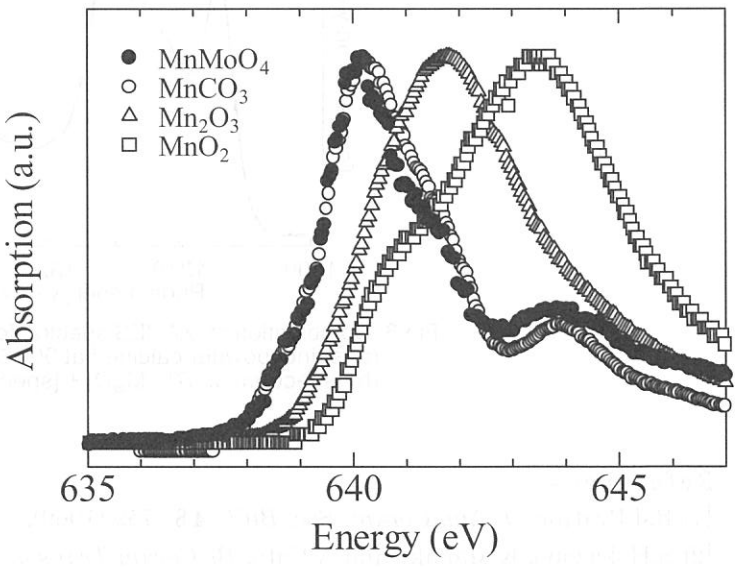

Fig.1. Mn *L*-edge XANES spectrum of $MnMoO_4$ and various Mn compounds as reference

value of Mo L_{23}-edge in MoO_3. Mn L_{23}-edge XANES was measured on BL8B1 beam line at UVSOR (Okazaki, Japan) with ring energy of 750 MeV in a mode of total electron yield at room temperature.

Mn and Mo XANES for synthesized powder also carried out to investigate the oxidation state of Mn and Mo and to verify the chemical formula. XANES results were shown in Fig.1 and Fig. 2 with reference materials that have various oxidation states. The Mn *L*-edge XANES shows two strong absorption features due to the spin-orbit splitting of the Mn 2p core hole. The absorption shown in Fig.1 about 640-645 eV is $2p_{3/2}$ (L3) edge. In Fig.1, the spectra for the edge jumps for $MnCO_3$ and $MnMoO_4$ are very close to each other, we can assume that Mn exists as Mn^{2+} in $MnMoO_4$. Mo L-edge XANES spectra of $MnMoO_4$ and MoO_3 presented in the Fig. 2 illustrate that the valence of Mo in $MnMoO_4$ should be +6. The oxidation state arrived from the XANES spectra and well-defined XRD pattern obtained for the prepared sample confirm that the compound is stoichiometric $MnMoO_4$. Furthermore, the spectra of Mo L-edge XANES of $MnMoO_4$ and MoO_3, which involves the transitions from the 2p core levels into the empty 4d orbital, show separation of two peaks clearly. Generally, in octahedral coordinated metal, the d-orbitals are splits into triply degenerate t_{2g} and doubly degenerate e_g orbitals. The electrons in e_g orbitals are repelled more strongly by the negative charge since electrons are located along the bonding axes than those of t_{2g} orbitals which point between the axes. Thus the t_{2g} orbitals lie lower in energy than the e_g orbitals, whereas, in tetrahedral coordination, triply degenerate t_2 orbitals lie higher in energy than doubly degenerate e orbitals. The Mo atoms in MoO_3 are in a octahedral environment, and Fig.2 indicate the typical 4d splitting in two sets of e_g and t_{2g} symmetry. On the other hand, the Mo atoms in $MnMoO_4$ are in a tetrahedral environment, and Fig.3(b) shows ligand field splitting parameter: (energy difference of t_2 and e) is about 1.6eV.

In order to obtain charge-discharge profile of $MnMoO_4$, cell was subjected to several cycles at constant current mode. The charge-discharge profiles obtained are depicted in Fig. 3. The initial charge capacity was about 1800Ah/kg and reversible capacity in consequent discharge process was around 1000Ah/kg. During the first charge, the lithium intercalation process exhibited a plateau around 0.8V versus Li/Li^+ which is not observed in the following cycles.

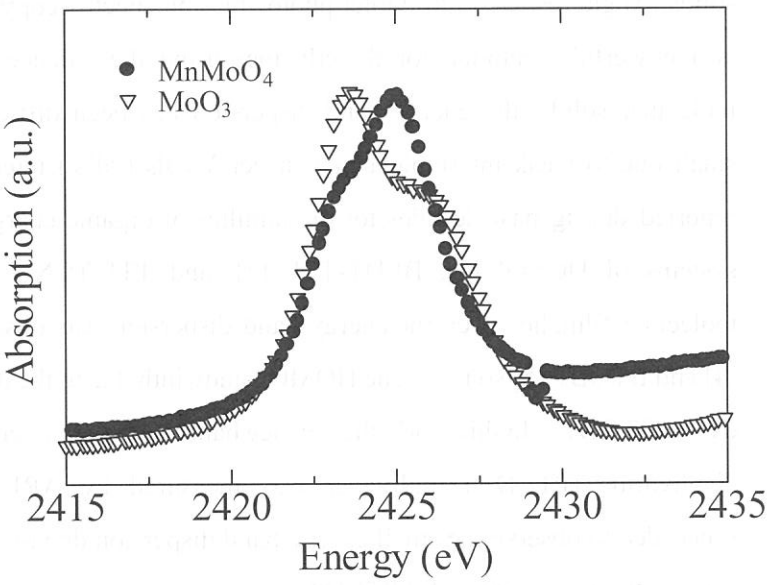

Fig.2. Mo *L*-edge XANES spectrum of $MnMoO_4$ and MoO_3.

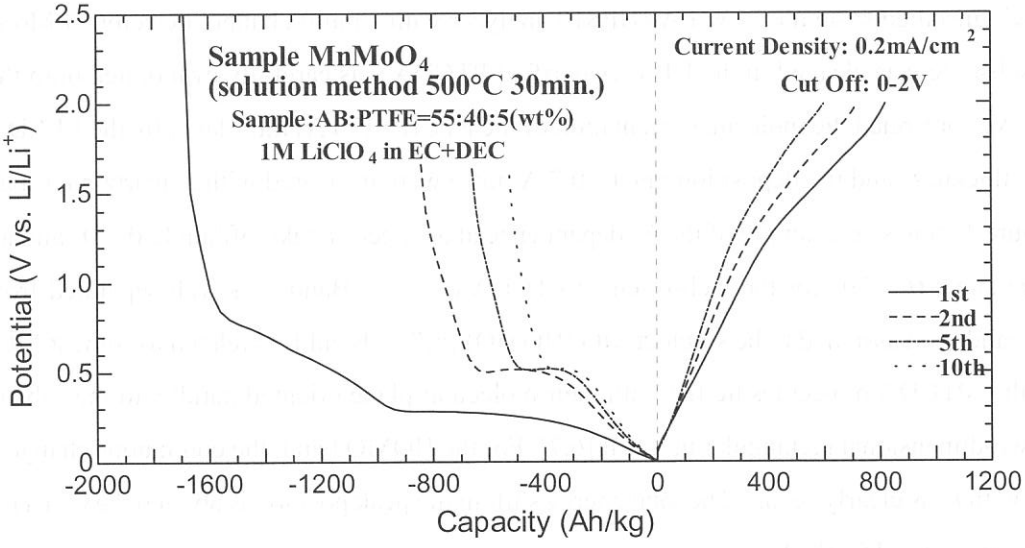

Fig.3 Charge-discharge voltage profile of $MnMoO_4$.

(BL8B2)

Intermolecular Energy-Band Dispersion in Well-Oriented PTCDA Multilayer by Angle-Resolved UV Photoemission

Satoshi KERA[a], Shinji TANAKA[a], Yosuke YABUUCHI[a], Tadaomi MORI[a], Hiroyuki YAMANE[a,b], Daisuke YOSHIMURA[b], Koji K. OKUDAIRA[b], and Nobuo UENO[a]

[a]*Graduated School of Science and Technology, Chiba University, Chiba 263-8522*

[b]*Institute for Molecular Science, Okazaki 444-8585*

The energy-band dispersion is a fundamental basis for understanding the basic properties of solids. Angle-resolved ultraviolet photoemission spectroscopy (ARUPS) using synchrotoron radiation is a powerful technique for directly measuring the valence band dispersion. For typical organic molecular solids, the energy-band dispersion has been difficult to observe, since the bandwidth is small due to weak intermolecular van der Waals (vdW) interaction. Some experiments have been reported during past decades for the families of organic charge transfer salts, such as metal complex systems of DCNQI [1], BEDT-TTF [2], and TTF-TCNQ [3]. In a single-component organic molecular film, however, the energy-band dispersion was observed for only two systems, that is, C_{60} [4] and BTQBT [5] so far. The HOMO bandwidth due to the dispersion is about 0.4 eV for C_{60} and 0.4 eV for BTQBT. In this work, the valence band of well-characterized perylene-3,4,9,10-tetracarboxylic dianhydride (PTCDA) multilayer was measured by ARUPS with synchrotoron radiation. We succeeded to observe the small energy-band dispersion due to the weak HOMO-HOMO interaction for a conventional organic solid PTCDA.

ARUPS measurements were carried out at the BL8B2 of UVSOR. ARUP spectra were measured by a newly installed system of a VG-ARUPS10 analyzer with a multi channel detector. A MoS_2 single crystal substrate was cleaved in the UHV. A purified PTCDA was carefully evaporated onto the MoS_2 surface. We confirmed the molecular orientation of the PTCDA (30 Å) multilayer by the LEED pattern. The film thickness and the deposition rate (~ 0.7 Å/min.) were measured with a quartz microbalance.

Figure 1 shows an example of the *hv* dependence at an electron take-off angle $\theta = 0°$ and a photon incidence angle $\alpha = 70°$ for the well-oriented PTCDA (30 Å). Band A is well separated from other valence bands and assigned to be single π MO (HOMO) [6,7]. Band B is related to some π MOs [6,7]. In this film, PTCDA molecules lie flat with their molecular plane oriented parallel to the substrate and form a two-dimensional rectangular unit cell [6,7]. For the HOMO band, the continuous change of peak position with *hv* is clearly seen. The total energy shift in the peak position is about 0.2 eV in a region of photon energy hv = 15–81 eV.

From Fig.1, the energy band dispersion relation along the surface normal was determined using the procedure described in the previous report [5], where assumed that (i) both energy and momentum of electrons are conserved for the ionization and (ii) the final continuum state is a parabolic free-electron like band in a constant inner potential V_0. In Fig.2, the best fit dispersion curve along with the experimental results calculated by a simple tight-binding model is shown, where inner potential V_0 is –8.5 eV, the binding energy of the band center is 7.43 eV, the lattice spacing is 3.7 Å, and the transfer integral is 0.05 eV. As seen in Fig.2, we could observe the energy-band dispersion over four Brillouin zones (3rd, 4th, 5th and 6th zones) with the bandwidth of about 0.2 eV. For V_0 value, further confirmation is now in progress using the low-energy transmission spectroscopy [8].

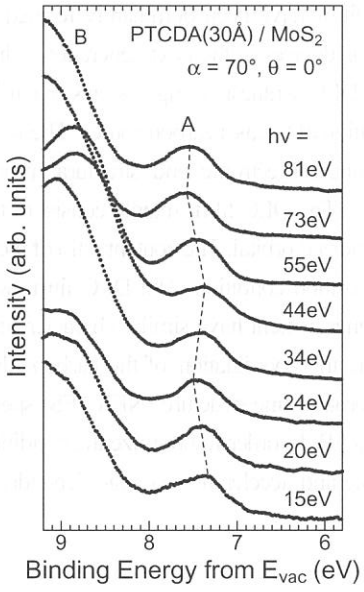

Fig.1 Photon energy dependence of ARUPS at normal emission for PTCDA (30Å) on MoS_2.

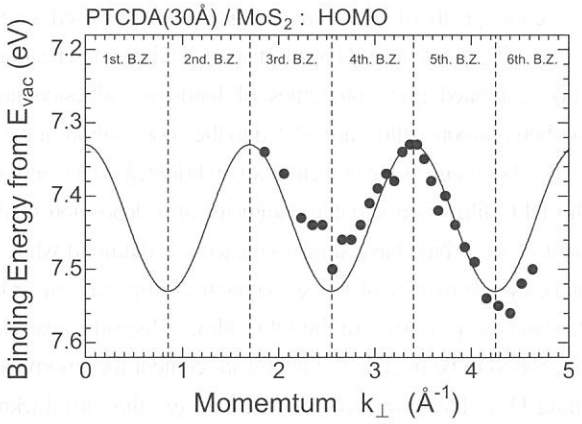

Fig.2 The experimental dispersion for the HOMO band (filled circles) and the best fit curve (line) in the tight-binding model.

[1] For example, D. Schmeisser et al., Solid State Commun. **81**, 827 (1992).

[2] For example, H. Mori et al., Physica C **357-360**, 103 (2001).

[3] For example, F. Zwick et al., Phys. Rev. Lett. **81**, 2974 (1998).

[4] G. Gensterblum et al., Phys. Rev. B **48**, 14756 (1993).

[5] S. Hasegawa et al., J. Chem. Phys. **100**, 6969 (1994).

[6] Y. Azuma et al., J. Appl. Phys. **87**, 766 (2000); J. Synchrotron Rad. **5**, 1044 (1998).

[7] S. Kera et al., Phys. Rev. B **63**, 115204 (2001).

[8] H. Yamane et al., Phys. Rev. B **64**, 113407 (2001).

(BL8B1)

Characterization of the diamond-like carbon films formed by Ar gas cluster ion beam assisted deposition

Teruyuki Kitagawa[1], Kazuhiro Kanda[2], Yutaka Shimizugawa[2], Yuichi Haruyama[2], Shinji Matsui[2], Mititaka Terasawa[1], Harushige Tsubakino[1], Isao Yamada[2,3], Tatsuo Gejo[4] and Masao Kamada[4]

[1] *Himeji Institute for Technology, Faculty of Engineering, Himeji, Hyogo, Japan*
[2] *Himeji Institute for Technology, Laboratory of Advanced Science and Technology for Industry, Kamigori, Hyogo, Japan*
[3] *Collaborative Research Center for Cluster Ion Beam Process Technology, Kyoto University, Sakyo, Kyoto, Japan*
[4] *Institute for Molecular Science, Okazaki, Aichi, Japan.*

Diamond-like carbon (DLC) films have been very interesting material in view of their numerous applications because of their high hardness, low friction coefficient and chemical inertness. DLC films have been dominantly formed by vapor phase methods [1,2], however their properties are not sufficient for the various devices in the next generation. In order to improve the quality of DLC film, our group has proposed a novel method in DLC synthesis using gas cluster ion beam [3]. The DLC films were formed by irradiating Ar cluster ion beam during evaporation of C_{60} as a carbon source. The films by this method exhibited good properties of hardness, adhesion and wear resistance. Electronic and structural properties of amorphous carbon films are related to the coordination of the carbon atoms. The DLC films mainly consist of two phase of carbon bonding. One of them is sp^2 hybridized orbital and other is sp^3 hybridized orbital. The content ratio of these phases in the DLC films is a variable parameter of a deposition method and a deposition condition. The DLC films with lower content of sp^2 orbital have similar character of diamond while those with higher content have similar character of graphite. That is, the estimation of the sp^2 content is important in order to determine the coordination of the carbon film and to understand the properties of the DLC film. Recently, near edge X-ray absorption fine structure (NEXAFS) spectroscopy was reported to be useable estimating sp^2 content for amorphous carbon films [4]. In order to optimize the condition on the forming DLC films with lower content of sp^2, the film thickness dependence and acceleration voltage dependence in the NEXAFS spectra were measured.

NEXAFS measurement was performed at the BL8B1 station of UVSOR [5]. The synchrotron radiation provided by the 0.75 GeV electron storage ring was dispersed by a constant-deviation constant-length spherical grating monochromator and was perpendicularly irradiated to the film surface. The NEXAFS carbon *K*-edge spectra were measured in the photon energy range 275-320 eV with 0.5 eV FWHM resolution. The detection of electrons emitted from sample was performed in the total electron yield mode. The details of the deposition method of DLC film by using GCIB assisted deposition have been described in the previous paper [3]. The accuracy in

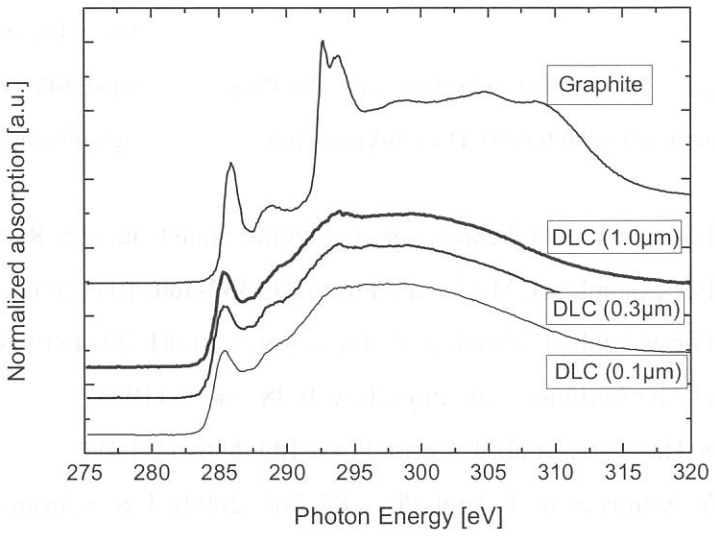

Fig.1 NEXAFS spectra of graphite and DLC films formed by Ar gas cluster ion beam (GCIB) assisted deposition. The films were deposited with various film thicknesses.

our NEXAFS spectra was confirmed by measuring the reference sample of graphite as shown fig. 1.

Fig. 1 shows the typical NEXAFS carbon *K*-edge spectra of the DLC films formed by GCIB assisted deposition with the spectra of graphite. The spectra of DLC films with various film thickness, which were deposited with 9kV acceleration voltage of GCIB, are shown. The NEXAFS spectra of various carbon films have been investigated previously [4,6,7]. A pre-edge resonance at 285.3 eV is due to transitions from C 1*s* level to unoccupied π^* orbital principally originating from sp^2 (C=C) hybridized orbital. This peak is not almost present in the diamond spectrum [8], because the diamond consists of only sp^3 (C-C) orbital. Therefore the intensity of the transitions at 285.3 eV represents as an index of sp^2 content.

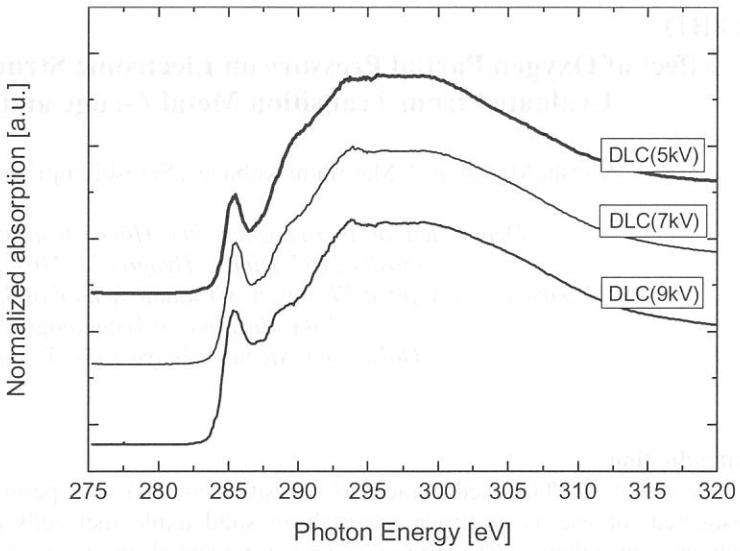

Fig.2 NEXAFS spectra of DLC films deposited with various acceleration voltage.

The established method for the quantitative determination of sp^2 content from EELS technique was applied to the NEXAFS measurements. The sp^2 content was estimated from the integral of the pre-edge peak at 285.3 eV. Further information for the determination of sp^2 content is denoted in the literature [9, 10]. In the fig. 1, the sp^2 contents of the DLC films with the various film thickness were almost same values. This result showed no dependence on the film thickness of the surface structure, since the total electron yield mode of this measurement detected the electrons from the film surface in the depth up to approximately 10 nm. That means homogeneous DLC films could be produced by GCIB assisted deposition under the constant acceleration voltage.

Fig. 2 shows the acceleration voltage dependence of NEXAFS spectra in the DLC films. The DLC films were deposited by varying the GCIB acceleration voltage from 5 to 9 kV with 0.3 μm of film thickness. The intensity of $1s \rightarrow \pi^*$ transitions increases with increasing the GCIB acceleration voltage. The film formed by Ar gas cluster ion beam assisted deposition with 5 kV acceleration voltages has a lowest sp^2 content under this voltage condition.

References

[1] J. Ullmann, Nucl. Instr. and Meth., Phys. Res. B, **127**, 910 (1997).

[2] H. Tsai and D.B. Bogy, J. Vac. Sci. Technol., A **5**, 3287 (1987).

[3] I. Yamada, T. Kitagawa, J. Matsuo and A. Kirkpatrick, Mass. Char. Trans. Inorg. Materials, 957 (2000).

[4] C. Lenardi, P. Piseri, V. Briois, C.E. Bottani, A. Li Bassi and P. Milani, J. Appl. Phys., **85**, 7159 (1999).

[5] A. Hiraya. E. Nakamura, M. Hasumoto, T. Kinoshita, K. Sakai, E. Ishiguro and M. Watanabe, Rev. Sci. Instrum, **66**, 2104 (1995).

[6] P. E. Batson, Phys. Rev. B **48**, 2608 (1993).

[7] M. Jaouen, G. Tourillon, J. Delafond, N. Junqua and G. Hug, Diamond Relat. Mater., **4**, 200 (1995).

[8] J. F. Morar, F. J. Himpsel, G. Hollinger, G. Hughes and J. L. Lordan, Phys. Rev. Lett., **54**, 1960 (1985).

[9] S. D. Berger, D. R. Mc Kenzie and P. J. Martin, Philos. Mag. Lett., **57**, 285 (1988).

[10] P. J. Fallon, V. S. Veerasamy, C. A. Davis, J. Robertson, G. A. J. Amaratunga, W. J. Milne and J. Koskinen, Phys. Rev. B **48**, 4777 (1993).

(BL8B1)

Effect of Oxygen Partial Pressure on Electronic Structure of (La,Sr)(Co,Fe)$O_{3-\delta}$ Evaluated from Transition Metal *L*-edge and O *K*-edge XANES

Atsushi Mineshige[A], Masafumi Kobune[A], Satoshi Fujii[A] and Yoshiharu Uchimoto[B]

[A]*Department of Applied Chemistry, Himeji Institute of Technology*
Shosha 2167, Himeji, Hyogo 671-2201, Japan
[B]*Department of Applied Chemistry, Graduate School of Science and Engineering,*
Tokyo Institute of Technology
Ookayama, Meguro, Tokyo 152-8552, Japan

1. Introduction

Some of La*M*O_3-based oxides (*M*; transition metals) with perovskite-type structure have been widely investigated for use as electrode materials in solid oxide fuel cells (SOFCs) and oxygen semi-permeable membranes since they exhibit high oxide ionic (O^{2-}) and electronic conductivities. Under operating conditions of such devices, the La*M*O_3-based oxides are exposed to gases with various oxygen partial pressures, $P(O_2)$, at elevated temperatures. There are, however, few studies on $P(O_2)$ dependence of their electrical conductivity (σ), although their ionic and electronic conductivities are much affected by a change in $P(O_2)$ because of a deviation in oxygen content from 3. The decrease in the oxygen content from 3 leads to a formation of the oxygen vacancies, paths of an oxide ion transport, and changes the electronic structure, which directly influences their electronic conductivity. In the present study, the change in the electronic structure of Sr-doped La$(Co_{0.2}Fe_{0.8})O_3$ as a function of $P(O_2)$ was studied. In this system, *p*-type electronic conduction is dominant, and σ tends to increase with Sr-doping into La-site or temperature rise (semiconductor-like behavior). The enhancement in σ with Sr content is due to a hole doping. In fact a nominal mean valence of transition metals (*n*) increases to about 3.3 for 40% Sr-doped La$(Co_{0.2}Fe_{0.8})O_3$, while *n* is about 3.0 for undoped sample [1]. The aim of this work is to evaluate a valence of each transition metal, as well as *n*, under several $P(O_2)$ conditions. In addition, the previous study [2] revealed that this system exhibited a curious *p*-type electronic conducting behavior at low $P(O_2)$; *i.e.*, the *p*-type electronic conduction under *n* less than 3. Hence, the relation between the change in its electrical conductivity and that in its electronic structure was also discussed.

2. Experimental

Powders of 40% Sm-doped La$(Co_{0.2}Fe_{0.8})O_3$, $La_{0.6}Sr_{0.4}Co_{0.2}Fe_{0.8}O_3$, which is regarded as one of the best candidate for the cathode material of SOFC, were synthesized from each metal nitrate. It was found that the molar ratio of each metal in the powders thus obtained was desirable by an ICP analysis. Its crystal structure was rhombohedrally distorted with a_r = 5.466 Å, and α_r = 60.33° confirmed by XRD. Then, samples were prepared by re-heating the powders in air at 1273 K, followed by annealing and cooling under various $P(O_2)$ [$10^{-8} \le P(O_2)/\text{atm} \le 0.2$]. The electrical conductivity during cooling was also measured using d.c. 4 probe method under the same $P(O_2)$ conditions. The Co L_{23}-edge, Fe L_{23}-edge and O *K*-edge X-ray Absorption Near Edge Structure (XANES) spectra were measured on the BL-8B1 beam line at UVSOR (Okazaki, Japan) with ring energy of 750 MeV in a mode of total electron yield at room temperature.

3. Results and discussion

Figure 1 shows the Fe *L*-edge XANES of $La_{0.6}Sr_{0.4}Co_{0.2}Fe_{0.8}O_3$ after annealing and cooling in various $P(O_2)$. For comparison, the spectra of $LaFeO_3$ and $SrFeO_3$ are also shown in this figure. A valence of iron is probably 3 in $LaFeO_3$, while iron exhibits two valences of Fe^{3+} and Fe^{4+} in $SrFeO_3$. The absorption at around 708-713 eV is the $2p_{3/2}$ (L_3) edge and that at around 720-725 eV is the $2p_{1/2}$ (L_2) edge. In the spectrum under higher $P(O_2)$, the peak shape resembled that of $SrFeO_3$, exhibiting mixed valences of Fe^{3+} and Fe^{4+}. The sample after cooling in air exhibits about 3.3 of nominal *B*-site mean valence and its oxygen nonstoichiometry (δ in $La_{0.6}Sr_{0.4}Co_{0.2}Fe_{0.8}O_{3-\delta}$) is about 0.05, determined from a weight loss during decomposition [1] and by iodometry [2]. With decreasing $P(O_2)$, no noticeable chemical shifts were observed, but the peak shape in the spectrum slightly changed. In the case of $P(O_2) = 10^{-8}$ atm, the spectrum of the sample and that of $LaFeO_3$ resembled each other. With a decrease in $P(O_2)$, the peak shape changed continuously from $SrFeO_3$-like to $LaFeO_3$-like. This is due to a reduction of Fe valence caused by the formation of oxygen vacancies. The total electrical conductivity (σ), *i.e.*, *p*-type electronic conductivity was about 10^2 and 10^{-1} Scm^{-1}, at room temperature after cooling in air and $P(O_2) = 10^{-4}$, respectively. Hence, it is found that the change in σ is well corresponded to the change in a concentration of charge carriers (electronic hole). It should be, however, noted that the Fe ions have mixed valences of Fe^{3+} and Fe^{4+} rather than Fe^{3+} alone, even in the strongly reducing

condition of $P(O_2) = 10^{-8}$ atm (Fig. 1). This indicates that the charge carriers still exist at that condition.

Figure 2 shows the Co *L*-edge XANES of the same samples. The spectra of $LaCoO_3$ and CoO are also shown in this figure for comparison. The absorption at around 775-782 eV is the $2p_{3/2}$ (L_3) edge and that at around 790-797 eV is the $2p_{1/2}$ (L_2) edge. The spectral features near 783 and 798 eV under the lower $P(O_2)$ conditions were unknown at present. The peak of $LaCoO_3$, exhibiting a valence of ca. 3 appeared at 779.22 eV, whereas that of CoO, exhibiting a valence of ca. 2 appeared at 776.92 eV. This figure shows that the mixed valences of cobalt in the samples changed from Co^{3+}-Co^{4+} to Co^{2+}-Co^{3+} with decreasing $P(O_2)$. Our previous work [2] revealed that *p*-type electronic conduction appeared in the $P(O_2)$ range [$10^{-11} \leq P(O_2)/\text{atm} \leq 1$ at 1273 K], while δ is equal to 0.28 (2.84 of nominal *B*-site mean valence) at 10^{-8} atm of $P(O_2)$ at the same temperature. Hence it is suggested that the appearance of Co^{2+} enabled the *p*-type electronic conduction to appear in the wide range of $P(O_2)$ even if the mean valence of *M* is less than 3. While the formation of Co^{2+} may not be preferable in view of the stability of the structure in $(La,Sr)CoO_3$ system, in the case of $(La,Sr)Co_{0.2}Fe_{0.8}O_3$, *B*-site sublattice, consisting mainly of Fe ions may stabilize Co^{2+} ions.

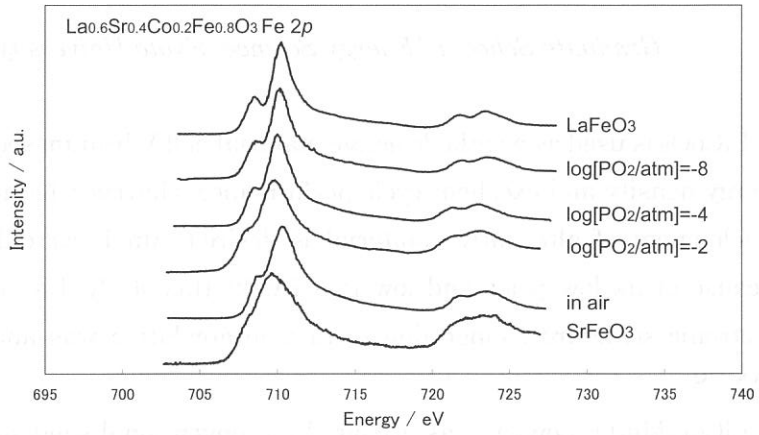

Fig. 1. Fe2*p* X-ray absorption spectra of samples.

Figure 3 shows the O *K*-edge XANES of the samples. The peak near 528 eV is attributed to the band derived from the mixing of the transition metal 3*d* states with O 2*p* states. The prepeak near 527 eV is attributed to the hole state, containing O 2*p* character caused by Sr-substitution. With decrease in $P(O_2)$, the prepeak disappeared along with the oxygen vacancy formation. Oxygen atoms containing this hole state with O 2*p* character may be transformed easily into neutral oxygen molecules under low $P(O_2)$, leaving the oxygen vacancies at the lattice. In conclusion, the role of each element to the electric conducting behavior was revealed by XANES studies on $La_{0.6}Sr_{0.4}Co_{0.2}Fe_{0.8}O_{3-\delta}$. In the further work, a quantitative observation regarding the hole concentration at each position has to be done.

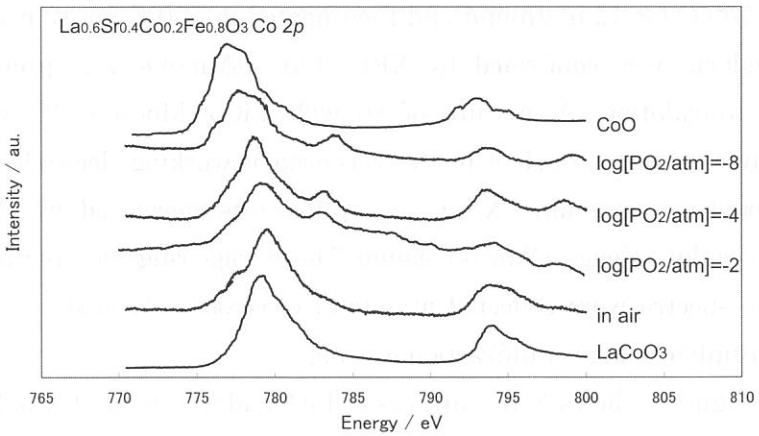

Fig. 2. Co2*p* X-ray absorption spectra of samples.

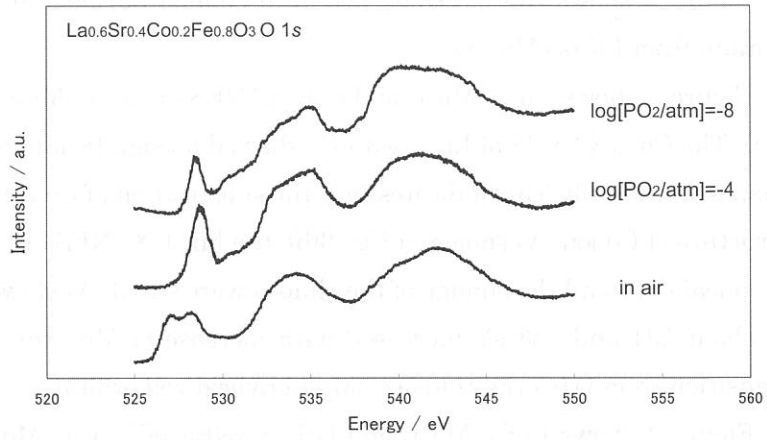

Fig. 3. O1*s* X-ray absorption spectra of samples.

References

[1] L-W. Tai, M. M. Nasrallah and H. U. Anderson, *J. Solid State Chem.*, **118,** 117 (1995).

[2] A. Mineshige, J. Izutsu, M. Nakamura, K. Nigaki, M. Kobune, S. Fujii, M. Inaba, Z. Ogumi and T. Yao, *Electrochemistry,* **68,** 515 (2000).

(BL-8B1)

Electronic Structure Change by Li deintercalation in $Li_xCo_{1-y}Mn_yO_2$ from Co-L, Mn-L and O-K XANES

Naoshi OZAWA, Yoshiharu UCHIMOTO, Hiroshi SAWADA and Takeshi YAO

Graduate School of Energy Science, Kyoto University, Kyoto, 606-8501 Japan

$LiCoO_2$ is used as a cathode active material of 4 V lithium secondary battery, because of its high energy density and excellent cycle performance. However, because Co is expensiveness and toxic, development of alternative material is desired. Mn is candidates for the alternative material because of its low price and low toxicity. In this study, $LiCo_{1-y}Mn_yO_2$ was synthesized and the electronic structure change due to Li deintercalation was analyzed from Co-L, Mn-L and O-K XANES.

$LiCo_{1-y}Mn_yO_2$ powder was prepared by conventional solid state reaction starting with lithium hydroxide (Wako Chemical Co. Inc., 99.9 %), cobalt hydroxide (Wako Chemical Co. Inc., 99.9 %), and manganese hydroxide (Wako Chemical Co. Inc., 99.9 %). Mixtures of low material was heated at 700°C for 12 h, ground and then heated at 800°C for 12 h in air. The crystal structure of the products was confirmed by XRD. $Li_xCo_{0.9}Mn_{0.1}O_2$ was prepared by electrochemical lithium deintercalation. A mixture of 80 wt% $LiCo_{0.9}Mn_{0.1}O_2$, 15 wt% acetylene black, and 5 wt% polytetrafluoropropylene binder was used as working electrode. The electrolyte was 1 M $LiClO_4$ in propylene carbonate. X-ray absorption was measured by BL-8B1 at UVSOR, Institute for Molecular Science, Okazaki, Japan. The storage ring was operating at electron energy of 750 MeV. The spectra were collected in a total electron yield mode at room temperature by an electron multiplier using G1 diffraction grating.

Figure 1 shows XRD patterns of $LiCo_{1-y}Mn_yO_2$ (y=0, 0.1, 0.2). The patterns were indexed to a rhombohedral lattice and $R\bar{3}m$ space group. For $LiCo_{0.8}Mn_{0.2}O_2$, tiny unknown peak was observed at about 37 °.

Figure 2 shows the electrode potential change during the electrochemical deintercalation of lithium from $LiCo_{0.9}Mn_{0.1}O_2$.

Figure 3 shows Co-L, Mn-L and O-K XANES of $LiCo_{1-y}Mn_yO_2$ (y=0, 0.1, 0.2). As shown in Fig. 3(a), The Co-L XANES of $LiCo_{1-y}Mn_yO_2$ showed no significant chemical shift and the change of the shapes were small. This indicates that the substitution of Co with Mn does not affect the electronic structure of Co ion. As shown in Fig. 3(b), the Mn-L XANES of $LiCo_{1-y}Mn_yO_2$ showed no significant chemical shift and the change of the shapes were small. As shown in Fig. 3(c), the peak intensities at about 531 and 533 eV increased with increase of Mn content. These peaks are attributed to transition from O1s orbital to O2p-Mn3d hybridized orbital[1].

Figure 4 shows Co-L, Mn-L and O-K XANES of $Li_xCo_{0.9}Mn_{0.1}O_2$ (x=0.2, 0.4, 0.6, 0.8, 1.0). As shown in Fig. 4(a), the Co-L XANES of $Li_xCo_{0.9}Mn_{0.1}O_2$ showed no remarkable chemical shift and

the change of the shapes were small. This indicates that the valence of Co ion was almost unchanged by deintercalation of Li from $LiCo_{0.9}Mn_{0.1}O_2$. As shown in Fig. 4(b), the Mn-L XANES of $Li_xCo_{0.9}Mn_{0.1}O_2$ showed no significant chemical shift and the change of the shapes were small. This indicates that the valence of Mn ion was almost unchanged by intercalation of Li from $LiCo_{0.9}Mn_{0.1}O_2$. As shown in Fig. 4(c), by extracting lithium from $LiCo_{0.9}Mn_{0.1}O_2$, the peak shape at about 529 to 533 eV changed and a new shoulder was observed at about 527 eV. This indicates that oxidation by lithium deintercalation is mainly related to the electrons in O2p orbital.

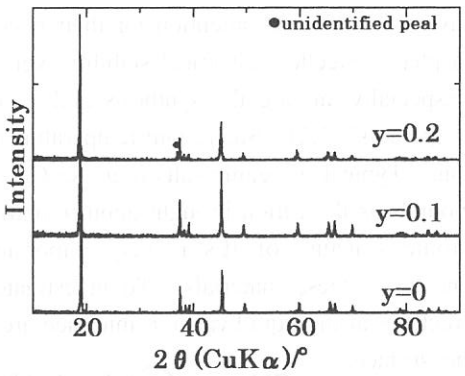

Fig.1 XRD patterns of $LiCo_{1-y}Mn_yO_2$ (y=0, 0.1, 0.2).

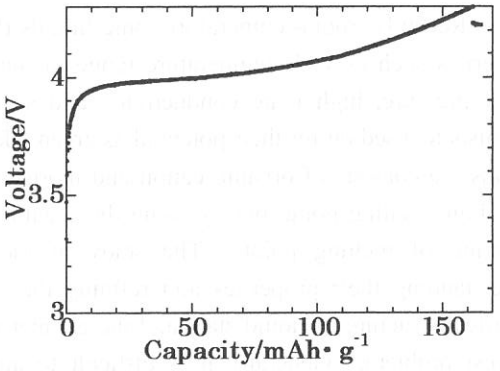

Fig.2 Electrode potential change of $LiCo_{0.9}Mn_{0.1}O_2$ electrode during the charge process.

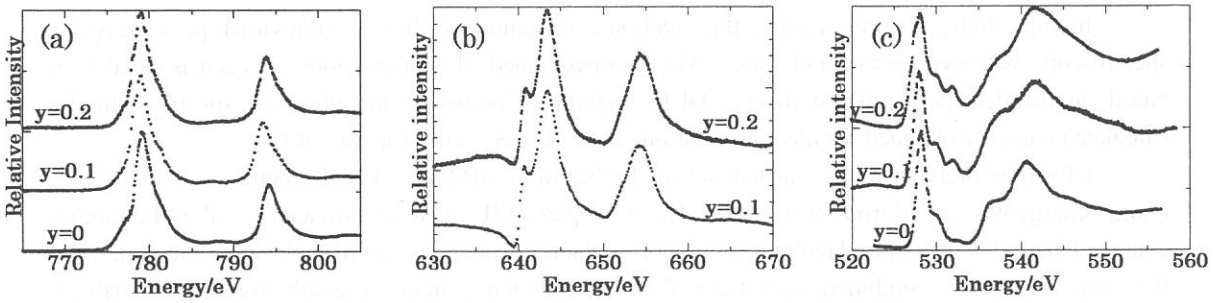

Fig.3 (a) Mn-L, (b) Co-L and (c) O-K XANES of $LiCo_{1-y}Mn_yO_2$ (x=0, 0.1, 0.2).

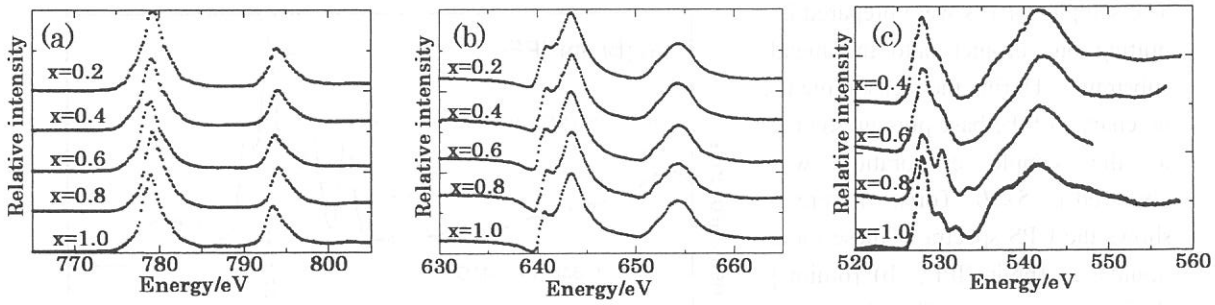

Fig.4 (a) Mn-L, (b) Co-L and (c) O-K XANES of $Li_xCo_{0.9}Mn_1O_2$ (x=0.2, 0.4, 0.6, 0.8, 1.0).

Reference

1) M.Abbate et. al., *Phys. Rev. B*, 46, 4551 (1992).

(BL8B2)

Electronic Structure of Ionic Liquids Studied by UV Photoemission

D. Yoshimura,[a,b] T. Yokoyama,[c] T. Nishi,[c] H. Ishii,[c] K. Seki,[a] R. Ozawa,[d] and H. Hamaguchi[d]

a) Research Center for Materials Science, Nagoya University, Chikusa-ku, Nagoya 464-8602, Japan

b) Institute for Molecular Science, Myodaiji, Okazaki 444-8585, Japan

c) Department of Chemistry, Graduate School of Science, Nagoya University, Chikusa-ku Nagoya 464-8602, Japan

d) Department of Chemistry, Graduate School of Science, The University of Tokyo, Hongo Tokyo 113-0033, Japan

Recently, room-temperature ionic liquids (ILs) have attracted much attention for their excellent properties such as wide temperature range of the liquid phase, excellent chemical stability, very low vapor pressure, high ionic conductivity, and so on. Especially, among the synthesis and catalysis chemists focused on for their potential as green "designer solvents".[1,2] Such room-temperature ionic liquids are consists of organic cation and inorganic anion. Typical inorganic salts (*e.g.* Na^+Cl^-) have very high melting point, but by using the organic compounds as the cation brought about remarkable lowering of melting point. The study of the electronic structure of ILs is very important to understanding their properties and refining the performance of these materials. To investigate the electrical structure of liquid state and the geometrical structures at the liquid/vacuum interface are also interest problem. Generally it is difficult to apply the surface scientific techniques to the liquid state sample. But the nature of very low vapor pressure of ILs enables us the measurement in ultra-high vacuum (UHV) condition. However, there have been few studies that directly observed the electronic structure of ILs.

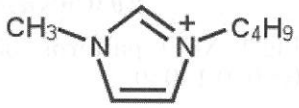

Fig.1 molecular structure of $bmim^+$

In this study, we investigated the electronic structures of ILs by ultraviolet photoemission spectroscopy with synchrotron radiation. We also performed MO calculations for each isolated ions based on the density functional theory (DFT) method. Comparing the observed spectra with the calculated ones, we obtained detailed information about the electronic structure of ILs.

UPS measurements were carried out at the beamline 8B2 of UVSOR facility. The incident photon energy was varied from 20-120eV. Three samples of ILs were investigated. All of the sample contain 1-buthyl-3-methylimidazolium ($bmim^+$) [3] which is known as one of typical organic cation for ILs, and this cation combined with three fluorine containing anions (hexafluorophosphate (PF_6^-), tetrafluoroboronate (BF_4^-), bis(trifluoromethanesulfonyl)imide ($CF_3(SO_2)_2N^-$; Tf_2N^-). All of these ILs are in the liquid phase at room temperature. In Figure 1, we show the molecular structure of $bmim^+$. The samples of ILs were prepared by putting one droplet onto the metal substrate. During the measurements, no change of the base pressure owing to the sample evaporation was observed (< 5×10^{-10}Torr). Figure 2 shows the UPS spectra of these ionic liquids; a) $[bmim^+]PF_6^-$, b) $[bmim^+]BF_4^-$, c) $[bmim^+]CF_3(SO_2)_2N^-$. The incident photon energies of the spectra were 80eV for Fig 2a and 60eV for Figs. 2b and 2c. The abscissa of the spectra is the binding energy relative to the vacuum level.

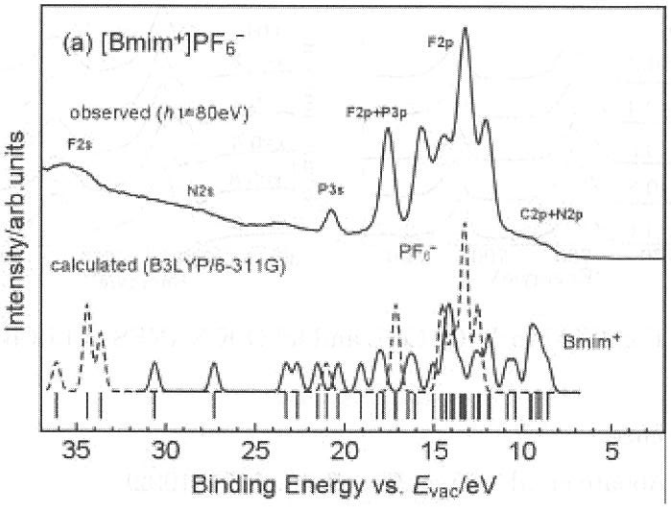

Fig 2(a)

Fig. 2(a) Observed and calculated spectra of $[bmim^+]PF_6^-$.

We also performed MO calculations for each isolated ions based on the density functional theory (DFT). The calculations were performed by GAUSSIAN98 with B3LYP parameters and 6-311G basis set. Below the observed spectra in Figs. 2, we show the calculated density of states (DOS) by convoluting each calculated states with a Gaussian function (FWHM = 0.5eV) under the assumption that the emission intensities from each orbital were the same. Each of the calculated DOS for the isolated ions was shifted in the energy scale for better correspondence with the observed spectra. The direction and the amount of the shifts were shown in Table 1, together with the experimentally obtained values of ionization potential (IP) of these ILs from the another UPS measurements.[2] Comparing the observed spectra with the simulated ones, there was fairly good agreement with each other. Therefore, it is concluded that the top of the valence band is derived from the HOMO of the $bmim^+$. We can assign the another peaks of ILs' spectra based on the calculation as shown in Figs. 2. In these figures, we can see the trend that the orbital energies of the cation ($bmim^+$) were unstabilized, and those of anions were stabilized against the predicted value by the calculations. Before the shift in the energy scale, the calculated HOMO of $bmim^+$ lay deeper than its counter anions. This inversion of the top of the valence states can be explained by the effect of Mudelung energy. Lastly, we mention that the molecular orientation of $bmim^+$ in the liquid phase from our recent results of NEXAFS measurements.[2] Next, we will try to obtain more detailed information about molecular orientation from ARUPS measurements.

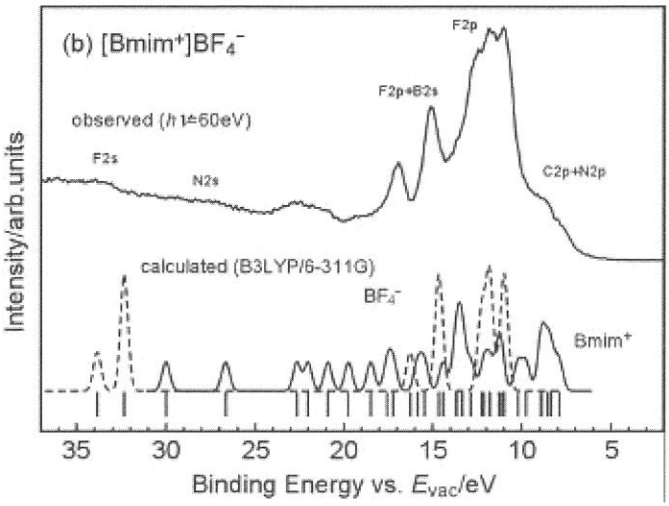

Fig. 2(b) Observed and calculated spectra of $[bmim^+]BF_4^-$.

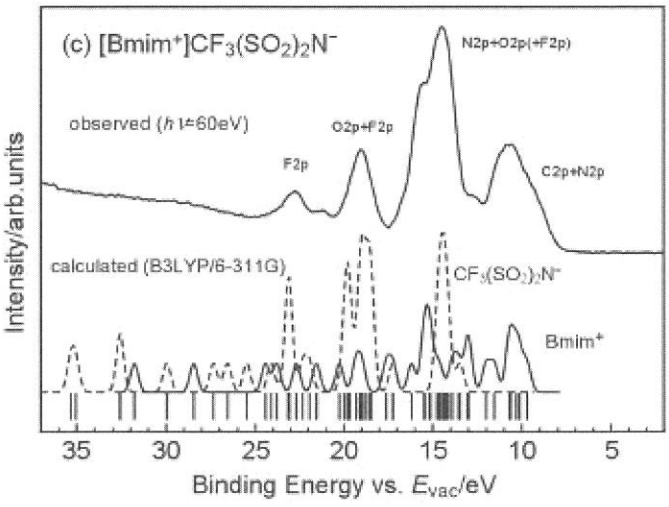

Fig. 2(c) Observed and calculated spectra of $[bmim^+]CF_3(SO_2)_2N^-$.

	I_{th}	Shifts in energy scale	
		Cation	Anion
$[bmim^+]PF_6^-$	7.85	-3.1	+6.9
$[bmim^+]BF_4^-$	6.68	-2.1	+9.3
$[bmim^+]Tf_2N^-$	7.82	-3.9	+6.8

(in eV)

Table 1. Ionization potential and the energy shifts.

References

[1] T. Welton, Chem Rev. **99** 2071 (1999).

[2] P. Wassescheid and W. Keim, Angew. Chem. Innt. Ed., **39** 3772 (2000).

[3] P.A.Z. Suarez, S. Einloft, J.E.L. Dullius, R.F. de Souza and J. Dupont, J. Chim. Phys. **95** 1626 (1998).

[4] T. Nishi, to be published.

Surface and Photochemistry

(BL2B1, 3A1, 4A1, 4A2, 5B, 6B, 8A)

(BL4A2)

SR etching of SiO_2 using a contact cobalt mask

C.Wang[1], Z.Wang[2], S.More[1], Y.Nonogaki[1], S.Yamamura[2], S.Fujiki[2], M.Takizawa[2], T.Urisu[1, 2]
[1]*Institute for Molecular Science,* [2]*The Graduate Univ. for Advanced Studies*

We have studied a new etching technique, which can be applied to the area selective deposition of SAM and biomaterial on silicon wafers. We use SF_6+O_2 as the reacting gas and a cobalt thin film as the contact mask. The cobalt mask was found to show strong resistibility for SR, while it can be easily removed with dilute acid. The roughness of the surface after the SR etching was sufficiently small to fabricate an well-ordered SAM on silicon wafers.

The silicon dioxide film (~ 205 nm) was thermally grown on n-type (80-120 ohm · cm) Si (100) wafer. A cobalt thin film (~ 200 nm), which was fabricated on the silicon oxide surface by using a sputtering technique was used as the contact mask. The gas pressure for O_2 and SF_6 was 0.05 torr and 0.002 torr, respectively. The beam current was about 200 mA. The irradiation dose of SR beam was about 2000 mA · min.

The depth profile (Fig. 1) of the etched pattern indicates that SR irradiation with flowing SF_6 and O_2 can effectively etch the silicon dioxide and completely stop on the silicon surface. The cobalt mask shows strong resistibility for SR etching. Furthermore, the cobalt was found to be easily removed by diluted HNO_3 or HF solution. Consequently, the cobalt can be used as a good mask for SR etching

The cross section of the etched pattern was observed with scanning electron microscopy (SEM). Due to the good directivity and short wavelength nature of synchrotron radiation beam, the SR etching for SiO_2 is anisotropic, and the sidewall of the etching pattern is very steeper. The AFM topography (Fig. 2) shows that the roughness of the surface after SR was about 1 nm. These flat surfaces are fit for depositing well-ordered SAM and biomaterials.

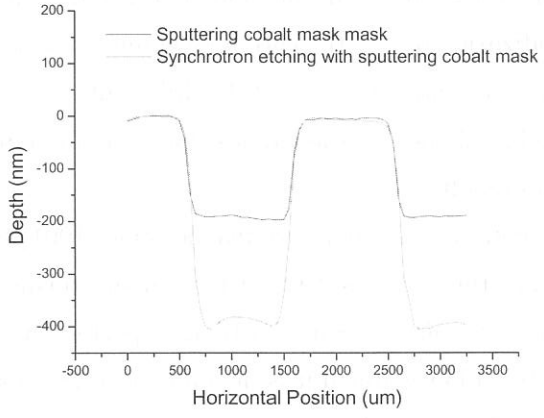

Fig. 1

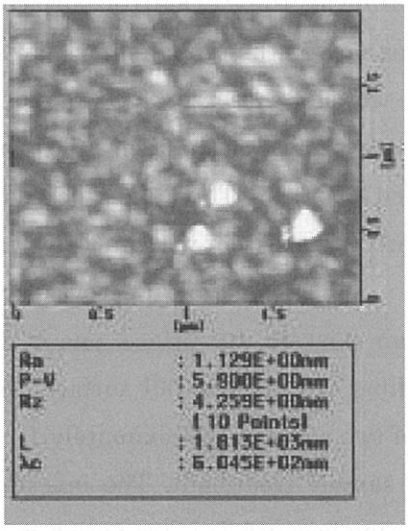

Fig. 2

(2B1)

Ion desorption from the $SrTiO_3(100)$ surface

S. Tanaka[1], K. Mase[2], and S. Nagaoka[3]

[1]*Department of Physics, Graduate School of Science, Nagoya University, Furo-cho, Chikusa, Nagoya 464-8602, Japan*

[2]*Institute of Material Structure Science, Tsukuba 305-0801, Japan*

[3]*Chemistry Group, Department of Fundamental Material Science, Faculty of Science, Ehime University, Matsuyama 790-8577, Japan*

Desorption induced by electronic transition (DIET) from solid surfaces has been studied extensively in recent decades, and a general mechanism of the ion desorption induced by core-level excitation was proposed by Knotek and Feibelman. It is based on the results they obtained when measuring the electron stimulated desorption (ESD) yield of O^+ from TiO_2, whose desorption threshold correlates with the Ti3p core excitation threshold but not with the O2s or the valence excitation. In the Knotek-Feibelman (KF) mechanism, a Ti3p core hole is produced by a primary excitation and decays by means of an *inter*atomic Auger process because there are no higher-lying occupied electronic states except for the O2s and O2p orbitals. (i.e., it is the "maximal valency" state). If two Auger electrons and an additional electron (due to, for instance, double Auger decay) are emitted by the oxygen atom, the remaining O^+ ion desorbs as a result of the Coulomb repulsion from the surrounding Ti^{4+} ions.

Recently, we have proposed another mechanism based on the investigation on the $TiO_2(110)$ and the ZnO(1010) surfaces by means of the electron-ion coincidence (EICO) spectroscopy. In the proposed mechanism, the creation and desorption of O^+ are driven by a charge transfer through the O2p-Ti3d hybridization due to the core hole potential at Ti (the Kotani-Toyozawa mechanism). TiO_2 has an unoccupied 3d orbital while ZnO has fully occupied 3d orbital. Thus, the proposed model predicts that the ion desorption occurs only on TiO_2, and is consistent with our experimental result.

$SrTiO_3$ is a typical perovskite-type metal oxide. There are two possible (100) planes that can exist on its surface; one is SrO, and the other is TiO_2. After ion-sputtering and annealing, the $SrTiO_3(100)$ surface contains both planes. Some authors reported that the ratio of two areas is approximately 1:1, but the other claimed it is dependent on the history of the sample treatment. The investigation of the ion desorption from this surface is of interesting because Ti is transition metal and Sr is not. Therefore, if one assumes a simple

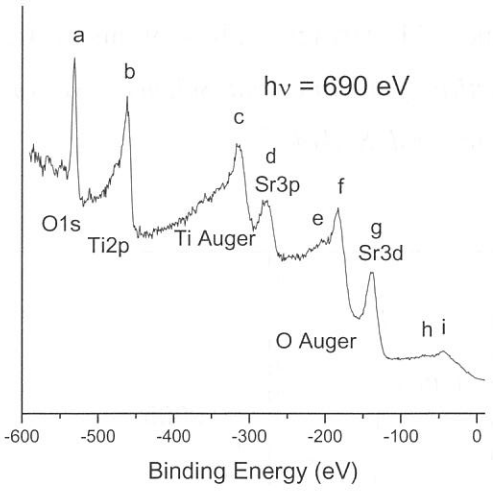

Figure 1

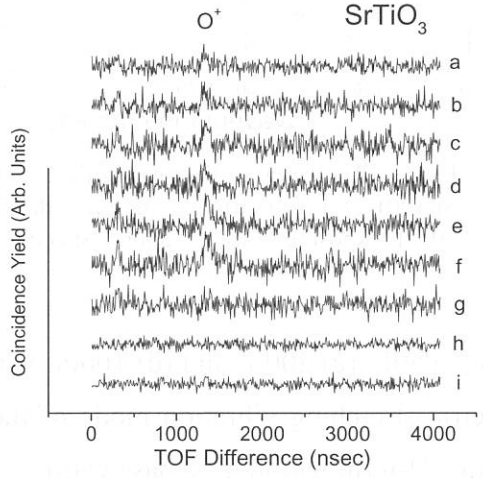

Figure 2

electronic configuration in which the bonding between Ti and O and that between Sr and O in $SrTiO_3$ are the same as those respectively in SrO and TiO_2, it is expected that the ion desorption occurs only on the excitation of the Ti-core level.

All the experiments were carried out at BL2B1 of UVSOR. The $SrTiO_3$(100) surface was Ar^+-sputtered and annealed in the vacuum and oxygen ($1x10^{-6}$ Torr) to obtain the stoichiometric surface with small number of oxygen vacancy. The ratio of SrO and TiO_2 domains is not known. Figure 1 shows the photoelectron spectrum of the taken at hν=690eV. Several peaks are observed, and indicated as a – i. These are photoelectron from the core-level and Auger electron emissions, as shown in the figure. Figure 2 shows EICO spectra of using the photoelectrons of a – i in Fig.1. O^+ desorption is observed for the curves of a – f, which are the photoelectron emission from the O-core (a), and Ti-core (b) levels, and Auger electron emission of O-core (e,f), and Ti-core (c,d) levels. Note that the peak d in Fig. 1 is also contributed from the Sr-core electron emission. Meanwhile, no peak is observed in the coincidence spectrum g, which indicates that the excitation of the Sr3d electron does not efficiently yield the ion desorption. This result is consistent with our proposal on the desorption mechanism, and contradict against the KF model, because the maximal valency condition is satisfied in SrO as well as TiO_2. However, according to the experimental results using a different photon energy, the the desorption induced by the Sr 3p and 3d electron excitation is clearly observed, even though their efficiencies are smaller than the Ti and O core-electron excitation. More work, including a quantitative comparison of ion desorption probabilities among the core-levels, is needed and in progress.

(BL4A2)

Reactivity of the Nearly Ideally H-terminated Si(100)-2×1 Surface with Water

Z.-H.Wang[1], H.Wanatabe[3], S. Nanbu[2], J. Maki[2], M. Aoyagi [1,2] , K. Ooi[3] and T. Urisu[2]

The Graduate Univ. for Advanced Studies[1] / Institute for Molecular Science[2], Nation. Insti. Advanc.Indust. Sci. Technol. Shikoku[3]

The ideally H-terminated Si(100) surface is very important from both viewpoints of surface science and semiconductor process technology. Surprisingly the detailed investigations are very few since the experimental difficulties on detection of surface species on one hand and theoretical expensive on the other hand. In this work, the BML-IRRAS technique was used to monitor the water reaction with ideally H-terminated Si(100)-2×1 surface for the first time. In Fig. 1, IR spectra of nearly ideally H-terminated Si(100) 2×1 surface (a), and the changes of the IR spectra by exposing the surface (a) to (b) 50L, (c) 200 L and (d) 1000L water vapor. The 2100 cm^{-1} peak is assigned to the symmetric stretching vibration mode of the coupled monohydride. From Fig. 1, it is clear that the H-termination has passivation effects for dissociative adsorption of water. But, it is also clear that the surface is still highly reactive with water and easily oxidized. The complex peak assignment is now under investigation combined with an ab initio molecular orbital (MO) calculation of the cluster model. The initial oxidation mechanism of water with H-terminated Si(100)-2×1 surface is also proposed.

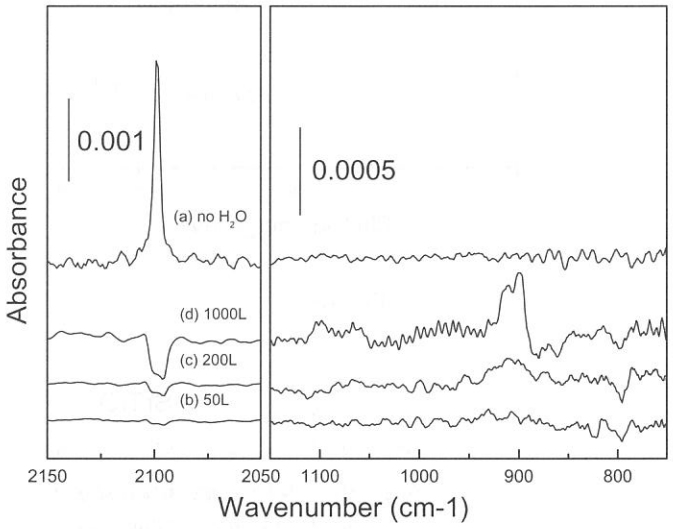

Fig. 1 IR spectra of (a) nearly ideally H-terminated Si(100)-2×1 and (b), (c), (d) after the 50, 200 and 1000L exposure to water vapor, respectively.

(BL4A2)

Nearly Ideally Hydrogen Terminated Si(100) Surface and IR-spectrum Width Broadening Due to Hydrogen Diffusion into the Subsurface

Z.-H. Wang[2], N. Yabumoto[3], T. Urisu [1,2] Wang@ims.ac.jp,

The Graduated Univ. for Advanced Studies[1] / Institute for Molecular Science[2], NTT Advanced Technology Corporation[3]

Nearly ideally H-terminated condition for Si(100)-2 × 1 surface is determined from the dependence of the peak intensity and the linewidth of the coupled monohydride symmetric stretching vibration on the hydrogen exposure and the exposure temperature, which has been investigated with infrared reflection absorption spectroscopy (IRRAS) using $CoSi_2$ buried metal layer substrate. It was found that even for nearly ideally H-terminated surfaces, the linewidth significantly changes depending on the hydrogen exposure and the exposure temperature. At low temperature region (<600K), the line width broadening was explained by the inhomogeneous of surface caused by dihydride species SiH_2 existence. At higher temperature region (>700K), the line width broadening was explained by the decomposition of coupled monohydride and background water adsorption contamination. In the region of (600K ~ 700K), the line width broadening can not simply explained by these effects since no dihydride species can be detected and no water contamination trace exist. The concentration of deuterium atoms incorporated in the Si bulk is measured by temperature programmed desorption. It is proportion with the line width. From these experimental facts it is concluded that hydrogen diffusion into the subsurface of Si has a significant influence on the linewidth broadening.

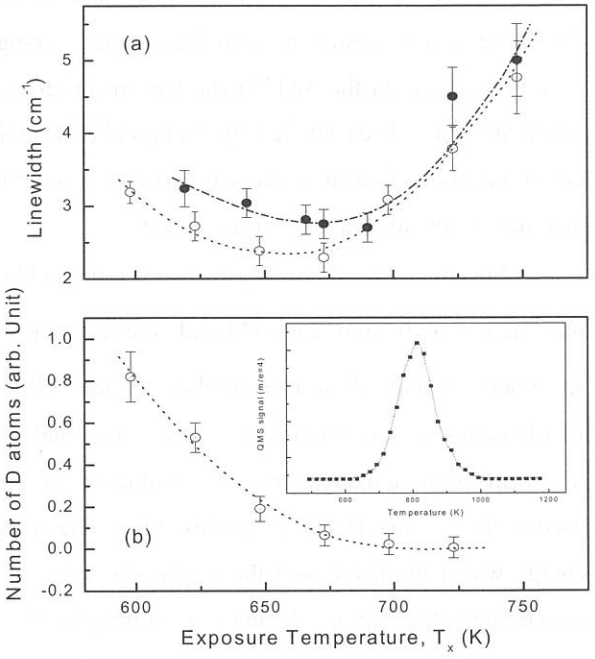

Fig. 1 Dependence of linewidth and desorption of D atoms incorporated into the bulk on the exposure temperature.

(BL5A)

Local atomic arrangement of Si(111)√3x√3-(Pb,Sn) surface

J. Yuhara, T. Takada, D. Nakamura†, K. Soda, M. Kamada*

Graduate School of Engineering, *Nagoya University, Nagoya, 464-8603, Japan*
*UVSOR, Institute for Molecular Science, Myodaiji, Okazaki 444-8585, Japan**

Recently, great attention has been focused on the understanding of atomic arrangement and electronic structure of binary adsorbates on the semiconductor surface to control crystalline growth mode, such as perfect flat interface and nano-dots. In the case of (Pb,Sn) binary adsorbates on the Si(111) surface, they form unique 2√7x3 and √7x√3 structures at the total coverage of 0.7 ~ 0.8 ML, although they are immiscible in bulk. We have also observed that co-adsorbates of Pb and Sn form a √3x√3 reconstruction at the total coverage of 1/3 ML. Therefore, it is interesting to study local atomic arrangements and electronic structures of (Pb,Sn) co-adsorbates at low coverage on the Si(111) surface. In this paper, the Si(111)√3x√3-(Pb,Sn) surface at single and binary adsorbates have been studied by topographic scanning tunneling microscopy (STM) and Pb 5*d* and Sn 4*d* core-level photoelectron spectroscopy (PES) in order to discriminate the adsorbate elements on the STM images and identify the local atomic arrangement.

Specimens were mirror-polished n-type Si(111) wafers with a resistivity of 3 Ω cm in sizes of 15x3x0.5 mm^3 and 15x6x0.5mm^3 for STM and core-level PES measurements, respectively. In the PES measurement, the specimen was placed on a manipulator under $5x10^{-9}$ Pa base pressure in the UHV chamber equipped with a LEED optics, a hemispherical electron energy analyzer ($\Delta E = 0.04$ eV) with an angular acceptance of ± 8° at the normal emission angle, and two evaporation sources for Pb and Sn. Excitation photon energy of 52 eV was used at the 45° incident angle in this study. The energy spread of excitation photon was 0.04 eV. The binding energy was determined from the Fermi edge of a Ta plate that holds the Si wafer. The total energy resolution including the thermal broadening was estimated to be about 0.10 eV from the Ta Fermi edge.

Typical topographic STM images of the Si(111)√3x√3-(Pb,Sn) surface are shown in Fig.1 (a) for the filled states and (b) for the empty states. Observed spots in the STM images can be classified into three type of spots; white and gray (α), gray and white (β), and black and gray (γ), in the filled- and empty-state images, respectively. The Pb 5*d* and Sn 4*d* core-level photoelectron spectra were measured for mosaic √3x√3-Pb, √3x√3-Pb, √3x√3-(Pb,Sn), √3x√3-Sn, and mosaic √3x√3-Sn surfaces to investigate the chemical states of Pb and Sn adsorbates. Typical core-level PES spectra are shown in Fig.2. As is seen in Fig.2 (b) and (d), the √3x√3-Pb and √3x√3-Sn surfaces show two major surface chemical shifted components in the Pb 5*d* and Sn 4*d* core-level spectra, respectively. This is ascribable to charge density wave or dynamical fluctuation of Sn adatoms between two different vertical positions above T4 site [1], which are detectable on PES but not in STM because of the z scale resolution limit and the difference in the probing time scale [2,3]. The peak positions and shape of Pb 5*d* and Sn 4*d* core-levels of the √3x√3-(Pb,Sn) surface are similar to those of the √3x√3-Pb and √3x√3-Sn surfaces. This suggests that there is no specific charge transfer between Pb and Sn at the √3x√3-(Pb,Sn) surface and that chemical states of Pb and Sn are almost the same as those of the √3x√3-Pb and √3x√3-Sn surfaces. Since the minimum atomic distance between adsorbates in the √3x√3 reconstruction at the coverage of 1/3 ML is 0.665 nm, it may be reasonable to have no direct interaction between Pb and Sn adsorbates. On the other hand, the Pb

5*d* and Sn 4*d* core level spectra of the mosaic √3x√3-Pb and mosaic √3x√3-Sn surfaces show one major component, respectively. The binding energies of Pb 5*d* and Sn 4*d* spectra of mosaic √3x√3-Pb and mosaic √3x√3-Sn surfaces are almost equal to those of lower binding energy component on the √3x√3-Pb and √3x√3-Sn surfaces, respectively. This result agrees well with the result reported previously [1,2,4]. These results indicate that Pb and Sn atoms are stabilized at certain height or in one charged state on the mosaic √3x√3 surfaces. These results also suggest that the Pb and Sn heights, or charged states, stabilized at the mosaic √3x√3 surface are similar to those at the √3x√3 surface.

From the topographic STM images including domain boundary of the 7x7 and √3x√3-Pb surfaces and that of the 7x7 and √3x√3-Sn surfaces, it is found that the averaged spot heights at Sn are 0.03~0.05 nm higher than those at Pb in the filled state image, while they are 0.05~0.07 nm lower in the empty state image. This bias dependence of the corrugation of Pb and Sn is closely related to those of the spots α and β on the √3x√3-(Pb,Sn) surface in Fig.1. Thus, we conclude that Sn and Pb are located at α and β positions, respectively. Since Si adatoms are easily replaced with Pb and Sn in √3x√3 surface and their STM images at the Si adatom position show black and gray spots in filled and empty state images, respectively [5], it is considered that Si adatoms are located at the γ position.

References

[1] J. Avila, A. Mascaraque, E. G. Michel, M. C. Asensio, G. Le Lay, J. Ortega, *et al*, Phys. Rev. Lett. 82 (1999) 442.

[2] M. Göthelid, M. Björkqvist, E. G. Michel, M. C. Asensio, G. Le Lay, C. J. Karlsson, Phys. Rev. B52 (1995) 14532.

[3] R. I. G. Uhrberg, H. M. Zhang, T. Balasubramanian, S. T. Jemander, N. Lin, and G. V. Hansson, Phys. Rev. B62 (2000) 8082.

[4] R. I. G. Uhrberg, H. M. Zhang, T. Balasubramanian, Phys. Rev. Lett. 85 (2000) 1036.

[5] J. M. G. Rodriguez, J.-Y. Veuillen, R. C. Cinti, Surf. Sci. 377/379 (1997) 45.

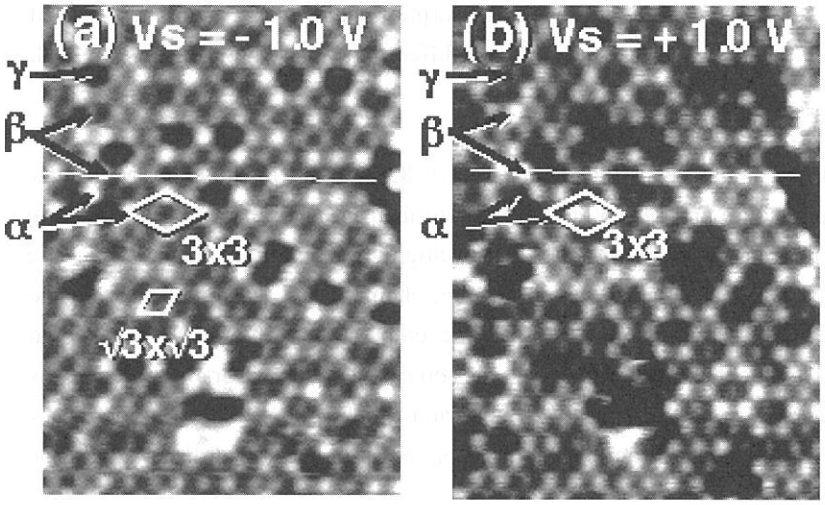

Fig.1 STM images obtained from the √3x√3-(Pb,Sn) surface at sample biases of -1.0 V (filled state) (a) and +1.0 V (empty state) (b). Spots are classified into three type of spots; white and gray (α), gray and white (β), and black and gray (γ) in the images (a) and (b), respectively. A √3x√3 unit cell is indicated in the figure as well as 3x3 unit cell.

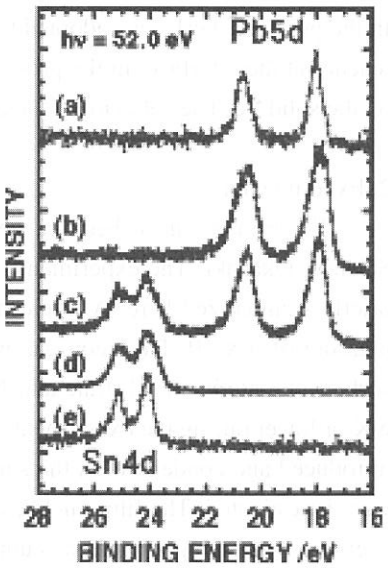

Fig.2 Pb 5*d* and Sn 4*d* photoelectron spectra of mosaic √3x√3-Pb surface with 1/6ML Pb (a), √3x√3-Pb with 1/3ML Pb (b), √3x√3-(Pb,Sn) (c), √3x√3-Sn with 1/3 ML Sn (d), and mosaic √3x√3-Sn with 1/6 ML Sn (e) after background subtraction.

(BL5B)

Measurements of Total Yields of Exciton-Induced Desorption from Argon Films Condensed on Solid Neon

Takashi Adachi, Takato Hirayama*, Ichiro Arakawa and Makoto Sakurai**

Department of Physics, Gakushuin University , Mejiro, Toshima, Tokyo 171-8588.
**Department of Physics, Rikkyo University , Nishi Ikebukuro, Toshima, Tokyo 171-0021.*
***Department of Physics, Kobe University, Rokkodai-cho, Nada-ku, Kobe 657-8501.*

1. Introduction

Electron or photon irradiation of the surface of rare gas solids produces the electronic excitations which can be followed by the desorption of various kinds of particles. Investigation of the desorption induced by electronic transitions (DIET) will reveal the dynamics of the electronic excitations and relaxations in solid and, especially, at the surface. DIET at the surface of rare gas solids has been extensively studied since 1980s [1]. We have reported the results of measurements of absolute photo-desorption yields from the surface of solid Ne [2], Ar [3, 4] and Kr [5] at excitonic excitation regime. At a film, which is thicker than 400 atomic layers, condensed on a metal substrate, the absolute photo-desorption yields are about 1.5, 0.2, and 0.03 atoms/photon for Ne, Ar, and Kr, respectively, at the excitation energy of the first order bulk exciton. The quantitative analysis of the absolute desorption yields and the thickness dependence reveal relaxation channels from the primary excitonic excitation to the desorption. The desorption yield of Ne was quantitatively explained by the internal sputtering mechanism [2]. In the case of Ar [3, 4] and Kr [5], the dominant desorption mechanism is the excimer dissociation which is followed by collision cascade.

The diffusion of excitons and these behavior at the interface between a solid rare gas and a substrate are important process to be considered for the estimation of the desorption yields and these thickness dependence. In the previous works, we adopted the assumption that the excitonic excitation is quenched immediately when it reaches at the interface. In the present study, we measured the photo-desorption yields from Ar films condensed on the solid Ne. The behavior of the exciton at the interface between two different rare gas solids are investigated.

2. Experimental

Experiments have been carried out at the beam line BL5B in UVSOR of the Institute for Molecular Science, Okazaki. The experimental procedure and set-up have been described in detail elsewhere [5] and are briefly summarized here. A liquid helium cryostat was installed in an ultrahigh-vacuum chamber with a base pressure of 5×10^{-9} Pa. Neon gas was introduced into the main vacuum chamber and was condensed on the surface of a platinum substrate attached to the liquid helium cryostat. The temperature of the sample was kept at 6 K or lower during the experiments. The thickness of the solid Ne was about 200 atomic layers. Argon gas was introduced and condensed on the surface of the solid Ne. Ar films of various thickness up to 800 atomic layers were investigated. The film thickness was calculated from the exposure on the assumption that the condensation coefficient of each gas at 6K was unity.

The absolute desorption yield was calculated from the absolute values of the intensity of the incident photons and of the number of Ar atoms desorbed. The absolute number of the incident light was monitored by measuring a photoelectron current emitted from the gold mesh which was installed in the beam line. The absolute number of the desorbed atoms was calculated from the rise of partial pressure of Ar, which was measured by a quadrupole mass spectrometer, during the irradiation of the sample and the total pumping speed for Ar.

3. Results and Discussions

The dependence of the total photo-desorption yields of Ar on the incident wavelength is shown in Fig. 1 for three different film thicknesses. For the film of 3 atomic layers in thickness, clear peaks are observed at 103 nm and 101 nm, which corresponds to the excitation energy of the first order bulk excitons, B1(3/2) and B1 (1/2), of solid Ar, respectively. For the film of 150 atomic layers, an additional peak appear at the wavelengths corresponding to the second order bulk (B2, 91 nm (3/2)) exciton. For the 520 atomic layers film, the small shoulder at 106 nm and the peak at 96 nm are observed, which corresponds to the creation of the second order surface (S2) and the first order surface (S1) excitons, respectively. The spectrum at 520 atomic layers is almost identical to that of the thick Ar film which is solely and directly condensed on the metal substrate.

Figure 2 shows the thickness dependence of the absolute desorption yields at B1 exciton excitation energy for two different systems; the Ar film condensed on the solid Ne and that on the metal substrate. The difference of the desorption yields between them at the thickness less than 10 atomic layers is originated from the difference in the behavior of the exciton at the interface. In the case of Ar on metal, the exciton is immediately quenched when it reaches at the surface of the metal substrate. In thin films, therefore, it results in low desorption yields. On the other hand, in the case of the Ar film condensed on solid Ne, the interface of Ar/Ne plays as a reflector for B1 exciton of Ar because the excitation energy of B1 exciton can not be transferred to solid Ne. Consequently the high desorption yields are observed at thin Ar film condensed on solid Ne. The quantitative analysis of the absolute desorption yields are now in progress.

References

[1] for recent review, see I. Arakawa, Molec. Crystal Liq. Crystal, **314**, 47 (1998), M. Runne and G. Zimmerer, Nucl. Instrum. Meth. Phys. Res. B **101**, 156 (1995).

[2] I. Arakawa, T. Adachi, T. Hirayama and M. Sakurai, Surf. Sci. **451**, 136 (2000).

[3] T. Adachi, T. Hirayama, I. Arakawa and M. Sakurai, UVSOR Act. Rep. 1999, UVSOR-**27**, 178 (2000).

[4] T. Adachi, T. Hirayama, I. Arakawa and M. Sakurai, UVSOR Act. Rep. 2000, UVSOR-**28**, 208 (2001).

[5] T. Adachi, T. Hirayama, I. Arakawa and M. Sakurai, in preparation.

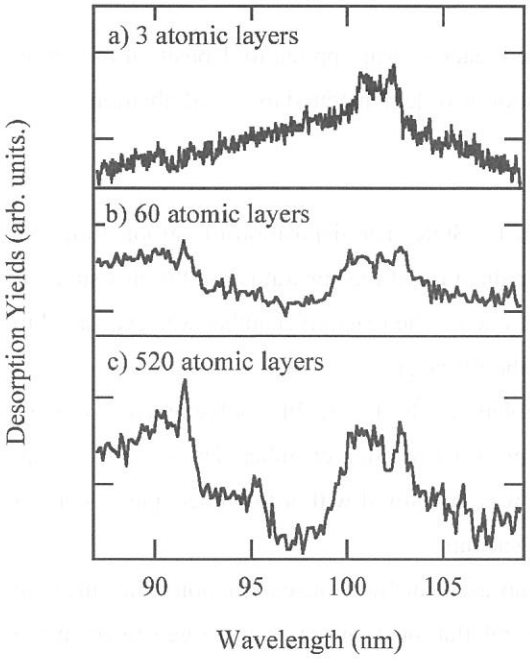

Fig. 1 Wavelength dependence of total desorption yields of Ar condensed on solid Ne.

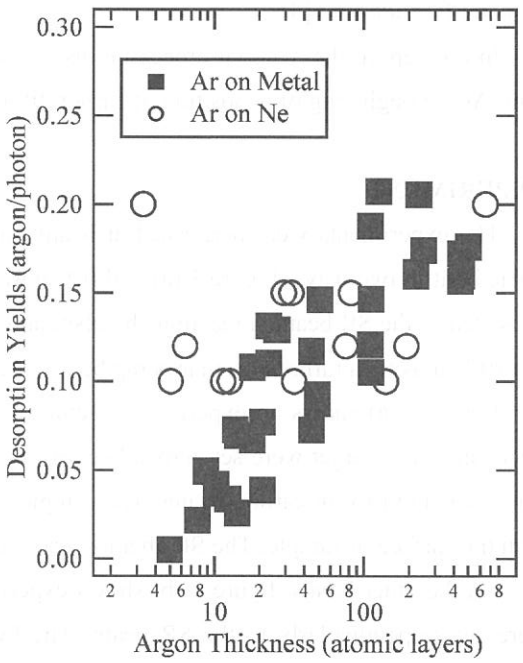

Fig. 2 Thickness dependence of absolute desorption yields at the excitation of B1 exciton.

(BL8A)

Deposition of Carbon Film Using Synchrotron Radiation Ablation

Hisao Nagai, Masaru Hori and Toshio Goto,
*Koji Katou, *Kouhei Ito and *Mineo Hiramatsu

Department of Quantum Engineering, Nagoya University,
Chikusa-ku, Nagoya, 464-8603
**Department of Electrical and Electronic Engineering, Meijo University,*
Tempaku-ku, Nagoya, 468-8502

INTRODUCTION

Electron field emission from various carbon materials has recently attracted much attention for their promising applications in displays and other microelectronic devices. Diamond, nanodiamond and diamond-like carbon are widely investigated and demonstrated to initiate emission at reasonably low fields. Among them, carbon materials such as nanodiamond and diamond-like carbon exhibit conspicuously excellent field emission characteristics, including very low threshold electrical fields, large emission current density, and high emission site density.

Previously, we demonstrated the anisotropic micromachining and film formation of Teflon (fluorocarbon polymer) using synchrotron radiation (SR) ablation process [1, 2]. Moreover, in order to clarify the mechanism of SR ablation, we have performed polytetrafluoroethylene (PTFE) micromachining by selecting the photon energy distribution of incident SR beam with carbon (C) membrane and carbon/magnesium fluoride / carbon (C / MgF_x / C) triple-layered membrane as filters. From these results, the photons with energy below 120 eV were found to contribute to the ablation of PTFE [3]. In addition, SR ablation was applied to pattern formation of metal fluoride film [4].

In this report, the material processing using the SR induced reaction was applied to deposition of carbon film. As the beginning of deposition of carbon film, the deposition was demonstrated using SR ablation.

EXPERIMENT

The experiments were performed at beam line BL-8A of UVSOR. The deposition of carbon film was carried out in two ways. Figure 1 (a) and (b) show a schematic diagram of the apparatus used in this study. It consisted of the SR beam, a reaction chamber, and a pumping system. The reaction chamber was evacuated to 1×10^{-4} Pa using a turbomolecular pump before irradiation by the SR beam.

Figure 1 (a) shows an experimental setup used for SR ablation. The PTFE, PE (polyethylene), $C_2H_2F_2$ thick films as a target were set perpendicularly to the SR beam in the reaction chamber. The sample heating was carried out using carbon heater. The sample temperature was monitored with a thermocouple in contact with the surface of sample. The SR ablation was carried out in vacuum.

On the other hands, figure 1 (b) shows experimental set up used for SR induced reaction. The substrate were set perpendicularly to the SR beam. The hydrocarbon and fluorocarbon gases were generated in the reaction chamber by evaporating PE and $C_2H_2F_2$ targets using carbon heater. The SR beam irradiated the target at 1×10^{-2} Pa.

RESULTS

Figure 2 shows a scanning electron microscopy (SEM) image of particles deposited on substrate using SR ablation of PTFE at dose of 1500 mA·min and a sample temperature of 500 °C. The size of particles were less than 1 μm.

Figure 3 shows a SEM image of particles deposited on the SR irradiation region on substrate using PE evaporation. The deposits with hemispherical shape of about 3 μm size were observed. In the case using $C_2H_2F_2$ evaporation, on the other hand, these deposits were not observed on the substraete.

Evaluation of deposits are being carried out using XPS and FT-IR. Moreover, emission characteristics will be investigated for the samples fabricated in this study.

REFERENCES

[1] M. Inayoshi *et al*, Jpn. J. Appl. Phys., **34**, L1675 (1995).

[2] M. Inayoshi *et al*, J. Vac. Sci. Technol., **B 17**, 949 (1999).

[3] H. Nagai *et al*, Applied Surface Science **183**, 284 (2001).

[4] H. Nagai *et al*, UVSOR Activity Report 182 (1999).

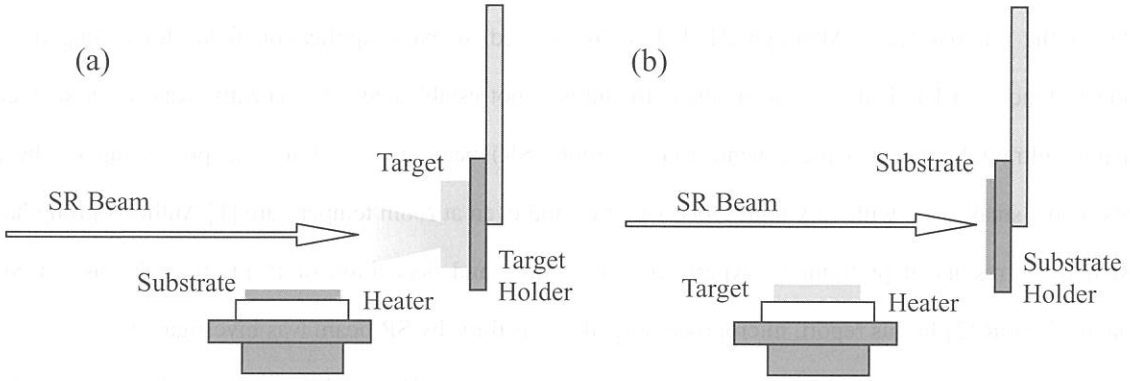

Fig. 1 Experimental set up used for (a) SR ablation and (b) SR induced reaction.

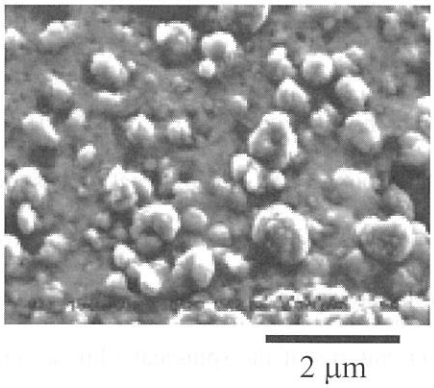

Fig. 2. SEM image of particles deposited on substrate using SR ablation of PTFE at substrate temperature of 500 °C.

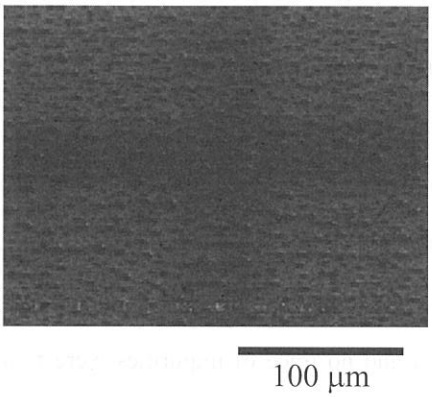

Fig. 3. SEM image of particles deposited on the SR irradiation region on substrate using PE evaporation.

(BL8A)

Formation of Polytetrafluoroethylene Microstructures by Synchrotron Radiation

H. Okada, E. Matsumoto, H. Yamada A. Wakahara and A. Yoshida

Department of Electrical and Electronic Engineering, Toyohashi University of Technology, Tempaku-cho, Toyohashi, 441-8580, Japan

Recent progress in micro-fabrication technique opens a new field of the microsystem such as the micro-machines, micro-sensors etc. Polytetrafluoroethylene (PTFE) is known to have unique properties: superior chemical stability, high thermal stability, high hydrophobicity and so on. These unique features of PTFE seems valuable for the microsystems. Although PTFE have been used in many application fields for a long time, formation technique of PTFE thin films or microstructures is not established yet. Recently, Kato *et al* showed that vacuum ultraviolet light in the synchrotron radiation (SR) beam is useful for the processing of these materials on the small scale with very high processing rate and even at room temperature.[1] Author's group has reported that the results of preliminary experiments of etching and deposition of PTFE films by use of SR radiation at UVSOR.[2] In this report, microprocessing of PTFE films by SR beam was investigated.

Experimental arrangement for a microprocessing is shown in Fig.1. The SR beam was incident through the same Ni mesh mask onto the spin-coated films. Thus, limited area ethicng of the PTFE film is expected here. Etching experiments were carried out in the reaction chamber having differential evacuation system was connected to the BL-8A port in UVSOR.

For the sample preparation, commercially available PTFE emulsion was used as a source of PTFE thin films. This source contains PTFE fine particles and surfactant. The rotational speed in the spin-coat process was 4000 rpm for 60sec, and the wafers were baked and filmed for 10min at the temperature of 513-673K. From x-ray photo-spectroscopy (XPS) spectrum of the deposited PTFE film shown in Fig.2, only C and F peaks were observed and no trace of impurities were found. From the XRD patterns of the spin-coat films a very strong sharp peak due to (100) plane of PTFE was observed. Thus, the crystalline quality of the films was obtained. The surface of the films was very smooth from atomic force microscope (AFM) observation, as shown in Fig.3.

The surface of PTFE is etched/ablated by irradiating SR beam and only irradiated surface region was easily etched through a mask. Nano-structured fabrication on the PTFE surface is possible with a suitably patterned mask. We tried the etching of commercially available PTFE sheet, and SR-induced and spin-coated PTFE thin

films through the Ni metal mask. The etching rate was very high (6mm/min for the electric current of 230mA in the storage ring), and was linearly dependent on the photon flux in proportion to the electron beam current in the storage ring. Figure 4 showed the SEM image of the etched surface of spin-coated PTFE films, and the PTFE surface was easily etched only on the area exposed to SR beam. By using SR-assisted process only, it is possible to deposit the crystalline PTFE films and succeedingly etch the surface of these films on a micro-scale. Since the SR beam is straightforwardly incident, the distance between a mask and the surface is allowed to be large even on a nano-structure. When the spin-coat method is accepted, the smooth and flat surface of PTFE is obtained even on complicated surface of the substrates.

REFERENCES
[1]T.Katoh and Y.Zhang, Appl.Phys.Lett., 68 (1996) 865
[2]M.Uchida, M.Ishizaka, H.Okada, A.Wakahara and A.Yoshida, UVSOR Activity Report 2000, (2000) 216

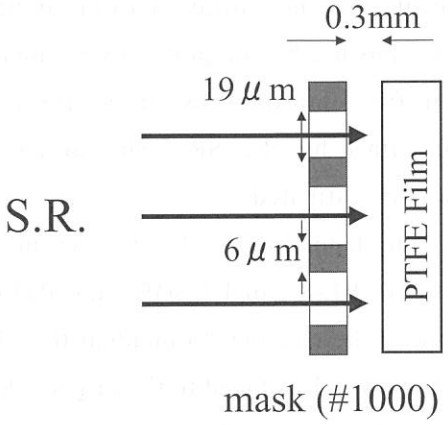

Fig.1: Experimental setup for etching.

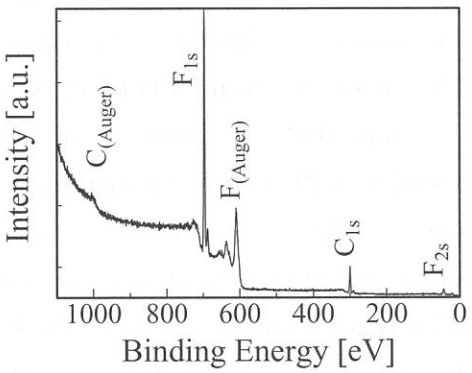

Fig.2: XPS spectrum of spin-coated PTFE film.

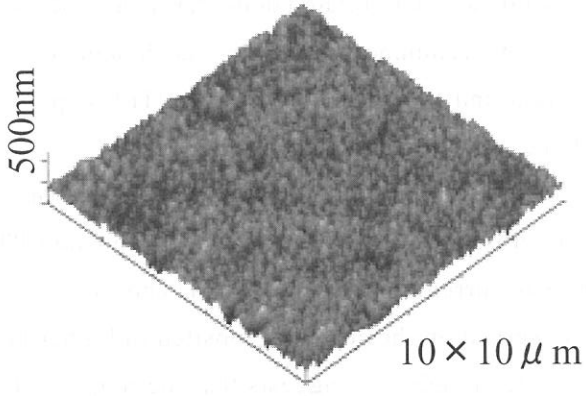

Fig.3: AFM image of spin-coated PTFE film.

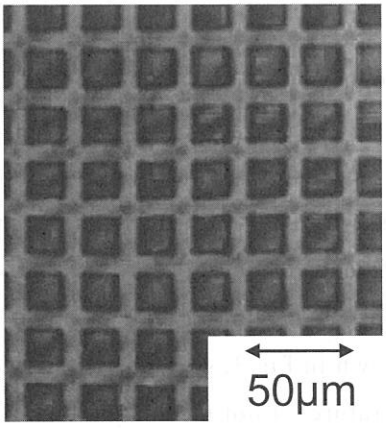

Fig.4: SEM image of etched film.

(BL8A)

Characteristics of Polytetrafluoroethylene Films Deposited by Synchrotron Radiation

A.Yoshida, E.Matsumoto, H.Yamada, H.Okada and A.Wakahara

Department of Electrical and Electronic Engineering, Toyohashi University of Technology, Tempaku-cho, Toyohashi, 441-8580, Japan

Polytetrafluoroethylene (PTFE) is a fascinating material due to its superior chemical stability, high thermal stability, high hydrophobicity and low surface tension. Adding to these, it also has excellent electrical characteristics, such as high breakdown voltage with low dielectric constant (ε_s=2.1). In spite of these features, formation or patterning of PTFE thin films are thought to be difficult due to the aforementioned nature. Recently, vacuum ultraviolet light in the synchrotron radiation (SR) beam utilized processing of PTFE films has been reported by Katoh *et al.*[1] They have ablated the PTFE target, and deposited thin film onto the substrate nearby the target. In this study, to obtain high quality PTFE thin films by the SR beam process, characteristics of PTFE thin film deposited by SR process was investigated.

Figure 1 shows experimental setup for PTFE thin film deposition[2, 3]. The vacuum chamber having differential evacuation system was connected to BL-8A of UVSOR ring. PTFE target, that is commercially available PTFE lump, was placed in the chamber to incident the SR beam directly. Deposition was made onto the p-Si(100) substrate which is faced to the target. The distance between the target and Si substrate was 3cm. Target heating can be achieved with a target heater.

Figure 2 showes Fourier transformation infrared (FTIR) spectrum of the PTFE thin film deposited at room temperature. Absorptions can be seen at the wavenumber of 1207、1152、630、553、 502cm^{-1}. Observed absorption peaks are assigned as CF_2 related bond that is a fundamental composition in PTFE. Weak peak observed at the wavenumber of 980cm^{-1} is thought to come from CF_3 bond. We have changed the beam current and target temperature in PTFE deposition, however, change was not observed in the FTIR spectrum from the deposited film.

Target temperature dependence of the surface morphology of the deposited film was investigated. Figure 3 shows the atomic force microscope (AFM) image of the deposited PTFE film for various target temperatures. Here, the beam current in storage ring was chosen at 220mA. As shown in Fig.3, granular-like structure was observed on the surface deposited in higher target temperatures. Root mean square (RMS) of the surface roughness suggests that the rough surfaces appear in higher target temperatures. Thus, target temperature affects the surface morphology.

As compared with the previous report in Ref.1, larger deposition rate was obtained in our results. From the sharpness of the XRD peak of the deposited film, the film deposited in this study seems to have good crystallinity. At present, fair comparison between two reports is

difficult, however, one possibility of the observed sharp XRD peak in this study is a utilization of focused SR beam in BL-8A. Indeed, the vacuum pressure of the chamber went up to 10^{-4}Torr during the deposition process. In such a situation, enhanced reaction is expected due to the existence of large amount of saturated fluorocarbon species in between the target and. This may lead to cause a high crystal PTFE film depostion.

REFERENCE
[1] T.Katoh, Y.Zhang, Appl. Phys. Lett. 68, 6 (1996) 865.
[2] M.Uchida, M.Ishizaka, H.Okada, A.Wakahara and A.Yoshida, UVSOR Activity Report 2000,(2000) 216.
[3] E.Matsumoto, M.Uchida, H.Okada, A.Wakahara and A.Yoshida, Technical Report of IEICE, SDM2001-30~43 (2001) 7.

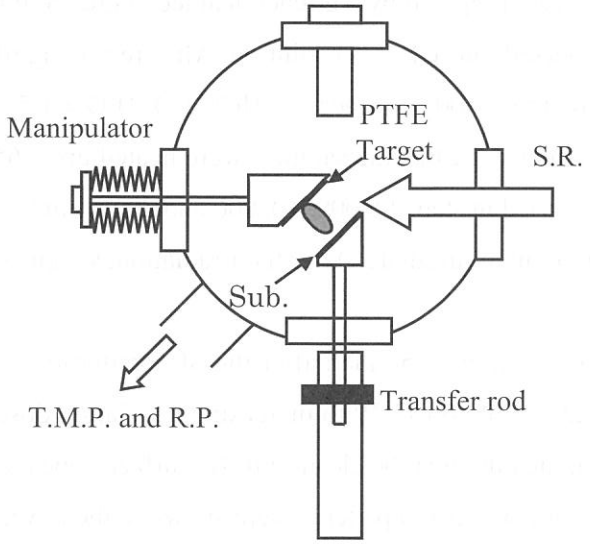

Fig.1 Experimental setup

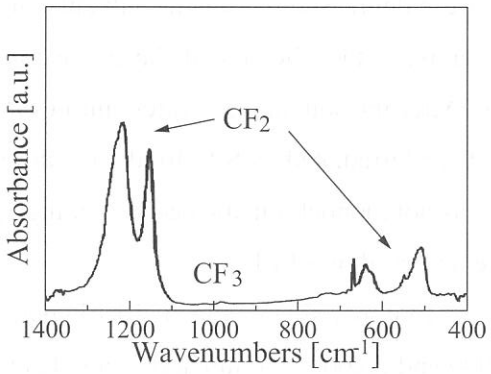

Fig.2 FTIR spectrum of PTFE thin film

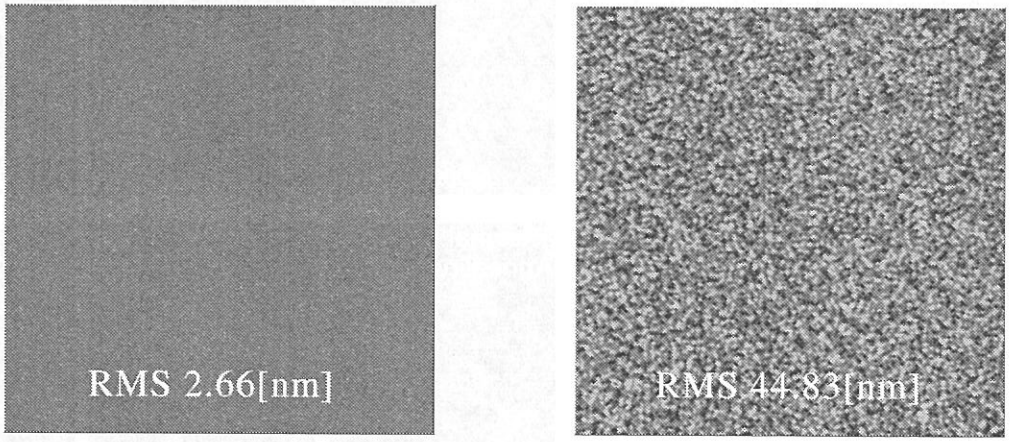

(a) Target Temperature R.T. (b) Target Temperature 210℃

Fig.3 AFM images of PTFE thin film(10×10 μm)

(BL6B)

Silicon Oxide on Si (001) Surfaces Removed by SR Stimulated Desorption

Youichi NONOGAKI and Tsuneo URISU

Institute for Molecular Science, Myodaiji, Okazaki 444-8585, Japan

By SR irradiation to the solid surfaces, various kinds of surface photochemical reactions occur due to strong interaction between VUV light and materials. So far, we have investigated SR stimulate silicon oxide desorption reaction on Si (111) surfaces by scanning tunneling microscope (STM) and low energy electron diffraction (LEED). From the STM observations, we have observed significant difference on the surface structures between usual thermal desorption and SR stimulated desorption on Si (111) surface. In this report, silicon oxide SR stimulated desorption on Si (001) by LEED observation.

Si (001) wafers covered by silicon oxide were prepared by wet-chemical technique. Si (001) wafers were degreased by organic solvents and immersed into HF (5%) solution. After removing of native silicon oxide, the silicon oxide layer was formed on the Si (001) surfaces by $HCl:H_2O_2:H_2O$ = 1:5:10 solution. After introducing the wafers into UHV chamber at BL6B, the samples were heated up to 650°C or 700°C and irradiated by SR. Irradiation dose was varied in step at 5,000, 10, 000 and 20,000 mA min. The SR was not monochromatic because of high photon flux to irradiate. After the irradiation, sample surfaces were observed by LEED.

In upper side of Fig. 1, LEED patterns were shown obtained after the SR irradiation of 5,000, 10,000 and 20,000 mA min at the sample temperatures of 700°C. With increasing irradiation dose, 2 x 1 pattern appears and the each spot becomes clear, indicating that the clean Si (001) surface appears and the area of clean surface increases gradually. For comparison, LEED patterns were shown in the lower side of Fig. 1 obtained after thermal annealing at the same temperature of 700°C without SR irradiation. The annealing times were set at 22, 49, 90 min, which corresponds to the duration time for 5,000, 10,000 and 20,000mA min irradiation of upper side samples. All the LEED images have no spots, indicating that surface oxide remains even for 90 min annealing.

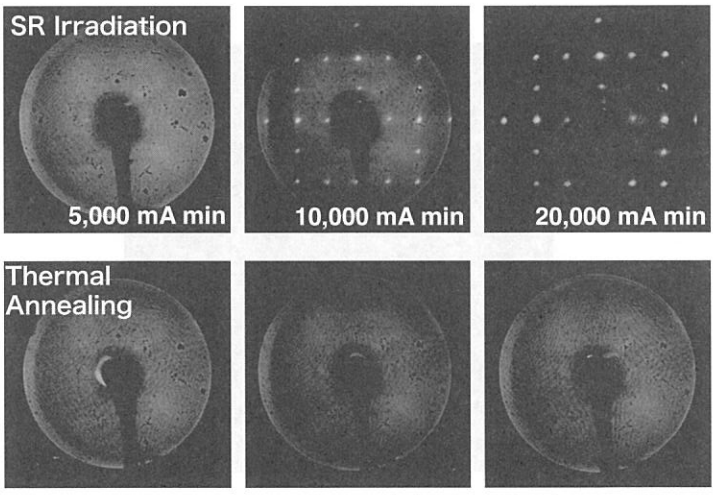

Figure 1: LEED patterns after SR irradiation at 700°C in upper side. In the lower side, LEED patterns after thermal annealing without SR irradiation

This result means that silicon oxide on Si (001) is removed by SR stimulation effect. This phenomenon can be applied to make silicon oxide patterns on Si (001) surfaces by the area selective desorption using SR irradiation.

Publications

LIST OF PUBLICATIONS (2001)

H. Aritani, O. Fukuda, A. Miyaji, and S. Hasegawa
Stryctural Change of Molybdenum on Silica-alumina in Contact with prorene Studied by ESR and Mo L_{III}-edge XANES
Appl. Surf. Sci., **180**, 261 (2001).

H. Aritani, S. Nishimura, M. Tamai, T. Yamamoto, T. Tanaka, and A. Nakahira
Local Structure of Framework Iron in Fe-Substituted Al-Mordenites by Fe Edge XAFS
Chem. Mater., **14**, 562 (2002).

H. Aritani, H. Yamada, T. Yamamoto, T. Tanaka, and S. Imamura
XANES Study of Li-MgO and Li-La_2O_3-MgO Catalysts for Oxidative Coupling of Methane
J. Synchrotron Rad., **8**, 593 (2001).

S. Asaka, M. Itoh, and M. Kamada
Ultraviolet Light Amplification within a Nanometer-sized Layer
Phys. Rev. B **63**, 081104(R) (2001).

J. Azuma, S. Asaka, T. Tsujibayashi, M. Itoh, M. Watanabe, O. Arimoto, S. Nakanishi, H. Itoh, and M. Kamada
Optical Detection System Using Time Structure of UVSOR for Combined Laser-SR Experiments
Nucl. Instr. Meth. Phys. Res. A **467-468**, 1455 (2001).

J. Azuma and K. Tanaka
Retrieved Anisotropy of One-dimensional Crystal Piperidinium Triblomoplumbate
International Journal of Modern Physics B **15**, 3646 (2001).

Y. Azuma, S. Akatsuka, K. K. Okudaira, Y. Harada, and N. Ueno
Angle-resolved Ultraviolet Photoelectron Spectroscopy of In-[perylene-3,4,9,10-tetracarboxylic dianhydride] System
J. Appl. Phys. **87**, 766 (2000).

M. Fujita, M. Itoh, M. Horimoto, Y. Usuki, M. Kobayashi, and M. Nikl
Optical Anisotropy of Exciton Band and Doping Effect in Scheelite $PbWO_4$ Crystals
J. Phys. Soc. Jpn. **70**, 1439 (2001).

T. Gejo, J. A. Harrison, and J. R. Huber
Depletion Spectrum of Ozone in a Molecular Beam. Evidence for Interference Effects in the Hartley Band Photodissociation
Chem. Phys. Lett. **350**, 558 (2001).

K. Hamaguchi, S. Machida, M. Nagao, F. Yasui, K. Mukai, Y. Yamashita, J. Yoshinobu, H. S. Kato, H. Okuyama, M. Kawai, T. Sato, and M. Iwatsuki

Bonding and Structure of 1,4-Cyclohexadiene Chemisorbed on Si(100)(2×1)
Phys. Chem. B **105**, 3718 (2001) .

S. Hasegawa, K. Yakushi, H. Inokuchi, K.Kamiya-Okudaira, N. Ueno, K. Seki, E. Morikawa and V. Saile
Calculated Photoelectron Angular Distributions of ω-(n-pyrrolyl)alkanethiol Self-assembled Monolayers for Distinguishing Between Different Arrangements of the Pyrrole Groups
J. Electr. Spectrosc. Relat. Phenom., **120**, 121 (2001) .

Y. Hikosaka, and K. Mitsuke
Formation and Autoionization of a Dipole-Forbidden Superexcited State of CS_2
J. Phys. Chem., **105**, 8130 (2001) .

S. Hino, K. Umishita, K. Iwasaki, M. Aoki, K. Kobayashi, S. Nagase, T.J.S. Dennis, T. Nakane, and H. Shinohara
Ultraviolet Photoelectron Spectra of Metallofullerenes, two $Ca@C_{82}$ Isomers
Chem. Phys. Lett., **337**, 65 (2001) .

S. Hino, K. Umishita, K. Iwasaki, T. Miyamae, M. Inakuma, and H. Shinohara
Ultraviolet Photoelectron Spectra of Sc@C82
Chem. Phys. Lett., **300**, 145 (1999) .

M. Hosaka, S. Koda, M. Katoh, J. Yamazaki, H. Hama,
FEL Induced Electron Bunch Heating Observed by a Method Based on Synchronous Phase Detection
Nucl. Instr. and Meth. A **474**, 217 (2001) .

T. Ibuki, K. Okada, K. Saito, T. Gejo, N. Saito, and I. H. Suzuki
Angle, Energy, and Mass-Resolved Ion Spectroscopy of Core-Excited Polyatomic Molecules
Nucl. Instr. and Meth. A **467**, 1505 (2001) .

H. Ishii, H. Oji, E. Ito, N. Hayashi, D. Yoshimura, and K. Seki
Energy Level Alignment and Band Bending at Model Interfaces of Organic Electroluminescent Devices
J. Luminescence, **87-89**, 61 (2000) .

M. Itoh, K. Hayakawa, and S. Oishi
Optical Properties and Electronic Structures of Layered MoO_3 Single Crystals
J. Phys.: Condens. Matter **13**, 6853 (2001) .

M. Itoh, amd S. Oishi
Optical Properties of $Na_2W_4O_{13}$ Crystals
Materials Research Bulletin **36**, 1495 (2001) .

M. Itoh, and M. Kamada
Comparative Study of Auger-Free Luminescence and Valence-Band Photoemission in Wide-Gap Materials
J. Phys. Soc. Jpn. **70**, 3446 (2001) .

K. Iwasaki, K. Umishita, S. Hino, K. Kikuchi, and Y.Achiba
Ultraviolet Photoelectron Spectra of Potassium Dosed Higher Fullerenes
Mol. Cryst. and Liq. Cryst. **340**, 623 (2000).

K. Iwasaki, K. Umishita, S. Hino, K. Kikuchi, Y.Achiba and H. Shinohara
Ultraviolet Photoelectron Spectra of Mono Metal Atom Encapsulated Fullerenes
Mol. Cryst. and Liq. Cryst. **340**, 643 (2000) .

K. Iwasaki, K. Umishita, S. Hino, T. Miyamae, K. Kikuchi, and Y.Achiba
Ultraviolet Photoelectron Spectra of C_{100} , C_{110},and Potassium-doped C_{110}
Phys. Rev. B **60**, 5044 (1999) .

M. Kamada, S. Tanaka, K. Takahashi, Y. Doi, K. Fukui, T. Kinoshita, Y. Haruyama, S. Asaka, Y. Fujita, and M. Itoh
Beam-line Systems for Pump-probe Photoelectron Spectroscopy Using SR and Laser
Nucl. Instr. and Meth. A **467-468**, 1441 (2001) .

A. Kameyama, A. Yokotani, and K. Kurosawa
Identification of Defects Associated with Second-order Optical Nonlinearity in Thermally Poled High-purity Silica Glasses
J. Appl. Phys. **89**, 4707 (2001) .

H. Kato, A. Masuzawa, T. Noma. K. S. Seol, and Y. Ohki
Thermally Induced Photoluminescence Quenching Centre in Hydrogenated Amorphous Silicon Oxynitride
J. Phys.: Condens. Matter **13**, 6541 (2001) .

H. Kato, A. Masuzawa, H. Sato, T. Noma, K. S. Seol, M. Fujimaki, and Y. Ohki
Visible Electroluminescence in Hydrogenated Amorphous Silicon Oxynitride
J. Appl. Phys. **90**, 2216 (2001) .

M. Katoh, K. Hayashi, T. Honda, Y. Hori, M. Hosaka, T. Kinoshita, S. Koda, Y. Takashima, J. Yamazaki,
New Lattice for UVSOR
Nucl. Instr. and Meth. A **467-468**, 68 (2001) .

T. Kawai, N. Ichimura, and S. Hashimoto
Origin of the Absorption Bands of Cesium Halides Doped with Tl^+ Ions
Phys. Stat. Sol.. **227** 587 (2001) .

S.-S. Kim, Y. Kadoma, H. Ikuta, Y. Uchimoto and M. Wakihara
Electrochemical Performance of Natural Graphite by Surface Modification Using Alumina
Electrochem. Solid-state Lett. **4**, A109-A112 (2001) .

S.-S. Kim, H. Ikuta and M. Wakihara
Synthesis and Characterization of MnV_2O_6 as a High Capacity Anode Material for a Lithium Secondary Battery
Solid State Ionics, **139**, 57 (2001) .

S.-S. Kim, S. Ogura, H. Ikuta, Y. Uchimoto and M. Wakihara
Synthesis of $MnMoO_4$ as High Capacity Anode Material for Li Secondary Battery
Chem. Lett. 760 (2001) .

S.-S. Kim, Y. Kadoma, H. Ikuta, Y. Uchimoto and M. Wakihara
Improvement of Electrochemical Properties of Surface Treated Natural Graphite by Aluminum
Electrochemistry **69**, 830 (2001) .

S. Kimura, M. Okuno, H. Iwata, H. Aoki and A. Ochiai
Temperature Dependence of Low-Energy Optical Conductivity of Yb4(As1-xPx)3 (x = 0, 0.05, 0.15)
J. Phys. Soc. Jpn., **70**, 2829-2832 (2001).

T. Kinoshita, H. P. N. J. Gunasekara, Y. Takata, S. Kimura, M. Okuno, Y. Haruyama, N. Kosugi, K. G. Nath, H. Wada, A. Mitsuda, M. Shiga, T. Okuda, A. Harasawa, H. Ogasawara, and A. Kotani
Spectroscopy Studies of Temperature-Induced Valence Transition on $EuNi_2(Si_{1-x}Ge_x)_2$ around Eu 3d-4f, 4d-4f and Ni 2p-3d Excitation Regions
J. Phys. Soc. Jpn. **71**, 148 (2002) .

M. Kitaura and H. Nakagawa
Origin of the Luminescence Bands in $PbCl_2$ Crystals Induced by UV Light at Low Temperatures
J. Phys. Soc. Jpn. **70**, 2462 (2001) .

S. Koda, M. Hosaka, J. Yamazaki, M. Katoh, H. Hama
Development of Longitudinal Feedback System for a Storage Ring Free Electron Laser
Nucl. Instr. and Meth. A **474**, 211 (2001) .

S. Matsuo, T. Nakano, S. Yamada, T. Matsuo, and H. Wakita
X-ray Absorption Spectral Studies on Stoichiometric Analysis of Amphiphilic Ruthenium (II) Polypyridine Complex on a Poly(methyl methacrylate) Film
J. Electron Spectrosc. Relat. Phenom. **113**, 193 (2001) .

T. Masuoka
Kinetic-energy Release and Intercharge Distance of the Sulfur Dioxide Dication (SO_2^{2+})
Int. J. Mass Spectrom. **209**, 125 (2001) .

T. Masuoka

Single- and Double-Photoionization Cross Sections of Sulfur Dioxide (SO_2) and Ionic Fragmentation of SO_2^+ and So_2^{2+}

J. Chem. Phys. **115**, 264 (2001) .

K. Mitsuke, and M. Mizutani

Laser Induced Fluorescence Spectroscopy of CN(X2 Σ+) Radicals Produced by Vacuum UV Photoexcitation of CH3CN with Synchrotron Radiation

J. Electron Spectrosc. Relat. Phenom. **119**, 155 (2001) .

K. Mitsuke, and M. Mizutani

UV and Visible Emission Spectra from Photodissociation of Carbonyl Sulfide Using Synchrotron Radiation at 15 - 30 eV

Bull. Chem. Soc. Jpn. **74**, 1193 (2001) .

T. Miyamae, S. Hasegawa, D. Yoshimura, H. Ishii, N. Ueno, and K. Seki

Intramolecular Energy-band Dispersion in Oriented Thin Films of n-$CF_3(CF_2)_{22}CF_3$ Observed by Angle-resolved Photoemission with Synchrotron Radiation

J. Chem. Phys. **112**, 3333 (2000) .

T. Miyazaki, M. Aoki, and O. Takayasu,

Photoemission Spectra of $LiNiO_2$ Catalyst for Oxidative Coupling of Methane

Jpn. J. Appl. Phys. **38**, 51 (1999) .

T. Miyamae, N. Ueno, S. Hasegawa, Y. Saito, T. Yamamoto, and K. Seki

Electronic Structure of Poly(1,10-phenanthroline-3,8-diyl) and Its K-doped States Studied by Photoelectron Spectroscopy

J. Chem. Phys. **110**, 2552 (1999) .

E. Morikawa, V. Saile, K. K. Okudaira, Y. Azuma, K. Meguro, Y. Harada, K. Seki, S. Hasegawa, and N. Ueno

Pendant Group Orientation of Poly(2-vinylnaphtalene) Thin Film Surface Studied by NEXAFS and ARUPS

J. Chem. Phys. **112**, 10476 (2000) .

A. Motogaito, M. Yamaguchi, K. Hiramatsu, M. Kotoh, Y. Ohuchi, K. Tadatomo, Y. Hamamura, and K. Fukui

Characterization of GaN-Based Schottky Barrier Ultraviolet (UV) Detectors in the UV and Vacuum Ultraviolet (VUV) Region Using Synchrotron Radiation

Jpn. J. Appl. Phys. **40**, L368 (2001) .

A. Motogaito, K. Ohta, K. Hiramatsu, Y. Ohuchi, K. Tadatomo, Y. Hamamura and K. Fukui

Characterization of GaN Based UV-VUV Detectors in the Range 3.4-25 eV by Using Synchrotron Radiation

Phys. Stat. Sol. (a) **188**, 337 (2001) .

H. Nagai, M. Inayoshi, M. Hori, T. Goto, M. Hiramatsu
On the Mechanisum of Polytetrafluoroethylene Ablation Using a Synchrotron Radiation-induced Photochemical Process
Appl. Surf. Sci., **183**, 284 (2001).

S. Nagaoka, S. Tanaka, and K. Mase
Site-Specific Fragmentation Following C:1s Core-Level Photoionization of 1,1,1-Trifluoroethane Condensed on a Au Surface and of a 2,2,2-Trifluoroethanol Monolayer Chemisorbed on a Si(100) Surface
J. Phys. Chem. B **105**, 1554 (2001).

K. G. Nath, Y. Haruyama, and T. Kinoshita
Surface Superstructure Formation, Electronic Structure Modification and Magnetic Stability of Co Films on Oxygen-rich Cu(001): Confirmation of Oxygen-Surfactant Effect
Surf. Sci. **486**, 185 (2001) .

K. G. Nath, Y. Haruyama, and T. Kinoshita
Observation of the Satellite Signal in Co 2p Photoemission Spectra: Evidence of a Localized Electronic Structure in Thin Films
Phys. Rev. B **64**, 245417 (2001) .

T. Noma, K. S. Seol, H. Kato, M. Fujimaki, and Y. Ohki
Origin of Photoluminescence around 2.6-2.9 eV in Silicon Oxynitride
Appl. Phys. Lett. **79**, 1995 (2001) .

H. Okamura, T. Koretsune, M. Matsunami, S. Kimura, T. Nanba, H. Imai, Y. Shimakawa and Y. Kubo
Charge dynamics in the colossal magneto-resistance pyrochlore Tl2Mn2O7
Phys. Rev. B **64**, 180409(R) (2001).

A. Ohnishi, K. Tanaka, M. Kitaura, T. Otomo, and T. Yoshinari
Optical Spectra of Inorganic-Organic Compounds $(C_2H_5NH_3)_2CdCl_4$ in 3-30 eV Range
J. Phys. Soc. Jpn **70,** 3424 (2001) .

N. Ohno, Y. Yamasaki, H. Yoshida, and M. Fujita
Optical Spectra of Orthorhombic $SnBr_2$ Crystals
Phys. Stat. Sol. (b) **223**, 723 (2001) .

H. Ohta, A. Ueda, S. Ono, Y. Ikeuchi, T. Nanba, A. Hirano, and R. Kanno
Millimeter Wave Reflection Measurement of Secondary Battery Substance $LiNiO_2$
Jpn. J. Appl. Phys. **39**, 409 (2000).

M. Ono, H. Yoshida, H. Hattori, and K. Mitsuke
Performance of the 18 m-Spherical Grating Monochromator Newly Developed in the UVSOR Facility
Nucl. Instrum. Meth. Phys. Res. A, **467-468**, 577 (2001) .

K. Okada, S. Tanimoto, T. Ibuki, K. Saito and T. Gejo
Assignment of the C K-Shell Photoabsorption Spectrum of CF_3CN Molecule
Chem. Lett.1046 (2001) .

K. K. Okudaira, E. Morikawa, S. Hasegawa, H. Ishii, Y. Azuma, M. Imamura, H. Shimada, K. Seki and N. Ueno
Surface Electronic Structure and Molecular Orientation of Poly(9-vinylcarbazole) Thin Film: ARUPS and NEXAFS
Nucl. Instr. and Meth. A, **467-468**, 1233 (2001) .

K. Seki, R. Mitsumoto, E. Ito, T. Araki, Y. Sakurai, D. Yoshimura, H. Ishii, Y. Ouchi, T. Miyamae, T. Narita, S. Nishimura, Y. Takata, T. Yokayama, T. Ohta, S. Suganuma, F. Okino, and H. Touhara
High-Energy Spectroscopic Studies of the Electronic Structures of Organic Systems Formed from Carbon and Fluorine by UPS, Vacuum-UV Optical Spectroscopy, and NEXAFS: Poly(hexafluoro-1,3-butadiene) $[C(CF_3)=C(CF_3)]_n$, Fluorinated Graphites (CF, C_2F, and C_6F), Perfluoroalkanes n-C_nF_{2n+2}, Poly (tetrafluoroethlene)$(CF_2)_n$, and Fluorinated Fullerenes ($C_{60}F_x$ and $C_{70}F_x$)
Mol. Cryst. Liq. Cryst. **355**, 247 (2001) .

K. Seki, E. Ito, H. Oji, D. Yoshimura, N. Hayashi, Y. Sakurai, Y. Hosoi, T. Yokoyama, T. Imai, Y. Ouchi, and H. Ishii
Organic/Metal Systems Studied by Electron Specroscopies and Other Techniques
Synth. Metals **119**, 19 (2001).

S. Tanaka, S.D. More, J. Murakami, M. Itoh, Y. Fujii, and M. Kamada
Surface Photovoltage Effects on p-GaAs(100) from Core-level Photoelectron Spectroscopy Using Synchrotron Radiation and a Laser
Phys. Rev. B **64**, 155308 (2001) .

T. Tokushima, T. Yanagihara, Y. Senba, H. Yoshida, and A. Hiraya
High Mass-resolution Electron-ion-ion Coincidence Measurements on Core-excited Organic Molecules
Nucl. Instr. and Meth. A, **467-468**, 1523 (2001) .

Y. Uchimoto, H. Sawada, and T. Yao
Changes in Electronic Structure by Li Ion Deintercalation in $LiNiO_2$ From Nickel L-edge and O K-edge XANES
J. Power Sources, **97-98**, 326 (2001) .

Y. Uchimoto, H. Sawada, and T. Yao
Changes in Electronic Structure by Li Ion Deintercalation in $LiCoO_2$ From Cobalt L-edge and Oxygen K-edge XANES
J. Synchrotron Rad., **8**, 872 (2001) .

N. Ueno
Angle-Resolved UPS Studies of Organic Thin Films
Jpn. J. Appl. Phys. **38**, 226 (1999).

H. Yasufuku, K. Meguro, S. Akatsuka, S. Setoyama, S. Kera, Y. Azuma, K.K. Okudaira, S. Hasegawa, Y. Harada, and N. Ueno
Surface States of Hydrogen-terminated Si(111) by Metastable Atom Electron Spectroscopy and Angle-resolved Ultraviolet Photoelectron Spectroscopy
Jpn. J. Appl. Phys. **39**, 1706 (2000).

J. Yoshinobu, Y. Yamashita, F. Yasui, K. Mukai, K. Akagi, S. Tsuneyuki, K. Hamaguchi, S. Machida, M. Nagao, T. Sato, and M. Iwatsuki
Reaction Mechanism and Absorbed States of Cyclohexene on Si(100)(2×1)
J. Electron Spectrosc. Relat. Phenom. **114-116**, 383 (2001).

(in Japanese)
T. Ito, T. Toyoda, N. Hirai, Y. Ohki
Photoliminescence in Polyropylene Induced by Ultraviolet Photons
Trans. IEE of Japan 121-A, 865 (2001).

M. Katoh
Upgrade Plan fpr UVSOR
J. Jpn. Soc. Synchro. Rad. Res. **14**, 27 (2001).

A. Motogaito, K. Ohta, K. Hiramatsu, Y. Ohuchi, K. Tadatomo, Y. Hamamura
and K. Fukui
Characterization of GaN Based Schottky UV Photodiode in Vacuum Ultraviolet Region
Technical Report of IEICE 101, 55 (2001) (ED2001-135, CPM2001-88)

Workshops

UVSOR Workshop VIII

Beamline Upgrade Project at UVSOR (I)

26 and 27 November 2001

26 Nov. (Mon) 13:00 – 18:00 (coffee break included)

<First half> Chair and discussion leader: E. Shigemasa (IMS)

UVSOR upgrade project

13:00 – 13:20	Introduction of UVSOR upgrade project	N. Kosugi (IMS)
13:20 – 13:45	Upgrade of the UVSOR storage ring	M. Kato (IMS)
13:45 – 14:10	Current status of the novel beamline BL4B at UVSOR	T. Gejo (IMS)
14:10 – 14:35	New undulator beamline BL7A at UVSOR	Y. Nonogaki (IMS)
14:35 – 15:00	Upgrade project of BL3 at UVSOR	T. Hatsui (IMS)
15:00 – 15:15	Coffee break	

<Second half> Chair and discussion leader: N. Kosugi (UVSOR, IMS)

Current circumstance and future prospect of surface science at BL2B1

15:15 – 15:45	Site specific photoion desorption induced by inner-shell excitations	T. Sekitani (Hiroshima Univ.)
15:45 – 16:15	Photoion desorption from transition metal oxide surfaces	S. Tanaka (Nagoya Univ.)
16:15 – 16:45	Present status of studies on site specific ion desorption at BL2B1 and their future prospect	S. Nagaoka (Ehime Univ.)
16:45 – 17:15	Studies on surfaces using coincidence spectroscopy at PF; Current status and future plans	K. Masa (KEK)
17:15 – 18:00	Comprehensive Discussion I	

27 Nov. (Tue) 9:00 – 14:30 (lunch and coffee break included)

<First half> Chair and discussion leader: E. Shigemasa (UVSOR, IMS)

Present situation and future perspectives of surface science at PF

9:00 – 9:50	Frontiers of surface molecular sciences; Geometrical and electronic structures of adsorbates and their magnetisms on metal surfaces	T. Yokoyama (Univ. of Tokyo)
9:50 – 10:30	Nano-scale science utilizing synchrotron radiation; A few examples from recent work at PF	K. Ono (Univ. of Tokyo)

Now and future for investigations in a gas phase at BL8B1

10:30 – 11:00	Dynamics following inner-shell excitations of large molecules	K. Okada (Hiroshima Univ.)
11:00 – 11:30	Photodissociation processes of inner-shell excited organic molecules studied by an Auger-electron–photoion coincidence technique	H. Yoshida (Hiroshima Univ.)
11:30 – 12:00	Future perspectives of gas phase experiments at HiSOR	A. Hiraya (Hiroshima Univ.)
12:00 – 13:00	Lunch	

<Second half> Chair and discussion leader: N. Kosugi (UVSOR, IMS)

13:00 – 14:30	Comprehensive Discussion II	

UVSOR Workshop IX

Beam line Upgrade II

~ Low-Energy Photoemission of Solids and Nano-Science at UVSOR ~

March 5 and 6, 2002

March 5, 2002

Upgrading UVSOR Chair: S. Kimura (Kobe Univ.)

1300-1320 Upgrading UVSOR — N. Kosugi (UVSOR)

1320-1340 Plan of upgrading UVSOR light source — M. Kato (UVSOR)

Present status of VUV monochromator Chair: S. Kimura (Kobe Univ.)

1340-1410 Present status of HiSOR BL-9 (Off-Plane Eagle) — M. Arita (Hiroshima Univ.)

1410-1440 Present status of UVSOR BL7B — K. Fukui (Fukui Univ.)

1440-1510 Present status and future plan of UVSOR BL5A — K. Takahashi (UVSOR)

1510-1530 Coffee break

High-resolution angle-resolved photoemission Chair: K. Soda (Nagoya Univ.)

1530-1600 Electronic structure of superconductors studied by high-resolution angle-resolved photoemission at low temperatures — T. Kiss (Tokyo Univ.)

1600-1630 Angle-resolved photoemission of transition metal oxides with one- and two-dimensional structure (Utilization of SSRL) — K. Mizokawa (Tokyo Univ.)

1630-1700 Electronic structure of Bi2Sr2CuO6+d studied by high-resolution angle-resolved photoemission (Utilization of SRC and ISSP) — T. Takeuchi (Nagoya Univ.)

1700-1730 High-resolution low-temperature photoemission of d- and f- electron systems at HiSOR — K. Shimada (Hiroshima Univ.)

1730-1800 Discussion

1800-1830 UVSOR tour

1900-2100 Banquet (Club house restaurant)

March 6, 2002

Photoelectron-emission microscopy Chair: S. Kimura (Kobe Univ.)

0900-0930 MCD-microscopy of core electron using high brilliance circularly-polarized soft x-ray — S. Imada (Osaka Univ.)

0930-1000 Structural study of metal-SiC, -Si, contact using soft X-rays: PEEM, SXES
J. Labis (Okayama Univ.)

1000-1030 Present status of PEEM experiment T. Kinoshita (Tokyo Univ.)

Multi-layered mirror Chair: S. Kimura (Kobe Univ.)

1030-1100 Development of wide band multi-layered mirror region and Schwarzschild optics for XUV region T. Ejima (Tohoku Univ.)

Nano-science using photoemission Chair: K. Takahashi (UVSOR)

1100-1130 Photoemission of low-dimensional nano-metals A. Tanaka (Tohoku Univ.)

1130-1200 ARUPS of organic materials at BL8B2 I: One-dimensional electronic structure of long chain molecules for nano-wire H. Ishii (Tohoku Univ.)

1200-1230 ARUPS of organic materials at BL8B2 I: Present status of new ARUPS spectrometer and study on organic thin films K. Okudaira (IMS)

1230-1300 Plan of SR in Saga Prefecture and study on nano-technology and materials
M. Kamada (Saga Univ.)

Appendix

ORGANIZATION

Director

Nobuhiro Kosugi	Professor	kosugi@ims.ac.jp

Accelerator Division

Masahiro Katoh	Associate Professor	mkatoh@ims.ac.jp
Masahito Hosaka	Research Associate	hosaka@ims.ac.jp
Shigeru Kouda	Research Associate	kouda@ims.ac.jp (-Aug.2001)
Akira Mochihashi	Research Associate	mochi@ims.ac.jp (Aug. 2001 -)
Toshio Kinoshita	Unit Chief Engineer	kinoshita@ims.ac.jp (- Mar. 2002)
Jun-ichiro Yamazaki	Unit Chief Engineer	yamazaki @ ims.ac jp
Kenji Hayashi	Engineer	h-kenji@ims.ac.jp

Beamline Division

Masao Kamada	Associate Professor	kamada@ims.ac.jp
Eiji Shigemasa	Associate Professor	sigemasa@ims.ac.jp
Tatsuo Gejo	Research Associate	gejo@ims.ac.jp
Kazutoshi Takahashi	Research Associate	ktakahashi@ims.ac.jp
Osamu Matsudo	Section Chief Engineer	mastudo@ims.ac.jp
Masami Hasumoto	Unit Chief Engineer	hasumoto@ims.ac.jp
Eiken Nakamura	Unit Chief Engineer	eiken@ims.ac.jp
Naonori Kondo	Engineer	kondo@ims.ac.jp
Suekichi Matsuo	Supporting Engineer	mastuo@ims.ac.jp
Bunichi Kamimoto	Supporting Engineer	kamimoto@ims.ac.jp

Guest Scientist

Yoichiro Hori	Associate Professor	yoichiro.hori@kek.jp(Apr.2001 -)
Junpei Azuma	JSPS Research Fellow	azuma@ims.ac.jp (Apr. 2001-)

Secretary

Hisayo Hagiwara	hagiwara@ims.ac.jp
Naoko Onitake	onitake@ims.ac.jp

Graduate Student

Senku Tanaka	senku@ims.ac.jp
Kousuke Hayakawa	hayakawa@ims.ac.jp(Apr. 2001- Mar. 2002)

STEERING COMMITTEE

(April 2000 - March 2001)

Nobuhiro Kosugi	UVSOR IMS	Chairperson
Masao Kamada	UVSOR IMS	
Masahiro Katoh	UVSOR IMS	
Eiji Shigemasa	UVSOR IMS	
Yoichiro Hori	KEK	
Tatsuhisa Katoh	IMS	
Tatsuya Tsukuda	IMS	
Hayao Kobayashi	IMS	
Tsuneo Urisu	IMS	
Toyohiko Kinoshita	Univ. of Tokyo	
Akira Yagishita	KEK	
Nobuo Ueno	Chiba Univ.	
Yasuo Udagawa	Tohoku Univ.	
Keiichiro Nasu	KEK	
Takao Nanba	Kobe Univ.	
Ken-ichiro Tanaka	Hiroshima Univ.	

JOINT STUDIES

(Financial Year 2001)

Cooperative Research Projects	: 25
Use-of-UVSOR Projects	: 157
Workshop	: 2
Machine Time for Users	: 35 weeks

Mr. Kinoshita's farewell party

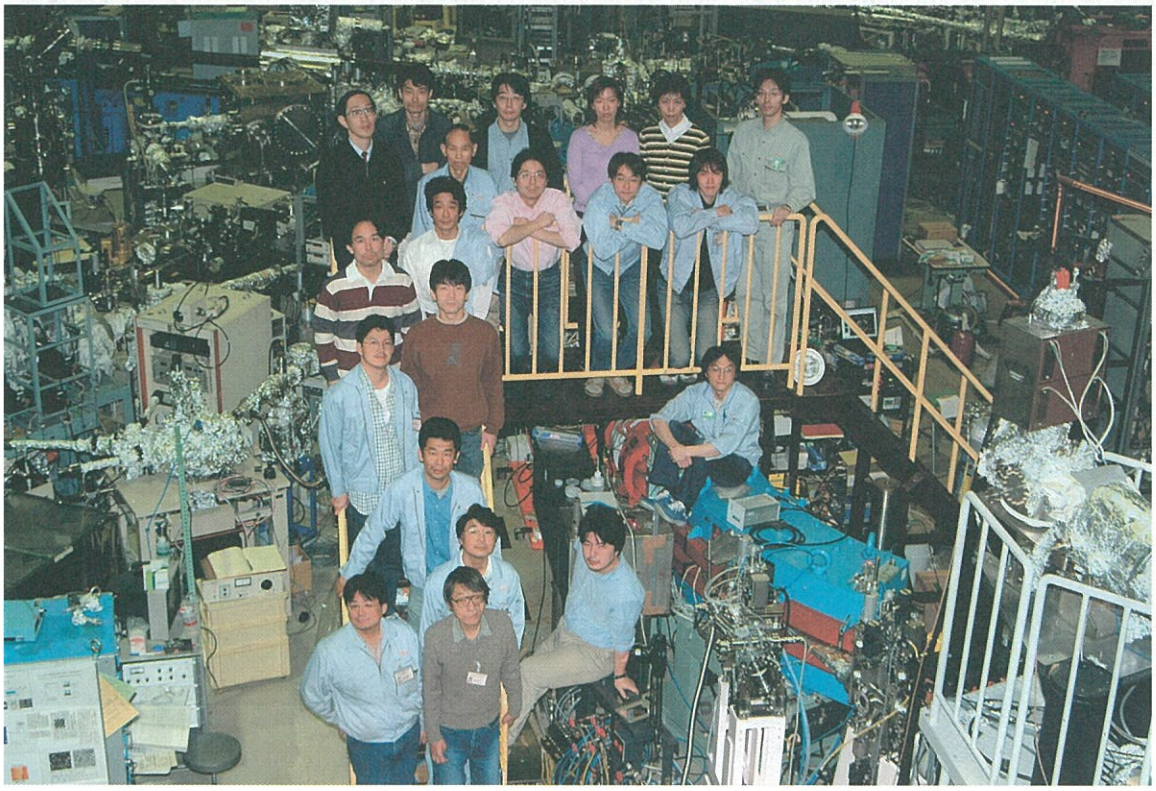

UVSOR staffs